Springer Series in Materials Science 308

Davide Peddis
Sara Laureti
Dino Fiorani *Editors*

New Trends in Nanoparticle Magnetism

Springer

Springer Series in Materials Science

Volume 308

The Springer Series in Materials Science covers the complete spectrum of materials research and technology, including fundamental principles, physical properties, materials theory and design. Recognizing the increasing importance of materials science in future device technologies, the book titles in this series reflect the state-of-the-art in understanding and controlling the structure and properties of all important classes of materials.

More information about this series at http://www.springer.com/series/856

Davide Peddis · Sara Laureti · Dino Fiorani
Editors

New Trends in Nanoparticle Magnetism

Springer

Editors
Davide Peddis
Department of Chemistry and Industrial Chemistry (DCIC)
Nanostructured Magnetic Materials (nM2) Lab, University of Genoa
Genoa, Italy

Institute of Structure of Matter (ISM)
Nanostructured Magnetic Materials (nM2) Lab, Italy National Research Council (CNR)
Rome, Italy

Dino Fiorani
Institute of Structure of Matter (ISM)
Nanostructured Magnetic Materials (nM2) Lab, Italy National Research Council (CNR)
Rome, Italy

Sara Laureti
Institute of Structure of Matter (ISM)
Nanostructured Magnetic Materials (nM2) Lab, Italy National Research Council (CNR)
Rome, Italy

ISSN 0933-033X ISSN 2196-2812 (electronic)
Springer Series in Materials Science
ISBN 978-3-030-60472-1 ISBN 978-3-030-60473-8 (eBook)
https://doi.org/10.1007/978-3-030-60473-8

This Springer imprint is published by the registered company Springer Nature Switzerland AG
The registered company address is: Gewerbestrasse 11, 6330 Cham, Switzerland

Preface

Magnetic nanoparticles continue to be the object of growing interest, from both fundamental and technological point of view, since the pioneering works of Louis Néel about 70 years ago. The reason is because nanoparticles are unique physical objects with remarkable magnetic properties which differ greatly from their massive materials. Such properties can be finely tuned trough control of the size, surface/interface structure, and nature and strength of interactions, allowing to design and synthesize a variety of magnetic nanostructures for a large number of applications.

In the last decades, there has been significant progress in understanding the fundamental magnetization processes in magnetic nanoparticles thanks to continuous advances in theory, materials preparation methods, structural and diagnostic techniques.

This book is aimed at providing an overview of new trends and challenging perspectives in the research on magnetic nanoparticles and their applications, highlighting emerging approaches in theoretical modeling, synthetic methodologies of new nanoparticle-based materials, fundamental issues and strategies to improve the magnetic properties, experimental techniques and frontier applications in strategic sectors. In particular, a special attention has been given to biomedicine, where magnetic nanoparticles hold great potential in medical diagnosis and therapy.

The book is arranged in topical sections providing a spectrum of the latest advances and accomplishments in nanoparticle magnetism covering (a) fundamental properties, by theoretical modeling, simulation and experimental investigations; (b) design and synthesis of new magnetic nanoarchitectures; (c) selected advanced structural and magnetic diagnostic techniques; (d) applications in selected strategic fields such as biomedicine, energy and life science.

This book will benefit to physicists, chemists and material scientists interested in the recent advances and new perspectives of research on magnetic nanoparticles and their applications. It is also recommended, for its multidisciplinary character, as additional literature for undergraduate and postgraduate students with majors in physics, chemistry, engineering and biology.

Genoa, Italy — Davide Peddis
Rome, Italy — Sara Laureti
Rome, Italy — Dino Fiorani

Contents

Contributors

Javier Alonso Department CITIMAC, Universidad de Cantabria, Santander, Spain

Livia Angeloni Department of Basic and Applied Sciences for Engineering, Sapienza University of Rome, Rome, Italy

Matteo Avolio Dipartimento di Fisica, INFN and INSTM, Università degli Studi di Pavia, Pavia, Italy

Chris Binns Instituto Regional de Investigación Científica Aplicada (IRICA), Ciudad Real, Spain

J. Blanco-Portals LENS-MIND, Electronics and Biomedical Engineering Department, Universitat de Barcelona, Barcelona, Spain;
Institut de Nanociència i Nanotecnologia (IN2UB), Universitat de Barcelona, Barcelona, Spain

Russell P. Cowburn Cavendish Laboratory, University of Cambridge, Cambridge, UK

César de Julián Fernández Institute of Materials for Electronics and Magnetism, Italian Research Council, Parma, Italy

Isabelle de Moraes Institut Néel, CNRS and Université Grenoble Alpes, Grenoble, France

José Angel de Toro Instituto Regional de Investigación Científica Aplicada (IRICA), Ciudad Real, Spain

Nora M. Dempsey Institut Néel, CNRS and Université Grenoble Alpes, Grenoble, France

S. Estradé LENS-MIND, Electronics and Biomedical Engineering Department, Universitat de Barcelona, Barcelona, Spain;
Institut de Nanociència i Nanotecnologia (IN2UB), Universitat de Barcelona, Barcelona, Spain

María Luisa Fdez-Gubieda Dpto. Electricidad y Electrónica, Universidad del País Vasco - UPV/EHU, Leioa, Spain;
Basque Center for Materials, Applications and Nanostructures, UPV/EHU Science Park, Leioa, Spain

Ana García-Prieto Basque Center for Materials, Applications and Nanostructures, UPV/EHU Science Park, Leioa, Spain;
Dpto. Física Aplicada I, Universidad del País Vasco - UPV/EHU, Bilbao, Spain

Òscar Iglesias UB and IN2UB, Barcelona, Spain;
Departament de Física de La Matèria Condensada and Institut de Nanociència i Nanotecnologia, Universitat de Barcelona, Barcelona, Spain

Claudia Innocenti Dipartimento di Chimica "U.Shiff", Università degli Studi di Firenze and INSTM, Sesto Fiorentino (FI), Italy;
ICCOM, CNR, Sesto Fiorentino (FI), Italy

Hamid Kachkachi UPVD and PROMES CNRS UPR8521, Perpignan, France

Hafsa Khurshid Department of Applied Physics and Astronomy, University of Sharjah, Sharjah, UAE

Armin Kleibert Paul Scherrer Institut, Swiss Light Source, Villigen PSI, Switzerland

Alessandro Lascialfari Dipartimento di Fisica, INFN and INSTM, Università degli Studi di Pavia, Pavia, Italy;
Dipartimento Di Fisica, INFN and INSTM, Università degli Studi di Milano, Milan, Italy

Isabelle Lisiecki Sorbonne Universités, UPMC Univ Paris 06, UMR 8233, MONARIS, Paris, France;
CNRS, UMR 8233, MONARIS, Paris, France

L. López-Conesa LENS-MIND, Electronics and Biomedical Engineering Department, Universitat de Barcelona, Barcelona, Spain;
Institut de Nanociència i Nanotecnologia (IN2UB), Universitat de Barcelona, Barcelona, Spain

Lourdes Marcano Dpto. Electricidad y Electrónica, Universidad del País Vasco - UPV/EHU, Leioa, Spain

George Margaris Institute of Nanoscience and Nanotechnology, NCSR Demokritos, Attiki, Greece

Manuel Mariani Dipartimento di Fisica, INFN and INSTM, Università degli Studi di Pavia, Pavia, Italy

C. Marquina Instituto de Nanociencia y Materiales de Aragón (INMA), Consejo Superior de Investigaciones Científicas (CSIC)-Universidad de Zaragoza, Zaragoza, Spain;
Departamento de Física de la Materia Condensada, Facultad de Ciencias, Universidad de Zaragoza, Zaragoza, Spain

Roland Mathieu Department of Materials Science and Engineering, Uppsala University, Uppsala, Sweden

Alicia Muela Basque Center for Materials, Applications and Nanostructures, UPV/EHU Science Park, Leioa, Spain;
Dpto. Inmunología, Microbiología y Parasitología, Universidad del País Vasco - UPV/EHU, Leioa, Spain

Sawako Nakamae Service de Physique de L'état Condensé, SPEC, CEA, CNRS, Université Paris-Saclay, CEA Saclay, Gif sur Yvette CEDEX, France

Zohreh Nemati Department of Electrical and Computer Engineering, University of Minnesota Twin Cities, Minneapolis, USA

Per Nordblad Department of Materials Science and Engineering, Uppsala University, Uppsala, Sweden

Peter Normile Instituto Regional de Investigación Científica Aplicada (IRICA), Ciudad Real, Spain

Iñaki Orue SGIker, Universidad del País Vasco - UPV/EHU, Leioa, Spain

Daniele Passeri Department of Basic and Applied Sciences for Engineering, Sapienza University of Rome, Rome, Italy;
Research Center for Nanotechnology Applied to Engineering of SAPIENZA University of Rome (CNIS), Rome, Italy

F. Peiró LENS-MIND, Electronics and Biomedical Engineering Department, Universitat de Barcelona, Barcelona, Spain;
Institut de Nanociència i Nanotecnologia (IN2UB), Universitat de Barcelona, Barcelona, Spain

C. Petit Sorbonne Universités, UPMC Univ Paris 06, UMR 8233, MONARIS, Paris, France;
CNRS, UMR 8233, MONARIS, Paris, France

Manh-Huong Phan Department of Physics, University of South Florida, Tampa, FL, USA

Francesco Pineider Department of Chemistry and Industrial Chemistry, University of Pisa, Pisa, Italy

J. M. Rebled LENS-MIND, Electronics and Biomedical Engineering Department, Universitat de Barcelona, Barcelona, Spain;
Institut de Nanociència i Nanotecnologia (IN2UB), Universitat de Barcelona, Barcelona, Spain

Johannes Richardi Sorbonne Université, CNRS, Laboratoire de Chimie Théorique, LCT, Paris, France;
CNRS, UMR 8233, MONARIS, Paris, France

Marco Rossi Department of Basic and Applied Sciences for Engineering, Sapienza University of Rome, Rome, Italy;
Research Center for Nanotechnology Applied to Engineering of SAPIENZA University of Rome (CNIS), Rome, Italy

Claudio Sangregorio ICCOM, CNR, Sesto Fiorentino (FI), Italy

Hariharan Srikanth Department of Physics, University of South Florida, Tampa, FL, USA

P. Torruella LENS-MIND, Electronics and Biomedical Engineering Department, Universitat de Barcelona, Barcelona, Spain;
Institut de Nanociència i Nanotecnologia (IN2UB), Universitat de Barcelona, Barcelona, Spain

Kalliopi Trohidou Institute of Nanoscience and Nanotechnology, NCSR Demokritos, Attiki, Greece

Marianna Vasilakaki Institute of Nanoscience and Nanotechnology, NCSR Demokritos, Attiki, Greece

Tarun Vemulkar Cavendish Laboratory, University of Cambridge, Cambridge, UK

Elin L. Winkler Centro Atómico Bariloche and Instituto Balseiro Comisión Nacional de Energía Atómica (CNEA), Consejo Nacional de Investigaciones Científicas Y Técnicas (CONICET), Universidad Nacional de Cuyo (UNCUYO), San Carlos de Bariloche, Río Negro, Argentina

Ll. Yedra LENS-MIND, Electronics and Biomedical Engineering Department, Universitat de Barcelona, Barcelona, Spain;
Institut de Nanociència i Nanotecnologia (IN2UB), Universitat de Barcelona, Barcelona, Spain

Roberto D. Zysler Centro Atómico Bariloche and Instituto Balseiro Comisión Nacional de Energía Atómica (CNEA), Consejo Nacional de Investigaciones Científicas Y Técnicas (CONICET), Universidad Nacional de Cuyo (UNCUYO), San Carlos de Bariloche, Río Negro, Argentina

Part I
Fundamentals and Theory

Chapter 1
Single Nanomagnet Behaviour: Surface and Finite-Size Effects

Òscar Iglesias and Hamid Kachkachi

Abstract In this chapter we discuss some intrinsic features of nano-scaled magnetic systems, such as finite-size, boundary, shape and surface effects. We mainly review in a succinct manner the main results of previous works. We first present the basics of theoretical models and computational techniques and their applications to individual nanomagnets. Results of both simulations and analytic calculations for specific materials, compositions and shapes are given based on these models.

1.1 Introduction

Nanomagnetism is the magnetism of nano-scaled objects. In general, the magnetic state of a body is characterized by its macroscopic property that is magnetization, which is the module of the statistical average of the magnetic moment vector, projected onto the applied field. The module and orientation of the latter are stable with respect to thermal fluctuations during a certain interval of time that depends on the underlying material, the size and shape of the magnetic body, as well as external environment parameters such as temperature and magnetic fields. Depending on the system's setup, the magnetic moment may adopt several possible orientations corresponding to the various minima of its energy, which are separated from each other by energy barriers that depend in turn on various intrinsic physical parameters of the system as well as on external ones. In bulk systems the energy barriers happen to be too high for the system to cross them (within the observation time) and to spontaneously switch from one state to another. On the opposite, in nano-scaled systems these barriers are drastically reduced leading to rather short switching times. Indeed, when the size of the system reduces from bulk to nanometric scales, the magnetic

Ò. Iglesias (✉)
UB and IN2UB, Barcelona, Spain
e-mail: oscariglesias@ub.edu

H. Kachkachi
UPVD and PROMES CNRS UPR8521, Perpignan, France
e-mail: hamid.kachkachi@promes.cnrs.fr

D. Peddis et al. (eds.), *New Trends in Nanoparticle Magnetism*,
Springer Series in Materials Science 308,
https://doi.org/10.1007/978-3-030-60473-8_1

properties are drastically modified owing to the fact that finite-size, boundary and surface effects then play a major role. Roughly, finite-size and boundary effects are due to the nanometric size and shape of the system, while surface effects emerge from the symmetry breaking of the crystal structure at the boundaries of the nano-object. As such, before addressing the study of nano-scaled magnetic systems, call them *nanomagnets* (NM), we ought to distinguish between these effects and try to assess their separate contributions, at least from the standpoint of theory. In reality all these effects are intertwined together and it is not possible to single out the impact of each effect on the macroscopic observable, for the simple reason that the surface is intimately connected with boundary, shape and size.

Accordingly, in this short review we will attempt to cover, with no pretension to be exhaustive, the main results of previous works on these effects. We first recall a simple comparison and clear distinction between finite-size, boundary and surface effects. Next, we will proceed through chosen examples to illustrate each one of these effects on the main physical observables which are relevant in the context of nanomagnetism [1]. We will then consider the magnetization reversal, relaxation time and blocking temperature and the (quasi-)equilibrium properties of the NMs such as the hysteresis loop, the "critical temperature", spin configuration and, of course, the magnetization itself. We will also discuss, where necessary, the main computing methods (analytical and numerical) employed.

1.1.1 Finite-Size Versus Boundary Effects

As discussed above, when dealing with confined magnetic systems, such as a NM, one should distinguish, at least from a theoretical point of view, between finite-size, boundary, and surface effects. For instance, for a cube with simple cubic (sc) lattice (see Fig. 1.1 left) with periodic boundary conditions (pbc), there is only one environment (crystal field) with coordination number $z = 6$.

In this case, the temperature behavior of the magnetization is marked by the well-known $M \sim 1/\sqrt{\mathcal{N}}$ tail in the critical region, where $\mathcal{N}$ is the total number of spins in the NM (Fig. 1.1, right). In the case of more realistic free boundary conditions (fbc), a cube with sc structure shows four different environments with $z = 3, 4, 5, 6$ (see Fig. 1.2 left). In this case, in addition to the previous finite-size effects, one is faced with boundary effects. These induce stronger fluctuations that suppress the magnetization of the system (see Fig. 1.2 right). Considering both cases of pbc and fbc allows for a separate estimation of the related effects. Now, if the boundary of a system with fbc is endowed with a surface anisotropy, which is indeed a consequence of boundary defects, we may then speak of surface effects, in addition to the finite-size and boundary effects (see below).

For both pbc and fbc, it can be shown [2] that the magnetization can be written in a simple form. At low temperature and zero field, M (when normalized) deviates from unity, its saturation value, according to

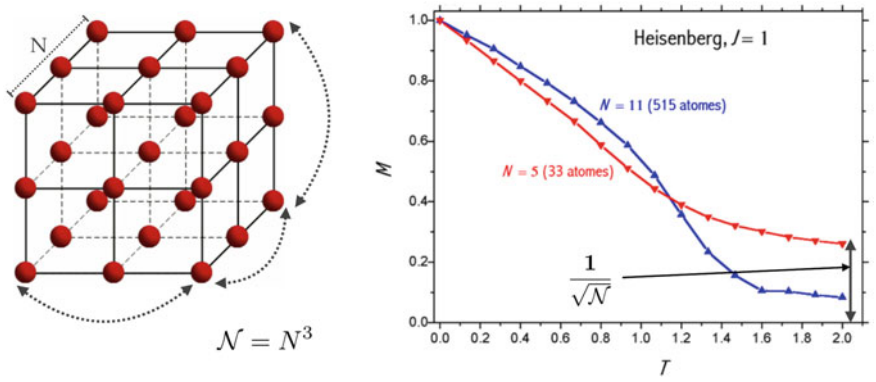

Fig. 1.1 Cubic system with pbc and thermal behavior of the magnetization for two sizes

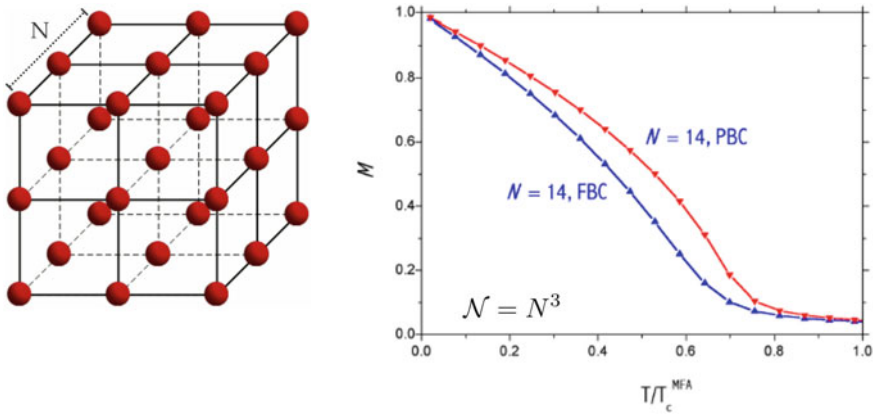

Fig. 1.2 Cubic system with fbc and thermal behavior of the magnetization for pbc and fbc systems

$$M \cong 1 - \frac{\theta}{2} W_N, \tag{1.1}$$

where

$$W_N = \frac{1}{\mathcal{N}} {\sum_{\mathbf{k}}}' \frac{1}{1 - \lambda_{\mathbf{k}}}, \theta = \frac{T}{T_c^{\mathrm{MFA}}} \tag{1.2}$$

and for a three-dimensional ($d = 3$) sc lattice $\lambda_{\mathbf{k}} = (\cos k_x + \cos k_y + \cos k_z)/d$. It is important to note that W_N in (1.2) for pbc and fbc differ only by the definition of the discrete wave vectors [2, 3], since

$$k_\alpha = \begin{cases} 2\pi n_\alpha / N, & \text{pbc} \\ \pi n_\alpha / N, & \text{fbc} \end{cases}, \qquad n_\alpha = 0, 1, \ldots, N-1 \tag{1.3}$$

where $\alpha = x, y, z$. This subtle difference is responsible for much stronger thermal fluctuations in the fbc model due to boundary effects. Indeed, the separation between two successive values of the wavenumber k for fbc is smaller than that for pbc. Therefore, more spin-wave modes are excited in the fbc system, thus leading to a weaker magnetization.

Surface Effects

Surface effects are due to the breaking of crystal-field symmetry at the boundary of the NM, and in reality they cannot be disentangled from boundary effects. In order to study surface effects one has to resort to microscopic theories capable of distinguishing between different atomic environments and taking account of physical parameters such as single-site surface anisotropy, exchange and dipolar interactions (DI), in addition of course to the magneto-crystalline anisotropy and magnetic field. Unfortunately, this leads to complex many-body problems which can only be efficiently dealt with, in general, using numerical approaches such as Monte Carlo simulations or numerical solutions of the Landau-Lifshitz equation (see Sect. 1.2.2).

Shape Effects

Apart from the finite-size, boundary and surface effects, the NM shape is also a distinctive property that has an influence not only on its magnetic properties but also on the optical, plasmonic and electric properties of nanostructured systems. The equilibrium states and hysteresis loops are clearly dependent on the NM's shape (see Sect. 1.3.2). Indeed, when the shape changes, the distribution of atomic spins changes and the core-to-surface ratio is thereby modified, leading to a change in the corresponding effective fields. There is even a drastic change in the distribution of local fields that lead to new spin configurations and thereby to new magnetic states with different macroscopic properties.

1.2 Basic Theoretical Models and Computing Tools

Building theoretical models for confined magnetic systems requires explicitly taking into account the local atomic environment with all its specificities which are strongly dependent on the size, shape and underlying material. On the other hand, the model have to account for the macroscopic behavior of the net magnetic moment which is rather sensitive to the external stimili such as heat and magnetic fields. Such a behavior is exemplified by *superparamagnetism*, which is a fast shuttling motion of the net magnetic moment between its energy minima. Low temperature magnetic order within the NM has to incorporate exchange coupling between the magnetic ions, the Zeeman coupling to the external field and the (local) magnetic anisotropy energy. Apart from this, the spatial lattice in which the magnetic ions reside has to reflect the real crystallographic structure of the material to be studied, since lattice geometry may play an essential role in establishing the minimum energy configurations by inducing competing orders and frustration. For these reasons, a reasonable

model and the corresponding Hamiltonian must necessarily make use of the atomic magnetic moment as its elementary building block. Consequently, the techniques for computing the various physical observables using such a Hamiltonian, generally borrowed from bulk systems, have to be adapted and extended to such nano-scaled systems, namely spin-wave theory, relaxation time theories, and Monte Carlo simulations, just to cite a few. In some limit, depending on the set of physical parameters, it is possible to investigate the magnetization reversal of a NM within an assembly using a macroscopic model which represents the NM through its net magnetic moment. Obviously, this model ignores any internal features of the NM and focuses on its global behaviour in an external magnetic field and/or in contact with a heat bath. There are several variants of such a model but all of them may be considered as extensions of the initial Stoner-Wohlfarth (SW) and/or the Néel-Brown (NB) models [4–10]. Up to scaling factors, these models are all *one-spin problems* and will then be referred to as OSP. On the other hand, *many-spin problems* which involve the atomic spins of the NM will be referred to as MSP. In this section we shall first succinctly present the macroscopic model (OSP) and the well known results they render for the magnetic moment of a NM under the usual conditions of temperature and magnetic field. Next, we will turn to the presentation of the MSP approach, the corresponding Hamiltonian and computational methods. In the subsequent sections, we will present the main results of the application of this approach to a NM, regarded as a many-spin crystal with its specific features.

1.2.1 Macrospin Approach

As discussed earlier, in the framework of the macroscopic model (OSP), one concentrates on the behaviour of the net magnetic moment, ignoring any (local) process that leads to its onset. Thus, the exchange energy becomes a constant and plays no role in the minimization of the total energy. Consequently, the Hamiltonian only includes the anisotropy and Zeeman energies, namely

$$\mathscr{H} = -\frac{KV}{M^2}(\mathbf{M}.\mathbf{e})^2 - (g\mu_B)\,\mathbf{H}\cdot\mathbf{M}, \tag{1.4}$$

where K is an effective uniaxial anisotropy constant, $\mathbf{e}$ the verse of its easy direction and V the volume of the NM. Upon writing $\mathbf{M} = M\mathbf{s}$, $\mathbf{H} = H\mathbf{e}_h$ and introducing the dimensionless anisotropy and field parameters

$$\sigma = \frac{KV}{k_B T}, \quad h = \frac{(g\mu_B)\,HM}{2KV}, \tag{1.5}$$

the energy in (1.4), measured with respect to thermal energy $k_{\mathrm{B}}T$, becomes

$$-\beta\mathscr{H} = \sigma\left[(\mathbf{s}\cdot\mathbf{e})^2 + 2h\mathbf{s}\cdot\mathbf{e}_h\right]. \tag{1.6}$$

T is the absolute temperature and k_{B} the Boltzmann constant $\beta \equiv 1/k_{\mathrm{B}}T$.

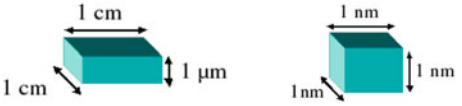

Fig. 1.3 A bulk system versus a nanoscale one. *Source* Reprinted with permission from [1]. Copyright (2020), Elsevier Books

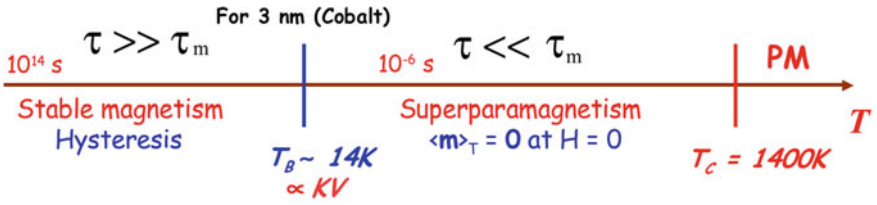

Fig. 1.4 Temperature axis

1.2.1.1 Relevant Time, Length and Energy Scales

To a first approximation, the (dimensionless) anisotropy-energy barrier in zero field is given by σ. For comparison, in Fig. 1.3 we evaluate the latter for two blocks of a given material, one of "bulk" dimensions (cm), on the left, and the other on the right with dimensions of the order of a nanometer.

To be more specific we consider cobalt for the underlying material at room temperature, $T = 300\,\mathrm{K}$, in the absence of a DC magnetic field. We find for the energy barrier $\sigma = \frac{KV}{k_B T} \sim 10^{15}$. This leads to a switching time between the two minima which is given by $\tau \propto e^{\sigma} \sim \exp(10^{15})$. On the other hand, for the cluster on the right $\sigma \sim 10^{-2}$ and $\tau \sim 10^{-10}$ s. This implies that as the magnet's size is reduced to the nanometer scale, the switching of the macroscopic magnetic moment between the various energy minima becomes possible at room temperature. In fact, even at much lower temperatures this switching becomes accessible to experiments. This fundamental new effect (i.e. superparamagnetism), induces a shift in the relevant temperature scale. Indeed, as depicted in Fig. 1.4, in nano-scaled systems the most relevant temperature is that which corresponds to the thermal energy that is sufficient for overcoming the energy barrier, rather than the Curie temperature, as is relevant for bulk systems. This new temperature is known as the *blocking temperature* and is denoted by T_B. In fact, its should be called the unblocking temperature because it is the temperature above which the magnetic moment climbs up the energy barrier and switches its orientation.[1]

In general, the energy barrier may be lowered by various mechanisms and/or different external stimuli:

[1]More precisely, for magnetic measurements with measuring time $\tau_m \sim 100$s (such is the case in magnetometry measurements), the superparamagnetic range is $0 \leq \Delta E/k_B T < \ln(\tau_m/\tau_0) \simeq 25$.

- At zero temperature, an applied static magnetic field h reduces the energy barrier as follows $\Delta E = \sigma\,(1-h)^2$. When h reaches a critical value h_c (here 1), the energy barrier is entirely suppressed and the magnetic moment of the system switches to the new available minimum. This hysteretic switching mechanism is well described by the so-called Stoner-Wohlfarth model [4, 8].
- At finite temperature, and even at zero magnetic field, the switching probability of the magnetic moment becomes nonzero owing to thermal fluctuations. Such a stochastic mechanism is well described by the so-called Néel-Brown model [5, 7, 9, 11]. Alongside the well-known work of Néel, Brown, and also that of Aharoni (1969), there is a fundamental approach developed by Langer (1967–69) for multivariate systems [12–15]. The only limitation of Langer's approach is that it applies to situations where the extrema of the energy potential are well defined in the sense that they are not flat. Indeed, this approach is based on the quadratic expansion of the energy potential at the various extrema (minima, maxima and saddle points). In practice, this turns out to be applicable to intermediate-to-high damping regimes.

For practical applications, such as information storage, one seeks to increase the storage density by using rather small magnetic elements. However, reducing the volume of these elements leads to rather low energy barriers and thereby to large switching rates, especially at room temperature. This drastically deteriorates the temporal stability of the information stored in the media. One way out consists in considering magnetic materials with large anisotropy constants K (as in CoPt), but then the critical field h_c required to suppress the energy barrier, which corresponds to writing a new information, becomes too large and inaccessible to nano-scaled devices. This is what we could call the *superparamagnetic tri-lemma*. Consequently, the nanomagnetism community sought for other alternatives while keeping in mind the two main objectives for practical applications, namely large storage densities and long temporal stability at room temperature. Two of such alternatives have been suggested: (i) add a time-dependent field on top of the static magnetic field [16–21], thus assisting the switching process without having to entirely suppress the energy barrier, and (ii) apply a laser beam to the system so as to locally reduce the anisotropy contribution. This is what it is called *heat-assisted magnetization reversal* (HAMR) mechanism.

1.2.2 Many-Spin Approach

In NMs of a diameter of the order of 10 nm (e.g. of cobalt), a great number of atoms is located on the outer shell. Now, we know that the latter undergoes lattice reconstructions and atomic rearrangements which in turn lead to a crystal-field symmetry breaking inducing strong local inhomogeneities. The consequence of this is *nonuniform atomic spin configurations*. For instance, as the surface anisotropy increases in intensity, the switching mechanism becomes less coherent and rather operates cluster-wise, leading to steps in the hysteresis loop and the limit-of-metastability

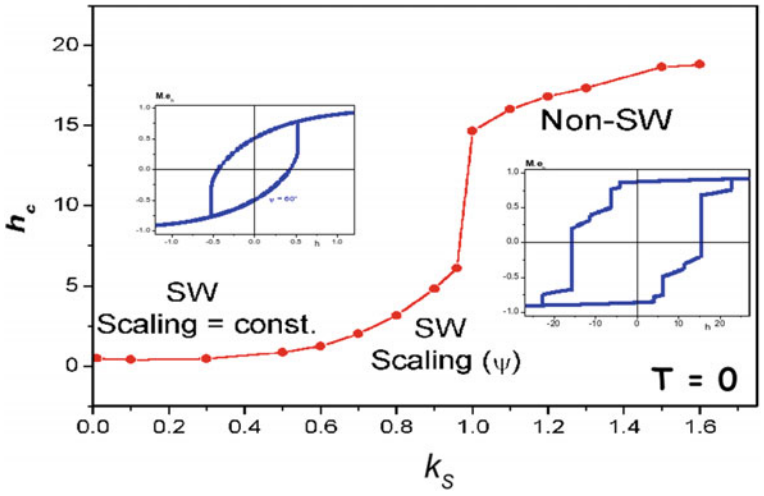

Fig. 1.5 Effects of surface anisotropy on the hysteresis loop and validity of the macrospin approach ($k_S \equiv K_S/J$). *Source* Reprinted with permission from [1]. Copyright (2020), Elsevier Books

curve can no longer be scaled with the Stoner-Wohlfarth astroid [22]. The situation can be summarized in Fig. 1.5, where the Stoner-Wohlfarth switching field is plotted against the ratio of surface anisotropy constant to exchange coupling ($k_S \equiv K_S/J$).

1.2.2.1 Hamiltonian

In order to account for and investigate the effect of spin noncolinearities, one has to resort to microscopic approaches that necessarily involve the atomic magnetic moment with continuous degrees of freedom as their building block. Such approaches then take account of the local environment inside the system, including the microscopic interactions and single-site anisotropy. Consequently, this amounts to adopting many-spin approaches in which the NM is considered as a crystal of $\mathcal{N}$ atomic magnetic moments $\boldsymbol{m}_i = (g\mu_B S)\,\boldsymbol{s}_i$, where $\mathbf{s}_i$ is the atomic unit spin vector ($\| \mathbf{s}_i \| = 1$) on site i. The interaction of these atomic moments is usually described with the help of the (classical) anisotropic Dirac-Heisenberg model [22]

$$\mathscr{H} = -\sum_{\langle i,j \rangle} J_{ij}\mathbf{s}_i \cdot \mathbf{s}_j + \mathscr{H}_Z + \mathscr{H}_{an}, \tag{1.7}$$

where J_{ij} is the exchange coupling which may be ferromagnetic or antiferromagnetic and whose nominal value depends on the nature of the link $i \leftrightarrow j$. So we may have

a different coupling for core-core (J_{cc}), core-surface (J_{cs}) and surface-surface (J_{ss}) links.[2]

Next,

$$\mathscr{H}_Z = -(g\mu_B)\mathbf{H} \cdot \sum_{i=1}^{\mathscr{N}} \mathbf{s}_i \tag{1.8}$$

is the Zeeman energy of interaction of the external magnetic field $\mathbf{H}$ with all atomic magnetic moments $\boldsymbol{m}_i$. Finally, $\mathscr{H}_{an}$ in (1.7) is the (uniaxial) single-site anisotropy energy

$$\mathscr{H}_{an} = -\sum_i K_i (\mathbf{s}_i \cdot \mathbf{e}_i)^2, \tag{1.9}$$

with easy axis $\mathbf{e}_i$ and constant $K_i > 0$. If the site i is located in the core, the anisotropy axis $\mathbf{e}_i$ is taken along some reference z axis and $K_i = K_c$. In fact, K_c is the effective anisotropy constant and $\mathbf{e}_i$ is the easy axis of the effective anisotropy that is usually assumed to include the NM's shape anisotropy. For NMs grown out of a magnetic material with cubic anisotropy, the term $\mathscr{H}_{an}$ may also comprise a cubic contribution. Altogether, in the absence of experimental data, the anisotropy constant K_c and easy direction are often assumed to be the same as those of the underlying bulk material. For surface spins, the anisotropy is also considered as uniaxial with a constant $K_i = K_s$ and an easy axis that is taken along the radial direction (i.e., transverse to the cluster surface), as illustrated in Fig. 1.6. Several works have also considered the same model with $K_i < 0$, i.e. with an easy axis that is tangential to the surface.

A more physically plausible model of surface anisotropy was introduced by Néel [6] with

$$\mathscr{H}_{an} = \frac{K_s}{2} \sum_i \sum_{j=1}^{z_i} (\mathbf{s}_i \cdot \mathbf{u}_{ij})^2, \tag{1.10}$$

where z_i is the coordination number of site i and $\mathbf{u}_{ij} = \mathbf{r}_{ij}/r_{ij}$ the unit vector connecting the site i to its nearest neighbors (see Fig. 1.7). This model sounds more realistic because the anisotropy at a given site occurs only when the latter loses some of its neighbors, e.g. when it is located at the boundary.

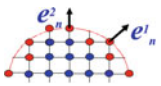

Fig. 1.6 Transverse Surface Anisotropy model. *Source* Reprinted with permission from [1]. Copyright (2020), Elsevier Books

[2]We define the core as the group of atomic spins whose coordination number z is equal to that of the bulk material (= 6 for a sc lattive and 12 for an fcc lattice). The other spins with lower z are considered as surface spins.

1.2.2.2 Weak Surface Effects

The study of the dynamics of NMs in the many-spin approach, along what was discussed in Sect. 1.2.1, presents tremendous difficulties related with the analysis of the energyscape (minima, maxima and saddle points), which is a crucial step in the calculation of relaxation rates and investigation of the magnetization reversal at finite temperatures. One may then address the question as to whether it is possible to establish some conditions under which one may adopt a (simpler) macroscopic approach and avail oneself from the corresponding full-fledged theory of magnetization dynamics. An answer to this question was provided in [23, 24] in the case of not-too-strong surface effects, i.e. when the surface anisotropy is not strong enough so as to consider the spin configuration as almost collinear (see Fig. 1.8).

Under this condition an *effective macroscopic model* was built for the net magnetic moment of the NM evolving in an effective energy potential. The latter turns out to be an infinite polynomial in the components of this macroscopic magnetic moment [23–26]. However, the 2nd- and the 4th-order terms are the leading contributions to the effective energy and the corresponding coefficients depend, both in magnitude and sign, on the underlying material, the size and shape of the NM, and the microscopic parameters (coupling, anisotropy, etc.) [26]. In the absence of a magnetic field, we then have the effective energy [23–26]

$$\mathscr{E}_{\text{eff.}} = -K_2\, m_z^2 + K_4(m_x^4 + m_y^4 + m_z^4). \tag{1.11}$$

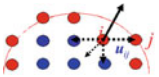

Fig. 1.7 Néel Surface Anisotropy model. *Source* Reprinted with permission from [1]. Copyright (2020), Elsevier Books

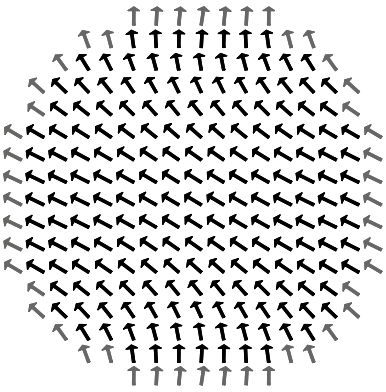

Fig. 1.8 Spin configuration of the middle plane of a spherical NM with relatively weak surface anisotropy and a net magnetic moment along the diagonal. *Source* Reprinted with permission from [1]. Copyright (2020), Elsevier Books

The coefficient K_2 of the second-order[3] contribution is in fact the result of two contributions, one stemming from the initial core uniaxial anisotropy and a new contribution that is induced by surface anisotropy (see below). The latter contribution is much smaller than the former because its coefficient contains the product $(K_c/J)(K_s^2/J) \ll 1$. The 4th-order coefficient K_4 in (1.11) was expressed in terms of the microscopic parameters as [23]

$$K_4^{(0)} = \kappa_2^{(0)} \frac{\mathcal{N} K_s^2}{zJ}, \tag{1.12}$$

where K_s, z, J are respectively the on-site surface anisotropy constant (transverse or Néel), the coordination number, and the exchange coupling of the many-spin NM. $\kappa_2^{(0)}$ is a surface integral that depends on the underlying lattice, the shape, and the size of the NM and also on the surface-anisotropy model. For instance, for a spherical NM (of ~ 1500 spins) cut from a simple cubic lattice with Néel's surface anisotropy, $\kappa_2^{(0)} \simeq 0.53465$.

To sum up, this effective macroscopic model provides us with an intermediate approach that: (i) involves a macroscopic magnetic moment whose dynamics is much easier to study since its potential energy is a function of only two variables, and (ii) does inherit the intrinsic features of the NM through the microscopic physical parameters entering the coefficients of the effective potential.

1.2.2.3 Validity of the Effective Models

The effective model (1.11) comes in as a handy tool for investigating the dynamics of the magnetization of NMs in a macroscopic approach that still captures some of the intrinsic features of the NMs [27, 28], see Sect. 1.3.1.1. However, it is not an easy matter to validate this model in experiments. The main reason is that the quartic term in (1.11) is a pure surface contribution that appears even in the absence of core anisotropy (see [23, 24]) and which may renormalize the cubic anisotropy of the (underlying) magnetic material the NM might be made of. Hence, it is not obvious how to disentangle this surface-induced 4th-order contribution from the intrinsic cubic anisotropy of magnetic materials. Nonetheless, at least for thin disks where the effective anisotropy is mostly of (boundary) surface origin, this quartic contribution may become dominant. An example of this situation was provided by cobalt nano-dots with enhanced edge magnetic anisotropy [29].

Obviously, for rather weak surface anisotropy the cubic contribution drops and the Stoner-Wohlfarth model is reinstated as a good approximation to the many-spin NM. Some experimental macroscopic estimates of the surface anisotropy constant yield, e.g. for cobalt $K_s/J \simeq 0.1$ [30], for iron $K_s/J \simeq 0.06$ [31], and for maghemite NMs $K_s/J \simeq 0.04$ [32]. However, one should not forget that this effective constant depends on the NM's size, among other parameters such as the material composition.

[3] With respect to the power of the components of the net magnetic moment.

Moreover, for a NM of diameter 2 nm, we may expect higher anisotropies. For such materials, the effective macroscopic model has been shown to be valid for $K_s/J \leq 0.25$ in a simple cubic lattice and $K_s/J \leq 0.35$ in a face-centred cubic lattice [26].

In Sect. 1.3.1.1 we discuss the effect of surface anisotropy on the relaxation rate in a study that has been made possible with the help of this effective model.

In the case of an assembly of magnetic NMs this model was used to compute the magnetization, the static susceptibility and the ac susceptibility. More precisely, the system studied is an ensemble of macrospins, each described with the help of the effective macroscopic model, and mutually interacting via the long-ranged dipolar coupling. In such a setup, it was possible to investigate the competition between (intrinsic) surface effects and dipolar interactions [28, 33–35] and to provide (semi-)analytical expressions for the observables mentioned above taking account of temperature, applied DC field, surface anisotropy and dipolar interactions. It is clear that such analytical developments would not be possible for an assembly of NMs treated as many-spin systems.

1.2.2.4 Strong Surface Anisotropy

When the conditions discussed above are not met, one has to deal with the Hamiltonian in (1.7) in its full generality with respect to the various energy contributions.

Thus, as discussed earlier, all techniques, both analytical and numerical, that are usually applied to bulk systems for investigating the magnetic properties, have to be adapted to nano-scaled systems. In particular, spin-wave theory, which is the study of the fluctuations of local spins, has to be extended so as to include the fluctuations of the net magnetic moment as well. This has been done in [2, 3] and references therein. The choice of the computing method depends on the observable of interest and on the approach considered. For equilibrium properties, the hysteresis loop and the switching field, for instance, is computed by numerically solving the deterministic Landau-Lifshitz equation without the Gaussian field. Within the macrospin approach, this equation is in fact a system of two (three) coupled equations in the system of spherical (Cartesian) coordinates, whereas within the many-spin approach this leads to a system of $2\mathcal{N}$ ($3\mathcal{N}$) coupled equations. However, in all cases the numerical procedure is quite straightforward and uses standard routines such as the Euler, Heun or Runge-Kutta methods [36, 37]. General magnetic properties of a many-spin system with, in principle, an arbitrary set of physical parameters, are also accessible to Monte Carlo simulations.

The classical Monte Carlo (MC) method based on the Metropolis algorithm is a standard technique [38] used in principle to simulate equilibrium statistical properties taking averages over a sample of possible spin configurations. At difference from atomistic simulations based on the Landau-Lifshitz equations, which are well suited for dynamic studies because they give the time evolution of magnetic moments, in MC simulations they are evolved through a sequence of MC steps with no real correspondence to real time. Even so, attempts have been made to establish a time quantification

of MC steps in some particular cases [39, 40] showing that this simulation technique can also be used to qualitatively understand dynamic magnetization processes such as magnetic relaxation or hysteresis. In brief, at each MC step, one selects a single spin from the lattice either randomly or sequentially and a change of its orientation is proposed, repeating the sequence a number of times equal to the total number of spins. At each selection, a new trial orientation of the spin, the corresponding energy change ΔE and Boltzmann probability $p(\Delta E, T) = \exp(-\Delta E/K_B T)$ are computed. Then the new spin orientation is accepted if either $\Delta E < 0$ or $p(\Delta E, T) > r$ [$r \in (0, 1)$ being a uniform random number], otherwise the trial is rejected and the initial spin orientation is kept. For Ising spins, there is one option to change the sign of the spin variable with probability $1/2$, but for Heisenberg spins, the new trial step can be chosen in different ways as long as detailed balance condition is met. Instead of using as trial moves random directions on a sphere, it turns out to be more convenient to perform trials inside a cone around the current spin direction whose aperture can be tuned, in order to keep a high trial acceptance rate [41–43]. It has been noticed that it is of crucial importance to use a combination of methods (random, inside a cone and spin flip) when simulating NM with inhomogeneous properties such as surface anisotropy or NM with core/shell structure (see Sects. 1.3.2.1 and 1.3.2.3).

In order to account for the superparamagnetic behavior of the NM net magnetic moment the MC method was extended in [3] by including global rotations of the net magnetic moment, in addition to the usual (local) rotations of the atomic spin. The semi-analytical expressions for the magnetisation in terms of temperature and magnetic field were derived it was shown that there are three field regimes separated by two critical values of the magnetic field, namely the one that suppresses the global rotation and the higher one that suppresses spin waves.

The dynamics of a many-spin NM can in principle be tackled by solving the set of coupled (stochastic) Landau-Lifshitz equations written for atomic spins [44, 45]. Indeed, solving the (stochastic) Landau-Lifshitz equation with a Langevin (thermal) field is a very versatile technique that can deal with multi-variate systems and is thus well suited for investigating equilibrium and dynamic behavior of such many-spin systems. However, this method inherently includes time consuming subroutines that are necessary for (i) generating sequences of arrays of stochastic numbers and (ii) computing averages over sufficiently large ensembles of time spin trajectories. The other technique would consists in solving the Fokker-Planck equation but this requires writing a hierarchy of equations that depend on the energy potential. This means that this procedure is somewhat model-dependent. Moreover, this technique is limited in practice to a small number of degrees of freedom, since otherwise this hierarchy becomes too cumbersome to write and rather costly to solve numerically. As such, and as far as NMs are concerned, this technique has been applied to a maximum of two coupled magnetic moments [46]. In conclusion, the study of the dynamics of NMs in the many-spin approach can only be done efficiently using the Landau-Lifshitz equation, even though this remains a tremendous numerical task.

1.3 Results

In the following sections we shall present a sample of our previous results on finite-size, boundary, shape and surface effects. We first present results for model NMs with a simple cubic lattice, spherical and cubic shapes. Next, we discuss the results for more specific situations with antiferromagnetic couplings and core/shell configurations.

1.3.1 Finite-Size Effects

1.3.1.1 Switching Field

For many-spin NMs of variable size, but which still exhibit a collinear spin configuration, the hysteresis loop can be scaled with that rendered by the macrospin Stoner-Wohlfarth model, even in the general case of a field applied at an arbitrary angle with respect to the core easy axis.

The effect of finite-size on the hysteretic properties of NMs have been investigated by many authors, see [36, 37, 47] and references therein.

In Fig. 1.9 we plot on the left the coercive field of a spherical NM and on the right the Stoner-Wohlfarth astroid. We see that the results for a many-spin NM with physical parameters within the range of the OSP model scale with those of the Stoner-Wohlfarth model. The scaling constant is the ratio of the number of core spins to

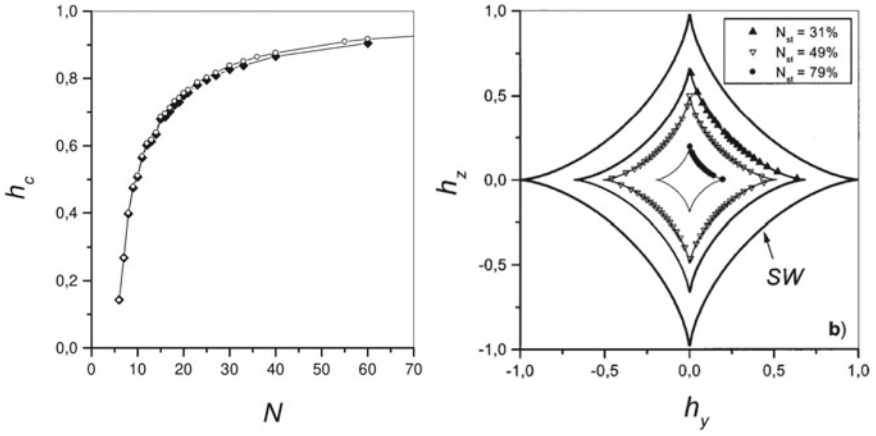

Fig. 1.9 Left: coercive field versus the linear size of a spherical NM. Right: Switching field of a spherical NM with $ks/j \simeq 0.01$, for different values of the surface-to-volume ratio $N_{st} = N_s/\mathcal{N}$. Calculations performed using the Landau-Lifshitz equation. *Source* Reprinted with permission from [37]. Copyright (2020), AIP Publishing LLC

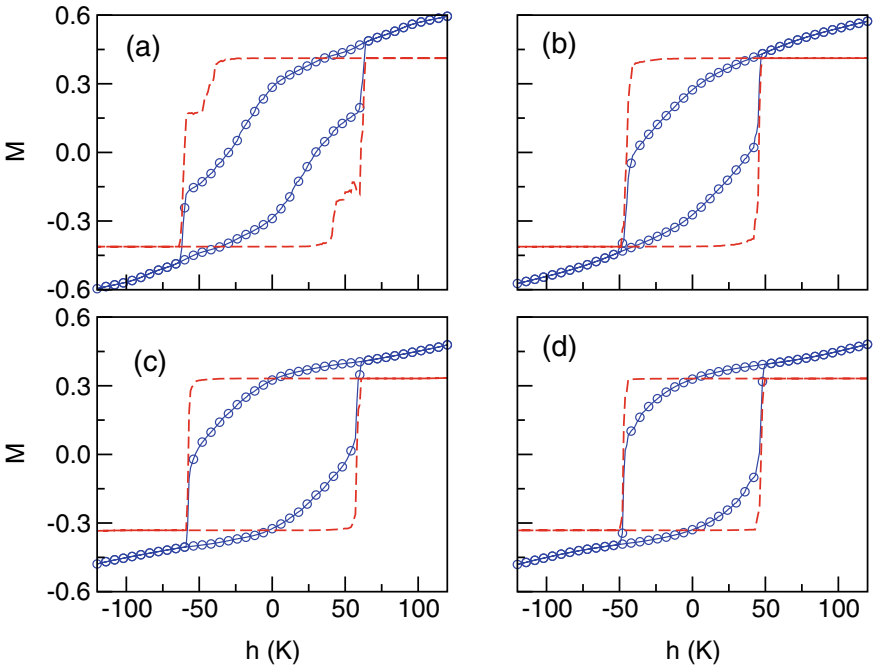

Fig. 1.10 Surface (continuous line) and core (dashed line) contributions to the hysteresis loop for NM of diameters $D = 3a$, $T = 10$ K (**a**); $D = 3a$, $T = 20$ K (**b**); $D = 6a$, $T = 10$ K (**c**); $D = 6a$, $T = 20$ K (**d**). Adapted from [48] Copyright 2020 American Physical Society

that of the NM's total number of spins. Moreover, the limit-of-metastability curves (astroids) for all sizes fall inside the Stoner-Wohlfarth astroid. This means that when boundary and surface effects, and the spin noncollinearities they entail, are ignored the magnetic properties of the NM can be described with the help of the macrospin model (or OSP).

Next, we consider the case of infinite uniaxial anisotropy thus restricting the orientation of the magnetic moments to that of Ising model. The reason for this choice is to study in pure form the effect of finite-size without interference from surface anisotropy effects. As a particular example with important applications, we consider a ferrimagnetic oxide such as maghemite. In this kind of oxides, Fe ions reside on a spinel structure where the spins have different coordination and antiferromagnetic couplings depending on the sublattice (tetra and octahedral) they belong to. The Ising variables interact through exchange interactions that may vary in value and sign from atom to atom depending on the spatial arrangement of the nearest neighbours [48, 49]. Since not all magnetic interactions can be fulfilled, and in spite of the collinear alignment of the spins, intrinsic geometrical frustration exists that is in part responsible for some of the peculiar properties of this kind of NM.

Then, in Fig. 1.10 we show hysteresis loops at different temperatures for NM with diameters $D = 3a, 6a$. First of all, we note that the saturation field and the high-field susceptibility increase as the NM size is reduced, since these quantities are mainly associated with the progressive alignment of the surface spins towards the field direction. Thus, the loops of the smallest NM resemble those found in ferrimagnetic NM [50–52] and other bulk systems with disorder [53, 54], increasing their squaredness (associated with the reversal of M as a whole) with the size. In fact, by plotting separately the contributions of the core and the surface to the total magnetization (see Fig. 1.10, dashed lines), we see that the loop of the core is almost perfectly squared independently of temperature and NM size, indicating a reversal of its magnetization with a well-defined ferrimagnetic moment. Instead, the loop of the surface reveals a progressive reversal of M, which is a typical feature associated to disordered or frustrated systems [53]. Nonetheless, for a wide range of temperatures and NM sizes, it is the reversal of the surface spins that triggers the reversal of the core. This is indicated by the fact that the coercive field of the core is slightly higher but very similar that of the surface. At zero temperature it was shown in [37] that the surface switches before the core in spherical NM with moderate surface anisotropy.

1.3.1.2 Magnetization Thermal Behaviour

In Fig. 1.11 we show the magnetization of a (model) spherical NM as a function of the reduced temperature. This is the ratio of temperature T to the critical temperature (T_{PBC}) of the cube-shaped NM with size of 40^3 and periodic boundary conditions. The corresponding magnetization is denoted M_{PBC}. This is compared with the magnetization of the core of a spherical NM of variable size and total number of spins $\mathcal{N} = 909, 3766, 6330$, with a surface contribution of 53%, 41%, 26%, respectively. For the details of the system and computing method see [55].

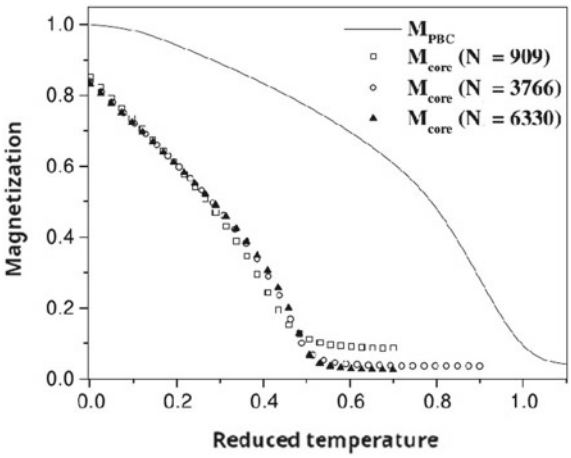

Fig. 1.11 Magnetization as a function of (reduced) temperature. Calculations performed using Monte Carlo simulations. *Source* Reprinted with permission from [56]. Copyright (2020), Springer

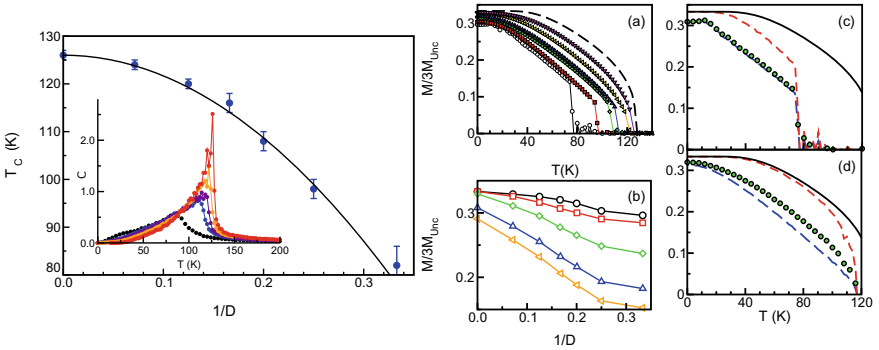

Fig. 1.12 Left panel: NM size dependence of the transition temperature T_c from paramagnetic to ferrimagnetic phases for spherical maghemite NM with fbc. The displayed values have been obtained from the maximum in the specific heat. The continuous line is a fit to (1.13) Inset: Thermal dependence of the specific heat for the same sizes as in the main panel. Right panel (**a**) shows the thermal dependence of the magnetization M obtained by progressive cooling from high T at a constant rate, $\delta T = -2$ K starting from a random configuration of spins, for NM of diameters $D = 3a, 4a, 6a, 8a, 10a, 14a$ (symbols) and pbc conditions, in a system of linear size $N = 14$ (dashed line). In panels (**c**) and (**d**) the contributions of the surface (blue dashed line) and core spins (red dashed line) have been distinguished from the total magnetization (circles) for NM with diameters $D = 3a, 8a$. The results for pbc conditions, in a system of linear size $N = 14$, have also been included for comparison (continuous line). Panel (**b**) displays the size dependence of M_{Total} at different temperatures 10, 20, 40, 60, 70 K from upper to lowermost curves. Adapted from [48] Copyright 2020 American Physical Society

It is clearly seen that the critical temperature and magnetization are dramatically reduced in the core of the NM. The reduction of the critical temperature is obviously due to the finite-size. There is a size-dependent reduction of the critical temperature by up to 50% for the smallest NM. The same result has been found by Hendriksen et al. [60] and many other authors.

Next, we discuss finite-size effects in some specific systems. Accordingly, for maghemite NM, and as a first example of purely finite-size effects on equilibrium properties, we present results of the ordering temperature dependence on the NM size for diameters varying between 3 and 14 unit cells (corresponding to real NM sizes of 2.5–12 nm) as extracted from the peak in the thermal dependence of the specific heat that signals a second-order transition from a paramagnetic to a ferrimagnetic order. In Fig. 1.12, we can see that T_C decreases with decreasing NM size, approaching the bulk value extracted from a simulation performed using pbc on a system with linear size $N = 14$. The obtained dependence can be fitted accurately to the predictions of finite-size scaling theory [57, 58] to a scaling law of the kind

$$\frac{T_c(\infty) - T_c(D)}{T_c(\infty)} = \left(\frac{D}{D_0}\right)^{-1/\nu}. \tag{1.13}$$

This expression fits nicely the MC data with $D_0 = (1.86 \pm 0.03)$a being a microscopic length scale (in this case, it is roughly twice the cell parameter), and a critical exponent $\nu = 0.49 \pm 0.03$, which seems to indicate a mean field behaviour [59]. This result can be ascribed to the high coordination of the O and T sublattices. The fitted curve is drawn in Fig. 1.12 where deviations from scaling are appreciable for the smallest diameters, for which corrections to the finite-size scaling in (1.13) may be important [57]. Thus, these results discard any important surface effects on the ordering temperature and are consistent with spin-wave calculations [60] and old MC simulations [61]. Similar finite-size effects have been found in fine NM [62] of $MnFe0_4$, but with a surprising increase of $T_c(D)$ as D decreases, which has been attributed to surface effects due to the interactions with the NM coating. More recently, other experimental [63–68] and theoretical [69–72] studies have reported similar scaling laws, although with different values of the scaling exponents depending on the NM composition and spin lattice.

The effects of the NM size can also be appreciated in the thermal dependence of the magnetization of an individual NM when going from the high temperature paramagnetic phase through T_C, the ordering temperature. Finite-size effects show up as changes in the $M(T)$ law with NM size D as compared to bulk behavior. To study the effects of a free surface and of finite size on the magnetization of the NM, we compare in Fig. 1.12a the results for four NM diameters ($D = 3$a, 4a, 6a, 8a, 10a, 14a, symbols) with those corresponding to $N = 14$ with pbc (representing the behavior of the bulk). The main feature observed is the reduction of the total magnetization M_{Total} with respect to the pbc case (continuous line) due to the lower coordination of the spins at the surface, which hinders ferrimagnetic order at finite temperatures. Figure 1.12c, d clearly show the role played by the surface (blue dashes) and the core (red dashes) in establishing the magnetic order. On one hand, independently of the NM size, the core tends to a perfect ferrimagnetic order at low T (marked by $M = 1/3$), progressively departing from the bulk behavior as T approaches T_c, this finite-size effect being more important as the NM size decreases. However, the surface magnetization does not reach perfect ferrimagnetic order at $T = 0$ even for $D = 8$ due to the reduced coordination of the spins. For this reason, a rapid thermal demagnetization is observed leading to M_{Surf} that significantly departs from the bulk behavior.

It is worthwhile to note that for all the diameters studied, there is a temperature range in which this demagnetization process is linear, this range being wider as the NM size decreases. In this linear regime, the NM demagnetization becomes dominated by surface effects since the core and surface behaviors are strongly correlated. Linear demagnetization is indicative of the effective 3D-2D dimensional reduction of the surface shell and has previously been observed in thin film systems [73, 74] and in simulations of rough FM surfaces [75]. M_{Total} is always strongly dominated by the surface contribution, progressively tending to the bulk behavior as the NM size is increased.

In Fig. 1.12b, we show the size dependence of the M_{Total} at different temperatures. All the curves follow a quasi-linear behavior with $1/D$ except for very small NM sizes ($D = 3$). This is consistent with the existence of a surface layer of constant

thickness Δr independent of D and with reduced magnetization with respect to the core. With these assumptions, the size dependence of M can be expressed as

$$M(D) = M_{\text{Core}} - \Delta M \frac{\Delta r S}{V} = M_{\text{Core}} - \Delta M \frac{6\Delta r}{D}, \tag{1.14}$$

where S and V are the surface and volume of the NM, and $\Delta M = M_{\text{Core}} - M_{\text{Surface}}$.

1.3.2 Effects of Shape and Surface Anisotropy

Recent advances in the synthesis methods and characterization techniques in the field of nanomagnetism have allowed us to have control on the production of NM with specific shapes and morphologies. It has been demonstrated that magnetic nanoparticles can be synthesized with precise control over their sizes, shapes, compositions, and structures [76–79]. In particular, the control of their shape can be used to tailor functional properties for specific biomedical and technological applications [80, 81]. In what follows, we will first present examples that illustrate how shape is related to distinct magnetic properties of NM and then will continue presenting three phenomena that illustrate how the existence of surface anisotropy and interfaces affect the magnetic properties of NM.

1.3.2.1 Effects of Shape in the Reversal of Oxide NPs

As a first example, let us consider two maghemite NM with spherical and cubic shape and similar radius and length of 20 nm, as the ones used in an experimental study of the heating properties relevant to hyperthermia applications [82]. Analyzing the hysteresis loops simulated by atomistic MC (see Fig. 1.13), we see that their shape and area undergo a substantial change just for the fact of changing their shape, since they have the same (real) values of the core and surface anisotropies. In particular, notice that the loop area of the cubic NM is larger than that of the spherical one. It has been checked that this is accomplished independently of the NM size, thus pointing to a genuine shape effect associated with changes occuring at the surface of the NM. Note that the difference in areas stems from qualitative loop shape differences around the coercive and closure field points that can be traced back to the different reversal processes of the surface spins as clearly observed on in the right panel of Fig. 1.13. Since the loop area is directly related to the specific absorption rate, these simulation results give a convincing explanation of experiments that show a systematic superior magnetic heating efficiency of cube-shaped NM as compared to spherical ones of similar sizes [82–87].

In our next example, we compare the phenomenology of spherical and ellipsoidal NM [88, 89]. Notice that, in contrast with the previous sections, the values of the

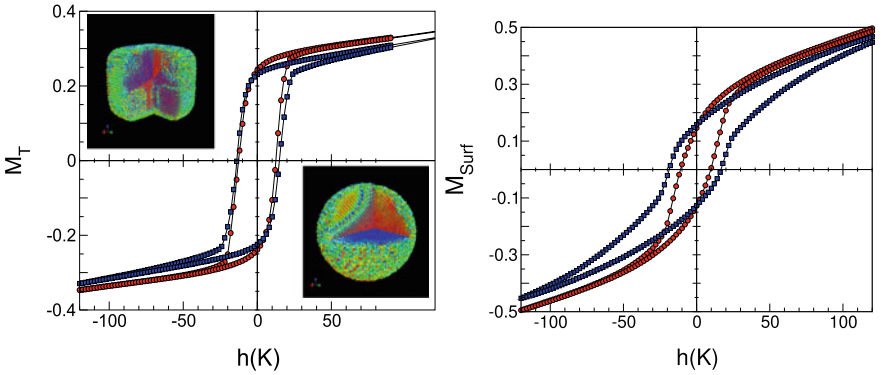

Fig. 1.13 Left panel: Hysteresis loop for a spherical (red circles, diameter 20 nm) and a cubic NM (blue squares, side 20 nm) obtained from MC simulations of an atomistic spin model of maghemite at low temperature. In both, uniaxial anisotropy at the core and Néel surface anisotropy have been considered. Snapshots show the spin configurations at the positive coercive field. Spins have been colored according to their projection onto the magnetic field direction (z axis) from red (+1) to blue (−1). Right panel: Contribution of the surface spins only to the hysteresis loop of a spherical (red circles) and a cubic NM (blue squares)

anisotropy constants here are given in temperature units and that they correspond to maghemite (see Sect. 1.3.2.2 for details).

By comparing, in Fig. 1.14, the loops for $k_S = 10$ to those for $k_S = 100$, we see that the coercive field increases and the remanence decreases with increasing surface anisotropy, independently of the elongation L of the NM. Moreover, the presence of disordered groups of spins at the surface, induced by surface anisotropy, makes the loops more elongated and increases the closure fields of the loops as found also in experiments on ferrimagnetic oxides [90]. The rounding of the loops near the coercive field clearly indicates a progressive departure from a uniform reversal mechanism with increasing k_S. When looking only at the M_z component, not much difference is appreciated between the loops for NM with different L because of the compensation of the spin components transverse to the field direction due to the symmetry of revolution of the NM around the z axis. However, upon further inspection of the ${M_n}^{\text{Surf}}$ and M_n^{Core} contributions and animated snapshots taken along the loops [91], the details of the reversal process can be better understood.

We first note that when k_S is increased from $k_S^\star$ the reversal mechanism changes from quasi-uniform (induced by the core) rotation at low k_S values, to a process in which the formation of surface hedgehog-like structures induce the non-uniform switching of the whole NM. In the first regime ($k_S = 10$ case in Fig. 1.14), the core and surface spins point mostly along the z axis ($M_n^{\text{Core}} \approx 1$, $M_n^{\text{Surf}} \ll 1$) except near the coercive field where they make short excursions towards the radial direction driven by the surface anisotropy (see the dips in M_n^{Core} and the cusps in ${M_n}^{\text{Surf}}$). However, for $k_S > k_S^\star$ ($k_S = 100$ case in Fig. 1.14), the surface spins remain near the local radial easy-directions ${M_n}^{\text{Surf}} \approx 1$) during the reversal, while the core spins

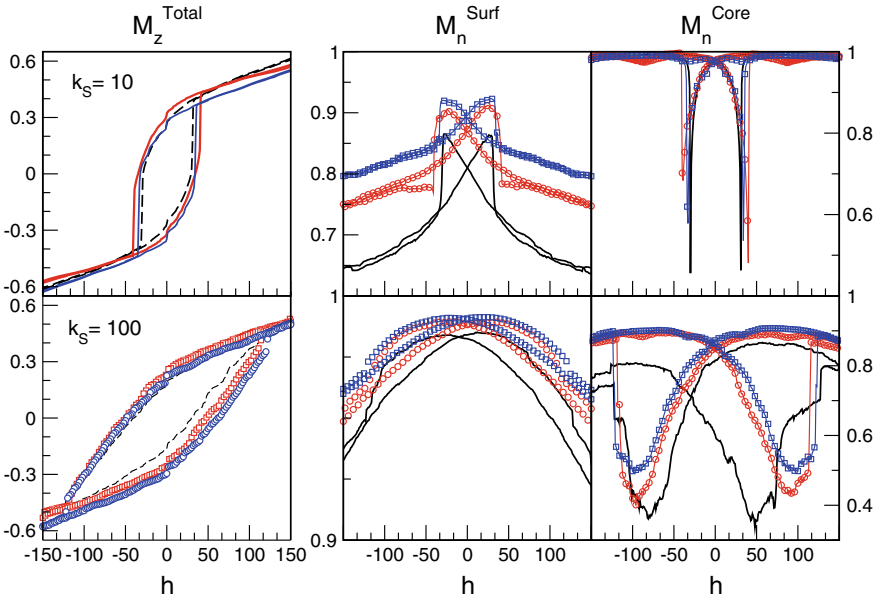

Fig. 1.14 Hysteresis loops for maghemite ellipsoidal NM with two values of the radial surface anisotropy constant $k_S = 10, 100$. Black lines are for a spherical NM with diameter $D = 3$, symbols are for an ellipsoidal NM with $D = 3$ and $L = 6$ (circles), 8 (squares). Left panels display the total magnetization while central and right panels show the surface and core contributions to M_n. Reprinted from [88] Copyright (2004), with permission from Wiley-VCH

are dragged away from the z local easy-axis by the surface spins during the reversal, except for values of h near the closure field. This is indicated by the widening of the dips in M_n^{Core} and the global decrease of M_n^{Core} values as k_S increases. Finally, let us remark also that, for all the k_S considered, the $M_n{}^{\text{Surf}}$ values along the whole hysteresis loops increase with increasing L, which indicates that the surface spins remain closer to the local radial direction during the reversal as the NM become more elongated. Upon increasing L, the dips in M_n^{Core} become less profound for $k_S > k_S^\star$, an indication that reversal of core spins along the radial direction is suppressed by the elongation. However, for weak anisotropy ($k_S < k_S^\star$), the more elongated the NM are, the greater the deviation of surface spins towards the radial direction during the reversal.

1.3.2.2 Surface Effects on the Thermal Dependence and Hysteresis of Oxide NP

In order to study surface effects in atomistic simulations, it is necessary to account for the three dimensional character of the atomic spins considering them as Heisenberg classical spins ($\mathbf{s}_i$) that can point in any direction in space (see (1.7)). Moreover,

apart from the exchange interaction, it is necessary to include magnetocrystalline anisotropy and to introduce the distinct surface Néel anisotropy term (1.10) for spins close to the surface with reduced coordination as compared to bulk. While the values of bulk anisotropy constants K_C can be obtained indirectly by magnetic measurements, the surface contribution K_S is more difficult to evaluate. However, for maghemite with $K_C \simeq 4.7 \times 10^4$ erg/cm^3 [92, 93], K_S has been estimated as $K_S \simeq 0.06$ erg/cm^2 from Mössbauer experiments [94, 95]. Therefore, in the simulations for maghemite NM, we will vary the core anisotropy values in the range $k_C = 0.01 - 1$ K and those of the surface anisotropy in the range $k_S = 1 - 100$ K.

We start again by examining the thermal dependence of the magnetization for different diameters, now with a variable k_S and fixed $k_C = 1K$. For small surface anisotropy ($k_S < 10$), the demagnetizing process has a linear dependence with T over a wide range of temperature for all NM sizes studied. This linear dependence is similar to that found for the model with Ising spins [96] in Sect. 1.3.1.2 . However, in that case, the linear dependence was blurred as the NM size increased and it was limited to a narrower range of temperatures. For Heisenberg spins, instead, this behavior is clearly observed for all the simulated D's and extends up to the ordering temperature, being more evident for the largest NM and for the core spins (see Fig. 1.15). This linear behavior is in agreement with the variation predicted by a surface spin wave theory and, therefore, is indicative of the effective 2D behavior of the surface shell, that completely dominates the magnetic behavior of the NM [97]. This is also in contrast with the results for FM NM (not shown, [98]) where, due to the absence of frustration, the core contribution dominates as indicated by a clear downward curvature of the $M(T)$ curves [98, 99]. Note also that the ordering temperature, marked by appearance of a non-zero M_z value, increases with the NM size as in the Ising model, but its value is lower.

Next, we focus on the magnetic order reached after the cooling process. For the real maghemite NM, the attained configurations are the result of the competition between

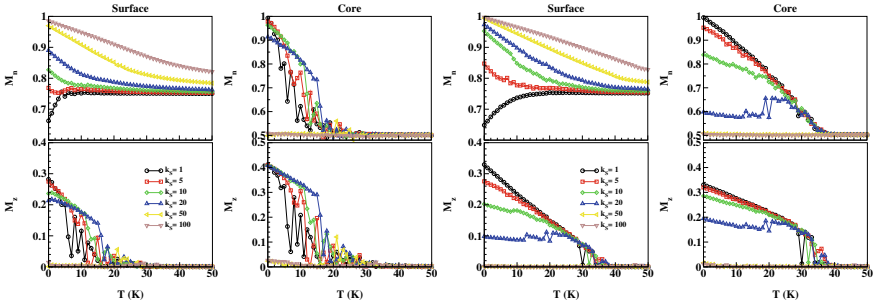

Fig. 1.15 Spherical NM ($D = 3$a for left panels and $D = 6$a right panels) with the real maghemite AF interactions. Thermal dependence of the surface (left column) and core (right column) contributions to M_z and to M_n during a progressive cooling from a high T at a constant rate $\delta T = -1$ K. Different curves correspond to different values of the surface anisotropy $k_S = 1, 5, 10, 20, 50, 100$ with $k_C = 1$. Reprinted from [100] Copyright (2004), with permission from Elsevier

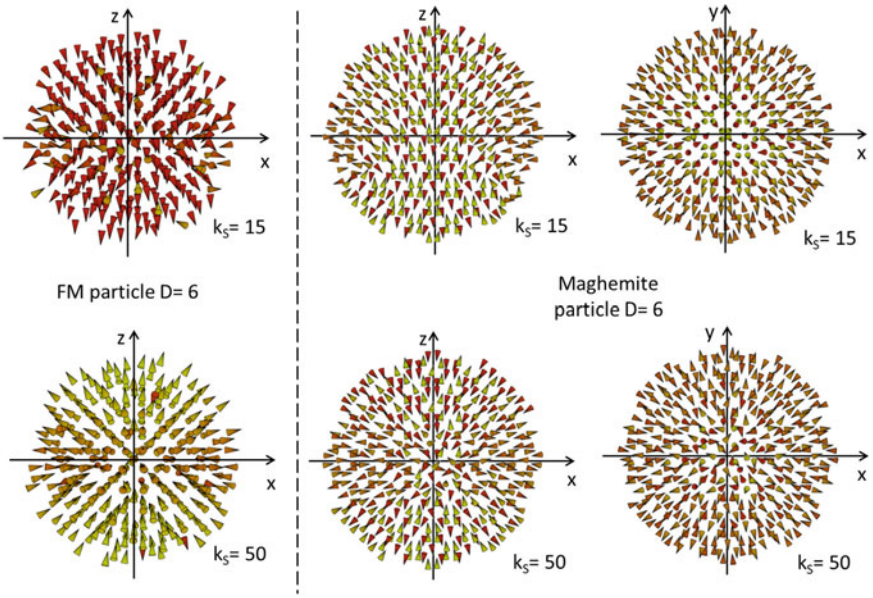

Fig. 1.16 Snapshots of the equilibrium configurations attained after cooling from a high temperature disordered state for FM (left column) and ferrimagnetic maghemite spherical (central and left columns) NMs with $D = 6a$ and maghemite lattice structure. Configurations are shown for two values of the surface anisotropy constant $k_S = 15$ and $k_S = 50$. The pictures display the central unit cell corresponding to a cut through an equatorial plane along the Z or XY axes

the frustration caused by the intra and intersublattice AF coupling of the spins and the distribution of local anisotropy directions at the surface. As a consequence, due to the dominant AF intersublattice coupling, a greater degree of disorder at the surface is induced with respect to the FM case [98]. For low k_S values ($k_S \lesssim 20$ curves in Fig. 1.15), the NM orders into a quasi-AF state in which spins in each sublattice are almost aligned along the core easy-axis, the states attained at $T = 0$ have core spins ordered in an AF state along the z-axis but surface spins that progressively depart from perfect alignment along the core easy-axis direction as k_S is increased. This is indicated by the approach of M_n towards 1 for core spins and towards 0.5 for surface spins as T is reduced (see the upper panels in Fig. 1.15). Note that while for the FM NM the maximum value of the total magnetization M_z is 1, this is not the case for the real maghemite NM since now the low T value of the total magnetization is given essentially by the contribution of noncompensated spins [96] (see Fig. 1.15).

With increasing k_S, this quasi-AF kind of ordering changes. $M_n^{\text{Surf}} \to 1$ at low T (see the upper panels in Fig. 1.15), which indicates that surface spins start to depart from the core easy-axis towards the local radial direction. Moreover, $M_n^{\text{Core}} \to 0.5$, a clear signature that the radial deviation of surface spins drive the core spins progressively towards the radial direction as k_S is increased. As a consequence throttled structures as those seen for $k_S = 15$, $D = 6$ in Fig. 1.16 start to form (similar results

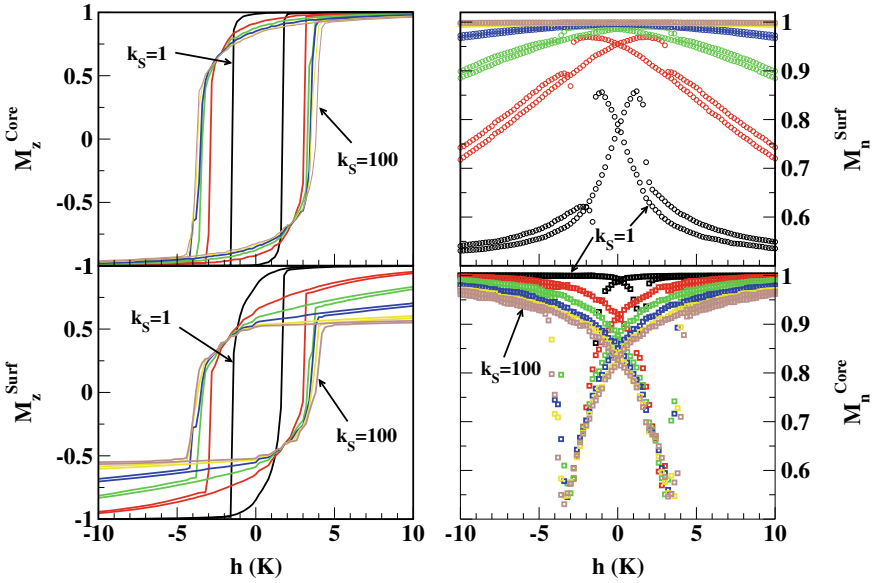

Fig. 1.17 Hysteresis loops for a spherical NM of diameter $D = 3a$ with FM interactions. The core anisotropy constant is $k_C = 1$, the results for several values of the surface anisotropy constant are displayed $k_S = 1, 5, 10, 20, 50, 100$. The magnetization component along the applied field direction is shown in lower right panel, the core contribution is displayed in the upper right panel. Right panels show the surface and core contributions to M_n, the sum of spin projections onto the local anisotropy axis. Reprinted from [100] Copyright (2004), with permission from Elsevier

have been found for other lattices and compositions in [71, 101–104]). Finally, for k_S above a critical value, $k_S^\star$, hedgehog-like configurations are favoured by the dominant radial anisotropy contribution (see for example the configuration for $k_S = 50$, $D = 6$ in Fig. 1.16). The direct visualization of equilibrium configurations presented in Fig. 1.16 shows that the reduction of the saturation magnetization with NM size observed experimentally in different fine NM of ferrimagnetic oxides, can be attributed to the random canting of surface spins caused by the competing AF interactions between sublattices [50, 105]. Moreover, as the results of our simulations confirm, the degree of disorder at the surface is larger than for the FM NM due to the complex interplay between the AF intralattice interactions and the local anisotropy easy-axes.

Next, we continue analyzing the influence of surface anisotropy on the reversal processes. First, we consider the results for a FM NM with the same lattice structure than maghemite shown in Fig. 1.17 for different values of k_S. For a FM NM, the hysteresis loops are dominated by the surface contribution for all values of k_S studied as indicated by the non-squaredness of the loops around the coercive field. For high values of the surface anisotropy ($k_S = 50, 100$), a magnetic field as high as $h = 20$ K is able to saturate the core, but the surface spins instead point along the radial direction during the magnetization process. This is more clearly reflected on the right panels of Fig. 1.17, where we see that for high k_S, M_n remains close to 1 at the

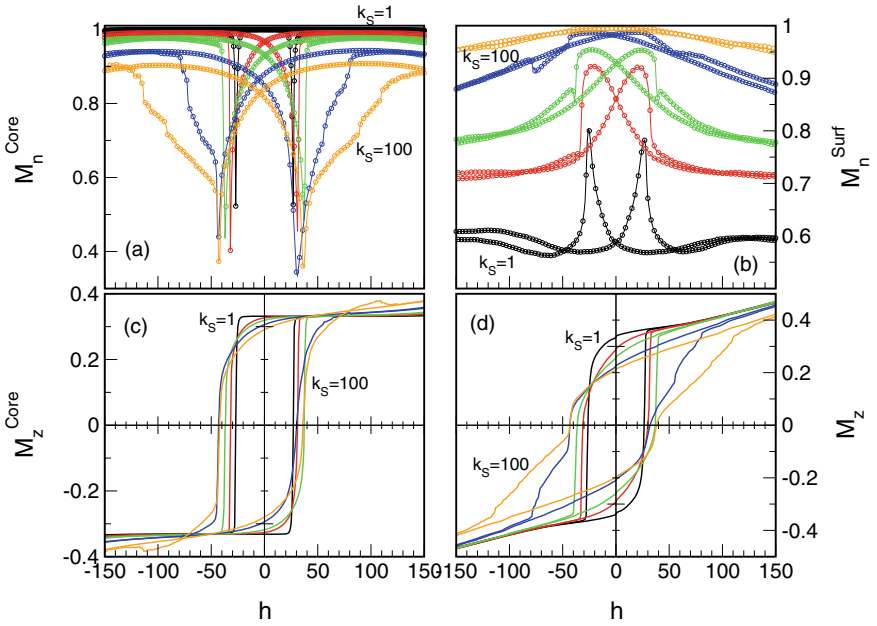

Fig. 1.18 Hysteresis loops for a real maghemite spherical NM with diameter $D = 6a$ for different values of the surface anisotropy constant $k_S = 1, 10, 20, 50, 100$. The different panels show the (**a**) core and (**b**) surface contributions to the projected magnetization along the local anisotropy axes (M_n), (**c**) the core contribution to the component of the magnetization along the field direction, and (**d**) the total magnetization

surface during all the reversal process, while the core spins depart from their easy directions ($M_n \sim 1$) dragged by the surface towards the radial direction close to the coercive field, where $M_n \sim 0.5$.

The hysteresis loops for the FM NM are to be compared with those for real ferrimagnetic maghemite NM presented in Fig. 1.18 for $D = 3a, 6a$ and k_S ranging from 1 to 100. Although the reversal process is still dominated by the surface spins, notice that now the loops for the ferrimagnetic NM become more elongated and have higher closure fields than those for the FM NM of the same size, indicating the frustrating character of the interactions in ferrimagnetic oxide NMs [106]. Moreover, a reduction in the high field susceptibility and an increase of the closure fields is also observed. These features are due to the dominance of surface anisotropy over exchange interactions that create surface disordered states which become more difficult to reverse by the magnetic field.

More importantly, there is a change in the magnetization reversal mechanism upon increasing k_S above $k_S^\star$, the value for which a change in the low T configurations was observed. For $k_S < k_S\star$ (see Fig. 1.18), the core and the surface have similar h_C and closure fields. The NM core reverses in a quasi-uniform manner with the spins pointing mostly along the z-axis ($M_n \approx 1$) except near h_c, and with the surface

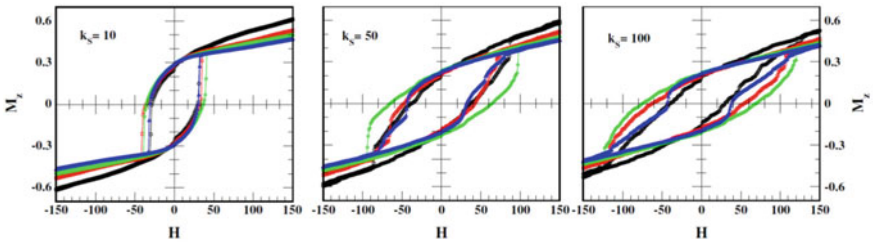

Fig. 1.19 Hysteresis loops of maghemite particles with diameters $D = 3a$ (black),$D = 4a$ (blue),$D = 5a$ (red),$D = 6a$ (green). Each panel corresponds to a different value of k_S as indicated

spins following the core reversal (with $M_n < 1$ indicating alignment close to the z direction) [107]. However, at higher k_S (see Fig. 1.18 for $k_S > k_S^\star$), surface spins remain close to the local radial direction ($M_n \approx 1$) during all the reversal process, driving the core spins away from their local easy axis and making their reversal non-uniform ($0.5 < M_n < 1$) due to the appearance of the hedgehog-like structures during the reversal [107]. Notice also that for $k_S > k_S^\star$ a series of steps in the hysteresis loops along the irreversibility line can be observed as also seen in [108]. Each step corresponds to the jump of a cluster of surface spins that are able to overcome the energy barrier induced by the high radial anisotropy at that field.

The influence of NM size on the hysteresis loop at $T = 0$ depends on the range of values of k_S, although some features are common to all of them, as can be seen in Fig. 1.19. As the NM size increases, the high field susceptibility decreases while the loops at different D all cross at $h = 0$. However, for k_S values below the critical one ($k_S < k_S^\star$), h_C is almost size independent, although the coercive field for the core spins of NM with high anisotropy is higher for the smaller NM. In contrast, for $k_S > k_S^\star$ (see the panels with $k_S = 50, 100$ in Fig. 1.19) h_C increases with increasing NM size except for the $D = 6$ NM. These results are in qualitative agreement with those reported by Morales et al. [109] for maghemite NMs with sizes ranging between 3 and 14 nm. They observed a slight increase of the coercive field with decreasing size for the range of sizes reported here.

1.3.2.3 Core-Shell NPs

For many technological applications, it has been shown to be useful to synthesize NP with non-homogenous materials having, for example, a gradient in composition when going from the inner to outer parts [110] or having a core and shell made of materials with different magnetic properties [111]. The last case is somehow unavoidable since most magnetic elements are easily oxidized when exposed to air or aqueous media. These NP can be otherwise produced by controlled chemical synthesis [112, 113] in a variety of morphologies and compositions. Magnetic core/shell nanoparticles with

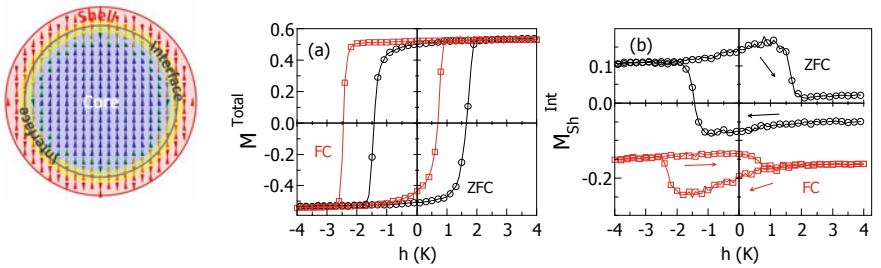

Fig. 1.20 Left: schematic drawing of model of a core/shell NM of total radius R used in the MC simulations. The spins sit on the nodes of a sc lattice. The AF shell has width R_{Sh} (red and yellow spins) and the FM core (blue and green spins) a radius $R_C = R - R_{Sh}$. The core/shell interface (green and yellow spins) is formed by the core (shell) spins having nearest neighbours on the shell (core). Right: Hysteresis loops for a core/shell NP with radius $R = 12\,a$ obtained from a ZFC state and after FC down to $T = 0.1$ in a field $h_{\rm FC}$ for $J_{\rm Sh} = -0.5 J_{\rm C}$ Panel (**a**) displays the total normalized magnetization component along the field direction. Panel (**b**) shows the normalized contributions of the shell spins at core/shell interface to the total magnetization of the loop. Adapted from [124] Copyright (2020) American Physical Society

functionalyzed shells and coatings are also necessary in biomedicine for applications in targeted delivery and diagnostics [81, 114–116].

An attractive composition results from the combination of a FM or AF core surrounded by an AF or FM shell (usually an oxide) coupled by the exchange interaction at the interface between them. Interesting proximity effects result from the structural modification and competition of different magnetic orderings at the FM/AFM interfaces [117–123]. In particular, the so-called exchange bias (EB) phenomenon which, in brief, consists in the shift of the hysteresis loop along the field axis after cooling the sample from high temperature through the Néel temperature of the AF, in the presence of a magnetic field [121]. For thin film FM/AF layers, different semi-analytical models (for a review see [121] and references therein) based on the macrospin approach have been proposed to account for the values of the observed EB fields, but none of them applies to NM, where the role played by the interface needs to be understood at an atomistic level. In order to unveil the microscopic origin of all the phenomenology associated to EB effects in NM, a minimum model that captures the main ingredients of a single NM with core/shell structure can be developed as depicted by the drawing shown in Fig. 1.20.

For simplicity, a core/shell NM is made of atomic spins placed on the nodes of a sc lattice inside a sphere of radius R (measured in multiples of the unit cell dimensions a) and inside which three regions are distinguished: core with radius R_C, shell of thickness $R_{Sh} = R - R_C$ and interface formed by the core (shell) spins having nearest neighbors on the shell (core). To account for the finite values of anisotropy in real systems, we consider Heisenberg spins interacting through the Hamiltonian of (1.7) with uniaxial anisotropy as in Fig. 1.6. Core/shell structures are typically made of a FM core and AF shell [121, 124–126], represented by $J_{\rm C,Sh} \lessgtr 0$ exchange constants respectively (hereafter fixed to $J_{\rm C} = 10$ and $J_{\rm Sh} = -0.5 J_{\rm C}$). The

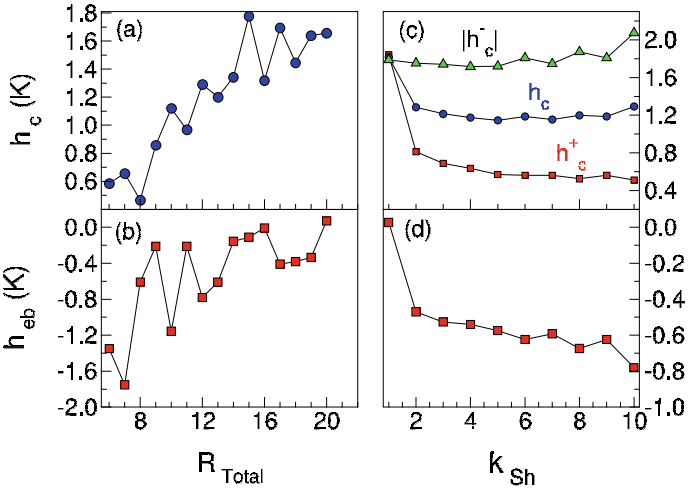

Fig. 1.21 Coercive and exchange bias fields for a spherical particle with $R = 12$, $R_{Sh} = 3$ and $k_C = 1$. The dependence on the particle radius is shown in panels (**a**) and (**b**), while in panels (**c**) and (**d**) the surface anisotropy k_{Sh} dependence is shown. Coercive fields at the decreasing and increasing field branches h_c^-, h_c^+ are also displayed in (**c**)

coupling at the interface is represented by $J_{\rm Int}$, that can be varied in sign and value to study the role played by the coupling across the core/shell interface on magnetic properties. Usually, $k_{\rm Sh} > k_{\rm C}$ is required in order for the shell spins not to reverse while cycling the magnetic field, so that EB is observed. Typically its value is higher than for the core due to reduced local coordination and will be fixed to $k_{\rm Sh} = 10$ K, in agreement with experiments [127, 128]. The core anisotropy will be fixed to $k_{\rm C} = 1$ K, which just sets the scale of the anisotropy field of the FM core.

Results of typical hysteresis loops obtained by MC simulation are shown in Fig. 1.20a for $J_{\rm Int} = -0.5 J_{\rm C}$, where the shift of the loop towards negative field values and a slightly increased coercivity for the loop after FC can be clearly seen. This can also be obtained for $J_{\rm Int} > 0$ [124]. In order to demonstrate that the origin of the loops shift is on the interface, we further computed the field dependence of the contribution of interface spins belonging to the shell, M_{Sh}^{Int}, to the total magnetization as displayed in Fig. 1.20b. The interfacial shell spins acquire a negative (or positive for AF coupling) net magnetization after FC which is higher than for the ZFC case [129], reflecting the fact that, after the FC process, a fraction of the interfacial spins are pinned and they remain so during the field reversal. In contrast, for the ZFC case, most of the interfacial spins follow the reversal of the FM core. The net magnetic moment, induced by the geometrical symmetry breaking and the alignment of groups of spins into the field direction, generates local fields on the core spins that point into the same direction as the external field, causing the shift of the hysteresis loops.

The results of the simulations allow us to understand that the origin of EB is a surface (interfacial) effect that, in contrast with those previously presented, scales with the number of uncompensated spins at the interface and not necessarily with

the surface size. However, the peculiarities of the shape of the interface in a NM depend on its size and, as a consequence, EB is also affected by finite-size effects. As can be seen in panels (a) and (b) of Fig. 1.21, for increasing NP size, h_C also exhibits an increasing trend attributed to a higher proportion of interfacial core spins that have to be reversed. For h_{eb}, the tendency is the contrary, although with clear oscillations that are in complete correspondence to the ones observed in M_{int} attained after the FC process [125, 130]. This demonstrates again the direct link between the net magnetization component of the shell interfacial spins and the loop shifts. Finally, notice that surface anisotropy also influences all this phenomenology. As seen on panels (c) and (d) of Fig. 1.21, there is a minimal value of k_{Sh} for the observation of EB. On increasing k_{Sh} above it, the bias field increases progressively as the proportion of interfacial spins pinned during the hysteresis loop increases, and finally saturates. In contrast, in the presence of EB, h_C is reduced with respect to the low-anisotropy case, but its value does not show appreciable variations with k_{Sh}.

1.3.2.4 Effects of Surface Anisotropy on the Dynamics of NM

Availing ourselves of the compromise provided by the EOSP approach, i.e. a macrospin capturing some of the intrinsic features of the NM, we can then investigate the effects of surface anisotropy on the switching field. Accordingly, the relaxation rate turns out to be a non monotonic function of the surface anisotropy constant K_s [27]. More precisely, owing to the variation of the energy barrier as a function of the surface anisotropy (see Fig. 1.22 left), the relaxation rate increases for (small) increasing K_s (see Fig. 1.22 right) since the (surface) quartic contribution to anisotropy induces saddle points at the equator. As K_s further increases, the quartic anisotropy starts to dominate, inducing much deeper energy minima and thereby much higher energy barriers, which finally makes the switching less likely.

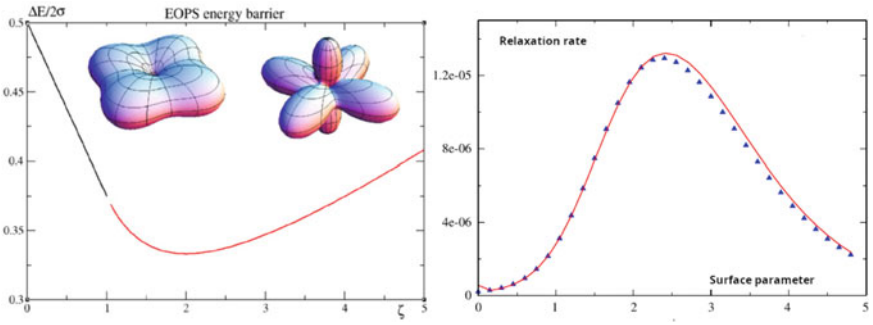

Fig. 1.22 Left: Energyscape with increasing surface anisotropy and the corresponding energy barrier. Right: Relaxation rate as a function of the surface parameter $\zeta = K_4/K_2$ (see (1.11)). *Source* Reprinted with permission from [1]. Copyright (2020), Elsevier Books

Compared to the effect of thermal fluctuations on the switching field, which is a simple scaling law, the effect of surface anisotropy depends on the direction of the applied field. This leads to a flattening of the switching field curve [27]. In the case of an assembly of magnetic NMs, this model is used to compute the ac susceptibility and to investigate the competition between (intrinsic) surface effects and dipolar interactions within an assembly of NM [28, 33–35].

1.3.2.5 Magnetic Excitations

When the conditions stated at the end of Sect. 1.2.2.2 regarding the limit of validity of the effective models are no longer satisfied, one has to adopt the full many-spin approach discussed earlier with the Hamiltonian in (1.7), and resort to fully numerical approaches, such as the Monte Carlo simulation method and/or the numerical solution of the Landau-Lifshitz equation, in order to study the equilibrium and dynamical properties of the NM. Among the results obtained for the equilibrium behavior, using the extended Monte Carlo approach that integrates both global and local spin rotations [2, 3], it has been shown that due to surface anisotropy the magnetization saturation requires relatively very strong magnetic fields ($\sim$ 10 T). In addition, as was discussed earlier, the hysteresis loop exhibits various jumps which account for a (cluster-wise) switching of groups of atomic spins, and thus showing that the magnetization reversal is not a coherent mechanism as in the Stoner-Wohlfarth model. Regarding the many-spin approach to the magnetization reversal, it was shown in [131, 132] that, under specific conditions, second-generation spin waves can develop within the NM which, through their coupling to the uniform mode, destabilize the latter and ultimately induce the magnetization switching. More precisely, it was shown that a box-shaped NM exhibit an exponential spin-wave instability in the case of a uniaxial anisotropy and a linear spin-wave instability for a random anisotropy, with the exponential instability leading to a faster relaxation than the linear instability.

We have also studied surface effects on ferromagnetic resonance in magnetic nanocubes [133]. The numerical method used consists in linearizing the Landau-Lifshitz equation around the equilibrium state of the system, thus leading to an eigenvalue problem whose solution renders the excitation spectrum. For a box-shaped NM, the results were also compared to those of the generalized spin-wave theory [2, 3]. We computed the absorbed power as a function of the excitation frequency and showed that it is possible to attribute the different contributions of the surface and those of the core spins to the various peaks obtained by our calculations. In particular, the low-energy peak, corresponding to the $k = 0$ mode, consists of equal contributions from the surface and core spins. Furthermore, in the case of less symmetric box-shaped samples with Néel surface anisotropy, we observe an elliptic precession of the spins whose signature could be seen in a parametric resonance experiment. For 8 nm iron nanocubes, we show that the absorbed power spectrum should exhibit a low-energy peak around 10 GHz, typical of the uniform mode, followed by other low-energy features that couple to the uniform mode but with a stronger contribution from the surface. There are also high-frequency exchange-mode peaks around 60 GHz.

Finally, in the [134], the authors investigated the effects of surface anisotropy (and the ensuing spin misalignment) on the magnetization dynamics of ferromagnetic nanocubes in the many-spin approach. It was shown that such inhomogeneous spin configurations induce nutation in the dynamics of the particle's magnetization. In addition to the ordinary precessional motion with a frequency of 10 GHz, it was found that the dynamics of the net magnetic moment exhibits two more resonance peaks with frequencies that are higher than the FMR frequency. In particular, a much higher frequency of 1 THz was attributed to the magnetization fluctuations at the atomic level driven by exchange interactions.

1.4 Conclusion

In this chapter, we have studied the equilibrium, and to a lesser extent the dynamic, properties of nano-scaled magnetic systems taking account of their "intrinsic" features, such as finite-size, boundary and surface effects. We deemed it necessary to first emphasize the difference between these effects illustrated through simple models of a nanomagnet. Then, we presented the various models and approximations employed for describing nanomagnets depending on the range of their physical parameters and their ratios. Next, we discussed the corresponding computing methods that have been developed for these specific systems, such as the Monte Carlo simulations, Landau-Lifshitz equation (with and without the Langevin field), and the spin-wave theory.

We have covered some of our previous results for the thermal and hysteretic behavior of the magnetization. We first did so for model NM so as to build a qualitative picture of the general behavior and a fair understanding of the underlying mechanisms. Then, we considered more realistic NM with maghemite as the underlying structure as well as nanomagnets in core-shell configurations. For the model NM and the more realistic iron oxide nanocubes, we have also succinctly reported on some of our works that dealt with the effects of surface anisotropy on the relaxation rate and the spectrum of spin-wave excitations.

The examples studied allow us to appreciate the wealth of novel features and physical phenomena, and on the other hand the big challenges, brought about by nano-scaled spin systems. Their reduced size has deep consequences on their internal magnetic state as well as their macroscopic behavior. Indeed, finite-size, boundary and surface effects induce nonuniform magnetic states (spin noncolinearities) which lead to incoherent switching and novel hysteretic properties, reduced critical temperature and complex magnetization processes. The reduced size also leads to the interesting phenomenon of superparamagnetism which has redefined the relevant temperature and time scales. The study of the dynamics of such systems is a daunting task that requires the analysis of a multi-valley energy potential. Nevertheless, it has been possible to build macroscopic and microscopic models for investigating these phenomena and for shedding light on the underlying mechanisms. In addition, these models have allowed us to make estimates of the various physical parameters and to

compare with experiments. It has thus been possible to figure out how the magnetization of the nanomagnet switches, to evaluate the corresponding relaxation time and the switching magnetic field. The macroscopic models such as the Stoner-Wohlfarth and Néel-Brown models have already been validated by experiments performed on nanomagnets for which these models are applicable. In the opposite situation induced by surface effects, we may say that only qualitative studies have been relatively successful, whereas any quantitative investigation still remains a challenge. However, the fast progress in synthesis, characterization and measurement has allowed for an unprecedented control of a whole set of properties of these nanomagnets and has made it to possible to shrink the gap between theory and experiments. In particular, the possibility of making well organised, nearly monodisperse assemblies of well defined nanomagnets, offers a real potential for studying the competition between, on one hand the intrinsic properties due to finite-size and boundary, shape and surface effects, and on the other the collective effects induced by mutual interactions between the nanomagnets and by their interactions with the hosting medium. This relatively favorable situation has triggered new impetus for further investigations of NMs assemblies with a plethora of promising practical applications.

Acknowledgements Ò.I. acknowledges financial support form the Spanish MINECO (No. MAT2015-68772 and No. PGC2018-097789-B-I00), Catalan DURSI (No. 2017SGR0598) and European Union FEDER Funds (una manera de hacer Europa), also CSUC for supercomputer facilities.

References

1. D.S. Schmool, H. Kachkachi, in *Single-Particle Phenomena in Magnetic Nanostructures* (Chap. 4), *Solid State Physics*, vol. 66, ed. by R.E. Camley, R.L. Stamps (Academic Press, 2015), pp. 301 – 423. https://doi.org/10.1016/bs.ssp.2015.06.001. http://www.sciencedirect.com/science/article/pii/S0081194715000053
2. H. Kachkachi, D.A. Garanin, Physica A **300**, 487 (2001). https://doi.org/10.1016/S0378-4371(01)00361-2
3. H. Kachkachi, D.A. Garanin, Euro. Phys. J. B **22**, 291 (2001). https://doi.org/10.1007/s100510170106
4. E.C. Stoner, E.P. Wohlfarth, Philos. Trans. R. Soc. London, Ser. A **240**, 599 (1948)
5. L. Néel, Compt. Rend. Acad. Sci. **228**, 664 (1949)
6. L. Néel, Compt. Rend. Acad. Sci. **237**, 1468 (1953)
7. W.F. Brown, Phys. Rev. **135**, 1677 (1963)
8. E.C. Stoner, E.P. Wohlfarth, IEEE Trans. Magn. **27**, 3475 (1991)
9. W.F. Brown, IEEE Trans. Magn. **15**, 1196 (1979)
10. A. Aharoni, *Introduction to the Theory of Ferromagnetism* (Oxford Science Pubs., 1996)
11. A. Aharoni, J. Appl. Phys. **83**, 3432 (1998). https://doi.org/10.1063/1.367113
12. J. Langer, Phys. Rev. Lett. **21**, 973 (1968)
13. J. Langer, Ann. Phys. (N.Y.) **54**, 258 (1969)
14. W.T. Coffey, D.A. Garanin, D.J. McCarthy, Adv. Chem. Phys. **117**, 483 (2001)
15. H. Kachkachi, J. Mol. Liquids **114**, 113 (2004)
16. T.L.S.I. Denisov, P. Hänggi, Phys. Rev. Lett. **97**, 227202 (2006)
17. G. Bertotti, I. Mayergoyz, C. Serpico, J. Appl. Phys. **91**, 7556 (2002)
18. Z.Z. Sun, X.R. Wang, Phys. Rev. B **74**, 132401 (2006)

19. C. Thirion, W. Wernsdorfer, D. Mailly, Nature Materials **2**, 524 (2003)
20. N. Barros, M. Rassam, H. Jirari, H. Kachkachi, Phys. Rev. B **83**, 144418 (2011)
21. N. Barros, M. Rassam, H. Kachkachi, Phys. Rev. B **88**, 014421 (2013)
22. H. Kachkachi, D.A. Garanin, in *Surface Effects in Magnetic Nanoparticles*, ed. by D. Fiorani (Springer, Berlin, 2005), p. 75
23. D.A. Garanin, H. Kachkachi, Phys. Rev. Lett. **90**, 065504 (2003). https://doi.org/10.1103/PhysRevLett.90.065504
24. H. Kachkachi, J. Magn. Magn. Mater. **316**, 248 (2007)
25. H. Kachkachi, E. Bonet, Phys. Rev. B **73**, 224402 (2006)
26. R. Yanes, O. Chubykalo-Fesenko, H. Kachkachi, D.A. Garanin, R. Evans, R.W. Chantrell, Phys. Rev. B **76**, 064416 (2007). https://doi.org/10.1103/PhysRevB.76.064416
27. Y. Kalmykov, P.-M. Déjardin, H. Kachkachi, J. Phys. D **41**, 134004 (2008)
28. F. Vernay, Z. Sabsabi, H. Kachkachi, Phys. Rev. B **90**, 094416 (2014)
29. S. Rohart, V. Repain, A. Thiaville, S. Rousset, Phys. Rev. B **76**, 104401 (2007)
30. R. Skomski, J.M.D. Coey, *Permanent Magnetism, Studies in Condensed Matter Physics*, vol. 1 (IOP Publishing, London, 1999)
31. K.B. Urquhart, B. Heinrich, J.F. Cochran, A.S. Arrott, K. Myrtle, J. Appl. Phys. **64**, 5334 (1988)
32. R. Perzynski, Yu.L. Raikher, in *Surface Effects in Magnetic Nanoparticles*, ed. by D. Fiorani (Springer, Berlin, 2005), p. 141
33. D. Ledue, R. Patte, H. Kachkachi, J. Nanosci. Nanotechnol. **12**, 4953 (2012)
34. G. Margaris, K. Trohidou, H. Kachkachi, Phys. Rev. B **85**, 024419 (2012)
35. Z. Sabsabi, F. Vernay, O. Iglesias, H. Kachkachi, Phys. Rev. B **88**, 104424 (2013). https://doi.org/10.1103/PhysRevB.88.104424
36. D.A. Dimitrov, G.M. Wysin, Phys. Rev. B **51**, 11947 (1995)
37. M. Dimian, H. Kachkachi, J. Appl. Phys. **91**, 7625 (2002)
38. K. Binder, D. Heermann, *Monte Carlo Simulation in Statistical Physics* (Springer, Berlin, 1992)
39. U. Nowak, R.W. Chantrell, E.C. Kennedy, Phys. Rev. Lett. **84**, 163 (2000). https://doi.org/10.1103/PhysRevLett.84.163
40. O. Chubykalo, U. Nowak, R. Smirnov-Rueda, M.A. Wongsam, R.W. Chantrell, J.M. Gonzalez, Phys. Rev. B **67**, 064422 (2003). https://doi.org/10.1103/PhysRevB.67.064422
41. U. Nowak, in *Annual Reviews of Computational Physics IX*, ed. by D. Stauffer (World Scientific, Singapore, 2001), chap. Thermally Activated Reversal in Magnetic Nanostructures, p. 105. https://doi.org/10.1142/9789812811578_0002
42. D. Hinzke, U. Nowak, Comp. Phys. Comm. **121–122**, 334 (1999). https://doi.org/10.1016/S0010-4655(99)00348-3
43. R.F.L. Evans, W.J. Fan, P. Chureemart, T.A. Ostler, M.O.A. Ellis, R.W. Chantrell, J. Phys.: Condens. Matter **26**, 103202 (2014). https://doi.org/10.1088/0953-8984/26/10/103202
44. D. Berkov, J. Magn. Magn. Mater. **186**, 199 (1998)
45. D.V. Berkov, N.L. Gorn, J. Phys.: Condens. Matter **13**, 9369 (2001)
46. S.V. Titov, H. Kachkachi, Y.P. Kalmykov, W.T. Coffey, Phys. Rev. B **72**, 134425 (2005). https://doi.org/10.1103/PhysRevB.72.134425
47. D.A. Dimitrov, G.M. Wysin, Phys. Rev. B **50**, 3077 (1994)
48. O. Iglesias, A. Labarta, Phys. Rev. B **63**, 184416 (2001). https://doi.org/10.1103/PhysRevB.63.184416
49. O. Iglesias, A. Labarta, F. Ritort, J. Appl. Phys. **89**, 7597 (2001)
50. R.H. Kodama, A.E. Berkowitz, E.J. McNiff, S. Foner, Phys. Rev. Lett. **77**, 394 (1996)
51. R.H. Kodama, S.A. Makhlouf, A.E. Berkowitz, Phys. Rev. Lett. **79**, 1393 (1997)
52. R.H. Kodama, A.E. Berkowitz, Phys. Rev. B **59**, 6321 (1999)
53. K. Binder, A.P. Young, Rev. Mod. Phys. **58**, 801 (1986)
54. H. Maletta, in *Excitations in Disordered Solids*, ed. by M. Thorpe (Plenum, New York, 1981)
55. H. Kachkachi, A. Ezzir, M. Noguès, E. Tronc, Surface effects in nanoparticles: Monte Carlo simulations. Eur. Phys. J. B **14**, 681 (2000)

56. H. Kachkachi, A. Ezzir, M. Nogués, E. Tronc, Eur. Phys. J. B **14**, 681 (2000)
57. D.P. Landau, Phys. Rev. B **14**, 255 (1976)
58. M.N. Barber, in *Phase Transitions and Critical Phenomena*, vol. 8, ed. by C. Domb, J.L. Lebowitz (Academic Press, New York, 1983), p. 145
59. H.E. Stanley, *Introduction to Phase Transitions and Critical Phenomena* (Oxford University Press, New York, 1987)
60. P.V. Hendriksen, S. Linderoth, P.-A. Lindgard, Phys. Rev. B **48**, 7259 (1993)
61. K. Binder, H. Rauch, V. Wildpaner, J. Phys. Chem. Sol. **31**, 391 (1970). https://doi.org/10.1016/0022-3697(70)90119-8
62. X. Obradors, A. Isalgue, A. Collomb, A. Labarta, M. Pernet, J.A. Pereda, J. Tejada, J.C. Joubert, J. Phys. C: Solid State Phys. **19**, 6605 (1986). https://doi.org/10.1088/0022-3719/19/33/010
63. J. Wang, W. Wu, F. Zhao, G.-m. Zhao, Appl. Phys. Lett. **98**, 083107 (2011). https://doi.org/10.1063/1.3558918
64. J. Wang, W. Wu, F. Zhao, G.-m. Zhao, Phys. Rev. B **84**, 174440 (2011). https://doi.org/10.1103/PhysRevB.84.174440
65. E. Skoropata, R.D. Desautels, B.W. Southern, J. van Lierop, Chem. Mater. **25**(9), 1998 (2013). https://doi.org/10.1021/cm303893h
66. L. Li, F.g. Li, J. Wang, G.m. Zhao, J. Appl. Phys. **116**(17), 174301 (2014). https://doi.org/10.1063/1.4900951
67. A.K. Pramanik, A. Banerjee, A. Banerjee, J. Phys.: Condens. Matter **28**(35), 35LT02 (2016). https://doi.org/10.1088/0953-8984/28/35/35lt02
68. X. Zhang, J. Wang, M. Gao, Mod. Phys. Lett. B **30**, 1650241 (2016). https://doi.org/10.1142/S0217984916502419
69. E. Velásquez, J. Mazo-Zuluaga, J. Restrepo, O. Iglesias, Phys. Rev. B **83**, 184432 (2011). https://doi.org/10.1103/PhysRevB.83.184432
70. E.A. Velásquez, J. Mazo-Zuluaga, D. Altbir, J. Mejía-López, Eur. Phys. J. B **87**, 61 (2014). https://doi.org/10.1140/epjb/e2014-40712-6
71. J. Alzate-Cardona, S. Ruta, R. Chantrell, O. Arbeláez-Echeverri, E. Restrepo-Parra, J. Magn. Magn. Mater. **424**, 451 (2017). https://doi.org/10.1016/j.jmmm.2016.10.108
72. E.S. Loscar, C.M. Horowitz, Phys. Rev. E **97**, 032103 (2018). https://doi.org/10.1103/PhysRevE.97.032103
73. B. Martínez, R.E. Camley, J. Phys.: Condens. Mat. **4**, 5001 (1992)
74. J.H. Park, E. Vescovo, H.J. Kim, C. Kwon, R. Ramesh, T. Venkatesan, Phys. Rev. Lett. **81**, 1953 (1998)
75. D. Zhao, F. Liu, D.L. Huber, M.G. Lagall, Phys. Rev. B **62**, 11316 (2000)
76. T. Hyeon, S.S. Lee, J. Park, Y. Chung, H.B. Na, J. Am. Chem. Soc. **123**, 12798 (2001). https://doi.org/10.1021/ja016812s
77. J. Park, K. An, Y. Hwang, J.G. Park, H.J. Noh, J.Y. Kim, J.H. Park, N.M. Hwang, T. Hyeon, Nat. Mater. **3**, 891 (2004). https://doi.org/10.1038/nmat1251
78. A. Labarta, X. Batlle, O. Iglesias, in *Surface Effects in Magnetic Nanoparticles*, ed. by D. Fiorani, Nanostructure Science and Technology (Springer, 2005), chap. From Finite-Size and Surface Effects to Glassy Behaviour in Ferrimagnetic Nanoparticles, pp. 105–140
79. L. Wu, A. Mendoza-Garcia, Q. Li, S. Sun, Chem. Rev. **116**, 10473 (2016). https://doi.org/10.1021/acs.chemrev.5b00687
80. A. Feld, A. Weimer, A. Kornowski, N. Winckelmans, J.P. Merkl, H. Kloust, R. Zierold, C. Schmidtke, T. Schotten, M. Riedner, S. Bals, H. Weller, ACS Nano **13**, 152 (2019). https://doi.org/10.1021/acsnano.8b05032
81. S. Tanaka, Y.V. Kaneti, N.L.W. Septiani, S.X. Dou, Y. Bando, M.S.A. Hossain, J. Kim, Y. Yamauchi, Small Methods **3**, 1800512 (2019). https://doi.org/10.1002/smtd.201800512
82. C. Martinez-Boubeta, K. Simeonidis, A. Makridis, M. Angelakeris, O. Iglesias, Sci. Rep. **3**, 1652 (2013). https://doi.org/10.1038/srep01652
83. P. Guardia, A. Riedinger, S. Nitti, G. Pugliese, S. Marras, A. Genovese, M.E. Materia, C. Lefevre, L. Manna, T. Pellegrino, J. Mater. Chem. B **2**, 4426 (2014). https://doi.org/10.1039/C4TB00061G

84. A.G. Kolhatkar, Y.T. Chen, P. Chinwangso, I. Nekrashevich, G.C. Dannangoda, A. Singh, A.C. Jamison, O. Zenasni, I.A. Rusakova, K.S. Martirosyan, D. Litvinov, S. Xu, R.C. Willson, T.R. Lee, ACS Omega **2**, 8010 (2017). https://doi.org/10.1021/acsomega.7b01312
85. E. Natividad, I. Andreu, in *Magnetic Characterization Techniques for Nanomaterials*, ed. by C.S. Kumar (Springer, Berlin, 2017), pp. 261–303. https://doi.org/10.1007/978-3-662-52780-1_8
86. Z. Nemati, J. Alonso, I. Rodrigo, R. Das, E. Garaio, J.Á. García, I. Orue, M.H. Phan, H. Srikanth, J. Phys. Chem. C **122**, 2367 (2018). https://doi.org/10.1021/acs.jpcc.7b10528
87. A.G. Roca, L. Gutiérrez, H. Gavilán, M.E.F. Brollo, S. Veintemillas-Verdaguer, M. del Puerto Morales, Advanced Drug Delivery Reviews **138**, 68 (2019). https://doi.org/10.1016/j.addr.2018.12.008
88. O. Iglesias, A. Labarta, Phys. Status Solidi C **1**, 3481 (2004). https://doi.org/10.1002/pssc.200405485
89. O. Iglesias, A. Labarta, J. Magn. Magn. Mater. **290–291**, 738 (2005). https://doi.org/10.1016/j.jmmm.2004.11.358
90. B. Martínez, X. Obradors, L. Balcells, A. Rouanet, C. Monty, Phys. Rev. Lett. **80**, 181 (1998)
91. Animated snapshots of the configurations along the hysteresis loops can be found at the web site: http://www.ffn.ub.es/oscar/SCM2004/SCM2004.html
92. S. Krupricka, K. Zaveta, in *Magnetic Oxides*, ed. by D.J. Craik (Wiley-Interscience, New York, 1975)
93. J.K. Vassiliou, V. Mehrotra, M.W. Russell, E.P. Giannelis, R.D. McMichael, R.D. Shull, R.F. Ziolo, J. Appl. Phys. **73**, 5109 (1993)
94. J.L. Dormann, F. D'Orazio, F. Lucari, E. Tronc, P. Prené, J.P. Jolivet, D. Fiorani, R. Cherkaoui, M. Nogués, Phys. Rev. B **53**, 14291 (1996)
95. F. Gazeau, E. Dubois, M. Hennion, R. Perzynski, Y.L. Raikher, Euro. Phys. Lett. **40**, 575 (1997)
96. O. Iglesias, A. Labarta, Phys. Rev. B **63**, 184416 (2001)
97. R.N. Bhowmik, R. Nagarajan, R. Ranganathan, Phys. Rev. B **69**, 054430 (2004). https://doi.org/10.1103/PhysRevB.69.054430
98. O. Iglesias, A. Labarta, Physica B **343** (2004). https://doi.org/10.1016/j.physb.2003.08.109
99. P.V. Hendriksen, S. Linderoth, P.-A. Lindgard, J. Phys.: Condens. Matter **5**, 5675 (1993)
100. O. Iglesias, A. Labarta, Physica B **343**, 286 (2004)
101. J. Restrepo, Y. Labaye, L. Berger, J.M. Greneche, J. Magn. Magn. Mater. **272–276**, 681 (2004). https://doi.org/10.1016/j.jmmm.2003.12.719
102. J. Mazo-Zuluaga, J. Restrepo, F. Muñoz, J. Mejía-López, J. Appl. Phys. **105**, 123907 (2009). https://doi.org/10.1063/1.3148865
103. Y. Labaye, O. Crisan, L. Berger, J.M. Greneche, J.M.D. Coey, J. Appl. Phys. **91**, 8715 (2002). https://doi.org/10.1063/1.1456419
104. L. Berger, Y. Labaye, M. Tamine, J.M.D. Coey, Phys. Rev. B **77**(10), 104431 (2008). https://doi.org/10.1103/PhysRevB.77.104431
105. J.Z. Jiang, G.F. Goya, H.R. Rechenberg, J. Phys.: Condens. Matter **11**, 4063 (1999)
106. E. Tronc, D. Fiorani, M. Nogués, A.M. Testa, F. Lucari, F. D'Orazio, J.M. Grenèche, W. Wernsdorfer, N. Galvez, C. Chenéac, D. Mally, J. Jolivet, J. Magn. Magn. Mater. **262**, 6 (2003)
107. Animated snapshots of the configurations along the hysteresis loops can be found at the web site: http://www.ffn.ub.es/oscar/HMM2003/HMMM2003.html
108. H. Kachkachi, M. Dimian, Phys. Rev. B **66**, 174419 (2002). https://doi.org/10.1103/PhysRevB.66.174419
109. M.P. Morales, S. Veintesmillas-Verdaguer, M.I. Montero, C.J. Serna, A. Roig, L. Casas, B. Martínez, F. Sandiumenge, Chem. Mater. **11**, 3058 (1999)
110. S.h. Noh, W. Na, J.t. Jang, J.H. Lee, E.J. Lee, S.H. Moon, Y. Lim, J.S. Shin, J. Cheon, Nano Lett. **12**, 3716 (2012). https://doi.org/10.1021/nl301499u
111. S.K. Sharma (ed.), *Exchange Bias: From Thin Film to Nanogranular and Bulk Systems* (CRC Press, 2017). https://doi.org/10.1201/9781351228459

112. M.A. Willard, L.K. Kurihara, E.E. Carpenter, S. Calvin, V.G. Harris, Int. Mater. Rev. **49**, 125 (2004)
113. S.B. Darling, S.D. Bader, J. Mater. Chem. **5**, 4189 (2005)
114. Q.A. Pankhurst, J. Connolly, S.K. Jones, J. Dobson, J. Phys. D **36**, R167 (2003)
115. P. Tartaj, M.P. Morales, T. González-Carreño, S. Veintemillas-Verdaguer, C. Serna, J. Magn. Magn. Matter **290–291**, 28 (2005)
116. K.M. Krishnan, A.B. Pakhomov, Y. Bao, P. Blomqvist, Y. Chun, M. Gonzales, K. Griffin, X. Ji, B.K. Roberts, J. Mater. Sci. **793**, 793 (2006)
117. J. Nogués, I.K. Schuller, J. Magn. Magn. Matter **192**, 203 (1999)
118. A.E. Berkowitz, K. Takano, J. Magn. Magn. Matter **200**, 552 (1999)
119. J. Nogués, J. Sort, V. Langlais, V. Skumryev, S. Suriñach, J. Muñoz, M. Baró, Phys. Rep. **422**, 65 (2005)
120. G. Salazar-Alvarez, J. Sort, S. Suriñach, M.D. Baró, J. Nogués, J. Am. Chem. Soc. **129**, 9102 (2007). https://doi.org/10.1021/ja0714282
121. O. Iglesias, A. Labarta, X. Batlle, J. Nanosci. Nanotechnol. **8**, 2761 (2008)
122. A.E. Berkowitz, G.F. Rodriguez, J.I. Hong, K. An, T. Hyeon, N. Agarwal, D.J. Smith, E.E. Fullerton, Phys. Rev. B **77**, 024403 (2008). https://doi.org/10.1103/PhysRevB.77.024403
123. A. López-Ortega, M. Estrader, G. Salazar-Alvarez, A.G. Roca, J. Nogués, Phys. Rep. **553**, 1 (2015). https://doi.org/10.1016/j.physrep.2014.09.007
124. O. Iglesias, X. Batlle, A. Labarta, Phys. Rev. B **72**, 212401 (2005). https://doi.org/10.1103/PhysRevB.72.212401
125. Ò. Iglesias, X. Batlle, A. Labarta, J. Phys. D **41**, 134010 (2008). https://doi.org/10.1088/0022-3727/41/13/134010
126. M.H. Phan, J. Alonso, H. Khurshid, P. Lampen-Kelley, S. Chandra, K. Stojak Repa, Z. Nemati, R. Das, Ó. Iglesias, H. Srikanth, Nanomaterials **6**, 221 (2016). https://doi.org/10.3390/nano6110221
127. E. Tronc, D. Fiorani, M. Nogués, A.M. Testa, F. Lucari, F. D'Orazio, J.M. Grenéche, W. Wernsdorfer, N. Galvez, C. Chanéac, D. Mailly, J.P. Jolivet, J. Magn. Magn. Mater. **262**, 6 (2003)
128. M.P. Morales, S. Veintemillas-Verdaguer, M.I. Montero, C.J. Serna, A. Roig, L. Casas, B. Martínez, F. Sandiumenge, Chem. Mater. **11**, 3058 (1999)
129. O. Iglesias, A. Labarta, Phys. B **372**, 247 (2006). https://doi.org/10.1016/j.physb.2005.10.059
130. D. De, O. Iglesias, S. Majumdar, S. Giri, Phys. Rev. B **94**, 184410 (2016). https://doi.org/10.1103/PhysRevB.94.184410
131. H.K.D.A. Garanin, L. Reynaud, Europhys. Lett. **82**, 17007 (2008)
132. D.A. Garanin, H. Kachkachi, Phys. Rev. B **80**, 014420 (2009)
133. R. Bastardis, F. Vernay, D.A. Garanin, H. Kachkachi, J. Phys. C: Condens. Matter **29**, 025801 (2017)
134. R. Bastardis, F. Vernay, H. Kachkachi, Phys. Rev. B **98**, 165444 (2018). https://doi.org/10.1103/PhysRevB.98.165444

Chapter 2
Interparticle Interactions: Theory and Mesoscopic Modeling

Marianna Vasilakaki, George Margaris, and Kalliopi Trohidou

Abstract In this chapter, we discuss the interparticle interaction effects in assemblies of magnetic nanoparticles. For our study, we have developed a mesoscopic scale model that takes into account: (a) the morphology of the assemblies and (b) the interplay between the interparticle and intra-particle characteristics of the nanoparticles. The hysteresis loops, the virgin magnetization curves and the temperature-dependent (Field Cooled (FC)/zero-field cooled (ZFC)) magnetization curves have been calculated with our model. Results are presented for three case studies of different nanoparticles' morphologies assemblies and they show that our mesoscopic model reproduces well the experimentally studied systems and reveals the origin of the observed magnetic behavior.

2.1 Introduction

Magnetic nanoparticles are commonly formed in random or ordered assemblies. Ferrofluids [1] and granular magnetic solids are usually characterized as random nanoparticle assemblies while patterned media and self-assembled arrays [2] are described as ordered ensembles. The crucial role in determining the magnetic behavior of both types of assemblies is played by the interparticle interactions, namely the long-range dipolar interactions and the short-range exchange interactions for nanoparticles in contact which are usually meet in the random assemblies. It has been demonstrated that the presence of interparticle exchange interactions changes the physical properties of a nanoparticles system [3]. If the strength of the interparticle interactions is relatively weak, namely the interparticle energy is much lower than the individual particle anisotropy energy, the interparticle interactions are considered just a perturbation to the superparamagnetic state; this leads to the so-called interacting superparamagnet model [4], where the static and dynamical

M. Vasilakaki · G. Margaris · K. Trohidou (✉)
Institute of Nanoscience and Nanotechnology, NCSR Demokritos, 15310, Aghia Paraskevi, Attiki, Greece
e-mail: k.trohidou@inn.demokritos.gr

D. Peddis et al. (eds.), *New Trends in Nanoparticle Magnetism*,
Springer Series in Materials Science 308,
https://doi.org/10.1007/978-3-030-60473-8_2

properties of the individual particles are only partially modified by the interaction with the neighboring particles. On the other hand, if the interparticle interactions are strong and randomness in the distribution of particle positions and in the anisotropy axes orientation exists, then a collective super spin glass state (SSG) is formed. This SSG state is observed in concentrated frozen ferrofluids [5] and in concentrated granular systems where single-domain particles are dispersed in a non-magnetic matrix [6, 7].

Various experiments demonstrated that the presence of dipolar interactions results to: (a) a reduction of remanence at low temperature and of the coercive field [8], (b) an increase of the blocking temperature (T_B) defined as the temperature that corresponds to the maximum of ZFC magnetization curve [9], (c) an increase of the energy barrier distribution width [9], (d) deviations of the ZFC magnetization curves from the Curie behavior [10], (e) differences between in-plane and out-of-plane remanence, and (f) an increase of the blocking temperature with the frequency of the applied field [11]. The first model that studied the magnetic interaction effects on the coercivity was presented by Néel [12] and it was generalized by Wohlfarth [13] taking into account the orientations and the geometrical arrangement of the particles. According to this model, the coercive field decreases with the increase of the particle concentration. Later, a detailed study on the effect of interparticle interactions was reported by Dormann et al. [14] where it was demonstrated that the total energy barrier increases with the dipolar interactions Monte Carlo simulations studies [15] confirmed the increase of the blocking temperature of a dipolarly interacting system with the increase of the concentration and that the magnetic properties of randomly located and oriented nanoparticle systems are determined by the interplay between the single-particle anisotropy energy and the dipolar interaction energy. Indeed, it has been demonstrated that the dense face-centered cubic (FCC) packing of the particles leads to more pronounced ferromagnetic (FM) behavior than the simple cubic (SC) packing; this behavior is characterized by FM domains of supermoments of particles, the so-called superferromagnetism [16]. The sample free boundaries and the corresponding demagnetizing field have also a strong effect on the remanence of the assembly while they produce a minor reduction to the coercivity [15]. Later, Lu et al. by performing MC simulations found that the coercive field (H_C) can be increased or decreased with dipole–dipole interactions, depending on the bonding angle between the easy axes of the nanoparticles [17]. On the other hand, Vargas et al. claimed that demagnetization role of dipole–dipole interactions reduces the H_C of the system [8]. However, Nadeem et al. observed an enhancement in H_C and blocking temperature of compacted Fe_3O_4 nanoparticles compared with the powder sample [18]. They attributed this result to the highlighting effect of interparticle interactions on the energy barrier between equilibrium states.

Overall, it becomes evident that the magnetic characteristics (hysteresis loops, blocking temperatures) of an assembly of magnetic nanoparticles depend not only on the strength of the interactions but also on the morphology of the samples [19].

In the recent years, the effort to reduce the nanoparticle size and at the same time to achieve high magnetic anisotropy led to the production of bi-magnetic nanoparticles with enhanced nanoparticle anisotropy due to the extra unidirectional anisotropy

along the interface called "exchange bias" [20]. In these structures, the interplay between internal nanoparticle structural characteristics and interparticle interaction leads to enhanced or novel magnetic properties [21, 22]. MC simulations have shown that in random assemblies of ferromagnetic (FM)/antiferromagnetic (AFM) nanoparticles, the exchange interparticle interactions play a major role causing the experimentally observed increase in the H_C and the exchange bias field H_{ex} with the concentration of the nanoparticles [21]. Therefore, the modification of the coercive and the exchange bias field in assemblies of nanoparticles with core/shell morphology, which results from the competition between the intra-particle exchange anisotropy and interparticle interactions, is a challenging issue. It is evident that the basic understanding of the magnetic properties of random assemblies of bi-magnetic nanoparticles is of crucial importance for the next generation of high performance magnetic nanomaterials.

Importantly, the improved production techniques enable the production of ultra-small nanoparticles below 5 nm in size. For these sizes, it has been demonstrated experimentally and numerically that the particle surface plays the dominant role in their magnetic behavior. Therefore, surface effects have to be taken explicitly into account in the calculations, in order to understand the magnetic properties of the assemblies [7].

Another factor that influences the magnetic behavior of the nanoparticles is the assembly's structure. For instance, clustering of nanoparticles in an assembly can be achieved by bringing magnetic nanoparticles at distances where they can strongly interact. In this case, either colloidal assemblies are produced and capping with molecules prevents the exchange coupling between them [23–25], or nanoparticles (NPs) are created by deposition techniques that they do not allow them to coalesce but retain a distinct boundary with a significant free volume among aggregates of exchange coupled particles [26]. Their observed magnetic behavior has been analyzed through numerical modeling, revealing interesting effects like stepwise behavior in the hysteresis loops and the virgin magnetization curves [27, 28].

Finally, there is experimental evidence that diluted assemblies of magnetic nanoparticles in a magnetic matrix exhibit exchange bias behavior and dynamical effects. Indeed, a diluted assembly of Co nanoparticles randomly embedded in magnetically and structurally disordered Mn matrix [29–31] shows enhanced exchange bias field and SSG state. These characteristics are attributed to the intra-particle characteristics, namely the Co/Mn alloying at the surface of Co nanoparticles, that create strong exchange interaction at the Co/Mn interface, and to the granularity of the matrix in mediating interparticle interactions, through exchange and dipole–dipole coupling between the uncompensated moments of Mn grains, as they are confirmed by Monte Carlo simulations [32].

Atomic scale modeling of assemblies of magnetic nanoparticles including interparticle interactions, especially for dense samples, demands a very big amount of CPU memory and time. For this reason, the single-spin treatment of the Stoner Wohlfarth (SW) coherent rotation model [33, 34] was usually implemented in the study of assemblies of magnetic nanoparties. However, in the recent years, modeling assemblies of ultra-small nanoparticles where core/shell or core/surface morphology affects

greatly their magnetic behavior becomes an excessively complicated computational issue, since the single-spin treatment becomes insufficient to describe their magnetic structure. We have developed a novel mesoscopic scale model for the study of these nanoparticle systems that consider more than one macrospin for the description of each nanoparticle together with the interparticle interactions [7, 21]. Our model gives the possibility for explicit treatment of all the regions inside each nanoparticle, namely the core, the shell, the core/shell interface and the surface [21, 35]. As we will describe below, the number of the effective spins for each nanoparticle depends on the characteristics of the studied system.

The Monte Carlo (MC) simulation technique with the implementation of the Metropolis algorithm [36, 37] has been proven a very powerful and reliable tool for the systematic study of the magnetic behavior of nanoparticle systems at finite temperature. Especially in the case of NPs with core–shell or core–surface morphology, the technique is advantageous because it gives the possibility to take into account explicitly the regions of each nanoparticle, so the details of their internal structure can be studied together with the interparticle interactions using the suitable mesoscopic model. The appropriate choice of a model Hamiltonian is the starting point of MC simulations, and then the random number generator is used to calculate statistical fluctuations in order to generate the correct thermo-dynamical probability distribution simulating a canonical ensemble [37].

In this chapter, we present for three cases our work on the magnetic behavior of assemblies of nanoparticles using numerical modeling. We describe in our mesoscopic model that takes into account: (a) the morphology of the macroscopic assemblies and (b) the interplay between the interparticle interactions and the intraparticle characteristics of each nanoparticle. For the numerical modeling of these systems, we use the Monte Carlo simulation technique with the implementation of the Metropolis algorithm [3] that includes explicitly the temperature. The characteristics of the hysteresis loops, magnetization curves as a function of the applied field and the temperature-dependent ZFC/FC magnetization are studied. A comparison with experimental findings is given in all cases.

2.2 Case Studies

2.2.1 Case Study 1: Magnetic Behavior of Nanoparticle Assemblies: Interplay of Nanoparticles Morphology (Core/Surface and Core/Shell) with the Interparticle Interactions

Here, we review our work on dense assemblies of nanoparticles where the nanoparticle's morphology is taken into account. We present results on (a) ferrite nanoparticles with core/surface morphology, more specifically for spherical γ-Fe_2O_3 nanoparticles covered with an organic surfactant in the case that only dipolar interparticle

interactions are present, and (b) on bi-magnetic nanoparticles with Co core/CoO shell morphology.

2.2.1.1 The Model

Despite the importance of interparticle interactions, atomic scale Monte Carlo approaches have been inadequate to simulate assemblies of nanoparticles with core/shell or core/surface morphology due to the prohibitively large computational requirements, since each nanoparticle includes a few hundreds up to a few thousands of spins. For this purpose, we have developed a simple mesoscopic model to simulate the magnetic properties of assemblies of magnetic nanoparticle, taking into account their internal structure, namely core/shell or core/surface morphology. Our mesoscopic method was based on the reduction of the amount of simulated spins to the minimum number necessary to describe the magnetic structure of the particles and on the introduction of the adequate exchange and anisotropy parameters between the different spin regions inside the nanoparticle. Our modeling is multi-scale because the magnetic moments are evaluated using data from our atomistic simulations of the core/shell nanoparticles [38], with the appropriate rescaling [21]. Then, we integrate them properly into the mesoscopic model going in this way from the atomic scale to the mesoscopic modeling.

Our model goes beyond the classical model of coherent rotation of a particle's magnetization of Stoner–Wohlfarth [33] in which each nanoparticle is described by a classical spin vector ($\boldsymbol{s}_i$). Here, each nanoparticle in the assembly is described by a set of three classical spin vectors one for the core and two for the two sublattices of the AFM or ferrimagnetic (FiM) shell or surface. The values of the different parameters in the simulation are set on the basis of their bulk values, if they exist, and their modifications are established considering the nanoparticles' morphology (e.g., reduced symmetry and reduced size) using a mean field approach and the data from atomistic simulations wherever it is possible. We have to note here that "surface" describes a layer of thickness approximately one lattice constant of the same material as that of the core and very high anisotropy while the term "shell" corresponds to a thicker layer that includes also the surface layer and it consists of a different material than that of the core. The core/shell model includes also interface effects.

In what follows, we consider an assembly of N bi-magnetic nanoparticles with FM core/AFM shell morphology or of N ferrimagnetic nanoparticles with core/surface morphology. These nanoparticles are spherical in shape with diameter d and they are located randomly at the nodes of a simple cubic lattice of lattice constant, a, inside a box of edge length $L\alpha$. Each nanoparticle is described by a set of three classical spin vectors, one for the core $\vec{\boldsymbol{s}}_{\mathbf{1}i}$ and two for the shell or the surface $\vec{\boldsymbol{s}}_{\mathbf{2}i}$ and $\vec{\boldsymbol{s}}_{3i}$ $i = 1, \ldots, N$ (total number of particles), with magnetic moments $m_n = M_n V_n / M_s V$, $n = 1$ stands for the core and $n = 2{,}3$ for the "up" and "down" shell or surface sublattices of the nanoparticle, respectively. V is the particle volume and M_S its saturation magnetization. V_n and M_n are the volume and the saturation magnetization of the core, the "up" and the "down" shell or surface sublattice spins.

Each spin has a uniaxial easy anisotropy axis with a certain orientation. Depending on the model, the three spins can have either one or two (different for the core spin) common randomly oriented anisotropy axes or each of the three spins can have each own randomly orientated anisotropy axis.

The total energy of the system for the N nanoparticles is:

$$
\begin{aligned}
E = & -\frac{1}{2}\sum_{i=1}^{N}\left[J_{c1}(\vec{s}_{1i}\cdot\vec{s}_{2i}) + J_{c2}(\vec{s}_{1i}\cdot\vec{s}_{3i}) + J_s(\vec{s}_{2i}\cdot\vec{s}_{3i})\right] \\
& - \sum_{i=1}^{N} K_c V_1\left(\vec{s}_{1i}\cdot\hat{e}_{1i}\right)^2 - \sum_{i=1}^{N} K_s\left[V_2\left(\vec{s}_{2i}\cdot\hat{e}_{2i}\right)^2 + V_3\left(\vec{s}_{3i}\cdot\hat{e}_{3i}\right)^2\right] \\
& - \frac{1}{2}g\sum_{i,j=1_{i\neq j}}^{N}\left(\sum_{n=1}^{3} m_{ni}\vec{s}_{ni}\right)D_{ij}\left(\sum_{n=1}^{3} m_{nj}\vec{s}_{nj}\right) \\
& - \frac{1}{2}J_{\text{inter}}\sum_{i=1}^{N}\sum_{\langle i,j\rangle}\left[\left(\vec{s}_{2i}\cdot\vec{s}_{3j}\right) + \left(\vec{s}_{3i}\cdot\vec{s}_{2j}\right)\right] - \sum_{i=1}^{N}\sum_{n=1}^{3} H m_{ni}\left(\vec{s}_{ni}\cdot\hat{e}_h\right) \qquad (2.1)
\end{aligned}
$$

The first and the second energy term describe the Heisenberg exchange interaction between the core spin and the two spins of the shell (or the surface) with exchange coupling strength J_{c1} and J_{c2}. The third energy term describes the Heisenberg exchange interaction between the two sublattice spins of the shell (or the surface) with exchange coupling strength J_s. The fourth and the fifth terms give the anisotropy energy for the core and the shell or surface ($\hat{e}_{1i}$, $\hat{e}_{2i}$, $\hat{e}_{3i}$ being the anisotropy easy-axis direction) with anisotropy strength K_c and K_s. The sixth term gives the dipolar interactions among all spins in the assembly where the magnetic moments of the three "macrospins" of each ith particle are defined as $m_{1i} = M_1V_1/M_sV$, $m_{2i} = M_2V_2/M_sV$, and $m_{3i} = M_3V_3/M_sV$, and D_{ij} is the dipolar interaction tensor [21]. The dipolar energy strength is defined as $g = \mu_0(M_SV)^2/4\pi d^3$ where d is the smallest distance between two nanoparticles equal to the particle's diameter d, V is the particle volume and M_S its saturation magnetization. For the dipolar energy calculation, the Ewald summation technique [21] has been implemented taking into account the long-range character of the dipolar interactions, using periodic boundaries in all directions. The next term exists only for those nanoparticles that are in physical contact. It describes the interparticle exchange interactions with coupling constant strength J_{inter}. The $\langle i, j\rangle$ denotes summation over nearest neighbors. This term refers to the interaction between the surface spins of the particles into contact for the ones with core/surface morphology, while for the bi-magnetic nanoparticles with a FM core surrounded by an AFM thin shell, this exchange terms additionally describe the exchange interaction between the core spins with the neighboring surface spins. The last term is the Zeeman energy ($\hat{e}_h$ being the direction of the magnetic field). The external magnetic field is H. The thermal energy is k_BT (where T is the temperature).

The above energy parameters, as they are entered into the simulations, have been normalized by a proper factor 10 K_cV that is the core volume anisotropy

of the nanoparticle, so they are dimensionless. Therefore, the normalized reduced anisotropy constants are k_c for the core, k_{shell} for the shell anisotropy or k_{srf} for the surface anisotropy. The effective exchange coupling constants between the core spin and the shell or the surface spins are $j_{c1}, j_{c2}, j_{shell}$ or j_{srf} and between the neighboring particles in contact j_{inter}. In what follows, we denote by H the reduced magnetic field, by g the reduced dipolar strength, by T and T_B the reduced values of the temperature and the blocking temperature respectively.

The calculation of the zero-field cooled (ZFC)/Field Cooled (FC) magnetization curves is a three steps process. First, we cool the system at a constant temperature rate ΔT from a high temperature, well above the ordering temperature, down to a very low temperature, close to zero temperature, at zero applied field. Then, we heat the sample from the low temperature to the high one at the same constant temperature rate applying a small magnetic field and we calculate the ZFC magnetization curve. Finally, we cool the system down to the lowest temperature, in the presence of the applied magnetic field, and we calculate the FC magnetization curve. The hysteresis loops are calculated after a field cooling procedure.

The Monte Carlo simulations results for a given temperature and applied field were averaged over 60–80 samples with various spin configurations, realizations of the easy-axes distribution and different spatial configurations for the nanoparticles.

2.2.1.2 Results and Discussion

(a) **Dipolarly interacting assemblies of ferrimagnetic nanoparticles with core/surface morphology**

Maghemite (γ-Fe_2O_3) nanoparticles of ~12.7 nm size covered by polyacrylic acid (PAA) surfactant were produced with volume fraction $x = 0.47$ [27]. Our mesoscopic model simulates this system as N identical spherical ferrimagnetic NPs of diameter $d = 13$ nm being located randomly at the nodes of a simple cubic lattice with lattice constant, a, inside a box of edge length $L = 10$ measured in units of a. The total number of NPs is $N = p \times (10\ a \times 10\ a \times 10\ a)$, where $p = 0.47$ is the concentration of the particles in the model. In accordance with the experimental findings, we consider core/surface morphology for each nanoparticle and we describe it by three spins with a common anisotropy easy axis. However, this axis is assumed to be randomly oriented from particle to particle. In addition, the parameters of the surface anisotropy (K_S) and magnetic moment (m) per particle were rationally chosen upon consideration of (a) the morphology of the NPs that is not completely spherical and (b) the approximate thickness of the surfactant layer, which appears to influence the degree of the defected surface coordination environment; the thicker the surface coordinating organic layer is, the lower the disorder of the uncompensated surface spins becomes [39]. Effectively, we consider a common anisotropy easy axis for spins in each nanoparticle resulting to a higher saturation magnetization, M_s than the corresponding bulk value [40] as observed experimentally [27].

The main parameters used in MC simulations are: $p = 0.47$ the particle concentration introduced in the model, $g = 0.884$ the dipolar energy strength, $m = 1.17$ the mean particle magnetic moment. Accordingly, the values of the intra-particle exchange energy among the core spin and the surface spins were taken as $j_{c1} = -7.77, j_{c2} = -1.35, j_{\text{srf}} = -0.091$ and the anisotropy energy of the core as $k_C = 0.1$, while that of the surface as $k_{\text{srf}} = 3.5$, since it is expected to be more than one order of magnitude larger than that of the core. These parameters are dimensionless as they are normalized by 10 $K_C V$. The particles in the assembly interact only through dipolar interactions since they are coated with the PAA surfactant ($j_{\text{inter}} = 0$) no interparticle exchange interactions are considered in our model.

We have performed MC simulations to calculate the hysteresis loops and the zero-field/field cooled (ZFC/FC) magnetization curves of the dense maghemite nanoparticles (Fig. 2.1). To get a better insight of the factors that influence the magnetic behavior of the system, we have first "switched off" the dipolar inerparticle interactions (Fig. 2.1) and next the intra-particle interaction term of the system (Fig. 2.2)

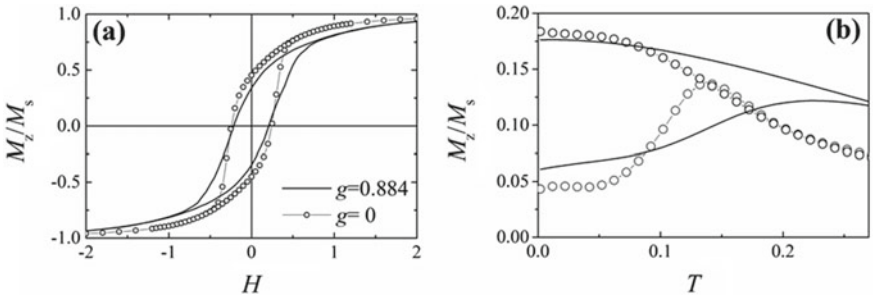

Fig. 2.1 Monte Carlo simulations of the isothermal magnetization curves at $T = 0.05$ (**a**) and ZFC/FC magnetization curves (**b**) for $p = 0.47$ for the dipolarly interacting nanoparticles ($g \neq 0$; full line) and in the case that the dipolar interactions are switched off ($g = 0$; line with circles)

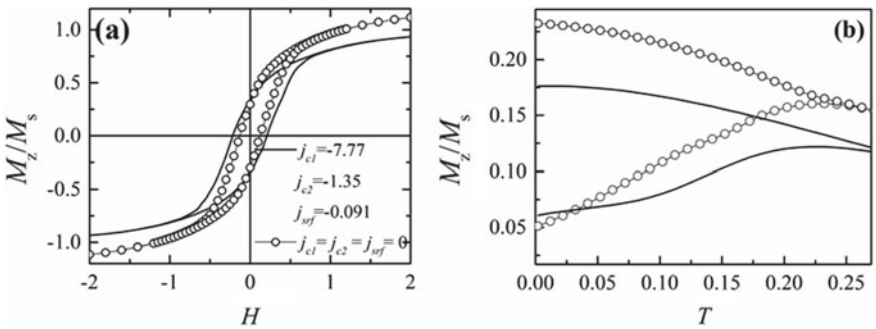

Fig. 2.2 MC simulations of the isothermal magnetization curves at $T = 0.05$ (**a**) and ZFC/FC magnetization curves (**b**) for $p = 0.47$ for the original model ($j_{c1}, j_{c2}, j_{\text{srf}}$ nonzero; lines) and in the case that the intra-particle interactions are switched off ($j_{c1} = j_{c2} = j_{\text{srf}} = 0$; circles)

and we have calculated the hysteresis loop and the ZFC/FC magnetization curves together with the fully interacting system.

As we can see from Fig. 2.1, when the dipolar strength is zero, consequently only the intra-particle exchange interactions and the anisotropy energy term contribute to the total energy, the blocking temperature of the non-interacting particle system decreases (Fig. 2.1b). The characteristics of the ZFC/FC magnetization curves (Fig. 2.1b) also indicate the movement from the super spin glass nanoparticle system to a non-interacting blocked assembly of nanoparticles. The coercive field does not seem to be affected, probably due to the strong competition between the intra-particle exchange coupling and the surface anisotropy.

On the other hand, in the absence of intra-particle interactions ($j_{c1} = j_{c2} = j_{srf} = 0$) (Fig. 2.2), the spins inside each nanoparticle do not interact with each other; thus, this frustration does not exist and the coercivity is decreased. The blocking temperature also is slightly decreased. Our results are in agreement with the experimental findings [27].

(b) **Core/shell nanoparticle dense assemblies interacting with dipolar and exchange interparticle interactions**

Next, we study the magnetic behavior of dense random assemblies of FM core/AFM shell nanoparticles. In this case, we take into account the interparticle dipolar and exchange interactions. The simulations are based on Co/CoO (FM/AFM) nanoparticles with 6 nm total diameter and a thin antiferromagnetic shell (~1 nm). Considering a dense assembly of Co/CoO nanoparticles with very thin CoO layer, we develop a three-spin model for the Co/CoO nanoparticle to simulate dense 2D and 3D assemblies [21, 41]. In each nanoparticle, the FM core was described by one spin and two spins described the thin AFM shell with the appropriate anisotropy ($k_c = 0.1$, $k_{shell} = 8.0$) and exchange parameters ($j_{c1} = 0.32, j_{c2} = 0.3, j_{shell} = -6$). The anisotropy axes of each nanoparticle were randomly oriented, one for the core and one common for the shell. The interparticle dipolar strength was taken as $g = 0.1$. If the nanoparticles are in direct contact, the interparticle exchange interactions are considered also between the core spins and the neighboring surface spins due to the very small shell thickness. Thus, additionally to the exchange coupling of the neighboring surface spins that is characterized by the strength parameter $j_{inter} = 2.5$, we consider also the exchange interaction of the core spin of the one nanoparticle with the surface spins of the other nanoparticle with strengths $j_{coreshell1} = 2.0$, $j_{coreshell2} = 0.5$. The interparticle exchange interactions in these systems are particularly strong.

We have demonstrated in Margaris et al. [21] the effectiveness of our mesoscopic method based on a Monte Carlo approach to simulate 2D large ensembles of bimagnetic core/shell nanoparticles and their important role on the exchange bias behavior of these system. Our MC simulation results of the effect of the exchange interactions on the exchange bias are in excellent agreement with the experimental results in the study of 2D random assemblies of Co/CoO core/shell nanoparticles [21]. Here, we simulate disordered arrays of nanoparticles where N particles are placed, randomly, on the nodes of a 3D cubic lattice inside a box of edge length $L = 10a$. We simulate the hysteresis loops (Fig. 2.3a, c) at $T = 0.02$ and the temperature

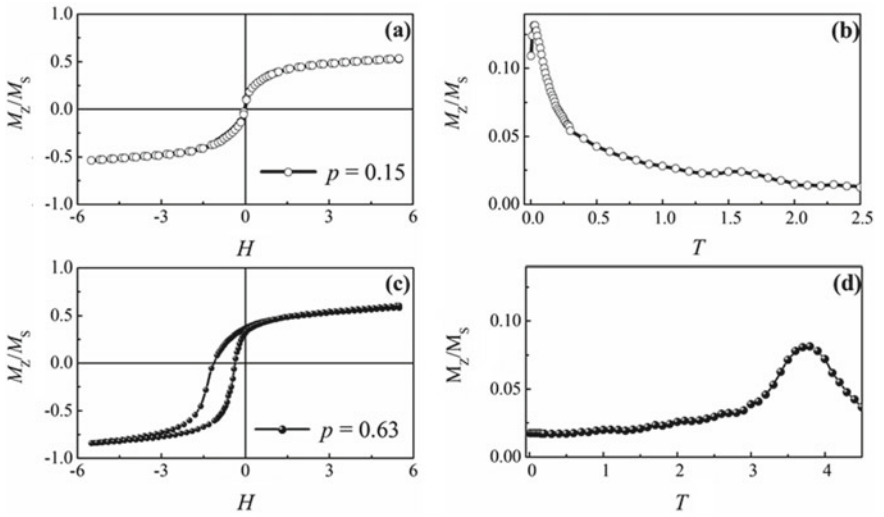

Fig. 2.3 **a**, **c** MC normalized hysteresis loops of 3D random arrays of Co/CoO core/shell nanoparticles with densities $p = 0.15$ and 0.63 at $T = 0.02$. **b**, **d** MC results for the ZFC temperature-dependent magnetization curves for the two densities

dependence of the magnetization, $M(T)$ (Fig. 2.3b, d) of a 3D random assembly of Co/CoO core/shell nanoparticles with concentrations $p = 0.15$ and 0.63 [3].

Our results gave a significant increase of both H_C and H_{ex} for the large concentration of nanoparticles. The most remarkable feature is that H_{ex} has larger value than H_C for $p = 0.63$. This is opposite from the $p = 0.15$ case. The increase in coercive and exchange bias field is due to the fact that as the number of particles increases, they come very close and they are in contact, consequently the "effective thickness" of the AFM layer increases. Namely, each core instead of "feeling" one shell, it "feels" two shells, thus the effective anisotropy energy increases. This "increase" in the AFM effective thickness leads to an enhancement of H_{ex} and H_C similar to what is observed for thin-film systems. Moreover, whereas the hysteresis loop appears rather symmetrical for $p = 0.15$, it is asymmetric for $p = 0.63$. Our results of 3D cubic lattice have the same features with those of the 2D square lattice [21]. The only difference is that in the 3D case, the effects are more pronounced because the number of nearest neighbor particles is increased from four (square lattice) to six (cubic lattice) so the strength of the interparticle interactions is larger.

Similarly, the results for ZFC the magnetization versus temperature *M(T)* show that for higher densities, the blocking temperature T_B increases dramatically, in agreement with experiments [42]. Furthermore, although the blocking temperature for the low concentration case is very low as in the 2D case ($T_B = 0.27$), for higher density $p = 0.63$ the $T_B = 3.77$ is larger than the case of 2D lattice ($T_B = 2.35$).

Importantly, the observed behavior is attributed to interparticle exchange interactions in the assembly and it is more pronounced in the 3D cubic lattice. Indeed, if

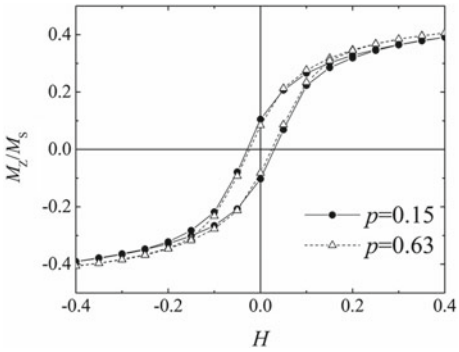

Fig. 2.4 MC simulations of the normalized hysteresis loops with $H_{\text{cool}} = 0.05$ of 3D random arrays of Co/CoO core/shell nanoparticles for $p = 0.15$ and 0.63, by switching off interparticle exchange interactions ($j_{\text{out}} = 0$) and for $g = 1$

we "switch off" the interparticle exchange interactions, (i.e., $j_{\text{out}} = 0$), but we keep the dipolar interactions, the behavior is completely different. Namely, in the pure dipolar case, the increase in the nanoparticle concentration leads to the decrease in H_C and H_{ex} due to the competition between anisotropy and dipolar energy (Fig. 2.4). Consequently, the exchange interparticle interactions in dense assemblies change the overall energy profile causing the increase in exchange and coercive field and blocking temperature. Obviously, the interplay between interparticle and intra-particle energies produces a complex magnetic behavior depending on the system.

2.2.2 *Case Study 2: Magnetic Behavior of Nanoparticle Assemblies: Effect of Assemblies Morphology (Nanoparticles Clustering)*

The combination of interparticle interactions and the assembly's morphology modifies the magnetic behavior of dense assemblies of nanoparticles with concentration well above the percolation threshold. The clustering between the nanoparticles has been studied with mesoscopic modeling [26–28, 43]. We examine two cases: (a) Dense assembly of Fe nanoparticles assembly: in this case, the Fe nanoparticles are forming tightly coupled clusters, some clusters are so close to each other that they are also exchange coupled and some of them are well separated and only dipolarly coupled, (b) maghemite nanoparticles which are forming well-separated clusters dipolarly coupled. In the latter case, each nanoparticle in the cluster has core/surface morphology structure.

2.2.2.1 The Model

We have developed a model of a non-uniform assembly of NPs with density well above the percolation threshold that includes explicitly the nanoparticles anisotropies, the dipolar interactions and the interparticle exchange interactions in case of nanoparticles that are in close contact, as it is described in Sect. 2.1.1. We are using the Monte Carlo simulations technique based on the Metropolis algorithm, to simulate a dense, random assembly of clusters of (a) Fe nanoparticles (Fig. 2.5 [28]) and (b) γ-Fe_2O_3 nanoparticles coated with organic surfactant in order to investigate the role of the assemblies morphology in the determination of their magnetic behavior.

In order to reproduce clusters of nanoparticles and isolated particles, we divide the lattice in eight areas of equal size but of different particle concentration in each area, under the constraint that the total concentration will be that of the assembly. So the condition $p = \left(\sum_{i=1}^{n_a} p_i N_i\right)/N$ must be held, where $n_a = 8$ is the number of areas and N_i and p_i are the number of lattice sites and partial concentration in each area, respectively. As a result of the different concentrations in the areas, clusters of different sizes are formed in each of them.

For example, for the concentration $p = 0.5$, we are well above the percolation threshold of the simple cubic lattice ($p_c = 0.3116$) [44]. Some of these areas will be dense and some diluted with partial concentrations smaller than the percolation threshold, so in some of them, more than one clusters will be formed. The number of the nearest neighbors of each particle (z_i) is a random variable and the average value in each area is different and depends on its concentration ($z_{i,\,avg} = 6\,p_i$).

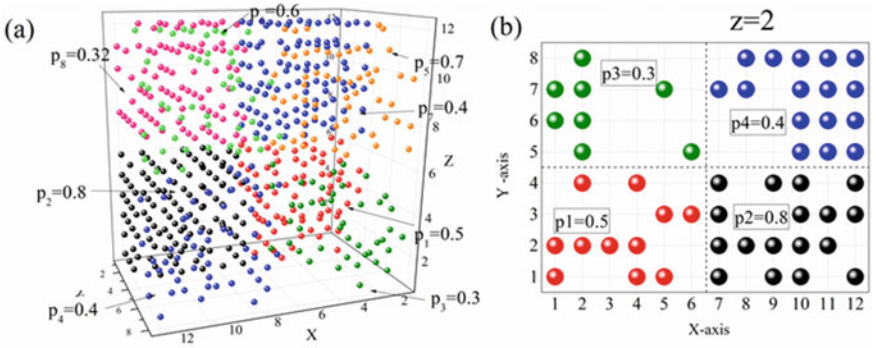

Fig. 2.5 Schematic representation of the non-uniform assembly of NPs. **a** The three-dimensional sketch of the non-uniform assembly of NPs. **b** Two-dimensional vertical intersection of the non-uniform assembly at the $z = 2$ plane [28]

2.2.2.2 Results and Discussion

(a) **Effect of the clustering on Fe nanoparticle assemblies**

Here, the role of the interparticle interactions and of the system's morphology in the magnetic behavior of dense assemblies of Fe nanoparticles is studied. To model the system, we consider N identical magnetic particles (grains) with spherical shape and diameter $d = 2.6$ nm. The magnetic particles are single domain, and we represent each of them as a three-dimensional classical unit spin vector with magnetic moment m_i (i $= 1, \ldots, N$). To each particle, a uniaxial easy axis is assigned, randomly distributed and its anisotropy constant equals to 1 in dimensionless units. In our study, the Fe particles produced by femtosecond pulsed laser deposition (fsPLD) + UV systematically show a disk-like shape, giving rise to a higher magnetic anisotropy, enhanced by shape and surface contributions. Also, the average saturation magnetization M_s of the NP is expected to have a value smaller than the bulk iron value ($M_{s,Fe} = 1.7 \times 10^6$ A/m), due to surface effects. Taking into account the above considerations, we expect that the dipolar interaction strength for the NPs is much smaller than the iron value for a spherical NP with $d = 2.6$ nm ($g_{Fe} \sim 0.6$). So here, we consider $g = 0.1$ [28].

We divide the lattice in eight areas with size $L_x \times L_y \times L_z = 6 \times 4 \times 6$ each and a different particle concentration p_i in each one of them, but under the constraint that the total concentration will be $p = 0.5$. We consider that each particle interacts with exchange forces of the same strength with a nearest neighbor, if they both belong in the same area. More specifically, p_i takes the values 0.50, 0.80, 0.30, 0.40, 0.70, 0.60, 0.40 and 0.30 in each of the eight areas, respectively. In the denser areas ($p_i \geq p$), the intra-cluster exchange interaction is $j_{inter} = 1.0$ and in the more diluted ones ($p_i < p$) is $j_{inter} = 8.0$ because, in this case, the whole cluster is considered to represent a bigger isolated particle. The exchange interaction strength between neighboring particles in different clusters is taken $j_{inter} = 0.1$. In general, we assume a small intercluster exchange constant which allows the cluster moments to be initially randomly oriented.

To study the magnetic behavior of the system, we calculate numerically [28] the virgin curve (VC), where we plot the normalized magnetization as function of the field, and the ZFC/FC magnetization curves, where the normalized magnetization is plotted as a function of the temperature. The calculated quantity is the normalized magnetization along the field direction, which is the z-axis direction,

$$M_z/M_s = \frac{1}{N M_s V} \sum_{i=1}^{N} m_{iz} = \frac{1}{N} \sum_{i=1}^{N} s_{iz} \tag{2.2}$$

The simulation of the VC starts from the zero field at a given temperature. In the initial configuration, the spins are randomly oriented. The field is increased gradually until the assembly magnetization reaches saturation (M_z/spin ~ 1). The simulations are repeated at two different temperatures. The simulations of the ZFC/FC magnetization versus temperature curves are also performed.

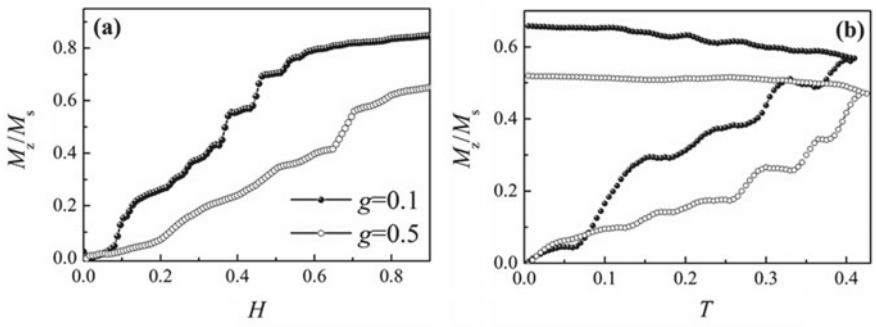

Fig. 2.6 Assembly of NPs interacting with two different dipolar interaction strengths g (assembly concentration $p = 0.5$). **a** Initial magnetization versus H curves (VC) at temperature $T = 0.005$ and **b** ZFC/FC magnetization versus T curves with $H_{\text{cool}} = 0.05$ [28]

We have to note that the strong effective interparticle exchange coupling ($j_{\text{inter}} \geq 1$) in an area and the uniaxial anisotropy result in a nonzero initial magnetization in each area even in the absence of a field, after a few steps. This fact and the small number of areas may result to an initial average value of the magnetization different from zero. This deviation is of the order of $1/2\sqrt{n_a}$ ($= 0.176$ for $n_a = 8$), under the condition that the interaction strength between the areas is weak. When the exchange interaction between particles in the different clusters is strong, the initial magnetization raises and specific initial configurations have to be chosen to reduce the problem [45].

The role of the dipolar strength in the magnetization behavior of the assembly is examined next, in the case of a dense non-uniform assembly ($p = 0.5$). Dipolar interactions give rise to collective effects [18]. As the dipolar coupling increases, dipolar interactions start playing a more important role, start competing initially and gradually dominating over the exchange interactions and the anisotropy. In this case, we have a slower increase of the magnetization at low fields and a slower approach to saturation in the virgin curve (Fig. 2.6a). The local dipolar field is the sum of the fields of all the randomly oriented dipoles and oscillates randomly on every node. As a result, in some cases, reversals of clusters may create locally large dipolar fields, helping other spins or clusters to overcome their energy barrier and triggering their reversal more easily. These local fluctuations are larger as the dipolar strength increases. Consequently, smaller steps are present, at different positions as the value of g increases (Fig. 2.6a and b). It is expected that with the increase of the dipolar strength, we have an increase in the maximum of the ZFC magnetization versus temperature curve [28].

We compare our results with those of the uniform morphology for the nanoparticles' assembly. In this case, we distribute the particles at random on the nodes of the lattice with occupation probability $p = 0.5$. All particles interact via exchange interaction of the same strength and dipolar interactions. In the case that the exchange coupling constant is equal to the anisotropy constant ($j_{\text{inter}} = k = 1$), there is a strong

competition between the anisotropy energy and the exchange energy. The average assembly concentration is uniform but density fluctuations may result in different local concentrations. As a result, we may have small agglomerates of particles more strongly connected, in sites that have bigger number of neighbors and anisotropy axis toward the same direction. So smaller clusters, compared to the ones of the non-uniform morphology, are formed but they are more strongly connected with other clusters or particles. We have to note that here the definition of a cluster is different from that in the non-uniform model. As a cluster in the non-uniform model, a set of connected particles of the same area is defined, each one with the coordination number $z_i \geq 1$, while here we require that $z_i \geq 3$. Figure 2.7a and b shows that steps in the curves may appear again but smaller than those in the non-uniform assembly of Fig. 2.6. The larger initial magnetization in the ZFC magnetization versus temperature curve, the larger initial slope and stronger temperature dependence in the VC curves are attributed to the simpler structure and to the stronger intercluster coupling.

Figure 2.7 shows that the main source of the stepwise behavior, in random anisotropy models, is the competition between the exchange and anisotropy energy when they have comparable values but the exact form of the initial plateau and steps is due to a more complicated structure where large clusters are formed.

(b) **Effect of the clustering on assemblies of nanoparticles with core/surface morphology**

Enhanced or collective magnetic properties have been observed in nanoscale systems made of multiple subunits self-assembled in cluster-like structures [27]. These complex structures may attain collective properties [46] due to the coupling mechanisms established across the interface or strongly coupled material nanodomains [47]. In addition, the magnetic behavior of these complex systems may be affected by microscopic phenomena associated with the surface coordination environment such as canted surface spins [48], intra- and interparticle interactions (dipolar or

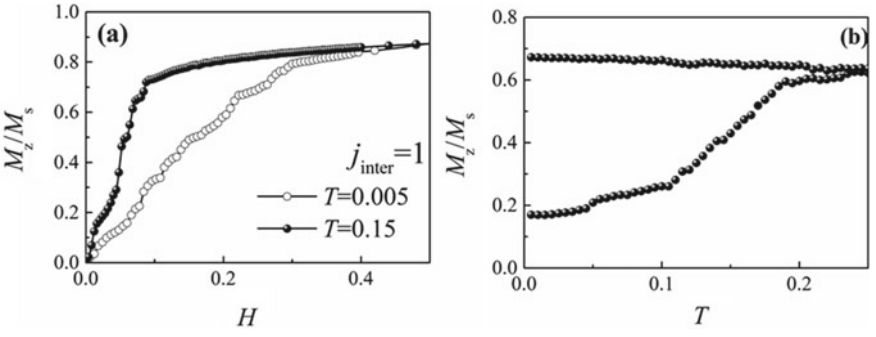

Fig. 2.7 Uniform assembly with $p = 0.5$ interacting with intermediate exchange forces ($j_{inter} = 1$). **a** Initial magnetization versus H curves (VC) for two temperatures T and **b** ZFC/FC versus T magnetization curves with $H_{appl} = 0.05$ [28]

exchange, involving surface spins among different particles) and even increased surface anisotropy [39].

We have studied controlled assemblies of single-crystal, colloidal maghemite nanoparticles which is facilitated via a high temperature polyol-based pathway. Structural characterization shows that size-tunable nanoclusters of 50 and 86 nm diameters, with high dispersibility in aqueous media, are composed of 13 nm crystallographically oriented nanoparticles. The interaction effects are examined against the increasing volume fraction, p, of the inorganic magnetic phase that goes from individual colloidal nanoparticles ($p = 0.47$) to clusters ($p = 0.60, 0.72$) [27]. In such nanoparticle assembled systems, with increased p, the role of the interparticle dipolar interactions and that of the constituent nanoparticles' surface spin disorder in the emerging spin glass dynamics is expected to be significant.

In order to model the clusters morphology of the assembly of nanoparticles, we consider N identical spherical ferrimagnetic NPs of diameter d being located randomly on the nodes of a simple cubic lattice with lattice constant, a, inside a box of edge length 10α measured in units α. The clusters have been produced by dividing the lattice into eight areas with size $5a \times 5a \times 5a$ each and a variable particle concentration per area, but under the constraint that the total concentration is the same as the experimental one. The total number of NPs is $N = p \times (10\,a \times 10\,a \times 10\,a)$, where p is the concentration of the particles in the model. In such a model, the total concentration $p = 0.60$ for small clusters and $p = 0.72$ for large clusters is spread into eight partial concentrations, namely [0.6, 0.7, 0.5, 0.6, 0.5, 0.7, 0.7, 0.5] and [0.72, 0.82, 0.52, 0.72, 0.82, 0.72, 0.82, 0.62], respectively. In all cases, due to the existence of the surfactant polymeric layer, it was assumed that there were no direct exchange interactions ($j_{\text{inter}} = 0$) between the nanoparticles, but instead they interacted only via dipolar forces with dipolar strength g.

In this case, we go beyond the classical model of coherent rotation of the particle's Stoner–Wohlfarth magnetization, in which each nanoparticle is described by a classical spin vector as in the case of Fe nanoparticles. Our mesoscopic model involves a set of three classical unit spin vectors, one for the core $\vec{s}_{1i}$ and two for the surface layer $\vec{s}_{2i}$, $\vec{s}_{3i}$ with magnetic moments $m_n = M_n V_n / M_s V$ $n = 1$ stands for the core and $n = 2, 3$ for the "up" and "down" shell or surface sublattices of the nanoparticle, respectively, as it is described in Sect. 2.1.1. In this way, surface effects were included for each i nanoparticle in the assembly.

The energy parameters in (2.1) are based on the bulk values of maghemite (M_s= 4.2×10^5 A/m and $K = 5 \times 10^3$ J/m^3), and their modifications are established considering the nanoparticles morphology (e.g., reduced symmetry and reduced size) using a mean field approach. Accordingly, the values of the intra-particle exchange energy among the core spin and the surface spins were taken as $j_{c1} = -7.77, j_{c2} = -1.35, j_{\text{srf}} = -0.091$ and the anisotropy energy of the core as $k_C = 0.1$, while that of the surface as $k_{\text{srf}} = 2.5$, since it is expected to be more than one order of magnitude larger than that of the core.

The dipolar strength energies (g) and magnetic moments (m) have been calculated taking into account the experimental values of the particle concentration (p) and the saturation magnetization (M_s) of the nano-architectures for the three different

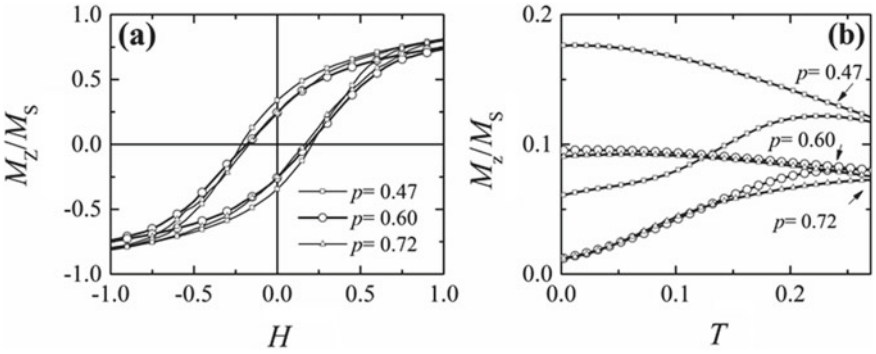

Fig. 2.8 Monte Carlo simulations of **a** hysteresis loops at $T = 0.05$ under zero-field cooled conditions and **b** ZFC and FC magnetization as function of temperature curves for $p = 0.47$ individual particles (squares) and clusters of NPs ($p = 0.60$ (circles) and $p = 0.72$ (triangles)). All the curves are normalized to the saturation magnetization (M_s) of the individual NPs

samples. As a result, the mean particle magnetic moment is taken $m = 0.87$, the mean dipolar energy strength is $g = 0.955$ for $p = 0.60$ and $m = 0.77$, $g = 0.865$ for $p = 0.72$.

In our model that describes the clusters ($p = 0.62, 0.70$), the core spin anisotropy axis for each nanoparticle in a cluster was assumed parallel from site to site, i, effectively resembling the crystallographic alignment of adjacent NPs in a cluster. On the other hand, the surface spin anisotropy at each site ($\hat{e}_i$) was modeled at a random direction with respect to the core [27]. The disorder between the two domains and the imposed intra-particle interactions ($j_{c1}, j_{c2}, j_{\text{srf}}$) describes well the experimental observations of a reduced saturation magnetization, M_s, in the clusters as compared to the individual NPs (Fig. 2.8a). This magnetic behavior is quite the opposite of that reported for multi-core γ-Fe_2O_3 particles ($D < 30$ nm). In the latter, the components were also crystallographically oriented, but as they were lacking any disorder between the surface spins and the spin of their core, no exchange coupling anisotropy was established [25]. However, in our study, the clusters display minimal, but resolvable exchange bias ($H_{\text{ex}} \sim 10$ Oe), which is progressively reduced at increasing p confirming the existence of internal core/surface structure. Our simulations were performed using (2.1) for the energy. The hysteresis loops for different p showed a progressive decrease of H_C and a lowering of the M_s (Fig. 2.8a) in good agreement with the experimental curves [27]. Furthermore, the calculated blocking temperature was growing with p and the temperature-dependent FC magnetization curves became flat (Fig. 2.8b) at $T \leq 0.05$, similarly to the measured ones [27] indicating the presence of spin glass dynamics [49].

Furthermore, to identify the factors dictating the spin glass behavior, we have examined the cases, where, either the dipolar interactions ($g = 0$) or the intra-particle spin-exchange interactions ($j_{c1} = j_{c2} = j_{\text{srf}} = 0$) were "switched off" in the case of clusters of nanoparticles ($p = 0.72$). When the $g = 0$ (Fig. 2.9 squares), the spins inside each nanoparticle tends to spontaneously couple ferrimagnetically (but with

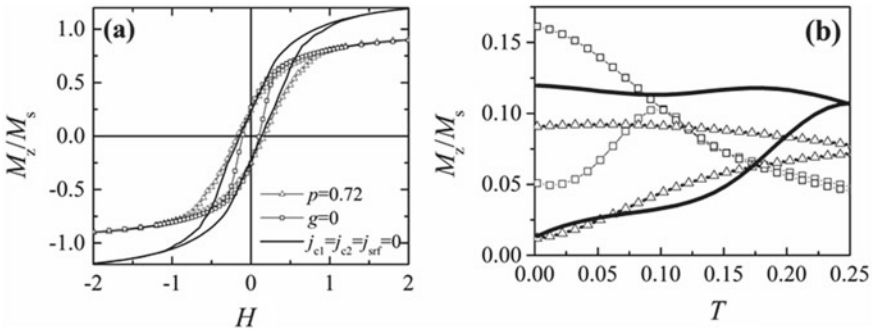

Fig. 2.9 Monte Carlo simulations of the isothermal magnetization curves at $T = 0.05$ and ZFC-FC magnetization curves for cluster type systems with $p = 0.72$ for the original model (g, j_{c1}, j_{c2}, j_{srf}, $\neq 0$; triangles), when the dipolar interactions are switched off ($g = 0$; squares) and when the intra-particle interactions are switched off ($j_{c1} = j_{c2} = j_{srf} = 0$; continuous line)

randomly oriented easy axis among sites), with effective decrease of their surface spin disorder and as such, the FC $M(T)$ curves present a short plateau (Fig. 2.9b squares) and the blocking temperature is reduced. On the other hand, for suppressed intra-particle interactions ($j_{c1} = j_{c2} = j_{srf} = 0$, curves with lines), the spins inside the nanoparticles do not interact with each other, permitting the surface moments to become decoupled from nearby spins (surface and core) and adopt a random configuration. The randomness in the spin arrangement leads to an increase in the M_S (Fig. 2.9a) and reduced T_B (Fig. 2.9b, lines). These results demonstrate that the intra-particle (dipole–dipole and exchange) interactions are non-negligible in the studied system.

In summary, Monte Carlo simulations suggest that a spin glass state arises (i) in the individual NPs from strong dipolar interactions and their impact on the surface spin disordering, whereas (ii) in the assembly of such NPs in clusters, with increased p, from the interplay of dipolar interactions with an additional spin disorder due to the defected nanoparticle surface coordination environment.

2.2.3 Case Study 3: Effect of an AFM Matrix in the Magnetic Behavior of Magnetic Nanoparticle Assemblies

Among the nanoparticle systems, the most studied ones are the granular solids, i.e., magnetic nanoparticles embedded in a metallic or non-metallic non-magnetic matrix. Recently, there is a growing interest in the study of magnetic nanoparticle embedded in a magnetic matrix with focus on the nanoparticle–matrix interface exchange coupling, because of its great impact on a number of technological applications. The understanding of its mechanisms and its interplay with the interparticle

interactions is a great challenge, since it would allow controlling equilibrium and non-equilibrium magnetization dynamics of exchange coupled nanoparticles systems and the fine tuning of their anisotropy. In what follows, we present our study on the influence of interparticle interaction on the exchange bias effect of a dilute assembly of Co nanoparticles embedded in a granular Mn matrix (5% volume fraction of Co particles in Mn matrix) using the three-spin mesoscopic model developed in ref [32]. Our simulations provide evidence that this interplay leads to a collective superspin glass behavior of the system.

2.2.3.1 The Model

For the numerical study of the Cobalt nanoparticles embedded in the Mn matrix, we have used the Monte Carlo simulation technique and the Metropolis algorithm. We consider an assembly of Co nanoparticles randomly placed on the nodes of a simple cubic lattice with lattice characteristic lengths L_x, L_y, L_z, with $L_x = L_y = L_z = 10\alpha$. The parameter α is defined as the smallest interparticle distance.

Each Co particle has spherical shape and diameter D. The magnetic particles are single domain and we represented each of them with a three-dimensional classical unit spin vectors $\hat{s}_i$. Their magnetic moments have magnitude $m_i = M_S V_i$ where M_S is the saturation magnetization and $V_i = \pi D^3/6$ is the particle's volume.

There is experimental evidence that the texture of the antiferromagnetic Mn matrix is granular and its magnetic behavior is typical of an assembly of uncompensated antiferromagnetic nanoparticles [31]. The Co particles were distributed at the lattice sites with occupation probability p_{Co}. From the experimental measurements, we know that the metal volume fraction of Co in the assembly is $x_{\mathrm{Co}} = 5\%$ so the occupation probability is $p_{\mathrm{Co}} = (6/\pi)\, x_{\mathrm{Co}} \sim 10\%$ and the total number of Co nanoparticles is $N_{Co} = p_{Co} \times (N_x \times N_y \times N_z)$ where $N_x = L_x/\alpha$, $N_y = L_y/\alpha$ and $N_z = L_z/\alpha$. A randomly distributed uniaxial easy axis $\hat{e}_i$ was assigned to each particle for the anisotropy vector. Each Mn grain has a small magnetic moment due to the uncompensated spins. To simulate the matrix, we assigned to each empty lattice site, i.e., non-occupied by Co nanoparticles, unit spin vectors with magnetic moment of a small magnitude $m_{Mn} = 0.1 m_{\mathrm{Co}}$ and a weak random uniaxial anisotropy $K_{Mn} = 0.1\, K_{Co}$. The Co particles interact via long-range dipolar forces and via exchange forces when they are sufficiently close. The exchange forces between two Co particles are ferromagnetic, yielding positive exchange constants ($j_{CoCo} = 1$). Due to the fact that occupation probability is much smaller that the percolation threshold ($p_{\mathrm{Co}} = 10\% < p_{\mathrm{C}} \approx 31\%$) very few Co particles have other Co nanoparticles as nearest neighbors [15, 34]. In Fig. 2.10, a 2D schematic representation of the nanoparticles system is given.

The Mn magnetic moments interact via long-range dipolar forces with all the other magnetic moments (Mn or Co). Furthermore, they interact via exchange forces with their nearest neighbors. To represent the antiferromagnetic character of the matrix, we have set the exchange constant between two Mn moments negative ($j_{MnMn} = -0.1$). The exchange coupling between a Co nanoparticle and its nearest Mn grains is taken ferromagnetic $j_{CoMn} = 0.3$.

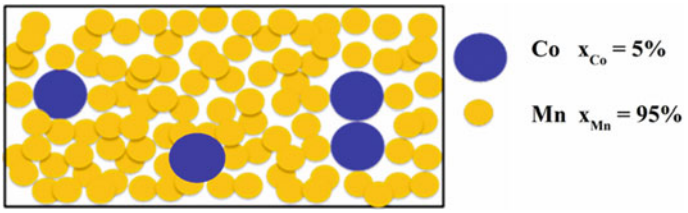

Fig. 2.10 A 2D schematic representation of the model for the assembly of Co nanoparticles (blue spheres) embedded in the Mn (yellow spheres) matrix

Experimental studies showed a significant alloying between the ferromagnetic Co nanoparticles and the antiferromagnetic matrix (Mn) along the Co/Mn interface [31]. To represent this alloying which is non-uniform, we have introduced a stronger exchange coupling randomly between the Co and one of the Mn grains at each Co/Mn interface of our system and we set for this stronger coupling $j'_{CoMn} = 1.0$.

The above description of the system gives the total energy of the N spins [35] equal to the sum of the Co and Mn spins ($N = N_{\mathrm{Co}} + N_{\mathrm{Mn}}$) by the sum of the Zeeman (due to interaction with an external field), the anisotropy, the exchange and the dipolar interaction energy terms, hence,

$$
\begin{aligned}
E = & -\mu_0 H \sum_{i=1}^{N_{Co}} m_{Co}\left(\hat{s}_i \cdot \hat{e}_h\right) - \mu_0 H \sum_{i=1}^{N_{Mn}} m_{Mn}\left(\hat{s}_i \cdot \hat{e}_h\right) \\
& - \sum_{i=1}^{N_{Co}} K_{Co} V_{Co}\left(\hat{s}_i \cdot \hat{e}_i\right)^2 - \sum_{i=1}^{N_{Mn}} K_{Mn} V_{Mn}\left(\hat{s}_i \cdot \hat{e}_i\right)^2 \\
& - \sum_{i=1}^{N} \sum_{\langle i,j \rangle} \left[j_{CoCo}\left(\hat{s}_i \cdot \hat{s}_j\right) + j_{CoMn}\left(\hat{s}_i \cdot \hat{s}_j\right) + j'_{CoMn}\left(\hat{s}_i \cdot \hat{s}_j\right) + j_{MnMn}\left(\hat{s}_i \cdot \hat{s}_j\right) \right] \\
& - g \sum_{i=1}^{N} \sum_{i>j} m_i m_j \hat{s}_i D_{ij} \hat{s}_j
\end{aligned}
\tag{2.3}
$$

where $\langle i\ ,j\rangle$ denotes summation over nearest neighbors only, and $\hat{e}_h$ and $\hat{e}_i$ are the directions of the magnetic field and the anisotropy axis of ith particle, respectively. The parameters entering (3) are the magnetic field H, the effective anisotropy constant of Co $K_{Co}V_{Co}$ and Mn $K_{Mn}V_{Mn}$ and the effective exchange constants j_{CoCo}, j_{CoMn}, j'_{CoMn}, j_{MnMn}. D_{ij} is the dipolar interaction tensor [28] and the magnetic moments m_{Co} and m_{Mn}.

In (3), we take the exchange interaction between the spins of Heisenberg type, so the strength of the exchange coupling along the interface depends also on the relative orientation of the vector spins.

The energy parameters entering our simulations have been divided by the Co particle anisotropy $k_{\mathrm{Co}} = K_{\mathrm{Co}}V_{\mathrm{Co}}$ so they are dimensionless. In these reduced units,

the anisotropy constant k_{Co} is always 1. The dipolar interaction strength is taken $g = 0.1$.

Periodic boundary conditions were used and the lattice was repeated periodically. We implemented the Ewald summation technique for the calculation of the long-range dipolar interactions so the values of the dipolar interaction tensor (D_{ij}) were the same used in the Ewald matrix.

2.2.3.2 Results and Discussion

The MC simulations of the ZFC/FC susceptibility curves are reported in Fig. 2.11a. Notably, they quite well reproduce the observed SSG-type behavior of the Co/Mn film [32]. Simulations were also performed removing from the Hamiltonian the interface Co/Mn coupling energy term ($j_{CoMn} = j'_{CoMn} = 0$; Fig. 2.11b) in order to check the role of the exchange coupling at the core/shell interface. In this case, the SSG behavior is not produced.

In Fig. 2.12a, the hysteresis loop of the MC simulations without field cooling and after field cooling ($H_{cooling} = 0.4$) procedure are reported. In our Hamiltonian, in order to take into account the non-uniform alloying, we have introduced two different j_{CoMn} values ($j_{CoMn} = 0.3$; $j'_{CoMn} = 1.0$). In Fig. 2.12b, we show the results for our system with uniform alloying by setting ($j_{CoMn} = j'_{CoMn} = 0.3$ along the interface. Notably, the comparison between the two simulation results shows that the disorder due to the alloying enhances the exchange bias field value (from 0.006, in Fig. 2.12b, to 0.048 in Fig. 2.12a).

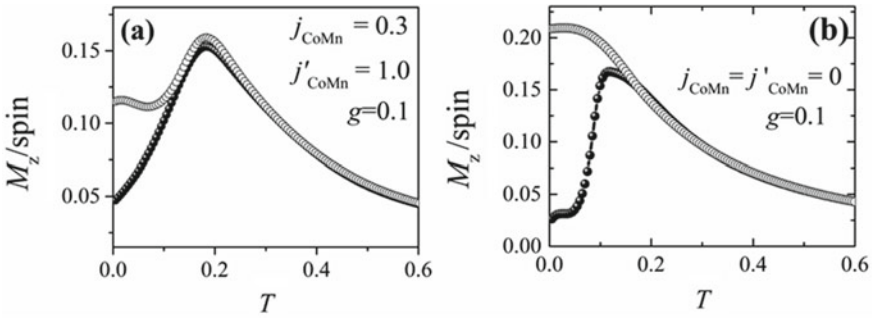

Fig. 2.11 Monte Carlo simulation results for Co/Mn system (**a**) and the system without taking into account interface effects ($j_{CoMn} = j''_{CoMn} = 0$) (**b**), under an applied field $H = 0.1$ [32]

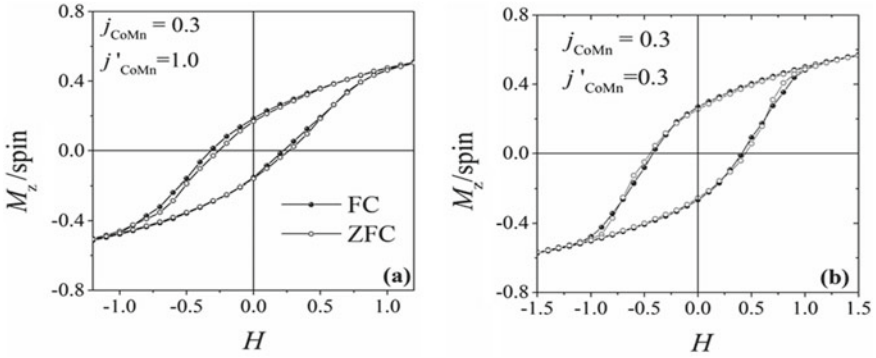

Fig. 2.12 **a** MC simulations of the hysteresis loops without field cooling (open circles) and after field cooling (closed circles) in a field of $H_{cool} = 0.4$, hysteresis loops considering non-uniform alloying ($j_{CoMn} = 0.3$; $j'_{CoMn} = 1.0$and **b** for uniform alloying ($j_{CoMn} = j'_{CoMn} = 0.3$) [32]

2.3 Concluding Remarks—Prospects

In this chapter, we have reviewed the effect of interparticle interactions on the magnetic behavior of assemblies of nanoparticles. We have presented a mesoscopic model that includes the assembly's and nanoparticle's morphology together, taking into account in this way the interplay between the intra-particle characteristics and the interparticle interactions. In the case of magnetic nanoparticles embedded in an antiferromagnetic matrix, the effect of the magnetic matrix on the magnetic behavior of an assembly of the nanoparticles has been discussed.

Our simulations showed that in the dense random assemblies of core/surface nanoparticles, strong dipolar interactions lead to the formation of SSG phase and strong surface effects. In the dense assemblies of nanoparticles with core/shell morphology, which are in contact, the important role in their exchange bias behavior is played by the interparticle exchange interactions.

Importantly, though our mesoscopic model has been developed for core/surface and core/shell nanoparticle assemblies, it can be easily extrapolated to the study of the magnetic properties of various ultra-small magnetic nanoparticle systems or multi-shell magnetic systems, by the proper choice of the number and the type of spins, characterizing the systems and their interactions. This opens new prospects toward the optimization of their performance in biomedical [50], magnetic recording [51, 52], permanent magnets applications [20] and more recently in magnetocaloric and thermoelectric devices [53, 54].

References

1. A. Joseph, S. Mathew, Ferrofluids: synthetic strategies stabilization, physicochemical features, characterization, and applications. Chempluschem **79**, 1382–1420 (2014)
2. S. Singamaneni, V.N. Bliznyuk, C. Binek, E.Y. Tsymbal, Magnetic nanoparticles: recent advances in synthesis, self-assembly and applications. J. Mater. Chem. **21**, 16819–16845 (2011)
3. M. Vasilakaki, G. Margaris, K.N. Trohidou, Magnetic Behavior of Composite Nanoparticle Assemblies, in *Magnetic Nanoparticle Assemblies*, ed. by K.N. Trohidou (Pan Stanford Publishing, USA, 2014), pp. 253–280
4. P. Allia, M. Coisson, P. Tiberto, F. Vinai, M. Knobel, M.A. Novak, W.C. Nunes, Granular Cu-Co alloys as interacting superparamagnets, Phys. Rev. B Condens. Matter Mater. Phys. **64**, 1444201–14442012 (2001)
5. S. Nakamae, C. Crauste-Thibierge, K. Komatsu, D. L'Hôte, E. Vincent, E. Dubois, V. Dupuis, R. Perzynski, Anisotropy-axis orientation effect on the magnetization of γ-Fe_2O_3 frozen ferrofluid. J. Phys. D Appl. Phys. **43**, 474001 (2010)
6. D. Peddis, C. Cannas, A. Musinu, G. Piccaluga, Coexistence of superparmagnetism and spin-glass like magnetic ordering phenomena in a $CoFe_2O_4$-SiO_2 nanocomposite. J. Phys. Chem. C **112**, 5141–5147 (2008)
7. M. Vasilakaki, G. Margaris, D. Peddis, R. Mathieu, N. Yaacoub, D. Fiorani, K. Trohidou, Monte Carlo study of the superspin glass behavior of interacting ultrasmall ferrimagnetic nanoparticles, Phys. Rev. B. **97**, 094413(6) (2018)
8. J.M. Vargas, L.M. Socolovsky, M. Knobel, D. Zanchet, Dipolar interaction and size effects in powder samples of colloidal iron oxide nanoparticles. Nanotechnology. **16**, S285–S290 (2005)
9. J.L. Dormann, D. Fiorani, E. Tronc, On the models for interparticle interactions in nanoparticle assemblies: comparison with experimental results. J. Magn. Magn. Mater. **202**, 251–267 (1999)
10. S.A. Majetich, M. Sachan, Magnetostatic interactions in magnetic nanoparticle assemblies: Energy, time and length scales. J. Phys. D Appl. Phys. **39**, R407–R422 (2006)
11. P. Allia, P. Tiberto, Dynamic effects of dipolar interactions on the magnetic behavior of magnetite nanoparticles. J. Nanoparticle Res. **13**, 7277–7293 (2011)
12. L. Néel, Le champ coercif d'une poudre ferromagnetique cubique á grains anisotropes, C. R. Acad. Sci., Paris. **224**, 1550–1551 (1947)
13. E.P. Wohlfarth, The Effect of Particle Interaction on the Coercive Force of Ferromagnetic Micropowders, Proc. R. Soc. A Math. Phys. Eng. Sci. **232**, 208–227 (1955)
14. J.L. Dormann, L. Bessais, D. Fiorani, A dynamic study of small interacting particles-superparamagnetic model and spin-glass laws. J. Phys. C-Solid State Phys. **21**, 2015–2034 (1988)
15. D. Kechrakos, K.N. Trohidou, Effects of dipolar interactions on the magnetic properties of granular solids. J. Magn. Magn. Mater. **1771**, 943–944 (1998)
16. S. Bedanta, W. Kleemann, Supermagnetism, J. Phys. D. Appl. Phys. **42**, 013001(28 pp) (2009)
17. J.J. Lu, M.-T. Lin, C.C. Kuo, H.L. Huang, Hysteretic behavior of magnetic particles with dipole interaction. J. Appl. Phys. **85**, 5558–5560 (1999)
18. K. Nadeem, H. Krenn, T. Traussing, I. Letofsky-Papst, Distinguishing magnetic blocking and surface spin-glass freezing in nickel ferrite nanoparticl. J. Appl. Phys. **109**, 13912 (2011)
19. T. Uusimäki, G. Margaris, K. Trohidou, P. Granitzer, K. Rumpf, M. Sezen, G. Kothleitner, Three dimensional quantitative characterization of magnetite nanoparticles embedded in mesoporous silicon: Local curvature, demagnetizing factors and magnetic Monte Carlo simulations. Nanoscale. **5**, 11944–11953 (2013)
20. A. López-Ortega, M. Estrader, G. Salazar-Alvarez, A.G. Roca, J. Nogués, Applications of exchange coupled bi-magnetic hard/soft and soft/hard magnetic core/shell nanoparticles. Phys. Rep. **553**, 1–32 (2015)
21. G. Margaris, K.N. Trohidou, J. Nogués, Mesoscopic model for the simulation of large arrays of Bi-magnetic core/shell nanoparticles. Adv. Mater. **24**, 4331–4336 (2012)

22. S.K. Sharma, J.M. Vargas, M. Knobel, K.R. Pirota, C.T. Meneses, S. Kumar, C.G. Lee, P.G. Pagliuso, C. Rettori, Synthesis and tuning the exchange bias in Ni–NiO nanoparticulate systems. J. Appl. Phys. **107**, 850 (2010)
23. A. Kostopoulou, S.K.P. Velu, K. Thangavel, F. Orsini, K. Brintakis, S. Psycharakis, A. Ranella, L. Bordonali, A. Lappas, A. Lascialfari, Colloidal assemblies of oriented maghemite nanocrystals and their NMR relaxometric properties. Dalt. Trans. **43**, 8395–8404 (2014)
24. A. Kostopoulou, A. Lappas, Colloidal magnetic nanocrystal clusters: variable length-scale interaction mechanisms, synergetic functionalities and technological advantages. Nanotechnol. Rev. **4**, 595–624 (2015)
25. L. Lartigue, P. Hugounenq, D. Alloyeau, S.P. Clarke, M. Lévy, J.C. Bacri, R. Bazzi, D.F. Brougham, C. Wilhelm, F. Gazeau, Cooperative organization in iron oxide multi-core nanoparticles potentiates their efficiency as heating mediators and MRI contrast agents. ACS Nano **6**, 10935–10949 (2012)
26. V. Iannotti, S. Amoruso, G. Ausanio, R. Bruzzese, L. Lanotte, A.C. Barone, G. Margaris, K.N. Trohidou, D. Fiorani, Stepwise behaviour of magnetization temperature dependence in iron nanoparticle assembled films. Nanotechnology. **24**, 165706 (2013)
27. A. Kostopoulou, K. Brintakis, M. Vasilakaki, K.N. Trohidou, A.P. Douvalis, A. Lascialfari, L. Manna, A. Lappas, Assembly-mediated interplay of dipolar interactions and surface spin disorder in colloidal. Nanoscale. **6**, 3764–3776 (2014)
28. G. Margaris, K.N. Trohidou, V. Iannotti, G. Ausanio, L. Lanotte, D. Fiorani, Magnetic behavior of dense nanoparticle assemblies: Interplay of interparticle interactions and particle system morphology. Phys. Rev. B. **86**, 214425 (2012)
29. N. Domingo, D. Fiorani, A.M. Testa, C. Binns, S. Baker, J. Tejada, Exchange bias in a superspin glass system of Co particles in Mn matrix. J. Phys. DAppl. Phys. **134009**, 41 (2008)
30. N. Domingo, A.M. Testa, D. Fiorani, C. Binns, S. Baker, J. Tejada, Exchange bias in Co nanoparticles embedded in an Mn matrix **316**, 155–158 (2007)
31. C. Binns, N. Domingo, A.M. Testa, D. Fiorani, K.N. Trohidou, M. Vasilakaki, J.A. Blackman, A.M. Asaduzzaman, S. Baker, M. Roy, D. Peddis, Interface exchange coupling in Co nanoparticles dispersed in a Mn matrix, J. Phys. Condens. Matter. **22**, 436005 (2010)
32. G. Margaris, M. Vasilakaki, D. Peddis, K.N. Trohidou, S. Laureti, C. Binns, E. Agostinelli, D. Rinaldi, R. Mathieu, D. Fiorani, Superspin glass state in a diluted nanoparticle system stabilized by interparticle interactions mediated by an antiferromagnetic matrix. Nanotechnology. **28**, 1–8 (2017)
33. E.C. Stoner, F.R.S. Wohlfarth, E.P. Wohlfarth, On a mechanism of magnetic hysteresis in heterogeneous alloys. Philos. Trans. Roy. Soc. London. **240**, 599 (1948)
34. G. Margaris, K. Trohidou, H. Kachkachi, Surface effects on the magnetic behavior of nanoparticle assemblies. Phys. Rev. B. **85**, 1–9 (2012)
35. M. Vasilakaki, K.N. Trohidou, D. Peddis, D. Fiorani, R. Mathieu, M. Hudl, P. Nordblad, C. Binns, S. Baker, Memory effects on the magnetic behavior of assemblies of nanoparticles with ferromagnetic core/ antiferromagnetic shell morphology, Phys. Rev. B. **88**, 140402(R)pp 1–5 (2013)
36. E. Metropolis, N., Rosenbluth, A., Rosenbluth, M., Teller, A., Teller, Equation of State Calculations by Fast Computing Machines, J. Chem. Phys. **21**, 1087–1092 (1953)
37. K. Binder, *Applications of the Monte-Carlo Method in Statistical Physics* (Springer-Verlag, NY, 1987)
38. E. Eftaxias, M. Vasilakaki, K.N. Trohidou, A Monte Carlo study of the exchange bias effects in magnetic nanoparticles with Ferromagnetic Core/Antiferromagnetic shell morphology. Mod. Phys. Lett. B **21**, 1169–1177 (2007)
39. P. Guardia, B. Batlle-Brugal, A.G. Roca, O. Iglesias, M.P. Morales, C.J. Serna, A. Labarta, X. Batlle, Surfactant effects in magnetite nanoparticles of controlled size. J. Magn. Magn. Mater. **316**, 756–759 (2007)
40. B.D. Cullity, C.D. Graham, *Introduction to Magnetic Materials, xvii* (Wiley, New Jersey, 2008)
41. M. Vasilakaki, G. Margaris, E. Eftaxias, K.N. Trohidou, Monte Carlo study of the Exchange Bias Effects in Magnetic Nanoparticles with Core-Shell Morphology, in *Exchange Bias: From*

Thin Film to Nanogranular and Bulk Systems, ed. by S.K. Sharma (CRC Press, Taylor and Francis Group, New York, 2018), pp. 127–157
42. J. Nogués, V. Skumryev, J. Sort, S. Stoyanov, D. Givord, Shell-driven magnetic stability in core-shell nanoparticles. Phys. Rev. Lett. **97**, 157203 (2006)
43. V. Iannotti, S. Amoruso, G. Ausanio, X. Wang, L. Lanotte, A.C. Barone, G. Margaris, K.N. Trohidou, D. Fiorani, Interplay between particle anisotropy and exchange interaction in Fe nanoparticle films, Phys. Rev. B Condens. Matter Mater. Phys. 83, 4–8 (2011)
44. P. Grassberger, Numerical studies of critical percolation in three dimensions. J. Phys. A: Math. Gen. **25**, 5867–5888 (1992)
45. D. Dimitrov, G. Wysin, Magnetic properties of superparamagnetic particles by a Monte Carlo method. Phys. Rev. B: Condens. Matter **54**, 9237–9241 (1996)
46. Z. Nie, A. Petukhova, E. Kumacheva, Properties and emerging applications of self-assembled structures made from inorganic nanoparticles. Nat. Nanotechnol. **5**, 15–25 (2010)
47. Q.K. Ong, X.-M. Lin, A. Wei, Role of frozen spins in the exchange anisotropy of core − shell Fe@ Fe_3O_4 Nanoparticles. J. Phys. Chem. C **115**, 2665–2672 (2011)
48. A. Espinosa, A. Muñoz-Noval, M. García-Hernández, A. Serrano, J. Jiménez De La Morena, A. Figuerola, A. Quarta, T. Pellegrino, C. Wilhelm, M.A. García, Magnetic properties of iron oxide nanoparticles prepared by seeded-growth route. J. Nanoparticle Res. **15**, 1514 (2013)
49. E. Winkler, R.D. Zysler, M. Vasquez Mansilla, D. Fiorani, D. Rinaldi, M. Vasilakaki, K.N. Trohidou, Surface spin-glass freezing in interacting core-shell NiO nanoparticles, Nanotechnology. **19**, 185702 (2008)
50. S. Hyun Noh, S.H. Moon, T.H. Shin, Y. Lim, J. Cheon, Recent advances of magneto-thermal capabilities of nanoparticles: From design principles to biomedical applications, Nano Today. **13**, 61–76 (2017)
51. R.L. Stamps, S. Breitkreutz, J. Åkerman, A. V. Chumak, Y. Otani, G.E.W. Bauer, J.U. Thiele, M. Bowen, S.A. Majetich, M. Kläui, I.L. Prejbeanu, B. Dieny, N.M. Dempsey, B. Hillebrands, The 2014 Magnetism Roadmap, J. Phys. D. Appl. Phys. **47** (2014)
52. A. Hirohata, K. Takanashi, Future perspectives for spintronic devices, J. Phys. D. Appl. Phys. **47** (2014)
53. K.S. Khattak, A. Aslani, C.A. Nwokoye, A. Siddique, L.H. Bennett, E. Della Torre, Magnetocaloric properties of metallic nanostructures, Cogent Eng. **2**, 1050324(pp 1–13) (2015)
54. T.J. Salez, B.T. Huang, M. Rietjens, M. Bonetti, C. Wiertel-Gasquet, M. Roger, C.L. Filomeno, E. Dubois, R. Perzynski, S. Nakamae, Can charged colloidal particles increase the thermoelectric energy conversion efficiency? Phys. Chem. Chem. Phys. **19**, 9409–9416 (2017)

Chapter 3
Collective Magnetic Behaviour

Roland Mathieu and Per Nordblad

Abstract The mechanisms responsible for magnetic interaction between nanoparticles are described and modelled in the previous chapter of this book. Here, the collective superspin glass state resulting from such interaction is discussed, using a collection of experimental results. Superspin glasses display qualitatively similar dynamical magnetic properties as canonical spin glasses, including ageing, memory and rejuvenation phenomena. In the Introduction, the dynamical properties of spin and superspin glasses are illustrated and contrasted. These properties are discussed in more detail in Case studies, taking into account the nanoparticle concentration, size and size distribution, using results from studies of ferrofluids and compacts of γ-Fe_2O_3 particles. The Outlook section illustrates recent findings suggesting that the temperature dependence of the low-field isothermal remanent magnetization (IRM) and magnetization as a function of magnetic field (hysteresis or M-H) curves of superspin glasses include information on the superspin dimensionality and magnetic anisotropy. The possibility to engineer nanocomposites with tailored magnetic interaction and anisotropy is also discussed.

3.1 Introduction

Interaction between particles in an ensemble of magnetic nanoparticles causes collective behaviour [1–5]. Figure 3.1 shows the temperature dependence of the zero-field-cooled (ZFC) and field-cooled (FC) magnetization of a dilute and a concentrated assembly of 8 nm maghemite nanoparticles prepared from the same batch. The magnetic response is altered by the dipolar interparticle interaction, yielding slowing down of the magnetization dynamics at low temperatures and a nonzero Weiss temperature (θ_w). The interparticle dipolar interaction transforms the nanoparticle system from being superparamagnetic to becoming a superspin glass (SSG). The

R. Mathieu (✉) · P. Nordblad
Department of Materials Science and Engineering, Uppsala University, Box 35, 751 03 Uppsala, Sweden
e-mail: roland.mathieu@angstrom.uu.se

D. Peddis et al. (eds.), *New Trends in Nanoparticle Magnetism*,
Springer Series in Materials Science 308,
https://doi.org/10.1007/978-3-030-60473-8_3

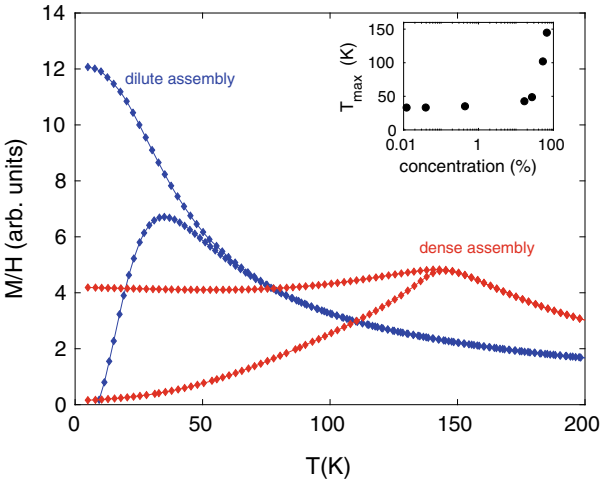

Fig. 3.1 Temperature dependence of the low-field ($H = 5$ Oe) ZFC and FC magnetization (M/H) of a dilute (blue) and a dense (red) assembly of 8 nm maghemite nanoparticles. The measured magnetization for the dense system has been corrected for demagnetization effects. The inset shows the variation of the temperature for the maximum in the ZFC curves ($T_{\max}$) as a function of particle concentration (logarithmic scale)

high-temperature behaviour follows the Curie–Weiss law: $\chi = C/(T-\theta_w)$, where C is assumed to be the same for the dilute and the dense system. The Weiss constant θ_w has from the measured data been derived to be about 90 K for the dense system and 0 K for the dilute system. There is thus a dominance of ferromagnetic interaction in the dense system.

3.1.1 Systems of Magnetic Nanoparticles

The magnetic behaviour of dilute (non-interacting) nanoparticle assemblies is governed by the sum of the response of each particle. The response of the individual particle depends on its magnetic moment ($m_{\rm sp}$) and its anisotropy ($E_{\rm ap}$). In an assembly of nanoparticles, there is a distribution of particle sizes and shapes and thus a corresponding distribution of $m_{\rm sp}(V)$ and $E_{\rm ap}(V)$ that is given by the composition and fabrication method of the particles. The building material of the particles can be ferromagnetic, ferrimagnetic or antiferromagnetic. The magnetic transition temperature of the particle material should be much higher than the temperatures where the magnetic properties of the particle system are studied.

3.1.2 Interaction Mechanisms

Dipolar interaction is always present and governed by the magnetic moment of the particles and the distance between particles. When the particles are touching, there is a possibility of direct or super-exchange interaction between particles. In a metallic matrix, interparticle interaction mediated via the conduction electrons becomes possible. If the matrix is antiferromagnetic, direct magnetic interaction at the interphase between matrix and particle occurs. Ferro- or ferrimagnetic matrices yield nanostructured magnets, which constitute a separate class of ordered magnetic materials. Figure 3.2 illustrates four different ways to suspend magnetic nanoparticles for physical property measurements. The two upper panels of Fig. 3.2 illustrate a ferrofluid, where the interparticle dipolar interaction is tuned by the concentration of particles and magnetic particles suspended in a matrix material. The matrix material can be a non-magnetic or an antiferromagnetic insulator or metal. In the two lower panels of Fig. 3.2, particles in the form of a powder or a compacted powder are illustrated. In these configurations, the interparticle distance can be tuned by the compacting pressure and the thickness of an insulating non-magnetic capping layer.

In the following, results obtained on compacts of γ-Fe_2O_3 maghemite, ferrofluids and nanocomposites, such as Fe nanoparticles embedded in Cr matrices, will be presented. The compacts will be referred to as "RCPx" (strongly interacting random closed-packed systems) and "REFx" (weakly interacting references), where "x" denotes the diameter of the constituting particles in nanometer [6]. Data obtained on spin glasses systems are included for comparison. Systems such as the Ag(11 at.%

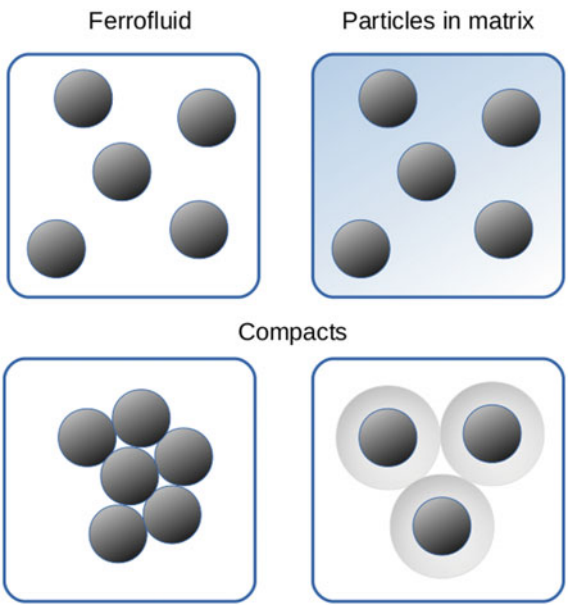

Fig. 3.2 Illustrations of magnetic particle assemblies: a ferrofluid (upper left), particles suspended in a solid matrix (upper right), bare compacted particles (lower left) and compacted particles with a capping layer (lower right)

Mn), Cu(13.5 at.% Mn) and Au(6 at.% Fe) will be referred to as Ag(Mn), Cu(Mn) and Au(Fe), respectively.

3.1.3 Time Scales

The dynamics of a magnetic nanoparticle is governed by the Arrhenius law $\tau_p = \tau_0 \exp(E_{\mathrm{ap}}/k_B T)$, where τ_{p} is the relaxation time of the particle, $\tau_0 \sim 10^{-11}$ s and k_B is the Boltzmann constant [7]. The thick black curve in Fig. 3.3 illustrates the evolution of the relaxation time of nanoparticles in an assembly of 8 nm maghemite particles (REF8) with quite narrow size distribution (using $E_{\mathrm{ap}} = \mathrm{KV}$ and $K \approx 50$ kJ/m^3) [8]. The corresponding data for smaller ($d = 7.5$ nm) and larger ($d = 8.5$ nm) particles is included using thin lines. The observation time (t_{obs}) range of conventional AC-susceptibility experiments is indicated by horizontal dashed lines ($t_{\mathrm{obs}} = 1/\omega$, where ω is the angular frequency of the AC-field). The particles become blocked when the relaxation time of the particles exceeds the observation time of the measurement. The distribution of particle sizes significantly broadens the region where blocking of the

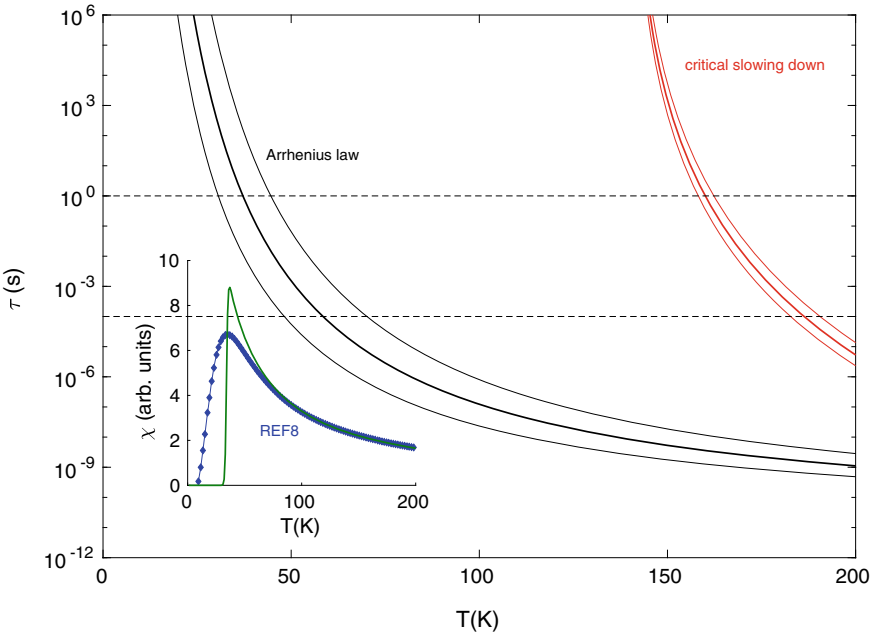

Fig. 3.3 Evolution of the particle relaxation time with temperature for dilute (grey) and dense (red) 7.5, 8 and 8.5 nm maghemite nanoparticles according to the Arrhenius law and assuming critical slowing down with $T_g = 140$ K, respectively. The inset shows the measured ZFC magnetization curve of REF8 and the calculated curve for a corresponding truly monodispersed 8 nm particle system

different particles occurs. The inset shows the measured low-field ZFC magnetization ($\chi = M/H$) of the dilute 8 nm assembly (REF8) and the calculated behaviour for a corresponding monodispersed 8 nm maghemite assembly (Debye AC susceptibility; $t_{obs} = 10$ s). Also drawn in Fig. 3.3 is the evolution of the relaxation time of the system assuming a compact nanoparticle system with dipolar interaction yielding $T_g = 140$ K. The individual particle relaxation time that corresponds to the volume of the particles and critical slowing down ($\tau_{crit} = \tau_p t^{-z\nu}$, $t = (T\text{-}T_g)/T_g$ [9] and $z\nu = 10$ the dynamic critical exponent) have been used to calculate the evolution of the critical relaxation time (τ_{crit}) of the dense particle assemblies (red curves; 7.5, 8 and 8.5 nm particles).

3.1.4 Model Behaviour Contra Collective Phenomena

A model superparamagnetic or superspin glass system would consist of monodispersed particles. However, such a system does not exist and the blocking behaviour of a non-interacting system of magnetic nanoparticles is always significantly broadened compared to a model calculation using the mean volume (see inset Fig. 3.3). The relaxation times of a model superspin glass approaching the glass temperature obey critical slowing down [10–13]. In spite of the inevitable size distribution of the nanoparticles, critical slowing down is observed in compact nanoparticle systems, with similar sharpness as that observed in archetypal atomic spin glasses [14]. On the other hand, nanoparticle systems with broader size distributions exhibit typical characteristics of collective dynamics in glassy magnetic systems such as ageing and memory phenomena although critical slowing down indicating a phase transition is not observed [15].

Figure 3.4 illustrates the correspondence between the ageing/memory behaviour of an archetypal spin glass (Cu(Mn)) [16] and a strongly interacting magnetic nanoparticle assembly (RCP8) showing superspin glass behaviour [6]. The main frames show low-field ZFC magnetization (M/H) versus temperature curves; a reference curve (red) where the system has been continuously cooled to a low temperature where the magnetic field is applied and the magnetization recorded on increasing temperature, and a memory curve (blue) where the sample has been kept at a halt temperature a wait time t_w during cooling. The memory curve shows a dip at the halt temperature as a memory of the halt [17]. The insets show ZFC magnetic relaxation at the halt temperatures using two different wait times (0 (red curves), and 3000 or 10,000 s (blue), respectively) at constant temperature before the magnetic field is applied. At an observation time of 100 s, the magnetization is lower when the system has been kept at constant temperature a longer wait time, this is in accord with the dip in the M versus T memory curves. The fact that the reference and memory M versus T curves coalesce at lower temperatures reflects the rejuvenation phenomenon (chaotic nature); the response of the (super)spin glass at lower temperatures is unaffected by the halt.

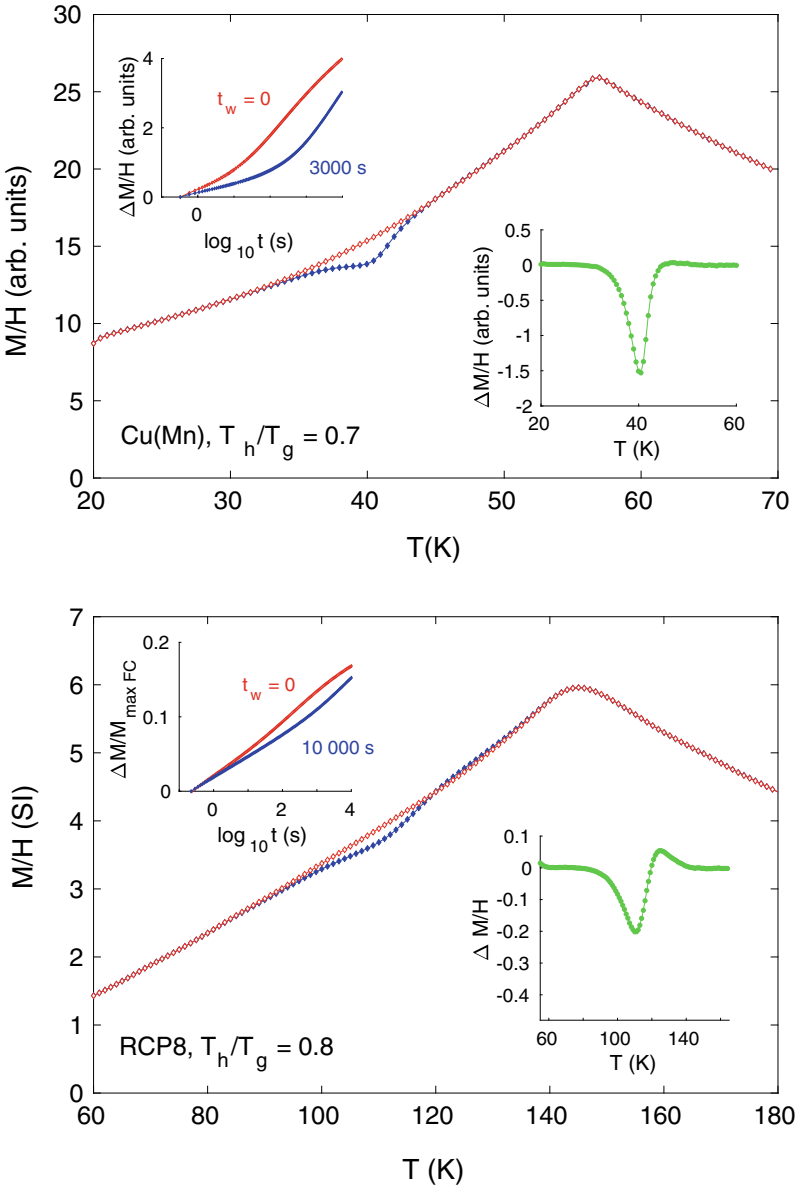

Fig. 3.4 M/H versus T (main frames) and M versus log (t) (upper insets) for an archetypal spin glass (top, Cu(Mn)) and a compacted ensemble of 8 nm maghemite nanoparticles (bottom, RCP8); $H =$ 0.5 Oe. In the latter case, corrections due to demagnetization effects have been made to extract the internal susceptibility. The main frames illustrate memory behaviour (lower insets show difference curves $\Delta M = M_{\text{mem}}$-$M_{\text{ref}}$) and the upper insets magnetization relaxation curves measured after two different wait times t_w as indicated in the figure

3.2 Case Studies: Superspin Glasses

Spin glasses are formed by atomic systems where there is structural disorder and competing ferro- and antiferromagnetic interaction giving rise to frustrated spins. The properties of model spin glasses such as Cu(Mn) and $Fe_{0.5}Mn_{0.5}TiO_3$ have been extensively studied and exhibit universal properties as to the existence of a second-order phase transition (revealed from static and dynamic scaling analyses) and infinite relaxation times and non-equilibrium dynamics manifested by ageing, memory and rejuvenation phenomena at temperature below T_g [18]. Measurable physical manifestations of superspin glass states are found in systems with strong enough dipolar interaction. Dipolar interaction can in randomly packed systems gives rise to dynamic frustration, i.e. depending on how neighbouring particles flip their magnetization direction, the dipolar moment on a specific particle changes sign with time. Strong enough means that the dipolar interaction strength causes a glass temperature that exceeds the blocking temperature (at the observation time (about 10 s) of magnetization versus temperature measurements) by a factor of two or more. For instance, if the dipolar interaction $E_{dd}/k_B = 100$ K, the anisotropy of the particles $E_{ap}/k_B < \log(\tau/\tau_{0)} \times T_B \sim 1250$ K (considering $T_B = 50$ K, on experimental observation time (10 s) and $\tau_0 = 10^{-11}$ s). Translated to observation times, this implies that the relaxation time of the particles at T_g, $\tau_p \sim 10^{-5}$ s. When T_g exceeds T_B by a factor of five, the relaxation time of the particles at T_g becomes $\tau_p \sim 10^{-9}$ s. To measure critical slowing down on the time scales of standard ac-susceptibility experiments (1–10,000 Hz, $t_{\text{obs}} = 1/\omega \sim 0.16$–$1.6 \times 10^{-5}$ s) the relaxation time of the slowest particles should always be much shorter than the observation time of the probe. In systems with weak interparticle interaction, this criterion is not fulfilled. On the other hand, as mentioned above (see Sect. 3.1.4), other manifestations of collective phenomena, such as ageing and memory, are readily observed in systems with wide distributions of particle sizes and comparably weak dipolar interparticle interaction.

3.2.1 Frozen Ferrofluids

Ferrofluids allow continuous tuning of the particle density and thus the strength of the interparticle dipolar interaction. Dense randomly packed frozen ferrofluids show magnetic ageing behaviour due to collective non-equilibrium dynamics introduced by dipolar dynamic frustration [14]. Interparticle interaction broadens the relaxation function at low temperatures and shifts the maximum in the low-field ZFC magnetization versus temperature curve to higher temperatures. In cases of strong dipolar interaction and narrow particle size distributions, critical slowing down indicating a spin glass like transition is observed on the time scales of AC-susceptibility experiments. An example of this is shown in Fig. 3.5 citing results from AC-susceptibility measurements on a system of FeC nanoparticles at different

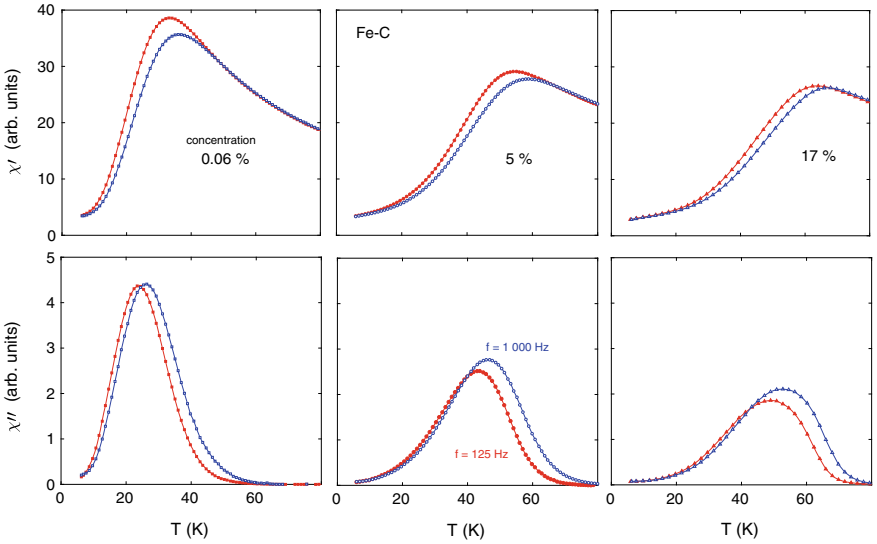

Fig. 3.5 In-phase (upper frame) and out-of-phase (lower frame) AC-susceptibility versus temperature at 125 Hz (red) and 1000 Hz (blue) for a frozen ferrofluid of amorphous Fe–C nanoparticles of different concentration; $h_{ac} = 0.1$ Oe. The figure is adapted from Fig. 3.1 in [10]

particle densities [10]. The sequence of curves elucidates the transformation of the particle assembly from superparamagnetic blocking behaviour to a superspin glass with increasing particle density and increased dipolar interaction strength. Analyses of the slowing down of the dynamics using wide frequency windows yield spin glass characteristic behaviour for the most dense sample, however with a microscopic relaxation time that corresponds the relaxation times of the particles near the derived glass temperature (T_g).

3.2.2 Compacts

Figure 3.1 showed ZFC-FC magnetization curves on assemblies of 8 nm maghemite nanoparticles with narrow size distribution (RCP8). The left panel of Fig. 3.6 shows the same ZFC/FC data for the compacted assembly together with the in- and out-of-phase components of the low-field AC-susceptibility measured at 10 Hz. The right panel shows the out-of-phase component of the AC-susceptibility data at different frequencies (0.17–510 Hz). The temperature for the onset of a finite out-of-phase component can be used as indicator of freezing of the magnetic moments on the time scale of that frequency. The dots near the onset indicate how the freezing temperatures (T_f) have been chosen for the different frequencies. Analysing the frequency dependence of the derived freezing temperatures according to critical slowing down, the best fit is found for $z\nu = 11$ and $\tau_p = 6 \times 10^{-12}$ s (see inset).

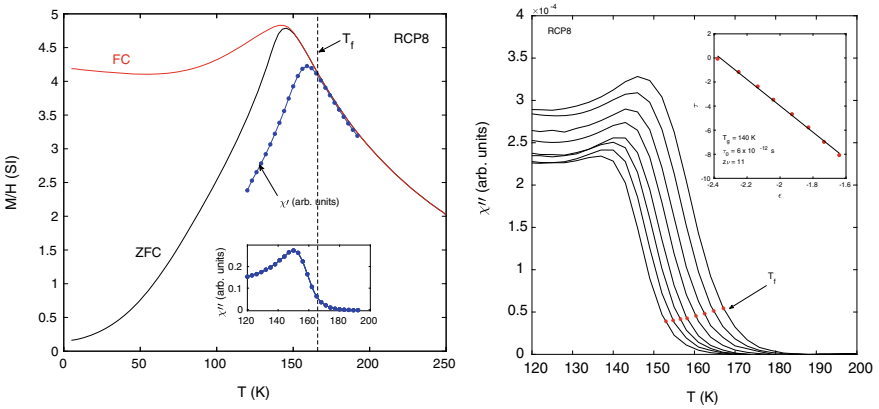

Fig. 3.6 DC and AC magnetic susceptibility versus temperature for RCP8. Left panel: ZFC and FC M/H ($H = 5$ Oe; corrected for demagnetizing effects) and $\chi'(T)$ and $\chi''(T)$ at 170 Hz ($h_{ac} = 4$ Oe). Right panel $\chi''(T)$ measured at 0.17–510 Hz and $h_{ac} = 4$ Oe. The inset shows the best fit of the data to critical slowing down

Corresponding systems of maghemite nanoparticles of other sizes have been investigated with the same experimental methods and found to exhibit critical slowing down [14]. Figure 3.7 shows the temperature dependence of the ZFC and FC magnetization (normalized to the magnetization value at the maximum of the ZFC curves) for compacted samples of sizes: 6, 8, 9 and 11.5 nm. The derived temperatures for the maximum in the ZFC magnetization versus temperature curves, T_{max}, are plotted as a function of particle volume in the inset together with the corresponding blocking temperatures for dilute samples of the same nanoparticles. The superspin glass temperatures derived from dynamic scaling analyses increase in a similar way

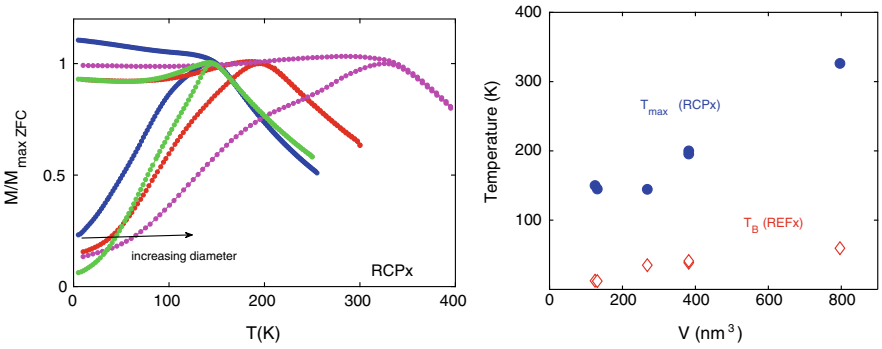

Fig. 3.7 Left panel: Normalized ZFC/FC magnetization versus temperature curves for compacted maghemite assemblies of 6, 8, 9 and 11.5 nm nanoparticles; $H = 5$ Oe. Right panel: T_{max} and T_B plotted versus the mean volume of the particles for the compact (RCP) and the dilute (REF) assemblies. The magnetization curves were not corrected for demagnetization effects [14, 20]

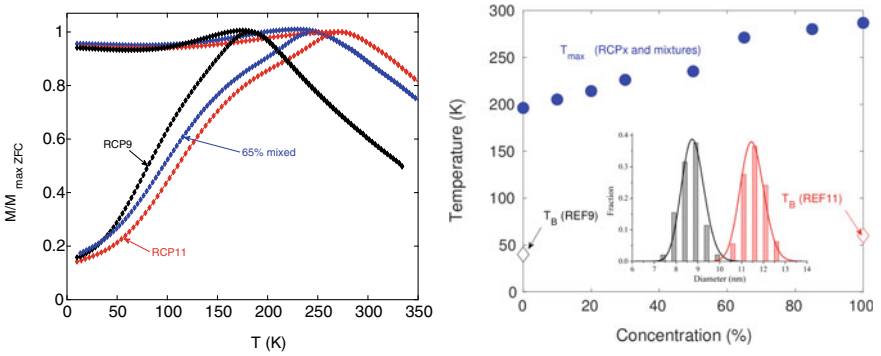

Fig. 3.8 Left panel: Normalized ZFC/FC magnetization versus temperature for compacted samples of 9 nm particles (RCP9), 11.5 nm particles (RCP11), and a mixture of 9 and 11.5 nm particles with 65% mixing fraction; $H = 5$ Oe. Right panel: $T_{\max}$ of the compacted mixed samples (RCP) versus concentration of large particles and T_B of the dilute 9 and 11.5 nm samples (REF9 and REF11, respectively). The inset shows the particle size distribution of the 9 and the 11.5 nm assemblies. The magnetization curves were not corrected for demagnetization effects [19, 20]

as $T_{\max}$ with particle volume. $T_{\max}$ (and T_g) exceeds T_B by a factor of 4 or more for all samples.

All the discussed compacted samples have similar and quite narrow particle size distributions and exhibit well-behaved critical slowing down indicating super-spin glass transitions [14]. Figure 3.8 shows ZFC and FC magnetization curves for compacted samples of 9 nm (RCP9) and 11.5 nm (RCP11) maghemite particles, as well as for a sample consisting of a mixture of 9 and 11.5 nm particles (65% mixing fraction). The volume ($2V$) of the 11.5 nm particles is about twice the volume (V) of the 9 nm particles. The size distributions of the two particle systems are shown as an inset in the right panel of Fig. 3.8. The evolution of the measured $T_{\max}$ with increasing fraction of larger particles is shown in the main frame of the right panel in Fig. 3.8. $T_{\max}$ increases linearly with the mixing fraction (mean particle size). Analyses of the frequency dependence of the freezing temperatures indicate that the assemblies of mixed particle sizes obey critical slowing down at all different mixing fractions from 0 to 100% of larger particles [19]. In all cases, the SSG temperature exceeds the blocking temperature of the dilute reference sample of the largest particles ($2V$) by at least a factor of three.

At low temperatures, where the particle moments are thermally blocked on the time scale of magnetization measurements, interparticle interaction can be revealed from a comparison between the field dependence of the isothermal remanent magnetization IRM(H) and the direct current demagnetization DCD(H) [21]. IRM is measured starting from a zero-field-cooled sample, applying a field pulse and then measuring the remanent magnetization M_{IRM} in zero field. DCD is measured starting from a high negative field ($-H_s$) that saturates the remanent magnetization (M_{RS}), applying a reversal field ($H_r \geq 0$), then removing this field and measuring the remanence M_{DCD} in zero field. The relative values of these remanences: $m_{IRM}(H) =$

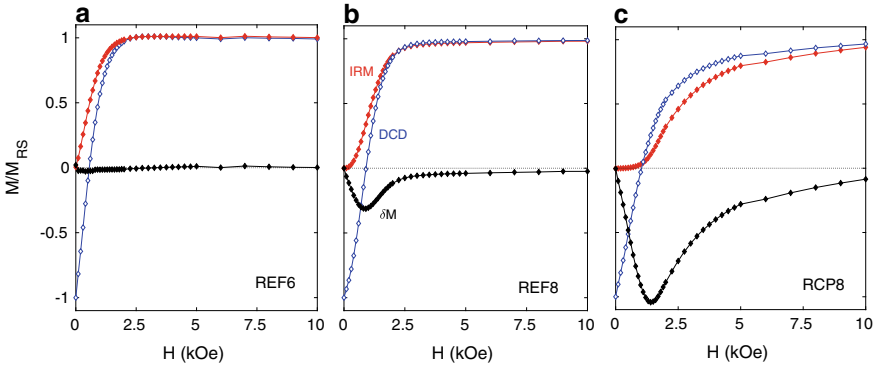

Fig. 3.9 m_{IRM}(H), m_{DCD}(H) and $\delta M(H)$ at $T = 5$ K for **a** non-interacting 6 nm particles **b** non-interacting 8 nm particles and **c** compact 8 nm particles [22]

$M_{\mathrm{IRM}}/M_{\mathrm{RS}}$, and $m_{\mathrm{DCD}}(H) = M_{\mathrm{DCD}}(H)/M_{\mathrm{RS}}$ are used to calculate $\delta M = m_{\mathrm{DCD}}$-(1–$2m_{\mathrm{IRM}}$). For a non-interacting system of ideal superspins $\delta M = 0$ at all fields, whereas for systems with interparticle interaction and/or non-ideal particle moments $\delta M(H) \neq 0$ at low fields [21]. The field dependences of IRM, DCD and δM of REF6, REF8 and RCP8 at 5 K are shown in Fig. 3.9 a–c. REF6 shows the expected behaviour of a non-interacting system of magnetic nanoparticles being switched according to the Stoner–Wohlfarth model, i.e. $\delta M(H) \approx 0$ at all fields. For REF8 on the other hand, $\delta M(H) \neq 0$ at low fields. The different behaviour of REF6 and REF8 reflects non-ideal behaviour of the 8 nm particles [22]; these particles exhibit finite exchange bias after field cooling, whereas the 6 nm particles do not. Figure 3.9c shows the very strong influence that interparticle interaction and collective behaviour of the compact 8 nm particle system (RCP8) has on the field dependence of δM.

At higher temperatures, thermal relaxation implies that the measures M_{IRM}, M_{DCD} and δM become time dependent: i.e. dependent on the duration of the magnetic field pulse (how long time H_r has been applied), the observation time of the measurement of the remanence and for an interacting system the wait time before the magnetic field is applied after zero-field cooling. This implies that also these time parameters need to be controlled when this kind of measurements is made at temperatures where significant magnetic relaxation occurs. The crucial influence that thermal relaxation has on the hysteresis behaviour of (super)spin and glasses is evidenced by first-order reversal curves (FORC) simulations of an Edwards-Anderson Ising spin glass at $T = 0$ and $T = 0.3\ T_g$, where finite temperature smoothens all sharp features of the FORC diagram (in accord with experimental results) and effectively wipes out the reversal field memory effect characteristic of 3D Ising spin glasses at $T = 0$ K [23]. FORC diagrams and magnetic hysteresis of Heisenberg spin glasses are on the other hand dominated by an induced excess moment that exhibits field-dependent exchange bias [24, 25]. FORC diagrams of RCP8 at low temperature are very different from those of the weakly interacting system (which primarily are controlled by the particle size distribution) but also very different from FORCs of atomic spin glasses [22].

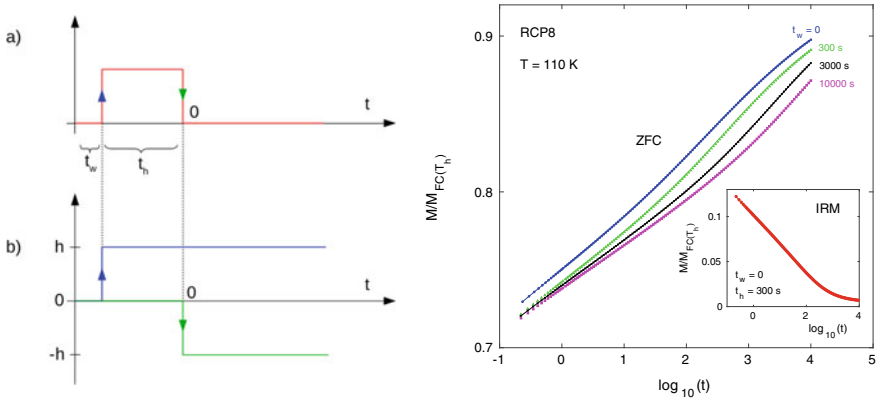

Fig. 3.10 Left: Equivalent field change sequence for a field pulse of duration t_h. Right: M_{ZFC} (t_w, t)/M_{FC} versus log(t) recorded in $H = 0.5$ Oe and calculated $m_{\mathrm{IRM}}(t)$ for RCP8 ($t_w = 0$)

At low fields, where the particle system obeys linear response to field applications, M_{IRM} reflects the relaxation function, $p(t_w, t)$ and the time dependence of $M_{\mathrm{IRM}}(t)$ obeys the principle of superposition. The relaxation function is directly measured by the ZFC relaxation after the application of a weak magnetic field (h): $p(t_w, t) = M_{\mathrm{ZFC}}(t_w, t)/h$ [26], where t is the time elapsed after the field application and t_w the wait time at constant field before the magnetic field is applied. The right panel of Fig. 3.10 shows zero-field-cooled magnetic relaxation, $M_{\mathrm{ZFC}}(t, t_w)$ versus log (t), of the compact 8 nm particle assembly (RCP8) measured at 110 K. The relaxation at temperatures below T_g (= 140 K) occurs over extended time scales stating from the individual particle relaxation time (τ_p) and continuing well beyond any experimental time scales.

The fact that there is a wait time dependence of the relaxation function implies that the system experiences magnetic ageing, as already the memory behaviour suggested (Fig. 3.4). The magnitude of the low-field IRM is controlled by the relaxation function $p(t_w, t)$: and given by: $M_{\mathrm{IRM}}(t) = hp(tw, t + t_h) - hp(t_w + t_h, t)$ [26]. Where the response function empirically is defined from the measured $M_{\mathrm{ZFC}}(t_w, \mathrm{t})$ curves. The inset of the right panel of Fig. 3.10 shows the calculated m_{IRM}(t) using the $t_w = 0$ and $t_w = 300$ s curves of the main panel and the field application sequence is indicated in the left panel of Fig. 3.10: a positive field is applied at $t = 0$ and a negative field change h (= 0.5 Oe) is made at time t_h (= 300 s). The remanence, m_{IRM} [$= M_{\mathrm{IRM}}/M_{\mathrm{FC}}(T_h)$], that has been attained after the field has been cut to zero can be frozen in by immediately cooling the sample to lower temperatures. Figure 3.11 shows the temperature dependence of M_{IRM} on cooling and heating (red dots) and on heating after the sample has been quenched to low temperature immediately after the field has been switched off (black dots) [27]. As can be seen by the red curve there is a rapid decrease of the magnetization in the temperature region close to the halt temperature (cf. the decay of $m_{\mathrm{IRM}}(t)$ on a linear scale shown in the inset of Fig. 3.11, the same m_{IRM} data as shown on a logarithmic scale in

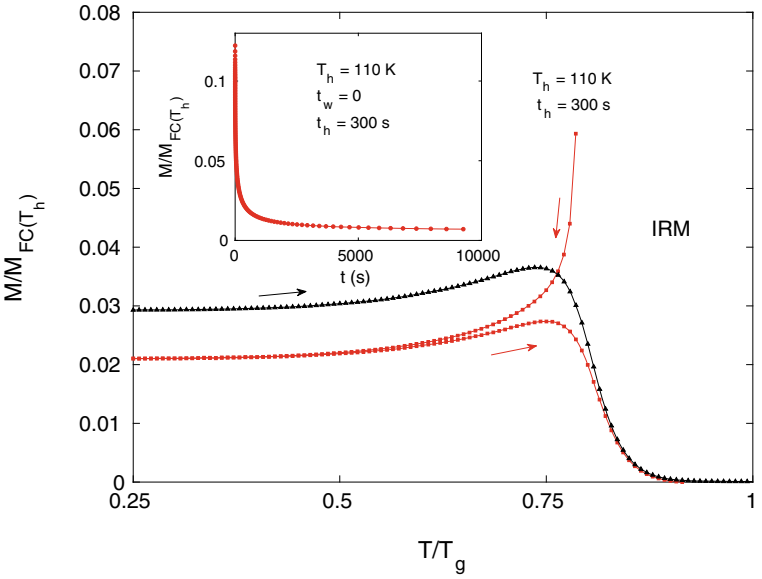

Fig. 3.11 $m_{\mathrm{IRM}}(T)$ measured on cooling and subsequent heating (red curves) and on heating after rapid cooling to low temperatures (black curve) (RCP8, $h = 0.5$ Oe). Inset: calculated $m_{\mathrm{IRM}}(t)$ for RCP 8 ($t_w = 0$) from Fig. 3.10 (linear scale)

Fig. 3.10). $m_{\mathrm{IRM}}(T)$ very rapidly decays towards zero when the temperature reaches near the temperature where it was attained. The frozen in magnetization attained in the time window 1–300 s rapidly relaxes when their relaxation times again reaches the order of the observation time of the magnetization measurement (~10 s).

3.3 Outlook

3.3.1 Superspin Dimensionality

Experiments on different spin glasses have shown that the frozen in $m_{\mathrm{IRM}}(T)$ can be used as an indicator of the spin dimensionality of the investigated spin glass [28]. The inset of the left panel of Fig. 3.12 shows the temperature dependence of m_{IRM} of an Ising and a Heisenberg spin glass as a function of T/T_g, where m_{IRM} has been frozen in at $T_h/T_g = 0.6$. There is a clear distinction between the behaviour of the two systems near T_h: the curve for the Ising spin glass smoothly decays whereas $m_{\mathrm{IRM}}(T)$ of the Heisenberg system exhibits a distinct maximum before decaying towards zero. The right panel of Fig. 3.12 shows corresponding curves for a compact of 8 nm maghemite particles (RCP8) with a superspin glass temperature of 140 K. Notable in the figure is that the low-temperature curves show a smooth decay of $m_{\mathrm{IRM}}(T)$ (Ising like)

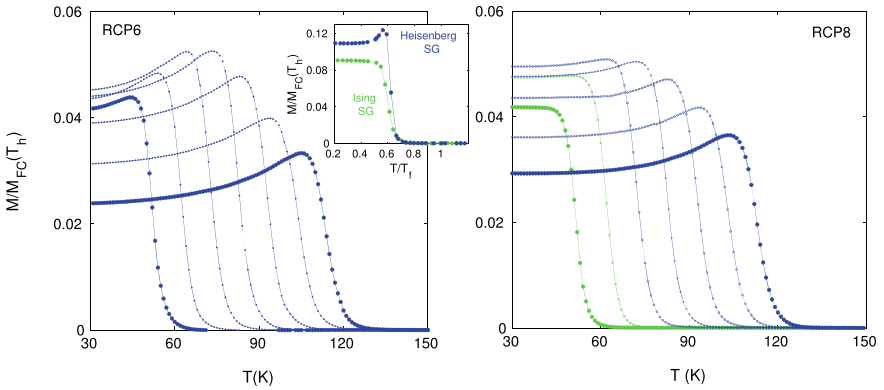

Fig. 3.12 Superspin dimensionality and relation to T_B for RCP6 and RCP8 (T_g ~ 140 K in both cases). $m_{\mathrm{IRM}}(T)$ is recorded on reheating after halts made at $T_h = 50$, 60, 70, 80, 90, 100 and 110 K ($h = 0.5$ Oe, $t_h = 300$ s) during the cooling. The inset shows $m_{\mathrm{IRM}}(T)$ for Ising and Heisenberg spin glasses, for T_h/T_g ~ 0.6–0.7 ($h = 10$ Oe, $t_h = 3000$ s) [28]

at lower temperatures, whereas the curves at higher temperatures exhibit a clear maximum (Heisenberg like) before the decay. All $m_{\mathrm{IRM}}(T)$ curves for the compact of 6 nm particles on the other hand exhibit a clear maximum (Heisenberg like) before rapidly decaying to zero at temperatures above T_h. The significant dynamic difference between the two systems is that the blocking temperatures of the non-interacting systems are significantly different although the superspin glass temperatures are the same (140 K) for the two compacts. $T_B = 12.5$ K for the non-interacting system 6 nm particles and $T_B = 35$ K for the compact 8 nm particle assembly. This difference between the two compacts hints that the crossover is related to the evolution of the relaxation times of the particles with temperature and that the particles behave Ising like at temperatures $T < T_B$ and Heisenberg like at $T \gg T_B$. At low temperatures, the particles are mainly confined to point along the anisotropy direction, whereas at higher temperature, $T \gg T_B$, they very rapidly switch between the two energy minima. This type of experiments reflects properties of the collective dynamics of the particle system and is only viable in the temperature region between T_B and T_g. At temperatures below T_B of the non-interacting system, the particles are essentially blocked on the time scales of the experiment and no remanence is induced from a field pulse of duration minutes.

The spin dimensionality has been found to affect the anisotropy and reversal of the magnetization of spin glasses [25]. For example strikingly different hysteresis curves are displayed by spin glasses such as Au(Fe) with an Ising character—brought forth by the single ion anisotropy of the Fe spins—and the above-discussed Cu(Mn) Heisenberg spin glass. As seen in Fig. 3.13 (main frames), the ZFC M(H) curves of the Heisenberg system include an excess moment (ΔM). Furthermore, as seen in inset, these curves, like the field-cooled ones recorded after cooling the system in H_{FC}, are exchange biased. The FC $M(H)$ data recorded after sweeping the magnetic field from H_{FC} to $-H_{FC}$ and back includes an excess moment and defines two switching fields.

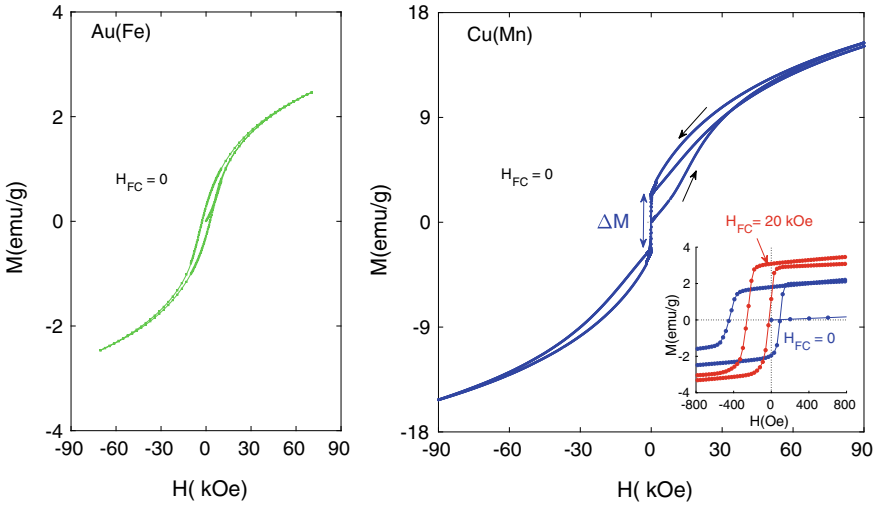

Fig. 3.13 Zero-field-cooled M(H) hysteresis loops at low temperatures ($T/T_g \sim 0.08$) for two spin glasses with Ising (Au(Fe), $T_g = 24$ K) and Heisenberg (Cu(Mn), $T_g = 57$ K) characters. The inset shows the zero-field-cooled and field-cooled ($H_{\mathrm{FC}} = 20$ kOe) on a smaller field scale for the Cu(Mn) spin glass; adapted from [29]

This behaviour has been interpreted in term of the chirality of the spin structure of Heisenberg systems, which may be affected by a small magnetic field applied during cooling, and the excess moment ΔM.

This brings forth unidirectional and uniaxial anisotropies and their respective switching fields [25]. The evolution of $m_{\mathrm{IRM}}(T)$ curves with T_h presented in Fig. 3.12, and the behaviour of FORC distributions for superspin glasses [22] suggest that such $M(H)$ experiments shall be relevant to superspin glasses.

3.3.2 Nanocomposites

Magnetic nanoparticles covered with an antiferromagnetic shell or dispersed in an AF-matrix have magnetic properties that emanate from direct exchange coupling at the interphase between the ferro- or ferrimagnetic core of the particles and the AF-coating/matrix. Unidirectional anisotropy and shifted FC hysteresis loops (exchange bias) were reported by Meiklejohn and Bean [30] in the mid 1950ies: "The material that exhibits this property is a compact of fine particles of Co (100–1000 Å) that have a cobaltous oxide coating". This phenomenon is illustrated in Fig. 3.14 which shows low-temperature hysteresis curve recorded after zero-field cooling and field cooling for amorphous Fe@(Fe,O) core-shell nanoparticles (core diameter ~8 nm, shell thickness ~2 nm). In the latter case, the $M(H)$ curve is recorded by increasing the magnetic field strength from its cooling value H_{FC} to the maximum ($H_{\mathrm{max}} = 50$ kOe),

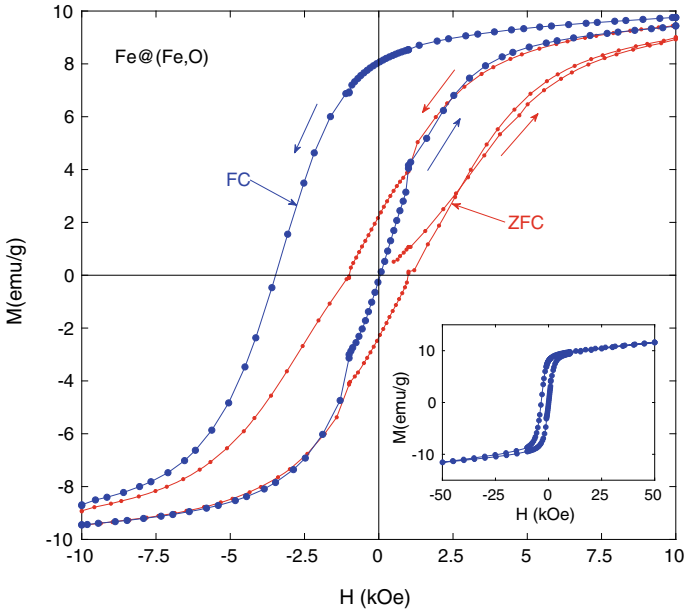

Fig. 3.14 Low-temperature hysteresis curves for a system of Fe@(Fe, O) core-shell nanoparticles recorded under zero-field-cooled and field-cooled ($H_{FC} = 10$ kOe) conditions. The inset shows a complete ZFC M(H) curve measured up to ± 5 T; adapted from [31]

and then cycling the magnetic field to $\pm H_{max}$ [31]. Some decades after Meiklejohn and Bean's discovery, in 2003, a corresponding system of Co nanoparticles with a Co core of 30–40 Å and a shell of CoO of about 10 nm was found "Beating the superparamagnetic limit with exchange bias" [32]. These particles were investigated embedded in a paramagnetic (Al_2O_3), as a compacted powder and embedded in an antiferromagnetic CoO matrix. The behaviour is remarkably different in between the three systems and indicates that the particles in Al_2O_3 behave as a superparamagnetic system with thermally blocked particles at temperatures below 10 K. When embedded in an antiferromagnetic CoO matrix, the particles become exchange coupled to the matrix and blocked up to the Neel temperature of CoO near room temperature [32]. In addition, the low-temperature FC hysteresis loops of the CoO embedded particles are strongly exchange biased, in accord with the Meiklejohn and Bean findings.

It was reported recently that including the Co@CoO core-shell particles in a Cu_2O matrix would enhance the interfacial morphology and exchange bias [33]. Interestingly, the matrix may have specific electrical and magnetic properties, which affect the magnetic interaction as well as exchange bias of the embedded particles. For example small (~2 nm diameter) Co nanoparticles embedded in a Mn matrix were found to interact magnetically, while the same particles in a Ag matrix show little interaction effects [34, 35].

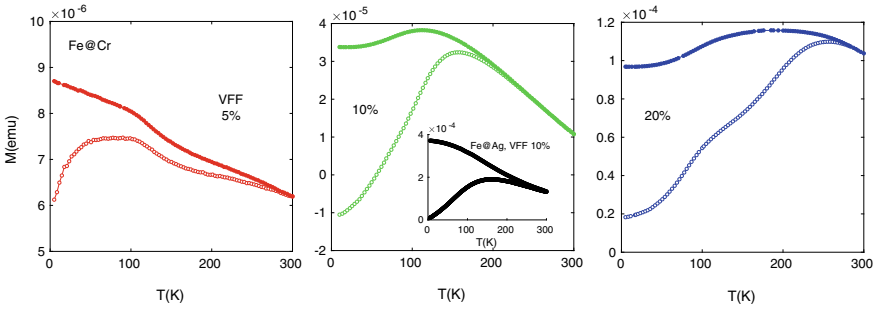

Fig. 3.15 ZFC/FC magnetization for Fe@Cr nanocomposites, consisting of 2 nm Fe particles embedded in a Cr matrix, with volume filling fraction (VFF) of 5, 10 and 20% ($H = 10$ Oe). The inset shows the corresponding magnetization curve for similar particles embedded in a non-magnetic Ag matrix (Fe@Ag) [36]

In the related system of similarly small Fe particles embedded in a Cr matrix, the magnetic anisotropy and interparticle interaction of the particles are greatly influenced by the Cr matrix [36]. As illustrated by the middle panel of Fig. 3.15, the magnetization curves of the Fe@Cr nanocomposite with a volume filling fraction of 10% are reminiscent to those superspin glasses (main frame). On the other hand, the Fe@Ag nanocomposite with the same filling fraction exhibits a superparamagnetic-like behaviour with a lower blocking temperature [36]. The evolution of the magnetization curves in Fig. 3.13 mimics those of the susceptibility curves depicted in Fig. 3.5 for a ferrofluid with increasing particle concentration. In the present case, a ferromagnetic-like response is observed for the largest volume filling fractions [2]. One could envisage that inversed magnetic nanoparticle systems such as non-magnetic nanoparticles (holes) in an antiferromagnetic matrix may provide collectively locked field-cooled excess moments with extraordinary high coercivity and paramagnetic zero-field-cooled behaviour.

Nanocomposites comprising two or more materials mixed on the nanoscale may be designed, in order to maximize the interaction between the two constituents. For example exchange-spring nanocomposites have been considered as a novel way to design permanent magnets [37, 38]. In spintronic nanocomposites including transition metal oxides, it was found that magnetoresistive [39] and magnetoelectric [40] properties could be tuned owing to the interaction of the two constituting phases. Hole-doped $La_{1-x}Ca_xMnO_3$ transition metal oxides (x is the hole concentration) are prototypical colossal magnetoresistance manganites [41]. Akin to the results of [39], it is expected that in nanocomposites of $La_{0.67}Ca_{0.33}MnO_3$ (LCMO) and $CoFe_2O_4$ (CFO), $CoFe_2O_4$ particles may exert a dipolar field onto the LCMO ones. Two types of composites have been considered, either the simple mechanical mixture (nanomixture) of the two nanosystems, or LCMO nanoparticles grown around the CFO ones (nanocomposite) [42]. Interestingly in this case, the CFO phase acts as hard phase for the soft LCMO. As seen in Fig. 3.16, owing to the more homogeneous core-shell-like morphology in the nanocomposite, interaction of the two phases is much

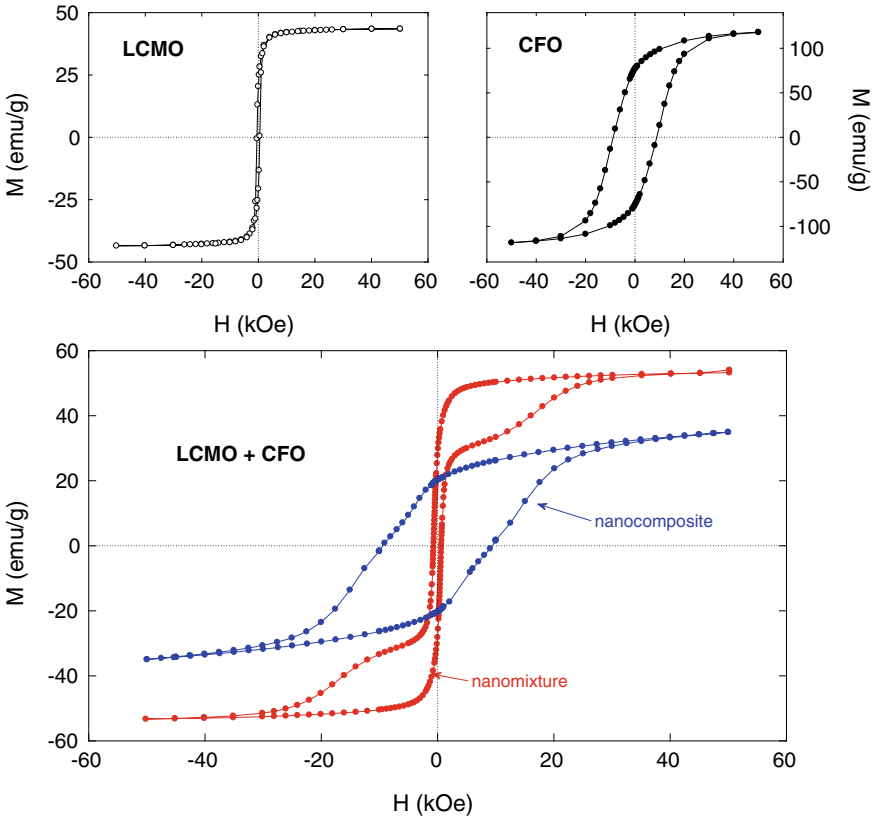

Fig. 3.16 Low-temperature M(H) hysteresis curves for (top panels) $La_{0.67}Ca_{0.33}MnO_3$ (LCMO) and $CoFe_2O_4$ (CFO), and (bottom panels) composite nanosystems (LCMO + CFO) [42]

stronger and switching is more coherent, akin to that observed in exchange-coupled nanocomposites [37, 38]. On the other hand, the M(H) curves of the nanomixture show two individual switchings, corresponding to the independent switching of the two phases. Interestingly, there are many parameters which may be varied to tune the magnetic (e.g. electrical) properties of such exchange-spring-like nanocomposites, for example phase volume fractions, magnetic properties (saturation magnetization, anisotropy) of the phases, and particles size.

3.3.3 Superstructures

The magnetic nanoparticle systems that we have discussed are all amorphous from a structural point of view, i.e. the particles are randomly distributed in space. Assemblies of nanoparticles are found to display magnetic properties determined by the

arrangements of the particles and orientational dependence of the magnetic interaction [43]. The organization of the particles results in the formation of three-dimensional structures, such as helices [44], superlattices [45], and other nanostructures [46] and mesoscopic systems [47, 48]. Systems built on spatial structural order provide possibilities of ordered magnetic structures. The fabrication and study of superferromagnets, superferrimagnets and superantiferromagnets provide a challenging field of collective experimental magnetism promoted by the possibility of 3D printing on the mesoscale [49].

Acknowledgements The authors are grateful to all their co-workers. This chapter includes results obtained in collaboration with M. S. Andersson, G. Muscas, P. Anil Kumar, M. Hudl, as well as D. Peddis, G. Singh, J. A. de Toro and their respective groups. The Swedish Research Council (VR) is thanked for financial support.

References

1. P. Jönsson, Adv. Chem. Phys. **128**, 191–248 (2004)
2. S. Bedanta, W. Kleemann, J. Phys. D Appl. Phys. **42**, 013001 (2009)
3. S. Mörup, M.F. Hansen, C. Frandsen, Beilstein J. Nanotechnol. **1**, 182–190 (2010)
4. S. Bedanta, O. Petracic, W. Kleemann, Supermagnetism in *Handbook of Magnetic Materials 23*, ed. by K. H. J. Buschow (Elsevier, 2017), pp. 1–83
5. D.S. Schmool, H. Kachkachi, Collective effects in assemblies of magnetic nanoparticles. in *Solid State Physics 67*, ed. by R.E. Camley, R.L. Stamps (Academic Press, 2016), pp. 1–97
6. J.A. De Toro, S.S. Lee, D. Salazar, J.L. Cheong, P.S. Normile, P. Muniz, J.M. Riveiro, M. Hillenkamp, F. Tournus, A. Tamion, P. Nordblad, Appl. Phys. Lett. **102**, 183104 (2013)
7. D.L. Leslie-Pelecki, R.D. Rieke, Chem. Mater. **8**, 1770 (1996)
8. M.S. Andersson, J.A. De Toro, S.S. Lee, P.S. Normile, P. Nordblad, R. Mathieu, Phys. Rev. B **93**, 054407 (2016)
9. K. Binder, A.P. Young, Rev. Mod. Phys. **58**, 801 (1986)
10. M.F. Hansen, P.E. Jönsson, P. Nordblad, P. Svedlindh, J. Phys. Condens. Matter **14**, 4901–4914 (2002)
11. C. Djurberg, P. Svedlindh, P. Nordblad, M.F. Hansen, F. Bödker, S. Mörup, Phys. Rev. Lett. **79**, 5154–5157 (1997)
12. J.L. Dormann, R. Cherkaoui, L. Spinu, M. Nogues, F. Lucari, F. D'Orazio, D. Fiorani, A. Garcia, E. Tronc, J.P. Jolivet, J. Magn. Magn. Mater. **187**, L139–L144 (1998)
13. K. Hiroi, K. Komatsu, T. Sato, Phys. Rev. B **83**, 224423 (2011)
14. M.S. Andersson, R. Mathieu, P.S. Normile, S.S. Lee, G. Singh, P. Nordblad, J.A. De Toro, Mater. Res. Express **3**, 045015 (2016)
15. T. Jonsson, J. Mattsson, C. Djurberg, F.A. Khan, P. Nordblad, P. Svedlindh, Phys. Rev. Lett. **75**, 4138 (1995)
16. R. Mathieu, M. Hudl, P. Nordblad, Europhys. Lett. **90**, 67003 (2010)
17. R. Mathieu, P. Jönsson, D.N.H. Nam, P. Nordblad, Phys. Rev. B **63**, 092401 (2001)
18. P.E. Jönsson, R. Mathieu, P. Nordblad, H. Yoshino, H. Aruga Katori, A. Ito, Phys. Rev. B **70**, 174402 (2004)
19. M.S. Andersson, R. Mathieu, P.S. Normile, S.S. Lee, G. Singh, P. Nordblad, J.A. De Toro, Phys. Rev. B **95**, 184431 (2017)
20. P.S. Normile, M.S. Andersson, R. Mathieu, S.S. Lee, G. Singh, J.A. De Toro, Appl. Phys. Lett. **109**, 152404 (2016)

21. J. García-Otero, M. Porto, J. Rivas, J. Appl. Phys. **87**, 7376–7381 (2000)
22. J.A. De Toro, M. Vasilakaki, S.S. Lee, M.S. Andersson, P.S. Normile, N. Yaacoub, P. Murray, E.H. Sanchez, P. Muniz, D. Peddis, R. Mathieu, K. Liu, J. Geshev, K.N. Trohidou, J. Nogues, Chem. Mater. **29**, 8258 (2017)
23. H. G. Katzgraber, D. Hérisson, M. Östh, P. Nordblad, A. Ito, H. Aruga Katori, Phys. Rev. B **76**, 092408 (2007)
24. M. Östh, D. Hérisson, P. Nordblad, J. Magn. Magn. Mater. **310**, e525–e527 (2007)
25. M. Hudl, R. Mathieu, P. Nordblad, Sci. Rep. **6**, 19964 (2016)
26. L. Lundgren, P. Nordblad, L. Sandlund, Europhys. Lett. **1**, 529–534 (1986)
27. M.S. Andersson, J.A. de Toro, S.S. Lee, R. Mathieu, P. Nordblad, Europhys. Lett. **108**, 17004 (2014)
28. R. Mathieu, M. Hudl, P. Nordblad, Y. Tokunaga, Y. Kaneko, Y. Tokura, H. Aruga Katori, A. Ito, Philos. Mag. Lett. **90**, 723 (2010)
29. P. Nordblad, M. Hudl and R. Mathieu, Exchange bias in dilute magnetic alloys in *Exchange Bias: From Thin Film to Nanogranular and Bulk Systems*, ed. by S.K. Sharma (CRC Press, 2017) p 71
30. W.H. Meiklejohn, C.P. Bean, Phys. Rev. **102**, 1413–1414 (1956); ibidem **105**, 904–913 (1957)
31. P. Anil Kumar, G. Singh, W.R. Glomm, D. Peddis, E. Wahlström, R. Mathieu, Mater. Res. Express **1**, 036103 (2014)
32. V. Skumryev, S. Stoyanov, Y. Zhang, G. Hadjipanayis, D. Givord, J. Nogués, Nature **423**, 850–853 (2003)
33. J.A. González, J.P. Andrés, R. López Antón, J.A. De Toro, P.S. Normile, P. Muniz, J.M. Riveiro, J. Nogués, Chem. Mater. **29**, 5200–5206 (2017)
34. N. Domingo, D. Fiorani, A.M. Testa, C. Binns, S. Baker, J. Tejada, J. Phys. D Appl. Phys. **41**, 134009 (2008)
35. G. Margaris, M. Vasilakaki, D. Peddis, K.N. Trohidou, S. Laureti, C. Binns, E. Agostinelli, D. Rinaldi, R. Mathieu, D. Fiorani, Nanotechnology **28**, 035701 (2017)
36. D. Peddis, M.T. Qureshi, S.H. Baker, C. Binns, M. Roy, S. Laureti, D. Fiorani, P. Nordblad, R. Mathieu, Philos. Mag. **95**, 3798 (2015)
37. H. Zeng, J. Li, J.P. Liu, Z.L. Wang, S. Sun, Nature **420**, 395 (2002)
38. B. Balamurugan, D.J. Sellmyer, G.C. Hadjipanayis, R. Skomski, Scripta Mater. **67**, 542–547 (2012)
39. P. Anil Kumar, D.D. Sarma, Appl. Phys. Lett. **100**, 262407 (2012)
40. H. Zheng, J. Wang, S.E. Lofland, Z. Ma, L. Mohaddes-Ardabili, T. Zhao, L. Salamanca-Riba, S.R. Shinde, S.B. Ogale, F. Bai, D. Viehland, Y. Jia, D.G. Schlom, M. Wuttig, A. Roytburd, R. Ramesh, Science **303**, 661–663 (2004)
41. Y. Tokura, N. Nagaosa, Science **288**, 462 (2000)
42. G. Muscas, P. Anil Kumar, G. Barucca, G. Concas, G. Varvaro, R. Mathieu, D. Peddis, Nanoscale **8**, 2081 (2016)
43. D. Peddis, C. Cannas, A. Musinu, A. Ardu, F. Orrù, D. Fiorani, S. Laureti, D. Rinaldi, G. Muscas, G. Concas, G. Piccaluga, Chem. Mater. **25**, 2005–2013 (2013)
44. G. Singh, H. Chan, A. Baskin, E. Gelman, N. Repnin, P. Král, R. Klajn, Science **345**, 1149–1153 (2014)
45. J. Chen, A. Dong, J. Cai, X. Ye, Y. Kang, J.M. Kikkawa, C.B. Murray, Nano Lett. **10**, 5103–5108 (2010)
46. G. Singh, H. Chan, T. Udayabhaskararao, E. Gelman, D. Peddis, A. Baskin, G. Leitus, P. Král, Rafal Klajn, Faraday Discuss. **181**, 403 (2015)
47. A. Fabian, M.T. Elm, D.M. Hofmann, P.J. Klar, J. Appl. Phys. **121**, 224303 (2017)
48. Elena V. Sturm, Helmut Cölfen, Crystals **7**, 207 (2017)
49. M.S. Saleh, C. Hu, R. Panat, Sci. Adv. **3**, e1601986 (2017)

Part II
Magnetic Nano Architectures Design

Chapter 4
Core/Shell Bimagnetic Nanoparticles

Elin L. Winkler and Roberto D. Zysler

Abstract The advances in the physical and chemical fabrication methods have enabled the possibility to produce artificial nanostructures whose properties are different from that of their constituent materials. The presence of interfaces in core/shell bimagnetic nanoparticles introduces additional interactions that could radically modify the static and dynamic magnetic behavior of the systems. The number of parameters that governs the magnetic behavior grows enormously and the opportunity to manipulate, control, and understand the role played by each one of them, opens a wide range of possibilities to design novel materials with suited properties. The magnetic response changes depend on the magnetic ordering and anisotropy of the phases, the core size and shell thickness, the quality of the interface, and the strength of the interface exchange coupling. In this chapter, we discuss the new properties found in core/shell bimagnetic nanoparticles and analyze the main characteristics that have to be taken into account to design a system with a particular response.

4.1 Introduction

The magnetism has had a tremendous impact on our daily life, and it has transformed our society, the way we see the world and the way we communicate each other. These days, it exist a huge demand of new materials to be used in numerous applications, and for developing new smaller devices and with improved performance. Large part of

E. L. Winkler (✉) · R. D. Zysler (✉)
Centro Atómico Bariloche and Instituto Balseiro Comisión Nacional de Energía Atómica (CNEA), Consejo Nacional de Investigaciones Científicas Y Técnicas (CONICET), Universidad Nacional de Cuyo (UNCUYO), Av. E. Bustillo 9500, R8402AGP San Carlos de Bariloche, Río Negro, Argentina
e-mail: winkler@cab.cnea.gov.ar

R. D. Zysler
e-mail: zysler@cab.cnea.gov.ar

D. Peddis et al. (eds.), *New Trends in Nanoparticle Magnetism*,
Springer Series in Materials Science 308,
https://doi.org/10.1007/978-3-030-60473-8_4

the research on field was driven by looking for harder and softer magnetic materials, and compounds for magnetic recording.

One important area in this field is the development of high-performance permanent magnets which requires hard magnetic materials with large energy product $(BH)_{max}$. Most of the progress in this area was reached from the design of new alloys that combines 3d ions coupled with rare-earth ions as $SmCo_5$, $Nd_2Fe_{14}B$, $Sm_2Fe_{17}N_3$, in this way compounds with large remanent magnetization and large coercive field are obtained. Novel ways to fabricate permanent magnets exploit the exchange length of the magnetic materials by combining at nanoscale soft with hard magnetic materials, composites with large magnetization, and also large magnetic anisotropy could be obtained. This strategy also opens new possibilities to fabricate new compounds with large energy products and rare-earth free magnets which would lower the cost of raw materials for manufacturing, and also simplify production due to the limitations of obtaining rare earth. The dimension of each component is determinant in this family of nanostructures and as a consequence fine control of the morphology and structure at nanoscale is mandatory.

The miniaturization of the magnetic devices and the increasing demand of high-density data storage materials also have driven the research in material science. The pushing toward high-density data storage in smaller dimensions has to face the well-known superparamagnetic limits so other approaches based on exchange coupling bimagnetic materials at nanoscale emerge as a possible solution. As it was mentioned previously, the current strategy does not go through the search for new compounds, although it cannot be ruled out to find a new phase with astonishing properties, but it is looking to design and manufacture new compounds from the possibility of manipulating and combining materials at the nanoscale. New synthesis and physical fabrication methods give a huge impulse to the area. The possibility of combining in a single nanoparticle two or more components, with controlled size and high quality of interfaces, opens a wide range of new possibilities.

The presence of interfaces in core/shell bimagnetic nanoparticles introduces additional interactions that could radically modify the static and dynamic magnetic behavior of the systems. The number of parameters that governs the magnetic behavior grows enormously and the opportunity to manipulate, control, and understand the role playing by each one of them opens a wide range of possibility to design novel materials with suited properties. The magnetic response changes depend on the magnetic ordering and anisotropy of the phases, the core size and shell thickness, the quality of the interface, and the strength of the interface exchange coupling. As a consequence, different behaviors named exchange spring, exchange bias, magnetic hardening, and proximity effects are observed. In this chapter, we are going to focus on the advances reached in the fabrication and the new properties found in core/shell bimagnetic nanoparticles, and we will discuss the main characteristics that have to be taken into account to design a particular system. The chapter is organized as follows: in Sect. 4.2, a brief summary of the most used synthesis methods is given. In Sect. 4.3, we will focus on the phenomenology and the physical parameters that determine the magnetic response of the core/shell system. In Sect. 4.4, we are going to present a case study, CoO-core/$Co_{1-x}Zn_xFe_2O_4$-shell nanoparticles with $x = 0$–1,

where the tuning of the coercive field, the thermal stability and the exchange bias will be attained by controlling the size and the interface exchange coupling. Finally, in the last section, future perspectives on the field will be described.

4.2 Synthesis and Production of Core/Shell Nanoparticles

The advances in the chemical and physical fabrication methods have enabled a continuous production of novel multifunctional nanostructures. In the particular case of bimagnetic nanoparticles, according to the technological challenge or basic research, different core/shell structures, including FM(FiM)-core/AFM-shell [1, 5, 9], FM-core/FiM-shell [66], hard/soft FiM-core/FiM-shell [11, 39], inverted AFMcore/FiM-shell [30, 36], doubly inverted AFM-core/FiM-shell ($T_N > T_C$) [53], and multishell nanoparticles [54], have been fabricated.

A physical approach to the fabrication of bimagnetic nanoparticles is based on obtaining the initial nanoparticles by known methods as gas condensation, thermal plasma, or spray pyrolysis. These initial particles can be formed, in general, by simple metals, alloys, or oxides. A second step, consisting of a post-treatment of partial reduction of oxides or oxidation of alloys (or overoxidation of certain oxides), provides a core/shell architecture to the nanoparticles. An example of oxidation of metallic particles has been reported in the initial paper of the exchange bias phenomena where cobalt particles were oxidized giving a Co/CoO ferromagnetic/antiferromagnetic core/shell structure [43]. Another example of oxidation of seeded nanoparticles is given by the Ni/NiO (ferromagnetic/antiferromagnetic) core/shell structures [23]. On the other hand, the reduction of transition metal oxides by annealing in reducing atmosphere (e.g., H_2) can also be used to obtain the desired core/shell nanostructures as the CoO (Co_3O_4)/Co antiferromagnetic/ferromagnetic inverted core/shell structure [63] or $CoFe_2O_4/CoFe_2$ [20].

The concept to produce core/shell nanoparticles by chemical route is similar. Single-phase nanoparticles are synthesized by a particular chemical method, and using the same concept of superficial post-treatment, an oxidation (reduction) is taking effect in order to obtain the core/shell structure. Many chemical routes give high control of composition, crystallinity, and size. There exists a large diversity of synthesis methods such as co-precipitation [13], sol–gel [64], cation exchange process [59], and thermal decomposition [35, 45]. Although it is very simple to obtain core/shell architecture by post-processing the surface, there are inherent drawbacks to the method that limit its application, i.e., it is very difficult to control independently the core and shell sizes, and the shell composition is determined (and limited) by the core composition. On the other hand, these manufacturing methods produce a low quality of the core/shell interface. The last point is a major problem in the observation of the exchange bias effect and/or the enhancement of the coercive field.

Another interesting approach is the seed-mediated growth method. This procedure consists in the synthesis of the core and shell in two stages which enable to control independently both composition and size of each component This opens up many

possibilities for manufacturing new systems, where proper materials can be chosen to optimize the exchange interaction between the two magnetic phases, i.e., by minimizing the crystalline mismatch, selecting compounds with particular magnetization and magnetic anisotropy, etc. The seed-mediated high-temperature thermal decomposition method has shown high efficiency in producing monodispersed nanoparticles with high quality of crystalline order and well-defined interfaces. These characteristics make it one of the most used methods which enabled the fabrication of many novel core/shell bimagnetic nanoparticles, e.g., $CoO/CoFe_2O_4$ [36], $CoO/NiFe_2O_4$ [31], $CoFe_2O_4/MnFe_2O_4$ [57], $Fe_3O_4/\gamma\text{-}Mn_2O_3$ [24], $ZnFe_2O_4/CoFe_2O_4$ [42]. Also, two-step co-precipitation methods have proven to be appropriate for creating core/shell architecture. Examples of that are $\gamma\text{-}Fe_2O_3/CoO$ [55], SmCo/Co [65], and $CoFe_2O_4/Fe_3O_4$ [16]. The mentioned chemical routes, among many others [15], show an enormous versatility and easy to produce a great variety of bimagnetic core/shell nanoparticles, which make this field promising for the design and fabrication of new systems for fundamental studies or for the development of nanoparticles for a wide range of applications.

4.3 Interface Coupling Phenomenology and Models

As the size of a magnetic material is reduced to nanometric scale, the surface-to-volume ratio increases and, as a consequence, the surface effects became more relevant. For example, approximately 1% of the atoms are located at the surface of single-phase nanoparticles of 100 nm, while the proportion increases over the 60% when the size diminishes to 3 nm. Surface defects, broken bonds, variation in the interatomic distance and surface local anisotropy induce magnetic disorder and magnetic frustration. In bimagnetic core/shell nanoparticles, besides the surface effects, the presence of the interface between the two magnetically ordered phases introduces additional interactions that could radically modify the static and dynamic magnetic behavior of the systems. This interface interaction can generate a new behavior that is not present in any of the original components as exchange bias effect, exchange spring, and anisotropy enhancement, which present characteristic hysteresis loops as illustrated in Fig. 4.1. There are good and complete reviews in the literature that discuss in detail the models that describe these effects [14, 22, 25, 39, 46, 48], below we are going to mention the main characteristics that has to be taken into account to predict the behavior and for designing a particular system.

4.3.1 Exchange Bias Effect

In bimagnetic nanostructures with FM/AFM interfaces, the exchange bias effect (E_B) is typically manifested by a field shift (H_{EB}) of the hysteresis loop when the material is field cooled from temperatures higher than the Néel temperature of the AFM (T_N)

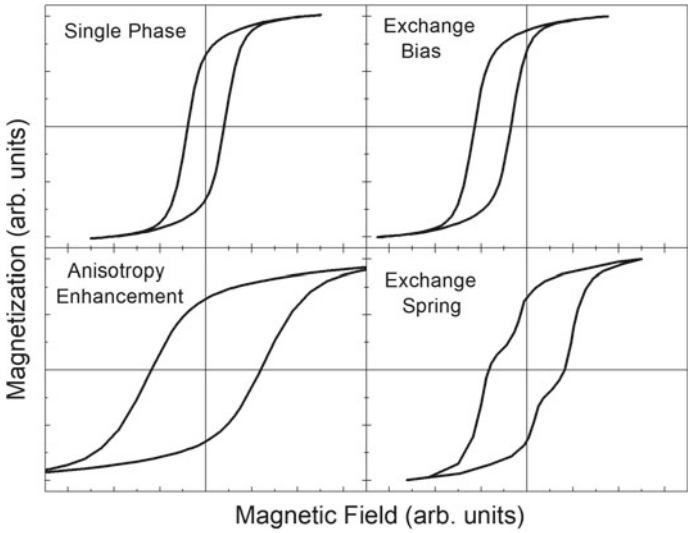

Fig. 4.1 Scheme of the magnetization loops for a single-phase magnetic nanoparticles and for different exchange coupled systems where exchange bias, anisotropy enhancement, and exchange spring behaviors are illustrated

and lower than the Curie temperature of the FM (T_C). The phenomenon is also related to other features as unidirectional anisotropy, coercive field enhancement, enhancement of the thermal stability of the nanoparticle magnetic moment, and vertical shift or asymmetric of the magnetization loop. Since the first observation of the unidirectional anisotropy in Co/CoO nanoparticles by Meilklejhon and Bean in 1956 [43], important advances have been made, both in the fabrication of new exchange bias structure and also in the development of theories explaining the origin of the observed behavior. Initially, most of the studies were made in thin films due to the high degree of control in the fabrication process, and they were impulsed by the crucial role played by the interfaces in technological application as read-head, high-density magnetic memories, spin valves, etc. Later, novel chemical route allowed a great control of the growing parameters of magnetic nanoparticles making it possible the design and fabrication of an enormous variety of biphase or even multiphase nanoparticles.

The physical origin of EB is usually explained by describing the pinning action exerted by the AFM over the FM(FiM) spins, as a consequence of the exchange coupling at the AFM/FM(FiM) interface. This interaction induces an extra torque to the magnetization reversal process and, depending to the ratio between the interface coupling energy and the anisotropy energy of the AFM, an asymmetry of the magnetization loops or enhancement of the coercive field, or both effects are observed. In a simple phenomenological model, considering the Zeeman interaction, the magnetic anisotropy of both phases, and the FM/AFM exchange interaction, the free energy of a FM/AFM coupled system can be expressed as:

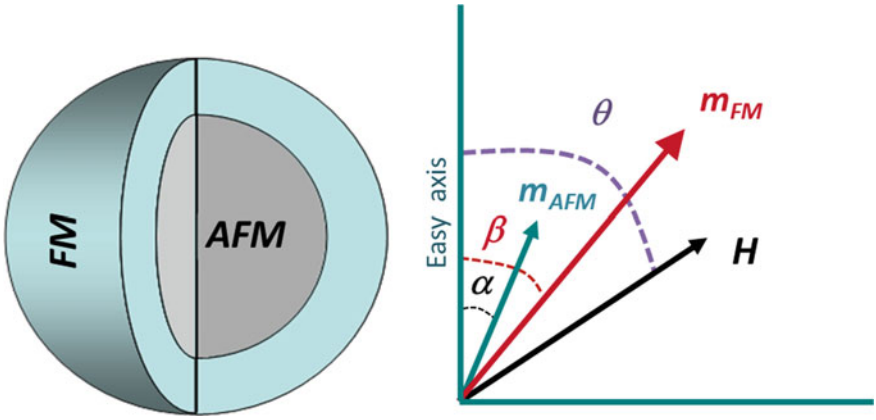

Fig. 4.2 Schematic representation of the magnetizations of the antiferromagnetic (m_{AFM}) and the ferromagnetic (m_{FM}) component of a core/shell nanoparticle, the magnetic field (H), and the angles involved in the description of the free energy

$$E = -Hm_{FM}V_{FM}.\cos(\theta - \beta) - Hm_{AFM}V_{AFM}\cos(\theta - \alpha) + K_{FM}V_{FM}\sin^2\beta + K_{AFM}V_{AFM}\sin^2\alpha - J_{EX}\cos(\beta - \alpha)$$

where H is the applied magnetic field, m_{FM} is the saturating FM magnetization normalized by the total FM volume (V_{FM}), m_{AFM} is the uncompensated AFM magnetization normalized by the total AFM volume (V_{AFM}), K_{FM} and K_{AFM} are the magnetic anisotropy of the FM and AFM phases, J_{EX} is the exchange coupling constant at the interface; the α, β, and θ are the angles between m_{AFM}, m_{FM}, and H with the easy axis direction, respectively, as shown in Fig. 4.2. The expression above includes two important approximations, the first one assumes a coherent rotation of the saturation magnetization with the field, and the second one assumes that the FM and AFM anisotropy easy axis are parallel.

From the above expression, two limit situations can be considered: $K_{AFM}V_{AFM} \gg J_{EX}$ and $K_{AFM}V_{AFM} \ll J_{EX}$. In the first case, $K_{AFM}V_{AFM} \gg J_{EX}$, after a field cooling process from a temperature $T_N < T < T_C$, the spins at the AFM interface align parallel (or antiparallel for $J_{EX} < 0$) to the FM phase in order to minimize the energy due to the interface exchange coupling. In this particular configuration, for $J_{EX} > 0$, the requested field to produce the inversion of the magnetization is higher in the opposite direction of the applied magnetic field which originates the characteristic unidirectional anisotropy and negative exchange bias field. In this approximation, the magnetic structure of the AFM phase remains unchanged during the magnetization reversal process. From (1), the equilibrium angles of magnetization can be easily calculated for $\alpha \sim 0$ and $m_{AFM} \sim 0$, and the exchange bias field can be obtained: $H_{EB} = -J_{EX}/(m_{FM}V_{FM})$.

As the real interfaces are far away to the ideal sharp AFM/FM interface, the predicted H_{EB} value is overestimated even by several orders of magnitude. Novel

experimental and theoretical approaches show the presence of pinned and unpinned spins at the interface, where only the AFM pinned spins, exchange coupled with the FM phase, give place to the loop shift after the field cool process. As a consequence, the coupling energy should be normalized by replacing it by an effective J_{EFF} value that accounts for the pinned spins faction ρ, $J_{EFF} = \rho J_{EX}$, which reduces the surface exchange energy consistently with the smaller H_{EB} observed [3, 49, 53]. Ohldag and co-workers [49, 40], from X-ray circular dichroism experiments on exchange bias multilayers, found that only a small fraction of interfacial spins ~4% is pinned to the AFM component. Similar results were reported in several core/shell systems as Fe@Cr [3], MnO@Mn_3O_4 [53, 67], Fe/γ-Fe_2O_3 [21], CoO@$Co_{1-x}Zn_xFe_2O_4$ [29]where the strength of the exchange coupling is correlated with the density of interfacial frozen spins. The exchange bias shift is often accompanied by a vertical shift displacement of the magnetization loop originated by the uncompensated AFM spins that remain pinned during the hysteresis loop. Size dependence studies show that the vertical shift, which is proportional to the number of pinned spins, has a non-monotonous dependence with the size as shown in Fig. 4.3 for the Fe/γ-Fe_3O_4

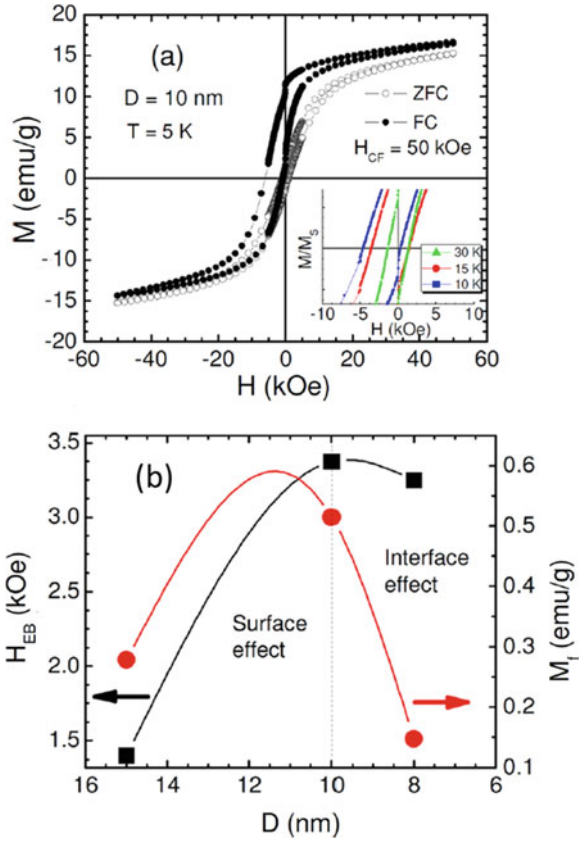

Fig. 4.3 **a** Zero-field cooling (ZFC) and field cooling (FC) magnetization loops taken at $T = 5$ K for 10 nm Fe/γ-Fe_2O_3 nanoparticles. The inset shows the FC $M(H)$ curves at different temperatures. **b**Exchange bias field (H_{EB}) and the net magnetic moment of the frozen spins (M_f) plotted as a function of particle. Reprinted from Khurshid et al. [21], with the permission of AIP Publishing

system [21]. However, although these quantities are related, the observation of a H_{EB} does not necessarily require the existence of uncompensated AFM spins.

Notice that the expression obtained for the exchange bias, within these approximation, does not depend on the magnetic anisotropy neither the size of the AFM phase. However, experimental evidence [41] shows that an AFM size threshold should be overcome to observe an exchange bias field. Figure 4.4 shows the dependence of $\mathbf{H_{EB}}$ of Fe_3O_4(FiM)core/CoO (AFM) shell nanoparticles as a function of the AFM shell thickness, where a non-monotonous dependence of the H_{EB} with the thickness is observed [38]. These results could be understood in terms of the diminution of the AFM anisotropy when the size of the AFM component diminishes beyond a critical thickness and, as a consequence, the AFM component is not longer pinned during the

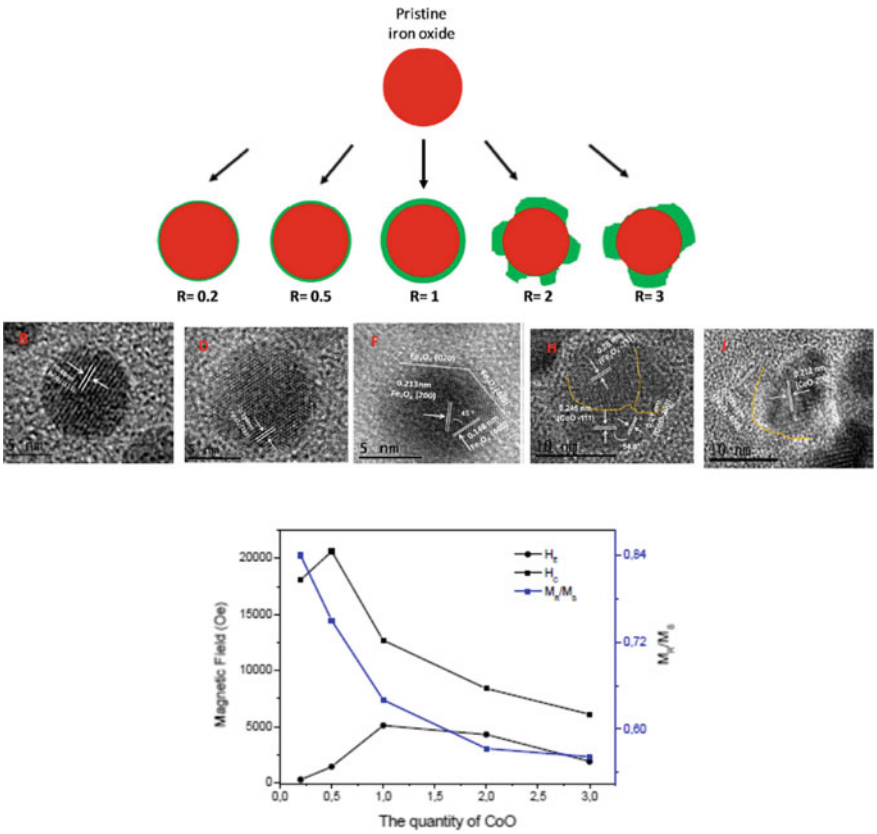

Fig. 4.4 Schematic and TEM image of the $Fe_{3-\delta}O_4$@CoO core/shell nanoparticles. The drawing shows the profile sections as a function of the Co(stearate)$_2$/Fe(stearate)$_2$ molar ratio *R*. $Fe_{3-\delta}O_4$ in red and CoO in green. The bottom graph shows the exchange bias field (H_E, ●) and the coercive field (H_C, ■), after FC and squareness (M_R/M_S, Bluebox) obtained from M(H) curves and plotted as a function of *R*. Adapted with permission from Liu et al. [38]. Copyright (2015) American Chemical Society

magnetization reversal mechanism. In spite of this, the authors call the attention on the complexity of the system that should be taken into account to interpret the results. On one hand, the growth process leads to a homogeneous CoO shell formation when the coating is thin, while polycrystalline discontinuous shell is found for thicker thicknesses. On the other hand, interdiffusion at the interface was found which leads a $CoFe_2O_4$ thin layer formation to be observed, only, in the thinner CoO shell. The presence of this hard/soft interface could result in the huge coercivity increase and the diminution of the exchange bias for the lower Co concentration.

Another parameter that plays a fundamental role in the exchange bias strength is the lattice mismatch between core and the shell phases. Depending of the system, different effects were reported. In the size dependence of Co-core/Co_3O_4-shell nanoparticles study it was found that the exchange bias field and the vertical shift present a maximum when the lattice mismatch is maximized. This result is associated with the increase of the interfacial magnetic anisotropy with the strain $\varepsilon_{Co} = (a_{Co} - a_{Co\text{-}bulk})/a_{Co\text{-}bulk}$, and also it is related with the increase of pinned spins with the lattice mismatch [8, 26, 51]. On the contrary, when the Co-core/CoO-shell nanoparticles are embedded in Cu_xO matrix, the exchange bias and the coercivity was optimized by diminishing the mismatch between the AFM shell and the matrix. In this case, by diminishing the mismatch, the highly anisotropic CoO phase is stabilized and also an increase of the number of pinned and unpinned uncompensated spins as a consequence of the interdiffusion of the Cu ions into the CoO shell is observed. This strategy could be reaches by modulating the oxygen partial pressure and therefore adjusting the Cu_xO phases, been Cu, Cu_2O, Cu_4O_3 or CuO, of the matrix [17]. These examples illustrate different approaches to maximize the anisotropy of the AFM phase and as a consequence optimize the EB effects.

Most of the researches on core/shell exchange bias systems report ferromagnetic coupling at the interface which is compatible with the negative H_{EB} usually observed. Different couplings were evaluated mainly from Monte Carlo simulations, however, only recently could be experimentally detected. Bimagnetic core/shell nanoparticles based on iron and manganese oxide were studied, and antiparallel coupling at the interface was found with the corresponding positive exchange bias field [11]. Interestingly, it was proved that the sign and the magnitude of the exchange bias field can be controlled by the cooling field, which give an additional tool to handle the EB effect.

Up to here we have discussed the reversal process when the AFM anisotropy energy is larger than the interface exchange energy, in the opposite situation: $J_{EX} \gg K_{AFM} V_{AFM}$, the AFM and FM phases are rigidly coupled and an enhancement of the magnetic anisotropy with the consequent coercivity increase is observed. From the equilibrium condition of the free energy, in the approximation $\alpha \sim \beta$ the coercivity field can be estimated:

$$H_C = \frac{2(K_{FM} V_{FM} + K_{AFM} V_{AFM})}{m_{FM} V_{FM} + m_{AFM} V_{AFM}},$$

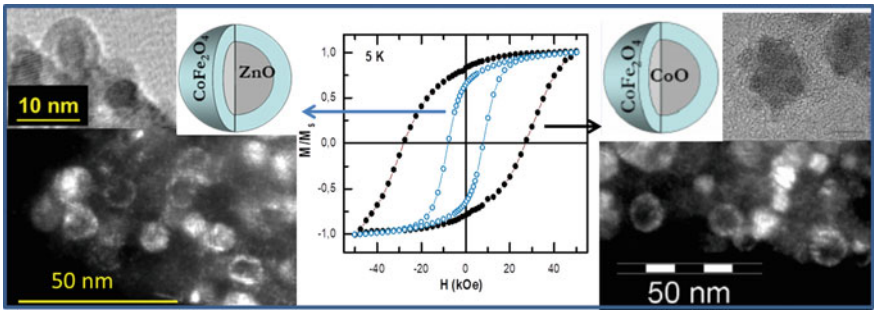

Fig. 4.5 TEM image of $ZnO/CoFe_2O_4$ and $CoO/CoFe_2O_4$ core/shell nanoparticles and the corresponding magnetization loops measured at $T = 5$ K, where the increase of the coercive field by the interface exchange coupled in the second sample is remarkable

where H_C results an average of the magnetic parameter of both phases. Figure 4.5 illustrates the coercivity enhancement by the interface exchange coupling observed in core/shell nanoparticles of 7.4 nm mean diameter [62]. In the figure, the magnetization loop of $CoFe_2O_4$ ferrite is compared when it grows over a diamagnetic ZnO or an AFM CoO core. In the former case, the coercivity result 7.8 kOe, instead in the exchange coupled $CoFe_2O_4/CoO$ system H_C increase more that 300% reaching the 27.8 kOe evidencing the magnetic hardening of the nanostructure by the interfacial exchange interaction.

The intrinsic complexity of core/shell nanoparticles makes it difficult the analysis of the exchange bias effect and the particularity of each system makes hard to including all the results in a single model. However, although the modified [43] phenomenological model fails to give a quantitative description, it provides a correct qualitative description of the systems, which results very useful for choosing suitable materials for designing nanostructures with tuned property.

4.3.2 Exchange Spring Behavior

The search of high-performance magnets has driven the development of nanostructured magnetic material that maximize the energy product $(BH)_{max}$, which can be achieved by increasing both the saturation magnetization and the coercive field. Therefore, the strategy is to combine at the nanoscale a FM (FiM) soft magnetic material, to maximize M_S, exchange coupled with a hard magnetic material, which usually presents lower M_S, to maximize H_C. This approach has the advantage of reducing the proportion of hard magnetic material based on rare earth with the corresponding cost reduction. However, as was settled by Kneller and Hawig in their pioneering work [22], when the fraction of FM soft material increases, a critical thickness, δ_c, is found. Below δ_c, both phases are rigidly exchange coupled and switch their magnetization simultaneously, whereas for larger thicknesses, the soft

phase nucleates and rotates reversibly at a lower magnetic field, as it is illustrated in Fig. 4.6. The critical thickness is related with the exchange length and results approximately twice the domain wall of the hard phase $d_H = \pi(A_H/K_H)^{1/2}$, where A_H and K_H are the exchange and anisotropy constant of the hard phase, respectively. Therefore, in hard/soft or soft/hard core/shell nanoparticles, when the thickness of the soft layer t_s is smaller than the δ_c, the magnetization of both materials is strongly coupled and invert simultaneously at a switching field H_{SW}, which results in an

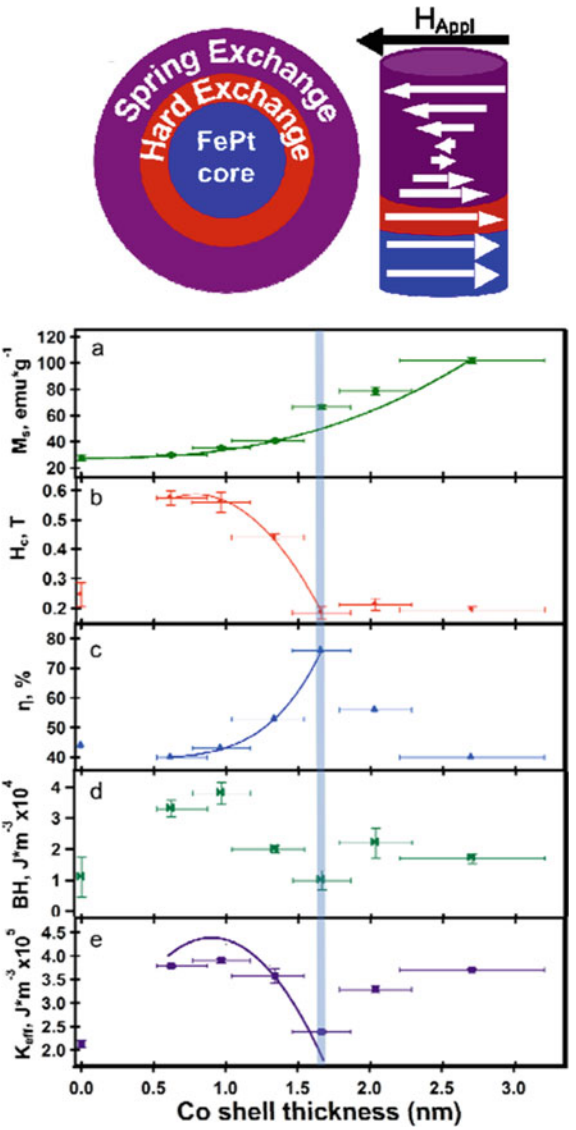

Fig. 4.6 Diagram of the proposed magnetic exchange regimes in the core/shell nanoparticles. Magnetic properties of FePt@Co nanoparticles as a function of the Co shell thickness: **a** saturation magnetization, Ms, **b** coercive field, Hc, **c** % remnant magnetization recovery, **d** energy product, BH, and **e** anisotropy constant, Keff. The blue shaded line indicates the maximum exchange-spring effect. Reprinted with permission from Carnevale et al. [4]. Copyright (2016) American Chemical Society

average of the parameters of both phases, $H_{SW} = 2(K_H V_H + K_S V_S)/(M_H V_H + M_S V_S)$, where K, M and V are the magnetic anisotropy, saturation magnetization, and volume, respectively, and the subindex S and H correspond to the soft and hard component.

When the thickness of the soft phase is larger than the critical thickness, $t_s > \delta_c$, the magnetization of both phases remains parallel until the Bloch-type domain wall nucleates in the soft phase at the magnetic field $H_N = \pi^2 AS/(2M_S tS^2)$, where A_S is the exchange constant of the soft component. For magnetic fields larger than H_N the domain wall moves toward the interface where the spins are pinned to the hard magnetic component (see Fig. 4.6). When H is further increased above H_{irr}, the domain wall will be compressed to the interface till the energy necessary for a displacement of the domain wall into the hard magnetic phase is reached. The irreversible field is usually smaller than the switching field of the hard phase but has the same order of magnitude. Below H_{irr} a reversible behavior of the magnetization is observed which resembled spring behavior, which originated the name of the process. Finally, when $t_s \gg \delta_c$ the magnetization inversion process corresponds to two independent phases.

The predicted evolution from rigid-coupled to exchange spring and beyond the exchange coupled behavior is nicely illustrated in the hard/soft $Fe_{0.65}Pt_{0.35}$-core/Co-shell nanoparticles case [4]. The system was synthesized by one-pot microwave chemical route which allows the control of the Co shell thickness from 0.6 to 2.7 nm over the hard fcc $Fe_{0.65}Pt_{0.35}$ of 5 nm of diameter. From the low-temperature hysteresis loop, the size dependence of the magnetic parameters was obtained as shown in Fig. 4.6. As expected, the saturation magnetization of the system systematically increases with the shell thickness, following a volumetric power law $M_S \propto r^3$. Conversely, the coercivity field follows non-monotonic size dependence. For a thinner Co layer, the H_C increases, a behavior ascribed to the improving of the hard magnetic properties due to the strong exchange coupling between the interface Co spins and the FePt core. When the thickness of the shell increases, the coercivity decreases due to the weaker pinning action exerted by the FePt hard magnetic phase over the outer Co layers, within this size range exchange spring process is observed. For a thicker shell, the magnetic behavior is dominated by the soft FM Co, as a consequence H_C diminishes and tends to an asymptotic value. An important consequence of the described behavior is the enhancement of the energy product which increases from 1.10(8) MGOe for FePt nanoparticles up to 3.82(5) MGOe when the core is encapsulated by a 1 nm thickness Co shell.

Finally, as the advanced chemical methods enabled to obtain monodispersed nanoparticle systems, large area of self-assembled nanoparticles can be fabricated. These systems look to optimize the core/shell nanoparticles as building blocks for advanced permanent magnetic applications reaching promising results at room temperature, as the FePt–Fe3O4 nanocomposites with an energy product of 20.1MGOe [65], FePt/Co [37], or rare-earth free core/shell nanoparticles $CoFe_2O_4/CoFe_2$ [56].

Much has been advanced in this time driven by new techniques of manufacture and characterization, and a large number of different materials has been fabricated

depending on the particular problem to be analyzed, or the magnetic response that it wanted to be achieved. In most of the cited examples, the magnetic response of bimagnetic nanoparticles is tuned by controlling the size of the core or shell components or by combining materials with different magnetocrystalline anisotropy. In the next section, we will discuss an alternative approach to control the magnetic properties as a function of the interface exchange energy.

4.4 Tuning the Magnetic Properties by the Interface Exchange Coupling

In Sect 4.3, the exchange bias effect was analyzed in AFM/FM(FiM) or FM(FiM)/AFM core/shell systems by comparing the magnetic anisotropy energy of the AFM phase with the interface exchange energy, where two limit situations were considered $K_{AFM}V_{AFM} \gg J_{EX}$ and $K_{AFM}V_{AFM} \ll J_{EX}$. Here, we present a model system to analyze the evolution of the exchange bias effect as a function of the interface coupling. With this aim CoO, AFM nanoparticles of ~3 nm of diameter were synthesized by high-temperature decomposition of organometallic precursor and encapsulated with a $Co_{1-x}Zn_xFe_2O_4$ shell of ~4 nm thickness. It is expected that by replacing the Co^{2+} ($3d^7$, $S = 3/2$) by Zn^{2+} ($3d^{10}$, $S = 0$) the strength of the interface exchange coupling would be reduced, therefore a change from rigid coupling ($K_{AFM}V_{AFM} < J_{EX}$) to exchange bias regime ($K_{AFM}V_{AFM} > J_{EX}$) could be obtained. In order to perform a systematic study, the CoO cores were synthesized in one step and split in five batches to overgrow the shells with different compositions, and this step assures that the properties of the AFM component are comparable in all the studied systems. Figure 4.7 shows TEM images of the five systems studied named Zn-x, where x corresponds to the Zn concentration that changed nominally as $x = 0, 0.25, 0.50, 0.75, 1$. All the systems present comparable size ~ 11 nm and similar morphology, also notice that the shell is formed by several nanograins in close contact as was observed in other core/shell system [36, 38].

From the FC and ZFC magnetization loops, the coercivity and the exchange bias fields were obtained and they are shown in Fig. 4.8. Also, for comparison, the field values for 8 and 5 nm $CoO/CoFe_2O_4$ core/shell bimagnetic nanoparticles [29] and the coercivity of $(Co_{1-x}Zn_x)Fe_2O_4$ single-phase nanoparticles [19, 18] are included. Several features of this figure call the attention: the coercivity field monotonically decreases with the Zn concentration, while the H_{EB} presents a maximum H_{EB} ~1500 Oe for $x = 0.25$; also, when the H_C values are compared with the obtained for the single-phase ferrite, the magnetic hardening of the system is evidenced. Moreover, it is noteworthy that H_C and H_{EB} can be systematically changed without producing a significant modification of the magnetization.

As it is known, the magnetocrystalline anisotropy is originated in the spin orbit coupling. In the cobalt ferrite, the Co^{2+} ($3d^7$, $S = 3/2$) occupy the octahedral site of the spinel structure resulting in a degenerate ground-state energy level with nonzero

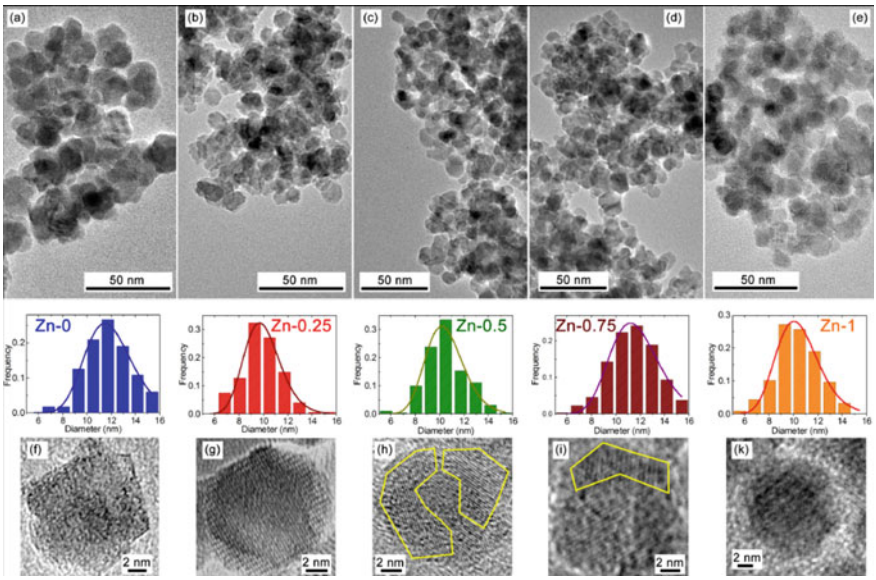

Fig. 4.7 **a–e** Transmission electron microscopy image, with the corresponding size histograms, and **f–k** high-resolution TEM images of CoO/ $Co_{1-x}Zn_xFe_2O_4$ ($x = 0$–1) core/shell nanoparticles (samples name Zn-x). Reproduced from Lavorato et al. [32] with permission from The Royal Society of Chemistry

orbital angular momentum [7, 47] (as a consequence the orbital magnetic moment interact with the spin originating large magnetocrystalline energy. The anisotropy constant reported for the Co ferrite at room temperature is K ~4 × 10^6 erg/cm^3 [46, 61]. On the contrary, the Zn^{2+} does not present spin orbit interaction because its outer configuration is fulfilled. Therefore, when the Zn concentration increases, it is expected a decrease of the effective magnetic anisotropy of the $(CoZn)Fe_2O_4$. This argument is consistent with the diminution of the coercivity observed with x, however it is not enough to explain the results because the magnitude of the H_C is more than 100% larger in the core/shell system that in the $(CoZn)Fe_2O_4$ single-phase nanoparticles of similar size. If the interface exchange coupling is considered, this interaction provides an additional source of anisotropy that explains the enhancement of H_C and also the presence of H_{EB}.

The interface coupling energy could be estimated from the experimental parameters as $E_{EX} = H_{EB}V_{FiM}M_S$, where V_{FiM} and M_S are the volume and the saturation magnetization of the ferrite. It is found that, for round nanoparticles systems of 11 nm with a core of 2.7 nm of diameter, E_{EX} vary approximately linearly with the Zn concentration from 1.5 × 10^{-13} erg for $x = 0.25$ to 0.4 × 10^{-13} erg for $x = 0$. Although for $x = 0$ no H_{EB} was observed, the coupling energy can be estimated from the linear extrapolation resulting E_{EX} ~ 2 × 10^{-13} erg, value close to the anisotropy energy of the CoO antiferromagnetic component $E_{AFM} = K_{AFM}V_{AFM}$~3.1 × 10^{-13} erg. Microscopically, this result could be interpreted from the modified Meilklejhon

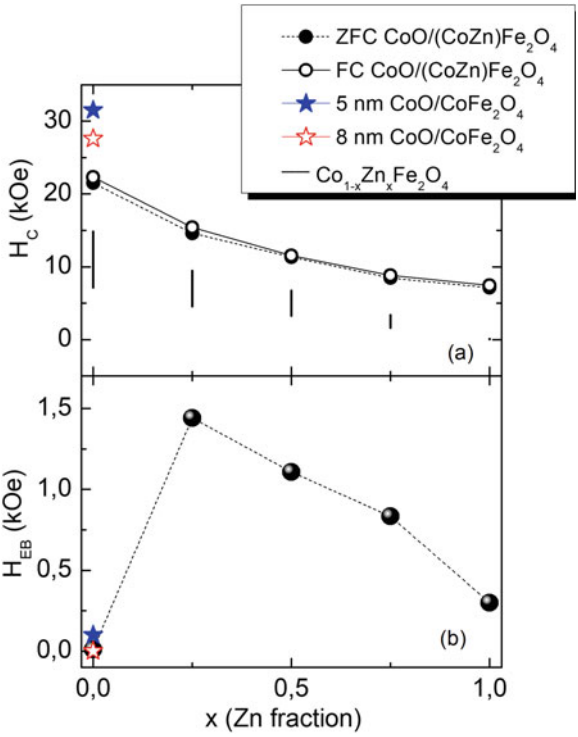

Fig. 4.8 **a** Zero-field-cooled and field-cooled (from 310 K with 10 kOe) H_C and **b** H_{EB} of $CoO/Co_{1-x}Zn_xFe_2O_4$ ($x = 0$–1) core/shell nanoparticles measured at 5 K. For comparison, the H_C of $Co_{1-x}Zn_xFe_2O_4$ [19] and [18], and also the H_C and H_{EB} values for 5 and 8 nm $CoO/CoFe_2O_4$ [29] are shown. Reproduced from Lavorato et al. [31], with permission from The Royal Society of Chemistry

and Bean model where the surface interface energy is normalized by the fraction of effective pinned spins, n, $E_{EX}/A_{int} = nJS_{FiM}S_{AFM}/a_{AFM}{}^2$, where A_{int} is the surface area, $J = J_{Co–Co} = 21.2$ K, $S_{AFM} = 3/2$, S_{FiM} is approximately 5/2, $a_{AFM} = 4.26$ Å. Figure 4.9 shows the evolution of the calculated energy and the fraction of pinned spins with the Zn concentration. The replacement of Co by the non-magnetic Zn ions induces a reduction of the interface coupling changing the relation between the involved energy E_{AFM} and E_{EX}, promoting the change of behavior from rigid coupling to exchange bias. When the Zn concentration further increases, the fraction of pinned spins continuously diminishes and the interface coupling is less effective, as a consequence the H_{EB} diminishes.

In summary, the presented approach provides a way to tune the magnetic hardening and the exchange bias field of the system by tuning the exchange coupling at the AFM/FiM interface of core/shell nanoparticles.

4.5 Future and Perspectives

The impressive advances in the physical and chemical fabrication methods have enabled the possibility to produce artificial nanostructures whose properties are

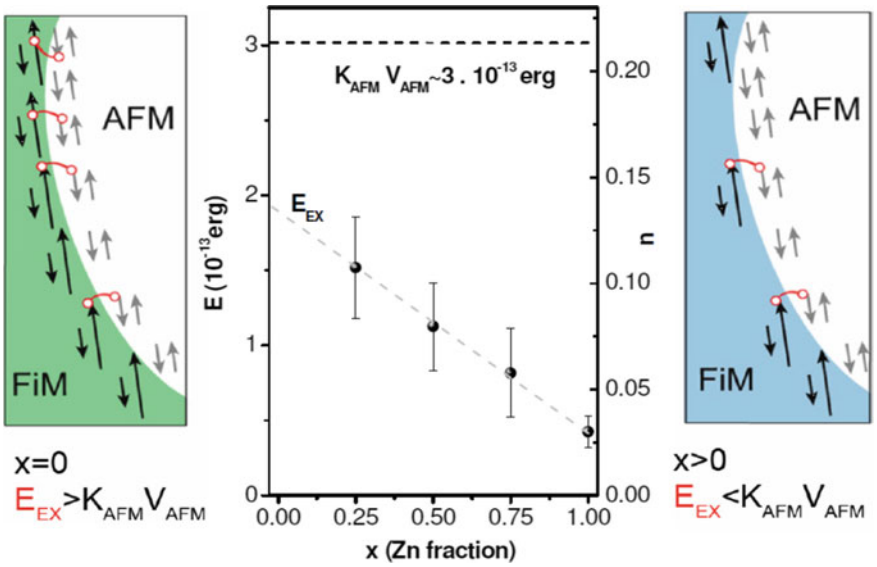

Fig. 4.9 Variation of the interface exchange coupling energy (E_{EX}) and the associated fraction of pinned uncompensated spins at the interface (n, right axis) with the Zn concentration (solid line) estimated from the experimental data (circles). The horizontal dotted line indicates the anisotropy energy of the AFM core estimated from the experimental data. The left ($x = 0$) and right ($x > 0$) panels show schematically the reduction in the effective number of exchange-coupling bonds at the interface when doping the Co ferrite with non-magnetic Zn atoms. Reproduced from Lavorato et al. [32], with permission from The Royal Society of Chemistry

different from that of their constituent materials. The core/shell nanoparticles systems have shown great versatility in the capacity to design *new materials* with tuned properties. In this chapter, we have shown that, by the interface exchange coupling, the magnetic hardening and the energy product for permanent magnets can be enhanced, and also the exchange bias can be tuned to produce an offset in the magnetization loops of great interest for spintronic and data storage applications. Recently, chemical method allows the fabrication of tunnel magnetoresistance devices based on bimagnetic nanoparticles or multicomponent superlattice [2, 6, 10, 27, 58, 60]. As it is well known, magnetic tunnel junction is composed by two ferromagnetic conducting layers separated by an insulating tunneling barrier, and the electrical resistance of the device switches between high and low resistance states as the magnetic field changes the relative orientation of the magnetizations of the two magnetic layers. In these nanostructures, the magnetic switching field is determined by the magnetic anisotropy of the system. Therefore, the possibility of combining ferromagnetic conductors with magnetic insulators in a single nanoparticle with core/shell structure would allow the manipulation the characteristic of switching field by tuning the interface exchange coupling, which would opens new and exciting possibilities to use the nanoparticles as the building blocks for new devises. The perspectives for improvement and innovation are huge, where different nanostructures can

be developed to obtaining multiple magnetotransport, or magnetoelectric responses. Different magnetic characteristics, i.e., exchange spring, exchange bias, can be tuned by choosing different hard/soft or soft/hard core/shell materials. Also, the tunnel barrier can be modulated by modifying the shell structure and composition.

The versatility and ease production of the core/shell nanostructures were also exploited in the biomedical field. For example, for magnetic fluid hyperthermia, it is necessary to tune the nanoparticles magnetic properties in order to produce the highest specific power loss for a given alternating magnetic field. Core/shell systems are the suit material to pursue this goal since, as we have showed previously, proper anisotropy and magnetization could be easily tuned by the exchange interaction [28, 34, 50]. The development of bifunctional nanoparticles also presents an exciting perspective. For example, the incorporapproximately linearly with the Zn concentrationation of optical functionalities to magnetic nanoparticles could contribute to the future development of magnetic fluid hyperthermia and its clinical application by monitoring their presence in the intracellular medium in vitro through fluorescence microscopy. In this area, we can mention the development of bifunctional $CoFe_2O_4$(core)/ZnO(shell) nanoparticles with simultaneous photoluminescence in the visible range (shell) and optimized magnetic properties (core), suited for produce AC magnetic losses for hyperthermia treatment [33], or for MRI contrast agent [61].

An important aspect that should be taken into account for biomedical applications is the biocompatibility of these nanostructures. The surface modification of the nanoparticles, or its encapsulation with a biocompatible shell, could expand the available materials in this area and its range of applications [12]. In particular, the nanoparticles can be coated with silica [52] or hydroxyapatite [44], which could improve the biocompatibility, the nanoparticle chemical stability, reduce the toxicity and also the coating could provides an ideal support for subsequent functionalizations with active organic molecules.

The challenge for the future is the development of new core/shell nanoparticles systems where the properties are fundamentally determined by the interfaces. It is a very active area where novel systems with new properties are continuously reported. It is also an interdisciplinary field, with a tremendous impact in our society, impulsed by the synergy between the advancement in the chemical and physical fabrication methods together with the technological development of new characterization tools, and with the impetus given by the huge demand for new magnetotransport and magnetoelectronic devices or innovative biomedical therapies.

References

1. W. Baaziz, B.P. Pichon, C. Lefevre, C. Ulhaq-Bouillet, J.-M. Greneche, M. Toumi, T. Mhiri, S. Bégin-ColinJ, Phys. Chem. C **117**, 11436 (2013)
2. C.T. Black, C.B. Murray, R.L. Sandstrom, S. Sun, Science **290**, 1131 (2000)
3. C. Binns, M.T. Qureshi, D. Peddis, S.H. Baker, P.B. Howes, A. Boatwright, S.A. Cavill, S.S. Dhesi, L. Lari, R. Kröger, S. Langridge, Nano Lett. **13**(7), 3334 (2013)
4. D.J. Carnevale, M. Shatruk, G.F. Strouse, Chem. Mater. **28**(15), 5480 (2016)

5. S. Chandra, H. Khurshid, W. Li, G.C. Hadjipanayis, M.H. Phan, H. Srikanth, Phys. Rev. B Condens. Matter **86**, 014426 (2012)
6. J. Chen, X. Ye, J.O. Soong, J.M. Kikkawa, C.R. Kagan, C.B. Murray, ACS Nano **7**, 1478 (2013)
7. S.O. Chikazumi, S.H. Charap, *Physics of Magnetism* (Wiley, New York, 1964)
8. D. De, O. Iglesias, S. Majumdar, S. Giri, Phys. Rev. B **94**, 184410 (2016)
9. A. Dobrynin, D. Ievlev, K. Temst, P. Lievens, J. Margueritat, J. Gonzalo, C.N. Afonso, S. Zhou, A. Vantomme, E. Piscopiello, G. Van Tendelloo, Appl. Phys. Lett. **87**, 012501 (2005)
10. A. Dong, J. Chen, P.M. Vora, J.M. Kikkawa, C.B. Murray, Nature **466**, 474 (2010)
11. M. Estrader, A. López-Ortega, S. Estradé, I.V. Golosovsky, G. Salazar-Alvarez, M. Vasilakaki, K.N. Trohidou, M. Varela, D.C. Stanley, M. Sinko, M.J. Pechan, D.J. Keavney, F. Peiró, S. Suriñach, M.D. Baró, J. Nogués, Nature Commun. **4**, 2960 (2013)
12. S. Foglia, M. Ledda, D. Fioretti, G. Iucci, M. Papi, G. Capellini, M. Grazia Lolli, S. Grimaldi, M. Rinaldi, A. Lisi, Sci. Rep. **7**, 46513 (2017)
13. N. Fukamachi, N. Tezuka, S. Sugimoto, J. Jpn. Inst. Met. **74**, 345 (2010)
14. E.E. Fullerton, J.S. Jiang, S.D. Bader, J. Magn. Magn. Mater. **200**, 392 (1999)
15. R. Ghosh Chaudhuri, S. Paria, Chem. Rev. **112**, 2373 (2012)
16. J.A. Gomes, M.H. Sousa, F.A. Tourinho, R. Aquino, G.J. da Silva, J. Depeyrot, E. Dubois, R. Perzynski, J. Phys. Chem. C **112**, 6220 (2008)
17. J. A. Gonzalez, J. P. Andrés, R. López Antón, J. A. De Toro, P. S. Normile, P. Muñiz, J. M. Riveiro, J. Nogués, Chem. Mater. **29**, 5200 (2017)
18. F. Gozuak, Y. Köseoglu, A. Baykal, H. Kavas, J. Magn. Magn. Mater. **321**, 2170 (2009)
19. H. Huang, Y. Zhang, Z. Huang, Z. Kou, X. Yuan, Z. Ren, Y. Zhai, J. Du, H. Zhai, J. Appl. Phys. **117**, 17E711 (2015)
20. J. Jin, X. Sun, M. Wang, Z.L. Ding, Y.Q. Ma, J. Nanopart. Res. **18**, 383 (2016)
21. H. Khurshid, M.-H. Phan, P. Mukherje, H. Srikanth, Appl. Phys. Lett. **104**, 072407 (2014)
22. E.F. Kneller, R. Hawig, IEEE Trans. Magn. **27**, 3588 (1991)
23. F. Einar Kruisa, H. Fissana, A. Peleda, J. Aerosol Sci. **29**, 511 (1998)
24. K.L. Krycka, J. Borchers, G. Salazar-Alvarez, A. López-Ortega, M. Estrader, S. Estrade, E. Winkler, R.D. Zysler, J. Sort, F. Peiró, M.D. Baró, C.-C. Kao, J. Nogués, ACS Nano **7**, 921 (2013)
25. M. Kiwi, J. Mag. Mag. Mat. **234**, 584 (2001)
26. Z.-A. Li, N. Fontaíña-Troitiño, A. Kovács, S. Liébana-Viñas, M. Spasova, R.E. Dunin-Borkowski, M. Müller, D. Doennig, R. Pentcheva, M. Farle, V. Salgueiriño, Sci. Rep. **5**, 7997 (2015)
27. F. Fabris, E. Lima Jr., C. Quinteros, L. Neñer, M. Granada, M. Sirena, R.D. Zysler, H.E. Troiani, V. Leborán, F. Rivadulla, E.L. Winkler, Phys. Rev. Appl. **11**, 054089 (2019)
28. F. Fabris, E. Lima, Jr., E. De Biasi, H.E. Troiani, M. Vásquez Mansilla, T.E. Torres, R. Fernández Pacheco, M. R. Ibarra, G.F. Goya, R.D. Zysler, E.L. Winkler. Nanoscale **11**, 3164 (2019b)
29. G.C. Lavorato, E. Lima Jr., D. Tobia, D. Fiorani, H.E. Troiani, R.D. Zysler, E.L. Winkler, Nanotechnology **25**, 355704 (2014)
30. G.C. Lavorato, D. Peddis, E. Lima Jr., H.E. Troiani, E. Agostinelli, D. Fiorani, R.D. Zysler, E.L. Winkler, J. Phys. Chem. C **119**, 15755 (2015)
31. G. Lavorato, E. Winkler, A. Ghirri, E. Lima Jr., D. Peddis, H.E. Troiani, D. Fiorani, E. Agostinelli, D. Rinaldi, R.D. Zysler, Phys. Rev. B **94**, 054432 (2016)
32. G.C. Lavorato, E. Lima Jr., H.E. Troiani, R.D. Zysler, E.L. Winkler, Nanoscale **9**, 10240 (2017)
33. G. Lavorato, E. Lima Jr., M. Vasquez Mansilla, H. Troiani, R. Zysler, E. Winkler, J. Phys. Chem. C **122**, 3047 (2018)
34. G.C. Lavorato, R. Das, Y. Xing, J. Robles, F. Jochen Litterst, E. Baggio-Saitovitch, M.-H. Phan, H. Srikanth, ACS Appl. Nano Mater. **3**(2), 1755–1765 (2020)
35. E. Lima Jr., E. De Biasi, M. Vasquez Mansilla, M.E. Saleta, F. Effenberg, L.M. Rossi, R. Cohen, H.R. Rechenberg, R.D. Zysler, J. Appl. Phys. **108**, 103919 (2010)
36. E. Lima Jr., E.L. Winkler, D. Tobia, H.E. Troiani, R.D. Zysler, E. Agostinelli, D. Fiorani, Chem. Mater. **24**, 512 (2012)

37. F. Liu, J. Zhu, W. Yang, Y. Dong. Y. Hou, C. Zhang, H. Yin, S. Sun, Angew. Chem. **53**, 2176 (2014)
38. X. Liu, B.P. Pichon, C. Ulhaq, C. Lefèvre, J.M. Grenèche, D. Bégin, S. Bégin-Colin, Chem. Mater. **27**, 4073 (2015)
39. A. Lopez-Ortega, M. Estrader, G. Salazar-Alvarez, A.G. Roca, J. Nogués, Phys. Rep. **553**, 1 (2015)
40. A. Lopez-Ortega, D. Tobia, E. Winkler, I. V. Golosovsky, G. Salazar-Alvarez, S. Estradé, M. Estrader, J. Sort, M. A. González, S. Suriñach, J. Arbiol, F. Peiró, R. D. Zysler, M. D. Baró, and J. Nogués. J. Am. Chem. Soc. **132**, 9398–9407 (2010). https://doi.org/10.1021/ja1021798
41. M. Lund, W. Macedo, K. Liu, J. Nogués, I. Schuller, C. Leighto, Phys. Rev. B **66**, 544221 (2002)
42. O. Masala, D. Hoffman, N. Sundaram, K. Page, T. Proffen, G. Lawes, R. Seshadri, Solid State Sci. **8**, 1015 (2006)
43. W.H. Meiklejohn, C.P. Bean, Phys. Rev. **102**, 1413 (1956)
44. S. Mondal, P. Manivasagan, S. Bharathiraja, M. Santha Moorthy, H. Hyun Kim, H. Seo, K. Dae Lee, J. Oh, Int. J. Nanomed. **12**, 8389–8410 (2017)
45. S. Mourdikoudis, K. Simeonidis, M. Angelakeris, I. Tsiaoussis, O. Kalogirou, C. Desvaux, C. Amiens, B. Chaudret, Modern. Phys. Lett. B **21**, 1161 (2007)
46. J. Nogues, J. Sort, V. Langlais, V. Skumryev, S. Suriñach, J.S. Muñoz, M.D. Baró, Phys. Rep. **422**, 65 (2005)
47. C.R. O'Handley, *Modern Magnetic Materials: Principles and Applications* (Wiley, 1999). 978-0-471-15566-9
48. K. O'Grady, L.E. Fernandez-Outon, G. Vallejo-Fernandez, J. Mag. Mag. Mat. **332**, 883 (2010)
49. H. Ohldag, A. Scholl, F. Nolting, E. Arenholz, S. Maat, A.T. Young, M. Carey, J. Stöhr, Phys. Rev. Lett. **91**, 017203 (2003)
50. V. Pilati, R. Cabreira Gomes, G. Gomide, P. Coppola, F.G. Silva, F.L.O. Paula, R. Perzynski, G.F. Goya, R. Aquino, J. Depeyrot. J. Phys. Chem. C **122**, 5, 3028–3038 (2018)
51. A. Pratt, L. Lari, O. Hovorka, A. Shah, C. Woffinden, S.P. Tear, C. Binns, R. Kröger, Nat. Mater. **13**, 26 (2014)
52. B. Sahoo, K. Sanjana P. Devi, S. Dutta, T.K. Maiti, P. Pramanik, D. Dhara, J. Colloid Inter. Sci. **431**, 31–41 (2014)
53. G. Salazar-Alvarez, J. Sort, S. Suriñach, M.D. Baró, J. Nogués, J. Am. Chem. Soc. **129**, 9102 (2007)
54. G. Salazar-Alvarez, H. Lidbaum, A. López-Ortega, M. Estrader, K. Leifer, J. Sort, S. Suriñach, M.D. Baró, J. Nogués, J. Am. Chem. Soc. **133**, 16738 (2011)
55. E. Skoropata, R.D. Desautels, C.-C. Chi, H. Ouyang, J.W. Freeland, J. van Lierop, Phys. Rev. B **89**, 024410 (2014)
56. J.M. Soares, F.A.O. Cabral, J.H. de Araújo, F.L.A. Machado, Appl. Phys. Lett. **98**, 072502 (2011)
57. Q. Song, Z.J. Zhang, J. Am. Chem. Soc. **134**, 10182 (2012)
58. S. Sun, C. Murray, D. Weller, L. Folks, A. Moser, Science **287**, 1989 (2000)
59. M. Sytnyk, R. Kirchschlager, M.I. Bodnarchuk, D. Primetzhofer, D. Kriegner, H. Enser, J. Stangl, P. Bauer, M. Voith, A.W. Hassel, F. Krumeich, F. Ludwig, A. Meingast, G. Kothleitner, M. Kovalenko, W. Heiss, Nano Lett. **13**, 586 (2013)
60. N. Taub, A. Tsukernik, G. Markovich, J. Magn. Magn. Mater. **321**, 1933 (2009)
61. N. Venkatesha, Y. Qurishi, H.S. Atreya, C. Srivastava, RSC Adv. **6**, 18843 (2016)
62. E.L. Winkler, E. Lima Jr., D. Tobia, M. Saleta, H.E. Troiani, E. Agostinelli, D. Fiorani, R.D. Zysler, Appl. Phys. Lett. **101**, 252405 (2012)
63. M. Wu, Y.D. Zhang, S. Hui, T.D. Xiao, S. Ge, W.A. Hines, J.I. Budnick, J. Appl. Phys. **92**, 491 (2002)
64. L. Xi, Z. Wang, Y. Zuo, X. Shi, Nanotechnology **22**, 045707 (2011)
65. H. Zeng, J. Li, J.P. Liu, Z.L. Wang, S. Sun, Nature **420**, 395 (2002)

66. H. Zeng, J. Li, Z.L. Wang, J.P. Liu, S. Sun, Nano Lett. **4**, 187 (2004)
67. A. López-Ortega, D. Tobia, E. Winkler, I.V. Golosovsky, G. Salazar-Alvarez, S. Estradé, M. Estrader, J. Sort, M.A. González, S. Suriñach, J. Arbiol, F. Peiró, R.D. Zysler, M.D. Baró, J. Nogués, J Am Chem Soc 132, 9398–9407 (2010). https://doi.org/10.1021/ja1021798

Chapter 5
Magneto-Plasmonic Nanoparticles

César de Julián Fernández and Francesco Pineider

Abstract Magnetoplasmonics nanoparticles encompass in a single nano-entity all the rich science and promising applications of the plasmonics and magnetic nanoworlds. The difficult liaison and a certain incompatibility between plasmonics and magnetic phenomena, due to the different chemical-physical origins and supporting materials, are overcome thanks to the design and synthesis of novel nanostructures. The variations of properties, interactions and synergies of both phenomena and materials demonstrate how rich and surprising the matter is at nanoscale and the promising applications. In fact, we show how not only light and magnetism can interplay but also other phenomena like forces, heat, electric field and chemical interactions, between others, can show synergism. Magnetoplasmonic systems are excellent benchmark materials to develop and investigate multi-responsive multifunctional nanosystems that now are required in an increasing number of technologies, such as biomedicine, pharmacy, catalysis, optoelectronics and data storage.

5.1 Introduction

Magneto-plasmonics (MPs) is new concept of multifunctional nanomaterials exhibiting simultaneously plasmonic and magnetic phenomena. MPs combine and intertwine two separated materials science worlds, magnetism and photonics, at the nanoscale. In general, MP materials are composed by the materials that originate each phenomenon: plasmonic materials are elements constituted by mainly Au, Ag and Cu while magnetic materials are formed by *3d* metals and their oxides. Since plasmonic phenomena mainly manifest in the nanometric range, also MP materials are designed in this dimension range. At this scale, both plasmonics and magnetic

C. de Julián Fernández (✉)
Institute of Materials for Electronics and Magnetism, Italian Research Council, Parma, Italy
e-mail: cesar.dejulian@imem.cnr.it

F. Pineider
Department of Chemistry and Industrial Chemistry, University of Pisa, Pisa, Italy
e-mail: francesco.pineider@unipi.it

D. Peddis et al. (eds.), *New Trends in Nanoparticle Magnetism*,
Springer Series in Materials Science 308,
https://doi.org/10.1007/978-3-030-60473-8_5

materials exhibit a rich phenomenology correlated to size and surface effects that will be present also in the MPs nanomaterials. In addition to size effects, the properties of the MP nanoparticles are affected by structural and electronic correlations between the two types of elements or materials, the final properties being different than those of bare magnetic or plasmonic materials and hence giving rise to novel properties. Moreover, very promising new phenomena and applications appear due to the synergy between the two moieties. For these reasons, nowadays MP materials are object of intense investigation in materials science. In addition, these new materials have given rise to the development of novel applications of each class of material—photonics for plasmonics and recording for magnetism—and multifunctional applications in the fields in which both materials are promising like in biomedicine and catalysis [1–5].

Focusing on the term *plasmonics*, [1, 6] this describes optical phenomena produced by the excitation of collective electron oscillations, the surface plasmon resonances (SPR), that are induced by an electromagnetic field (EMF) propagating in a metal/dielectric interface. In the case of nanoparticles, the SPR is denominated localized surface plasmon resonance (LSPR), but SPR can be generated in other morphologies as disks, thin films (propagating SPR), holes, gratings and a wide number of structures [1–9]. Plasmonics opens in photonics the possibility of new ways to manipulate the light, new optical properties of matter, and the possibility of engineering light at the nanoscale [1–3].

The possibility of obtaining a single material with both strong plasmonic and magnetic properties is nowadays an unsolved issue. Plasmonic phenomena require the presence of free electrons, hence metals with a partially-filled *s*-band at the Fermi level [1, 8–10]. On the opposite, magnetism is mainly correlated to bound electrons in the *d* and *f* bands [11]. Hence both properties are correlated to materials with very different electronic features that are not compatible in the same electronic structure. In fact, the main plasmonic materials, Au and Ag, are diamagnetic while most of magnetic metals like Fe, Co and Ni exhibit weak plasmon resonances.

Figure 5.1 shows a selection of the wide variety of MP NPs that have been grown so far [12–15]. Between all, magnetic metal NPs should be most simple MPs system that can exhibit magnetic and plasmonic properties simultaneously in a single entity. Also NPs composed by a solid solution of the magnetic and plasmonic elements—like AuFe, AgFe, AgCo should be good candidates. However, as we will discuss later, the electronic structure of the single phase and the solid-solution NPs is such that one or both plasmonic and magnetic properties are typically damped. The design of hetero-structures in which plasmonic and magnetic moieties are separated but in direct physical and electronic contact is a second approach to design MP systems. A wide variety of morphologies have been created, such as core@shell (CS), flowers, heterodimers (HSs), hybrid-cigars, stars, nanodomes, etc. These MP systems have nanometric dimension, hence the size and surface effects have a key role in their properties. Their sizes are smaller or of the order of the characteristic lengths of plasmonic and magnetic phenomena, i.e. visible light wavelength, electron mean free path and domain wall length. Then, the magnetic and plasmonic properties should be affected

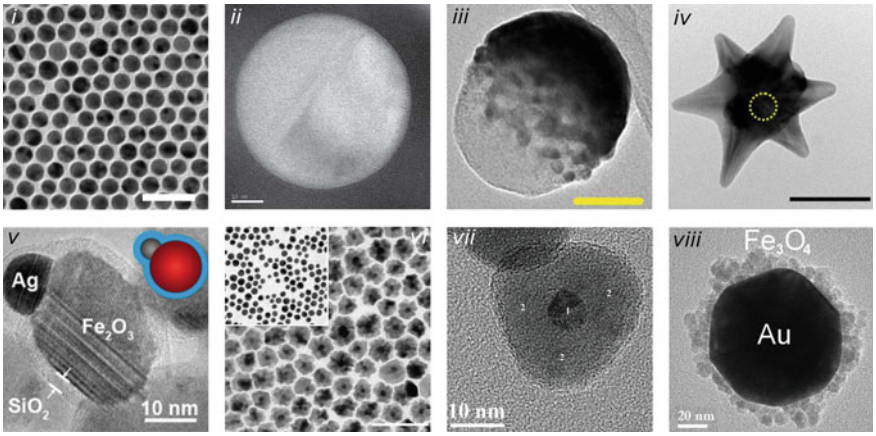

Fig. 5.1 Transmission Electron Microscopy (TEM) images of a variety of MP nanostructures. **i** Bare Au NPs, scale bar is 40 nm [229] (Adapted with permission from [229]. Copyright (2013) American Chemical Society). **ii** Solid solution AuFe NP, Energy Field TEM mapping at the Au N-edge (83 eV) [27] Adapted by permission of The Royal Society of Chemistry. **iii** MP nanodome with 20 nm Fe core and 20 nm Au layer, the scale bar 50 nm [135] (Adapted by permission from Elsevier). **iv** Au nanostar with superparamagnetic core outlined by the dashed circle, the scale bar is 50 nm [175]. Adapted with permission from [175]. Copyright (2009) American Chemical Society. **v** Asymetric SiO_2-coated Ag-Fe_2O_3 HD [165]. Adapted with permission from [165]. Copyright (2013) American Chemical Society. **vi** Flower-like Au@iron-oxide CS NPs. Inset Au nanocrystals seeds, scale bar is 100 nm [89]. Adapted with permission from [89]. Copyright (2012) American Chemical Society. **vii** Au@iron-oxide CS NPs [81]. Adapted by permission of The Royal Society of Chemistry. **viii** Fe_3O_4-decorated Au NPs [124] Adapted with permission from [124]. Copyright (2013) American Chemical Society

and correlated considering different coupling mechanisms: interparticle electromagnetic or magnetic dipolar interactions and intraparticle chemical, structural and electronic couplings. In fact, some studies show that the plasmonic and magnetic properties of the MP systems are different from the independent plasmonic and magnetic moieties. In addition, the MP properties of this variety of nanostructures can be correlated to their morphology but also to the mechanisms of magnetic and optical coupling. In the first section of this chapter, we will discuss the way in which plasmonic and magnetic moieties are correlated in the different morphologies developed so far. In the second part, their possible applications will be presented. In the third section, we will discuss the specific case of the plasmon assisted magneto-optical phenomena and finally discuss on the perspectives of these materials.

5.2 Optical and Magnetic Properties of MP Nanoparticles

Let us consider first the LSPR in small plasmonic and magnetic single metallic particles. The simplest description of the LSPR corresponds to the Mie model, [1,

6–8] that solves Maxwell's equations of propagation of an electromagnetic field in a metallic sphere. Plasmon resonances can correspond to single-mode or multi-mode electronic excitations that modify the scattering and the attenuation of the light [1, 6–8]. In the case of nanoparticles with sizes below 30 nm-case that will be mainly discussed here—the wavelength of the exciting light (for Vis or nIR light, between 275 and 1000 nm) is larger than the particle size. Considering other conditions such as the absence of interparticle electrical interactions and that the medium is a pure, non-lossy (i.e. non-absorbing) dielectric, the electrodynamic behavior of a particle can be described as that of a dipole in which the phase of the incoming electromagnetic field is constant over the particle volume [1, 3, 8]. The absorption spectrum is determined by the attenuation phenomenon (scattering is negligible, thus extinction ≈ absorption) at which corresponds an absorption cross section σ_{ext} of:

$$\sigma_{ext} = \frac{24\pi^2 R^3 \varepsilon_m^{3/2}}{\lambda} \frac{\varepsilon_2}{(\varepsilon_1 + 2\varepsilon_m)^2 + \varepsilon_2^2} \tag{5.1}$$

Absorption depends on the nanoparticle radius, R, on the light wavelength, λ, on the dielectric constant of the medium, ε_m, and on the real and the complex dielectric constant of the metal of the nanoparticle, $\varepsilon_1 + i\varepsilon_2$, The plasmonic resonance occurs at the wavelength λ_p at which when the denominator of the second part of 5.1 is zero or minimum, denominated Mie resonant conditions:

$$\left(\varepsilon_1(\lambda_p) + 2\varepsilon_m\right)^2 + \varepsilon_2^2(\lambda_p) = 0 \tag{5.2}$$

The calculated σ_{ext} using 5.1 of selected plasmonic and magnetic nanoparticles with a $R = 5$ nm dispersed in silica medium ($\varepsilon_m = 2.16$) are represented in Fig. 5.2c, d.

Figure 5.2a and b represent respectively the wavelength dependence of the dielectric constants of the main plasmonic materials, Au and Ag, as well as the Ni of some magnetic metals and alloys: Ni, Co, Fe, $Fe_{80}Ni_{20}$ (Permalloy) and FePt (in L_{10} structure). Optical data were obtained from [16–18]. As can be seen in Fig. 5.2c, both Au and Ag exhibit a very strong increase of absorption at the plasmonic resonance, followed by a decrease of the absorption in the IR range. In comparison, the SPR peak of the Ni is quite weak (observe that Fig. 5.2c is in powers of ten scale), while absorption is almost constant toward the IR spectral region. Figure 5.2d shows that Fe and FePt exhibit broader SPR peaks, while the SPR of Co and $Fe_{80}Ni_{20}$ should be at lower wavelength. The differences in strength and energy for the excitation of the SPR between the plasmonic and magnetic materials can be correlated to their electronic structures. In first instance, considering the dielectric functions of the metals in terms of the Drude-Sommerfeld model of free electrons [1, 9, 20], plasmon resonance of magnetic metals should be strongly damped and blue shifted with respect to the plasmonic metals. This is due to the larger density of electrons at the Fermi level [20] that shift the bulk plasmon resonance to high energies and to higher relaxation times [9, 10] of the magnetic metals. A more realistic approach to describe the dielectric

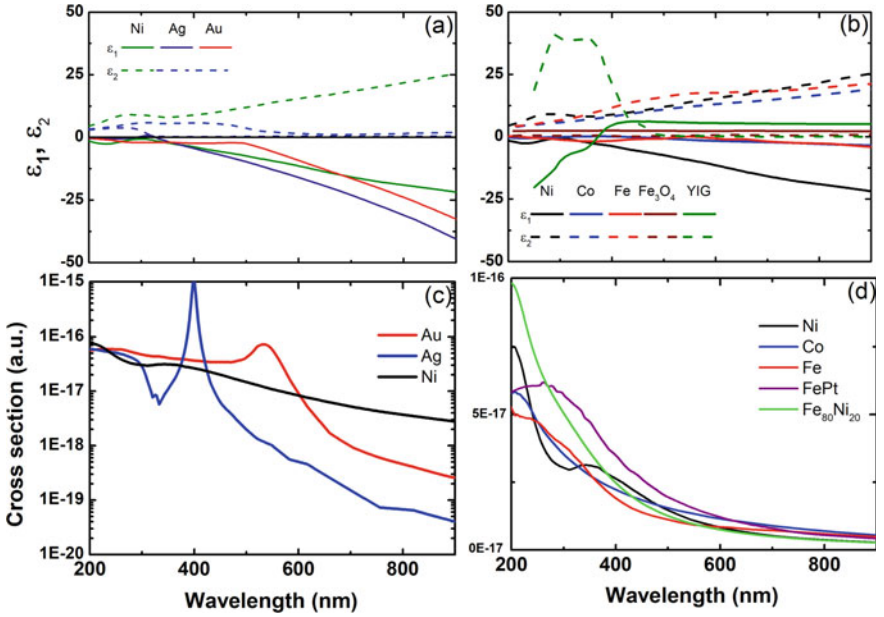

Fig. 5.2 **a** Dielectric constants of Au, Ag, Ni, **b** dielectric constants of Ni, Co and Fe and Fe_3O_4 (magnetite) and YIG. Plasmon cross sections calculated with 5.1 for 5 nm particles of **c** Au, Ag, Ni and **d** Ni, Co, Fe, FePt and $Fe_{80}Ni_{20}$

function of metals takes into account the contribution of both intraband and interband optical transitions. Intraband transitions occur in the conduction band and they can be described in terms of free electron model [1, 8–10]. They are directly involved in the SPR excitation. Interband transitions occur between different bands (like *d* and *p*) and the conduction band. In metallic magnetic materials the localized *3d* band reaches the Fermi level. This increases the probability of interband transitions to occur, giving rise to an increase of non-radiative relaxation processes. Spin–orbit coupling, characteristic also of *3d* electrons, determines further relaxation processes that damp free electron oscillations. The overlapping of the interband and the intraband transitions in correspondence of the SPR of magnetic metals gives rise to the SPR damping. In fact, no overlapping of the two type of transitions is present at the SPR of Ag, while in Au overlapping occurs only at high energy region of the SPR. In magnetic metals, the interband transitions are allowed in all the Vis and nIR spectrum [9, 21, 22]. Then the optical absorption (mainly represented by ε_2) of the magnetic metals is larger than that of the Au and Ag. This explains the damping of plasmon resonance in magnetic nanomaterials. Different experimental studies confirm qualitatively but not quantitatively the plasmonic phenomenology of magnetic metallic nanoparticles [21–24]. In fact, this description does not include a realistic contribution of size and surface effects that affect critically the electronic structure of magnetic metals and, even more simply, effects as oxidation or morphology.

An alternative simple approach to develop MP materials is using single particles composed by a solid solution of magnetic and plasmonic elements. The most important plasmonic elements, the Ag and Au, are poorly soluble in Fe and Co in the bulk, but their alloying has been experimentally demonstrated in nanoparticles [25–29]. Size and surface effects allow overcoming the thermodynamic equilibrium immiscibility [29–31] but the synthesis of alloy MP NPs is nowadays a challenge. As a consequence of the mixing of both elements, electronic hybridization occurs between the *5d6s* bands (for gold) and the *3d4s* bands of the plasmonic and magnetic metals, respectively, which gives rise to larger electronic densities at Fermi level and a broad spectral overlap of the inter and intraband transitions [26, 27, 29]. This leads to a significant damping of the plasmon resonance. At difference with single metal and hybrid nanostructures, the SPR of the alloys can either blue shift or red shift [29] depending on the metal composition. The optical properties of these alloys are different than those corresponding to the weighted combination of the constants of the containing elements, as demonstrated by Amendola et al. [27], who simulated the SPR spectrum of AuFe nanoparticles first considering the dielectric properties measured from AuFe films, then using theoretical values obtained combining elemental weighted dielectric constants of the Au and Fe. Significantly better agreement with the experiment was found using the former set of optical constants.

A second class of systems are the hybrid heterostructures constituted by a plasmonic and a magnetic moiety that are in direct contact. In this case the optical properties of the two moieties are intertwined by their proximity (dipolar fields), but also influenced by their mutual structural arrangement (epitaxy) and electronic hybridization at the contact interface [13, 31–36]. In general the plasmonic properties depend critically on the geometry and the materials that are selected. When the magnetic moiety is metallic, the LSPRs of the two moieties could be excited separately, since they are separated in energy. However, the SPR of the plasmonic moiety can be damped by the absorption of the counterpart (Fig. 5.3v), but also electronic excitations coupling between the two moieties can occur [37–41]. For instance, Sachan et al. [40] employed Energy Electron Loss experiments to observe locally the plasmonic excitation of the two moieties of CoFe–Ag HDs (Fig. 5.3 **iii**). They determined that both moieties exhibit distinct LSPR modes that are split in energy, the LSPR of the magnetic moiety being red shifted with respect to the one of Ag. Interestingly, isolated CoFe NPs do not exhibit LSPR. Moreover, a plasmon resonance was observed at the CoFe–Ag interface corresponding to a hybridized state. In the case that the magnetic part is an oxide, this material behaves as a dielectric medium (i.e. real part of $\varepsilon_m > 1$) with also large absorption ($\varepsilon_2 > 2$). See for example, in Fig. 5.2 the dielectric functions of the most investigated oxide, the magnetite (Fe_3O_4), and the promising oxide Yttrium iron garnet (YIG, $Y_3Fe_5O_{12}$) [42, 43]. Regarding morphology, in the case that the plasmonic nanoparticles are surrounded totally (in CS NPs) or partially (as in HDs) by the oxide, plasmon resonance could be analyzed by using a mean field approach (the Maxwell–Garnett, MG, model, for example) considering an absorbent medium or a multilayer structure [35, 44, 45]. As can be seen in Fig. 5.3**iv**, both in CS and HD morphologies, plasmon resonance

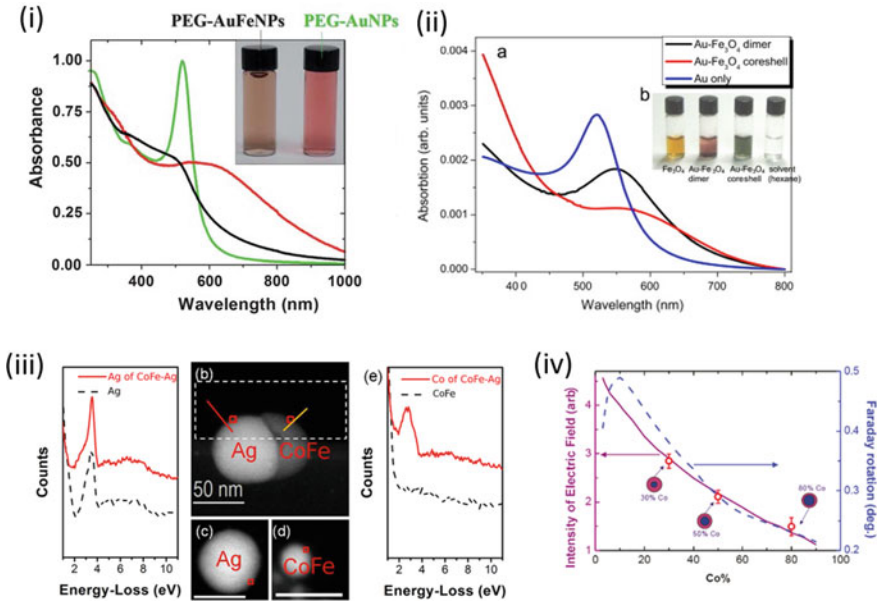

Fig. 5.3 **i** Optical spectra of AuFeNPs in ethanol (red line), of PEG–AuFeNPs in water (black line) and of PEG coated AuNPs (green line). Inset, PEG–AuFeNPs in water are reddish in color (left), different from the purple color of pure AuNPs (right) [27] (Reproduced from [27], with the permission of the Royal Society of Chemistry). **ii** Optical spectra of Au, Au–Fe_3O4 dimer and core–shell NPs; and b image of Fe_3O_4 and Au–Fe_3O_4 HNP's suspensions in hexane [160] (Reprinted from [160] with permission from Elsevier). **iiia** Experimental EELS spectra from the surface of the Ag region in a CoFe–Ag HDs NP (solid line) and isolated Ag NP (dashed line). HAADF image of **b** a CoFe–Ag HD NP, **c** an isolated Ag NP, and **d** an isolated CoFe NP. **e** Experimental EELS spectra from the surface of the CoFe region in a CoFe–Ag NP (solid line) and isolated CoFe NP (dashed line). The spectra were taken from the regions marked by square-boxes in the respective NPs. The scale bar for each HAADF image is 50 nm [40] (Reprinted from [40] with permission of the American Chemical Society). **iv** Calculated intensity of the electric field within the Co core in Co–Ag core–shell nanoparticles at resonance (continuous violet line) and maximum Faraday rotation of Co–Ag nanoparticles embedded in oil ($n = 1.5018$) (dashed blue line) as a function of the Co concentration [38] (Reprinted from [38] with permission of the American Chemical Society)

is red shifted and broadened, depending on the relative sizes of the two components. In the case of the HDs, the spectrum is the convolution of all the optical absorption spectra corresponding to all the different orientations of the MP couples respect to the propagation of light [46, 47]. The CS NPs constituted by a plasmonic shell is a different case. In general, a plasmonic crown exhibits two plasmonic modes at lower and higher energies than the plasmon resonance of the particle [39, 40, 48–50]. Including the magnetic dielectric core, both resonances are weaker and red shifted [37, 50]. Often however, the plasmonic shell is not constituted by a continuous shell but by packed plasmonic nanoparticles (Fig. 5.1h). In this morphology multimodal resonances due to interparticle dipolar interactions give rise also to the broadening of the absorption and to scattering processes. Finally, in the case that the magnetic shell

is metallic several studies show that these CS structures exhibit a single plasmonic peak that is red shifted and broader as the percentage of magnetic moiety is larger but also blue shift by modifying the size of the magnetic moiety [38]. The study by López-Ortega et al. [51] obtains a reasonable agreement of the plasmonic properties of Ag@CoFe CS with the simulations.

Previous discussions on the plasmonic properties of the hybrid systems considered a static description of the plasmon resonance, i.e. the solution of Maxwell'equations of the system. However, the dynamics of the plasmons needs also to be considered [52]. Only few different pump and probe studies [53–56] have been performed on Au–Fe oxide HDs and other morphologies, showing that the plasmon resonance is characterized by a faster electron relaxation process than that of bare Au NPs. Considering the previous described experiments on magnetic metal-plasmonic heterostructures (CoFe–Ag [38] and Ag@CoFe [51]), the hypothesis of a charge-transfer process from the plasmonic to the magnetic moiety can be proposed. Cosmin et al. [56], in contrast, proposed that the observed relaxation is due to the spill-out of electron density from gold electron at the gold/magnetic interface excluding a charge transfer mechanism. Further studies are required considering a controlled interface and chemical states of the magnetic oxide.

Composites or mixtures of isolated magnetic and plasmonic particles are the simplest MP systems. A large variety of materials have been synthesized: micro and nano capsules containing a mixture of the two classes of NPs [35]; capsules containing only one kind of nanomaterial, magnetic for example, that are decorated by the plasmonic counterpart [57, 58]; multilayers or onion-like particles in which plasmonic and magnetic moieties are separated by a dielectric layer like SiO_2 or TiO_2 [41, 59–66]. MP effects have been investigated even in mixtures or simple solutions containing the two types of NPs [67, 68]. In all these cases, the interparticle dipolar electromagnetic interactions and the absorption of the magnetic NPs determine the changes of the plasmonic resonance respect to bare plasmonic nanoparticles. Depending on the interparticle distance, the geometry of the particles and the magnetic/plasmonic nanoparticle concentration ratio, the coupling can have different strength. In very diluted systems the dielectric contribution of the magnetic moiety could be included in the term of the dielectric medium (ε_m) using a mean-field model [68, 69]. However, SPR should be calculated considering that the medium surrounding the plasmonic particles is absorbent [69–71]. A red shift and damping of the LSPR is expected as previously discussed. If interparticle distance is small (nanometers), strong confinement of the EMF occurs, and the so called "hot spots", can be present even between plasmonic and metallic magnetic nanoparticles [72, 73]. This can give rise to blue shift of the LSPR. Finally, superstructures composed by networks of the two classes of materials have been also synthesized [74, 75].

Also magnetic properties of the MP structures appear different compared to equivalent bare magnetic particles, even if plasmonic materials are diamagnetic. In first instance, the hybrid nature of MP structures determines that the growth mechanism is different to that of bare magnetic nanoparticles. For example, the synthesis of hybrid structures like CS and HDs requires a two-step process in which heteronucleation

and particle growth are involved [13, 33, 35, 44]. Crystal growth, shape and composition of the magnetic moiety can be different than bare magnetic NPs. While most studies compare bare nanoparticles with hybrid ones, in which the nucleation process is different, recent studies [78–81] have compared hybrid systems with the corresponding NPs or hollow NPs obtained after the elimination of the plasmonic moiety. Even if the morphology is similar, the two nanomaterials exhibit different magnetic properties, such as saturation magnetization and hysteresis [81]. This demonstrates the critical role in the magnetic properties of the plasmonic-magnetic interface.

More deeply investigated cases correspond to heterostructures as CS nanoparticles and HDs in which Ag and Au are combined with Fe oxide. The first effect is the modification of the magnetization of the magnetic moiety, consisting in a strong decrease of saturation magnetization of Fe_3O_4 in comparison to the bare nanoparticles. This decrease is typically correlated to the presence of a magnetic disordered layer, called dead layer, at the free surface or at the Au-interface of the magnetic moiety [45, 82–87]. In the case of CS the presence of antiferromagnetic phase boundaries in the intergranular regions of the multigrain or petals of Fe_3O_4 can also give rise to a decrease of the magnetization [61, 88]. In addition, the presence of an antiferromagnetic FeO wustite layer in the interface region between the Fe_3O_4 and Au moieties could also cause of the decrease of magnetization [61, 89, 90]. However, such behavior is not always observed as in some studies the specific magnetization is near the bulk value (80–90 emu/g), [91–93] suggesting the above proposed problem could be overcome. Further studies on the physico-chemical properties and chemical stability of these structures are required.

A significant question that illustrates the complexity of the magnetic order in hybrid system is the magnetic observation of the Verwey temperature. This is a specific fingerprint of magnetite, Fe_3O_4, not present in other Fe oxides, which corresponds to a metal-to-insulator transition around 120 K. The change of the electric nature of the Fe_3O_4 at this transition corresponds also with changes in the magnetic and optical properties of the oxide and hence plasmonic coupling features in a hybrid system could be influenced. In many studies, including both HDs and CS [81, 89, 93–95] structures the Verwey transition is observed at or below the bulk temperature value, while in other cases it is absent [45, 61, 85, 87, 96, 97]. The absence of this transition could be a fingerprint of the size effects in the oxide. However, changes in the stoichiometry or the partial oxidation of the Fe_3O_4, composed of Fe^{2+} and Fe^{3+}, to maghemite (γ-Fe_2O_3) or other oxides composed of only Fe^{3+} are more possibly the origin of these changes.

MP hybrid nanostructures exhibit also differences in the reversal process mechanism of the magnetization. In principle, most of the investigated MPs have the magnetic moieties with a dimension below the 20–30 nm, being near or below the single domain range [11]. In such case, the dominant mechanism of reversal of the magnetization is the coherent rotation of all the spins. The hysteresis loops, described by the Stoner-Wohlfarth model [11, 98], should have open loops with maximum coercive field correlated to the anisotropy field of the material. However, local and global surface and size effects determine mainly the reversal process and all the magnetic properties of the magnetic particles [11, 98, 99]. In addition, thermal

activation processes are dominant [98] and the superparamagnetic effect occurs at room temperature. This behavior has been reported in a wide number of works investigating Au–Fe_3O_4 heterodimers and Ag–Fe_3O_4 [45, 89, 93–97, 100]. The blocking temperature, i.e. the threshold between the blocked and superparamagnetic regimes, is determined by the size distribution of the particles, their magnetic anisotropy, as well as the magnetic interparticle interactions. HDs and CS NPs appear to exhibit different behavior [95, 96, 101]. In the case of HDs, some works [85, 87, 90] have shown that the magnetic moiety exhibits a spin-glass behavior due to the spin-disorder in the structure. Different is the case of the CS NPs [96, 100, 101], if the shell is magnetic and depending on the morphology of this shell—continuous shell or discontinuous layer of particles—the reversal process could take place by incoherent rotation modes or by the dipolar competition of the particles. Here, in addition to the spin-glass behavior, also exchange bias effects have been observed [87, 90, 93] even if the presence of an antiferromagnetic material counterpart, necessary for the exchange bias effect, was not detected. Chandra et al. [85] propose this behavior is possible in the Au@Fe_3O_4 CS NPs due to the presence of inner or intergranular spin disordered regions. On the other hand, Zhu et al. [87] propose that the exchange bias is due to the coupling of weak magnetic layer at the Au–Fe_3O_4 interface and the Fe_3O_4 overlayer. However, these effects are not present in all the investigated structures: other studies [89, 102] show the classical superparamagnetic behavior in which interparticle interactions are dominant even if magnetic moiety is composed by ferromagnetic (Fe_3O_4 or γ-Fe_2O_3) and antiferromagnetic (α-Fe_2O_3) phases.

The magnetic properties of alloy-based MP nanoparticles, that combine magnetic and non-magnetic elements, are completely different to those of the hybrid family. As previously mentioned, the formation of this type of alloys is not straightforward, but it is even more difficult to obtain magnetic properties at room temperature. The out-of-equilibrium nature of nanomaterials allows the growth of these alloys, but also other possible morphologies, such as segregated particles or inhomogeneous mixtures, are possible. On the other hand, the solid solution of non-magnetic and magnetic elements gives rise to the decrease of the magnetic moment of the magnetic elements resulting in the decrease of the total magnetization of the particle and the weakening of exchange interactions with the consequent decrease of the Curie temperature. In a few alloys, for example NiCu [103] or FeCuPt [104] alloys, the solid solution of the two element is possible and the magnetization and the Curie temperature decrease (non-linearly) as the non-magnetic content increases. In the case of AuFe [105–107] and AgCo [108, 109] solid solutions, in addition to this evolution, also spin-glass and diamagnetic behaviors can occur for the large content of non-magnetic elements. In fact, in these cases the decrease of the magnetization and One relevant point is thatthe Curie temperature is due to the decrease of the direct exchange interactions and the increasing role of the indirect exchange interactions (RKKY) though the *s*-bands of the non-magnetic elements. In such case the magnetic behavior can pass from ferromagnetic, to spin-glass, paramagnetic and diamagnetic, depending of the non-magnetic content but also on the temperature.

The discussions above show that the preservation of both magnetic and plasmonic properties is possible both in hybrid and in alloy nanostructures, but a fine

control of the nanostructural and compositional features is required. On the other hand, the synergistic behavior between the two moieties has been evidenced investigating other properties and effects. The main case corresponds to the magneto-optical (MO) properties of these materials that will be discussed in the next section. Another synergistic effect is the observation of a spin and orbital moments in non-magnetic atoms of alloy-based AuFe nanoparticles [26, 27]. In fact, several studies have shown the spin polarization of the *d* and *s* bands of Au and also Ag elements when are alloyed with magnetic ones [107, 110–112]. The magnetic moment of these heavy non-magnetic elements exhibits a large orbital-to-spin ratio as expected due to their characteristic large spin–orbit coupling. Similar spin polarization of plasmonic element was observed in Au-Fe_3O_4 hybrid NPs. In this case, a charge transfer mechanism at the metal-oxide interface could give rise to the spin polarization of Au [89]. This demonstrates other paths of coupling mechanisms between the magnetic and plasmonic moieties.

5.3 General Applications of MP Nanoparticles

Let us consider first optical applications of MP nanoparticles. In principle, optical properties of MP NPs follow the same behavior of the plasmonic materials, taking into account the optical changes induced by the presence of a magnetic moiety. Even considering the expected resonance shift and spectral broadening, MP NPs exhibit the same characteristics that allow to design the color, light scattering and contrast, and optical spectral features required in several photonics and imaging applications [113–116]. The modification of plasmon resonance under the variation of the environment—a key concept for refractometric sensing devices—has been shown [117–120]. The strong localization and confinement of light at the SPR, giving rise to modification of the linear and non-linear optical properties of the capping molecules or materials is also possible. This is the working principle of many optoelectronics, sensing and monitoring applications. In particular, Surface-enhanced Raman scattering (SERS) spectroscopy, a spectroscopic technique that uses the plasmon-induced enhancement of Raman signal to detect a wide variety molecules and compounds, have been demonstrated both in hybrid MPs systems [121–126] as well in alloy-based MPs structures [127–129]. Photo-thermal effects were also demonstrated in MP nanostructures. This consists in the generation of heat by NPs due to the excitation of the LSPR and is a well-established subject in applications concerning nanoparticles in biomedicine [130–136] and catalysis [137]. One of the features that has brought the interest for MP nanostructures is the possibility to tune the SPR down to the n-IR region. Nowadays, this is a researched property for photonics in telecommunications and biomedical applications. In telecommunications, the scope is the reduction of losses and the coupling with telecom lasers [9, 10]. The employment of plasmonic effects and techniques under in-vivo conditions for biomedicine applications is limited by the complete absorption of light in the visible range by the skin and other bio-tissues [138, 139]. MP NPs can be prepared to exhibit the SPR in the

n-IR region where the first optical window, at around 700–800 nm, is present. This allows the development of in-vivo plasmon-assisted imaging techniques, but also for the application of photo-thermal therapy [130, 132, 134, 135] for deeper tissues.

Besides their plasmonic properties, gold nanostructures are investigated in biomedicine for their low cytotoxicity, biocompatibility and inertness [4, 93, 139, 140] and/or the established and wide possibilities of functionalization of Au surfaces with large number of molecules and materials [4, 5, 139, 141, 142]. The plasmonic moiety—attached to another active component—can assure the protection of the active component to chemically and biologically reactive or aggressive media. The gold moiety can cover the active component in such a way to reduce its toxicity or its release rate. Hence, plasmonic nanostructures are considered as key actuators for biomedical applications like drug delivery and genetic manipulation but also for environment sustainability [4, 8, 139, 141]. These questions are particularly important for applications in which magnetic nanoparticles are involved: except the Fe oxides (magnetite or maghemite), most of magnetic compounds are chemically oxidisable, reactive, and considered cytotoxic [140, 143, 144]. Hence the term "magnetoplasmonic" is also employed to define also hetero-nanostructures in which the magnetic moiety is covered by an Au layer or by Au NPs. Nowadays strong activity is performed in the understanding of the clearance, retention and toxicity of several MP nanostructures [145–148].

Concerning magnetic applications, MP NPs are now appealing for biomedical applications (some cases represented in Fig. 5.4), and are being considered also for catalysis and environmental applications. Like bare magnetic nanoparticles, the MP NPs can be moved and placed or concentrated in a region, tissue or on device using magnetic fields [113, 149]. These systems allow also the active particle concentration and guiding for in-vivo and in vitro biomedical applications [35, 36, 113, 133, 134, 149, 150] and improvements of concentration or separation for biomedical analysis [151–157]. They have also been employed as *contrast agents* using Nuclear Magnetic Resonance (NMR) [36, 62, 66, 157–162] and ultrasound biomedical imaging techniques [163, 164]. Several studies have demonstrated the improved relaxivity features of MP NPs, faster relaxation times (T1) than the commercial particles and promising T2 dephasing times. This has been observed both in Au–Fe_3O_4 heterostructures [157, 161, 162] and in weakly magnetic AuFe alloy-based NPs [27, 128] showing how the novel magnetic structures of these hybrid materials can improve the properties of bare magnetic particles. Finally, the heat generation of the MP NPs irradiated by radiofrequency magnetic field and its employment for cancer therapy was demonstrated [62, 81, 92, 94, 97, 121, 165–168]. The aim is to produce externally a local heating that can induce the apoptosis of cancer cells, the thermal induced release of drug or the activation or increase of efficiency of drugs. In addition, a novel approach of cancer therapy based on magnetomotive activity, mechanical or stress-induced damages produced by the rotation of the magnetic particles into the cellular target, was developed considering MP nanostructures [169, 170]. In this case the capping of Au layer of the magnetic moiety allows the surface functionalization, low cytotoxicity and it ensures the chemical and mechanical stability during the rotation or vibration of the particles into the cells.

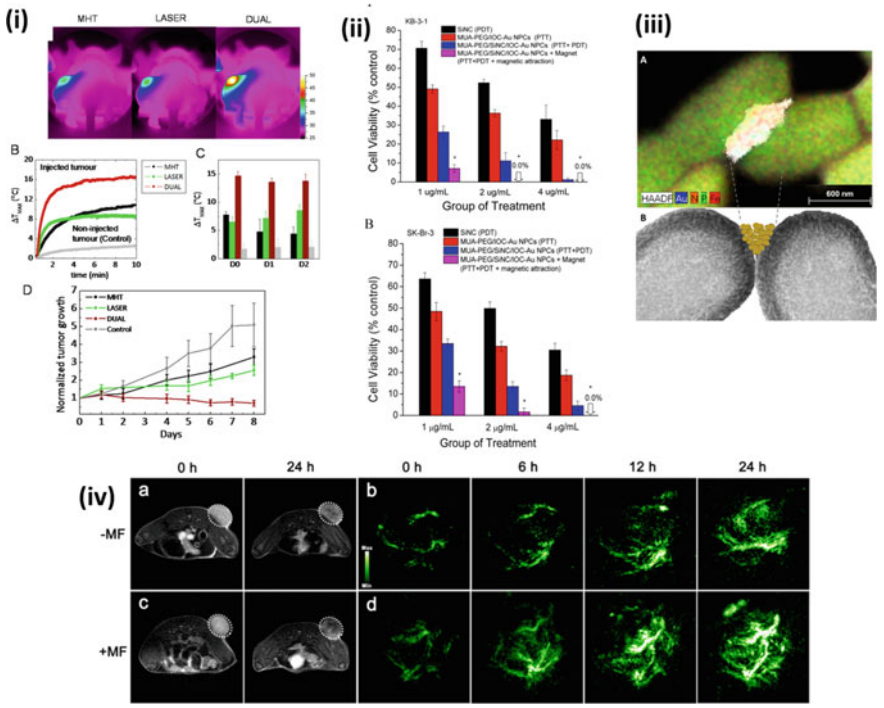

Fig. 5.4 **ia** Thermal images obtained with the IR camera in mice, after intratumoral injection of nanocubes in the left-hand tumor, and after 10 min application of magnetic hyperthermia (MHT, 110 kHz, 12 mT), NIR-laser irradiation (LASER, 808 nm at 0.3 W/cm^2), or DUAL (both effects). **b** Corresponding thermal elevation curves for all treatments and for the noninjected tumor in the DUAL condition. **c** Average final temperature increase obtained after 10 min on day 0 (1 h after injection) and 1 and 2 days after injection and for non-injected tumors. **d** Average tumor growth (groups of six tumors each in non-injected mice submitted to no treatment (Control) and in nanocube-injected mice exposed to MHT, LASER, and DUAL during the 8 days following the 3 days of treatment [183] (Reprinted from [183] with permission of the American Chemical Society). **ii** Comparison of the efficacy of different combinations of Photo-thermal therapy (PTT) with Photodynamic therapy (PDT) and magnetic attraction against KB-3-1 (**a**) and SK-BR-3 (**b**) cells using Au capped Fe oxide NPs (IOC-Au) capped with a capping layer of near-infrared absorbing photosensitizer silicon 2,3-naphthalocyannie dihydroxide (SiNC) and/or poly(ethylene glycol) (PEG) linked with 11-mercaptoundecanoic acid (MUA) [133] (Reprinted with permission from [133]. Copyright 2017 American Chemical Society). **iiia** STEM-electron dispersive energy micrograph map of colistinated FeOx/Au nanoclusters binding to A. baumannii. b Schematic of FeOx/Au nanoclusters binding to A. baumannii bacterium (STEM micrograph) [156] (Reprinted with permission from [156]. Copyright 2017 American Chemical Society). **iv** In vivo T2-weighted MR images of 4T1 tumor-bearing mice at various time points post-injection of gold nanorods @ Fe oxide core@shell particles load with doxorubicin (GNR@IOs-DOX) without (a) or with (c) magnetic tumor targeting. White circles indicate the positions of tumors. b, d In vivo Photoacustic images of the tumor sites at different time points postinjection of GNR@IOs-DOX without (b) or with (d) magnetic targeting [134] (Reprinted with permission from [134]. Copyright 2016 American Chemical Society)

Among the most appealing properties of MP NPs is the combination of magnetic and plasmonic properties and the *multifunctional approach* that can be reached with these structures. Magnetoplasmonic systems were first considered to overcome many of the limitations of plasmonic systems. MPs was one of the first concepts considered to develop "*active plasmonics*" [171], i.e., plasmonics devices which SPR, and hence the optical properties, could be manipulated externally [12, 14, 171–174]. The optical properties of the MP particles are modulated by an external magnetic field as a consequence of the change of their magneto-optical properties (see next section). Another path to modulate the optical properties is the design of asymmetric structures, as stars, in which a rotating magnetic field induces the movement (rotation) of the particles that gives rise to time-dependent changes of the reflectivity [27, 175, 176].

A second contribution of MPs concerns the improvement of the possibilities of *manipulation* of the plasmonic systems for biomedical targeting therapies (Fig. 5.4ii, iii, iv). In fact, the efficiency of plasmonic structures for drug or gene delivery, for targeting and for separation is determined by the possibilities of functionalization and anchoring to the targets [151]. Adding the possibilities of the spatial manipulation with a magnetic field gradient it is possible to improve the drug-delivery, tracking, intracellular drag update, and the particle retentivity in in-vivo applications [150, 177, 178]. In in-vitro tests and lab-on-chip applications it is possible to drag the particles, to localize and to concentrate the target molecules, genes, DNA and hence to improve sensibility of devices between other properties [153–157, 179].

Regarding the *thermal therapy* approach, both photo-thermia and magnetic hyperthermia methods can be simultaneously applied in MP NPs [35, 97, 121, 151, 180, 181]. As was previously discussed, the choice of MP structures can improve critical questions related to the employment of each class of particles in therapy, i.e. the cytotoxicity and the elimination of magnetic particles and the application of plasmon-assisted photo-thermal therapy in the NIR. In fact, photo-thermia can only be applied to targets placed at few centimeters from the skin, employing NIR radiation, while magnetic fields can be designed to reach deeper areas. Recent studies have outlined the improvement of the local thermal heating combining simultaneously the two procedures [97, 133, 180, 183] (Fig. 5.4i). Some studies indicate that the improvement is due to combination of the two thermal processes rather than to a synergistic effect [97, 182, 183].

Considering the activity of the plasmonic and magnetic moieties as probes, optical (photoacoustic, pholuminescence) and magnetic (NMR, ultrasound, magnetic, magneto-motive) imaging techniques can be combined in a *multimodalapproach* [15, 63, 65, 117, 128, 130, 134, 151, 177, 184, 185] with MPs NPs (Fig. 5.3iii, iv). Different types of imaging probes, like Vis and IR light, ultrasounds and radiofrequency (NMR), new imaging methods, like optical magneto-motive [163, 164] and magneto-optical techniques designed with MP NPs, and other clinical tests like positron emission Tomography or X-ray computed tomography [128, 179, 184–186] can be simultaneously employed to obtain images at penetration larger than the optical threshold of each probe. In addition better spatially resolved and complementary information can be obtained. Also enhanced imaging sensitivity and accuracy is

expected in such a way to get a better understanding of biomedical systems and an accurate anatomical and functional information from inside the body and in bio-tests.

MP nanostructures can be considered for *multiple theranosticapproaches* in biomedicine [187, 188] (Fig. 5.4ii). Theranostics considers the simultaneous or consecutive combination of diagnostic and therapeutic methods for a personalized, faster and efficient medical treatment. Independently, both plasmonics and magnetic nanoparticles, are considered for a theranostic approach mostly focused to cancer treatments. With MP nanoparticles, a wider range of targeting, diagnostic and therapeutic possibilities is available, as demonstrated the increasing number of studies [59, 60, 62, 131, 132, 135, 147, 178, 189–193].

5.4 Magneto-Optical Effects in MP Nanoparticles

Considering that the plasmonic phenomenon is mainly an optical effect, the direct cross-linking between the magnetism and plasmonics is the magneto-optical (MO) effect [172, 174]. This term describes a wide number of optical phenomena correlated to the interaction between light and matter in which the properties of light change after interacting with a magnetic material or any material under a magnetic field [194, 195]. In this chapter, we will discuss the main MO linear effects correlated to magnetic materials: the Faraday effect, Magnetic Circular Dichroism (MCD) and the Kerr effects. The MCD and the Kerr effect—in transverse configuration—involve changes in the light absorption, while the Faraday and Kerr effect—in longitudinal and polar configurations—give rise to the change the polarization of the light producing the change of the angle of polarization and give rise to an ellipticity. These MO effects are proportional to the magnetization of the magnetic material and hence change as a function of applied magnetic field and temperature. In fact, MO can be regarded also as a magnetometric technique that allows to measure the hysteresis loops of surfaces, films and also nanoparticles. The information on the magnetic properties coming from the MO effects depends on the penetration depth of light in matter at the specific wavelength and can range from some tens of nanometers for metals to centimeters for magnetic dielectrics (YIG, for example).

MO effects are due to optical transitions that follow the dipole selection rules i.e. requiring a change of the angular momentum of ± 1. Hence MO spectroscopy gives complementary information to other spectroscopic techniques as MO transitions can depend on crystal symmetry and spin-electronic structure, in particular concerning bands split by the Spin–Orbit (SO) coupling [194–196].

These MO effects are incorporated in the description of optical phenomena by describing the optical properties of the material with a complete dielectric tensor that includes the non-diagonal magneto-optical terms [14, 19]:

$$\varepsilon = \begin{pmatrix} \varepsilon_{xx} & \varepsilon_{xy} & \varepsilon_{xz} \\ -\varepsilon_{xy} & \varepsilon_{yy} & \varepsilon_{yz} \\ -\varepsilon_{xz} & -\varepsilon_{yz} & \varepsilon_{zz} \end{pmatrix} \tag{5.3}$$

where ε_{ii} and ε_{ij} $(i, j = x, y, z)$ compose the complex dielectric function that depend on the magnetization state in the respective directions.

The coupling of MO and plasmonic phenomena is currently being investigated in a wide number of MP morphologies, like nanoparticles, films, hollow films, gratings, disks, and more complex morphologies [14, 19, 174, 197]. NPs are probably one of the least investigated classes of MP candidates, due to the previously discussed complexity in their structure and composition. Many of the phenomena that will be discussed on the NPs have been theoretically predicted and observed in other morphologies. In particular, results on plasmonic nanodisks that also exhibit LSPR will be proposed as a reference.

In single-phase nanoparticles, the dielectric tensor of the material can be used in Mie equations to obtain the single-particle absorption and scattering cross sections; [198, 199] as an alternative, an effective medium such as the generalized Maxwell–Garnett (MG) approximation can be used to describe the system [22, 23, 200, 201]. In the case of the Faraday and MCD experiments, that are performed in transmission configuration, for optically isotropic magnetic materials, the dielectric tensor is simplified as $\varepsilon_{xx} = \varepsilon_{yy} = \varepsilon_1 + i\varepsilon_2$ and $\varepsilon_{xz} = \varepsilon_{yz} = 0$. Considering the MG equation for diluted particles the angle of plane rotation (θ) and the ellipticity (ϵ) of the polarization in the Kerr configuration is [202–204]:

$$\theta + i \in = \frac{2\varepsilon_m}{(\varepsilon_{xx} - \varepsilon_m)(\varepsilon_{xx} + 2\varepsilon_m)} \varepsilon_{xy} \tag{5.4}$$

As in the case of the 5.2, resonant conditions for the MO signal should appear as in the denominator reaches a minimum. In this case it occurs under two conditions (a) $\varepsilon_{xx} = -2\varepsilon_m$, hence to the excitation of the SPR corresponds an amplification of the MO effect and (b) $\varepsilon_{xx} = \varepsilon_m$, hence, MO amplification can occur upon a different excitation of the SPR.

Amplification of MO effects at the SPR have been observed in a wide number of single phase metallic NPs of Fe [21, 205], Ni [23] and Co [22, 24] as well as FeCo [206] and FePt [207] alloys nanoparticles, phenomenologically confirming the existence of the effect. The change of MO signal as a function of different structural factors, such as the particle size in the Fe NPs [21] and in the Co NPs [208, 209] (see Fig. 5.5i), the packing factor in Co nanoparticles [24], and the nature of the medium surrounding Co NPs [210–212], follow the behavior of the SPR. As was previously discussed, SPR in magnetic metallic NPs is blue shifted in comparison to plasmonic NPs. This is also observed in the MO spectrum, but the MO line shape can be a peak or a dispersive curve depending on type of MO effect that is measured. However, in most of these studies there is not a good agreement between the theoretical calculations and experimental MO measurements. In most of the

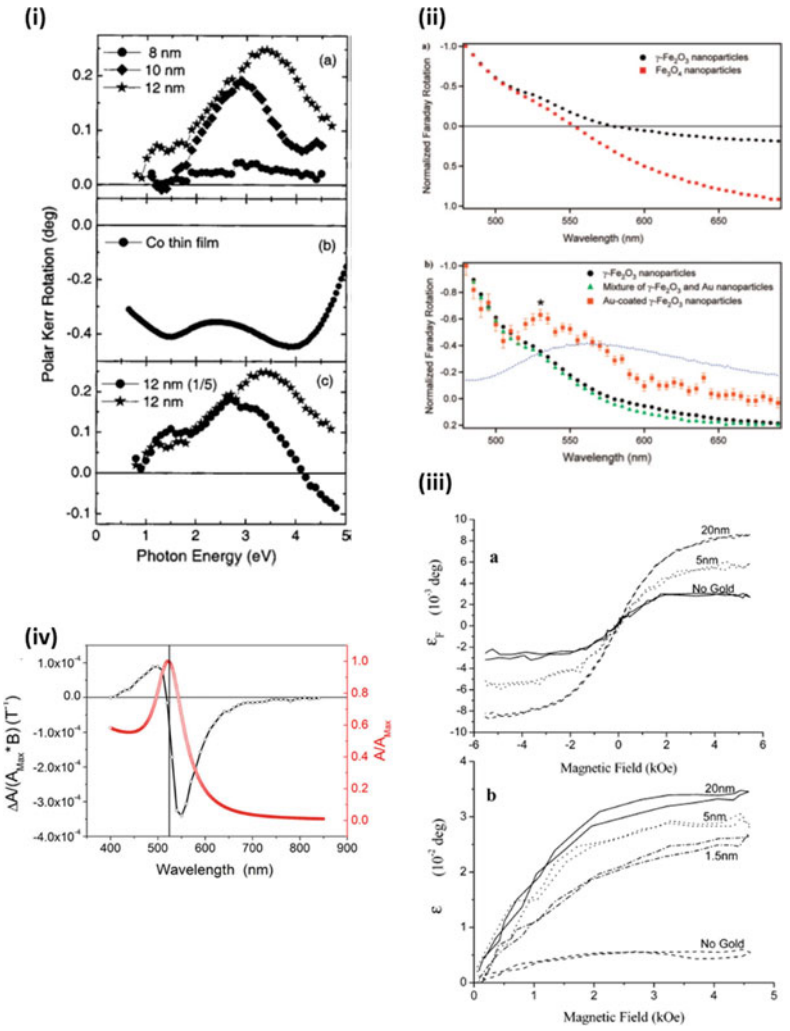

Fig. 5.5 **ia** MOKE spectra of thin films consisting of 8, 10, and 12 nm size Co particles deposited on Al substrate. **b** Co thin film reference spectrum. **c** Influence of solution dilution of the particles on the MOKE signal [208] (Reprinted from [208], with the permission of AIP Publishing). **iia** Normalized Faraday rotation spectra of γ-Fe_2O_3 and Fe_3O_4 nanoparticles. **b** Normalized Faraday rotation spectra of γ-Fe_2O_3 nanoparticles, gold-coated γ-Fe_2O_3 nanoparticles, and a mixture of γ-Fe_2O_3 and gold nanoparticles. The absorbance spectrum showing the plasmon resonance band of the gold-coated γ-Fe_2O_3 nanoparticles is indicated by the dotted blue curve [222] (Reprinted with permission from [222], Copyright 2009 American Chemical Society). **iii** Comparison between MCD magnetization curves for magnetite nanocrystal monolayers with and without a rough gold film measured in transmission (**a**) and reflection (**b**) configurations [217] (Reprinted with permission from [217], Copyright 2002 American Chemical Society). **iv** Optical absorption spectrum (red ○), and MCD (black ○) of the gold nanoparticles. Optical absorption (A) is given in normalized units at peak maximum (A/A_{Max}); dichroism (ΔA) is scaled in accordance ($\Delta A/A_{Max}$) [229] (Reprinted with permission from [229], Copyright 2009 American Chemical Society)

previous studies it has been argued that such differences come from the difficulty in accurately determining the optical and magneto-optical properties of magnetic materials composing the nanostructures, since they can be affected by oxidation processes and by surface and size effects, resulting in a dielectric tensor with can be very different from the starting bulk material, and very hard to characterize. Vlasin et al. [213] propose to take into account the diamagnetic MO contribution of the medium, to adequately perform the theoretical calculations with the MG model.

The amplification of the MO signal has been theoretically calculated with the Maxwell–Garnett effective field approximation in bimetallic CS and onion-like nanostructures [201, 214, 215] and observed in Ag@Co [38] and Ag@CoFe CS NPs [51] and Au top-capped Ni wires [216]. López-Ortega et al. [51] compares the plasmonics and MO properties of CoFe NPs to those of Ag@CoFe NPs (Fig. 5.3iv). The bare magnetic NPs do not present SPR and their MO signal is weaker than that of the MPs CS NPs that have a SPR and Faraday effects at coincident wavelength. Interestingly, the MO signal exhibits a similar shift in energy as the SPR when the surrounding medium is changed, indicating the possibility to apply the MO technique for chemical and biochemical sensors.

Wang et al. [38] investigated the evolution of the plasmon-induced MO signal of Au@Co CS NPs as function of the Co shell thickness. They observe an increase of the Faraday signal and of the SPR as Co layer was thinner even if bare Co NPs had small MO signal and no SPR. This behavior was in agreement with the simulations employing MG model confirming the expected damping of the SPR induced by the strong absorption of the magnetic component. However, the authors correlate the stronger MO activity of the CS NPs with thinner magnetic layer to an amplification effect of the EMFs induced at the LSPR. In fact, the local enhancement of the EMFs at the plasmonic resonance is a well-known and exploited optical effect that can give rise to the amplification of a wide number of optical effects. For example, Shemer et al. [217] showed that the Kerr effect in Fe_3O_4 NPs increases up to 3 times when placed in the proximity of plasmon-active rough metallic surfaces (Fig. 5.3iii). The proof of concept for this plasmon-amplified MO effect was demonstrated in composites of Au nanoparticles dispersed in garnet films [218–220]. The majority of available studies currently involve CS and HDs NPs [221–223] with magnetite (Fe_3O_4), maghemite (γ-Fe_2O_3) or spinel oxides doped with a second transition metal cation, due to the easier synthesis and their possible application in biomedicine. Jain et al. [222] reported the amplification of the Faraday signal of Au-coated maghemite nanoparticles (Fig. 5.3ii). Li et al. [221] observed an increase of the Faraday rotation and a change of its sign in Ag–$CoFe_2O_4$ HDs, but not at the SPR wavelength. In fact, the comparison between the MO properties of the bare magnetic moiety and in the hybrid nanostructures is not straightforward, due to the previously discussed magneto-structural differences between the two systems.

Several studies investigated the MO properties of mixtures of magnetic and plasmonic NPs, in which direct contact is excluded and mainly near field EMF interactions modify the MO signal. Several studies have shown the amplification [224, 225] or the reduction [68] of MO signal and the change of its sign [224], considering different interparticle distances and hence different dipolar strength. Discrete

Dipole Approximation calculations predict in Ag and $CoFe_2O_4$ packed NPs a non-monotonic dependence of the MO signal on the interparticle distance, the maximum being at 20 nm interparticle distance [226].

The overlapping of the SPR with a MO transition has been also taken into account. Campo et al. [68] investigated the effect of the SPR on the different MO transitions of $CoFe_2O_4$ NPs dispersed in a solvent with a small concentration of Au NPs (<1%). This oxide exhibits three bands associated to different interband and intraband optical transitions. The broad SPR peak of the composite overlaps with the interband charge-transfer (CT at 1.8 eV) transition and a crystal field (CF at 2.0 eV) transition of the Co^{2+} ions, which result in distinct MO spectral features. While the MO signal at the CF transition decreases, the one of the CT transitions that fully overlaps with the SPR, evolve to several weak MO transitions. On the other hand, plasmon-induced amplification of the MO signal of single-molecule magnet molecules (terbium(III) bis-phthalocianinate) deposited of Au discs was recently observed [227]. In this case the SPR of the substrate discs almost overlaps with the MO transitions related to the main absorption band of the molecule. A moderate, but very clear fivefold enhancement of the MO signal from the magnetic molecule was observed in this case.

One relevant point is that also non-magnetic plasmonic nanostructures exhibit MO effects at the SPR [203, 228, 229]. In fact, the interaction of light with free electrons in presence of a magnetic field perpendicular to the oscillating electric field of light gives rise to magneto-optical effects due to the Lorenz force [198, 230]. This results in Kerr or Faraday rotations due to the modification of the propagation plane. The magnetic field-induced change of the electron oscillation momentum implies that the SPR energy also varies and hence the plasmon frequency shifts in the presence of an applied magnetic field [203]. When using circularly polarized light, circular plasmonic modes with right and left polarization are split in energy in presence of a magnetic field parallel to the propagation direction giving rise to MCD nearby the SPR [229] (Fig. 5.3 iv). Nowadays different Kerr, Faraday and MCD effects have been demonstrated in Au [231], Ag [232, 233] and even in plasmonic semiconductors [234, 235] on nanoparticles, discs, rods and other morphologies. The MO effect of plasmonics nanoparticles varies linearly with the magnetic field, and it requires strong magnetic fields to be significant [229, 236]. In fact, it is significantly smaller than that of magnetic materials due to their different electronic origin.

5.5 Perspectives

In previous chapters we showed several examples of the multifunctionality of the MP nanostructures. However, a wide number of difficulties must be overcome to obtain high performance MP materials and devices. Such difficulties are linked to the nature of the involved materials and to the difficulties in the chemical design of the researched morphologies. From the optical point of view, the large optical losses of the most investigated magnetic materials: magnetite and maghemite, and Fe, Co, Ni,

give rise to the damping of the plasmonic properties in the different nanostructures. Alternatively, more transparent magnetic materials, like magnetic garnets (YIG) or magnetic metal-doped semiconductors, like ferromagnetic Co doped ZnO [237] or paramagnetic CeF_3 [238] are known, but their synthesis as nanoparticles or similar is currently a challenge. In this case, a more promising design would be the synthesis of metallic multicomponent alloys, semiconductors or multicomponent oxides in which the optical, plasmonic and magnetic properties could be optimized thanks to the control of the composition. Also, the search of alternative plasmonic materials should be interesting to develop MP nanostructures, since the vastly employed Ag and Au are not fully optimal materials [10]. For example, even if Ag has low optical losses in the visible optical range, the nanoparticles are not stable as Ag oxidizes easily. Au is more chemically stable, but it has large losses. These metals have large absorption in the NIR region where many applications—like telecommunications (TC) and biomedicine—are now working. Strong research activity is currently focused on novel plasmonic materials [9] and the development of MP structures with these compounds will be interesting.

The previous question is crucial also for the development of MP-based magneto-optical devices. In fact, the magneto-optical figure of merit, i.e. the parameter that defines the efficiency of a material for MO applications, is inversely proportional to the absorption. Magnetic garnets and Eu-chalcogenides, that have smaller MO signal than Fe or Co metals, are however employed in optical telecom devices due to their small losses in the Vis and IR [14]. The synthesis of MP NPs with materials with better transparency, as was previously discussed, or the employment of magnetic materials with high MO properties as half-metallic or Heusler phases [240] holds great promise. However, the synthesis of nanoparticles of these materials has not been developed at the moment. An alternative is the design of single phase and hybrid MP NPs with a morphology in which MO and SPR signals are not directly coupled. For example, in asymmetric structures, like ellipsoidal discs, the main SPR and the plasmon MO resonance occurs at different energies as are correlated with different orientations of discs. As shown by Chen et al. [241] in ellipsoidal Ni discs or by Macaferri et al. [242] in ellipsoids while the optical SPR can be excited along the main axis of the ellipsoid, the plasmonic MO excitation occurs along the orthogonal short axis at different wavelength. On the other hand, similar gap between MO and SPR has been observed in 2D arrays in which a mixture of plasmonics (Au) and magnetic (Ni) discs are arranged. Depending on the relative orientation of light and the array structure, different dipolar coupling processes between the plasmonic and magnetic discs (Ni–Ni and Au–Ni) are possible [243, 244], giving rise to high MO signal in a low absorption regime. Theoretical studies show that the development of MP photonic crystals composed of mixtures or single NPs could give rise to high magneto-optical performances.

Directly correlated with MO effects is the use of MPs for magnetic storage technologies [245, 246]. Heat Assisted Magnetic Recording (HARM) [247] is a commercial technology that takes advantage of the interplay between magnetic and plasmonic units to reach record (2 Tb/in.^{2}) density of magnetic storage [248]. This technology employs ultrafast switching of the magnetization of bits thanks to the local heating

produced by plasmon induced confinement of light. This is obtained by coupling a plasmonic antenna to a continuous magnetic medium [197]. Alternatively, all-optical magnetic recording has also been proposed as an ultrafast technology in the THz regime to switching the magnetization in magnetic memory and logic spintronic devices [250–253]. Ultrafast and high-power laser pulses allow magnetic erasing and writing processes thanks to a phenomenon known as the inverse Faraday effect. The incorporation of plasmonic structures should enhance the EMFs while at the same time allowing subwavelength spatial resolution inverse Faraday effects [251, 254, 255] and hence facilitate the incorporation of this technology in the on-chip submicrometric devices. While these two technologies are now investigated in films, 3D dots will be the further progress technology—for example, heated dot magnetic recording (HDMR) promises up to 10 Tb/in.^{2} [256]. Some works have investigated the possibility of MO writing and reading employing MP multilayer dots [255]. Here the aim is to overcome the limit of magneto-optical imaging in terms of spatial resolution [246]. MP nanoparticles should be the prototypes to investigate future developments of these technologies.

While the former technology (HAMR) takes advantage of the heat-induced demagnetization process, a different type of photo-induced switching mechanism activated by plasmonic resonance was proposed in Bogani et al. [257]. In this study the MO-detected hysteresis loops of AuFe nanoparticles with high coercive field were measured under the simultaneous irradiation with low power light at different wavelengths. The authors observed a faster magnetic relaxation of the nanoparticles when irradiating at the SPR wavelength. Different tests excluded that the observed phenomena were due to plasmon induced thermal or inverse Faraday effects. The authors propose that spin scattering processes are activated by the plasmon-induced electronic excitations.

Another field in which the multifunctional capabilities of MP NPs are very attractive is that of biomedical applications [246]. The development of theranostic approaches, *i.e.* diagnostic, imaging and therapeutic capabilities on a single platform for efficient and personalized treatment of cancer and other diseases, is a field in which the combination of the different performances of the plasmonics and magnetic moieties of the MP NPs can bring significant momentum. The benefit is also the possibility of overcoming the natural limits of each technique: the red-shift of SPR of the MP NPs allows imaging and treatment using IR radiation, while radio frequency-induced hyperthermia allows to perform thermal therapy in deeper regions of the body, unreachable to light, or to increase local temperature combining magneto- and photo-thermia. First demonstrations have been shown [258]; however, one of the main limitations for these applications is the restriction to Au for plasmonic and Fe oxide for the magnetic moiety taking into account cytotoxicity criteria. On the other hand, Ag has a stronger and narrower SPR compared to Au, while the Co-ferrite or FeCo alloys have larger anisotropy and magnetization respectively than the Fe oxides. However, these better compounds are chemically unstable in the body and cytotoxic.

Currently, different plasmonic diagnostic and sensing devices or platforms, using LSPR effects, are under investigation. MP NPs are gathering interest due to the possibility to combine the plasmonic application and an improvement in the efficiency to separate, concentrate or localize the analyte thanks to magnetic control in such a way to increase the sensibility, selectivity and detection rate. On the other hand, MO effects are being considered for the detection method. Recently, MCD and Kerr effects have been demonstrated to be high performance techniques for optical sensing of non-magnetic plasmonic structures [229]. However, since the MO signal of the magnetic materials is larger than that of the plasmonic ones and it can be reached applying smaller magnetic fields, the performance of magnetic structures should be better. On the other hand, MO spectroscopy could be useful to improve the selectivity of optical detection. Taking advantage of the phase change of the MO signal near the SPR proposed in [259], Macaferri et al. [260] developed an ultrasensitive and label-free molecular-level detection using ellipsoidal Ni nanodiscs and Kerr effect detection.

The employment of MP nanostructures for optimizing catalytic processes is another interesting application for magnetic-plasmonic hybrid structures. Most of the investigations exploit the bifunctionality of these structures, using for instance the capability of magnetic concentration, or the functionalization of the plasmonic surface. However, new scenarios that benefit from the properties of these hybrid structures are becoming clear: in hybrid structures like Au@Fe-oxides, the charge transfer mechanism and the charge depletion region can modulate the surface charge for catalytic reactions [90, 261–263]. On the other hand, plasmon-mediated catalytic processes are activated thanks to the local heat induced at the resonance [137]. In the case of MP NPs, the combination of photothermal and magnetic induced hyperthermia can be a new approach for controlling catalytic processes.

Another interesting perspective regards spin-plasmonics, i.e. the effects correlated to the net spin-polarization of the electrons involved in the plasmonic excitations. The spin polarization of *s*-band should not occur in pure plasmonic materials since they are diamagnetic, while it occurs in the *s* and *d* bands at the Fermi lever of the magnetic metals. In these materials, the spin-unbalance of *s*-electrons at the Fermi level is much smaller than the one corresponding to localized *d*-electrons. Several experiments based on X-Ray Magnetic Circular Dichroism spectroscopy have demonstrated the possibility to magnetize plasmonic elements. This has been observed in MPs metallic alloy based nanoparticles, like in AuFe [26, 27] NPs, or in metal@oxide hybrid heterostructures like Au@Fe_3O_4 CS NPs [89] as previously discussed. In magnetic materials, different intrinsic and extrinsic spin scattering mechanisms can give rise to different magneto-transport effects which are the base of magnetoresistance sensors and other spintronic devices. The effects due to a spin population and the spin scattering process in the SPR resonance has not been considered at the moment.

The landscape of new effects and applications of Magneto-plasmonic materials that is progressively appearing shows an increasing crossover of the MP effects with thermal effects. Several cases were discussed above in which magnet/plasmon/thermal effects are correlated, in particular to the photothermal

and magnetic hyperthermia effects therapies and plasmon driven demagnetization process. However, other crossing mechanisms can be outlined. Martin et al. [264] theoretically showed that the spatial thermal diffusion of the plasmon-induced heat between MP nanoparticles can be controlled by the MO effects. Experiments by Temnov et al. [265, 266] demonstrate the modulation of the non-linear optical properties of propagating plasmons in magnetoplasmonic multilayers induced by the thermal process at the magnetic interfaces. In addition, in MP NPs, single phase or hybrid, phononic and magnonic excitations are affected, and coupled, by size effects of the moieties, the inter and intra particle coupling and by the particle morphology. The fact that an increasing number of novel properties are being observed in magnetic and plasmonic nanostructures using other external stimulus—like chirality light, electrical and electrochemical fields or mechanical forces—[14, 72, 171, 174, 197, 251] involves that MPs will be excellent benchmark materials to design and investigate multi-responsive, multifunctional nanomaterials.

Acknowledgements This work has been supported by the European Union's Horizon 2020 Research and Innovation program under Grant agreement No. 737093 (FEMTOTERABYTE https://www.physics.gu.se/femtoterabyte) and by the University of Pisa through project PRA_2017_25.

References

1. S.A. Maier, *Plasmonics: Fundamentals and Applications* (Springer, New York, 2007)
2. J.A. Schuller, E.S. Barnard, W. Cai, Y.C. Jun, J.S. White, M.L. Brongersma, Nat. Mater. **9**, 193 (2010)
3. D.K. Gramotnev, S.I. Bozhevolnyi, Nat. Photon. **4**, 83 (2010)
4. O. Tokel, F. Inci, U. Demirci, Chem. Rev. **114**, 5728 (2014)
5. J. Langer, S.M. Novikov, L.M. Liz-Marzán, Nanotechnology **26**, 322001 (2015)
6. U. Kreibig, M. Vollmer, *Optical Properties of Metal Cluster* (Springer, Berlin, 1995)
7. S.K. Ghosh, T. Pal, Chem. Rev. **107**, 4797 (2007)
8. M.A. García, J. Phys. D: Appl. Phys. **44**, 283001 (2011)
9. S. Kim, J.M. Kim, J.E. Park, J.M. Nam, Adv. Mater. **30**, 1704528 (2018)
10. B. Doiron, M. Mota, M.P. Wells, R. Bower, ACS Photon. **6**, 240 (2019)
11. J.M.D. Coey, *Magnetism and Magnetic Materials* (Cambridge University Press, New York, 2010)
12. G. Armelles, A. Cebollada, A. García-Martín and M. Ujué González, Adv. Opt. Mater. **1**, 10 (2013).
13. R. Scarfiello, C. Nobile, P.D. Cozzoli, Front. Mater. **3**, 1 (2016)
14. D. Floess, H. Giessen, Rep. Prog. Phys. **81**, 116401 (2018)
15. V.T. Tran, J. Kim, L.T. Tufa, S. Oh, J. Kwon, J. Lee, Anal. Chem. **90**, 225 (2018)
16. P.B. Johnson, R.W. Christy, Phys. Rev. B **6**, 4370 (1972)
17. P.B. Johnson, R.W. Christy, Phys. Rev. B **9**, 5056 (1974)
18. K.K. Tikuišis, L. Beran, P. Cejpek, K. Uhlírová, J. Hamrle, M. Vaňatka, M. Urbánek, M. Veis, Mater. Design. **114**, 31 (2017)
19. G. Armelles, D. Weller, B. Rellinghaus, R.F.C. Farrow, M.F. Toney, P. Caro, A. Cebollada, M.I. Alonso, IEEE Trans. Magn. **33**, 3419 (1997)
20. N.W. Ashcroft, N.D. Mermin, *Solid State Physics* (Saunders College, Philadelphia, 1976)

21. J.L. Menéndez, B. Bescós, G. Armelles, R. Serna J. Gonzalo, R. Doole, A.K. Petford-Long, M.I. Alonso, Phys. Rev. B **65**, 205413 (2002)
22. H. Amekura, Y. Takeda, N. Kishimoto, Nucl. Instr. Meth. Phys. Res. B **222**, 96 (2004)
23. C. Clavero, A. Cebollada, G. Armelles, Y. Huttel, Phys. Rev. B **72**, 024441 (2005)
24. S. Ozaki, H. Kura, H. Maki, T. Sato, J. Appl. Phys. **105**, 113913 (2009)
25. C.Y. You, Z.Q. Yang, Q.F. Xiao, I. Škorvánek, Eur. Phys. J. Appl. Phys. **28**, 73 (2004)
26. C. de Julián Fernández, G. Mattei, E. Paz, R.L. Novak, L. Cavigli, L. Bogani, F.J. Palomares, P. Mazzoldi, A. Caneschi, Nanotechnology **21**, 165701 (2010)
27. V. Amendola, M. Meneghetti, O.M. Bakr, P. Riello, S. Polizzi, D.H. Anjum, S. Fiameni, P. Arosio, T. Orlando, C. de Julián Fernández et al., Nanoscale **5**, 5611 (2013)
28. N. Chen, Di Wang, T. Feng, R.A. Kruk, Nanoscale **7**, 6607 (2015)
29. P. Srinoi, Y.T. Chen, V. Vittur, M.D. Marquez, T.R. Lee, Appl. Sci. **8**, 1106 (2018)
30. R. Ferrando, J. Jellinek, R.L. Johnston, Chem. Rev. **108**, 846 (2008)
31. H. Zeng, S. Sun, Adv. Func. Mater. **18**, 391 (2008)
32. F.H. Lin, R.A. Doong, J. Coll. Interf. Sci. **417**, 325 (2014)
33. L. Carbone, P.D. Cozzoli, Nano Today **5**, 449 (2010)
34. M.B. Cortie, A.M. McDonagh, Chem. Rev. **111**, 3713 (2011)
35. K.C.F. Leung, S. Xuan, X. Zhu, D. Wang, C.P. Chak, S.F. Lee, W.K.W. Hob, B.C.T. Chung, Chem. Soc. Rev. **41**, 1911 (2012)
36. T.T. Nguyen, F. Mammeri, S.A. Nguyen, Nanomaterials **8**, 149 (2018)
37. C.S. Levin, C. Hofmann, T.A. Ali, A.T. Kelly, ACS Nano **3**, 1379 (2009)
38. L. Wang, C. Clavero, Z. Huba, K.J. Carroll, E.E. Carpenter, D. Gu, R.A. Lukaszew, Nano Lett. **11**, 1237 (2011)
39. W. Brullot, V.K. Valev, T. Verbiest, Nanomed. NBM **8**, 559 (2012)
40. R. Sachan, A. Malasi, J. Ge, S. Yadavali, H. Krishna, ACS Nano **8**, 9790 (2014)
41. E.A. Chaffin, S. Bhana, R.T. O'Connor, X. Huang, Y. Wang, J. Phys. Chem. B **118**, 14076 (2014)
42. W.F.J. Fontijn, P.J. van der Zaag, M.A.C. Devillers, V.A.M. Brabers, R. Metselaar, Phys. Rev. B **56**, 5432 (1997)
43. V. Doormann, J.P. Krumme, H. Lenz, J. Appl. Phys. **68**, 3544 (1990)
44. W. Shi, H. Zeng, Y. Sahoo, T.Y. Ohulchanskyy, Nano Lett. **6**, 875 (2006)
45. V. Velasco, L. Muñoz, E. Mazarío, N. Menéndez, P. Herrasti, A. Hernando, P. Crespo, J. Phys. D Appl. Phys. **48**, 035502 (2015)
46. B. Wang, S. Qu, Appl. Surf. Sci. **292**, 1002 (2014)
47. M. Wang, C. Gao, L. He, Q. Lu, J. Zhang, C. Tang, S. Zorba, Y. Yin, J. Am. Chem. Soc. **135**, 15302 (2013)
48. E. Prodan, P. Nordlander, N.J. Halas, Chem. Phys. Lett. **368**, 94 (2003)
49. C. Radloff, N.J. Halas, J. Chem. Phys. **120**, 5444 (2004)
50. A. Mahmed, A. Mehaney, M. Shaban, A.H. Aly, Mater. Res. Express **6**, 085073 (2019)
51. A. López-Ortega, M. Takahashi, S. Maenosono, P. Vavassori, Nanoscale **10**, 18672 (2018)
52. G.V. Hartland, Chem Rev **111**, 3858 (2011)
53. Y. Li, Q. Qiang Zhang, A.V. Nurmikko, S. Sun, Nano Lett. **5**, 1689 (2005)
54. K. Korobchevskaya, C. George, A. Diaspro, L. Manna, R. Cingolani, A. Comin, Appl. Phys. Lett. **99**, 18 (2011)
55. K. Korobchevskaya, C. George, L. Manna, A. Comin, J. Phys. Chem. C **116**, 26924 (2012)
56. A. Comin, K. Korobchevskaya, C. George, A. Diaspro, Nano Lett. **12**, 921 (2012)
57. C. Caruntu, B.C. Cushing, G. Caruntu, C.J. O'Connor, Chem. Mater. **17**, 3398 (2005)
58. F. Carlà, G. Campo, C. Sangregorio, A. Caneschi, C. de Julián Fernández, L.I. Cabrera, J. Nanopart. Res. **15**, 1813 (2013)
59. I. Urries, C. Muñoz, L. Gomez, C. Marquina, V. Sebastián, M. Arruebo, J. Santamaria, Nanoscale **6**, 9230 (2014)
60. X. Hou, X. Wang, R. Liu, H. Zhang, X. Liu, X. Liu, Y. Zhang, RSC Adv. **7**, 18844 (2017)
61. E.V. Shevchenko, M.I. Bodnarchuk, M.V. Kovalenko, D.V. Talapin, Adv. Mater. **20**, 4323 (2008)

62. W. Chen, N. Xu, L. Xu, L. Wang, Z. Li, W. Ma, Y. Zhu, C. Xu, N.A. Kotov, Macromol. Rapid. Commun. **31**, 228 (2010)
63. Y. Jin, C. Jia, S.-W. Huang, M.O. 'Donnell, X. Gao, Nat. Commun. **1**, 41(2010)
64. H. Mohammad-Beigi, S. Yaghmaei, R. Roostaazad, A. Arpanaei, Physica E **49**, 30 (2013)
65. X. Jin, H. Li, S. Wang, N. Kong, H. Xu, Q. Fu, H. Gua, J. Ye, Nanoscale **6**, 14360 (2014)
66. E.D. Smolensky, M.C. Neary, Y. Zhou, T.S. Berquo, V.C. Pierre, Chem. Comm. **47**, 2149 (2011)
67. M. Zhang, D.J. Magagnosc, I. Liberal, Y. Yu, H. Yun, H. Yang, Y. Wu, J. Guo, W. Chen, Y.J. Shin, A. Stein, J.M. Kikkawa, N. Engheta, D.S. Gianola, C.B. Murray, C.R. Kagan, Nat. Nanotech. **12**, 228 (2017)
68. G. Campo, F. Pineider, E. Fantechi, C. Innocenti, A. Caneschi, C. de Julián Fernández, J Nanosci. Nanotechnol. **19**, 4946 (2019)
69. A.C. Templeton, J.J. Pietron, R.W. Murray, P. Mulvaney, J. Phys. Chem. B **104**, 564 (2000)
70. C.F. Bohren, D.P. Gilra, J. Coll. Interf. Sci. **72**, 215 (1979)
71. I.W. Sudiarta, P. Chylek, J. Opt. Soc. Am. **67**, 561 (2001)
72. N. Passarelli, L.A. Pérez, E.A. Coronado, ACS Nano **8**, 9723 (2014)
73. M. Xiong, X. Jin, J. Jian Ye, Nanoscale **8**, 4991(2016)
74. E.V. Shevchenko, D.V. Talapin, C.B. Murray, S. O'Brien, J. Am. Chem. Soc. **128**, 3620 (2006)
75. W. Brullot, R. Strobbe, M. Bynens, M. Bloemen, P.J. Demeyer, W. Vanderlinden, S. De Feyter, V.K. Valev, T. Verbiest, Mater. Lett. **118**, 99 (2014)
76. P. Crespo, R. Litrán, T.C. Rojas, M. Multigner, J.M. de la Fuente, J.C. Sánchez-López, M.A. García, A. Hernando, S. Penadés, A. Fernández, Phys. Rev. Lett. **93**, 087204 (2004)
77. G.L. Nealon, B. Donnio, R. Greget, J.P. Kappler, E. Terazzi, J.L. Gallani, Nanoscale **4**, 5244 (2012)
78. Y. Lee, M.A. García, N.A. Frey Huls, S. Sun, Angew. Chem. Int. Ed. **49**, 1271 (2010)
79. C. Wang, Y. Wei, H. Jiang, S. Sun, Nano Lett. **9**, 4544 (2009)
80. C. George, A. Genovese, F. Qiao, K. Korobchevskaya, Nanoscale **3**, 4647 (2011)
81. F. Vita, C. Innocenti, A. Secchi, F. Albertini, V. Grillo, A. Fiore, P.D. Cozzoli, C. de Julián Fernández, J. Mater. Chem. C (2018)
82. R.H. Kodama, A.E. Berkovitz, E.J. Mcni, S. Foner, Phys. Rev. Lett. **77**, 394 (1996)
83. K. Kachkachi, A. Ezzir, M. Nogués, E. Tronc, Eur. Phys. J. B **14**, 681 (2002)
84. C. Martínez-Boubeta, K. Simeonidis, M. Angelakeris, N. Pazos-Pérez, M. Giersig, A. Delimitis, L. Nalbandian, V. Alexandrakis, D. Niarchos, Phys. Rev. B **74**, 054430 (2006)
85. S. Chandra, N.A. Frey Huls, M.H. Phan, S. Srinath, M.A. García, Y. Lee, C. Wang, S. Sun, O. Iglesias, H. Srikanth, Nanotechnology **25**, 055702 (2014)
86. A. Luchini, G. Vitiello, F. Rossi, O. Ruiz de Ballesteros, A. Radulescu, G. D'Errico, D. Montesarchio, C. de Julián Fernández, L. Paduano, Phys. Chem. Chem. Phys. **17**, 6087 (2015)
87. L. Zhu, X. Deng, Y. Hu, J. Liu, Nanoscale **10**, 21499 (2018)
88. P. Tancredi, L. Souza da Costa, S. Calderón, O. Moscoso-Londoño, L. M. Socolovsky, P.J. Ferreira, D. Muraca, D. Zanchet, M. Knobel, Nano Res. **12**, 1781 (2019)
89. F. Pineider, C. de Julián Fernández, V. Videtta, E. Carlino, A. al Hourani, F. Wilhelm, A. Rogalev, P.D. Cozzoli, P. Ghigna, C. Sangregorio, ACS Nano **7**, 857 (2013)
90. M. Feygenson, J.C. Bauer, Z. Gai, C. Marques, M.C. Aronson, X. Teng, D. Su, V. Stanic, V.S. Urban, K.A. Beyer, S. Dai, Phys. Rev. B **92**, 054416 (2015)
91. M. Kim, H. Song, J. Mater Chem C **2**, 4997 (2014)
92. P. Guardia, S. Nitti, M.E. Materia, G. Pugliese, N. Yaacoub, J.-M. Greneche, C. Lefevre, L. Manna, T. Pellegrino, J. Mater. Chem. B **5**, 4587 (2017)
93. A. Pariti, P. Desai, S.K.Y. Maddirala, N. Ercal, K.V. Katti, X. Liang, M. Nath, Mater. Res. Express **1**, 035023 (2014)
94. M.E.F. Brollo, J.M. Orozco-Henao, R. López-Ruiz, D. Muraca, C.S.B. Dias, K.R. Pirota, M. Knobel, J. Magn. Magn. Mater. **397**, 20 (2016)
95. P. Tancredi, O. Moscoso Londoño, P.C. Rivas Rojas, U. Wolff, L.M. Socolovsky, M. Knobel, D. Muraca, J. Phys. D Appl. Phys. **51**, 295303 (2018)
96. N.A. Frey, S. Srinath, H. Srikanth, C. Wang, S. Sun, IEEE Trans. Magn. **43**, 3094 (2007)

97. J.G. Ovejero, I. Morales, P. de la Presa, N. Mille, J. Carrey, M.A. García, A. Hernando, P. Herrasti, Phys. Chem. Chem. Phys. **20**, 24065 (2018)
98. M. Knobel, W.C. Nunes, L.M. Socolovsky, E. De Biasi, J. Nanosci. Nanotechnol. **8**, 2836 (2008)
99. X. Batlle, A. Labarta, J. Phys. D: Appl. Phys. **35**, R15 (2002)
100. P. Singh, M. Shukla, C. Upadhyay, Nanoscale **10**, 22583 (2018)
101. N.A. Frey, N.H. Phan, H. Srikanth, S. Srinath, J. Appl. Phys. **105**, 07B502 (2009)
102. L. León-Félix, J. Chaker, M. Parise, J.A.H. Coaquira, Hyperfine Interact. **224**, 179 (2014)
103. M. Bozorth, *Ferromagnetism* (Van Nostrand, Toronto, 1951)
104. D.A. Gilbert, L.W. Wang, T.J. Klemmer, J.U. Thiele, C.H. Lai, K. Liu, Appl. Phys. Lett. **102**, 132406 (2013)
105. A.P. Murani, J. Phys. F Met. Phys. **4**, 757 (1974)
106. B. Verbeek, J. Mydosh, J. Phys. F Met. Phys. **8**, L109 (2001)
107. F. Wilhelm, P. Poulopoulos, V. Kapaklis, J.P. Kappler N. Jaouen, A. Rogalev, A.N. Yaresko, C. Politis, Phys. Rev. B **77**, 224414 (2008)
108. J.R. Childress, C.L. Chien, Phys. Rev. B **43**, 8089 (1991)
109. J. Noetzel, A. Handstein, A. Mucklich, F. Prockert, J. Magn. Magn. Mater. **205**, 183 (1999)
110. N. Jaouen, F. Wilhelm, A. Rogalev, J. Goulon, J. Phys. Condens. Matter **20**, 095005 (2008)
111. J. Bartolomé, L.M. García, F. Bartolomé, F. Luis, R. López-Ruiz, F. Petroff, C. Deranlot, F. Wilhelm, A. Rogalev, P. Bencok et al., Phys. Rev. B **77**, 184420 (2008)
112. C. Maurizio, N. Michieli, B. Kalinic, V. Mattarello, V. Bello, F. Wilhelm, K. Ollefs, G. Mattei, Appl. Surf. Sci. **433**, 596 (2018)
113. J.K. Lim, S.A. Majetich, Nano Today **8**, 98 (2013)
114. I. Schick, D. Gehrig, M. Montigny, B. Balke, M. Panthöfer, A. Henkel, F. Laquai, W. Tremel, Chem. Mater. **27**, 4877 (2015)
115. J. Canet-Ferrer, P. Albella, A. Ribera, J.V. Usagre, S.A. Maier, Nanoscale Horiz. **2**, 205 (2017)
116. Y. Song, V.T. Tran, J. Lee, A.C.S. Appl, Mater. Interf. **9**, 24433 (2017)
117. J. Zeng, M. Gong, D. Wang, M. Li, W. Xu, Z. Li, S. Li, D. Zhang, Z. Yan, Y. Yin, Nano Lett. **19**, 3011 (2019)
118. H. Wang, D.W. Brandl, F. Le, P. Nordlander, N.J. Halas, Nano Lett. **6**, 827 (2006)
119. Y. Chen, N. Gao, J. Jiang, Small **9**, 3242 (2013)
120. Z. Li, J.J. Foley IV., S. Peng, C.J. Sun, Y. Ren, G.P. Wiederrecht, S.K. Gray, Y. Sun, Angew. Chem. Int. Ed. **54**, 8948 (2015)
121. Z. Li, A. López-Ortega, A. Aranda-Ramos, J.L. Tajada, J. Sort, C. Nogues, P. Vavassori, J. Nogues, B. Sepúlveda, Small **14**, 1800868 (2018)
122. B.H. Jun, M.S. Noh, J. Kim, G. Kim, H. Kang, M.S. Kim, Y.T. Seo, J. Baek, J.H. Kim, J. Park, S. Kim, Y.K. Kim, T. Hyeon, M.H. Cho, D.H. Jeong, Y.S. Lee, Small **6**, 119 (2010)
123. X. Zhou, W. Xu, Y. Wang, Q. Kuang, Y. Shi, L. Zhong, Q. Zhang, J. Phys. Chem. C **114**, 19607 (2010)
124. A. Mezni, I. Imen Balti, A. Mlayah, N. Jouini, L.S. Smiri, J. Phys. Chem. C **117**, 16166 (2013)
125. C. Yuen, Q. Liu, Analyst **138**, 6494 (2013)
126. Z. Sun, J. Du, F. Duan, K. He, J. Mater. Chem. C **6**, 2252 (2018)
127. V. Amendola, S. Scaramuzza, S. Agnoli, S. Polizzi, M. Meneghetti, Nanoscale **6**, 1423 (2014)
128. V. Amendola, S. Scaramuzza, L. Litti, M. Meneghetti, Small **10**, 2476 (2014)
129. S. Scaramuzza, S. Polizzi, V. Amendola, Nanoscale Adv. **1**, 2681 (2019)
130. Y.H. Lim, M.Y. Cho, J.K. Kim, S. Hwangbo, B.H. Chung, ChemBioChem **8**, 2204 (2007)
131. R. Bardhan, W. Chen, M. Bartels, C. Pérez-Torres, M.F. Botero, R.W. McAninch, A. Contreras, R. Schiff, R.G. Pautler, N.J. Halas, A. Joshi, Nano Lett. **10**, 4920 (2010)
132. D.K. Kirui, D.A. Rey, C.A. Batt, Nanotechnology **21**, 105105 (2010)
133. S. Bhana, G. Lin, L. Wang, H. Starring, S.R. Mishra, G. Liu, X. Huang, A.C.S. Appl, Mater. Interf. **7**, 11637 (2015)
134. L. Huang, L. Ao, D. Hu, W. Wang, Z. Sheng, W. Su, Chem. Mater. **28**, 5896 (2016)
135. Z. Li, A. Aranda-Ramos, P. Güell-Grau, J.L. Tajada, L. Pou-Macayo, S. Lope Piedrafita, F. Pi, A.G. Roca, M.D. Baró, J. Sorte, et al., Appl. Mater. Today **12**, 430 (2018)

136. C. Multari, M. Miola, F. Laviano, R. Gerbaldo, G. Pezzotti, D. Debellis, E. Verné, Nanotechnology **30**, 255705 (2019)
137. Q. Ding, H. Zhou, H. Zhang, Y. Zhang, G. Wang, H. Zhao, J. Mater. Chem. A, **4**, 8866 (2016)
138. V.J. Pansare, S. Hejazi, W.J. Faenza, R.K. Prud'homme, Chem. Mater. **24**, 812 (2012)
139. B. Pelaz, C. Alexiou, R.A. Alvarez-Puebla, F. Alves, A.M. Andrews, S. Ashraf, L.P. Balogh, L. Ballerini, A. Bestetti, C. Brendel, S. Bosi et al., ACS Nano **11**, 2313 (2017)
140. N. Lewinski, V. Colvin, R. Drezek, Small **4**, 26 (2008)
141. B.R. Smith, S.S. Gambhir, Chem. Rev. **117**, 901 (2017)
142. D. Lombardo, M.A. Kiselev, M.T. Caccamo, J. Nanomater. 3702518 (2019). https://doi.org/10.1155/2019/3702518
143. L.H. Reddy, J.L. Arias, J. Nicolas, P. Couvreur, Chem. Rev. **112**, 5818 (2012)
144. Q. Feng, Y. Liu, J. Huang, K. Chen, J. Huang, K. Xiao, Sci. Rep. **8**, 2082 (2018)
145. J.T. Jenkins, D.L. Halaney, K.V. Sokolov, L.L. Ma, H.J. Shipley, S. Mahajan, C.L. Louden, R. Asmis, T.E. Milner, K.P. Johnston, M.D. Feldman, Nanomed. Nanotechn. Biol. Med. **9**, 356 (2013)
146. J. Kolosnjaj-Tabi, Y. Javed, L. Lartigue, J. Volatron, D. Elgrabli, I. Marangon, G. Pugliese, B. Caron, A. Figuerola, N. Luciani et al., ACS Nano **9**, 7925 (2015)
147. L. Li, S. Fu, C. Chen, X. Wang, C. Fu, S. Wang, W. Guo, X. Yu, X. Zhang, Z. Liu et al., ACS Nano **9**, 7094 (2016)
148. F. Mazuel, A. Espinosa, G. Radtke, M. Bugnet, S. Neveu, Y. Lalatonne, G.A. Botton, A. Abou-Hassan, C. Wilhelm, Adv. Funct. Mater. **27**, 1605997 (2017)
149. J.K. Lim, C. Lanni, E.R. Evarts, F. Lanni, R.D. Tilton, S.A. Majetich, ACS Nano **5**, 217 (2011)
150. E. Lueshen, I. Venugopal, J. Kanikunnel, T. Soni, Future Med. (2013). https://doi.org/10.2217/nnm.13.69
151. H. Zhou, F. Zou, K. Koh, J. Lee, J. Biomed. Nanotechnol. **10**, 2921 (2014)
152. X. Jin, H. Yu, N. Kong, J. Chang, H. Li, J. Ye, J. Mater. Chem. B **3**, 7787 (2015)
153. H.L. Liu, C.H. Sonn, J.H. Wu, K.M. Lee, Y.K. Kim, Biomaterials **29**, 4003 (2008)
154. Y.H. Bai, J.Y. Li, J.J. Xu, H.Y. Chen, Analyst **135**, 1672 (2010)
155. J. Li, Q. Xu, X. Wei, Z. Hao, J. Agric. Food Chem. **61**, 1435 (2013)
156. C.S. Bell, R. Mejías, S.E. Miller, J.M. Greer, M.S. McClain, T.L. Cover, T.D. Giorgio, ACS Appl. Mater. Interf. **9**, 26719 (2017)
157. R. Tavallaie, J. McCarroll, M. Le Grand, N. Ariotti, W. Schuhmann, E. Bakker, R.D. Tilley, D.B. Hibbert, M. Kavallaris, J.J. Gooding, Nat. Nanotech. **13**, 1066 (2018)
158. C. Xu, J. Xie, D. Ho, C. Wang, N. Kohler, N. Kohler, E.G. Walsh, J.R. Morgan, Y.E. Chin, S. Sun, Angew. Chem. Int. Ed. **47**, 173 (2008)
159. H. Jaganathan, R.L. Gieseck, A. Ivanisevic, J. Phys. Chem. C **114**, 22508 (2010)
160. E. Umut, F. Pineider, P. Arosio, C. Sangregorio, M. Corti, F. Tabak, A. Lascialfari, P. Ghigna, J. Magn. Magn. Mater. **324**, 2373 (2012)
161. T. Orlando, A. Capozzi, E. Umut, L. Bordonali, M. Mariani, P. Galinetto, F. Pineider, C. Innocenti, P. Masala, F. Tabak, M. Scavini, P. Santini, M. Corti, C. Sangregorio et al., J. Phys. Chem. C **119**, 1224 (2015)
162. F. Sousa, B. Sanavio, A. Saccani, Y. Tang, I. Zucca, T.M. Carney, A. Mastropietro, P.H.J. Jacob Silva, R.P. Carney, K. Schenk, et al., Bioconjugate Chem. **28**, 161 (2017)
163. J. Li, B. Arnal, C.W. Wei, J. Shang, M. O'Donnell, X. Gao, ACS Nano **9**, 1964 (2015)
164. J.G. Ovejero, S.J. Yoon, J. Li, A. Mayoral, X. Gao, M. O'Donnell, M.A. García, P. Herrasti, A. Hernando, Microchim. Acta **185**, 130 (2018)
165. G.A. Sotiriou, M.A. Visbal-Onufrak, A. Teleki, E.J. Juan, Chem. Mater. **25**, 4603 (2013)
166. R. Di Corato, A. Espinosa, L. Lartigue, M. Tharaud, S. Chat, T. Pellegrino, C. Ménager, F. Gazeau, C. Wilhelm, Biomaterials **35**, 6400 (2014)
167. F. Mohammad, G. Balaji, A. Weber, R.M. Uppu, Z. Sheng, W. Su, J. Phys. Chem. C **114**, 19194 (2010)
168. E. Fantechi, P.M. Castillo, E. Conca, F. Cugia, C. Sangregorio, M.F. Casula, Interface Focus **6**, 20160058 (2016)

169. D.H. Kim, E.A. Rozhkova, I.V. Ulasov, S.D. Bader, T. Rajh, M.S. Lesniak, V. Novosad, Nat. Mater. **9**, 169 (2010)
170. S. Leulmi, X. Chauchet, M. Morcrette, G. Ortiz, H. Joisten, P. Sabon, T. Livache, Y. Hou, M. Carrière, S. Lequiena, B. Dieny, Nanoscale **7**, 15904 (2015)
171. N. Jiang, X. Zhuo, J. Wang, Chem. Rev. **118**, 3054 (2018)
172. G. Armelles, A. Cebollada, A. García-Martín, J. García-Martín, M.U. González, J.B. González-Díaz, E. Ferreiro-Vila, J.F. Torrado, J. Opt. A Pure Appl. Opt. **11**, 114023 (2009)
173. V. Temnov, G. Armelles, U. Woggon, D. Guzatov, A. Cebollada, A. García-Martín, J.M. García-Martín, T. Thomay, A. Leitenstorfer, R. Bratschitsch, Nat. Photon. **4**, 107 (2010)
174. D. Bossini, V.I. Belotelov, A.K. Zvezdin, A.N. Kalish, A.V. Kimel, ACS Photon. **38**, 1385 (2016)
175. Q. Wei, H.M. Song, A.P. Leonov, J.A. Hale, D. Oh, Q.K. Ong, K. Ritchie, A. Wei, J. Am. Chem. Soc. **131**, 9728 (2009)
176. H.M. Song, Q. Wei, Q.K. Ong, A. Wei, ACS Nano **4**, 5163 (2010)
177. A. Tomitaka, H. Arami, Z. Huang, A. Raymond, E. Rodriguez, Y. Cai, M. Febo, Y. Takemura, M. Nair, Nanoscale **10**, 184 (2018)
178. W.P. Li, P.Y. Liao, C.H. Su, C.S. Yeh, J. Am. Chem. Soc. **136**, 10062 (2014)
179. W. Shi, X. Liu, C. Wei, Z. J. Xu, S. S. Wei Sim, L. Liu, C. Xu, Nanoscale **7**, 17249 (2015)
180. R. Di Corato, G. Béalle, J. Kolosnjaj-Tabi, A. Espinosa, O. Clément, A.K.A. Silva, C. Ménager, C. Wilhelm, ACS Nano **9**, 2904 (2015)
181. E. Cazares-Cortes, S. Cabana, C. Boitard, E. Nehlig, Adv. Drug Deliv. Rev. **138**, 233 (2019)
182. A. Espinosa, M. Bugnet, G. Radtke, S. Neveu, G.A. Botton, C. Wilhelm, A. Abou-Hassan, Nanoscale **7**, 18872 (2015)
183. A. Espinosa, R. Di Corato, J. Kolosnjaj-Tabi, P. Flaud, T. Pellegrino, C. Wilhelm, ACS Nano **10**, 2436 (2016)
184. M. Carril, I. Fernández, J. Rodríguez, I. García, S. Penadés, Part. Part. Syst. Charact. **31**, 81 (2014)
185. J. Zhu, Y. Lu, Y. Li, J. Jiang, Nanoscale **6**, 199 (2014)
186. T.H. Shin, Y. Choi, S. Kim, J. Cheon, Chem. Soc. Rev. **44**, 4501 (2015)
187. S.S. Kelkar, T.M. Reineke, Bioconj. Chem. **22**, 1879 (2011)
188. H. Kang, S. Hu, M.H. Cho, S.H. Hong, Y. Choi, H.S. Choi, Nano Today **23**, 59 (2018)
189. J. Lee, J. Yang, H. Ko, S.J. Oh, J. Kang, J. Kang, J.H. Son, K. Lee, S.W. Lee, H.G. Yoon, J.-S. Suh et al., Adv. Funct. Mater. **18**, 258 (2008)
190. L.S. Lin, X. Yang, Z. Zhou, Z. Yang, O. Jacobson, Y. Liu, A. Yang, G. Niu, J. Song, H.H. Yang, X. Chen, Adv. Mater. **29**, 1606681 (2017)
191. Z. Abed, J. Beik, S. Laurent, N. Eslahi, T. Khani, E.S. Davania, H. Ghaznavi, A. Shakeri-Zadeh, J. Cancer Res. Clin. Oncol. **145**, 1213 (2019)
192. M.V. Efremova, V.A. Naumenko, M. Spasova, A.S. Garanina, M.A. Abakumov, A.D. Blokhina, P.A. Melnikov, A.O. Prelovskaya, M. Heidelmann, Z.-A. Li et al., Sci. Rep. **8**, 11295 (2018)
193. M.V. Efremova, Y.A. Nalench, E. Myrovali, A.S. Garanina, I.S. Grebennikov, P.K. Gifer, M.A. Abakumov, M. Spasova, M. Angelakeris, A.G. Savchenko et al., Beilstein J. Nanotechnol. **9**, 2684 (2018)
194. A.K. Zvezdin, V.A. Kotov, *Modern Magnetooptics and Magnetooptical Materials* (IOP Publishing Ltd., Bristol, 1997)
195. P.M. Oppeneer in *Handbook of Magnetic Materials*, vol. 13, ed. by K.H.J. Buschow (Elsevier Science, 2001)
196. P. Oppeneer, V. Antonov, in *Spin-Orbit-Influenced Spectroscopies of Magnetic Solids*, eds. by H. Ebert, G. Schütz (Springer, Berlin/Heidelberg, 1996), p. 29
197. N. Maccaferri, J. Opt. Soc. Am. B **36**, E112 (2019)
198. H. Feil, C. Haas, Phys. Rev. Lett. **58**, 65 (1987)
199. D. Lacoste, B.A. Tiggelen, G.L.J.A. Rikken, A. Sparenberg, J. Opt. Soc. Am. A **15**, 1636 (1998)
200. J.S. Ahn, K.H. Kim, T.W. Noh, D.H. Riu, K.H. Boo, H.E. Kim, Phys. Rev. B **52**, 15244 (1995)

201. M. Abe, T. Suwa, Phys. Rev. B **70**, 235103 (2004)
202. P.H. Lissberger, P.W. Saunders, Thin Solid Films **34**, 323 (1976)
203. B. Sepúlveda, J.B. González-Díaz, A. García-Martín, L.M. Lechuga, G. Armelles, Phys. Rev. Lett. **104**, 147401 (2010)
204. J.B. González-Díaz, B. Sepúlveda, A. García-Martín, G. Armelles, Appl. Phys. Lett. **97**, 043114 (2010)
205. A. Bourzami, O. Lenoble, C. Féry, J.F. Bobo, M. Piecuch, Phys. Rev. B **59**, 11489 (1999)
206. L. Fernández García, C. Pecharromán, A. Esteban-Cubillo, P. Tiemblo, N. García, J.L. Menéndez, J. Nanopart. Res. **15**, 2119 (2013)
207. A. Miles, Y. Gai, P. Gangopadhyay, X. Wang, R.A. Norwood, J.J. Watkins, Opt. Mater. Express. **7**, 2126 (2017)
208. B. Kalska, J.J. Paggel, P. Fumagalli, M. Hilgendorff, M. Giersig, J. Appl. Phys. **92**, 7481 (2002)
209. C. Clavero, B. Sepúlveda, G. Armelles, Z. Konstantinović, M. García del Muro, A. Labarta, X. Batlle, J. Appl. Phys. **100**, 074320 (2006)
210. B. Kalska, K. Schwinge, J. Paggel, P. Fumagalli, M. Hilgendorff, M. Giersig, J. Appl. Phys. **98**, 044318 (2005)
211. C. Clavero, G. Armelles, J. Margueritat, J. Gonzalo, M. García del Muro, A. Labarta, X. Batlle, Appl. Phys. Lett. **90**, 182506 (2007)
212. D. Martín-Becerra, J.M. García-Martín, Y. Huttel, G. Armelles, J. Appl. Phys. **117**, 053101 (2015)
213. O. Vlasin, O. Pascu, A. Roig, G. Herranz, Phys. Rev. Appl. **2**, 054003 (2014)
214. P. Varytis, N. Stefanou, A. Christofi, N. Papanikolaou, J. Opt. Soc. Am. B **32**, 1063 (2015)
215. P. Varytis, P.A. Pantazopoulos, N. Stefanou, Phys. Rev. B **93**, 214423 (2016)
216. B. Toal, M. McMillen, A. Murphy, W. Hendren, M. Arredondo, R. Pollard, Nanoscale **6**, 12905 (2014)
217. G. Shemer, G. Markovich, J. Phys. Chem. B **106**, 9195 (2002)
218. S. Tomita, T. Kato, S. Tsunashima, S. Iwata, M. Fujii, S. Hayashi, Phys. Rev. Lett. **96**, 167402 (2006)
219. R. Fujikawa, A.V. Baryshev, J. Kim, H. Uchida, M. Inoue, J. Appl. Phys. **103**, 07D301 (2008)
220. A.V. Baryshev, H. Uchida, M. Inoue, J. Opt. Soc. Amer. B **30**, 2371 (2013)
221. Y. Li, Q. Zhang, A.V. Nurmikko, S. Sun, Nano Lett. **5**, 1689 (2005)
222. P.K. Jain, Y. Xiao, R. Walsworth, A.E. Cohen, Nano Lett. **9**, 1644 (2009)
223. R.K. Dani, H. Wang, S.H. Bossmann, G. Wysin, J. Chem. Phys. **135**, 224502 (2011)
224. F.E. Moolekamp III., K.L. Stokes, IEEE Trans. Magn. **45**, 4888 (2009)
225. M. Caminale, L. Anghinolfi, E. Magnano, F. Bondino, A.C.S. Appl, Mater. Interf. **5**, 1955 (2013)
226. D. Smith, K.L. Stokes, Opt. Express **14**, 5746 (2006)
227. P. Pineider, E. Pedrueza-Villalmanzo, M. Serri, A.M. Adamu, E. Smetanina, V. Bonanni, G. Campo, L. Poggini, M. Mannini, C. de Julián Fernández, et al., Mater. Horiz. **6**, 1148 (2019)
228. M.A. Zaitoun, W.R. Mason, C.T. Lin, J. Phys. Chem. B **105**, 6780 (2001)
229. F. Pineider, G. Campo, V. Bonanni, C. de Julián Fernández, G. Mattei, A. Caneschi, D. Gatteschi, C. Sangregorio, Nano Lett. **13**, 4785 (2013)
230. P. Haefnere, E. Luck, E. Mohle, Phys. Stat. Sol. B **185**, 289 (1994)
231. B. Han, X. Gao, L. Shi, Y. Zheng, K. Hou, J. Lv, J. Guo, W. Zhang, Z. Tang, Nano Lett. **17**, 6083 (2017)
232. Y. Ishikawa, H. Yao, Chem. Phys. Lett. **609**, 93 (2014)
233. T. Shiratsu, H. Yao, Phys. Chem. Chem. Phys. **20**, 4269 (2018)
234. A.V. Malakhovskiia, A.E. Sokolova, A.S. Tsipotan, S.M. Zharkova, V.N. Zabluda, Phys. Lett. A **382**, 980 (2018)
235. P. Yin, Y. Tan, H. Fang, M. Hegde, P.V. Radovanovic, Nat. Nanotechnol. **13**, 463 (2018)
236. G. Weick, D. Weinmann, Phys. Rev. B **83**, 125405 (2011)
237. G. Varvaro, A. Di Trolio, A. Polimeni, A. Gabbani, F. Pineider, C. de Julián Fernández, G. Barucca, P. Mengucci, A. Bonapasta, A.M. Testa, J. Mater. Chem. C **7**, 78 (2019)

238. P. Molina, V. Vasyliev, E.G. Víllora, K. Shimamura, Opt. Express **19**, 11786 (2011)
239. J.F. Dillon, J. Appl. Phys. **39**, 922 (1968)
240. T. Graf, C. Felser, S.S.P. Parkin, Prog. Solid State Chem. **39**, 1 (2011)
241. J. Chen, P. Albella, Z. Pirzadeh, P. Alonso-González, Florian Huth, S. Bonetti, V. Bonanni, J. Åkerman, J. Nogués, P. Vavassori, et al., Small **7**, 2341 (2011)
242. N. Maccaferri, J.B. González-Díaz, S. Bonetti, A. Berger, M. Kataja, S. van Dijken, J. Nogués, V. Bonanni, Z. Pirzadeh, A. Dmitriev et al., Opt. Expr. **21**, 9875 (2013)
243. M. Kataja, T.K. Hakala, A. Julku, M.J. Huttunen, S. van Dijken, P. Törmä, Nat. Commun. **6**, 7072 (2015)
244. M. Kataja, S. Pourjamal, N. Maccaferri, P. Vavassori, T.K. Hakala, M.J. Huttunen, P. Törmä, S. van Dijken, Opt. Exp. **24**, 3652 (2016)
245. R.L. Stamps, S. Breitkreutz, J. Åkerman, A. Chumak, Y.C. Otani, G.E.W. Bauer, J.U. Thiele, M. Bowen, S.A. Majetich, M Kläui, et al., J. Phys. D Appl. Phys. **47**, 333001 (2014)
246. D. Sander, S.O. Valenzuela, D. Makarov, C.H. Marrows, E.E. Fullerton, P. Fischer, J. McCord, P. Vavassori, S. Mangin, P. Pirro et al., J. Phys. D Appl. Phys. **50**, 363001 (2017)
247. W.A. Challener, C. Peng, A.V. Itagi, D. Karns, W. Peng, Y. Peng, X. Yang, X. Zhu, N.J. Gokemeijer, Y.-T. Tsia et al., Nature Photon. **3**, 220 (2009)
248. E. Gage, K.Z. Gao, J.G. Zhu, in *Energy-Assisted Magnetic Recording, Ultrahigh-Density Magnetic Recording, Storage Materials and Media Designs,* ed. by G. Varvaro, F. Casoli (Pan Stanford Publishing, Singapore, 2016), Chap. 4
249. B.C. Stipe, T.C. Strand, C.C. Poon, H. Balamane, T.D. Boone, J.A. Katine, J.-L. Li, V. Rawat, H. Nemoto, A. Hirotsune, O. Hellwig, et al., Nature Phot. **4**, 484 (2010)
250. C.D. Stanciu, F. Hansteen, A.V. Kimel, A. Kirilyuk, A. Tsukamoto, A. Itoh, Th. Rasing, Phys. Rev. Lett. **99**, 47601 (2007)
251. I.S. Maksymov, Nanomaterials **5**, 577 (2015)
252. J. Walowski, M. Münzenberg, J. Appl. Phys. **120** 140901 (2016)
253. A.L. Chekhov, A.I. Stognij, T. Satoh, T.V. Murzina, I. Razdolski, A. Stupakiewicz, Nano Lett. **18** 2970 (2018)
254. T.M. Liu, T. Wang, A.H. Reid, M. Savoini, B. Koene, P. Granitzka, C.E. Graves, D.J. Higley, Z. Chen, G. Razinskas et al., Nano Lett. **15**, 6862 (2015)
255. A. Dutta, A.V. Kildishev, V.M. Shalaev, A. Bolasseva, R.E. Marinero, Opt. Mater. Express **7** 4317 (2017)
256. https://www.kitguru.net/components/hard-drives/anton-shilov/seagate-demos-hamr-hdds-vows-to-start-commercial-shipments-in-late-2017.
257. L. Bogani, L. Cavigli, C. de Julián Fernández, P. Mazzoldi, G. Mattei, M. Gurioli, M. Dressel, D. Gatteschi, Adv. Mater. **22**, 4054 (2010)
258. H. Hao Yan, W. Shang, X. Sun, L. Zhao J. Wang, Z. Xiong, J. Yuan, R. Zhang, Q. Huang, K. Wang, et al., Adv. Func. Mater. **28**, 1705710 (2018)
259. V. Bonanni, S. Bonetti, T. Pakizeh, Z. Pirzadeh, J. Chen, J. Nogués, P. Vavassori, O.R. Hillenbrand, J. Åkerman, A. Dmitriev, Nano Lett. **11**, 5333 (2011)
260. N. Maccaferri, E. Keith. K.E. Gregorczyk, T.V.A.G. de Oliveira, M. Kataja, S. van Dijken, Z. Pirzadeh, A. Dmitriev, J. Åkerman, M. Knez, P. Vavassori, Nature Comm. **6**, 6150 (2015)
261. S. Liu, S. Q Bai, Y. Zheng, K. Wei Shah, M.-Y. Han, ChemCatChem **4**, 1462 (2012)
262. L. Shang, Y. Liang, M. Li, G.I.N. Waterhouse, P. Tang, D. Ma, L.Z. Wu, C.H. Tung, T. Zhang, Adv. Func. Mater. **27**, 1606215 (2017)
263. S. Sarveena, D. Muraca, P. Mendoza Zélis, Y. Javed N. Ahmad, J.M. Vargas, O. Moscoso-Londoño, M. Knobel, M. Singha, S.K. Sharma, RSC Adv. **6**, 70394 (2016)
264. R.M.A. Ekeroth, A. García-Martín, J.C. Cuevas, Phys. Rev. B **95**, 235428 (2017)
265. V.V. Temnov, Nat. Photon. **6**, 728 (2012)
266. V.V. Temnov, I. Razdolski, T. Pezeril, D. Makarov, D. Seletskiy, A. Melnikov, K.A. Nelson, J. Opt. **18**, 093002 (2016)

Chapter 6
Hollow Magnetic Nanoparticles

Hafsa Khurshid, Zohreh Nemati, Óscar Iglesias, Javier Alonso, Manh-Huong Phan, and Hariharan Srikanth

Abstract Hollow magnetic nanoparticles present a characteristic morphology that gives rise to interesting magnetic behaviors and novel applications. In this chapter, we describe the synthesis methods utilizing the Kirkendall effect and the magnetic properties of these nanoparticles, with a focus on the analysis of their enhanced surface anisotropy, spin disorder, and exchange bias effect. The experimental studies are complemented by atomistic Monte Carlo simulations. Finally, we review a variety of applications of these nanoparticles, especially in biomedicine, batteries, sensing, and data storage, and also discuss some of the limitations that need to be overcome for their implementation.

H. Khurshid
Department of Applied Physics and Astronomy, University of Sharjah, Sharjah 27272, UAE
e-mail: hkhurshid@sharjah.ac.ae

Z. Nemati
Department of Electrical and Computer Engineering, University of Minnesota Twin Cities, Minneapolis 55455-0132, USA
e-mail: znematip@umn.edu

Ó. Iglesias
Departament de Física de La Matèria Condensada and Institut de Nanociència i Nanotecnologia, Universitat de Barcelona, 08028 Barcelona, Spain
e-mail: oscariglesias@ub.edu

J. Alonso
Department CITIMAC, Universidad de Cantabria, 39005 Santander, Spain
e-mail: javier.alonsomasa@unican.es

M.-H. Phan · H. Srikanth (✉)
Department of Physics, University of South Florida, Tampa, FL 33620, USA
e-mail: sharihar@usf.edu

M.-H. Phan
e-mail: phanm@usf.edu

D. Peddis et al. (eds.), *New Trends in Nanoparticle Magnetism*,
Springer Series in Materials Science 308,
https://doi.org/10.1007/978-3-030-60473-8_6

6.1 Introduction

Magnetic nanoparticles (MNPs) have attracted a lot of attention in the scientific community during the last decades due to their novel magnetic properties and their promising applications [1–4]. These nanoparticles can exhibit a series of interesting magnetic phenomena, such as superparamagnetism, exchange bias, and surface disorder [6, 7], and they have been used for a wide variety of applications from data storage [2, 8] to biomedicine [9, 10]. Many of these magnetic nanoparticles are usually iron oxide based, due in part to their relatively large magnetic moment, biocompatibility, and well-established synthetic methods that afford good reproducibility, narrow size distributions, and a high degree of control over their characteristics. Since the magnetic properties of these nanoparticles strongly depend on their structural and morphological characteristics, advances in the ability to synthesize these nanoparticles have motivated different groups to develop MNPs with novel properties and applications [11, 12].

In order to further extend the possibilities of these MNPs, researchers have tried to tune their magnetic properties by changing their shape, size, and morphology. In particular, recently, MNPs with a cavity inside making them hollow have been fabricated. From a magnetic point of view, this "hollow" morphology is especially interesting because the presence of both inner and outer surfaces contributes to increase of the total surface area of the MNPs, and this can lead to enhanced surface disorder and therefore to higher surface anisotropy and exchange bias [13–19]. Several different kinds of hollow MNPs with enhanced properties have recently been reported in the literature. Many of them are based on ferrites and magnetic oxides materials. For example, Jaffari et al. [20] have described an enhancement of the surface spin disorder in hollow $NiFe_2O_4$ nanoparticles. And Shin et al. [21] have recently synthesized 20 nm hollow manganese oxide nanoparticles with a paramagnetic behavior around room temperature.

In addition, hollow MNPs with tunable shell thickness and composition are promising building blocks for new advanced materials with lots of potential applications. In principle, hollow morphology allows encapsulating different contents inside the MNPs for various applications [1, 2, 22–24]. For example, anticancer drugs can be encapsulated inside the hollow MNPs used for drug delivery applications. The anticancer drug is camouflaged and protected inside the MNPs on its way toward the target once introduced into the body. These hollow MNPs can be guided toward the tumor area with an external magnetic field and make them release the anticancer drug in a localized and controlled way without affecting other regions of the body [22, 25, 26]. In the same way, hollow MNPs have also been proposed for other applications such as lithium-ion batteries. Hollow MNPs can store Li-ions inside, and they offer fast diffusion for Li-ions uptake/removal [27]. Likewise, the void space in hollow particles has been used to modulate refractive index, lower density, increase active area for catalysis, etc. [28]. Therefore, hollow MNPs have potential applications in a wide variety of areas, including catalysis, memristors, batteries, targeted drug delivery, and environmental treatment.

However, these pure magnetic materials can present some limitations, especially in biomedical applications, and recently other strategies have been proposed in order to create composite hollow MNPS. These have mainly focused on the use of a non-magnetic shell made of biocompatible materials, such as silica or carbon, and a magnetic phase in the interior of the shell in order to grant the composite magnetic response. For example, Son et al. [29] have synthesized silica nanotubes with a layer of magnetite (Fe_3O_4) on the inner surface for magnetic-field-assisted bioseparation, biointeraction, and drug delivery. Magnetic carbon nanocages have been introduced by Quin et al. [30] as efficient and recycled adsorbents in the removal of dye staff from textile wastewater. And Zhou et al. [31] have fabricated hollow silica nanospheres with Fe_3O_4 nanoparticles in the core. In addition, in the last years, a great progress has been made in the fabrication of multishelled hollow MNPs, with two or more shells, such as metal oxides and metal ferrites, which would provide additional tunability and improved applicability, as has been reported by Qi et al. [32], although the synthesis procedure becomes more complex.

In this book chapter, we focus on iron-oxide-based hollow MNPs, presenting a comprehensive report about their interest, properties, and applications. First, we analyze the synthesis procedures and describe the most relevant magnetic properties of these nanoparticles, including surface anisotropy, shell thickness dependence, exchange bias, etc. Then, we show how the structure and magnetism of the nanoparticles evolves as they become hollow through Kirkendall effect. The experimental findings are complemented with Monte Carlo simulations. Finally, we describe in detail some of the most relevant applications for these hollow MNPs, ending the chapter with a summary and future outlook.

6.2 Synthesis of Hollow MNPS

During the past years, there have been several reports on various physical and chemical methods to synthesize hollow nanoparticles, both magnetic and non-magnetic (CuO, C, NiO, SiO_2, CoSe, Al_2O_3, etc.) [19, 28, 33, 34]. Hollow nanoparticles can be essentially prepared by using two different fabrication methods, i.e., template-assisted method and template-free method. The template-mediated growth of hollow nanoparticles usually gives particles of microscale size and is more favorable to synthesize silicates, polymer-latex colloids, and polystyrene-magnetite hollow composites [35]. The template-free methods are more versatile to produce hollow MNPs and can be either hydrothermal or solvothermal reactions [36]. In the case of hollow MNPs, most of the fabrication methods reported follow chemical routes, such as templating approach, nanoscale etching, Ostwald ripening, or layer-by-layer growth [28, 37–43]. For example, monodisperse magnetite hollow MNPs with 400 nm average diameter and 60 nm shell thickness have been prepared through a one-pot solvothermal process based on Ostwald ripening [44].

The most facile method to produce monodisperse hollow MNPs is based on the Kirkendall effect. This method is a two-step procedure; at first, core/shell MNPs

are produced and the hollow nanostructures are obtained by oxidizing them [45]. Kirkendall effect was first reported by Kirkendall and Smigelkas in [46] and is based on the different diffusion rates of core and shell materials. This will be analyzed in more detail later in the book chapter.

It is to be noted that in these core/shell MNPs, the core is metallic while the shell is an oxidized form of the core material, being the end product a metal-oxide core/shell MNP [47]. These core/shell structures can be initially synthesized either by physical or chemical routes. For example, core/shell structured $(Ni_{33}Fe_{67})/(NiFe_2O_4)$ nanoparticles synthesized by the inert gas condensation method were used as the seeds to obtain $NiFe_2O_4$ hollow MNPs [20]. To obtain the hollow morphology, the core/shell particles were annealed above 350o52C. Later $CoFe_2O_4$ nanoparticles were obtained by following similar physical synthesis routes, that is by annealing $Co_{33}Fe_{67}/CoFe_2O_4$ (core/shell) nanoparticles [48].

In order to obtain iron-oxide-based hollow MNPs, thermal decomposition synthesis routes have been frequently employed. A typical setup for thermal decomposition is presented in Fig. 6.2a. During a thermal decomposition process, core/shell nanoparticles are synthesized by thermally decomposing organometallic compounds at high temperature in the presence of organic solvents and hydrophobic surfactants, oleic acid (OA), oleyl amine (OY), trioctyle phosphine, octanoic acid, etc. [49]. These surfactants play a very important role in stabilizing as well as in obtaining monodisperse and controlled particle size of core/shell nanoparticles that will eventually be transformed into hollow. Thermal decomposition of $Fe(CO)_5$ in the presence of organic surfactants is a common synthesis technique used to obtain to obtain iron-based core/shell MNPs [50]. The resultant core/shell MNP is usually composed of iron and iron oxide (either maghemite or magnetite) [51]. During a second step, the reaction product is heated again under flow of oxygen, aiding the Kirkendall effect and hence leading to a hollow morphology.

As an illustrative example, in Fig. 6.2b, we present the synthesis route for hollow γ-Fe_2O_3 (maghemite) nanoparticles [16]. Briefly, a three-necked flask was charged with oleylamine, 70%, and 1-octadecene, 90%, and the mixture was stirred at 140 °C under a mixture of 95% Ar + 5% H_2 gases for two hours to make sure that there was no trace of moisture or air in the flask. The temperature was raised subsequently to 220 °C where iron pentacarbonyl, Fe $(CO_2)_5$, was injected and left to reflux for 20 min. After injection, the iron pentacarbonyl immediately decomposed into iron fragments, which are the onset for nanoparticle formation (black precipitate). Acetone and/or CO gas formed in the reaction vessel (white smoke) and the reaction temperature raised a few degrees because of its exothermic nature. The injection temperature is important to have a narrow size distribution. Following reflux, the sample was cooled down to room temperature. The average particle size of the core/shell nanoparticles can be controlled by varying the injection temperature and/or amount of oleylamine. The obtained MNPs consist of a Fe core and a γ-Fe_2O_3 shell. To create hollow γ-Fe_2O_3 MNPs, the core/shell sample was annealed at 180 °C for one hour under a flow of oxygen. Both core/shell and hollow nanoparticles were washed with a mixture of 3 ml hexane, 95%, and 97 ml ethanol, $\geq$99.5%.

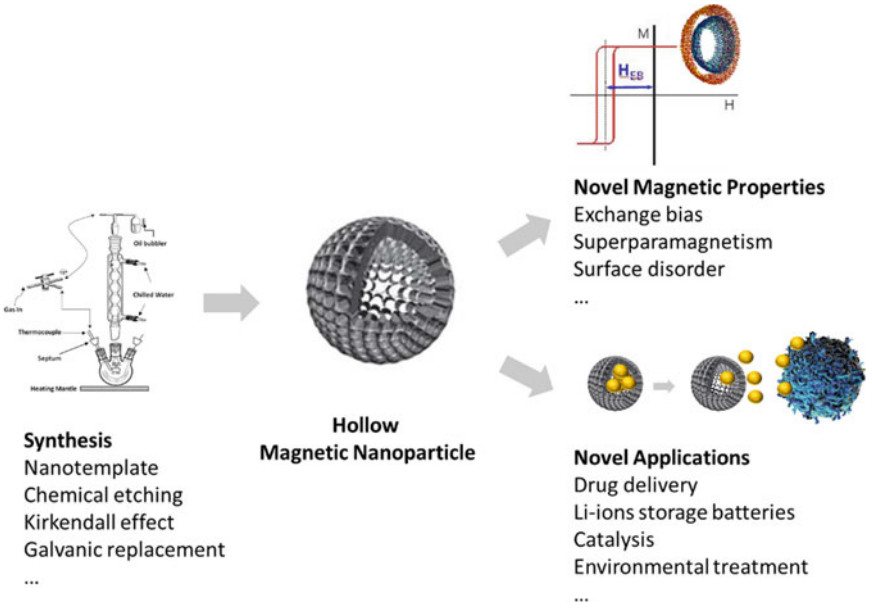

Fig. 6.1 Schematic depiction of some of the synthesis methods, magnetic properties, and applications of hollow MNPs

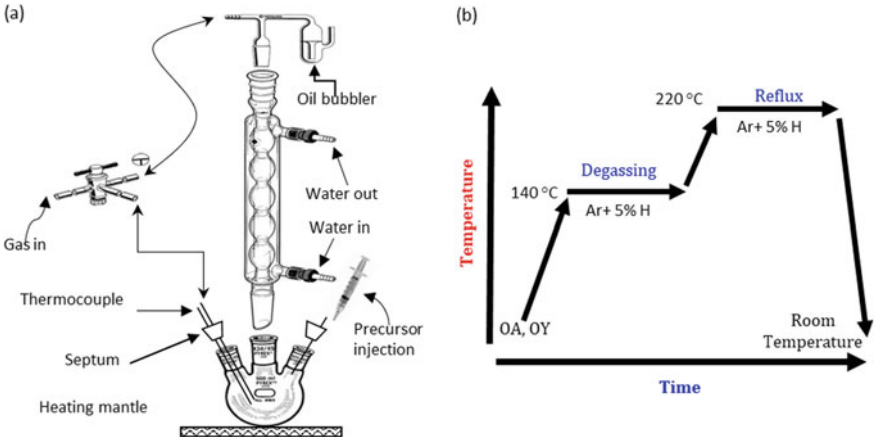

Fig. 6.2 **a** Thermal decomposition synthesis setup, and **b** schematic of the reaction route for hollow γ-Fe_2O_3 MNPs

Figure 6.3 shows the TEM and HRTEM images of the core/shell and hollow MNPs. In the case of the core/shell MNPs, both the core and shell are crystalline. The measured lattice spacing of the core corresponds to the (110) lattice planes of alpha iron and that of the shell to the (311) planes of the spinel iron oxide. The Fe core is single crystalline, however, the oxide shell is composed of small crystallites which are oriented randomly. In the case of the hollow MNPs, the shell is composed of randomly oriented grains that stick together to make a hollow shell.

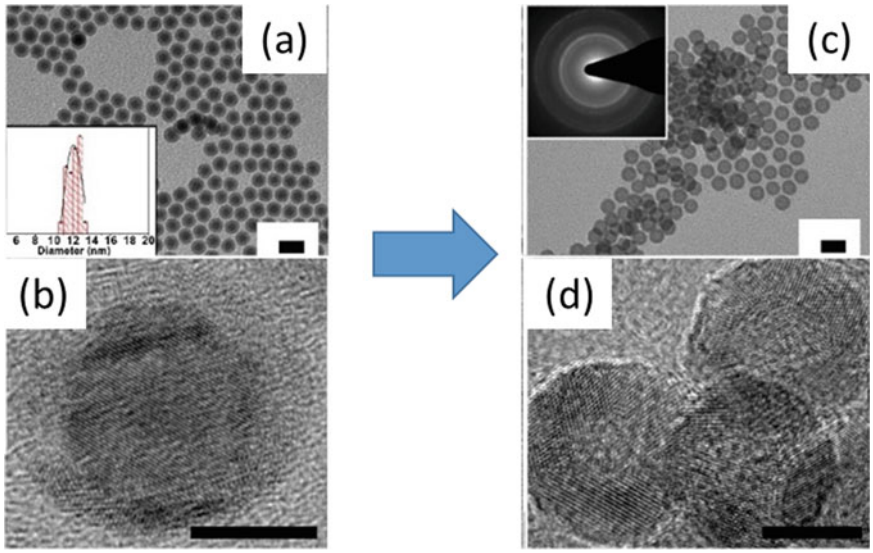

Fig. 6.3 TEM and HRTEM images of the core/shell Fe/γ-Fe_2O_3 (**a**, **b**) and hollow γ-Fe_2O_3 (**c**, **d**) MNPs; Inset (**a**) shows a histogram of the particle size distribution and inset (**c**) shows SAD pattern of hollow nanoparticles. The scale bar is 20 nm in Fig. (**a**, **c**) and is 5 nm in Fig. (**b**, **d**)

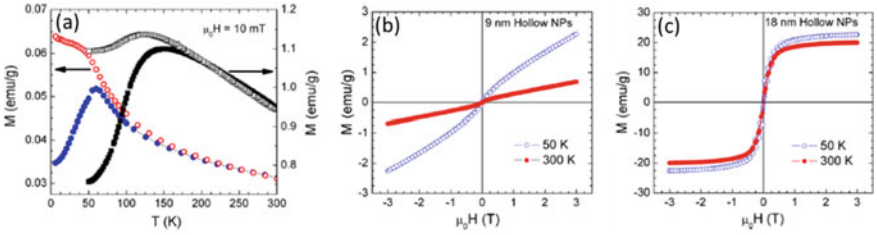

Fig. 6.4 **a** ZFC (solid symbols) and FC (open symbols) magnetization versus temperature curves for 9 nm (spheres) and 18 nm (squares) hollow γ-Fe_2O_3 MNPs. M–H loops taken at 300 and 50 K for the 9 nm (**b**) and 18 nm (**c**) hollow γ-Fe_2O_3 MNPs. Reprinted from [15], with the permission of AIP Publishing

6.3 Magnetic Properties of Hollow MNPs

Hollow MNPs exhibit interesting magnetic properties, which are rather different from those of their solid counterparts. In general, the nanoparticles' magnetic response is based on the combination of surface effect, finite-size effect, inter and intra-particles interactions, etc. In the case of hollow MNPs, increase in the surface area due to the appearance of the inner surface can give rise to distinct magnetic properties, including reduced magnetization, spin canting, and a strong increase in effective anisotropy and exchange bias [15, 20]. Therefore, hollow MNPs provide an excellent model to study these effects.

6.3.1 Basic Magnetic Behavior

The magnetic response of the hollow MNPs as a function of the temperature and the applied magnetic field presents several clear differences in comparison with their solid counterparts.

In the zero-field-cooled/field-cooled ZFC/FC curves obtained from measuring the magnetization as a function of temperature (Fig. 6.4a), hollow iron oxide MNPs normally present a maximum at low temperatures, corresponding to the magnetic blocking of the hollow MNPs, followed by a continuous decrease of the magnetization with increasing temperature. For sizes size below 10 nm, the blocking usually takes place at very low temperatures <50 K. As the size of these MNPs increases, so it does their blocking temperature. This value of the blocking temperature tends to be appreciably smaller than the one corresponding to solid MNPs of equivalent volume. This indicates that the blocking process in hollow MNPs is more related to the individual blocking of the nanograins that compose the hollow shell, than to the overall blocking of the whole nanoparticle, as it is usually the case for solid MNPs. However, even for the smallest hollow MNPs, the blocking temperature obtained tends to be larger than the one that would correspond to the isolated nanograins. This can be related to the presence of magnetic interactions among these nanograins and/or an enhanced value of the anisotropy energy due to the spins surface disorder. On the other hand, for the hollow nanoparticles, some separation between the ZFC and FC magnetization branches can also be typically observed. The irreversibility between the ZFC and FC curves can persist even at 300 K, far above the blocking temperature, and it can be attributed to increased anisotropy in the system and the effects of inter-particle and intra-particle interactions.

Concerning the magnetic hysteresis, M–H, loops (see Fig. 6.4b, c), at very low temperatures (~5 K), hollow MNPs usually present an elongated shape with a pronounced increase of the coercivity, decrease of the remanence, and a high field slope in comparison with solid ones. The M–H loop for the hollow MNPs, especially at low temperatures, resembles those of frustrated and disordered random anisotropy magnets. This is related to the high magnetic frustration present in the spins of these

hollow MNPs. As the size of the nanoparticles decreases, the slope of the M–H curves tends to increase indicating that the proportion of disordered surface spins increases with decreasing size of the hollow MNPs. As the temperature increases, the M–H loops resemble more and more those of magnetic nanoparticles with superparamagnetic + paramagnetic behavior. The superparamagnetic behavior is related to the core spins of the nanograins in the shell, while the paramagnetic behavior can be related to the surface spins of these nanograins. Their relative contribution can vary depending upon the size and number of nanograins (size and shell thickness).

6.3.2 Surface Anisotropy and Spin Disorder

Since both inner and outer surfaces of a hollow nanoparticle contribute to enhance its total surface area and hence surface anisotropy K_s, this contributes to increase the effective anisotropy (K_{eff}) of the whole system via: $K_{eff} = K_c + 6K_s/D$, where K_c is the anisotropy associated with the core spins and D is the mean diameter of the nanoparticle. The effective anisotropy of these MNPs can be estimated from the blocking temperature, using the standard formula $K_{eff}V = 25k_BT_B$, where T_B corresponds with blocking temperature and V with the volume of the nanograins in the shell. For hollow γ-Fe_2O_3 MNPs, effective anisotropies around ~10^{6-7} erg/cm^3 have been reported [13, 15, 20, 52, 53], which can be up to two orders of magnitude higher than those corresponding to solid maghemite nanoparticles (~10^5 erg/cm^3). Other estimations of the effective anisotropy, for example by means of AC susceptibility measurements, tend to yield similar values. This increase of the effective anisotropy can be attributed to the enhanced contribution from both surface and finite-size effects in hollow MNPs. The spins lying at the surface and interface of the magnetic nanograins can give rise to a great enhancement of the surface anisotropy.

To quantify the surface spins contribution toward magnetic properties, we can analyze the magnetization vs magnetic field, M–H, loops. In an ensemble of MNPs, the uncompensated surface spins are well known to provide a linear contribution (paramagnetic) to the magnetization. To extract paramagnetic contribution to the magnetization, the experimental M–H data can be fitted to the Langevin function with an added linear term (6.1)

$$M(H) = M_S^{MSP}[\coth\left(\frac{\mu H}{KT}\right) - \left(\frac{KT}{\mu H}\right)] + \chi^{PM}H \tag{6.1}$$

where $M_S{}^{SPM}$ is the saturation magnetization of the SPM part (corresponding to the "core" spins inside the shell), μ is the average magnetic moment of SPM particles, and χ^{PM} is the susceptibility of the paramagnetic contribution (corresponding to the "surface" spins at the shell) that is linear with the magnetic field H.

As an example, in Fig. 6.5 we present the M–H loops and corresponding fittings to (6.1) for 9 and 18 nm hollow γ-Fe_2O_3 MNPs. As depicted, for 9 nm hollow MNP

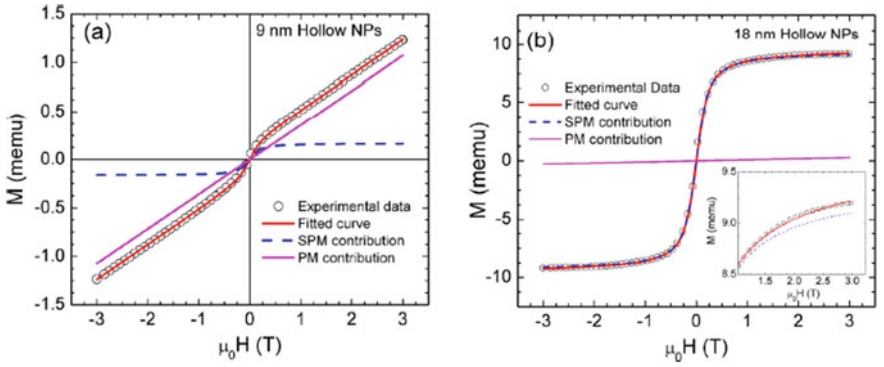

Fig. 6.5 Magnetic hysteresis, M–H, loops taken at 300 K for **a** 9.2 nm and **b** 18.7 nm hollow γ-Fe_2O_3 MNPs. The curves are fitted (red) to (6.1); the blue and magenta curves represent the simulated SPM and PM contributions, respectively. Reprinted from [15], with the permission of AIP Publishing

of iron oxide, the SPM susceptibility contributes to only 13% of the total magnetic moment, while the rest of it (87%) comes from the surface spins (paramagnetic susceptibility). Interestingly, by increasing the nanoparticles size up to 18 nm, the SPM susceptibility contribution increased to 97% while only 3% contribution comes from the PM susceptibility. Such a larger PM contribution in the smaller hollow MNPs suggests a larger number of disordered surface spins present.

It is important to mention that in 9 nm hollow γ-Fe_2O_3 MNPs, the shell thickness is usually around 2 nm only [13], and it increases to 4.5 nm thickness for 18 nm hollow γ-Fe_2O_3 MNPs. Therefore, the surface spin contribution is strongly related to the shell thickness. Bigger thickness will accommodate more and bigger nanocrystals in the shell, and this will reduce the number of surface spins present and therefore the surface contribution to the magnetism of the MNPs.

6.3.3 Exchange Bias Versus Minor Loops

Owing to broken exchange bonds and lower crystal symmetry, the highly disordered surface spin layers in hollow MNPs can enter a spin-glass-like state at a low temperature. Due to their very high surface anisotropy and large number of frustrated spins, hollow MNPs are very interesting candidates to investigate spin-glass and the exchange bias phenomenon. The field-cooled M–H loops show unusually large horizontal and vertical shifts in hollow MNPs below 10 nm [13, 15] that keep increasing with cooling field, giving rise to large exchange bias, EB, values.

In the case of solid MNPs, it has been reported that EB can be related to the exchange coupling between the shell of disordered spins and the core of ordered spins [54]. In the case of hollow MNPs, EB studies were carried out on 9 and 18 nm

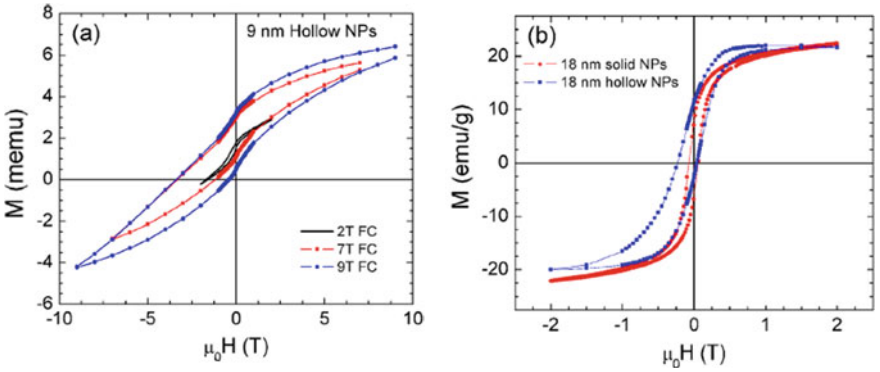

Fig. 6.6 Field-cooled M–H loops taken at 5 K for **a** 9.2 nm and **b** 18.7 nm hollow γ-Fe_2O_3 MNPs. Reprinted from [15], with the permission of AIP Publishing

hollow γ-Fe_2O_3 MNPs. The samples were cooled down from room temperature down to 5 K in high magnetic fields and the M–H loops were recorded afterward. Unusually large horizontal and vertical shifts were observed in both cases, as depicted in Fig. 6.6. In addition, it can be seen that for the 9 nm sample, the M–H loops are not closed when the maximum field is applied, as if the applied field is lower than the irreversibility field of the samples. Considering this, it is not correct to refer to the observed loop shifts as EB effects, and rather we should consider them as minor loop effects, since we are not saturating the magnetization of the sample in our recorded M–H loops. This huge magnetic irreversibility can be attributed to the large portion of disordered spins locating at the innermost or outermost surfaces of the shell and at the interfaces between the nanograins. It is very interesting to note that unlike the case of the 9 nm hollow MNPs, the loop shift observed for the 18 nm hollow MNPs represents an intrinsic EB effect. These results clearly point to the important role of inner and outer surface spins in enhancing the observed EB effect in the hollow MNPs.

When exchange bias studies were performed in 18 nm solid iron-oxide MNPs (see Fig. 6.6b), they showed much lower EB field. Such a difference in EB in solid versus hollow nanoparticles points to the important role of inner surface spins in enhancing the EB effect. Moreover, in case of smaller hollow nanoparticles (below 10 nm), the tremendous increase in surface-to-volume ratio directly impacts the spin disorder, and hence, a minor hysteresis loop is obtained under field-cooled conditions.

6.4 Evolution from Core–Shell to Core–Void–Shell to Hollow

Core/shell MNPs are composed of a core and shell with different magnetic phases such as ferromagnet–antiferromagnet (FM–AFM), ferromagnet/spin glass, ferrimagnet/ferrimagnet, etc. [11, 12, 55–57]. This kind of nanocomposite systems presents great potential for a wide range of applications: for example, Fe–Fe oxide core/shell MNPs have been studied for biomedical applications motivated by the increase in magnetization due to the Fe core, while keeping the intrinsic biocompatibility of the Fe oxide due to the shell [53, 58]. In addition, core/shell MNPs can exhibit exchange bias (EB), which is a byproduct of the coupling of the core–shell interface and gives rise to a horizontal shift in the hysteresis loop after cooling in a magnetic field [59, 60]. This phenomenon has attracted great interest in the recent years since it has been proposed as a promising approach to overcome the superparamagnetic limit in MNPs, a critical bottleneck for magnetic data storage applications [12].

One of the most commonly employed methods to obtain hollow MNPs is via the nanoscale Kirkendall effect. As was mentioned before, this effect can be employed to transform core/shell MNPs to hollow. A depiction of how a core/shell nanoparticle transforms into the core/void/shell and then hollow morphology is presented in Fig. 6.7, and a more detailed description can be found in Ong et al. [61] and Jaffari et al. [20]. Essentially, the process is based on the different diffusion rates of core and shell materials. During the Kirkendall effect, the migration of ions from the core to the shell and vice versa produces vacancies at the interface. The supersaturation of these vacancies causes void formation, and these voids eventually condense together to form a hole at the center of the particle. This way a core/void/shell nanoparticle is obtained. Eventually, the core completely shrinks and disappears, giving rise to a hollow shell MNP.

As a result of this process, the morphology of the MNPs changes drastically, and these morphological changes are going to significantly influence their static and dynamic magnetic properties. As the MNPs become hollow, the core becomes progressively smaller while the shell thickness increases, thereby increasing the average particle diameter. To this respect, we cannot think of the shell as a single crystalline and uniform entity, like the core, but as a composition of small crystallites

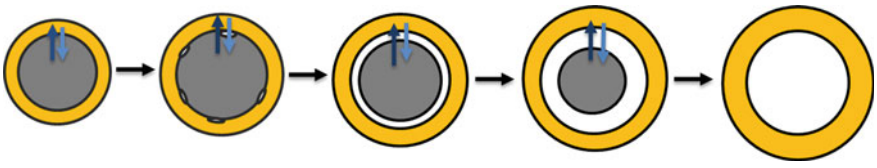

Fig. 6.7 Depiction of the evolution of the MNPs from core/shell to core/void/shell and to hollow morphology, as a result of the Kirkendall effect

or nanograins, as has been described in the literature [13, 16, 61]. These nanograins tend to dominate the magnetic behavior of the hollow nanoparticles.

In order to better understand this, we can focus on the particular case of the evolution from core/shell to hollow of Fe/γ-Fe_2O_3 MNPs [16]. In this work, we analyzed the "hollowing" process of two core/shell nanoparticles, with different sizes, around 8 and 12 nm, respectively. For the smaller core/shell MNPs, the Fe core occupies ~6% of the total volume of the MNP, while for the bigger ones, it occupies ~23%. Therefore, the influence of the magnetic core is more relevant in the case of the bigger MNPs. For the 12 nm core/shell MNPs, the obtained overall magnetic behavior is similar to an ensemble of interacting MNPs with a collective freezing into a super spin glass state at low temperatures [16]. As the morphology changes into core/void/shell and then hollow, dipolar interactions between the MNPs decrease, the magnetic moment per nanoparticle greatly decreases, and the effective anisotropy increases due to the growing number of surface disordered spins. This leads to a frustrated cluster glass-like behavior at low temperatures. However, for the smaller sizes (8 nm), both the core/shell and the hollow MNPs exhibit a very similar spin glass like magnetic behavior mediated by the grains in the shell, independently of the morphology of the MNPs.

Even more interesting is the evolution of the EB effect in these MNPs. For the bigger 12 nm MNPs, EB greatly increases as the particle becomes hollow, going from 1500 Oe for the core/shell MNP to a maximum value of 7000 Oe for the hollow ones. This great increase in the EB value can be related to the increase in the shell thickness when the MNPs become hollow (see Fig. 6.8). The shell can be understood as composed of two kind of spins, those occupying the interior of the shell (magnetically reversible) and those placed on the (inner and outer) exterior surfaces of the shell (magnetically irreversible) [13]. In the case of the 12 nm core/shell MNPs, the EB arises mainly due to the interaction between the disordered spins in the shell and the ordered spins in the core (1 interface, as depicted in Fig. 6.8a). However, as the MNPs become hollow and the shell thickness increases, two new interfaces are formed, between the ordered atoms in the interior of the shell and the disordered atoms on the exterior surfaces (Fig. 6.8b). This can give rise to an enhanced EB effect in comparison with the core/shell MNPs [52, 16]. This EB enhancement requires of a minimum shell thickness in order to be appreciable: in the case of the 8 nm core/shell and hollow MNPs, the shell is thinner and the volume occupied by the interior spins is significantly reduced, leading to the disappearance of the increase in the EB effect with changing morphology.

Therefore, analyzing the change of the morphology and magnetic behavior of these MNPs as they evolve from core/shell to core/void/shell and finally to hollow can provide a deeper insight into the surface and finite-size effects in magnetic nanoparticle systems, with special relevance to the EB effect. The combination of MNP diameter and shell thickness plays a crucial role in determining the final magnetic behavior of these MNPs, and by carefully tuning these two parameters, the magnetic response can be manipulated according to the desired application.

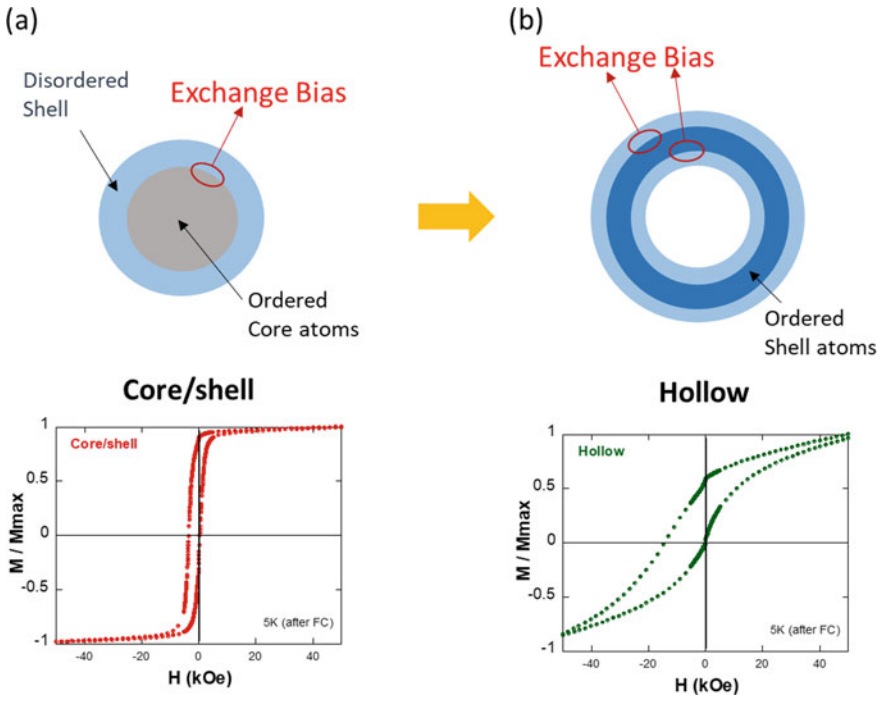

Fig. 6.8 Depiction of the evolution of the interfaces playing a role in the exchange coupling of the core/shell and hollow MNPs, which gives rises to the horizontally shifted (EB) hysteresis loops after field-cooling down to low temperatures

6.5 Monte Carlo Simulations

In order to understand the peculiarities of the magnetic behavior of hollow magnetic structures from a theoretical point of view, one has to revert to a simulation approach that is able to take into account not only the characteristics of their geometry, but also the peculiarities of their specific composition and interactions among the spins at the atomistic level. Although micromagnetic calculations in the continuum approximation [33] have been conducted to study the possible equilibrium magnetic order of ferromagnetic hollow MNPs, they can only give a first approximation to the real situation since they are neither suitable for antiferromagnets such as magnetic oxides, nor can they take into account the disorder at the inner and outer surfaces. For this purpose, simulations at the atomistic level are required, describing the magnetic ions by Heisenberg spins placed at the nodes of real magnetic oxide structures like the one for maghemite that has spins in two sublattices characterized by tetrahedral and octahedral coordination and different values and signs of the exchange interactions. Moreover, we have seen experimentally that MNPs might not be homogeneous from the structural point of view, so an atomistic approach can easily model variations

in local anisotropy directions or values of microscopic parameters characterizing a particular material.

Therefore, a minimal classical Hamiltonian representing the NP at the atomistic level comprises the following terms [13, 62]:

$$H/k_{\mathrm{B}} = -\sum_{<i,j>} J_{ij}\left(\vec{S}_i \cdot \vec{S}_j\right) - \sum_i \vec{h} \cdot \vec{S}_i + E_{\mathrm{anis}} \tag{6.2}$$

where the J_{ij} stand for the exchange constants, $\vec{h}$ is the magnetic field in reduced units, and the last term accounts for the magnetocrystalline anisotropy:

$$E_{\mathrm{anis}} = k_S \sum_{i\in S}\sum_{j\in nn}\left(\vec{S}_i \cdot \hat{r}_{ij}\right)^2 - k_C \sum_{i\in C}\left(\vec{S}_i \cdot \hat{n}_i\right)^2 \tag{6.3}$$

Here, the first term is for surface spins (both at the inner and outer regions of the MNP) having Neél anisotropy and the second one is for core spins with uniaxial anisotropy along direction $\hat{n}_i$. In order to better reproduce the real morphology of the hollow MNP, we have divided the shell in equal volume crystallites each having uniaxial anisotropy directions $\hat{n}_i$ at random. Using this model, low temperature hysteresis loops for maghemite hollow nanoparticles with sizes in the range of those found experimentally have been simulated.

Simulations of an annealing process from a high temperature disordered phase show that the equilibrium configurations at zero field for particles with uniform crystallographic composition can be tuned from quasi-uniform to throttled and hedgehog-like with increasing k_{S} [17, 63]. However, when including the crystallites, the configurations have most of the surface spins in a quasi-disordered state induced by the competition between the surface anisotropy and antiferromagnetic exchange interactions. In contrast, core spins still tend to order ferrimagnetically along the local easy axes of each crystallite, showing that the overall magnetic behavior is dominated by the crystallographic anisotropy of the individual crystal domains forming the shell [13].

Simulations have also been proved useful in simulating the dynamic behavior of hollow nanoparticles. By simulating hysteresis loops after cooling in the presence of different applied fields, it has been shown that the experimentally observed loop shifts along the negative field axis can be erroneously ascribed to exchange bias effects when the applied field is not enough to saturate even the core spins [13]. Moreover, simulation of loops using different number of Monte Carlo steps to average magnetization at each point in the loop have been useful in mimicking the training effects usually observed in hollow MNPs assemblies. The simulations show that coercive fields and remanence present a dynamic evolution that can be associated to the spin-glass-like state observed experimentally that evolves at long times into more stabilized state where surface spins attain a frozen configuration [52, 64].

The distinct magnetic behavior between solid and hollow MNPs is reflected notably in the change in magnetization reversal process as exemplified in Fig. 6.9a, where simulated loops for solid and hollow maghemite nanoparticles with the same size are compared. The loop for the hollow MNPs show increased coercivity, decreased remanence, and remain open to larger fields with no saturation. Results for decreasing values of the shell thickness indicate a progressive change in the magnetic response of the particles: as the shell thickness is decreased to the experimental value, the increasing number of surface spins of the crystallites, together with their random anisotropy directions, is responsible for the magnetic behavior of the nanoshells.

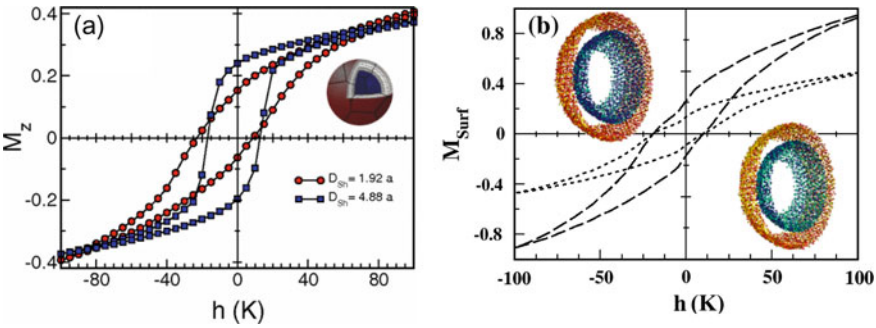

Fig. 6.9 **a** Simulated hysteresis loops for maghemite MNPs with surface anisotropy $k_S = 30$ K, $k_C = 0.01$ K and outer diameter of 8.1 nm ($a = 0.83$ nm). Blue squares are for a solid particle, and red circles correspond to a hollow MNP with 1.6 nm thick shell (inset presents a sketch of the crystallites forming the shell). **b** Contributions of the spins at the inner (long dashed lines) and outer (short dashed lines) surfaces of a hollow particle with diameter 12.5 nm and shell thickness 3.25 nm to the total hysteresis loop with. Insets show snapshots of the magnetic configuration of a slice of the inner and outer surfaces taken close to the maximum applied field (upper inset) and near the remanent state on the descending field branch (lower inset)

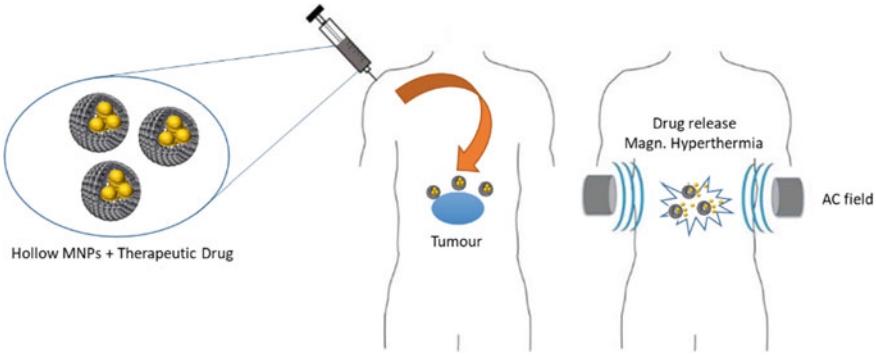

Fig. 6.10 Hollow magnetic nanoparticles loaded with anticancer drug can be injected into the body, targeting only the tumor area, and releasing therapeutic doses of heat and anticancer drug when activated by an external AC magnetic field

Another salient feature that can be elucidated from the simulations is the distinct behavior of the inner and outer surfaces along the hysteresis loop. By looking only at the global shape of the hysteresis loops of surface spins, it might be concluded that surface spins behave similarly in solid and hollow MNPs since the coercive field and loop shifts for the surface contribution are almost identical for both morphologies. However, the core contributions are different and, therefore, the difference in magnetic behavior between both morphologies have to ascribed to the additional inner surface spins in the hollow nanoparticles. In fact, by computing separately the contribution of the spins at the core and at the inner and outer surfaces to the total magnetization this can be corroborated. The results presented in Fig. 6.9b show that inner surface spins are more easily magnetized than spins at the outer surface, and that their associated hysteresis loops present a reduced vertical shift. The reversal behavior of the interior spins is clearly influenced by the existence of additional surface spins at the inner surface of the hollow nanoparticle. A further confirmation can be obtained by detailed inspection of snapshots taken (see insets in Fig. 6.9b for two representative examples) at different points of the hysteresis loop. These provide a clear indication that the change in dynamic properties of spins at the inner and outer surfaces is a consequence of the different range of effective energy barriers governing their relaxation.

6.6 Applications

Hollow MNPs, in general, present a lot of promising applications in a wide variety of areas including biomedicine, data storage, capacitors, etc. [22, 27, 65].

On the field of biomedicine, one of the most promising applications of hollow MNPs is in targeted drug delivery. This is a method of delivering medication to a patient based on the use of MNPs that can be externally guided (i.e., through magnetic fields), so that they release the therapeutic drug only into the affected area that needs to be treated, maximizing this way the efficiency of the medication and minimizing collateral damage [66] (see Fig. 6.10). Conventionally, the drug is attached onto the surface of the MNPs and released by an external stimuli (e.g., pH change, heat, etc.) once in the target area. For an efficient MNPs mediated drug delivery, several factors need to be optimized, including the magnetic response of the MNPs against an external magnetic field (which is proportional to their saturation magnetization), the drug loading capacity of the MNPs (which depends on their surface area), the drug release capacity and rate, etc. To this respect, hollow MNPs present a series of advantages compared to conventional solid MNPs for drug release treatment. On the one hand, the surface area available to attach drugs on hollow MNPs is much higher than in the case of solid MNPs, because of the existence of both the inner and outer surfaces, increasing their loading capacity. Since the drug can be encapsulated inside the hollow MNP instead of being attached to the surface, the drug is effectively “camouflaged” and protected on its way to the target [26]. All these results have led to several groups investigating different types of hollow

MNPs for drug delivery [2, 21, 22, 29, 67]. For example, Xing et al. have shown that human serum albumin (HSA)-coated iron oxide hollow MNPs can encapsulate more anticancer drug (doxorubicin, DOX) than solid MNPs, being more effectively uptaken by drug resistant cells than the free DOX, and consequently, becoming more effective in killing the cancer cells [26]. In addition, hollow MNPs can exhibit additional capacities in biomedicine, such as contrast agents for magnetic resonance imaging or heating agents for hyperthermia treatment of cancer [22]. For example, recently Li et al. [25] showed that hollow ferrite nanoparticles exhibited good heating capacities under the actuation of an alternating magnetic field and therefore could be used for both infrared and thermal imaging. These hollow ferrite nanoparticles also can provide temperature activated drug release and hyperthermia, demonstrating great potential for in vivo cancer therapy. Despite the growing interest of hollow MNPs in biomedical application, there are relatively few in vitro and in vivo studies. In addition, the hollowing process can create great strain and fragmentation of the shell that eventually can lead to a deterioration of their properties [68]. Therefore, further research in this area is still needed.

Another field of interest for the application of these hollow MNPs is water remediation and treatment. Unfortunately, there is a rising amount of water pollution and waste. This has led the scientific community to develop materials that can adsorb and remove organic and inorganic contaminants from water. In particular, in the last years, nanomaterials have been investigated for this task [69]. Magnetic nanoparticles, displaying large surface area and functionalized with an appropriate coating, can bind to specific pollutants in water, and thanks to their magnetic properties, they can be easily separated from water, removing this way the contaminants [70, 71]. In particular, iron-oxide-based MNPs have been investigated for the removal of heavy metals (Cr, Pb, Co, As …) from water, but there have been only a few reports on the use of hollow MNPs in this area. The large effective specific surface area of hollow MNPs, double if we compare them with conventional solid MNPs, is of strong interest for increasing the adsorption capacity of these nanomaterials. In particular, Balcells et al. have developed very stable iron oxide hollow nanocuboids that exhibit high efficiency in the absorption of both As(III) and As(V) (326 and 192 mg/g) [72]. As an alternative, some studies have focused on the combination of carbon-based and iron-oxide-based nanomaterials in order to develop magnetic "nanocages" with high surface area, capable of binding heavy metals on both carbon and iron oxide surfaces [73]. Along these lines, hollow MNPs can also be used for other tasks that require capture and removal of specific elements, such as bioseparation [29].

Another interesting application of hollow MNPs is related to Li-ion batteries. Batteries are considered essential to maximize the efficiency in energy use. In battery applications, ideal electrodes should be cheap, have high capacity and rate performances, and last long. For these reasons, iron-oxide-based nanomaterials have become attractive candidates as electrodes in Li-ion-based batteries [74, 75]. In particular, hollow iron oxide MNPs have great potential for these applications. The larger surface area of these hollow MNPs enables an increased electrode–electrolyte contact area as well as more Li-ion storage sites, the hollow morphology allows faster diffusion for Li-ions uptake/removal as compared to solid MNPs; and

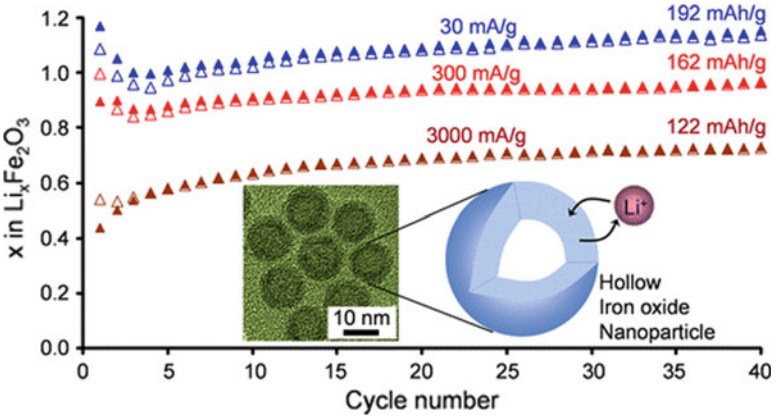

Fig. 6.11 Hollow iron oxide nanoparticles present high capacity, superior rate performance, and excellent stability for Li-ion-based batteries. Reprinted with permission from [27]. Copyright (2018) American Chemical Society

in addition, they can better tolerate the strain associated with the electrochemical cycling. Recent studies by Koo et al. [27] have shown that hollow maghemite MNPs contain a high concentration of cation vacancies that can be efficiently utilized for reversible Li-ion intercalation without structural change. Cycling in high voltage resulted in high capacity (~132 mAh/g at 2.5 V), 99.7% Coulombic efficiency, enhanced rate performance (133 mAh/g at 3000 mA/g), and excellent stability (see Fig. 6.11). Other studies with multishelled hollow MNPs also showed that the performance of these materials as electrode materials can be further improved by controlling their morphology [32]. These results indicate that further optimization of size, morphology, and composition of hollow MNPs can potentially lead to further improvement in their electrochemical performance.

Catalysis is a key factor both in chemical research and chemical industry. In the last decades, the use of nanoparticles as catalytic materials to speed up and favor chemical reactions has been heavily investigated. In the same way as in previous applications, this has led to the consideration of hollow MNPs as possible candidates for catalysis. Hollow MNPs present a series of potential advantages, such as their capacity to effectively isolate catalytic species, the increased surface area available for the catalytic reactions, and the possibility of separating and recovering them through magnetic fields [76]. For example, Zn doped Fe_3O_4 hollow nanospheres have exhibited enhanced catalytic performance on the degradation of rhodamine B (RhB) and cephalexin under visible-light irradiation, thanks to their hollow nanostructure and Zn doping (Sang Nguyen et al.). In addition, these nanospheres also present high stability and can be easily separated and recycled by an external magnetic field. In addition, other strategies to create hollow magnetic nanostructures for catalysis have also been studied, such as hollow carbon nanospheres with entrapped Fe_3O_4 MNPs which have also shown high catalytic activity and reusability [77].

The high surface area of these hollow MNPs is also advantageous for chemical and gas sensing. Sensors are widely used in industrial process control and safety applications. In the case of hollow MNPs, the enhanced porosity and the cavity of these MNPs seems to facilitate the diffusion of analytes into the MNPs leading to an increase in their sensitivity. In most of the cases, the sensing with these materials is carried out through measurements of change of resistivity produced by adsorption–desorption of a targeted analyte on the surface of the MNPs. For example, Wu et al. have reported that hematite composite hollow nanostructures exhibited high gas sensitivity toward formaldehyde and ethanol at room temperature, improving the results obtained with solid hematite MNPs [65].

One of the major potential applications of MNPs is in the field of data storage (hard drives, DVDs, etc.). The underlying idea is to replace the large randomly oriented magnetic grains employed in conventional media by single MNPs, in order to exponentially increase the data storage density. The smaller the MNPs, the higher the density. To attain this, the magnetic moment of the MNPs has to be very stable with time. To this regard, FePt MNPs have been proposed as ideal candidates due to their high anisotropy and stability [78]. However, as the MNPs become smaller, the thermal disorder tends to overcome the anisotropy of the MNPs and their magnetic moments are no longer stable. This is the so-called "superparamagnetic limit" and, in principle, imposes restrictions on our capacity to increase the data storage density. However, in the last few years, a way to overcome this limit has been proposed, based on the use of "exchange bias" (EB) [12]. The EB effect generates an additional effective anisotropy that allows reducing the size of the MNPs below the "superparamagnetic limit," and still obtaining a stable magnetization. As we explained before, hollow MNPs exhibit enhanced EB effect, making them promising candidates for data storage and similar applications [56]. Despite the promising results obtained in hollow MNPs, for now, the EB effect is mainly appreciable at very low temperatures (<50 k), and therefore, further work is needed to develop hollow magnetic nanostructures with appreciable EB at temperatures closer to ambient.

These are only a few examples of applications of hollow MNPs, but they already provide an overall idea of the wide use of these MNPs, and their potential applicability in other promising research areas such as spintronics or magneto-optical devices.

6.7 Summary and Future Outlook

In this book chapter, we have reviewed the main characteristics of hollow magnetic nanostructures in general, and iron-oxide-based hollow MNPs in particular. We have shown that the hollow morphology is particularly interesting because the presence of the additional surface area in these nanostructures gives rise to enhanced magnetic phenomena toward improved applications.

We have shown that hollow MNPs can be synthesized using either physical or chemical methods, but in the case of iron oxide ones, thermal decomposition and similar chemical synthesis routes are often employed. These synthesis methods let

us finely tune the morphology of hollow MNPs by controlling different reaction parameters, such as annealing temperature and/or surfactant concentration. We have also described in detail how iron-oxide-based hollow MNPs can be obtained from the evolution of an original core/shell nanoparticle, first into a core/void/shell, and then into a hollow morphology (i.e., Kirkendall effect). The shell in these hollow MNPs is typically composed of small randomly oriented nanograins that play a crucial role in the magnetic response of these nanoparticles. The static and dynamic magnetic properties of hollow MNPs are radically different from those observed in their solid counterparts. The high number of surface spins present, together with the nanogranular nature of the shell, gives rise to high magnetic frustration and spin glass like behaviors. As a result, surface anisotropy is greatly enhanced, leading often to the appearance of a prominent exchange bias effect. In particular, we have described how this EB phenomenon depends on the thickness of the shell, by carefully analyzing the evolution of EB as a function of the morphology, from core/shell to hollow. We have shown that a minimum shell thickness is crucial in enabling the presence of additional interfaces (i.e., reversible and irreversible spins) that enhances the EB effect. These experimental studies have been complemented with Monte Carlo simulations. Atomistic simulations confirm the presence of strongly disordered surface layers in the hollow particle morphology, with complex energy landscapes that underlie both glass-like dynamics and magnetic irreversibility. Finally, potential applications of the hollow MNPs have been reviewed, especially in the fields of biomedicine, catalysis, batteries, sensing, and data storage.

With the continuous improvement in synthesis techniques and the development of novel and facile synthesis routes, it is anticipated that we will attain a better control over the morphology and other characteristics of hollow MNPs. This will allow us to overcome several of the main limitations currently associated with these systems, such as reduced magnetic response, non-uniform hollow structure, instability of the hollow morphology, limited encapsulation/release efficiency, and reduced EB effect at room temperature. We foresee that the progressive work on this field will eventually lead toward multifunctional hollow MNPs with enhanced properties and novel applications.

References

1. K. Cheng, S. Peng, C. Xu, S. Sun, J. Am. Chem. Soc. **131**, 10637 (2009)
2. K. Cheng, N.A. Frey, S. Sun, S. Peng, K. Cheng, S. Sun, Chem. Soc. Rev. **38**, 2532 (2009)
3. G.A.O. Jinhao, G.U. Hongwei, X.U. Bing, Acc. Chem. Res. **42**, 1097 (2009)
4. A.H. Lu, E.L. Salabas, F. Schüth, Angew. Chemie. Int. Ed. **46**, 1222 (2007)
5. D. Weller, A. Moser, IEEE Trans. Magn. **35**, 4423 (1999)
6. R.D. Desautels, E. Skoropata, Y.-Y. Chen, H. Ouyang, J.W. Freeland, J. van Lierop, Appl. Phys. Lett. **99**, 262501 (2011)
7. M. Knobel, W.C. Nunes, L.M. Socolovsky, E. De Biasi, J.M. Vargas, J.C. Denardin, (n.d.)
8. B.D. Terris, T. Thomson, J. Phys. D. Appl. Phys. **38**, R199 (2005)
9. T. Neuberger, B. Schöpf, H. Hofmann, M. Hofmann, B. Von Rechenberg, in J. Magn. Magn. Mater. (2005), pp. 483–496

10. Q.A. Pankhurst, J. Connolly, S.K. Jones, J. Dobson, J. Phys. D. Appl. Phys. **36**, R167 (2003)
11. H. Khurshid, W. Li, S. Chandra, M.-H. Phan, G.C. Hadjipanayis, P. Mukherjee, H. Srikanth, Nanoscale **5**, 7942 (2013)
12. V. Skumryev, S. Stoyanov, Y. Zhang, G. Hadjipanayis, D. Givord, J. Nogués, Nature **423**, 850 (2003)
13. A. Cabot, A.P. Alivisatos, V.F. Puntes, L. Balcells, Ò. Iglesias, A. Labarta, Phys. Rev. B **79**, 094419 (2009)
14. S. Chandra, A. Biswas, H. Khurshid, W. Li, G.C. Hadjipanayis, H. Srikanth, J. Phys. Condens. Matter **25**, 426003 (2013)
15. H. Khurshid, W. Li, M.-H. Phan, P. Mukherjee, G.C. Hadjipanayis, H. Srikanth, Appl. Phys. Lett. **101**, 022403 (2012)
16. Z. Nemati, H. Khurshid, J. Alonso, M.H. Phan, P. Mukherjee, H. Srikanth, Nanotechnology **26**, 405705 (2015)
17. F. Sayed, Y. Labaye, R. Sayed Hassan, F. El Haj Hassan, N. Yaacoub, J.-M. Greneche, J. Nanoparticle Res. **18**, 279 (2016)
18. S. Yan, J. Tang, P. Liu, Q. Gao, G. Hong, L. Zhen, J. Appl. Phys. **109**, 07B535 (2011)
19. L. Yu, X.Y. Yu, X.W. (David) Lou, Adv. Mater. (2018)
20. G.H. Jaffari, A. Ceylan, C. Ni, S.I. Shah, J. Appl. Phys. **107**, 013910 (2010)
21. J. Shin, R.M.M. Anisur, M.K.K. Ko, G.H.H. Im, J.H.H. Lee, I.S.S. Lee, Angew. Chemie **48**, 321 (2009)
22. Q. He, Z. Wu, C. Huang, J. Nanosci. Nanotechnol. **12**, 2943 (2012)
23. P. Podsiadlo, S.G. Kwon, B. Koo, B. Lee, V.B. Prakapenka, P. Dera, K.K. Zhuravlev, G. Krylova, E.V. Shevchenko, J. Am. Chem. Soc. **135**, 2435 (2013)
24. S.J. Son, X. Bai, S.B. Lee, Drug Discov. Today **12**, 650 (2007)
25. J. Li, Y. Hu, Y. Hou, X. Shen, G. Xu, L. Dai, J. Zhou, Y. Liu, K. Cai, Nanoscale **7**, 9004 (2015)
26. R. Xing, A.A. Bhirde, S. Wang, X. Sun, G. Liu, Y. Hou, X. Chen, Nano Res. **6**, 1 (2013)
27. B. Koo, H. Xiong, M.D. Slater, V.B. Prakapenka, M. Balasubramanian, P. Podsiadlo, C.S. Johnson, T. Rajh, E.V. Shevchenko, Nano Lett. **12**, 2429 (2012)
28. X.W. Lou, L.A. Archer, Z. Yang, Adv. Mater. **20**, 3987 (2008)
29. S.J. Son, J. Reichel, B. He, M. Schuchman, S.B. Lee, J. Am. Chem. Soc. **127**, 7316 (2005)
30. H. Qin, Y. Huang, S. Liu, Y. Fang, X. Li, S. Kang, J. Nanomater. (2015)
31. J. Zhou, W. Wu, D. Caruntu, M.H. Yu, A. Martin, J.F. Chen, C.J. O'Connor, W.L. Zhou, J. Phys. Chem. C **111**, 17473 (2007)
32. J. Qi, X. Lai, J. Wang, H. Tang, H. Ren, Y. Yang, Q. Jin, L. Zhang, R. Yu, G. Ma, Z. Su, H. Zhao, D. Wang, Chem. Soc. Rev. **44**, 6749 (2015)
33. D. Goll, A.E. Berkowitz, H.N. Bertram, Phys. Rev. B Condens. Matter Mater. Phys. **70**, 1 (2004)
34. J.G. Railsback, A.C. Johnston-Peck, J. Wang, J.B. Tracy, ACS Nano **4**, 1913 (2010)
35. C. Song, J. Du, J. Zhao, S. Feng, G. Du, Z. Zhu, Chem. Mater. **21**, 1524 (2009)
36. P. Guo, M. Lv, G. Han, C. Wen, Q. Wang, H. Li, X.S. Zhao, Materials (Basel). **9** (2016)
37. K. An, S.G. Kwon, M. Park, H. Bin Na, S.I. Baik, J.H. Yu, D. Kim, J.S. Son, Y.W. Kim, I.C. Song, W.K. Moon, H.M. Park, T. Hyeon, Nano Lett. **8**, 4252 (2008)
38. F. Caruso, Chem. Eur. J. **6**, 413 (2000)
39. F. Caruso, R.A. Caruso, H. Möhwald, Science (80), **282** (1998)
40. W. Ding, H. Lin, Z. Sheng, J. Dai, X. Zhu, X. Tang, Z. Hui, Y. Sun, Cryst. Eng. Comm. **18**, 6134 (2016)
41. J. Huang, L. He, Y. Leng, W. Zhang, X. Li, C. Chen, Y. Liu, Nanotechnology **18**, 415603 (2007)
42. J.S. Lee, S.S. Im, C.W. Lee, J.H. Yu, Y.H. Choa, S.T. Oh, J. Nanoparticle Res. **6**, 627 (2004)
43. Y. Yin, C. Erdonmez, S. Aloni, A.P. Alivisatos, J. Am. Chem. Soc. **128**, 12671 (2006)
44. P. Hu, L. Yu, A. Zuo, C. Guo, F. Yuan, J. Phys. Chem. C **113**, 900 (2009)
45. K. An, T. Hyeon, Nano Today **4**, 359 (2009)
46. A.D. Smigelskas, E.O. Kirkendall, Trans. Am. Inst. Mining Metall. Pet. Eng. **171**, 130 (1947)
47. S. Peng, S. Sun, Angew. Chemie **119**, 4233 (2007)

48. G.H. Jaffari, A. Ceylan, H.P. Bui, T.P. Beebe, S. Ozcan, S.I. Shah, J. Phys. Condens. Matter **24**, 336004 (2012)
49. H. Khurshid, W. Li, V. Tzitzios, G.C. Hadjipanayis, Nanotechnology **22**, 265605 (2011)
50. C. Caizer, Mater. Sci. Eng. B Solid-State Mater. Adv. Technol. **100**, 63 (2003)
51. L. Signorini, L. Pasquini, L. Savini, R. Carboni, F. Boscherini, E. Bonetti, A. Giglia, M. Pedio, N. Mahne, S. Nannarone, Phys. Rev. B **68**, 1 (2003)
52. H. Khurshid, J. Alonso, Z. Nemati, M.H. Phan, P. Mukherjee, M.L. Fdez-Gubieda, J.M. Barandiarán, H. Srikanth, J. Appl. Phys. **117**, 17A337 (2015)
53. G. Zhang, Y. Liao, I. Baker, Mater. Sci. Eng. C **30**, 92 (2010)
54. T.N. Shendruk, R.D. Desautels, B.W. Southern, J. Van Lierop, Nanotechnology (2007)
55. C. Binns, M.T. Qureshi, D. Peddis, S.H. Baker, P.B. Howes, A. Boatwright, S.A. Cavill, S.S. Dhesi, L. Lari, R. Kreger, S. Langridge, Nano Lett. **13**, 3334 (2013)
56. M.-H. Phan, J. Alonso, H. Khurshid, P. Lampen-Kelley, S. Chandra, K. Stojak Repa, Z. Nemati, R. Das, Ó. Iglesias, H. Srikanth, Nanomaterials **6**, 221 (2016)
57. X. Sun, N.F. Huls, A. Sigdel, S. Sun, Nano Lett. **12**, 246 (2012)
58. C.G. Hadjipanayis, M.J. Bonder, S. Balakrishnan, X. Wang, H. Mao, G.C. Hadjipanayis, Small **4**, 1925 (2008)
59. O. Iglesias, A. Labarta, X. Batlle, J. Nanosci. Nanotechnol. **8**, 2761 (2008)
60. W.H. Meiklejohn, C.P. Bean, Phys. Rev. **105**, 904 (1957)
61. Q.K. Ong, X.-M. Lin, A. Wei, J. Phys. Chem. C **115**, 2665 (2011)
62. K. Simeonidis, C. Martinez-Boubeta, O. Iglesias, A. Cabot, M. Angelakeris, S. Mourdikoudis, I. Tsiaoussis, A. Delimitis, C. Dendrinou-Samara, O. Kalogirou, Phys. Rev. B Condens. Matter Mater. Phys. (2011)
63. F. Sayed, N. Yaacoub, Y. Labaye, R.S. Hassan, G. Singh, P.A. Kumar, J.M. Greneche, R. Mathieu, G.C. Hadjipanayis, E. Agostinelli, D. Peddis, J. Phys. Chem. C (2018)
64. H. Khurshid, P. Lampen-Kelley, Ò. Iglesias, J. Alonso, M.-H. Phan, C.-J. Sun, M.-L. Saboungi, H. Srikanth, Sci. Rep. **5**, 15054 (2015)
65. Z. Wu, K. Yu, S. Zhangand, Y. Xie, J. Phys. Chem. C **112**, 11307 (2008)
66. J. Dobson, Drug Dev. Res. **67**, 55 (2006)
67. S.-W. Cao, Y.-J. Zhu, M.-Y. Ma, L. Li, L. Zhang, J. Phys. Chem. C **112**, 1851 (2008)
68. Z. Nemati, J. Alonso, H. Khurshid, M.H. Phan, H. Srikanth, RSC Adv. **6**, 38697 (2016)
69. M.T. Amin, A.A. Alazba, U. Manzoor, Adv. Mater. Sci. Eng. **2014**, 1 (2014)
70. J. Liu, Z. Zhao, G. Jiang, Environ. Sci. Technol. **42**, 6949 (2008)
71. A.-F. Ngomsik, A. Bee, M. Draye, G. Cote, V. Cabuil, Comptes Rendus Chim. **8**, 963 (2005)
72. L. Balcells, C. Martínez-Boubeta, J. Cisneros-Fernández, K. Simeonidis, B. Bozzo, J. Oró-Sole, N. Bagués, J. Arbiol, N. Mestres, B. Martínez, A.C.S. Appl, Mater. Interf. **8**, 28599 (2016)
73. E. Petala, Y. Georgiou, V. Kostas, K. Dimos, M.A. Karakassides, Y. Deligiannakis, C. Aparicio, J. Tuček, R. Zbořil, A.C.S. Sustain, Chem. Eng. **5**, 5782 (2017)
74. J.B. Goodenough, Y. Kim, Chem. Mater. **22**, 587 (2010)
75. J. Zhou, H. Song, X. Chen, L. Zhi, S. Yang, J. Huo, W. Yang, Chem. Mater. **21**, 2935 (2009)
76. G. Prieto, H. Tüysüz, N. Duyckaerts, J. Knossalla, G.H. Wang, F. Schüth, Chem. Rev. **116**, 14056 (2016)
77. Q. Sun, C.Z. Guo, G.H. Wang, W.C. Li, H.J. Bongard, A.H. Lu, Chem. Eur. J. **19**, 6217 (2013)
78. G. Reiss, A. Hütten, Nat. Mater. **4**, 725 (2005)

Chapter 7
Nature Driven Magnetic Nanoarchitectures

María Luisa Fdez-Gubieda, Lourdes Marcano, Alicia Muela, Ana García-Prieto, Javier Alonso, and Iñaki Orue

Abstract Magnetotactic bacteria are aquatic microorganisms that have the ability to align in the geomagnetic field lines, using a chain of magnetic nanoparticles biomineralized internally (called magnetosomes) as a compass needle. Here we describe the biogenesis of magnetosomes, focusing in the formation of the mineral core. We then discuss the magnetic properties of the magnetosomes and the chain of magnetosomes, a natural paradigm of a magnetic 1D nanostructure. Finally, we review the use of magnetosomes and magnetotactic bacteria in biomedical and biotechnological applications, with special mention to the application in magnetic hyperthermia treatments.

M. L. Fdez-Gubieda (✉) · L. Marcano
Dpto. Electricidad y Electrónica, Universidad del País Vasco - UPV/EHU, 48940 Leioa, Spain
e-mail: malu.gubieda@ehu.eus

L. Marcano
e-mail: lourdes.marcano@ehu.eus

M. L. Fdez-Gubieda · A. Muela · A. García-Prieto
Basque Center for Materials, Applications and Nanostructures, UPV/EHU Science Park, 48940 Leioa, Spain
e-mail: alicia.muela@ehu.eus

A. García-Prieto
e-mail: ana.garciap@ehu.eus

A. Muela
Dpto. Inmunología, Microbiología y Parasitología, Universidad del País Vasco - UPV/EHU, 48940 Leioa, Spain

A. García-Prieto
Dpto. Física Aplicada I, Universidad del País Vasco - UPV/EHU, 48013 Bilbao, Spain

J. Alonso
CITIMAC, Universidad de Cantabria, 39005 Santander, Spain
e-mail: javier.alonsomasa@unican.es

I. Orue
SGIker, Universidad del País Vasco - UPV/EHU, 48940 Leioa, Spain
e-mail: inaki.orue@ehu.eus

D. Peddis et al. (eds.), *New Trends in Nanoparticle Magnetism*,
Springer Series in Materials Science 308,
https://doi.org/10.1007/978-3-030-60473-8_7

7.1 An Introduction to Magnetotactic Bacteria

Magnetotactic bacteria (MTB) are microorganisms able to passively align parallel to the Earth's geomagnetic field lines while they actively swim. This behavior, known as magnetotaxis, is due to the presence of unique intracellular magnetic organelles called magnetosomes [1–4]. The magnetosomes are intracellular inclusions composed by a core of magnetic iron mineral, typically magnetite (Fe_3O_4) or greigite (Fe_3S_4), enclosed by a thin membrane. Both MTB and magnetosomes spark interest among scientific community due to their special magnetic and structural characteristics that make them good candidates for nanotechnological applications [5–11]. The magnetotactic behavior in bacteria was first observed by Salvatore Bellini (1963) [12] in freshwater samples. He observed bacteria swimming northward persistently, and then suggested the presence of an internal magnetic compass responsible of the orientation of the cells. More than ten years later, R. P. Blakemore, in 1975 [13], observed the magnetic organelles within the bacterial cells and coined the term *magnetosome* to refer to them.

Magnetotactic bacteria are aquatic motile microorganisms widespread in freshwater and marine environments [14]. They are easily detected in chemically and redox stratified sediments and water columns, predominantly at the oxic-anoxic transition zones (OATZ). Bacteria living in OATZ, with vertical chemical gradients, are continually searching the optimal position in the stratified water column in order to satisfy their nutritional requirement. Under these circumstances, magnetotaxis is thought to be a great advantage by increasing the efficiency of chemotaxis [1]. Due to the inclination, the geomagnetic field lines act as vertical pathways in a stratified environment, therefore the bacteria aligned in the Earth's field reduce a three dimensional search to a single dimension, swimming up-downwards the stratified column (Fig. 7.1). Another possible role of the magnetosomes has been suggested as detoxifying agents scavenging metal ions or reactive oxygen species [15, 16].

At present, all the MTB described are motile gram-negative bacteria although they show a great diversity based on the morphology and physiology. The morphotypes observed, see Fig. 7.2 (top), include curved (a), spirilla (b), cocci (c), rods (d) and even some colonial bacteria, which form multicellular aggregates [3, 17]. The only signature trait they share is the ability to swim along the lines of magnetic fields, including the Earth's field.

The characteristics of the magnetosomes differ among the different types of magnetotactic bacteria but are consistent within a single species. This fact clearly reflects that the formation of these biogenic nanoparticles is under strict biological control. The morphologies of the crystals fit to three main patterns, see Fig. 7.2 (bottom): cubooctahedral (a), elongated prismatic (b, c) and bullet- or tooth-shaped (d, e). The size of the magnetic crystals also varies among species, ranging from around 35 to 120 nm. Nevertheless, each species synthesizes magnetosomes with a characteristic size and a narrow size distribution. Interestingly, the diameter range of the magnetosomes always remains within the range of the room-temperature stable single-magnetic domain particles [1, 3, 19, 20]. Two different phases can be differ-

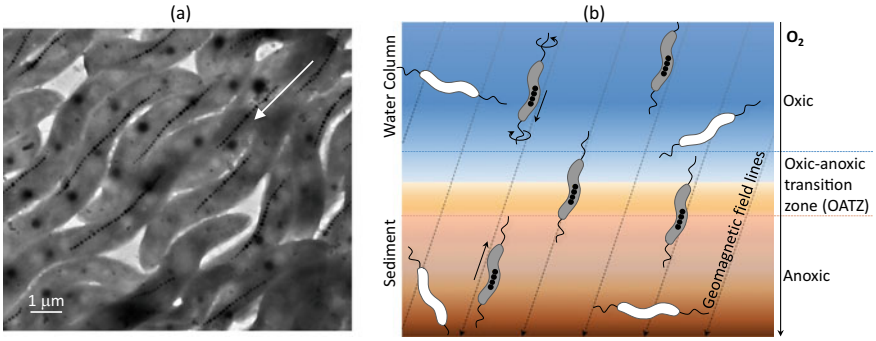

Fig. 7.1 Magnetic response in magnetotactic bacteria. **a** Transmission electron microscope image (TEM) of *Magnetospirillum gryphiswaldense* exposed to 0.5 T external magnetic field. Cells are oriented in the direction of the applied magnetic field. **b** Schematic model of magnetotaxis in the oxic-anoxic transition zone (OATZ). Magnetotactic bacteria (black) swim along the Earth's field lines (one dimensional search). Other non-magnetotactic bacteria (white) swim randomly (three dimensional search)

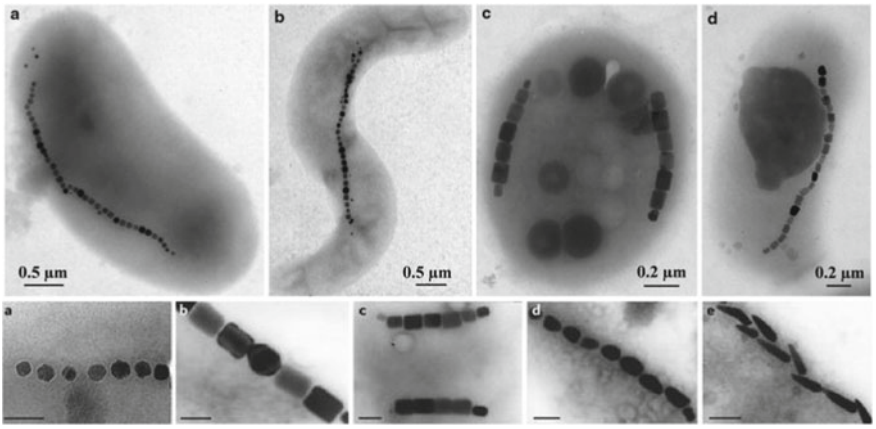

Fig. 7.2 TEM images of magnetotactic bacteria and magnetosomes. Top: Diversity of bacterial shapes: **a** curved; **b** spirillum; **c** coccus and **d** rod. Bottom: Crystal morphologies and intracellular arrangement of magnetosomes: **a** cubooctahedral; **b**, **c** elongated prismatic; **d** tooth-shaped and **e** bullet-shaped. The magnetosomes are arranged in one (**a**) or two (**c**) chains. Adapted, with permission, from [3] (top) and from [18] (bottom)

entiated in the magnetosome: the mineral core and the organic envelope. The mineral core presents high chemical purity, being magnetite, Fe_3O_4, in most of the species, but some of them synthesize greigite, Fe_3S_4. The magnetic core is surrounded by a proteinaceous lipid membrane that controls the biomineralization process [21–23]. The magnetosome membrane is originated by invagination of the cytoplasmic membrane and can be observed within the cell, as empty vesicles, before the formation of the mineral phase [22, 24]. As expected, the lipid composition of the magnetosome

membrane is similar to that of the cytoplasmic membrane. However, the inserted proteins are special functional proteins involved the synthesis of the magnetic core [25]. The magnetosomes are mainly arranged in one or more chains positioned in the long axis of the cell. Each chain, of variable length, may contain 10–20 magnetosomes. This arrangement causes the sum of the moments of the individual magnetosomes and turn the cell into a single magnetic dipole that functions as a magnetic needle enabling the bacteria to passively align in magnetic fields [19, 26]. The formation of the chain is guided by specific cytoskeletal elements, which also anchor the chain in a certain position within the cell [24, 27, 57]. The underlying biological control is the reason why the size, shape, chemical composition and intracellular arrangement varies among species but remain nearly invariant in each one.

Despite their ubiquity and abundance in the environment, MTB are fastidious microorganisms, difficult to grow and maintain in the laboratory [14]. At present,

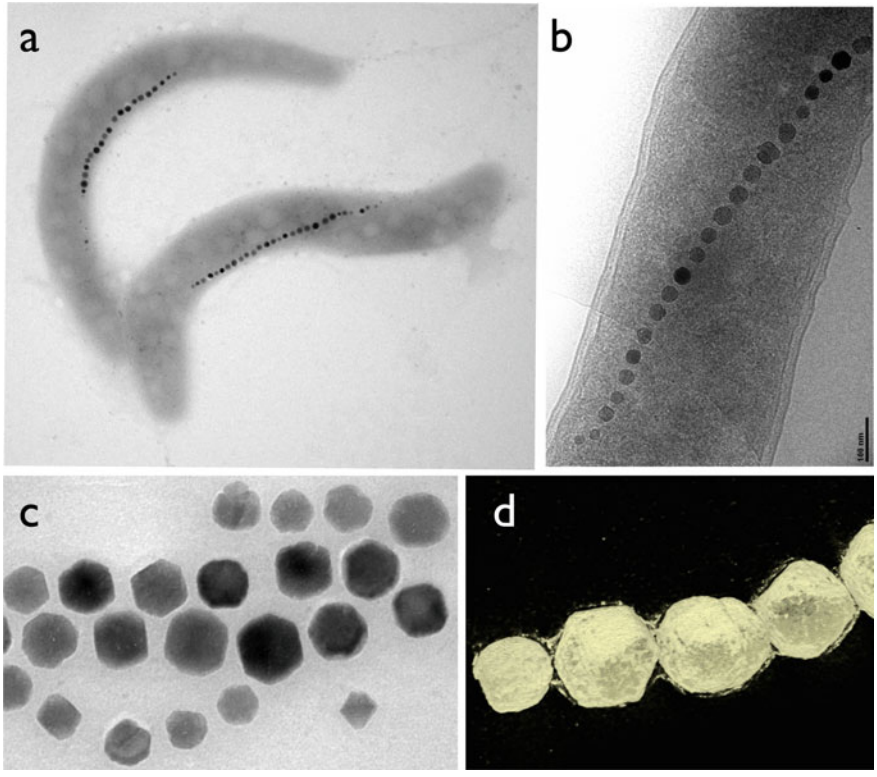

Fig. 7.3 Electron micrographs of cells and magnetosomes of *M. gryphiswaldense*. **a** TEM image of bacteria with the chain of magnetosomes along the long axis and one flagellum in each pole; **b** Cryoelectron tomographic slice showing a chain of magnetosomes lined along the long axis of the cell; **c** TEM image of isolated and purified cubooctahedral magnetosomes; **d** cryoelectron tomography of isolated magnetosomes

only a few representatives have been isolated in axenic culture and deposited in bioresource centers. This explains why most of the knowledge rests on the two first species isolated and easy-cultured, *Magnetospirillum magneticum* AMB-1 and *Magnetospirillum gryphiswaldense* MSR-1. They were isolated from freshwater sediment in the early 1990s [28, 29]. Both strains are spirilla and biomineralize cubooctahedral magnetite crystals arranged in a single chain. In Fig. 7.3 we show TEM and cryoelectron tomography images of *M. gryphiswaldense* and the isolated magnetosomes.

7.2 Biomineralization Process of the Magnetosome

The biomineralization of magnetosomes is a complex biochemical process genetically controlled. Up to date, more than 30 specific genes implicated in magnetosome biomineralization have been identified [18, 30]. Even though the biomineralization process is not well understood yet, different steps have been well described [21, 23, 31].

First, the magnetosome vesicles are formed in the cell by invagination of the cytoplasmic membrane. The vesicle acts as a 'nano-reactor' in which the conditions of the nanocrystal nucleation and growth (pH, redox, etc.) can be controlled, and at the same time, protects the cell from harmful byproducts [16, 32]. The vesicle will grow up to a certain size before the magnetite nucleation process starts. This seems to allow supersaturation of Fe to facilitate nucleation [33]. Second, once the vesicles are formed, the magnetosome membrane is targeted by several proteins (MamA, MamP, MamY, etc.), most of which are encoded in a conserved genomic segment named the magnetosome island (MAI) [34], although it is still not well known how the process works [23]. These proteins will control, among other things, the size, shape and morphology of the biomineralized nanoparticles. Third, iron is transported into the vesicle and mineralized as a nanocrystal. Finally, magnetosomes are aligned into chains through the interaction of the magnetosomes with a cytoskeletal filament that traverses the cell. All four steps are regulated by a complex genetic machinery which has been thoroughly described in the literature [18]. A schematic representation of the different steps can be seen in Fig. 7.4.

The intracellular formation of the magnetite nanocrystal inside the magnetosomes requires first the transport of iron from the surrounding environment into the cell. Three possible routes have been proposed for the iron uptake: (i) iron is introduced into the vesicle when the magnetosome is still attached to the cell membrane, (ii) (alternative to i) but not mutually exclusive) iron is first taken up by cellular iron transport systems and then introduced into the magnetosomes through specific transporters, and (iii) iron is transported from the cytoplasmic membrane to the magnetosome membrane by ligation to unknown organic substrates [18]. Previous studies seem to indicate that in some species the Fe is stored as a compound inside the cytoplasm before being introduced into the magnetosomes [35]. It has also been shown that magnetotactic bacteria are capable of taking up either Fe^{2+} or Fe^{3+}, and this process involves in some cases the use of iron chelators called siderophores [36].

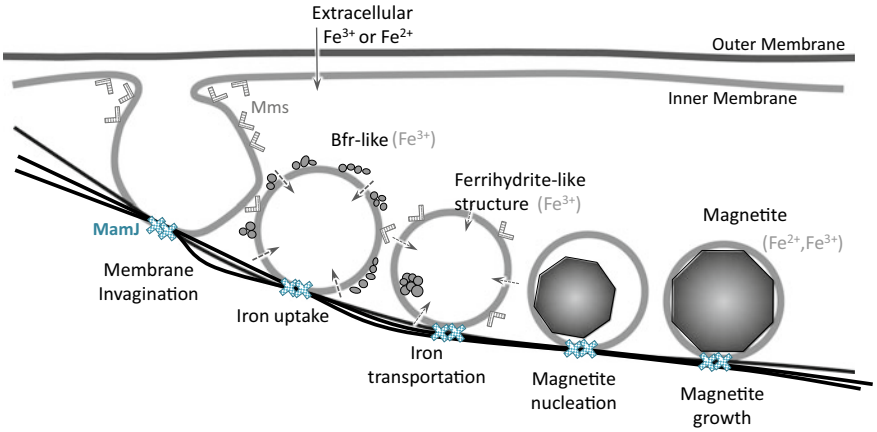

Fig. 7.4 Model of the biomineralization of magnetite in the magnetosomes of magnetotactic bacteria. Modified from Arakaki et al. [5]

Although no mechanism common to all the magnetotactic bacteria has been revealed yet, several proteins involved in this process have been identified. In order to synthesize magnetite nanocrystals, the conditions of the reaction need to be carefully adjusted inside the magnetosome (oxygen level, pH, etc.). Environmental conditions seem to also influence the physicochemical conditions in the interior of the magnetosomes. The nucleation of the magnetite nanocrystals starts when iron ions crystallize under optimal conditions (pH $>$ 7 and low redox potential).

Conventionally, two possible routes have been considered for the formation of magnetite in magnetotactic bacteria: co-precipitation of Fe^{2+} and Fe^{3+} in a ratio of 1:2, and either reduction of a ferric precursor such as ferrihydrite or oxidation of a precursor rich in ferrous content [37]. The existence of a precursor phase in the magnetite formation has been a matter of debate and only recently certain consensus has been reached thanks to the combined use of powerful structural analysis techniques such as High resolution TEM and X-ray Absorption Spectroscopy. To this respect, previous studies seem to show that iron transforms into magnetite from a ferrihydrite-like phase [35, 38, 39]. Precisely, our group carried out a time dependent biomineralization study in which the evolution of the different mineral phases was followed by a combination of structural and magnetic studies carried out in *M. gryphiswaldense* MSR-1 (see Fig. 7.5). The nonmagnetic bacteria were initially introduced into an Fe(III)-citrate supplemented medium and then at specific time intervals between 0 and 360 min, the bacteria were collected. The samples were measured magnetically by VSM magnetometry and Fe-*K* edge X-ray absorption near edge spectroscopy (XANES) measurements were carried out in each sample at the XAFS beamline of the Elettra Sincrotrone Trieste, Italy (Fig. 7.5a). The results indicated that at the early stages of the biomineralization, a phosphorous rich ferrihydrite-like phase is predominant inside the bacteria, and as the biomineralization process evolves (t $>$ 60 min), the bacteria rapidly mineralize magnetite probably following a reduc-

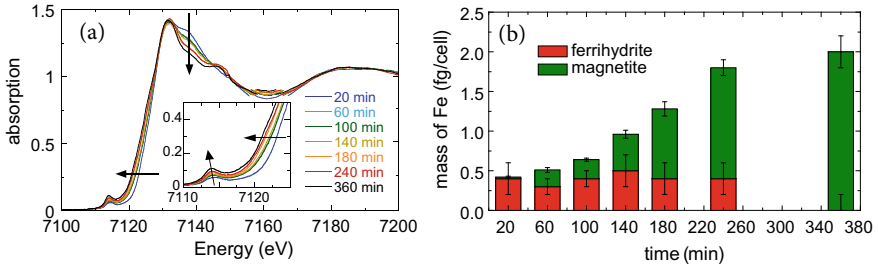

Fig. 7.5 Time resolved magnetic and structural study of the biomineralization process in *M. gryphiswaldense*. **a** Normalized XANES spectra at the Fe *K*-edge obtained at specific time intervals after iron incubation. The inset is a zoom-in of the pre-edge region. **b** Distribution of the mass of Fe per cell in the two identified phases: ferrihydrite-like and magnetite. Adapted from [38] with permission

tive route (Fig. 7.5b). In addition, it has been found that other magnetotactic bacteria (in particular, *Desulfovibrio magneticus* RS-1) seem to follow oxidative routes for the mineralization of magnetite [37]. These latest results suggest that depending on the prevalence of ferric or ferrous iron in the medium, the bacteria will accommodate different synthesis routes.

Finally, the magnetosomes are assembled into a chain. By aligning the magnetosomes into a chain structure the individual magnetic moments can be summed up in order to maximize the magnetotactic response of the bacteria. Depending on the growth conditions, the chains of magnetosomes can contain more than 100 magnetosomes. Although magnetic attraction between the magnetosomes tends already to give rise to chain formations [40, 57], these chains are mainly anchored by cytoskeletal filaments that cross the bacteria. These filaments are mainly formed by MamK, which is an actin-like protein that is mostly linked to magnetotactic bacteria. The magnetosomes are attached to the MamK filament thanks to a connector protein. There are however some differences in the formation of these chains, and in some strains the magnetosome chain extends across the entire bacteria, while in other cases several short chains have been observed [41]. In addition, to ensure proper segregation and equal inheritance of magnetosomes during cell division, magnetosome chains are usually positioned at the middle of the bacteria.

As has been seen, bacterial biomineralization is a complex process involving several steps. Despite the advancements, there are still several open questions that remain to be addressed, such as direct measurements of the conditions for the reaction inside the magnetosomes (pH, redox potential, etc.) [42]. Nevertheless, the better understanding of the biomineralization process and the different elements involved has led to promising studies in different research areas, such as chemical synthesis and biomedicine. For example, several groups have developed synthesis routes bioinspired by the magnetotactic bacteria in order to obtain magnetite nanoparticles with controllable size and morphology [43, 44]. In addition, other groups have studied the possibility of genetically modifying other cells (such as human stem cells) in order to make them express magnetic nanoparticles [45, 46].

7.3 Magnetic Properties of Magnetosomes and Magnetosome Chains in *Magnetospirillum gryphiswaldense*

As introduced in Sect. 7.1, the morphology and size of the magnetosomes are specific of each bacterial species. In particular, *M. gryphiswaldense* synthesize cube-octahedral magnetite nanoparticles with an average diameter of ≈45 nm and a narrow size distribution ≈8 nm. Transmission electron microscopy (TEM) and cryo-tomography techniques reveal that the magnetosome presents faceted morphology where the [111] axes define the growth directions of the hexagonal faces (Fig. 7.9a, b). The bacteria organize the magnetosomes forming a chain where the hexagonal faces are disposed face to face being the total magnetic moment oriented along the chain axis. In this configuration the magnetosome chain behaves as a compass needle and under the action of an external magnetic field, the magnetic torque reorients the bacteria towards the field direction.

7.3.1 The Verwey Transition in the Magnetosomes

Electron micro-diffraction on a single magnetosome confirms that they are single magnetite crystals, Fe_3O_4. Figure 7.6a shows the electron diffraction pattern of a [111] axis of magnetite. The magnetic response of the cells also corresponds to pure magnetite, as confirmed by the evolution of the magnetization as a function of temperature ($M(T)$) measured at 5 mT (Fig. 7.6b). $M(T)$ curves display a marked irreversibility in the whole analyzed temperature range, with the blocking temperature 300 K as expected owing to the large size of magnetosomes. The zero-field cooled (ZFC) curve shows a sharp transition at $T_V = 107$ K corresponding to the well-known Verwey transition, a cubic-to-monoclinic crystallographic phase transition characteristic of magnetite. It should be noted that although this Verwey transition occurs at 120 K in bulk magnetite, lower values (between 102 and 117 K) are found in magnetosomes [47–49]. The fact that the Verwey transition is so abrupt reflects the homogenous stoichiometry of the magnetite of magnetosomes. At 30 K the ZFC presents a shoulder attributed to the ordering of electron spins in magnetite at low temperature [50–52]. The Verwey transition is also observed in the field cooled (FC) curve. This time, the magnetization decreases only slightly below T_V remaining constant down to 5 K. In the FC curve the low-temperature transition is absent.

7.3.2 Magnetic Interactions in the Magnetosome Chain

The magnetosome chain inside the bacteria consists of ≈20 to 30 magnetic nanoparticles each of them surrounded by a lipid bilayer membrane with a thickness of 4 nm

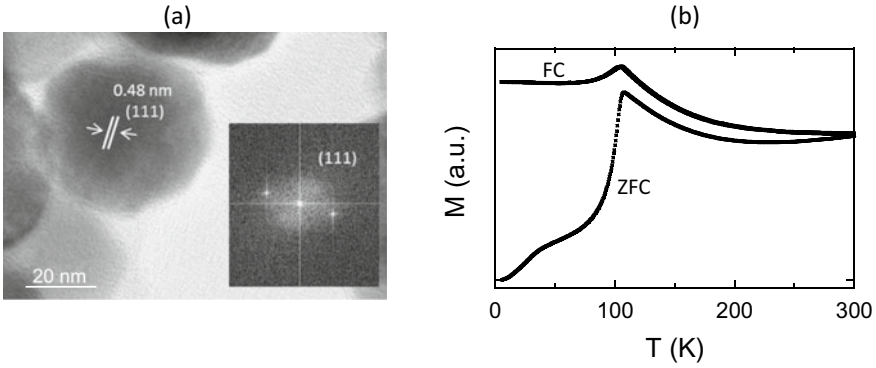

Fig. 7.6 **a** Electron micro-diffraction and Fourier transform of a single magnetosome. **b** $M(T)$ curve of *M. gryphiswaldense* measured at 5 mT. The sharp transition observed 107 K is the Verwey transition

and a distance between the surface of the particles of ≈10 nm. This construction is a natural 1D nanostructure and constitutes an ideal linear arrangement of magnetic single domains where the role of the magnetic interactions in the magnetic behavior can be studied [53].

A useful way to quantify the interparticle interactions and to study the effect on the magnetization reversal is to perform remanence magnetization studies through the Henkel plot. In this representation, two remanent magnetizations, M_{IRM} and M_{DCD}, obtained by different approaches, are plotted one against the other. One approach is the Isothermal Remanent Magnetization, IRM, curves. In an IRM experiment, the starting point is the demagnetized sample, at a fixed temperature, then a small magnetic field is applied and after 10 s the field is switched off and the remanence is measured, M_{IRM}. The process is repeated applying higher magnetic fields until the sample reaches saturation. The other approach is the Direct Current Demagnetization, DCD, remanence curves. For the DCD experiment, the starting point is the magnetic saturated sample after applying a magnetic field of −5 T, then a positive reverse field is applied and after 10 s the field is switched off and the remanent magnetization M_{DCD} is measured. The sequence is repeated increasing the field until the saturation is reached in the opposite direction of the initial state. Figure 7.7a represents the M_{IRM} and M_{DCD} as a function of applied magnetic field measured at 5 K for a sample of randomly oriented bacteria [54].

Note that M_{IRM} starts at 0, demagnetized state, and saturates at the maximum remanent magnetization M_R, while M_{DCD} starts at -M_R (reversal magnetized state) and finishes at M_R (magnetized in the direction of reversal pulses). For single domains

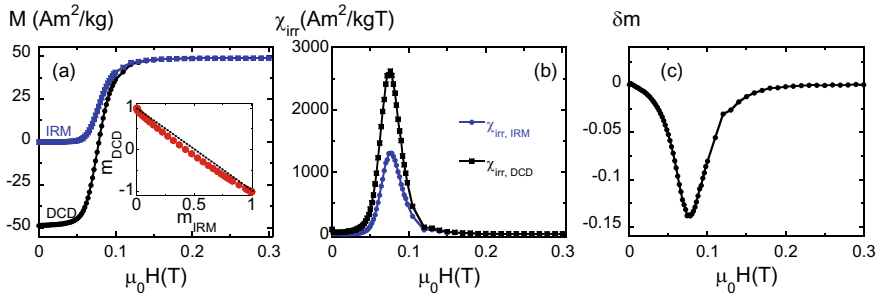

Fig. 7.7 **a** M_{IRM} and M_{DCD} curves, the inset displays the Henkel plot; **b** irreversible susceptibilities; **c** δm as a function of applied magnetic field measured at 5 K for a sample of randomly oriented bacteria

oriented at random and considering a non-interacting system, M_{IRM} and M_{DCD} should verify a quite simple linear relation [55]:

$$m_{\mathrm{DCD}} = 1 - 2m_{\mathrm{IRM}}, \tag{7.1}$$

where $m_{\mathrm{DCD/IRM}} = \frac{M_{\mathrm{DCD/IRM}}}{M_R}$.

However if single domains are indeed interacting with each other, via dipolar or exchange mechanisms, the relation between m_{IRM} and m_{DCD} is expected to deviate from that given in 7.1. The inset displayed in Fig. 7.7a presents the Henkel plot, m_{IRM} versus m_{DCD}. A slight deviation from the relation (7.1) is found, a clear indication that the system behaves as an almost not interacting system.

This is also supported by irreversible susceptibilities calculated as the derivatives of $\chi^{\mathrm{irr}}_{\mathrm{IRM}} = dM_{\mathrm{IRM}}/dH$ and $\chi^{\mathrm{irr}}_{\mathrm{DCD}} = dM_{\mathrm{DCD}}/dH$. These quantities represent a map of switching field distribution. From the fact that $\chi^{\mathrm{irr}}_{\mathrm{IRM}}$ and $\chi^{\mathrm{irr}}_{\mathrm{DCD}}$ present a maximum at the same value of the field amplitude, the interaction is supposed to be quite small (see Fig. 7.7).

At this point it is convenient to define a new variable, δm, as the difference between the experimental M_{DCD} and the non-interacting limit given by 7.1:

$$\delta m = m_{\mathrm{DCD}} - (1 - 2m_{\mathrm{IRM}}) \tag{7.2}$$

Depending on the sign of δm, interaction promotes demagnetizing ($\delta m < 0$) or magnetizing ($\delta m > 0$) effects, as discussed in the literature [56].

In our case, as observed in Fig. 7.7c, δm is small but negative what is usually explained as the interaction being originated by dipolar interactions between nanoparticles that favor antiparallel configuration.

Here we must point out that magnetosome chains are surrounded by bacteria's cytoplasm and this places a separation between chains of at least 1–2 microns. Chains of different bacteria are virtually magnetically isolated with each other so leading to very small inter-chain dipolar interactions: this is the type of interactions we

are indeed considering as negligible in the previous discussion of the Henkel plot in Fig. 7.7a. This argument implicitly assumes that the whole chain composed of 20–30 magnetosomes behaves mostly as a large magnetic domain or equivalently that magnetization rotation of magnetosomes belonging to a given chain is mostly coherent. To further check this line of reasoning, it might be useful to recap the information contained in the hysteresis loops of magnetotactic bacteria.

7.3.3 *Magnetization Process of the Chain: The Stoner-Wohlfarth Approach*

Figure 7.8 shows the experimental hysteresis loops obtained in a sample of randomly oriented bacteria at (a) 300 K and (b) 5 K. Above the Verwey transition $T \geq 107$ K, the hysteresis loops are almost perfectly superimposed with only slight changes of the coercive field $\mu_0 H \approx 20$–22 mT and reduced remanence magnetization $M_R/M_s \approx 0.5$ (see Fig. 7.8c, d). Below the Verwey transition, $T \leq 107$ K, the hysteresis starts to widen noticeably, showing a large increase of the coercive field, what is expected given that the crystal phase of magnetite changes from cubic to monoclinic below T_V, as commented previously. In contrast, the reduced remanence, $M_R/M_s \approx 0.5$ in all the temperature range studied (see Fig. 7.8d). This clearly indicates that we have a uniaxial magnetic anisotropic single domain randomly distributed, the magnetosome chain. This means that the magnetic moment of each magnetosome along the chain is subjected to the same energetic condition and in a first approximation they respond to

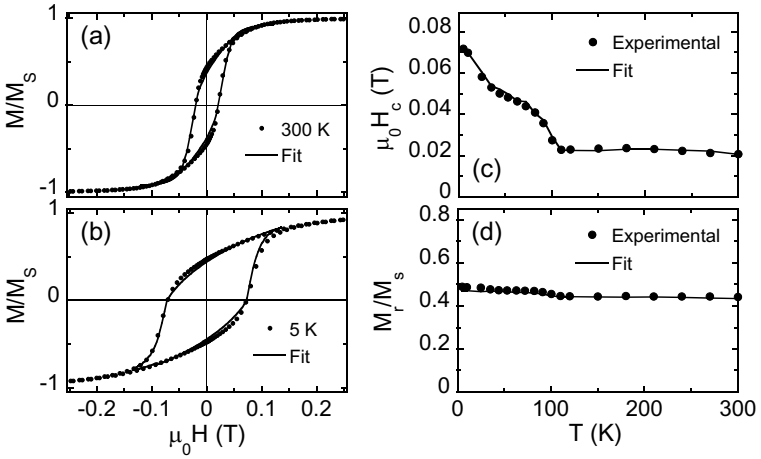

Fig. 7.8 Experimental hysteresis loops obtained from randomly oriented bacteria at **a** 300 K and **b** 5 K. **c** Temperature dependence of the coercive field and **d** reduced remanence magnetization, obtained from the hysteresis loops measured at different temperatures 5–300 K. Continuous lines represent the simulated hysteresis loops obtained as explained in the text

an external magnetic field in a coherent way. Therefore the physical problem can be implemented by using a single particle approach, the Stoner-Wohlfarth model, where the position of the magnetization is given by counterbalancing between the anisotropy energy, E_{ani}, and the Zeeman contribution. Being the energy density $E(\theta, \varphi, H)$ in spherical coordinates:

$$E(\theta, \varphi, H) = E_{\text{ani}} - \mu_0 M H_0(\hat{u}_H \cdot \hat{u}_m) \tag{7.3}$$

where $\hat{u}_H$ and $\hat{u}_m$ are the unit vectors that define the direction of the applied magnetic field and the magnetization, respectively.

There are several sources to the anisotropy energy: the magnetocrystalline contribution of the magnetite phase, E_c, which retains the cubic symmetry of the lattice and produces 8 equivalent easy axes above the Verwey transition directed along the $\langle 111 \rangle$ crystallographic directions; shape anisotropy of magnetosome due to the morphology, and the intra-chain dipolar interactions. The two last terms are typically of uniaxial nature and can be expressed as an effective uniaxial anisotropy K_{uni} (see Fig. 7.9a, b). As recently reported by Orue et al. [53, 57], due to compromise effects of shape anisotropy and dipolar interactions between magnetosomes, the effective magnetic moment of individual magnetosomes is tilted out of the [111] crystallographic easy axis of magnetite (see Fig. 7.9a, b). Then, the expression 7.3 can be written as:

$$E(\theta, \varphi, H) = E_c + K_{\text{uni}}[1 - (\hat{u}_u \cdot \hat{u}_m)^2] - \mu_0 M H_0(\hat{u}_H \cdot \hat{u}_m) \tag{7.4}$$

Note that an uniaxial anisotropy constant as small as 3 kJ/m^3 [53] is enough to overcome the small magnetocrystalline contribution of the magnetite ($K_c = -11$ kJ/m^3).

The hysteresis loops have been calculated following a dynamical approach in which the single domain magnetization can switch between the available energy minima states, at a rate determined by a Boltzmann factor ($\exp(-\frac{V\Delta E}{k_B T})$), where ΔE is the energy density barrier between each pair of minima states as it is well explained in [40, 58, 59]. Aiming to achieve the best match between experiment and theory, K_c and K_{uni} have been adjusted at each temperature in each simulation. As shown in Fig. 7.8, this model accurately reproduces the experimental hysteresis loops and the thermal evolution of the coercive field and the reduced remanence magnetization.

Figure 7.9 displays the thermal evolution obtained for K_c and K_{uni}. From 300 K down to the Verwey temperature T_V, the tendency of K_c reproduces the values and trend reported in the bibliography for bulk single-crystalline magnetite (at 300 K, $K_c = -11$ kJ/m^3) [60]. K_{uni} remains constant (11–12 kJ/m^3) down to T_V, suggesting that the shape anisotropy and the strength of magnetic interactions are basically temperature-independent in the whole studied temperature range. Below T_V, the magnetocrystalline anisotropy changes from cubic to essentially uniaxial along the $\langle 100 \rangle$ directions of the original cubic structure. Therefore, below T_V, the effective anisotropy is purely uniaxial and results from the competition between the magnetocrystalline uniaxial anisotropy, the shape anisotropy and the dipolar interaction

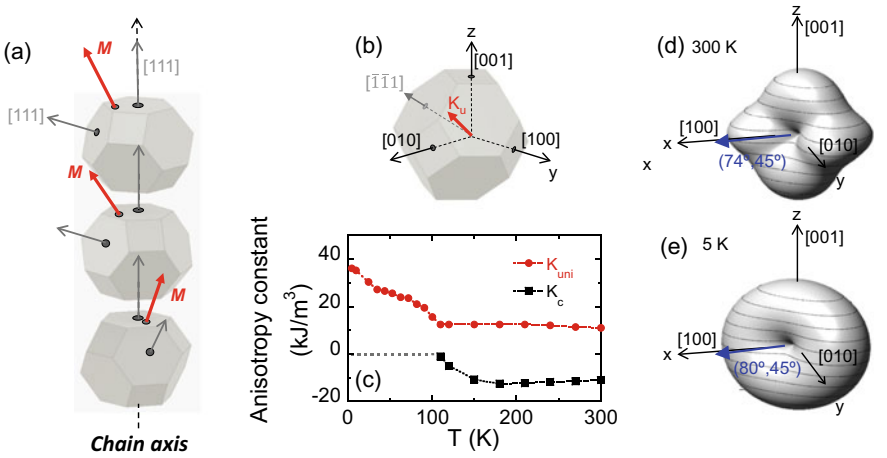

Fig. 7.9 **a** Schematic representation of magnetosome chain composed by three magnetosomes where the hexagonal faces are disposed face to face in the ⟨111⟩ direction. **b** Detailed depiction of an individual magnetosome where x, y and z conform the coordinate axes selected in the simulations coincident to ⟨100⟩ directions. Uniaxial axis (red arrow) forms 25° with the ⟨111⟩ direction. **c** Temperature evolution of the uniaxial anisotropy constant (K_{uni}) and the cubic magnetocrystalline anysotropy constant (K_c). Zero-field energy landscapes at (**d**) 300 K and (**e**) 5 K, respectively, obtained from the simulations as explained in the text. The blue arrows represent the effective easy axes, whose directions are given by (θ,φ), where θ is the polar angle and φ the azimuthal angle

contribution. The resulting uniaxial anisotropy constant K_{uni} increases substantially from 11 to 12 kJ/m^3 at T_V up to 37 kJ/m^3 at 5 K, as reported previously [61].

The implications of the anisotropy constant values in the effective easy axes are reflected in the zero-field energy surfaces plotted in Fig. 7.9d, e at 300 K and 5 K, respectively. At 300 K (see Fig. 7.9d) the energy surface displays one single minimum, proving that the effective anisotropy is uniaxial. The position of this minimum defines the direction of the corresponding easy axis, which in this case is ($\theta = 74°,\ \varphi = 45°$). Even though the cubic magnetocrystalline contribution (E_c) corresponding to a negative K_c (⟨111⟩ easy axes) is well distinguished in the shape of the energy surface at 300 K, it definitely plays a minor role in the overall energy, and its main contribution is to tilt slightly the direction of the uniaxial term set at ($\theta = 80°, \varphi = 45°$). At 5 K (Fig. 7.9e), when $K_c = 0$, the energy surface resembles a toroid. It is thus a pure uniaxial anisotropy with the uniaxial easy axis directed to $\theta = 80°, \varphi = 45°$) [62].

7.4 Applications

The outstanding properties of magnetosomes make them ideal candidates for a number of technological applications. On top of their uniform size and shape, chemical

purity, and easy reproducibility, they display a high magnetic moment and, very importantly, they are surrounded by a lipid-protein membrane, which confers them stability avoiding aggregation of extracted magnetosomes, easy functionalizability, and biocompatibility. Here we will review some of the potential applications of magnetosomes and MTB, with special focus on biomedical applications, and will discuss the main drawbacks that are delaying the transfer of the magnetosome-based technology to the market.

Magnetic hyperthermia is a therapy that aims at debilitating cancer cells by delivering heat to them. In magnetic hyperthermia the magnetic nanoparticles are attached to or internalized into the tumor cells and an alternating magnetic field (AMF) is applied. Under the action of the AMF, the magnetic moment of the nanoparticles describes a hysteresis loop, whose area is proportional to the dissipated energy that increases the temperature of the tumor. By reaching temperatures around 40–45 °C in the tumor area, the cancer cells can be 'deactivated' (dead or driven to apoptosis) without affecting the healthy ones. The study of magnetic nanoparticles with high heating capability, namely large hysteresis loop area for a given magnetic field intensity H and frequency f, has generated wide interest. In this context, magnetosomes from *M. gryphiswaldense* [63–66] and *M. magneticum* [66, 67] have been proven to exhibit large specific absorption rate (SAR) values at AMFs within the clinical limits ($H \cdot f \leq 5 \times 10^9$ $\mathrm{Am^{-1}s^{-1}}$ [68]), constituting ideal candidates for magnetic hyperthermia. The SAR values observed for magnetosomes are considerably higher than those for chemically synthesized magnetite nanoparticles [69–71]. This is mainly attributed to the magnetosomes being single magnetic domains stable at room temperature, a condition met by magnetosomes due to their size (between 30 and 50 nm for *M. gryphiswaldense* and *M. magneticum*), sizes that otherwise are hardly achievable with synthetic procedures.

As an example, Fig. 7.10a shows the SAR values normalized by the frequency (SAR/f) for magnetosomes from *M. gryphiswaldense* dispersed in water as a function of the applied magnetic field amplitude. For the studied field and frequency ranges the SAR/f values are independent of the frequency, evidencing a linear dependence of SAR with frequency. The efficiency of these magnetosomes as hyperthermia agents at 24 kA/m and 149 kHz has been tested on macrophages [64]. Results show that the hyperthermia treatment causes both cell death and inhibition of cell proliferation. Specifically, only 36% of the treated macrophages remained alive 2 h after alternating magnetic field exposure, 24 h later the percentage fell to 22% (see Fig. 7.10b).

The magnetosome membrane provides a matrix for the functionalization of the magnetosomes with biomolecules of interest and is a unique characteristic of magnetosomes over synthetic magnetic nanoparticles. Functionalization is possible either by chemical modification of the isolated particles or by genetic engineering of magnetosome membrane proteins. Genetic approaches involve fusing magnetosome membrane proteins to other enzymes or proteins of interest [72]. Functionalization opens up a wide range of applications in which magnetosomes bind specifically to cells, proteins, or nucleic acids of interest that are subsequently separated, detected or guided with magnetic fields [4]. For example, Ginet et al. [73] engineered a nanobiocatalyst

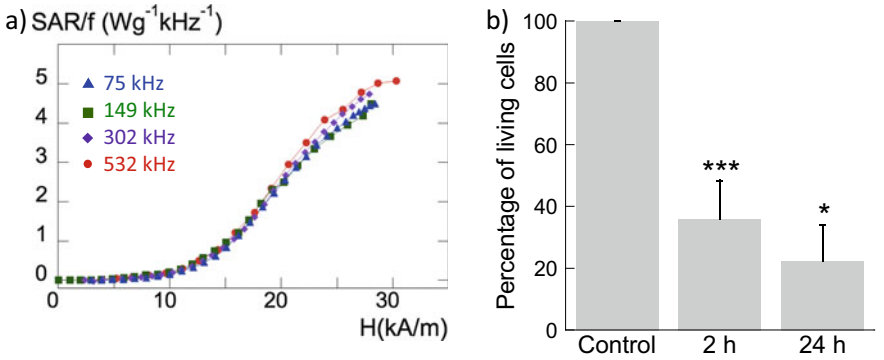

Fig. 7.10 **a** Specific absorption rate (SAR) values normalized to the field frequency for magnetosomes from *M. gryphiswaldense* dispersed in water (blue: 75 kHz; green:149 kHz; purple: 302 kHz; red: 532 kHz). **b** Effect of hyperthermia treatment on macrophage populations. Magnetosome-loaded macrophages were exposed to an AMF ($H = 24$ kA/m, $f = 149$ kHz) 30 min and the effect was evaluated 2 h and 24 h after the exposure. Natural untreated macrophages were used as control. Data represent the mean $\pm$ standard deviation. *, $P < 0.05$; ***, $P < 0.001$ [64]

to degrade ethyl-paraoxon, a commonly used pesticide, by genetically functionalizing the membrane surrounding the magnetite particles of *M. magneticum* with a phosphohydrolase and subsequently sequestering (and reusing) the particles with a magnet. Magnetosomes functionalized with anti-tumour drugs have been proposed as potential carriers for targeted cancer therapies. In vitro studies demonstrate the suitability of anti-cancer drug-loaded magnetosomes from *M. gryphiswaldense* [74] and *M. magneticum* [75] as drug carriers, but it is still to be proven the magnetic guiding capability and controlled drug release.

In this sense, instead of the isolated magnetosomes, the whole MTB have been proposed as potential biorobots with the ability to target and destroy cancer cells [76]. Since MTB incorporate the magnetosome chain, they can be externally detected, manipulated, and guided. In addition, MTB naturally migrate towards their preferred oxygen concentration region, which is close to, or below, the oxic-anoxic transition zone. This faculty is very appropriate for cancer treatment because since the tumor area is low in oxygen due to the tumor tendency to rapidly outgrow its blood supply, MTB are inherently attracted towards these hypoxic regions of the tumor. Therefore, targeting the tumor area with live MTB could become easier and more efficient than with nanoparticles. Preliminary works in this field have shown that *M. magneticum* can navigate in capillaries and target multicellular tumors [77], and that *Magnetococcus marinus* carrying drug-containing nanoliposomes can be magnetically guided towards hypoxic regions of colorectal xenografts [78], with 55% of the injected cells penetrating into the hypoxic regions of the tumour.

The potential of magnetosomes as diagnosis tools has been also demonstrated. It is well known that superparamagnetic iron oxide nanoparticles (SPION) can be used as magnetic resonance imaging (MRI) contrast agents as they shorten the T_2

relaxation time. Recently, Mériaux et al. [79] have demonstrated that magnetosomes show an improved MRI contrasting perfomance as compared to commercially available SPIONs, attributed to the particles being monodomain and magnetically stable at room temperature. Indeed, in vitro relaxometry measurements showed that magnetosomes of *M. magneticum* AMB-1 and *Magnetovibrio blakemorei* MV-1 display a transverse relaxivity r_2 between three and four times higher than commercial SPIONs that leads to a significant gain in MRI sensitivity. The improved MRI contrasting potential of MV-1 magnetosomes with respect to commercial SPIONs was demonstrated in in vivo tests aimed at visualizing mouse brain angiograms after systemic injection. These experiments did also prove that a lower dose of iron was needed when using magnetosomes as contrast agents instead of commercial SPIONs. As a step forward, magnetosomes have been proposed as probes for molecular imaging. Molecular imaging is a technique that combines MRI imaging with cell tracking and/or molecular targeting via the functionalization of the magnetosome membrane. A proper functionalization allows not only detecting with MRI where a tumour is located in the body, but also the activity and expression of specific molecules. The feasibility of using magnetosomes as molecular imaging probes to target breast cancer cells [80] and brain tumor in a mouse model of human glioblastoma [81] have been recently demonstrated. In the latter work, magnetosomes of *M. magneticum* AMB-1 were genetically modified so that their outer surface expressed the RGD peptide, whose binding efficiency to $\alpha_v\beta_3$ integrin receptors overexpressed by tumor cells has been largely demonstrated. In vivo MRI 11.2 T revealed the enhanced retention time of the RGD-labelled magnetosomes within the tumor compared to the unlabelled magnetosomes. The combined activity of magnetosomes as diagnosis and therapeutic agents (as molecular imaging probes and drug carriers/hyperthermia agents) has also been proposed [63].

Given the potential of magnetosomes in biomedical applications, their biocompatibility must be addressed before they can be of clinical use, although a good compatibility is expected due to the natural membrane surrounding the magnetic cores, as preliminary in vitro and in vivo studies suggest [66, 82–85].

Although being magnetosomes the result of a genetically controlled biomineralization process assures their reproducibility and outstanding properties, the feasibility of tuning their magnetic properties could expand their potential applications. In this sense, exposure of MTB to transition metal elements (Co, Mn, and Cu) has been shown to change the magnetic properties of magnetosomes [62, 86–89]. In particular, Co doping of magnetosomes from *M. magneticum* increases the magnetic coercivity [88], which could improve the heating power of these magnetosomes for hyperthermia applications. Doping of magnetosomes is generally achieved upon addition of the doping element to the growth medium, but other routes involving genetic modifications have been explored based on the expression of a metallophore specific for Co and/or Ni in magnetospirilla [90].

Other biotechnological potential applications involve the use of MTB as biosorbents for trace radionuclides and heavy metals in environmental bioremediation [91]. MTB are being investigated in this field because unlike other microorganisms usable

for bioremediation, MTB allow recovering the metal from the medium by subsequently trapping the MTB with a magnet.

There are additional nanotechnological applications of magnetosomes not necessarily related to biotechnology. Owing to their uniform shape and size, magnetosomes can be self-assembled forming regularly ordered 2D superstructures [40] with potential applications as miniaturized high-density data storage materials or biosensors. Magnetite nanoparticles can be fabricated by a biomimetic approach, that is, mimicking the MTB biomineralization process in vitro, by using one of the biomineralization proteins that control the formation of the magnetite crystals within the cell, namely Mms6 [92]. In this way a novel strategy for the production of magnetic arrays has been reported that involves the fabrication of biotemplates of the Mms6 with interferometric lithographic patterning, resulting in arrays of uniform magnetite nanoparticles (86 ± 21 nm) with a period of 357 nm [93]. Finally, magnetosome chains form natural 1D magnetic nanostructures that have inspired the fabrication of highly anisotropic structures for magnetic field detection in electronic devices, biosensing or biometric techniques [94].

Although the advantages of magnetosomes and MTB as potential (bio)technological agents are largely demonstrated, the commercial exploitation has not yet been achieved, primarily because MTB are slow and difficult to culture outside their natural environment, and also because of the fastidious process needed to extract magnetosomes from the bacteria. Despite advances in scaling up the bacterial production in large bioreactors for *M. gryphiswaldense* [95] and *M. blakemorei* [96], an alternative strategy to overcome this problem comes from instigating the magnetosome biogenesis in alternative microbes easier to grow in the laboratory. In this sense, gene clusters of *M. gryphiswaldense* have been transferred into the photosynthetic bacterium *Rhodospirillum rubrum*, a microorganism with 90% genetic similarity with *M. gryphiswaldense*, and magnetosome biogenesis with a formation of well-ordered magnetosome chains has been achieved [46]. Magnetosomes bisoynthesized by *R. rubrum* are however slightly smaller than those of *M. gryphiswaldense* and so does the mass of magnetite per cell.

7.5 Future Perspectives

The field of nanomagnetism is currently a hot topic and the research on magnetotactic bacteria has definitely a significant role in it. Current challenges in this field include understanding the biomineralization process towards reproducing the outstanding magnetite crystals, using magnetosomes as models where to study nanoscale magnetism in a size range hardly reachable by chemical synthesis methods, scale up the magnetosome production, and optimize the technological potential applications of magnetosomes and MTB and explore new ones.

Acknowledgements The Spanish Government is acknowledged for funding under projects number MAT2017-83631-C3-R. The Basque Government is acknowledged for funding under project number IT-1245-19.

References

1. D.A. Bazylinski, R.B. Frankel, Nat. Rev. Microbiol. **2**(3), 217 (2004). https://doi.org/10.1038/nrmicro842
2. D. Faivre, D. Schüler, Chem. Rev. **108**(11), 4875 (2008). https://doi.org/10.1021/cr078258w
3. D.A. Bazylinski, C.T. Lefèvre, D. Schüler, in *The Prokaryotes*, ed. by E. Rosenberg, E.F. DeLong, S. Lory, E. Stackebrandt, F. Thompson (Springer, Berlin 2013), pp. 453–494
4. D.A. Bazylinski, C.T. Lefèvre, B.H. Lower, in *Nanomicrobiology*, ed. by L.L. Barton, D.A. Bazylinski, H. Xu (Springer, New York, 2014), chap. 3, pp. 39–74. https://doi.org/10.1007/978-1-4939-1667-2
5. A. Arakaki, H. Nakazawa, M. Nemoto, T. Mori, T. Matsunaga, J. R. Soc. Interface **5**(26), 977 (2008). https://doi.org/10.1098/rsif.2008.0170
6. E. Alphandéry, Front. Bioeng. Biotechnol. **2**, (2014). https://doi.org/10.3389/fbioe.2014.00005
7. E. Alphandéry, A. Idbaih, C. Adam, J.Y. Delattre, C. Schmitt, F. Guyot, I. Chebbi, J. Controlled Release **262**. https://doi.org/10.1016/j.jconrel.2017.07.020. http://linkinghub.elsevier.com/retrieve/pii/S0168365917307290
8. A. Araujo, F. Abreu, K. Silva, D. Bazylinski, U. Lins, Marine Drugs **13**(12), 389 (2015). https://doi.org/10.3390/md13010389. http://www.mdpi.com/1660-3397/13/1/389
9. S. Taherkhani, M. Mohammadi, J. Daoud, S. Martel, M. Tabrizian, ACS Nano **8**(5), 5049 (2014). https://doi.org/10.1021/nn5011304
10. S. Martel, Biomicrofluidics **10**(2), 021301 (2016). https://doi.org/10.1063/1.4945734
11. D. Gandia, L. Gandarias, I. Rodrigo, J. Robles-García, R. Das, E. Garaio, J. Á. García, M.-H. Phan, H. Srikanth, I. Orue, J. Alonso, A. Muela, M.L. Fdez-Gubieda, Small **15**, 1902626 (2019). https://doi.org/10.1002/smll.201902626
12. S. Bellini, Instituto di Microbiologia dellUniversita di Pavia (1963)
13. R. Blakemore, Science **190**(4212), 377 (1975)
14. C.T. Lefèvre, D.A. Bazylinski, Microbiol. Mol. Biol. Rev. **77**(3), 497 (2013). https://doi.org/10.1128/MMBR.00021-13
15. F.F. Guo, W. Yang, W. Jiang, S. Geng, T. Peng, J.L. Li, Environ. Microbiol. **14**(7), 1722 (2012). https://doi.org/10.1111/j.1462-2920.2012.02707.x
16. D. Muñoz, L. Marcano, R. Martín-Rodríguez, L. Simonelli, , A. Serrano, A. García-Prieto, M.L. Fdez-Gubieda, A. Muela, Sci. Rep. **10**, 11430 (2020). https://doi.org/10.1038/s41598-020-68183-z
17. F. Abreu, J.L. Martins, T.S. Silveira, C.N. Keim, H.G.P.L. de Barros, F.J.G. Filho, U. Lins, Int. J. Syst. Evol. Microbiol. **57**(6), 1318 (2007). https://doi.org/10.1099/ijs.0.64857-0
18. R. Uebe, D. Schüler, Nat. Rev. Microbiol. **14**(10), 621 (2016). https://doi.org/10.1038/nrmicro.2016.99
19. R.B. Frankel, Ann. Rev. Biophys. Bioeng. **13**(1), 85 (1984). https://doi.org/10.1146/annurev.bb.13.060184.000505
20. B. Lower, D. Bazylinski, J. Mol. Microbiol. Biotechnol. **23**(1-2), 63 (2013). https://www.karger.com/DOI/10.1159/000346543
21. D. Schüler, FEMS Microbiol. Rev. **32**(4), 654 (2008). https://doi.org/10.1111/j.1574-6976.2008.00116.x
22. A. Komeili, H. Vali, T.J. Beveridge, D.K. Newman, Proc. Natl Acad Sci USA **101**(11), 3839 (2004)
23. A. Komeili, FEMS Microbiol. Rev. **36**, 232 (2012). https://doi.org/10.1111/j.1574-6976.2011.00315.x

24. A. Komeili, Z. Li, D.K. Newman, Science **311**(5758), 242 (2006). https://doi.org/10.1126/science.1116804
25. K. Grünberg, E.C. Müller, A. Otto, R. Reszka, D. Linder, M. Kube, R. Reinhardt, D. Schüler, Appl. Environ. Microbiol. **70**(2), 1040 (2004). https://doi.org/10.1128/AEM.70.2.1040
26. R.B. Frankel, R.P. Blakemore, J. Magn. Magn. Mater. **15**, 1562 (1980)
27. E. Katzmann, A. Scheffel, M. Gruska, J.M. Plitzko, D. Schüler, Mol. Microbiol. **77**(1), 208 (2010). https://doi.org/10.1111/j.1365-2958.2010.07202.x
28. T. Matsunaga, T. Sakaguchi, F. Tadakoro, Appl. Microbiol. Biotechnol. **35**(5), 651 (1991)
29. K.H. Schleifer, D. Schüler, S. Spring, M. Weizenegger, R. Amann, W. Ludwig, M. Köhler, Syst. Appl. Microbiol. **14**(4), 379 (1991). https://doi.org/10.1016/S0723-2020(11)80313-9
30. H.C. McCausland, A. Komeili, PLoS Genet. **16**(2), e1008499 (2020). https://doi.org/10.1371/journal.pgen.1008499
31. C. Jogler, D. Schüler, Ann. Rev. Microbiol. **63**(1), 501 (2009). https://doi.org/10.1146/annurev.micro.62.081307.162908
32. S. Barber-Zucker, R. Zarivach, ACS Chem. Biol. **12**(1), 13 (2017). https://doi.org/10.1021/acschembio.6b01000
33. E. Cornejo, P. Subramanian, Z. Li, G.J. Jensen, A. Komeili, mBio **7**(1), 1 (2016). https://doi.org/10.1128/mBio.01898-15
34. D. Murat, A. Quinlan, H. Vali, A. Komeili, Proc. Natl Acad. Sci. **107**(12), 5593 (2010). https://doi.org/10.1073/pnas.0914439107
35. J. Baumgartner, A. Dey, P.H.H. Bomans, C. Le Coadou, P. Fratzl, N.a.J.M. Sommerdijk, D. Faivre, Nat. Mater. **12**(4), 310 (2013). https://doi.org/10.1038/nmat3558
36. J. Baumgartner, D. Faivre, in *Molecular Biomineralization*, *Progress in Molecular and Subcellular Biology*, vol. 52, ed. by W.E.G. Müller (Springer, Berlin, 2011), chap. 1, pp. 3–27. https://doi.org/10.1007/978-3-642-21230-7
37. J. Baumgartner, N. Menguy, T.P. Gonzalez, G. Morin, M. Widdrat, D. Faivre, J. R. Soc. Interface **13**, 124 (2016). https://doi.org/10.1098/rsif.2016.0665
38. M.L. Fdez-Gubieda, A. Muela, J. Alonso, A. García Prieto, L. Olivi, J.M. Barandiarán, R. Fernández-Pacheco, ACS nano **7**, 3297 (2013)
39. E. Firlar, T. Perez-Gonzalez, A. Olszewska, D. Faivre, T. Prozorov, J. Mater. Res. pp. 1–9 (2016). https://doi.org/10.1557/jmr.2016.33
40. A.M. Huízar-Félix, D. Muñoz, I. Orue, C. Magén, A. Ibarra, J.M. Barandiarán, A. Muela, M.L. Fdez-Gubieda, Appl. Phys. Lett. **108**, 6 (2016). https://doi.org/10.1063/1.4941835
41. E. Katzmann, F.D. Müller, C. Lang, M. Messerer, M. Winklhofer, J.M. Plitzko, D. Schüler, Mol. Microbiol. **82**(6), 1316 (2011). https://doi.org/10.1111/j.1365-2958.2011.07874.x
42. D. Faivre, T.U. Godec, Angewandte Chemie - International Edition **54**(16), 4728 (2015). https://doi.org/10.1002/anie.201408900
43. A. Dey, J.J.M. Lenders, N.A.J.M. Sommerdijk, Faraday Discuss. **179**, 215 (2015). https://doi.org/10.1039/C4FD00227J
44. J.J.M. Lenders, G. Mirabello, N.A.J.M. Sommerdijk, Chem. Sci. **7**, 5624 (2016). https://doi.org/10.1039/C6SC00523C
45. A. Elfick, G. Rischitor, R. Mouras, A. Azfer, L. Lungaro, M. Uhlarz, T. Herrmannsdörfer, J. Lucocq, W. Gamal, P. Bagnaninchi, S. Semple, D.M. Salter, Sci. Rep. **7**(January), 1 (2017). https://doi.org/10.1038/srep39755
46. I. Kolinko, A. Lohße, S. Borg, O. Raschdorf, C. Jogler, Q. Tu, M. Pósfai, E. Tompa, J.M. Plitzko, A. Brachmann, G. Wanner, R. Müller, Y. Zhang, D. Schüler, Nat. Nanotechnol. **9**(3), 193 (2014). https://doi.org/10.1038/nnano.2014.13
47. R. Prozorov, T. Prozorov, S. Mallapragada, B. Narasimhan, T. Williams, D.A. Bazylinski, Phys. Rev. B **76**(5), 1 (2007). https://doi.org/10.1103/PhysRevB.76.054406
48. L. Marcano, A. García-Prieto, D. Muñoz, L. Fernández Barquín, I. Orue, J. Alonso, A. Muela, M. Fdez-Gubieda, Biochimica et Biophysica Acta (BBA) - General Subjects **1861**(6), 1507 (2017). https://doi.org/10.1016/j.bbagen.2017.01.012
49. J. Fock, L.K. Bogart, D. González-Alonso, J.I. Espeso, M.F. Hansen, M. Varón, C. Frandsen, Q.A. Pankhurst, J. Phys. D: Appl. Phys. **50**(26), 265005 (2017). https://doi.org/10.1088/1361-6463/aa73fa

50. H. Fischer, G. Mastrogiacomo, J.F. Loffler, R.J. Warthmann, P.G. Weidler, A.U. Gehring, Earth Planetary Sci. Lett. **270**(3–4), 200 (2008). https://doi.org/10.1016/j.epsl.2008.03.022
51. H. Kronmuller, F. Walz, Philosophical Maga. Part B **42**(3), 433 (1980). https://doi.org/10.1080/01418638008221886
52. A.R. Muxworthy, E. McClelland, Geophys. J. Int. **140**(1), 101 (2000). http://gji.oxfordjournals.org/content/140/1/101.short
53. D. Gandia, L. Gandarias, L. Marcano, I. Orue, D. Gil-Cartón, J. Alonso, A. García-Arribas, A. Muela, M.L. Fdez-Gubieda, Nanoscale **30**, 16081–16090 (2020). https://doi.org/10.1039/D0NR02189J
54. P. Bender, L. Marcano, I. Orue, D. Alba Venero, D. Honecker, L. Fernández Barquín, A. Muela, M.L. Fdez-Gubieda, Nanoscale Adv. **2**, 1115–1121 (2020). https://doi.org/10.1039/C9NA00434C
55. E.P. Wohlfarth, J. Appl. Phys. **29**(3), 595 (1958). https://doi.org/10.1063/1.1723232
56. K. O'Grady, R. Chantrell, in *Magnetic Properties of Fine Particles*, J.L. Dormann D. Fiorani edn. (Elsevier, 1992), pp. 93–102
57. I. Orue, L. Marcano, P. Bender, A. García-Prieto, S. Valencia, M.A. Mawass, D. Gil-Cartón, D. Alba Venero, D. Honecker, A. García-Arribas, L. Fernández Barquín, A. Muela, M.L. Fdez-Gubieda, Nanoscale **10**(16), 7407 (2018). https://doi.org/10.1039/C7NR08493E
58. L.J. Geoghegan, W.T. Coffey, B. Mulligan, Adv. Chem. Phys. **100**, 475 (1997)
59. J. Carrey, B. Mehdaoui, M. Respaud, J. Appl. Phys. **109**, 083921 (2011)
60. L.R. Bickford, J.M. Brownlow, R.F. Penoyer, Proc. IEE-Part B: Radio Electron. Eng. **104**(5S), 238 (1957)
61. K. Abe, Y. Miyamotto, S. Chikazumi, J. Phys. Soc. Jpn. **41**, 6 (1976)
62. L. Marcano, D. Muñoz, R. Martín-Rodrguez, I.n. Orue, J. Alonso, A. García-Prieto, A. Serrano, S. Valencia, R. Abrudan, L. Fernández Barquín, A. García-Arribas, A. Muela, M.L. Fdez-Gubieda, J. Phys. Chem. C **122**(13), 7541 (2018). https://doi.org/10.1021/acs.jpcc.8b01187
63. R. Hergt, R. Hiergeist, M. Zeisberger, D. Schüler, U. Heyen, I. Hilger, W.a. Kaiser, J. Magn. Magn. Mater. **293**(1), 80 (2005). https://doi.org/10.1016/j.jmmm.2005.01.047
64. A. Muela, D. Muñoz, R. Martín-Rodríguez, I. Orue, E. Garaio, A. Abad Díaz de Cerio, J. Alonso, J.Á. García, M.L. Fdez-Gubieda, J. Phys. Chem. C **120**(42), 24437 (2016). https://doi.org/10.1021/acs.jpcc.6b07321
65. T. Orlando, S. Mannucci, E. Fantechi, G. Conti, S. Tambalo, A. Busato, C. Innocenti, L. Ghin, R. Bassi, P. Arosio, F. Orsini, C. Sangregorio, M. Corti, M.F. Casula, P. Marzola, A. Lascialfari, A. Sbarbati, Contrast Media Mol. Imaging **11**(2), 139 (2015). https://doi.org/10.1002/cmmi.1673
66. E. Alphandéry, I. Chebbi, F. Guyot, M. Durand-Dubief, Int. J. Hyperthermia: Official J. Euro. Soc. Hyperthermic Oncol. North Am. Hyperthermia Group **6736**, 1 (2013). https://doi.org/10.3109/02656736.2013.821527
67. M. Timko, A. Dzarova, J. Kovac, A. Skumiel, A. Jzefczak, T. Hornowski, H. Gojewski, V. Zavisova, M. Koneracka, A. Sprincova, O. Strbak, P. Kopcansky, N. Tomasovicova, J. Magn. Magn. Mater. **321**(10), 1521 (2009). https://doi.org/10.1016/j.jmmm.2009.02.077. Proceedings of the Seventh International Conference on the Scientific and Clinical Applications of Magnetic Carriers
68. S. Dutz, R. Hergt, Int. J. Hyperthermia : Official J. Euro. Soc. Hyperthermic Oncol. North Am. Hyperthermia Group **29**(8), 790 (2013). https://doi.org/10.3109/02656736.2013.822993
69. C. Martinez-Boubeta, K. Simeonidis, A. Makridis, M. Angelakeris, O. Iglesias, P. Guardia, A. Cabot, L. Yedra, S. Estradé, F. Peiró, Z. Saghi, P.a. Midgley, I. Conde-Leborán, D. Serantes, D. Baldomir, Sci. Rep. **3**, 1652 (2013). https://doi.org/10.1038/srep01652
70. E. Alphandéry, S. Faure, O. Seksek, F. Guyot, I. Chebbi, ACS Nano **5**(8), 6279 (2011). https://doi.org/10.1021/nn201290k
71. K.D. Bakoglidis, K. Simeonidis, D. Sakellari, G. Stefanou, M. Angelakeris, IEEE Trans. Magn. **48**(4), 1320 (2012). https://doi.org/10.1109/TMAG.2011.2173474
72. C. Lang, D. Schüler, D. Faivre, Macromol. Biosci. **7**(2), 144 (2007). https://doi.org/10.1002/mabi.200600235

73. N. Ginet, R. Pardoux, G. Adryanczyk, D. Garcia, C. Brutesco, D. Pignol, PLoS ONE **6**(6), e21442 (2011). https://doi.org/10.1371/journal.pone.0021442
74. J.B. Sun, J.H. Duan, S.L. Dai, J. Ren, L. Guo, W. Jiang, Y. Li, Biotechnol. Bioeng. **101**(6), 1313 (2008). https://doi.org/10.1002/bit.22011
75. Q. Deng, Y. Liu, S. Wang, M. Xie, S. Wu, A. Chen, W. Wu, Materials **6**(9), 3755 (2013). https://doi.org/10.3390/ma6093755
76. M.L. Fernández-Gubieda, J. Alonso, A. García-Prieto, A. García-Arribas, L. Fernandez Barquín, A. Muela, J. Appl. Phys. **128**, 070902 (2020). https://doi.org/10.1063/5.0018036
77. M.R. Benoit, D. Mayer, Y. Barak, I.Y. Chen, W. Hu, Z. Cheng, S.X. Wang, D.M. Spielman, S.S. Gambhir, A. Matin, Clin. Cancer Res. **15**(16), 5170 (2009). https://doi.org/10.1158/1078-0432.CCR-08-3206
78. O. Felfoul, M. Mohammadi, S. Taherkhani, D. de Lanauze, Y. Zhong Xu, D. Loghin, S. Essa, S. Jancik, D. Houle, M. Lafleur, L. Gaboury, M. Tabrizian, N. Kaou, M. Atkin, T. Vuong, G. Batist, N. Beauchemin, D. Radzioch, S. Martel, Nat. Nanotechnol. **11**(August), 941 (2016). https://doi.org/10.1038/nnano.2016.137
79. S. Mériaux, M. Boucher, B. Marty, Y. Lalatonne, S. Prévéral, L. Motte, C.T. Lefèvre, F. Geffroy, F. Lethimonnier, M. Péan, D. Garcia, G. Adryanczyk-Perrier, D. Pignol, N. Ginet, Adv. Healthcare Mater. **4**(7), 1076 (2015). https://doi.org/10.1002/adhm.201400756
80. Z. Xiang, X. Yang, J. Xu, W. Lai, Z. Wang, Z. Hu, J. Tian, L. Geng, Q. Fang, Biomaterials **115**(Supplement C), 53 (2017)
81. M. Boucher, F. Geffroy, S. Prvral, L. Bellanger, E. Selingue, G. Adryanczyk-Perrier, M. Pan, C. Lefèvre, D. Pignol, N. Ginet, S. Mriaux, Biomaterials **121**, 167 (2017)
82. L. Xiang, J. Wei, S. Jianbo, W. Guili, G. Feng, L. Ying, Lett. Appl. Microbiol. **45**(1), 75 (2007). https://doi.org/10.1111/j.1472-765X.2007.02143.x
83. R. ting Liu, J. Liu, J. qiong Tong, T. Tang, W.C. Kong, X. wen Wang, Y. Li, J. tian Tang, Prog. Nat. Sci.: Mater. Int. **22**(1), 31 (2012)
84. L. Qi, X. Lv, T. Zhang, P. Jia, R. Yan, S. Li, R. Zou, Y. Xue, L. Dai, Scientific Reports **6**(December 2015), 26961 (2016)
85. T. Revathy, M.A. Jayasri, K. Suthindhiran, 3 Biotech **7**, 126 (2017)
86. S.S. Staniland, W. Williams, N. Telling, G. Van Der Laan, A. Harrison, B. Ward, Nat. Nanotechnol. **3**(3), 158 (2008)
87. M. Tanaka, R. Brown, N. Hondow, A. Arakaki, T. Matsunaga, S. Staniland, J. Mater. Chem. **22**(24), 11919 (2012). https://doi.org/10.1039/c2jm31520c
88. J. Li, N. Menguy, M.A. Arrio, P. Sainctavit, A. Juhin, Y. Wang, H. Chen, O. Bunau, E. Otero, P. Ohresser, Y. Pan, J. R. Soc. Interface 13(121). Article No. **20160355**, (2016)
89. L. Marcano, I. Orue, A. García-Prieto, R. Abrudan, J. Alonso, L. Fernández Barquín, S. Valencia, A. Muela, M. Luisa Fdez-Gubieda, J Phys. Chem. C **124**(41), 22827–22838 (2020). https://doi.org/10.1021/acs.jpcc.0c07018
90. D. Pignol, M. SABATY, P. Arnoux, J. ABBE. Modified magnetotactic bacteria expressing a metallophore specific for cobalt and/or nickel (2017). https://encrypted.google.com/patents/WO2017077114A1?cl=nl. WO Patent App. PCT/EP2016/076,856
91. W. Zhou, Y. Zhang, X. Ding, Y. Liu, F. Shen, X. Zhang, S. Deng, H. Xiao, G. Yang, H. Peng, Appl. Microbiol. Biotechnol. **95**(5), 1097 (2012)
92. Y. Amemiya, A. Arakaki, S.S. Staniland, T. Tanaka, T. Matsunaga, Biomaterials **28**(35), 5381 (2007). https://doi.org/10.1016/j.biomaterials.2007.07.051
93. S.M. Bird, O. El-Zubir, A.E. Rawlings, G.J. Leggett, S.S. Staniland, J. Mater. Chem. C **4**, 3948 (2016)
94. X. Jiang, J. Feng, L. Huang, Y. Wu, B. Su, W. Yang, L. Mai, L. Jiang, Adv. Mater. **2016**, 1 (2016). http://doi.wiley.com/10.1002/adma.201601609
95. U. Heyen, D. Schüler, Appl. Microbiol. Biotechnol. **61**(5–6), 536 (2003). https://doi.org/10.1007/s00253-002-1219-x
96. K.T. Silva, P.E. Leão, F. Abreu, J.A. López, M.L. Gutarra, M. Farina, D.A. Bazylinski, D.M.G. Freire, U. Lins, Appl. Environ. Microbiol. **79**(8), 2823 (2013). https://doi.org/10.1128/AEM.03740-12

Chapter 8
Magnetic Self-Assembling of Spherical Co Nanoparticles Used as Building Blocks: Syntheses, Properties and Theory

Johannes Richardi, C. Petit, and Isabelle Lisiecki

Abstract In this chapter, we show that thanks to the use of micellar and organometallic approaches, one can favor the growth of uniform spherical Co NPs with controlled surface passivation (dodecanoic acid or oleylamine), tunable size (from around 4 to 9 nm) and tunable nanocrystallinity (from fcc to hcp structure). As a result of the balance between van der Waals attractions between the metallic NPs, magnetic interactions between the magnetic NPs and solvent-mediated interactions between ligands, these uniform colloidal NPs can be used as building units to form a full set of assemblies which morphology depends on the deposition strategy, involving solvent evaporation. In the case of spontaneous self-assembling of magnetic NPs, compact hexagonal 2D arrays and 3D superlattices called supercrystals can form. In the latter case, either face-centered cubic supercrystalline films or single colloidal crystals can be obtained. Mesostructures of hexagonally ordered columns, labyrinths and void structures can result from assisted self-assembling, induced by the application of an external magnetic field. In highly ordered superlattices, individual NPs act as "artificial atoms" and occupy the lattice sites to form repetitive, periodic "artificial planes". From a fundamental point of view, these artificial solids constitute good models for investigating crystallization behavior. Resulting from collective interactions between neighboring NPs, they exhibit novel magnetic properties. The magnitude of these interactions, and then, the magnetic properties, can be tuned by various parameters including (1) the (crystallographic) nature of the magnetic NP, (2) the NP size, (3) the nature of the coating agent, (4) the nature

J. Richardi (✉)
Sorbonne Université, CNRS, Laboratoire de Chimie Théorique, LCT, F. 75005 Paris, France
e-mail: johannes.richardi@sorbonne-universite.fr
URL: https://www.lct.jussieu.fr/pagesperso/richardi/jrichardi.html

C. Petit · I. Lisiecki (✉)
Sorbonne Universités, UPMC Univ Paris 06, UMR 8233, MONARIS, 75005 Paris, France
e-mail: isabelle.lisiecki@upmc.fr

C. Petit
e-mail: christophe.petit@upmc.fr

J. Richardi · C. Petit · I. Lisiecki
CNRS, UMR 8233, MONARIS, 75005 Paris, France

D. Peddis et al. (eds.), *New Trends in Nanoparticle Magnetism*,
Springer Series in Materials Science 308,
https://doi.org/10.1007/978-3-030-60473-8_8

of the solvent, (5) the evaporation rate and (6) if appropriate, the application of an external field during the solvent evaporation. On the one hand, simulations based on a flory-type solvation theory using Hansen solubility colloidal parameters allow to predict the cobalt NP size. On the other hand, Monte Carlo simulations and free energy theories are able to predict the size and type of patterns appearing during the evaporation of a solution of magnetic NPs under a magnetic field.

8.1 Introduction

Self-assemblies of inorganic nanoparticles (NPs) into micrometer-scale ordered arrays and original mesostructures constitute a new generation of advanced materials [1–3]. Depending on the deposition strategy, involving solvent evaporation of a colloidal solution, various types of assemblies can be obtained. In the case of spontaneous self-assembling of magnetic NPs (MNPs), compact hexagonal 2D arrays [4, 5] and 3D superlattices called supercrystals [6] can form. Mesostructures of hexagonally ordered columns, labyrinths and void structures can result from assisted self-assembling, induced by the application of an external magnetic field [7]. In highly ordered superlattices, individual NPs act as “artificial atoms” and occupy the lattice sites to form repetitive, periodic “artificial planes". From a fundamental point of view, these artificial solids constitute good models for investigating crystallization behavior. In addition, their properties are determined by both individual NPs and their collective interactions. Resulting from collective interactions between neighboring NPs, they exhibit new mechanical, [8] transport, [9] optical, vibrational, [10] chemical (stability against oxidation and coalescence) and magnetic properties [11].

Fundamentally, one of the prerequisites to create assembly into well-defined superstructures is the use of NPs with uniform size and shape. The necessary conditions to form such populations are (1) a short nucleation step followed by (2) a slower growth step of the nuclei. Focusing on cobalt, size-controlled colloidal synthesis of spherical metallic NPs, remains, to this day, challenging. Such uniform MNPs have to be characterized by a high stability against oxidation and coalescence but not only. Regarding to the applications, high anisotropy of NPs is mainly required, it is then crucial to obtain preferentially highly crystallized hcp-Co NPs, rather than the two other possible structures, i.e., epsilon and fcc ones. The existing strategies to address these challenges are based on decomposition of organometallic precursors and metal-salt reduction, including the micellar method. In the case of decomposition of organometallic precursor, a precursor (e.g., $Co_2(CO)_8$) is rapidly decomposed at high temperatures in presence of surfactants and the NP size is tuned by tailoring the reaction time, reaction temperature, precursor injection time, surfactant to precursor ratio and chemistry of reagents and surfactants. For Co, this approach has been initiated by Dinega and Bawendi who obtained epsilon-Co NPs with however a rather high size polydispersity [12]. The first example of uniform size and shape tunable Co NPs using this approach has been reported by Puntes et al. [13] who obtained epsilon-Co NPs coexisting however with hcp-Co nanodisks. Thereafter, keeping unchanged the

precursor but varying the surfactants, populations of tunable size have been obtained characterized by either epsilon [13], fcc [14] or a mixing of hcp/fcc [15] structure. Another approach for formation of size-controlled spherical Co NPs is the reduction approach. In this method typically, a reducing agent is injected into a hot solution of metal-salt precursor either inorganic or organic ($CoCl_2$ or $Co(CH_3COO)_2$) in the presence of surfactants. Inorganic metal-salt chemical reduction first reported by Murray and Sun [16] allows the formation of uniform size tunable epsilon-Co NPs [14]. The group of Chaudret, using an organic metal-salt as precursor, Co(η3-C8H13)(η4-C8H12), that readily decomposes at lower temperature (around 150 °C) under a pressure of dihydrogen (usually 3 bars), synthesized Co NPs with an fcc/hcp structure [17]. Using a variant of the inorganic metal-salt reduction where the reducing agent also plays the role of the solvent (polyol method), Murray et al. published the first example of hcp-Co NPs. Recently, Mezziane et al. developed a simple organometallic approach based on the combination of oleylamine and $ClCo(PPh_3)_3$ and evidenced the formation of pure monodisperse spherical hcp-Co NPs, ferromagnetic at room temperature [18]. The reduction in reverse micelles, performed at room temperature, also allows the formation of uniform size tunable Co NPs, characterized by an fcc polycrystalline structure [19–21]. Using the appropriate annealing treatment and taking advantage of their high thermal stability, Co polycrystals can transform into hcp single-crystalline NPs [22, 23]. For all these approaches, surfactant is a key parameter not only to stabilize the NPs against coalescence and oxidation but also to mediate the NP growth.

The assembly of NPs can be obtained through the evaporation of a colloidal solution. As a result of the balance between van der Waals attractions between the metallic NP, magnetic interactions between the MNPs and also solvent-mediated interactions between ligands, uniform colloidal MNPs can assemble into various mesostructures. The magnitude of these interactions can be tuned by various parameters including (1) the nature of the MNP, (2) the NP size, (3) the nature of the coating agent, (4) the nature of the solvent (5) the evaporation rate and (6) if appropriate, the application of an external field during the solvent evaporation. In the absence of external field, MNPs can self-assemble into 2D and 3D ordered arrays. The first reports of nanocrystal superlattices were published by Bentzon [24, 25] and coworkers in 1989 with iron oxide NPs used as building blocks. Then after, significant progress has been made in preparing long-range 2D and 3D superlattices of MNPs. 2D superlattices composed for example of spherical MNPs (Co [6], Ni [26], Fe [27] and Fe_2O_3 [28]), are characterized by a hexagonal packing and can be obtained at the micrometer scale. Besides, self-organization of MNPs into 3D supercrystals has been, however in a less extend, evidenced by several groups. Depending on the experimental conditions, two growth processes are observed (1) onto a substrate (heterogeneous nucleation and growth) or (2) in solution (homogeneous nucleation and growth). In the first case, film morphology is obtained whereas in the latter ones, the colloidal crystals obtained are characterized by well-defined shape. The first example of long-range ordered 3D supercrystal film of MNPs has been published in 2003 by Lisiecki et al. [6]. These artificial solids are made of several hundred monolayers of fcc-Co NPs, which order in an fcc "super" structure. 3D supercrystal films have been also obtained using Ni

[26], magnetite [28] and Fe_3O_4 [29] NPs. Even more rarely, only some colloidal crystals made of MNPs have been, at this day, reported in the literature, which can be attributed to the difficulty to meet all the conditions to growth them. They have been obtained using Ni [26], γ-Fe_3O_4-Fe_2O_3 [30] and Fe_3O_4 [29].

Physico-chemical properties, especially magnetic ones of assemblies of NPs, are known to be significantly impacted by a set of parameters including (1) MNP size, (2) nanocrystallity, (3) interparticle gap, (4) degree and type of ordering of the superlattice, (5) morphology. In this chapter, we cover the results obtained in our group on (1) the colloidal synthesis of uniform and spherical cobalt NPs, (2) their use for the elaboration of 2D and 3D assemblies by means of spontaneous and assisted assembling and (3) their magnetic properties. The key factors for the synthesis of uniform Co NPs and their assemblies will be discussed. We will also present theories and simulations, which predict the size and shape of mesostructures obtained from evaporation of MNP solutions under a magnetic field.

8.2 Synthesis of Uniform Spherical Co Nanoparticles

8.2.1 Synthesis by Micellar Approach

8.2.1.1 Cobalt Nanoparticle Size Polydispersity Control

Co NPs are synthesized by solution-phase reduction approach, at room temperature [20]. The precursor used is the cobalt (II) bis(2-ethylhexyl) sulfosuccinate, $Co(AOT)_2$. 5×10^{-2} M $Co(AOT)_2$ solution is prepared using isooctane as bulk solvent [31]. The amount of water concentration defined as $w = [H_2O]/[AOT] = 32$. This prepared microemulsion is vigorously shaken for a few minutes for equilibrium and form reverse micelles [32]. The reducing agent used is sodium tetrahydroborate, and its concentration is given by R ($R = [NaBH_4]/[Co(AOT)_2]$). R value varies from 0.5 to 8 by varying the volume of a fixed concentration ($[NaBH_4] = 1$ M) added to the micellar solution. Under vigorous shaking, the solutions instantaneously turn from pink to black indicating the formation of Co NPs. Above $R = 0.5$, resulting from the large amount of water brought by the reducing agent injected, reverse micelles are instantaneously destroyed [32, 33]. After the synthesis, whatever the R value is, Co NPs are extracted from the AOT surfactant by adding highly concentrated dodecanoic acid solution ($[C_{12}H_{25}COOH] = 0.2$ M). After washing several times with ethanol, the NPs are dispersed in hexane and then centrifuged to precipitate bulky material. Only the upper phase containing dodecanoic acid coated NPs is collected. All the steps are carried out in a nitrogen glove box using deoxygenated solvents to prevent metal oxidation. Transmission electron microscopy (TEM) investigation is performed after depositing some drops of the colloidal solutions onto a carbon TEM grid and complete evaporation of the solvent. As can be observed in TEM images (Fig. 8.1), the populations of NPs significantly depend on R value. At $R =$

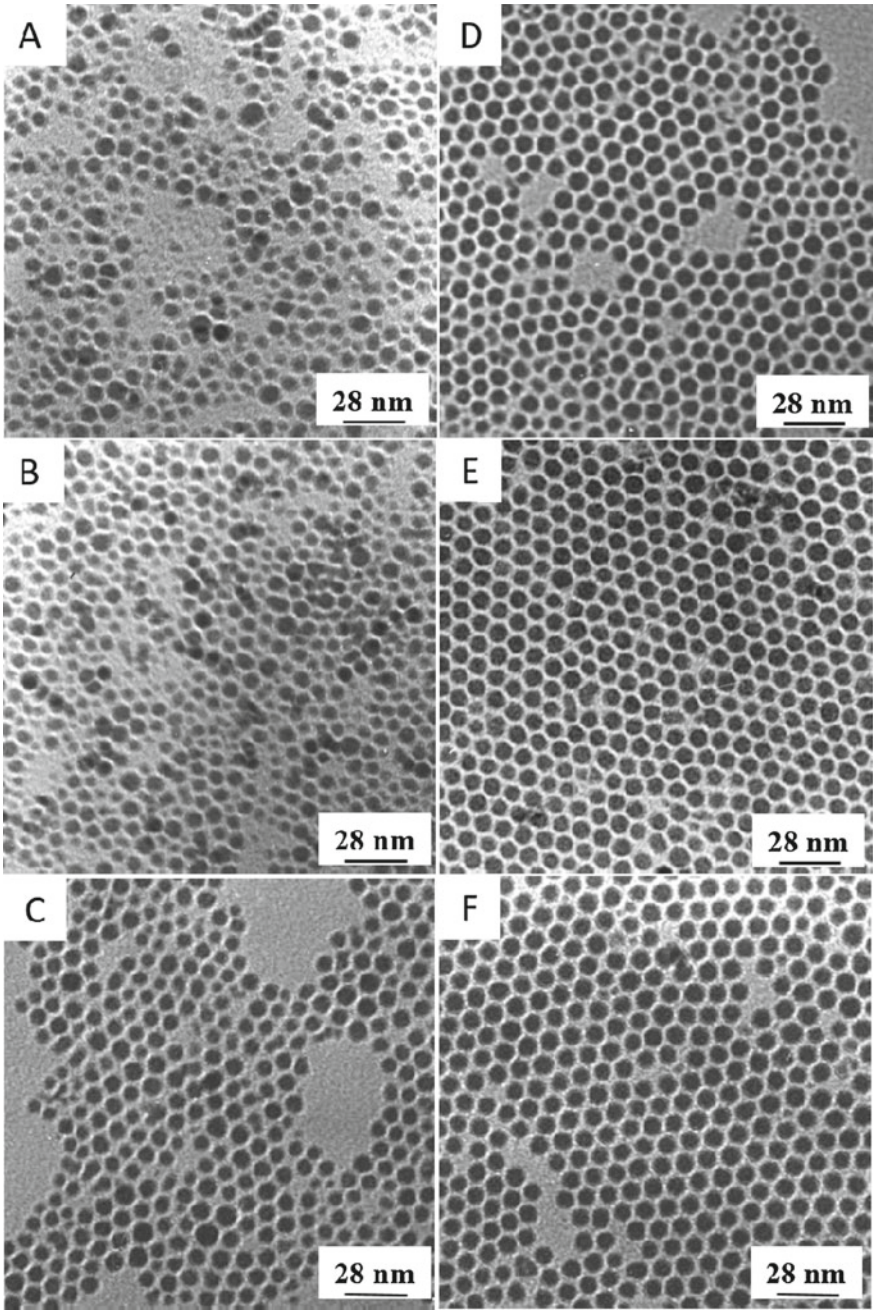

Fig. 8.1 TEM images of cobalt nanoparticles synthesized by the micellar approach, at various sodium tetrahydroboride concentrations, *R*. **a** ($R = 0.5$), **b** ($R = 1$), **c** ($R = 2$), **d** ($R = 4$), **e** ($R = 6$) and **f** ($R = 8$)

Table 8.1 Average diameter of C_O nanoparticles D, and size distributions, σ, at various R values

R	0.5	1	2	4	6	8
D (nm)	6	7	7	7	7	8
σ (%)	30	18	13	12	12	8

0.5, the mean diameter is 6 nm (Table 8.1), with a large size polydispersity, around 30%. By increasing R value, the more important change is the decrease in the size polydispersity which drops from 30 to 8%. In a lesser extend, the mean diameter slightly increases from 6 to 8 nm. Such feature is attributed to the increase in the yield of the reduction reaction that is not complete below $R = 8$ [34]. This statement is well illustrated by the concentration increase of the colloidal solution, by a factor of almost 5, when R increases from 0.5 to 8. Higher the R value, larger the NP diameter. The mean diameter increase combined to the size selection occurring at the end of the synthetic process explains the reducing agent concentration effect. This result shows that the best condition to promote the growth of uniform Co NPs, initiating in AOT reverse micelles, is to work in a saturation regime in reducing agent.

8.2.1.2 Cobalt Nanoparticle Size Control

Revisiting the chemical reduction approach of $Co(AOT)_2$ precursor presented below, a novel strategy based on the change of the bulk solvent gives rise to uniform colloidal Co NPs with tunable size [21]. Six different micellar solutions of 5×10^{-2} M $Co(AOT)_2$ are prepared using xylene (sample S1), cyclohexane (sample S2), cumene (sample S3), decane (sample S4), octane (sample S5) and isooctane (sample S6). w value is fixed at 2. Whatever the bulk solvent is, reverse micelles form [32–36]. Taking into account the importance of the saturation in reducing agent on Co size polydispersity, R value is fixed at 6. The rest of the protocol is similar to the previous one. At the end of the synthesize, six colloidal solutions with dodecanoic acid (C_{12}) coated Co NPs are obtained with hexane used as solvent. For clarity, this latter solvent is called "C_{12}-NP solvent" against "AOT solvent" for the initial bulk solvent use to form initial reverse micelles. TEM investigation performed on the six populations of Co NPs reveals that the growth of Co NPs drastically depends on the nature of the AOT solvent (Fig. 8.2 and Table 8.2). Indeed, the mean diameters of Co NPs for xylene, cyclohexane, cumene, decane, octane and isooctane are found equal to 3.9, 4.6, 4.7, 7.0, 7.6 and 7.7 nm, respectively. It is noticeable that all the samples are characterized by a rather low size polydispersity, i.e., around 12%. Co NP synthesize is occurring in an out-of-equilibrium ternary component system composed of $Co(AOT)_2$, oil and water. Despite the complexity of such a reaction system, size control of Co NPs can be explained by solvent-mediated AOT-AOT interactions. The NP formation is separated into two steps, (1) the nucleation step and (2) the growth step. The nucleation step mainly depends on the Co–Co interactions. DFT calculations show that the interactions between the solvent and the cobalt atoms are significantly weaker than the Co–Co interactions [37]. Therefore, an eventual

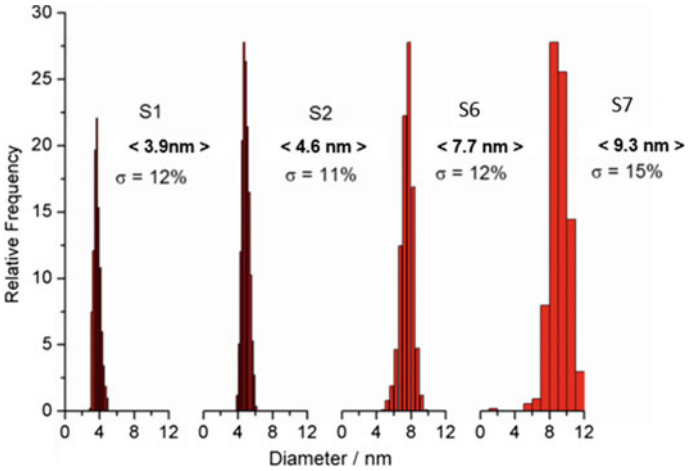

Fig. 8.2 Size distribution of Co nanoparticles synthesized by the micellar approach with different combinations of AOT solvent/C_{12}-NP solvent: xylene/hexane (S1), cyclohexane/hexane (S2), isooctane/hexane (S3) and isooctane/cyclohexane (S4)

Table 8.2 Average diameter (D) and size distribution (σ) of Co NP populations obtained with various solvent-ligand pairs used in the experiments. χ_{12} is the interaction parameter calculated for the various solvent-ligand pairs

Solvent-ligand (sample)	D (nm)	σ (%)	χ_{12} (J mol^{-1})
Octane—AOT (*S5*)	7.6	11	0.02375
Isooctane—AOT (*S6*)	7.7	12	0.02412
Decane—AOT (*S4*)	7.0	12	0.05058
Cyclohexane—AOT (*S2*)	4.6	11	0.17272
Cumene—AOT (*S3*)	4.7	11	0.44645
Xylene—AOT (*S1*)	3.9	12	0.49455
Hexane—C12 (*S6*)	7.7	12	0.06424
Cyclohexane—C12 (*S7*)	9.3	15	0.03062

impact of the solvent on the nucleation can be ruled out. However, the growth of NP is driven by the AOT adsorption on the metal surface through the attractions between the cobalt atoms and the polar head groups of AOT but also by AOT/AOT interactions [38]. Changing the nature of the solvent impacts the AOT solvation and then the AOT/AOT interactions, that in turn, the final NP size. This statement is supported by the calculation of interaction parameters χ_{12} for the various solvent-AOT pairs, using the Hansen solubility parameters [21]. In Fig. 8.3, the NP diameter is plotted against the χ_{12} parameter using a logarithmic scale. It can be seen that the NP size decreases as the χ_{12} parameter increases. A linear regression gives

$$\log(d) = 0.944 - 0.211 \log(c_{12})$$

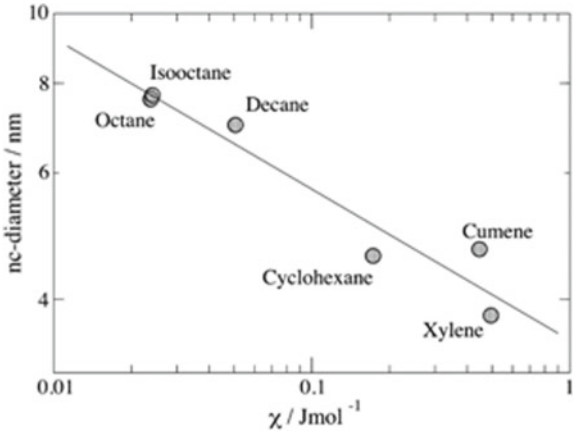

Fig. 8.3 Log–log plot of the experimental cobalt nanoparticle size and the interaction parameter

d and χ_{12} are expressed in nm and J mol^{-1} respectively. Based on the experimental results, this formula yields the NP diameter within an error of around 1 nm.

For cyclohexane, xylene and cumene, the larger χ_{12} values favor the attraction between the AOT, resulting in the increase in the stability of the ligand layer and thus the hindering of the growth of the NPs. At the opposite, an increase in the χ_{12} value results in smaller NPs as observed for octane, isooctane and decane.

The importance of the interaction parameter on the NP size control is also well illustrated by the following experiment. After removing the upper hexane colloidal solution from sample S6, a part of the precipitate containing C_{12}-Co NPs, is dispersed in cyclohexane (*sample S7*). TEM study reveals that the mean diameter of this "second dispersion" is 9.3 nm against 7.7 nm for the first dispersion (in hexane). The size distribution slightly increases from 12 to 15% (Fig. 8.2 and Table 8.2). The χ_{12} parameter calculated for dodecane (used for dodecanoic acid) using cyclohexane is 0.0306 J mol^{-1} against 0.0642 J mol^{-1} for hexane used as solvents (Table 8.2). The lower χ_{12} value indicates that cyclohexane is a better solvent for C_{12}-NPs, thus hindering the particle aggregation. This explains that, in this case, extraction from the precipitate of larger NPs is occurring, conversely to the use of hexane.

This novel strategy using the solvent-mediated ligand interaction allows to control accurately the NP size, but also to use a unique ligand to stabilize the NPs, e.g., dodecanoic acid that covalently binds to the Co surface ensuring high stability against oxidation and coalescence processes. It is noticeable that such a strategy would provide an efficient guide in the choice of the solvent for controlling the NP size of any material.

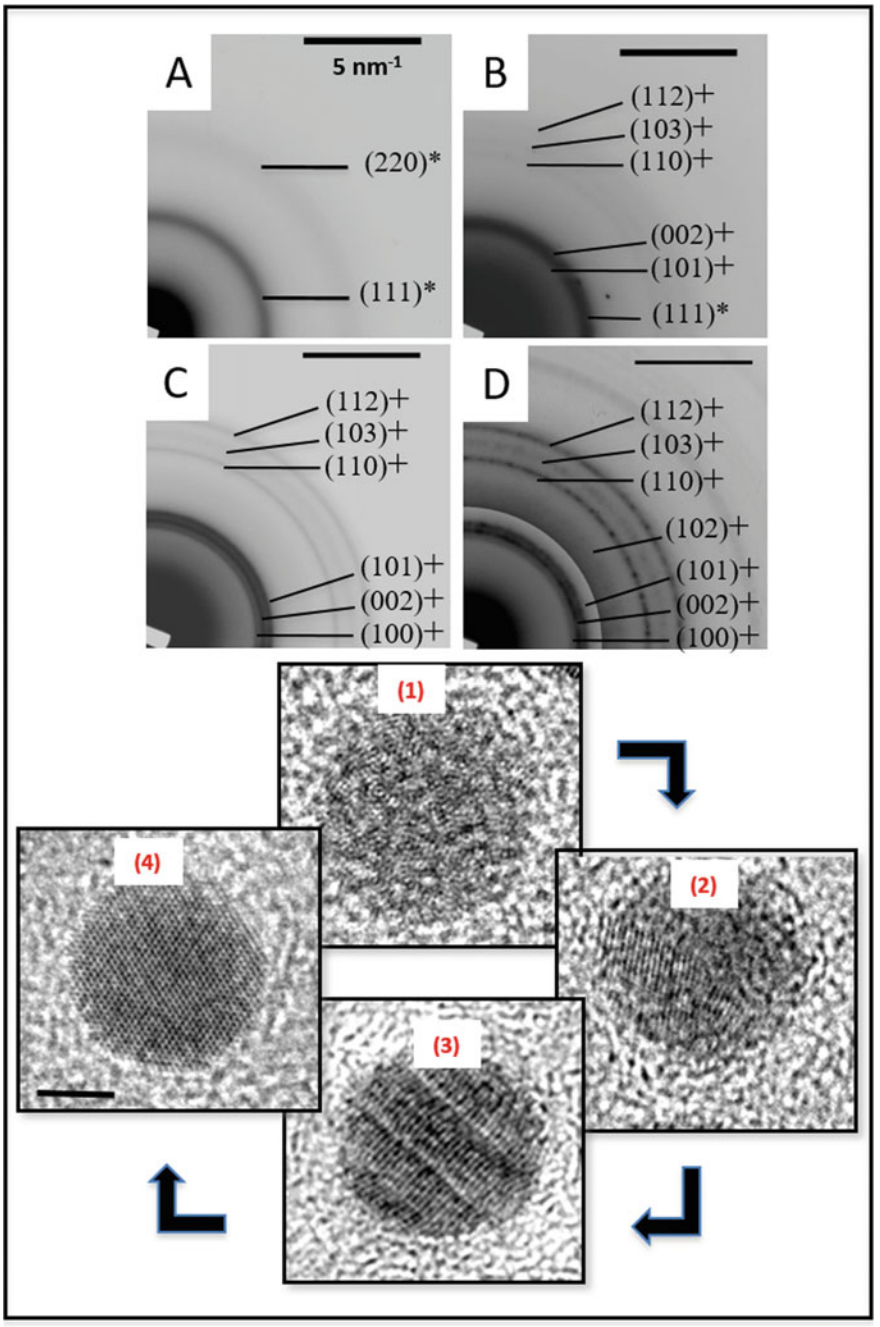

Fig. 8.4 Electron diffraction patterns of 7.5 nm Co nanoparticles obtained by the micellar approach not annealed (**a**) and annealed at 250 °C (**b**), 300 °C (**c**) and 350 °C (**d**). Reflections corresponding to the fcc (*) and hcp (+) structures. (1–4) Representative HRTEM images of Co nanoparticles annealed at various temperatures

8.2.1.3 Cobalt Nanoparticle Crystalline Structure Control

In order to improve the crystalline structure (nanocrystallinity) of the as-synthesized dodecanoic acid coated Co NPs (fcc polycrystals) obtained by the micellar approach, annealing treatments by (1) dry- and (2) solution-phase protocols are performed.

(1) Dry annealing is performed on 7.2 nm-NPs deposited on a TEM grid. The grid is placed in a close quartz ampule with a nitrogen atmosphere, finally placed in a furnace at various temperatures (250, 300 and 350 °C) for 15 min [23]. Electron diffraction and HRTEM (Fig. 8.4a, 4-1) reveal that the as-synthesized Co NPs are nearly amorphous with few ordered fcc domains less than 1 nm in size. After annealing at 250 °C, the structure is mainly hcp with some remaining fcc (Fig. 8.4b, 4-2). After annealing at 300 °C, pure hcp-Co NPs are obtained (Figs. 8.4c, 4-3), the defects of which tend to disappear at 350 °C (Figs. 8.4d, 4-4). Within error, the average diameter of the annealed NPs is unchanged.

(2) Recrystallization of fcc-Co into hcp-Co can be also driven by the solution-phase heating protocol. Using this novel strategy and conversely to the previous one, annealed NPs can be freely manipulated. Different protocols exist, always taking place in a refluxing bath, under nitrogen flux [2]. For instance, as-synthesized Co NPs are dispersed in high boiling point solvent, i.e., octyl ether. The solution is heated at 220 °C with a heating rate of 10 °C per minute up to 140 °C then more slowly with a heating rate of 2 °C per minute. Once the temperature is reached, NPs are maintained in the hot solution without aging or aged for 30, 90 and 180 min before a cooling step. Electron diffraction and HRTEM studies indicate the disappearance of the cfc phase just after reaching 220 °C, in favor of hcp-Co. After aging for 180 min, hcp-Co single crystals are obtained with a slight decrease in the mean diameter (6.5 nm against 7.2 nm for the native NPs).

Due to the high thermal stability of the dodecanoic acid coating, we show that dry- and solution-phase annealing treatments give rise to the structural transition from fcc-Co polycrystals to hcp-Co single crystals. No trace of Co oxide is detected. It is noticeable that reports in the literature of colloidal hcp-Co single crystals are very rare [14, 18].

8.3 Synthesis by Organometallic Approach

Besides the micellar soft chemical approach developed above, polyol synthesis of NPs appears to be one of the “simplest” routes to prepare NPs involving reduction of inorganic salt at high temperature (depending on the polyol) [39–41]. This is also the most representative approach of a complicated mixture synthesis of NPs as variations on the polyols, cobalt salt, surfactant, even bi-surfactant mixture, ruthenium seeds additive allow to reach different shapes, sizes and phases (mainly fcc-Co and hcp-Co) of nanocrystals [42–44]. As mentioned above, two other processes have been developed to produce monodispersed Co NPs in milder conditions using Co(0) or (I)

organometallic precursors instead of inorganic. The first one is related to carbonyl metal complexes (CMC, $CO_2(CO)_8$) and their thermal decomposition to generate NPs [16, 18]. The second one is dealing with hydrocarbyl complexes (HC) such as $Co(\eta^3\text{-}C_8H_{13})$ $(\eta^4\text{-}C_8H_{12})$ that readily decompose at lower temperature under a high pressure of dihydrogen [17]. However, the use of carbon monoxide as ligand (CMC approach) or a pressure of hydrogen (HC approach) still requires specific equipment in the laboratory. Moreover, these organometallic precursors are not readily available on a large scale and often as for the micellar route, annealing is necessary to reach pure hcp-Co phases (See above).

Based on the cobalt(II) salt and the cobalt(0 or I) organometallic approaches, a novel strategy has been developed by using a well-defined cobalt (I) halide complexes $(ClCo(PPh_3)_3)$ in presence of oleylamine (OAm) which should act as the solvent, the surfactant and as the reducing reagent [18]. Using this Co(I) complex heating in degassed OAm at 190 °C during 1 h, the formation of spherical monodispersed Co NPs is demonstrated by TEM study (Fig. 8.5). They are 9.2 nm spherical Co NPs, characterized by a very low size polydispersity of 6%. It is important to notice that no post-synthetic treatment is necessary to reach this control of the size distribution. TEM investigation allows a complete structural characterization of the cobalt NPs. A typical electronic diffraction pattern (Fig. 8.5A) obtained for a collection of NPs (Fig. 8.5c) consists of 7 diffractions rings characterized by 0.216 nm, 0.203 nm, 0.190 nm, 0.146 nm, 0.125 nm, 0.114 nm and 0.106 nm distances from center to outward, respectively. These distances correspond to the (100), (002), (101), (102), (110), (103) and (201) planes of the hcp structure of cobalt metal, when compared with the bulk values.

Magnetic characterization confirms the ferromagnetic behavior of these cobalt NPs even at room temperature, which is expected for these 9.2 nm in size hcp cobalt NPs [18, 45].

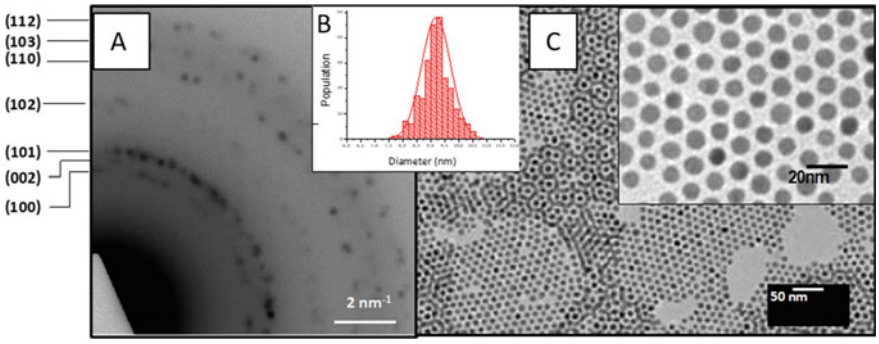

Fig. 8.5 TEM characterization of 9.2 nm hcp cobalt nanoparticles obtained by the organometallic approach. **a** SAED, **b** size histogram, **c** TEM images

8.4 Assemblies of Cobalt Nanoparticles

8.4.1 Key Parameters Involved in the Nanoparticle Organization

For a long time, experimentalists and theoreticians have sought the optimal conditions to obtain well-defined self-organization of NPs in 2D and 3D lattices. Here, we will focus on the self-assembly in solution. Three major parameters have become evident for this process: the speed of evaporation, the monodispersity of the particle size and the interaction between the NPs.

Concerning the *evaporation speed*, it has been observed that it has too be sufficiently small to allow the cluster of nanoparticles to come together to form mesostructures. This is usually empirically reached by a confinement of the beaker used for the evaporation.

Concerning the *monodispersity*, experiments have shown that well-ordered superlattices are observed at polydispersities lower than 5%, while polydispersities larger than 12% suppress ordered assemblies [46]. The theoretical study of solid–fluid transitions in hard-sphere systems using Monte Carlo simulations has given explanation for this observation [47, 48]. It reveals the existence of a terminal polydispersity above which, no crystallization can occur. The highest polydispersity is 5.7% for the solid and about 12% for the fluid. Fractionation enables a fluid of larger polydispersity to crystallize into several solids of smaller polydispersity and different average size. Therefore, a batch of nanocrystals synthesized with an average polydispersity smaller than 12% may form superlattices by fractionation, while within a large superlattice, the average polydispersity should be smaller than 6%. Simulations have shown that kinetic factors are the reason for the existence of the terminal polysdispersity [49]. Usually the free energy barrier to nucleation continuously decreases with increasing concentration enabling the formation of crystals. The simulations show that in polydisperse samples, the free energy barrier passes through a minimum, thus suppressing crystallization. Recent simulations have also shown that the fractionation may be a complex process [50]. We have carried out simulations in the 2D case using Lennard–Jones potential, which show this transition from an ordered to a disordered state when the polydispersity is increased. For a polydispersity of 6%, the left side of Fig. 8.6 shows an ordered assembly characterized by well-defined spots in the two-dimensional pair distribution function (see insert). This order disappears for a polydispersity of 15% on the right side of Fig. 8.6.

The third key parameter is the *interaction potential between the NPs*. To obtain a self-assembly purely by confinement due to the evaporation of the solvent, this interaction has to be repulsive even at the end of evaporation. In general, the interaction for two magnetic particles covered with chain-like ligands in a solvent may be expressed in the following way [51–53]:

$$u_{\mathrm{tot}}(r) = u_{vdW}(r) + u_{\mathrm{elastic}}(r) + u_{\mathrm{mix}}(r) + u_{\mathrm{ionic}}(r) + u_{\mathrm{dipole}}(r) \qquad (8.1)$$

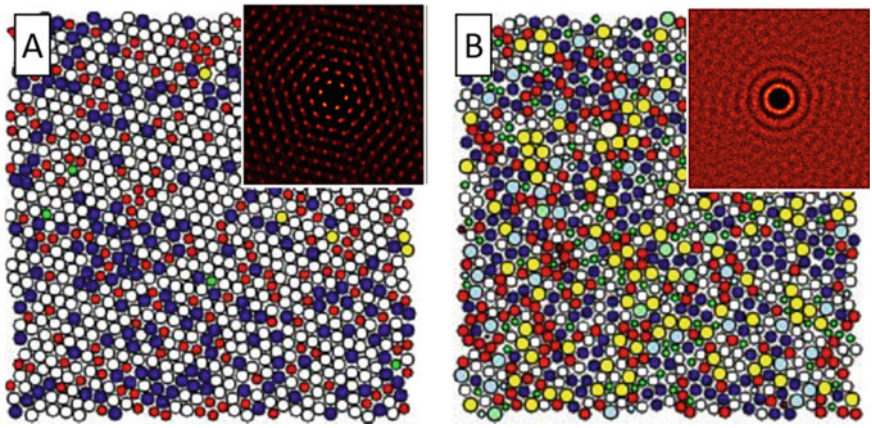

Fig. 8.6 Snapshots of the final configuration of particle assemblies obtained by 2D Monte Carlo simulations for two polydispersities **a** 6%, **b** 15%. The different colors correspond to various particle sizes. The inserts show the two-dimensional pair distribution functions for the given particle assemblies

$u_{vdW}(r)$ corresponds to the van der Waals attraction between the cores of the particles. It is calculated from the effective Hamaker constant reduced with respect to its value in vaccuum due to the presence of the solvent medium. $u_{\text{elastic}}(r)$ is the repulsion due to elastic compression of the ligands. $u_{\text{mix}}(r)$ described the free energy due to the mixing of the thiol ligands, when the two particle approach. This is accompanied by a demixing of solvents and ligands. This term may be attractive or repulsive depending on the solvent. The equations for the last three terms are given in reference 53. When the nanoparticles are dissolved in an aqueous ionic solution, an additional repulsive term $u_{\text{ionic}}(r)$ appears due to the formation of a cloud of counter-ions around charged nanoparticles. This can be for example described by a DLVO term or by the integral equation theories. Finally, we have the dipolar term $u_{\text{dip}}(r)$ due to the magnetism of the particles, which can be estimated from the magnetization at saturation of the magnetic material. With the help of the code NanoForceG developed in our laboratory, the interaction potential in (8.1) can be easily calculated. In Fig. 8.7, the interaction potentials for cobalt nanoparticles coated with dodecanoic acid are shown. Figure 8.2a gives the potential for various nanoparticle sizes using decane as solvent. For particles smaller than 10 nm, the attraction between the nanoparticles is sufficiently weak to ensure the formation of well ordered assemblies. At larger nanocrystal size, the van der Waals interaction due to the metallic cores becomes important. Moreover, for size larger than 15 nm the dipolar term is sufficiently strong to influence the nanoparticle assembly. This may lead to the formation of chains, which have been experimentally observed for magnetic nanoparticles of this size [54–56]. In Fig. 8.7b, the influence of the solvent for cobalt nanoparticles of 5 nm is shown. As expected, the alkanes are good solvents which lead to a repulsion between the nanoparticles, while protic and polar solvents such as water and acetone are bad solvent. However, it is interesting to observe that there is an intermediate case,

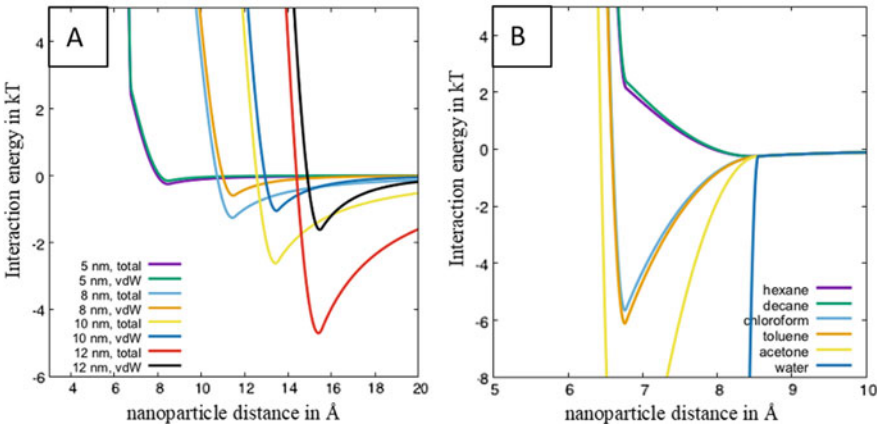

Fig. 8.7 Interaction energy between cobalt nanoparticles coated with dodecanoic acid. Figure **A** shows the evolution with solvent for a nanoparticle size of 5 nm. Figure **B** gives the dependence on the nanocrystals size for decane as solvent. The total potential and the one without the dipolar term (denoted vdW) are plotted

neither really good nor bad, where solvents such as chloroform or toluene induce some attraction. This attractive force can be used to assemble the nanoparticle in a controlled way in the solution without evaporation of the solvent. Thus, well-defined supercrystals made of nanoparticles can be grown in solution [53, 54]. This opens up a new way to fabricate nanomaterials. We would conclude this section with a short discussion of the ionic term, which appears in aqueous solutions. During evaporation, the salt concentration increases which leads to a collapse of the ionic cloud and may induce an uncontrolled aggregation of the particle due to the van der Waals term. This explains why non-aqueous systems are usually preferred to obtain controlled nanoparticle assemblies. However, this does not exclude aqueous solutions of nanoparticles to obtain mesostructures. Under specific conditions, the formation of isolated chains has also been experimentally observed, which has been explained by simulations [57].

8.5 2D Self-Organizations of Cobalt Nanoparticles Synthesized by Micellar Approach

2D self-organizations of Co NPs are prepared by depositing 1 drop of a colloidal solution of either (1) as-synthesized fcc-Co polycrystals with various sizes 3.9 nm (S1), 4.6 nm (S2), 7.7 nm (S6), 9.3 nm (S7) or (2) solution-phase annealed 7.1 nm hcp-Co single crystals on a highly ordered pyrolytic graphite (HOPG) grid. The concentration of NPs is fixed at 5.5 10^{-7} M. Subsequently to their deposition in

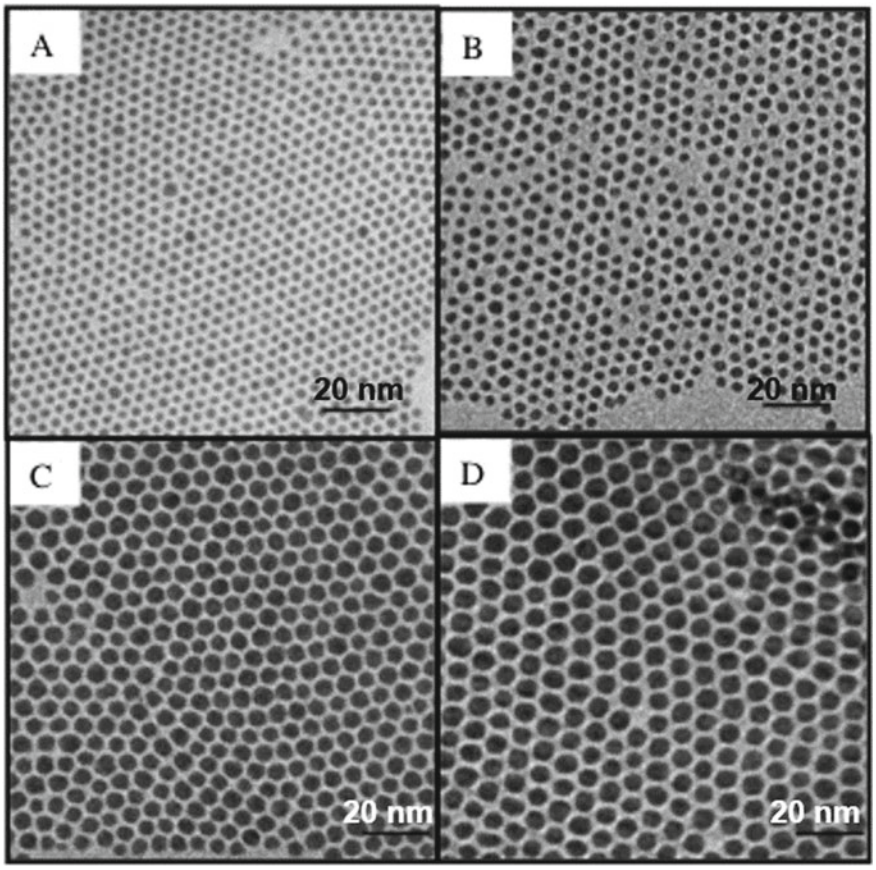

Fig. 8.8 TEM images of 2D ordered arrays of native fcc-Co polycrystals obtained by the micellar approach **a** 3.9 nm (S1), **b** 4.6 nm (S2), **c** 7.7 nm (S6), **d** 9.3 nm (S7)

2D ordered arrays, the as-synthesized fcc-Co polycrystals can be submitted to a dry-annealing process (3).

(1) Whatever the size of the as-synthesized fcc-Co polycrystals, TEM study (Fig. 8.8a–d) shows the formation of 2D ordered arrays with hexagonal symmetry [21]. These organizations are determined by both the diameter and the length of the C12 coating agent. For 3.9 nm, the mean center-to-center distance between particles (Dc-c) and interparticle gap (Di-p) are 5.9 nm and 2.1 nm, respectively (Table 8.3). Taking into account length of dodecanoic acid in the cis–trans configuration, i.e., 1.77 nm, the low $D_{i\text{-}p}$ value indicates interdigitation between the C12 alkyl chains. The use of larger Co NPs, e.g., 4.6, 7.7 and 9.3 nm results in a significant decrease of the Di-p values found equal to 2.3, 1.6 and 1.4 nm, respectively. This behavior is attributed to the van der Waals attractions between the metallic core, which magnitude increases with the particle volume.

Table 8.3 Structural characteristics of 2D ordered arrays presented in Figs. 8.5 and 8.6 and obtained by deposition of Co NPs characterized by an average diameter D and a size distribution σ. $D_{c\text{-}c}$; center-to-center nanoparticle distance; $D_{i\text{-}p}$: inter-particle distance

Sample	D (nm)	σ (%)	$D_{c\text{-}c}$ (nm)	$D_{i\text{-}p}$ (nm)
Co_{fcc} (*S1*)	3.9 ± 0.1	12	5.9 ± 0.1	2.1 ± 0.1
Co_{fcc} (*S3*)	4.6 ± 0.1	11	6.9 ± 0.1	2.3 ± 0.1
Co_{fcc} (*S6*)	7.7 ± 0.1	12	9.3 ± 0.1	1.6 ± 0.1
Co_{fcc} (*S7*)	9.3 ± 0.1	15	10.5 ± 0.1	1.4 ± 0.1
Co_{hcp} (S_{ann} 1)	7.1 ± 0.2	8	9.8 ± 0.2	2.7 ± 0.2
Co_{hcp} (S_{ann} 2)	7.0 ± 0.2	10	10.3 ± 0.2	3.3 ± 0.2

(2) Similarly to the native fcc-Co polycrystals, the deposition of solution-phase annealed 7.1 nm hcp-Co single crystals (Fig. 8.9a and Table 8.3) gives rise to 2D long-range ordered arrays characterized by center-to-center distance and interparticle gap of 9.8 nm and 2.7 nm, respectively (*Sample Sann* 1) [58]. The increase in the $D_{i\text{-}p}$ of around 1 nm compared to the arrays composed of similar size native NPs is attributed to the presence of larger amount of coating agent, related to the annealing protocol. By slightly increasing the concentration of the colloidal solution, ordered multilayers can also be obtained (Fig. 8.9b).

(3) 2D arrays of hcp-Co single crystals can also result from dry annealing at 350 °C of 2D ordered arrays of as-synthesized Co polycrystals. Such 2D arrays are characterized by NP diameter, $D_{c\text{-}c}$ and $D_{i\text{-}p}$ values equal to 7.0, 10.3 and 3.3 nm, respectively (Fig. 8.9c, Table 8.3). The $D_{i\text{-}p}$ increases after annealing, while the $D_{c\text{-}c}$ remains almost unchanged [23, 58]. NP size decrease is partly attributed to the structural transition of the NPs from the poorly crystalline phase to the hcp-Co single-crystalline phase. As shown in Fig. 8.9d, when the dry annealing is performed on ordered multilayers of Co polycrystals, the assembly keeps their integrity.

Whatever the protocol used is, 2D and thin 3D arrays of Co NPs can be obtained. We show that the characteristics of these organizations can be tuned by varying the mean diameter and the nanocrystallinity of the Co NPs, as well as the mean center-to-center distance between particles and interparticle gap. The high stability of these assemblies, especially in the dry and solution-phase annealing cases, is due to the high thermal stability of dodecanoic acid coating agent.

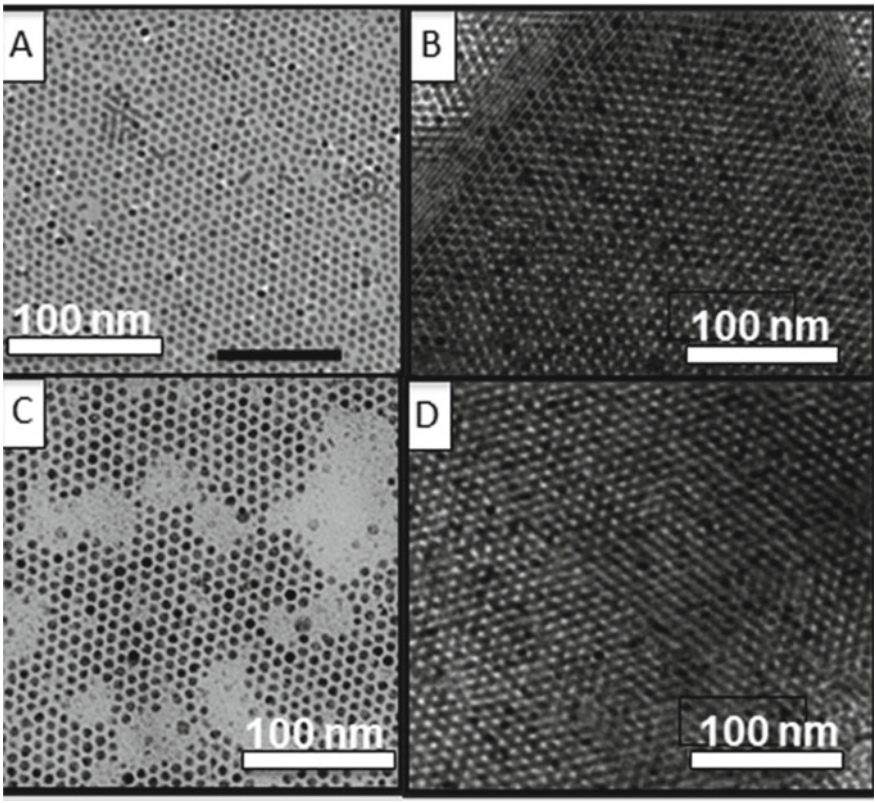

Fig. 8.9 TEM images of a monolayer (**a**) and a multilayer (**b**) of solution-phase annealed 7.1 nm hcp-Co single crystals obtained by the micellar approach. TEM images of a monolayer (**c**) and a multilayer (**d**) of 7.0 nm hcp-Co single crystals obtained by dry annealing of a native monolayer and multilayer of fcc-Co polycrystals

8.6 2D Self-Organizations of Cobalt Nanoparticles Synthesized by Organometallic Approach

The self-assembly process is not dependent of the route used to synthesize the cobalt NPs. As presented above, the 9.2 nm spherical Co NPs coated by oleylamine (OAm) are characterized by low size dispersity (0.6%). By simply depositing a drop of a colloidal solution of these NPs dispersed in toluene, onto amorphous carbon substrates, they self-organize in a long-range 2D hexagonal ordering (Fig. 8.10a) and thin 3D assemblies. When a concentrated solution is allowed to slowly evaporate on graphite substrate, well-developed supercrystals sitting on their larger flat facets are observed. (Fig. 8.10b, c). This is characteristic of the formation of the so-called supercrystals resulting from 3D periodic arrangement of the NPs either in fcc or hcp organization.

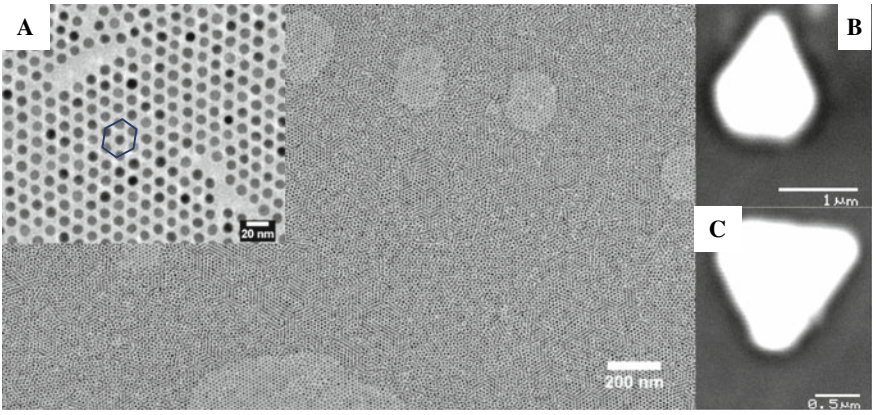

Fig. 8.10 9.2 nm spherical cobalt nanoparticles with 6% polydispersity obtained by the organometallic approach self-organized in **a** 2D and thin 3D assemblies as obtained by drop deposition on amorphous carbon. **b** and **c** Superlattices obtained by slow evaporation at room temperature on graphite substrate

As mentioned above, this is due to the attractive Van der Waals interactions between the metallic cores, the "chemical bonds" of self-assemblies resulting from the interdigitation of the ligand molecules (OAm). It should be noticed that from Fig. 8.10a, the deduced interparticle distance is 4.1 nm, which drastically limit the interparticle interaction. As a consequence, no aggregation occurs in the solvent or on the substrates during the deposition process. Indeed, the 2D patterns are purely hexagonal patterns as well as in the thin 3D organization (Fig. 8.10). In case of dipole–dipole interaction, non-close packed superlattices are often observed, which is not the case here. Indeed we can claim that no aggregation occurs in solution due to dipolar interaction.

8.6.1 3D Self-Organizations of Cobalt Nanoparticles

8.6.1.1 Control of the Mesoscopic Structure in 3D Assemblies of Co NPs

Dodecanoic acid coated Co NPs synthesized by micellar approach can be used as building blocks to form 2D ordered arrays but also long-range 3D superlattices also called supercrystals. For this aim, an HOPG substrate is horizontally immersed in 200 µl of a highly concentrated colloidal solution (5.5×10^{-7} M) of 7.2 nm. The solvent evaporates under nitrogen flux and the substrate temperature vary from 10 to 45 °C [59]. At 10 °C, TEM study shows the formation of a thin film with a smooth surface (Fig. 8.11a). The diffractogram shows a broad and low intensity Bragg peak indicating the absence of long-range ordering of NPs (Fig. 8.11b). By increasing the temperature from 25 to 45 °C, the film appears cracked and the size of the resulting isolated domains increases with increasing the substrate temperature (Fig. 8.11c,

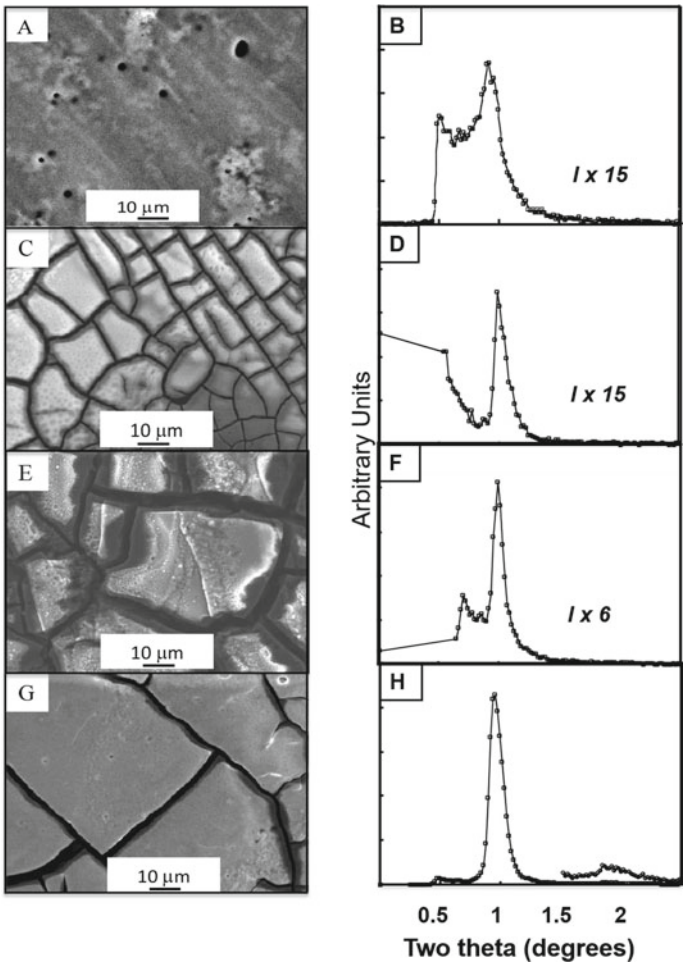

Fig. 8.11 SEM images obtained by depositing of fcc-cobalt nanoparticles obtained by the micellar approach, on HOPG substrate at various temperatures: **a** 10 °C, **c** 25 °C, **e** 35 °C, **g** 45 °C. **b**, **d**, **f** and **h**, corresponding diffractograms

e, g). For temperatures equal to 25, 35 and 45 °C, the average domain areas are 400, 1000 and 2500 μm^2, respectively, and their thickness can reach 5 µm. SAXS study clearly indicates a long-range fcc ordering of the NPs [59]. For instance, the X-ray diffraction pattern of the sample obtained at 45 °C (Fig. 8.12) shows various spots which coordinates, when compared to the theoretical values of various structures, correspond to an fcc structure [6]. At 25 °C, the (111) reflection shown in the diffractogram (Fig. 8.11d) is intense and nearly resolution limited (i.e., 0.05 nm^{-1}), indicating long-range ordering out of the plane. The interparticle distance is found around 3.60 nm (Table 8.4). By increasing the temperature from 25 to 45 °C, the peak with $\delta q_{1/2}$ decreases from 0.05 to 0.035 and 0.034 nm^{-1}, respectively, and become

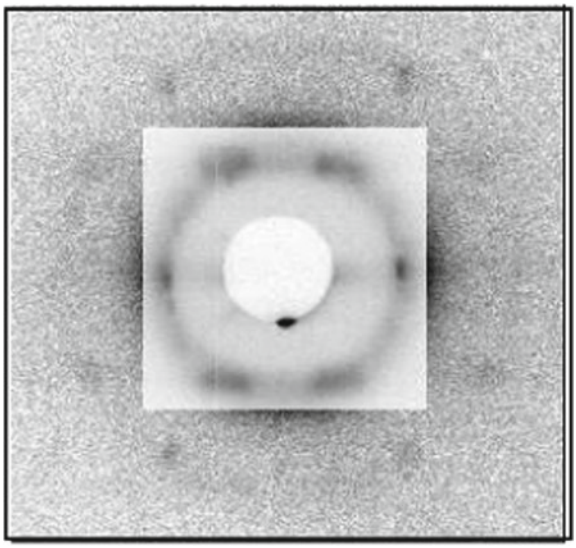

Fig. 8.12 X-ray diffraction pattern of sample obtained by depositing fcc-cobalt nanoparticles obtained by the micellar approach, on HOPG substrate at 45 °C

Table 8.4 Structural characteristics of 3D assemblies of Co NPs (7.2 nm) obtained at various temperatures and extracted from the diffractograms presented in Fig. 8.7. $\delta q_{1/2}$: the half width at half maximum; $D_{c\text{-}c}$: center-to-center nanoparticle distance; $D_{i\text{-}p}$: inter-particle distance

Substrate temperature	$\delta q_{1/2}$ (nm^{-1})	$D_{c\text{-}c}$ (nm)	$D_{i\text{-}p}$ (nm)
12 °C	0.190	11.75 ± 0.2	4.55 ± 0.2
25 °C	0.050	10.80 ± 0.2	3.60 ± 0.2
35 °C	0.035	10.80 ± 0.2	3.60 ± 0.2
45 °C	0.034	10.60 ± 0.2	3.45 ± 0.2

increasingly intense (Table 8.4). This behavior clearly evidences an increase in both the size and the coherence length of fcc crystallized domains, i.e., the supercrystals. By increasing the temperature from 25 to 45 °C, the mean interparticle distance decreases from 3.60 to 3.45 nm (Table 8.4) that further evidences the improvement of the mesoscopic ordering.

Hence, by just controlling the substrate temperature, mesoscopic ordering of 3D assemblies of Co NPs can be tuned from disordered to highly fcc ordered assemblies. This behavior is explained by the control of the diffusion of NPs within the solution and on the HOPG substrate.

8.6.1.2 Collective Magnetic Properties in 3D Assemblies of MNPs

Within a NP, small enough to have a single magnetic domain, all atomic spins are aligned in the same direction, and thus, the particle can be considered as a point dipole (or superspin) with a large magnetic moment. Some remarkable phenomena have been observed in MNPs; the most well-known among them being that of superparamagnetism (SPM) of non-interacting NPs, where the magnetic moments of each NPs act independendly [60]. Superparamagnetic NPs have found their use in many fields of applied technology including, but not limited to, biomedicine [61], magnetic resonance imaging [62] data storage [60, 63].

In an assembly of highly concentrated NPs, the materials' magnetic properties can be greatly influenced by the dipolar interactions between NPs. It has been found that at sufficiently high concentrations, the interparticle dipolar interactions can produce "collective states" below a system-dependent transition temperature T_c. The observed collective states are almost invariably "disordered" and thus called "superspin glasses" (SSG) as they show many of the phenomenology found in atomic spin glasses [64, 65]. Further increasing inter-particle correlations, the SSG state is predicted to transform into long-range ordered dipolar superferromagnetic (SFM) state. However, a clear-cut experimental evidence of a dipolar SFM state in real 3D NP assemblies has not yet been reported. This is likely due to the stringent geometrical conditions for inducing such a complex state: i.e., long ellipsoidal sample shape, highly ordered fcc or bcc lattice structure and parallel alignment of anisotropy-axis [66, 67]. Due to their structural characteristics, fcc supercrystals of Co NPs are considered as good candidates to display dipolar SFM properties [68, 69]. In the superferromagnetic transition region (from superparamagnetic to superferromagnetic), enhanced magnetocaloric effect is expected, bringing this novel class of material one step close to application in the field of energy efficiency (refrigeration) [70, 71].

8.6.1.3 Collective Magnetic Properties in 3D Fcc Supercrystals of Fcc-Co Polycrystals

The first aim is here (1) to study the effect of the mesoscopic order in 3D assemblies of fcc-Co polycrystals (characterized by a low anisotropy) on the magnetic properties by DC susceptibility measurements. The second one is (2) to study the possibility of superspin glass behavior in the same system by AC susceptibility measurements.

(1) The effect of the structural order of 3D assemblies on magnetic properties is studied by considering highly ordered fcc supercrystals and disordered assemblies. Both ordered and disordered samples are made with the same batch of 7.5 nm fcc-Co polycrystals. The zero field cooled (ZFC) magnetization versus temperature is measured by cooling the sample in zero applied field from 300 to 5 K, applying a field of 20 Oe and then measuring the magnetization as the

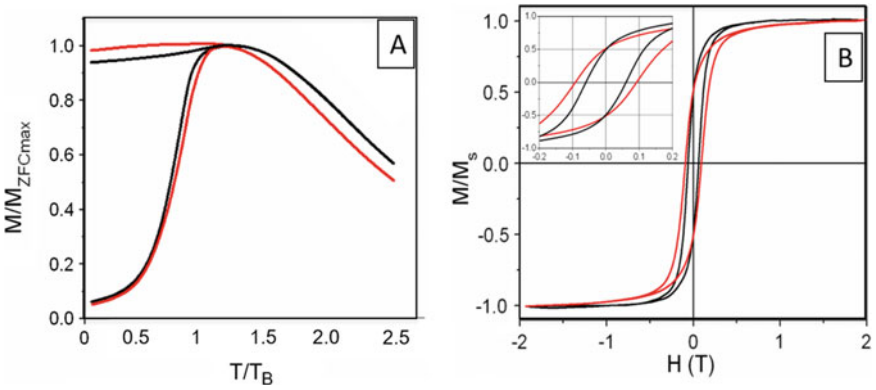

Fig. 8.13 **A** ZFC magnetization versus T/T_B curves for a supercrystalline film (red) and a disordered 3D assembly of 7.5 nm-Co nanoparticles (black). **B** Magnetization versus field curves at 5 K, normalized to M_S of a supercrystalline film (red) and disordered 3D assembly (black). Inset: Magnification of the low field region

sample is heated. To measure the field cooled (FC) magnetization versus temperature, a field of 20 Oe is applied at 300 K before cooling the sample to 5 K and subsequently measuring the magnetization from 5 to 300 K. The magnetization versus field measurements are carried out at 5 K after zero field cooling of the sample. All magnetic measurements are performed with the applied field parallel to the substrate. Figure 8.13a shows the ZFC and FC curves normalized (ZFC_{norm} and FC_{norm}) to the blocking temperature, T_B, of both the ordered (black) and disordered (red) samples [69].

In ZFC measurements, the sample has been cooled in zero field; hence, there is no net alignment of the superspins at 5 K and the magnetization is close to zero. As the temperature increases, the superspin become progressively "unblocked," aligning toward the field direction and the magnetization increases until reaching a maximum defined as the blocking temperature, T_B. Above T_B, the behavior is superparamagnetic. That is, the thermal energy increases to such an extend that that the increase dynamic rotation of the superspins prevents alignment in the field direction and the magnetization decreases with increasing temperature. In the FC curve, the magnetization remains almost constant from 5 K to T_B. Above T_B, the behavior is superparamagnetic and the magnetization decreases with increasing temperature. Whatever the mesoscopic ordering is, T_B does not vary significantly, it value is around 100 K. This is significantly higher value than has previously been observed for dilute systems of similar Co NPs [2] and indicating strong dipolar interactions between the NPs. Besides, the ZFC_{norm} peak of the disordered sample is significantly enlarged compared to that of the ordered sample. The width of the ZFC peak depends on the distribution of energy barriers, E_b, in the assemblies: larger the distribution, broader the peak. The barrier energy is the sum of the anisotropy energy ($E_a = k_a V$ where k_a is the anisotropy constant and V is the NP volume) and the interparticle dipole

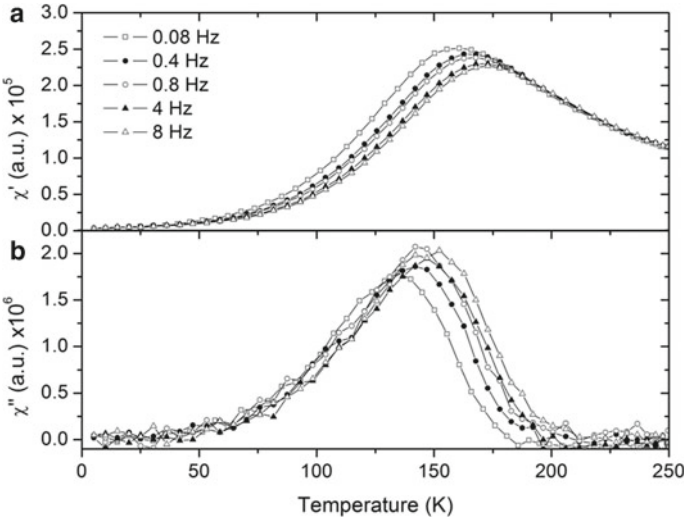

Fig. 8.14 **a** In-phase and **b** out-of-phase part of the AC susceptibility versus temperature, measured at frequencies between 0.08 and 8 Hz of a supercrystalline film of 8 nm-Co nanoparticles

interaction energy (E_{dd}) [72]. Because both ordered and disordered samples are made with the same batch of NPs, we can rule out any effect of NP volume distribution and anisotropy. The behavior observed is explained by the mesoscopic ordering of the assemblies. Indeed, the dipolar interactions are known to be highly directionally sensitive [69]. In highly ordered fcc supercrystal sample, each NP has the same geometrical coordination and the interparticle distance between NPs is uniform. This is not true in the disordered sample. Then, the distribution of E_{dd} and hence E_b, in the disordered sample is greater compared to the supercrystal sample, inducing the broadening of the ZFC peak for the disordered sample.

Figure 8.13b shows the corresponding magnetization versus field curves. For the supercrystal sample, the coercive field, H_c, is increased compared to that of the disordered sample (900 and 600 Oe respectively). This is attributed to a more collective behavior in the supercrystal sample arising from the long-range ordered fcc structure, which inhibits the rotation of the superspins. Besides, the approach to saturation is slower in ordered sample than in the disordered sample. This last feature in good agreement with the variation of H_c, is explained by a higher anisotropy in ordered sample compared to the disordered sample [73, 74].

This result constitutes the first example of collective magnetic properties due to the mesoscopic ordering in 3D assemblies of MNPs.

(2) In order to study the possibility of superspin glass (or SFM) state behavior in fcc supercrystals of 8 nm fcc-Co polycrystals, in addition to DC susceptibility measurements (See below), AC susceptibility measurements are also performed [75]. The latter measurements are required to define the characteristics relaxation times present in the system. The in-phase (χ') and out-of-phase

(χ'') components of the AC susceptibility versus temperature, are measured in a range of AC frequencies varying by 2 decades in magnitude (Fig. 8.14a, b). Both the χ' and χ'' components show a clear frequency dependence, where the temperature at which the maximum susceptibility is observed (T_{peak}) increases with increasing frequency. T_{peak} is defined as the temperature at which the relaxation time of the system, τ, is equal to the observation time, t, which is related to the measurement frequency by $t = 1/\omega$, where $\omega = 2\pi f$. In order to differentiate between superparamagnetic and superspin glass behaviors, which display both the same frequency dependence in an AC measurement, the change in T_{peak} with frequency has to be quantitatively analyzed and hence extract a value of τ_0. For a superparamagnet, characterized by negligible dipolar interactions between the magnetic moments, the frequency dependence should follow an Arrhenius law $\tau = \tau_0 e^{\frac{Ea}{k_b T}}$ where is the angular inverse attempt frequency, E_a is the anisotropy energy, and k_B is the Boltzmann constant. By plotting $\log_{10}\tau$ versus $1/T_{\text{peak}}$ and fitting the data to a straight line, the value of τ_0 can be extracted and in this case we find $\tau_0 = 10^{-31}$ s [75]. This unphysically small value indicates that this system cannot be described by simple energy barrier blocking and thermal activation. Actually and analogously to a spin glass, the magnetic response is also influenced by interparticle interaction we have to take into account. In spin glass systems, the dynamic behavior shows a critical slowing down, and hence, the characteristic relaxation time diverges to a finite static glass temperature T_g, according to a critical power law $\tau = \tau^* (T_{\text{peak}}/{T_g}^{-1})^{-z\nu}$, where τ^* is the relaxation time of an individual NP moment and $z\nu$ is a critical exponent. T_g is taken as the maximum in the DC ZFC magnetization curve. Fitting the data yields $\tau^* = 10^{-9\pm3}$ s and $z\nu = 12 \pm 2$. This value of τ^* is in good agreement with values found for spin glasses, and $z\nu$, although slightly high, is also compatible within error to that expected for spin glasses [76–78].

Spin glass and superspin glass materials are known to show aging and memory effects, which can be demonstrated by a simple DC magnetization experiment. The sample is zero field cooled from above T_g to a temperature T_s typically equal to 0.7 T_g where a waiting time of $t_w = 104$ s is imposed before continuing cooling down to low temperature. A small field is then applied and the magnetization is measured on heating. A deviation from the reference ZFC curve (with no stop during cooling) is observed at T_s, which is known as a "memory dip," so-called as the system has "remembered" the relaxation toward a zero magnetization value (aging) that occurred during the cooling process.

The results of these AC and DC susceptibility investigations provide strong evidence for superspin glass behavior in long-range ordered fcc supercrystals made of low anisotropy 8 nm fcc-Co polycrystals.

8.6.1.4 Collective Magnetic Properties in Fcc Supercrystals of Hcp-Co Single Crystals

The aim is here to investigate the effect of fcc supercrystals anisotropy on the super-spin glass behavior and the possibility for these systems to undergo a transition toward a dipolar SFM state. For this aim, 3D fcc supercrystals of Co polycrystals are submitted to the same thermal treatment used to anneal the 2D ordered arrays, at 250, 300 and 350 °C [23]. SEM study (Fig. 8.15a, c, e, g) indicates that heating process induces the formation of cracks in the supercrystalline film. The beginning of the formation of cracks is observed at 250 °C (Fig. 8.15c). With increasing the temperature, the process is progressively intensifying to give rise, at 350 °C, to isolated domains (Fig. 8.15g). GISAXS study clearly indicates that, whatever the heating temperature is, the fcc superstructure is maintained but not only. We observe both (1) a progressive decrease of the width at half maximum ($\delta 1/2$) of the first-order (111) Bragg peak and (2) an increase in the second-order reflection intensity (Fig. 8.15b, d, f, h and Table 8.5). This clearly indicates an increase in the coherence length of the fcc supercrystals. Besides, the interparticle distance between NPs progressively decreases from 3 to 2.2 nm (Table 8.5). This result shows that we are able to control both the crystalline structure of Co NPs and their 3D superstructure. Hence, heating the fcc supercrystals at 350 °C allows the formation of long-range ordered fcc supercrystals composed of hcp-Co single crystals.

The thermal treatment performed on the fcc supercrystals induces drastic changes in the magnetic behavior [11]. As shown in Fig. 8.16a–d, the blocking temperature, T_B, progressively increases from 112 K for the native sample to 280 K for the sample annealed at 350 °C. This behavior is mainly explained by the crystallographic transition from almost amorphous NPs to hcp-Co single crystals. After the annealing at 250 °C, the normalized ZFC peak to the T_B (Fig. 8.16e) is broadened compared to the native sample. At this temperature, the crystallographic transition is not complete as evidenced by electron diffraction study, leading to a distribution of the anisotropy in the sample and then to a distribution of the barrier energies. Annealing performed at higher temperature, 300 and 350 °C, induces a progressive narrowing of the ZFC_{norm} peak until the native width is recovered. This behavior is attributed to the crystallographic transition that is complete at 350 °C.

The AC susceptibility as a function of temperature and frequency shows usual "critical slowing down" behavior indicating the existence of collective states below T_c in all fcc supercrystals [79]. Using the Vogel-Fulcher model for weakly interacting systems, the particle anisotropy energy E_a and the effective temperature (related to the interaction energy between NPs) are extracted. As a general trend, the "interaction-to-anisotropy" energy ratio becomes larger with heating of the sample, i.e., with both improving Co nanocrystallinity and decreasing the interparticle gap. Such a behavior is favorable for the formation of a dipolar SFM state.

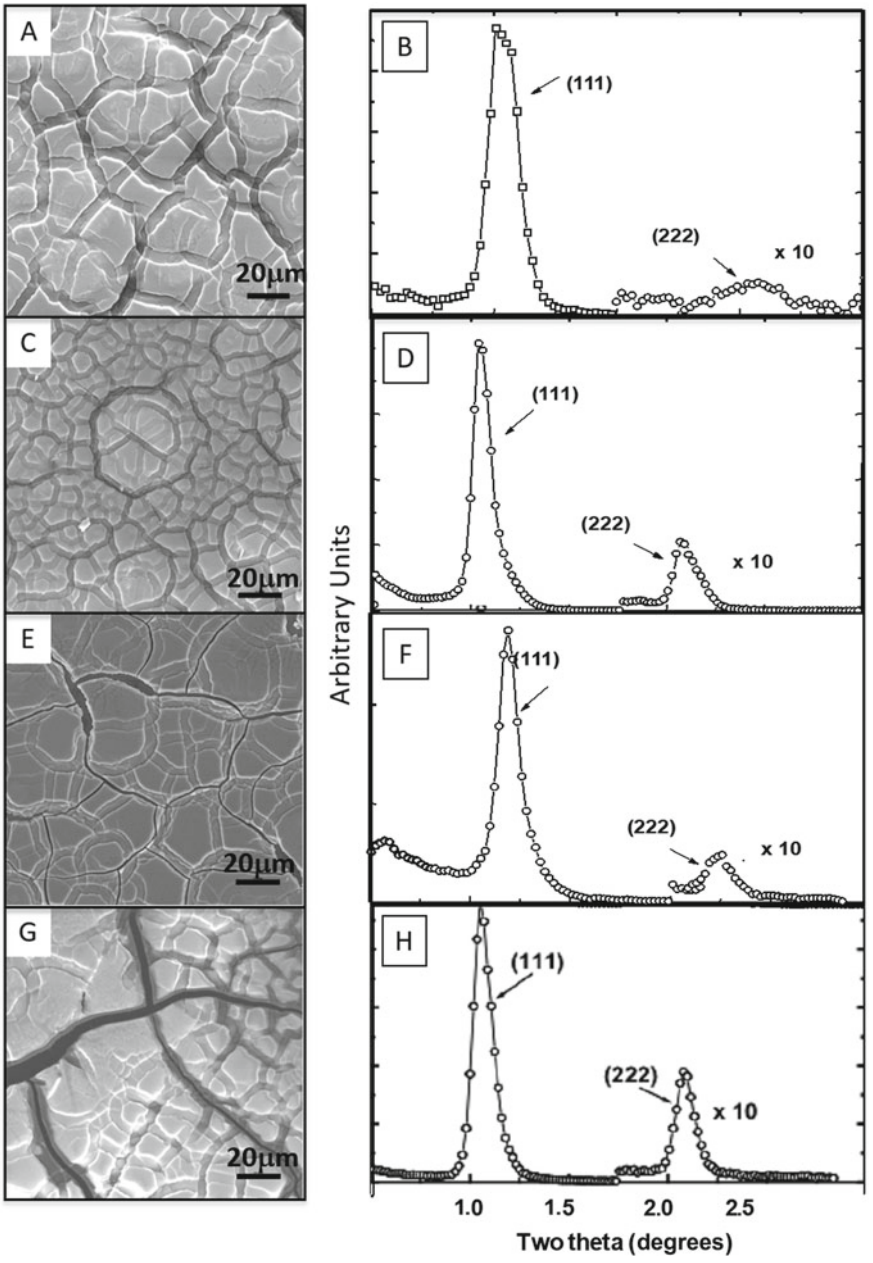

Fig. 8.15 SEM images of a supercrystalline film (thinner region) of 7.5 nm Co nanoparticles obtained by the micellar approach, not annealed (**a**), annealed at 250 °C (**c**), at 300 °C (**e**) and at 350 °C (**g**). **b**, **d**, **f** and **h** Corresponding diffractograms

Table 8.5 Structural and magnetic parameters extracted from the GISAXS patterns, the ZFC magnetization curves and the hysteresis. $\delta q1/2$: the half width at half maximum; $D_{c\text{-}c}$: center-to-center NC distance; $D_{i\text{-}p}$: border to border distance of NCs considering a NC size of 7.5 nm; T_B: blocking temperature; M_s: saturation magnetization; Msnat/Msann: ratio of native M_s to annealed M_s; H_c: coercivity

Sample	$D_{c\text{-}c}$ (nm)	$D_{i\text{-}p}$ (nm)	T_B (K)
Co_{fcc} (*Native*)	10.5 ± 0.1	3.0 ± 0.5	112 ± 3
Co_{hcp} (*Annealed at* 350 °C)	9.7 ± 0.1	2.2 ± 0.5	280 ± 3

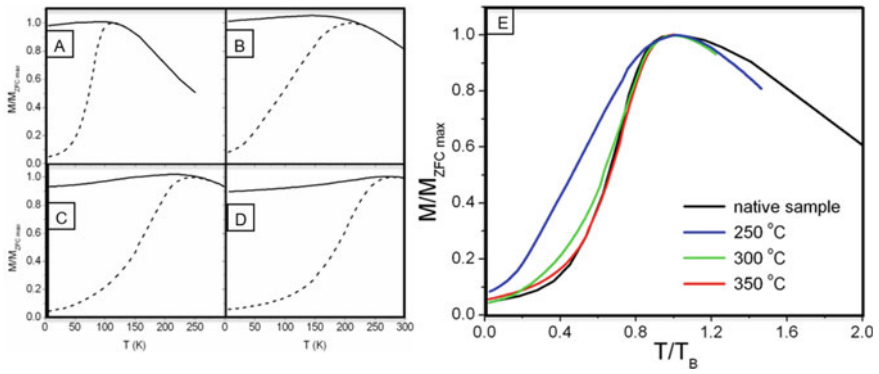

Fig. 8.16 FC (full lines), and ZFC (dashed lines) magnetization versus T curves of a supracrystalline film of **a** native and annealed at **b** 250 °C, **c** 300 °C, **d** 350 °C. **e** Corresponding ZFC magnetization versus T/T_B curves

8.7 Theory of Self-Organization of Magnetic Nanoparticles Under Magnetic Field

The application of a magnetic field during the evaporation leads to the formation of mesostructures. Thus, when the field is parallel to the substrate, chain and columns made of magnetic NPs are observed. The appearance of these structures is surprising, since chains are usually only observed for high dipolar parameters which is defined as the ratio between the magnetic dipolar and thermal energy. Thus, for the maghemite NPs of 10 nm coated with octanoic acid, the dipolar parameter is 0.69 compared to a threshold of 4 where chain formation is usually observed. However, for these NPs, chains are well observed. Brownian dynamics simulations have shown that the mesostructures can be attributed to an interplay of dipolar and van der Waals interactions between the NPs [80, 81]. This also explains why these mesostructures

may disappear when ligands with longer alkyl chains such as dodecanoic acid are used. In this case, the van der Waals attraction is reduced due to the larger contact distance between the particles and cannot participate in the mesostructure formation.

Mesostructure formation as observed for MNPs has been widely modeled as confined Stockmeyer fluid in gas–liquid coexistence. The Stockmeyer potential is made of the two terms essential for the mesostructure formation as discussed above: a Lennard–Jones term describing the van der Waals attraction and a magnetic dipole potential. This fluid is confined between two walls describing the film, which is formed during the evaporation. The mesostructure formation is interpreted as a coexistence of a gas and a condensed phase made of the colloidal particles. The condensed phase forms the mesostructures observed in the experiments.

The confined Stockmeyer potential is completely described by five parameters: the dipole strength μ, the density ρ, the temperature T, the film thickness L and the field strength H. These parameters are usually expressed in reduced units. To observe mesostructures, a large number of particles up to 12,000 have to be used. The long-range dipole interaction must be correctly handled using Ewald sums. Several Monte Carlo simulation studies have been carried out for this system and we will summarize the principal results [7, 81–84].

In the literature [85–98], usually particles with high dipole moments are studied by simulations studied have. Thus, the cluster distribution and spacing has been studied for low-density systems made of dipolar hard spheres in a slit geometry [93, 94]. Also the orientational order of dipolar soft spheres has been investigated showing an enhancement of ferroelectric order due to confinement [95, 96].

Concerning mesostructure formation, we will first discuss the simulation results for Stockmeyer fluids when a *field parallel to the film* is applied. Figure 8.17a shows the formation of an array of regularly spaced columns of similar diameter at a height of $L = 10$ [83]. For higher dipoles, the same number of columns is observed, but the particles form an ordered assembly of body-centered tetragonal type. When the height is larger than 10, the diameter of the columns stay close to the value observed for $L = 10$, which leads to the formation of several layers of columns (Fig. 8.17b). When the height is smaller than 10, the columns appear flattened (Fig. 8.17c). When diluted NP solutions are used, the formation of one layer of columns is observed as in Fig. 8.17a. For concentrated solutions corresponding to the case in Fig. 8.17b, several layers of columns are obtained.

The self-organization of magnetic NPs has also widely been studied in the case of *a field perpendicular to the film* [7, 82]. This case is fundamentally different from the parallel one previously discussed. This is explained in the following. The dipoles of the MNPs follow the field direction, which leads to a layer of dipoles pointing in the same direction at the surface of the evaporation film. The aligned dipoles repel each other, which would lead to a separation of the NPs. On the other hand, the NPs are attracted for example by short-range van der Waals attractions as mentioned above. This interplay of short-range attraction and long-range dipolar repulsion leads to the formation of pattern such as hexagonal arrays of columns or labyrinths. This phenomenon can be described by a free energy approach taking into account the repulsion between the aligned dipoles and the energy corresponding to the surface

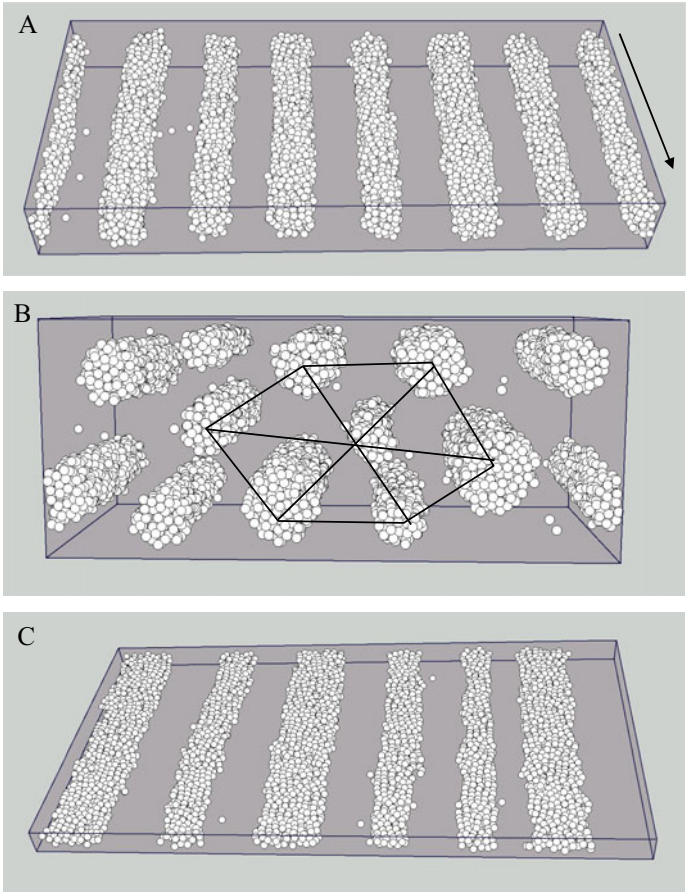

Fig. 8.17 Snapshots of configurations for a confined Stockmayer fluid at $\mu = 2.0$, $\rho = 0.2$, $T = 1.25$, and $H = 20$. **a** $L = 10$, **b** $L = 27$, **c** $L = 4$

created by the pattern. This approach has been widely applied [99–102] and leads to the following general results: the pattern size such as the radius of columns and the width of labyrinth decreases with the magnetic field strength to reach saturation at high field strength. The ratio of the pattern size and height decreases with the height. A transition between different kinds of patterns is not induced by a change in pattern height or field strength. These transitions are mainly determined by the volume fraction defined as the ratio of the volume occupied by the magnetic phase to the total volume of the film. The self-organization of MNPs in a perpendicular field has also been studied by Monte Carlo simulations using a confined Stockmeyer fluid in the gas–liquid coexistence [7, 103]. System parameters have been chosen close to cobalt NPs coated with dodecanoic acid. The decrease of the pattern size with field strength is in good agreement with the results from free energy approaches

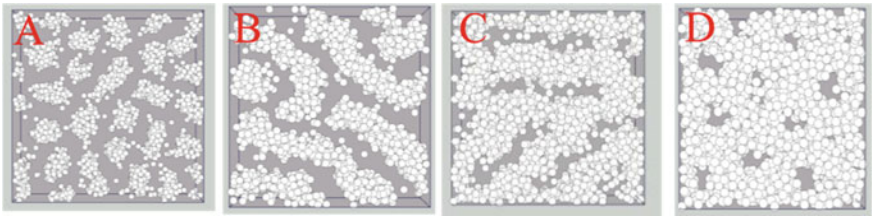

Fig. 8.18 Snapshots of configurations for a confined Stockmayer fluid at $\mu = 2.0$, $T = 1.25$, $L = 10$ and $H = 30$. **a** $\rho = 0.1$, **b** $\rho = 0.3$, **c** $\rho = 0.4$, **d** $\rho = 0.5$

[102]. Also in the simulations, the volume fraction appears the key parameter for the formation of various patterns [7, 103]. At low volume fractions, only arrays of columns are observed (Fig. 8.18a). For volume fractions close to 0.3, columns and labyrinthine patterns coexist. At even higher volume fraction, a pure labyrinth appears (Fig. 8.18b). At higher volume fractions, two void structures were observed for the first time by simulations. At volume fractions larger than 0.7, a void structure made of elliptical-like holes is obtained (Fig. 8.18c), while from a volume fraction of 0.83 voids with circular base appear (Fig. 8.18d). These void structures were also found in experiments with cobalt NPs at the volume fractions predicted by the simulations [7].

Some years ago, a novel "gel-like" phase was experimentally reported in colloidal suspensions and granular media obtained by *application of an electric field* [101, 104]. These void structures were observed at very low-density $\rho\sigma^3$ between 0.006 and 0.1. To investigate self-organizations at these densities, systematic Monte Carlo simulations were carried out varying the confinement, the short-range interactions and the dipolar moment [84]. Only isolated particles or single chains for large dipoles have been observed at very low density, but no evidence for a void structure was found. It is interesting to note that for larger dipoles, the end of the columns close to the confining walls become broadened. This is explained by the repulsion between the parallel dipoles and has been experimentally observed on ferrofluid emulsions [100, 105].

Using purely repulsive short-range interactions such as hard-sphere repulsion or the Weeks-Chandler-Anderson potential usually leads to the suppression of pattern formations such as columns or voids (see Fig. 8.19a–c). This is in good agreement with observation cited above that the van der Waals interactions are crucial for the formation of pattern.

Surprisingly using bulk-like boundary conditions, we observed the formation of columns even with dipolar hard spheres (Fig. 8.19d). We called this novel unattended phenomenon dipolar assembly with repulsive coupling (DARC). Two conditions must apply for this mesostructure formation without attractive short-range potential. First, quasi bulk-like conditions must exist which are observed for metallic particles in an electric field or magnetic particles in very thick films. Second, the repulsive potential must be very steep [81]. Test calculations have shown that so steep potential may for example apply for NPs stabilized by electrostatic potential.

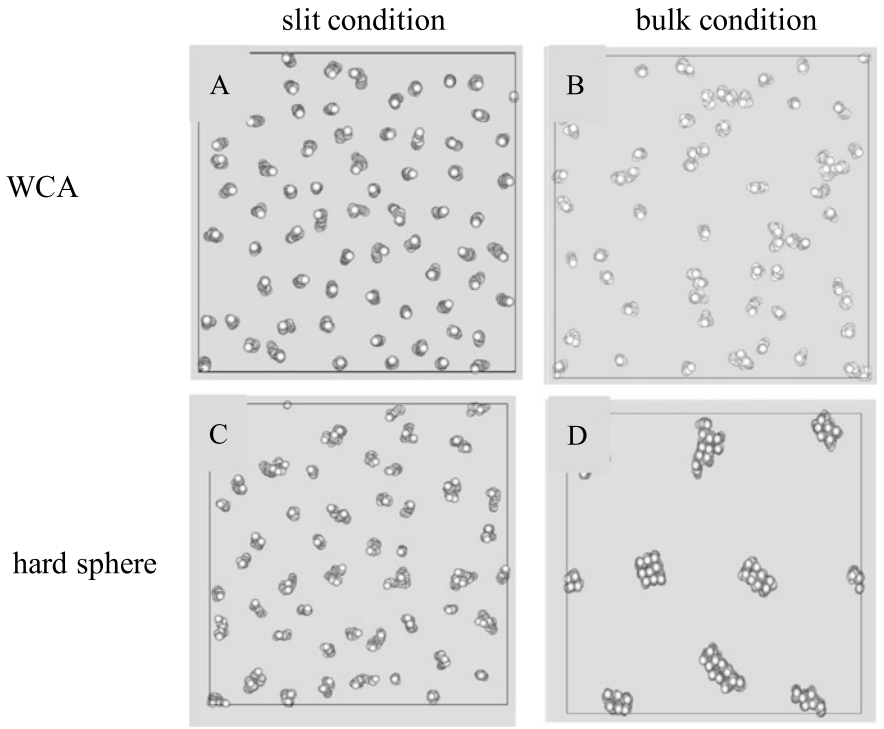

Fig. 8.19 Snapshots of configurations for a confined dipolar fluid at $\mu = 3.0$, $\rho = 0.1$, $T = 1.0$, $L = 20$ and $H = 40$. In the first and second lines, the repulsion corresponds to the Weeks-Chandler-Anderson (WCA) or the hard-sphere potential. On the left side, slit conditions apply for the simulation box, while on the right side, periodic bulk conditions are used

8.8 Conclusion

In this chapter, we show that both micellar and organometallic approaches allows the formation of uniform spherical Co NPs coated either by dodecanoic acid or **oleylamine**, which size can be tuned from **3.8 to 9.2 nm**. Thanks to an annealing process or directly after the synthesis, they are characterized by a hcp crystallinity. Due to their high stability against oxidation and coalescence, these MNPs self-organize into long-range ordered 2D and 3D superlattices. Magnetic properties evidence both the NP crystallinity effect as well as the mesoscopic ordering effect in the 3D supercrystals. We show that there are three key factors for a good assembly of NPs: slow evaporation speed, low size dispersity and the choice of a good solvent. For a specific class of solvents such as toluene, NP assembly can be observed within the solution. Monte Carlo simulations and free energy theories are able to predict the size and type of patterns appearing during the evaporation of a solution of MNPs. They show the importance of short-range attractive forces for the formation of these structures. However, recent simulations have shown that for particles with a steep repulsive

potential such additional short-range attractive forces might not be necessary for pattern formation.

Acknowledgements The research leading to these results has been supported by a grant ANR-CE08-007 from the ANR French Agency.

References

1. I. Lisiecki, From the Co nanocrystals to their self-organizations: towards ferromagnetism at room temperature. Acta Phys. Pol. A **121**, 426–433 (2012)
2. A.M. Kalsin, M. Fialkowski, M. Paszewski, S.K. Smoukov, K.J.M. Bishop, B.A. Grzybowski, Electrostatic self-assembly of binary nanoparticle crystals with a diamond-like lattice. Science **312**(80), 420–424 (2006)
3. M.A. Boles, M. Engel, D.V. Talapin, Self-assembly of colloidal nanocrystals: from intricate structures to functional materials—chemical reviews (ACS Publications). Chem. Rev. **116**, 11220–11289 (2016)
4. A. Demortière, C. Petit, First synthesis by liquid−liquid phase transfer of magnetic CoxPt100-X nanoalloys. Langmuir **23**, 8575–8584 (2007)
5. S. Sun, C.B. Murray, D. Weller, L. Folks, A. Moser, Monodisperse FePt nanoparticles and ferromagnetic FePt nanocrystal superlattices. Science **287**(80), 1989–1992 (2000)
6. I. Lisiecki, P.-A. Albouy, M.-P. Pileni, Face-centered-cubic "supracrystals" of cobalt nanocrystals. Adv. Mater. **15**, 712–716 (2003)
7. C. Salzemann, J. Richardi, I. Lisiecki, J.-J. Weis, M.P. Pileni, Mesoscopic void structures in cobalt nanocrystal films formed from drying concentrated colloidal solutions. Phys. Rev. Lett. **102**, 144502 (2009)
8. M. Gauvin, N. Yang, E. Barthel, I. Arfaoui, J. Yang, P.A. Albouy, M.P. Pileni, Morphology, nanocrystallinity, and elastic properties of single domain ε co supracrystals. J. Phys. Chem. C **119**, 7483–7490 (2015)
9. J.J. Urban, D.V. Talapin, E.V. Shevchenko, C.R. Kagan, C.B. Murray, Synergism in binary nanocrystal superlattices leads to enhanced P-type conductivity in self-assembled PbTe/Ag_2Te thin films. Nat. Mater. **6**, 115–121 (2007)
10. A. Courty, I. Lisiecki, M.P. Pileni, Vibration of self-organized silver nanocrystals. J. Chem. Phys. **116**, 8074–8078 (2002)
11. D. Parker, I. Lisiecki, C. Salzemann, M. Pileni, M. Curie, Emergence of new collective properties of cobalt nanocrystals ordered in Fcc supracrystals : II. Magn. Invest. 12632–12638 (2007)
12. D. Dinega, M. Bawendi, A solution-phase chemical approach to a new crystal structure of cobalt. Angew. Chemie Int. … 1788–1791 (1999)
13. V.F. Puntes, K.M. Krishnan, A.P. Alivisatos, Colloidal nanocrystal shape and size control: the case of cobalt. Science 291(80), 2115–2117 (2001)
14. C.B. Murray, S. Sun, W. Gaschler, H. Doyle, T.A. Betley, C.R. Kagan, Colloidal synthesis of nanocrystals and nanocrystal superlattices. IBM J. Res. Dev. **45**, 47–56 (2001)
15. J.I.L. Park, N.J. Kang, Y.W. Jun, S.J. Oh, H.C. Ri, J. Cheon, Superlattice and magnetism directed by the size and shape of nanocrystals. ChemPhysChem **3**, 543–547 (2002)
16. S. Sun, C.B. Murray, Synthesis of monodisperse cobalt nanocrystals and their assembly into magnetic superlattices (invited). J. Appl. Phys. **85**, 4325 (1999)
17. L. Zadoina, K. Soulantica, S. Ferrere, B. Lonetti, M. Respaud, A.-F. Mingotaud, A. Falqui, A. Genovese, B. Chaudret, M. Mauzac, In situ synthesis of cobalt nanoparticles in functionalized liquid crystalline polymers. J. Mater. Chem., 6988. (2011)

18. L. Meziane, C. Salzemann, C. Aubert, H. Gérard, C. Petit, M. Petit, Hcp cobalt nanocrystals with high magnetic anisotropy prepared by easy one-pot synthesis. Nanoscale **8**, 18640–18645 (2016)
19. C. Petit, M.P. Pileni, Cobalt nanosized particles organized in a 2D superlattice: synthesis, characterization, and magnetic properties. J. Phys. Chem. B **103**, 1805–1810 (1999)
20. I. Lisiecki, M.P. Pileni, Synthesis of well-defined and low size distribution cobalt nanocrystals: the limited influence of reverse micelles. Langmuir **19**, 9486–9489 (2003)
21. S. Costanzo, G. Simon, J. Richardi, P. Colomban, I. Lisiecki, Solvent effects on cobalt nanocrystal synthesis—a facile strategy to control the size of Co nanocrystals. J. Phys. Chem. C **120**, 22054–22061 (2016)
22. C. Petit, Z.L. Wang, M.P. Pileni, Ferromagnetic cobalt nanocrystals achieved by soft annealing approach-from individual behavior to mesoscopic organized properties. J. Magn. Magn. Mater. (2007)
23. I. Lisiecki, C. Salzemann, D. Parker, P. Albouy, M. Pileni, P. Marie, I. Lisiecki, C. Salzemann, M. Pileni, M. Curie, Emergence of new collective properties of cobalt nanocrystals ordered in Fcc supracrystals : I. Struct. Invest. 12625–12631 (2007)
24. M.D. Bentzon, A.R. Thölén, Phase contrast from a regular stacking of equally sized iron-oxide spheres. Ultramicroscopy **38**, 105–115 (1991)
25. M.D. Bentzon, J. van Wonterghem, S. Mørup, A. Thölén, C.J.W. Koch, Ordered aggregates of ultrafine iron oxide particles: "super crystals." Philos. Mag. Part B **60**, 169–178 (1989)
26. M. Li, Y. Chen, N. Ji, D. Zeng, D.L. Peng, Preparation of monodisperse Ni nanoparticles and their assembly into 3D nanoparticle superlattices. Mater. Chem. Phys. **147**, 604–610 (2014)
27. M. Okuda, Y. Kobayashi, K. Suzuki, K. Sonoda, T. Kondoh, A. Wagawa, A. Kondo, H. Yoshimura, Self-organized inorganic nanoparticle arrays on protein lattices. Nano Lett. **5**, 991–993 (2005)
28. T. Hyeon, S.S. Lee, J. Park, Y. Chung, H.B. Na, Synthesis of highly crystalline and monodisperse maghemite nanocrystallites without a size-selection process. J. Am. Chem. Soc. **123**, 12798–12801 (2001)
29. L. Meng, W. Chen, Y. Tan, L. Zou, C. Chen, H. Zhou, Q. Peng, Y. Li, Fe_3O_4 octahedral colloidal crystals. Nano Res. **4**, 370–375 (2011)
30. O. Kasyutich, R.D. Desautels, B.W. Southern, J. Van Lierop, Novel aspects of magnetic interactions in a macroscopic 3D nanoparticle-based crystal. Phys. Rev. Lett. **104**, 1–4 (2010)
31. C. Petit, P. Lixon, M.P. Pileni, Structural study of divalent metal bis(2-ethylhexyl) sulfosuccinate aggregates. Langmuir **7**, 2620–2625 (1991)
32. I. Lisiecki, P. André, A. Filankembo, C. Petit, J. Tanori, T. Gulik-Krzywicki, B.W. Ninham, M.P. Pileni, Mesostructured fluids. 1. Cu(AOT)2−H_2O−isooctane in oil rich regions. J. Phys. Chem. B **103**, 9168–9175 (1999)
33. I. Lisiecki, P. André, A. Filankembo, C. Petit, J. Tanori, T. Gulik-Krzywicki, B.W. Ninham, M.P. Pileni, Mesostructured fluids. 2. Microstructure and supra-aggregation. J. Phys. Chem. B **103**, 9176–9189 (1999)
34. G.N. Glavee, K.J. Klabunde, C.M. Sorensen, G.C. Hadjipanayis, Sodium borohydride reduction of cobalt ions in nonaqueous media. Formation of ultrafine particles (nanoscale) of cobalt metal. Inorg. Chem. **32**, 474–477 (1993)
35. J. Eastoe, T.F. Towey, B.H. Robinson, J. Williams, R.K. Heenan, Structures of metal bis(2-ethylhexylsulfosuccinate) aggregates in cyclohexane. J. Phys. Chem. **97**, 1459–1463 (1993)
36. J.A. Gutierrez, M. Alejandra Luna, N. Mariano Correa, J.J. Silber, R. Darío Falcone, The impact of the polar core size and external organic media composition on micelle–micelle interactions: the effect on gold nanoparticle synthesis. New J. Chem. **39**, 8887–8895 (2015)
37. N.P. Adhikari, X. Peng, A. Alizadeh, S. Ganti, S.K. Nayak, S.K. Kumar, Multiscale modeling of the surfactant mediated synthesis and supramolecular assembly of cobalt nanodots. Phys. Rev. Lett. **93**, 1–4 (2004)
38. Q. Zeng, X. Jiang, A. Yu, G.M. Lu, Growth mechanisms of silver nanoparticles: a molecular dynamics study. Nanotechnology **18**, 35708 (2007)

39. D. Larcher, R. Patrice, Preparation of metallic powders and alloys in polyol media: a thermodynamic approach. J. Solid State Chem. **154**, 405–411 (2000)
40. F. Bonet, V. Delmas, S. Grugeon, R. Herrera Urbina, P.Y. Silvert, K. Tekaia-Elhsissen, Synthesis of monodisperse Au, Pt, Pd, Ru and Ir nanoparticles in ethylene glycol. Nanostruct. Mater. **11**, 1277–1284 (1999)
41. F. Fievet, J.P. Lagier, M. Figlarz, Preparing monodisperse metal powders in micrometer and submicrometer sizes by the polyol process. MRS Bull. **14**, 29–34 (1989)
42. Y.H. Kim, D.K. Lee, H.G. Cha, C.W. Kim, Y.S. Kang, Synthesis and characterization of antibacterial Ag-SiO_2 nanocomposite. J. Phys. Chem. C **111**, 3629–3635 (2007)
43. S.I. Cha, C.B. Mo, K.T. Kim, S.H. Hong, Ferromagnetic cobalt nanodots, nanorices, nanowires and nanoflowers by polyol process. J. Mater. Res. **20**, 2148–2153 (2005)
44. R.J. Joseyphus, T. Matsumoto, H. Takahashi, D. Kodama, K. Tohji, B. Jeyadevan, Designed synthesis of cobalt and its alloys by polyol process. J. Solid State Chem. **180**, 3008–3018 (2007)
45. C. Petit, M. Petit, C. Aubert, L. Meziane, H. Gerard, C. Salzemann, Ambient-temperature ferromagnetic cobalt nanoparticles, production method thereof and uses of same (2017)
46. P.N. Pusey, W. Van Megen, Phase behaviour of concentrated suspensions of nearly hard colloidal spheres. Nature **320**, 340–342 (1986)
47. D.A. Kofke, P.G. Bolhuis, Freezing of polydisperse hard spheres. Phys. Rev. E **59**, 618–622 (1999)
48. P.G. Bolhuis, D.A. Kofke, Monte Carlo study of freezing of polydisperse hard spheres. Phys. Rev. E **54**, 634–643 (1996)
49. S. Auer, D. Frenkel, Suppression of crystal nucleation in polydisperse colloids due to increase of the surface free energy. Nature **413**, 711–713 (2001)
50. L.A. Fernández, V. Mart'in-Mayor, B. Seoane, P. Verrocchio, Separation and fractionation of order and disorder in highly polydisperse systems. Phys. Rev. E **82**, 21501 (2010)
51. S.J. Khan, F. Pierce, C.M. Sorensen, A. Chakrabarti, Self-assembly of ligated gold nanoparticles: phenomenological modeling and computer simulations. Langmuir **25**, 13861–13868 (2009)
52. N. Goubet, J. Richardi, P.A. Albouy, M.P. Pileni, How to predict the growth mechanism of supracrystals from gold nanocrystals. J. Phys. Chem. Lett. **2**, 417–422 (2011)
53. N. Goubet, J. Richardi, P.A. Albouy, M.P. Pileni, Which forces control supracrystal nucleation in organic media? Adv. Funct. Mater. **21**, 2693–2704 (2011)
54. K. Butter, P.H. Bomans, P.M. Frederik, G.J. Vroege, A.P. Philipse, Direct observation of dipolar chains in ferro uids in zero eld using cryogenic electron microscopy. Direct **15** (2003)
55. M. Klokkenburg, R.P.A. Dullens, W.K. Kegel, B.H. Erné, A.P. Philipse, Quantitative real-space analysis of self-assembled structures of magnetic dipolar colloids. Phys. Rev. Lett. **96**, 37203 (2006)
56. M. Klokkenburg, B.H. Erné, J.D. Meeldijk, A. Wiedenmann, A.V. Petukhov, R.P.A. Dullens, A.P. Philipse, In situ imaging of field-induced hexagonal columns in magnetite ferrofluids. Phys. Rev. Lett. **97**, 4–7 (2006)
57. J. Richardi, One-dimensional assemblies of charged nanoparticles in water: a simulation study. J. Chem. Phys. **130** (2009)
58. Z. Yang, M. Cavalier, M. Walls, P. Bonville, I. Lisiecki, M.-P. Pileni, A Phase-solution annealing strategy to control the cobalt nanocrystal anisotropy: structural and magnetic investigations. J. Phys. Chem. C **116**, 15723–15730 (2012)
59. I. Lisiecki, P.-A. Albouy, M.-P. Pileni, "Supra" crystal: control of the ordering of self-organization of cobalt nanocrystals at the mesoscopic scale. J. Phys. Chem. B **108**, 20050–20055 (2004)
60. S. Bedanta, W. Kleemann, Supermagnetism. J. Phys. D. Appl. Phys. **42** (2009)
61. A.G. Roca, R. Costo, A.F. Rebolledo, S. Veintemillas-Verdaguer, P. Tartaj, T. González-Carreño, M.P. Morales, C.J. Serna, Progress in the preparation of magnetic nanoparticles for applications in biomedicine. J. Phys. D. Appl. Phys. **42**, 224002 (2009)

62. J.S. Weinstein, C.G. Varallyay, E. Dosa, S. Gahramanov, B. Hamilton, W.D. Rooney, L.L. Muldoon, E.A. Neuwelt, Superparamagnetic iron oxide nanoparticles: diagnostic magnetic resonance imaging and potential therapeutic applications in neurooncology and central nervous system inflammatory pathologies, a review. J. Cereb. Blood Flow Metab. **30**, 15–35 (2010)
63. A. Moser, K. Takano, D.T. Margulies, M. Albrecht, Y. Sonobe, Y. Ikeda, S. Sun, E.E. Fullerton, Magnetic recording: advancing into the future. J. Phys. D. Appl. Phys. **35** (2002)
64. S. Mørup, Superferromagnetic nanostructures. Hyperfine Interact. **90**, 171–185 (1994)
65. P.E. Jönsson, Superparamagnetism and spin glass dynamics of interacting magnetic nanoparticle systems. Adv. Chem. Phys. 191–248 (2004)
66. S. Bedanta, T. Eimiller, W. Kleemann, J. Rhensius, F. Stromberg, E. Amaladass, S. Cardoso, P.P. Freitas, Overcoming the dipolar disorder in dense CoFe nanoparticle ensembles: superferromagnetism. Phys. Rev. Lett. **98**, 10–13 (2007)
67. J.P. Bouchaud, P.G. Zérah, Dipolar ferromagnetism: a monte carlo study. Phys. Rev. B **47**, 9095–9097 (1993)
68. S. Bedanta, W. Kleemann, Supermagnetism. J. Phys. D Appl. Phys. **42**, 13001 (2009)
69. I. Lisiecki, D. Parker, C. Salzemann, M.P. Pileni, Face-centered cubic supra-crystals and disordered three-dimensional assemblies of 7.5 Nm cobalt nanocrystals: influence of the mesoscopic ordering on the magnetic properties. Chem. Mater. **19**, 4030–4036 (2007)
70. S. Hariharan, J. Gass, Superparamagnetism and magneto-caloric effect (MCE) in functional magnetic nanostructures. Rev. Adv. Mater. Sci. **10**, 398–402 (2005)
71. H. Zeng, J. Zhang, C. Kuang, M. Yue, Magnetic entropy change in bulk nanocrystalline Gd metals. Appl. Nanosci. **1**, 51–57 (2011)
72. J. Dormann, L. Spinu, E. Tronc, J. Jolivet, F. Lucari, F. D'Orazio, D. Fiorani, Effect of interparticle interactions on the dynamical properties of γ-Fe_2O_3 nanoparticles. J. Magn. Magn. Mater. **183**, L255–L260 (1998)
73. J. Tuaillon, J.P. Perez, V. Dupuis, A. Perez, Of Iron and Nickel **8853**, 437–438 (1995)
74. J. Filippi, V.S. Amaral, B. Barbara, High-field magnetization curve of random-anisotropy amorphous magnet: observation of a crossover and link to structural short-range order. Phys. Rev. B **44**, 2842–2845 (1991)
75. D. Parker, I. Lisiecki, M.P. Pileni, Do 8 Nm co nanocrystals in long-range-ordered face-centered cubic (Fcc) supracrystals show superspin glass behavior? J. Phys. Chem. Lett. **1**, 1139–1142 (2010)
76. J. Mydosh, Spin Glasses: An Experimental Introduction (Taylor & Francis, London, 1993)
77. P. Svedlindh, P. Nordblad, M.F. Hansen, Spin glass like transition in a highly concentrated Fe-C nanoparticle system **139**, 1999–2000 (2000)
78. M.F. Hansen, P.E. Jönsson, P. Nordblad, P. Svedlindh, Critical dynamics of an interacting magnetic nanoparticle system. J. Phys. Condens. Matter **14**, 4901–4914 (2002)
79. I. Lisiecki, S. Nakamae, Crystalline order effects on the magnetic properties of superlattices made of cobalt nanocrystals. J. Phys. Conf. Ser. **521**, 12007 (2014)
80. Y. Lalatonne, J. Richardi, P.M.P. Van Der, Waals versus dipolar forces controlling mesoscopic organizations of magnetic nanocrystals. Nat. Mater. **3**, 121–125 (2004)
81. Y. Lalatonne, L. Motte, J. Richardi, M.P. Pileni, Influence of short-range interactions on the mesoscopic organization of magnetic nanocrystals. Phys. Rev. E **71**, 11404 (2005)
82. J. Richardi, M.P. Pileni, J.-J. Weis, Self-organization of magnetic nanoparticles: a Monte Carlo study. Phys. Rev. E **77**, 61510 (2008)
83. J. Richardi, M.P. Pileni, J.J. Weis, Self-organization of confined dipolar particles in a parallel field. J. Chem. Phys. **130** (2009)
84. J. Richardi, J.J. Weis, Low density mesostructures of confined dipolar particles in an external field. J. Chem. Phys. **135** (2011)
85. R. Tao, Q. Jiang, Simulation of structure formation in an electrorheological fluid. Phys. Rev. Lett. **73**, 205–208 (1994)
86. A. Satoh, Development of effective Stokesian dynamics method for ferromagnetic colloidal dispersions (cluster-based Stokesian dynamics method). J. Colloid Interf. Sci. **255**, 98–106 (2002)

87. M. Mohebi, N. Jamasbi, J. Liu, Simulation of the formation of nonequilibrium structures in magnetorheological fluids subject to an external magnetic field. Phys. Rev. E **54**, 5407–5413 (1996)
88. J.E. Martin, R.A. Anderson, C.P. Tigges, Simulation of the athermal coarsening of composites structured by a uniaxial field. J. Chem. Phys. **108**, 3765–3787 (1998)
89. J.E. Martin, R.A. Anderson, C.P. Tigges, Thermal coarsening of uniaxial and biaxial field-structured composites. J. Chem. Phys. **110**, 4854 (1999)
90. J.E. Martin, K.M. Hill, C.P. Tigges, Magnetic-field-induced optical transmittance in colloidal suspensions. Phys. Rev. E **59**, 5676–5692 (1999)
91. Z. Wang, H. Fang, Z. Lin, L. Zhou, Simulation of field-induced structural formation and transition in electromagnetorheological suspensions. Phys. Rev. E **61**, 6837–6844 (2000)
92. A.-P. Hynninen, M. Dijkstra, Phase diagram of dipolar hard and soft spheres: manipulation of colloidal crystal structures by an external field. Phys. Rev. Lett. **94**, 138303 (2005)
93. R. Haghgooie, P.S. Doyle, Transition from two-dimensional to three-dimensional behavior in the self-assembly of magnetorheological fluids confined in thin slits. Phys. Rev. E Stat. Nonlinear Soft Matter Phys. **75**, 1–13 (2007)
94. R. Haghgooie, P.S. Doyle, MR fluid structure in quasi-2D. Europhys. Lett. **77**, 18002 (2007)
95. J. Jordanovic, S.H.L. Klapp, Field-induced layer formation in dipolar nanofilms. Phys. Rev. Lett. **101**, 38302 (2008)
96. R.A. Trasca, S.H.L. Klapp, Structure formation in layered ferrofluid nanofilms. J. Chem. Phys. **129** (2008)
97. S.C. Ferreira, C. Castellano, R. Pastor-Satorras, Epidemic thresholds of the susceptible-infected-susceptible model on networks: a comparison of numerical and theoretical results. Phys. Rev. E **86**, 41125 (2012)
98. J. Richardi, M.P. Pileni, Towards efficient methods for the study of pattern formation in ferrofluid films. Eur. Phys. J. E **13**, 99–106 (2004)
99. J. Richardi, D. Ingert, M.P. Pileni, Theoretical study of the field-induced pattern formation in magnetic liquids. Phys. Rev. E **66**, 46306 (2002)
100. M. Ivey, J. Liu, Y. Zhu, S. Cutillas, Magnetic-field-induced structural transitions in a ferrofluid emulsion. Phys. Rev. E **63**, 11403 (2000)
101. A.K. Agarwal, A. Yethiraj, Low-density ordered phase in brownian dipolar colloidal suspensions. Phys. Rev. Lett. **102**, 198301 (2009)
102. V. Germain, J. Richardi, D. Ingert, M.P. Pileni, Mesostructures of cobalt nanocrystals. 1. Experiment and theory. J. Phys. Chem. B **109**, 5541–5547 (2005)
103. M.P. Pileni, Self organization of inorganic nanocrystals: unexpected chemical and physical properties. J. Colloid Interface Sci. **388**, 1–8 (2012)
104. A. Kumar, B. Khusid, Z. Qiu, A. Acrivos, New electric-field-driven mesoscale phase transitions in polarized suspensions. Phys. Rev. Lett. **95**, 258301 (2005)
105. J. Liu, E.M. Lawrence, A. Wu, M.L. Ivey, G.A. Flores, K. Javier, J. Bibette, J. Richard, Field-induced structures in ferrofluid emulsions. Phys. Rev. Lett. **74**, 2828–2831 (1995)

Part III
Advanced Characterization Techniques

Chapter 9
Magnetism of Individual Nanoparticles Probed by X-Ray Photoemission Electron Microscopy

Armin Kleibert

Abstract Magnetic nanoparticles are of great interest for applications in fields ranging from biomedicine to spintronics. However, despite considerable work, their size-dependent magnetic properties are still poorly understood. In this chapter, we will introduce x-ray photoemission electron microscopy (XPEEM) as a spectromicroscopy technique ideally suited for the investigation of the magnetic properties of large numbers of individual nanoparticles in extended ensembles. Moreover, XPEEM can be combined with other microscopy techniques to achieve a direct correlation between magnetism, size, shape, and structure of the very same nanoparticles. This approach has led to the discovery of novel magnetic states in 3*d* transition metal nanoparticles characterized by strongly enhanced magnetic energy barriers, attributed to the strong impact of structural defects rather than to surface or interface contributions to the total magnetic anisotropy.

9.1 Introduction

Magnetic nanoparticles are of interest for many applications in fields ranging from spintronics to magnetic data storage, energy conversion, and biomedicine [1, 2]. This interest is due to the unique finite size effects that can occur in nanoparticles, such as single domain states, superparamagnetism, enhanced magnetic moments or magnetic anisotropy energies [3, 4]. Such properties hold great potential for novel applications and are therefore extensively investigated. However, till today a quantitative understanding or control of size-dependent properties of magnetic nanoparticles has not been achieved. Instead, even for mono-disperse nanoparticle samples of the canonical 3*d* transition metals, experiments yield widely scattering magnetic anisotropy energies and magnetic moments [5]. This diversity is often explained by shape, surface, structure or interface effects, but a quantitative interpretation of the data is difficult, since most experiments concern integral measurements where the

A. Kleibert (✉)
Paul Scherrer Institut, Swiss Light Source, Forschungsstrasse 111, 5232 Villigen PSI, Switzerland
e-mail: armin.kleibert@psi.ch

D. Peddis et al. (eds.), *New Trends in Nanoparticle Magnetism*,
Springer Series in Materials Science 308,
https://doi.org/10.1007/978-3-030-60473-8_9

magnetic properties are averaged over large ensembles with distributions of particle sizes, morphologies, structures, defects, and orientations. Therefore, it remains often unclear whether the mean values obtained by integral measurements yield representative information about the actual nanoparticle properties or whether averaged data mask a more complex distribution of properties within the ensembles.

In order to unambiguously address this issue it is necessary to be able to probe the magnetism of individual nanoparticles and different experimental approaches are available today for this purpose [6]. For instance, microSQUIDs have been used to determine the magnetic anisotropy energy of isolated nanoparticles in great detail [7], while electron holography is used to study the magnetic structure in isolated or interacting nanoparticles [8]. In this chapter we focus on x-ray photoemission electron microscopy (XPEEM), a magnetic spectromicroscopy technique suited to the investigation of the magnetic properties and chemical composition of individual nanoparticles under ultrahigh vacuum (UHV) conditions [9, 10]. Moreover, XPEEM allows one to probe simultaneously many individual nanoparticles (typically a few hundred) in large ensembles, giving direct insight into the distribution of the magnetic properties in typical samples. Further, magnetic and chemical properties can be directly correlated with the actual size, shape, orientation and structure of the very same nanoparticles by combining XPEEM with other microscopy techniques such as scanning electron microscopy (SEM) or atomic force microscopy (AFM). Moreover, it is possible to follow the evolution of the magnetic properties as a function of temperature, magnetic fields, and during in situ chemical reactions. Finally, XPEEM provides not only access to the properties of ferromagnetically ordered systems, but is also suitable to investigating the magnetic properties of antiferromagnetically ordered nanoparticles.

XPEEM is a well established technique for the study of magnetic phenomena in systems ranging from films to nanodevices [11–18]. The first XPEEM investigations on individual 3*d* transition metal containing nanoparticles likely date back to 2002 [19]. This study focused on chemically synthesized and surfactant capped γ-Fe_2O_3 particles dispersed on Si wafers. Somewhat later, an investigation of ambient air exposed cobalt nanoparticles with a native oxide shell deposited on Si wafers was reported [20]. Both experiments demonstrated that x-ray absorption spectra of individual nanoparticles can be obtained, but the signal to noise ratio of the data was low and no magnetism was detected. These issues were successfully addressed in subsequent in situ experiments, where sample preparation, transfer and XPEEM characterization were carried out under UHV conditions [21, 22]. This approach yielded a significantly increased signal to noise ratio and the detection of magnetism in individual nanoparticles. It also enabled the first investigations of the pristine properties of individual 3*d* transition metal nanoparticles without the influence of surfactants, oxide shells, or matrix materials.

To demonstrate the potential of XPEEM for nanoparticle research, we will review the recent work on 3*d* transition metal nanoparticles with sizes ranging from 8 to 20 nm. We will mostly focus on iron nanoparticles, because they are often found as spherical or cubic single crystalline nanoparticles with bulk-like bcc structure and magnetic moments comparable to that of their bulk counterpart. These character-

istics seem to suggest a relatively simple behavior with predictable size dependent properties such as magnetic structure and anisotropy energy. However, as we will discuss in more detail below, ensemble measurements reveal a large variety and sometimes contradictory findings [23–32], making it impossible to establish an ambiguous understanding of the size-dependent magnetic properties of iron nanoparticles. By combining magnetic characterization of a large number of iron nanoparticles using XPEEM with structural characterization using SEM and AFM of the very same particles, it was possible to demonstrate that the apparently contradictory experimental observations can be actually explained by the existence of iron nanoparticles in two distinct magnetic states: one state with strongly enhanced magnetic anisotropy and another one with bulk-like magnetic anisotropy energy, irrespective of the size of the particles. Moreover, the enhanced magnetic anisotropy is not due to shape, surface or interface contributions, but is rather attributed to local structural defects in the particle volume, such as dislocations.

Similarly, integral measurements on cobalt and nickel nanoparticles revealed a wide scattering of magnetic properties. However, in contrast to the case of iron nanoparticles, cobalt and nickel nanoparticles are known to exist or coexist in a rich variety of different structures ranging from hcp to fcc single crystalline and multiply twinned structures, often with defects such as stacking faults, making the interpretation of averaged data even more difficult. First XPEEM experiments on fcc cobalt nanoparticle samples confirm the existence of at least two types of nanoparticles with distinct magnetic properties, similar to the observations in the case of bcc iron nanoparticles, while in fcc nickel nanoparticle samples so far only one type with low magnetic anisotropy was found. However, to determine the intrinsic magnetic properties of the different structural motifs and the impact of the different defects in cobalt and nickel nanoparticles requires one to combine magnetic characterization by means of XPEEM with techniques capable of structural characterization with atomic resolution, such as high resolution TEM, of the very same nanoparticles, which is the goal of future work.

This chapter is organized as follows: In Sect. 9.2 we will present the basics of XPEEM with focus on nanoparticle experiments, including instrumentation, sample requirements, and the fundamentals of chemical and magnetic nanoparticle characterization in XPEEM. In Sect. 9.3 we will review the recent XPEEM investigations on iron, cobalt, nickel and iron–cobalt-alloy nanoparticles with sizes ranging from 8 to 20 nm, and Sect. 9.4 concludes the chapter with a perspective for XPEEM in future nanoparticle research and an outlook for remaining challenges.

9.2 X-Ray Photoemission Electron Microscopy

XPEEM is a special case of low energy electron microscopy (LEEM) [9]. The samples in XPEEM are usually investigated under UHV conditions employing synchrotron x-ray radiation for illumination. An electron optical set-up is used to obtain an amplified image of the sample by detecting the x-ray photo-excited electrons [9]. XPEEM

is a versatile technique with a variety of detection modes and is used in many research fields ranging from magnetism, mineralogy, catalysis, organic matter, electrochemistry, to battery research and nanodevices [9, 10]. In the following sections we will briefly introduce the instrumentation needed for XPEEM investigations of individual nanoparticles, the working principle of XPEEM for magnetism studies, and the particular sample requirements for experiments on individual nanoparticles.

9.2.1 Instrumentation

XPEEM investigations on magnetic systems require highly intense, tunable and monochromatic radiation with variable polarization. In the soft x-ray range one probes most frequently the L edges of the $3d$ transition metals and the M edges of the rare earth elements at dedicated beamlines of large scale synchrotron facilities. A recent list of beamlines equipped with XPEEM instruments can be found in [33]. Access to XPEEM instruments is usually possible through user operation programs of the individual facilities. Figure 9.1a displays the schematics of an XPEEM instrument suited for nanoparticle studies. The x-rays impinge at a grazing angle of incidence with respect to the sample surface. For XPEEM imaging the sample is placed in the x-ray beam at a typical working distance between 1 and 2 mm in front of the objective lens. Usually, the sample is held at a negative high voltage in a range from –10 to –20 kV in order to accelerate the photo-excited electrons to high energies and into the electron optics. The latter consists of an energy analyzer and a number of electromagnetic or electrostatic lenses used for fast switching between different imaging/detection modes and field of views, which usually range from 1 to 100 μm. The instrument illustrated in Fig. 9.1a is in addition equipped with an electron gun used for spectroscopic LEEM (SPELEEM) applications. A more detailed description of the various possible instrument configurations and operation modes used in low energy electron microscopy can be found in [9]. As detector, a microchannel plate assembly combined with a phosphorescent screen and a charge-coupled device (CCD) camera are mostly used. More recently, pixelated direct electron detectors with enhanced quantum efficiency, virtually infinite dynamic range, and calibrated flat field have been introduced [34]. Such detectors may in future offer advanced detection schemes such as single electron time–of–flight detection with promising potential for nanoparticle investigations.

9.2.2 XPEEM Fundamentals

Magnetic and chemical characterization in XPEEM is usually achieved by probing the local x-ray absorption cross-section via spatially resolved detection of secondary electrons. The latter originate from non-radiative intra-atomic relaxation processes following the primary absorption of an x-ray photon [36]. The formation of secondary

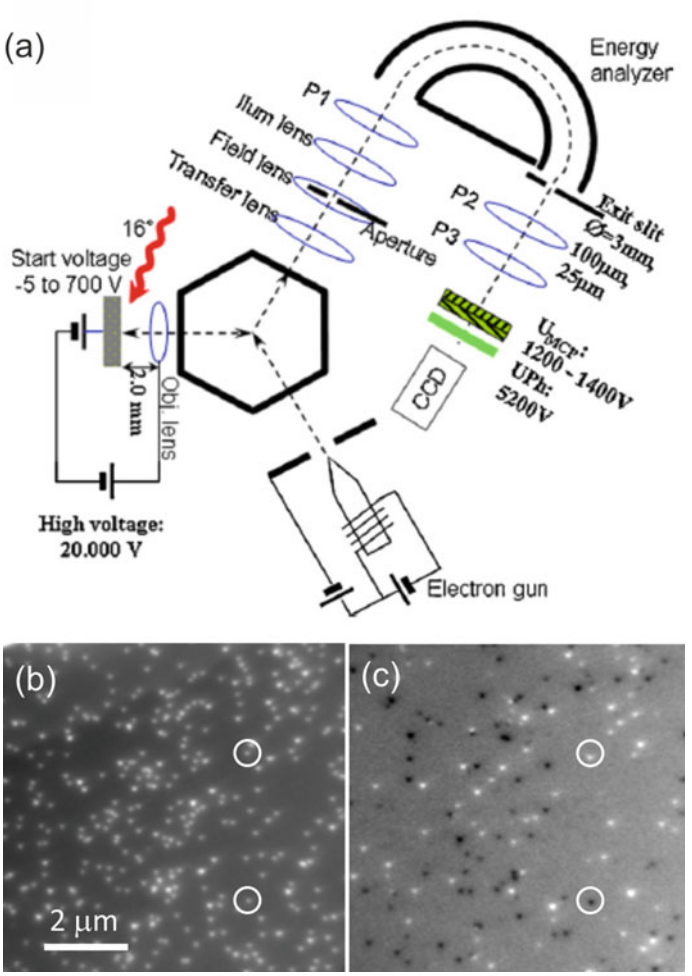

Fig. 9.1 **a** Schematic of a SPELEEM instrument used for XPEEM investigations at the Surface/Interface:Microscopy (SIM) beamline of the Swiss Light Source (SLS). Reprinted from [35], Copyright (2012), with permission from Elsevier. **b** Elemental contrast map, and **c** magnetic contrast map, respectively, of cobalt nanoparticles on a silicon substrate

electron cascades leads to an intrinsic signal amplification in XPEEM. The effective escape depth of the secondary electrons limits the probing depth of XPEEM typically to the upper 3–5 nm of a sample. When using secondary electrons for imaging, a spatial resolution of 30–100 nm can be achieved in instruments without additional aberration corrections [9, 37]. For nanoparticle experiments this implies that the inner structure of typical nanoparticles cannot be directly resolved using XPEEM. Moreover, to facilitate the detection of the signal of individual nanoparticles, suffi-

ciently diluted samples with a typical density of a few nanoparticles per μm^2 on the surface are required.

Magnetic investigations of ferromagnetically ordered systems in XPEEM are based on the spatially resolved detection of the x-ray magnetic circular dichroism (XMCD) effect occuring for instance at the $L_{2,3}$ edges of the $3d$ transition metals or the $M_{4,5}$ edges of the rare earth elements [11–18]. In investigations on $3d$ transition metal nanoparticles, elemental and magnetic contrast maps recorded at the respective L_3 edges are used to visualize the spatial distribution of the nanoparticles and their individual magnetization, as illustrated in Fig. 9.1b, c [5]. In this example, the nanoparticles appear as bright spots with a diameter that corresponds to the spatial resolution of the instrument, which is larger than the actual nanoparticle size. Magnetic contrast maps yield grey tones for the individual nanoparticles, which can range from bright to dark depending on the orientation of the magnetization **m** relative to the propagation vector **k** of the incident circularly polarized x-rays according to $\mathbf{m} \cdot \mathbf{k}$ [21]. The latter relation allows one to quantitatively determine the actual orientation of **m** when varying the azimuthal sample orientation [21, 35]. Further details regarding the data acquisition in XPEEM and processing can be found for instance in [5]. Another important aspect in XPEEM investigations of magnetic nanoparticles is the time τ_x required to record a magnetic contrast map. This time ranges typically between a few tens of seconds to several minutes. Only nanoparticles with a magnetic relaxation time $\tau_r > \tau_x$ can exhibit a detectable magnetic contrast in XPEEM [38].

9.2.3 Sample Requirements

Substrates for nanoparticles studies using XPEEM should possess a flattness in the nanometer range in order to achieve high spatial resolution (to avoid electric field perturbations at surface protrusions [39]). Further, the substrates should be sufficiently conductive to avoid charging of the sample. For instance, Si(100) wafers passivated with a native, amorphous oxide layer with a thickness of 1–2 nm have been proven to be suitable substrates for many studies. The native oxide layer is chemically inert and thermally stable up to about 1000 K. Lithographically prepared gold marker structures are ideally suited for the identification of the same nanoparticles in different microscopes, see Fig. 9.2. Marker structures further aid sample alignment and focusing of the instrument. For investigations of individual nanoparticles, the particle density on the substrate should not exceed a few nanoparticles per μm^2. In XPEEM, organic cappings, oxide shells or residuals of solvents on the sample usually attenuate the detectable signal significantly and, therefore, should be either thin (1–2 nm) or completely avoided.

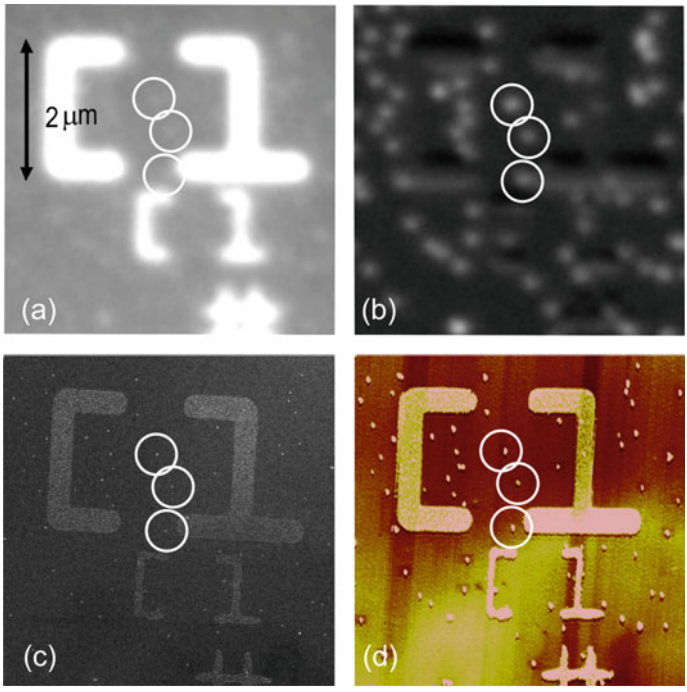

Fig. 9.2 **a** Raw XPEEM image of a Si wafer substrate with gold marker structures and of iron nanoparticles prepared in situ, measured with the photon energy set to the Fe L_3 edge. **b** Elemental contrast map of the same sample area as in **a**. **c** Ex situ SEM is used to determine the shape of the selected nanoparticles with high spatial resolution. **d** Ex situ AFM is used to determine their height. The same three nanoparticles are highlighted with circles in all images. Reprinted with permission from [5]. Copyright (2017) by the American Physical Society

9.3 XPEEM Investigations of 3*d* Transition Metal Nanoparticles

In this section we review the recent XPEEM investigations on pure and alloyed 3*d* transition metal nanoparticles with sizes ranging from 8 to 20 nm with a focus on iron nanoparticles, which are in many studies found as nano-sized single crystals with the bcc lattice known from bulk iron, allowing one to compare the magnetic properties of the nanoparticles with the bulk properties. This situation is significantly different for cobalt and nickel nanoparticles, which have been found in a large variety of structures ranging from single crystalline fcc to hcp or ϵ-phases and multiple twinned structures in various shapes [40–43]. Most of these structures have no bulk counterpart for comparison, and their magnetic properties are therefore much more difficult to assess.

Studies of the magnetic properties of nano-sized iron aggregates date back as early as the 19th century [44], but extensive efforts in the development of prepa-

ration and characterization techniques were needed until the first systematic and detailed investigations of mono-disperse iron nanoparticle samples became possible. However, despite considerable achievements, an unambiguous understanding of the magnetic properties of iron nanoparticles has still not been achieved. For instance, extensive size- and temperature-dependent investigations of iron nanoparticles were reported by Gangopadhyay et al. [23]. By combining TEM, with integral SQUID and Mössbauer spectroscopy, the authors could explain the frequent reports of a reduced magnetization in iron nanoparticles when compared to bulk iron by the formation of a thin native oxide shell around a metallic iron core with bulk-like magnetic moments. The authors also noticed a significantly enhanced magnetic anisotropy in the iron nanoparticles when compared to the magneto-crystalline anisotropy of bulk iron, which they assigned to the core–shell-type particle morphology and a strong interaction between the oxide shell with the iron core in addition to surface effects. Indeed, a subsequent Mössbauer spectroscopy study of metallic iron nanoparticles without oxide shell, which were prepared by reduction of ferric nitrate at 600 K in hydrogen atmosphere, revealed mostly bulk-like properties including a smaller, size-dependent surface contribution to the magnetic anisotropy which the authors assigned to smaller deviations from spherical symmetry [24]. However, high magnetic anisotropies were later found in another work on metallic iron nanoparticles deposited on copper surfaces under UHV conditions [28, 45]. Uniaxial and large anisotropy was also found by means of vibrating sample magnetometry of silver- or SiO_2-capped iron nanoparticles [25]. Similarly, microSQUID investigations of individual iron nanoparticles embedded in a niobium matrix revealed a dominant uniaxial anisotropy and a reduction of the magnetic moment due to the interaction with the matrix. The uniaxial anisotropy was assigned to surface- and shape anisotropy contributions originating from shape deviation from a perfect truncated dodecahedron [27]. Bulk-like magnetic anisotropy was later found in wet-chemically prepared iron nanocubes in [29]. As a last example, we may mention iron nanoparticles prepared by a high pressure magnetron sputtering technique, which revealed enhanced magnetic anisotropies with decreasing size [30].

These examples illustrate the large scatter of reported properties, and in particular the difficulty to disentangle the impact of the sample preparation technique, chemical state and the matrix material on the magnetic anisotropy of iron nanoparticles from ensemble measurements. In the following we will show that, by combining in situ XPEEM with SEM and AFM investigations, it is possible to directly correlate the magnetic properties of a large number of individual nanoparticles in extended ensembles with their actual size, shape, and orientation. Such approach overcomes the major uncertainties in averaging ensemble measurements, namely the impact of the inherent distribution of particle sizes, shapes, orientations, and the possible contribution of clusters of interacting nanoparticles to the measured mean values, and can therefore resolve previously controversial observations. Moreover, in situ XPEEM allows one to study the pristine state of the nanoparticles on various supports without the additional influence of organic or oxide shells or a matrix material.

9.3.1 Enhanced Magnetism and Metastable Properties in Iron Nanoparticles

We start the discussion with XPEEM investigations of iron nanoparticles in contact with non-magnetic silicon substrates passivated with a native, amorphous oxide layer [5, 38]. The iron nanoparticles, with sizes ranging from 8 to 20 nm, are generated in a gas phase condensation process using a UHV-compatible arc cluster ion source (ACIS) [46] and then deposited under soft-landing conditions on clean silicon substrates. Figure 9.3a, b display typical elemental and magnetic contrast maps of these samples recorded at room temperature using XPEEM. The data reveal that a sizable fraction of nanoparticles is in a magnetically blocked state and exhibits stable magnetic contrast over many hours with grey tone levels ranging from black to white such as nanoparticles "B" and "C" in Fig. 9.3, while other nanoparticles exhibit no magnetic contrast as for instance nanoparticle "A". A detailed quantitative analysis of the magnetic contrast levels of the magnetically blocked nanoparticles reveals a random orientation of their magnetic moments [38]. This finding is consistent with the random crystallographic orientation of the nanoparticles on the substrate, which was confirmed by means of in situ reflection high energy electron diffraction (RHEED) experiments [5]. The RHEED investigations showed in addition that the iron nanoparticles possess the bcc crystal lattice known from bulk iron.

The magnetic state of the nanoparticles was further investigated by recording magnetization curves in XPEEM using an external magnetic field. It was found that nanoparticles which initially exhibited no magnetic contrast were easily magnetized with magnetic fields of the order of a few mT, see Fig. 9.3c. This behaviour showed that these nanoparticles were also ferromagnetically ordered, but in a superparamagnetic state. This finding revealed that magnetically blocked and superparamagnetic iron nanoparticles coexist on the silicon substrates. A similar coexistence of superparamagnetic and magnetically blocked iron nanoparticles was also inferred from earlier ensemble measurements [30], where a critical size of 9 nm was estimated for the onset of superparamagnetic behavior within the samples. A direct determination of this critical size can be achieved by combining XPEEM with structural characterization by means of SEM and AFM. When correlating the magnetic state, magnetically blocked or superparamagnetic, with the size of the very same nanoparticles, no critical size was observed [38]. Instead, the analysis showed that iron nanoparticles can exist in both states at any size in the investigated range from 8 to 20 nm. In case of the iron nanoparticles in the *as deposited* state on silicon substrates, about one half of the nanoparticles were found in a magnetically blocked state, while the other half was found in a superparamagnetic state, with both fractions exhibiting nearly the same distribution of sizes as shown in Fig. 9.6g. Another surprising finding was that some of the magnetically blocked nanoparticles changed their behavior spontaneously and developed a superparamagnetic behaviour during the experiments, carried out at room temperature in a time span of several hours, see for instance Fig. 9.3e and f. This transition could be promoted by thermal treatment of the sample, in particular heating 420 K led to superparamagnetic behavior at room

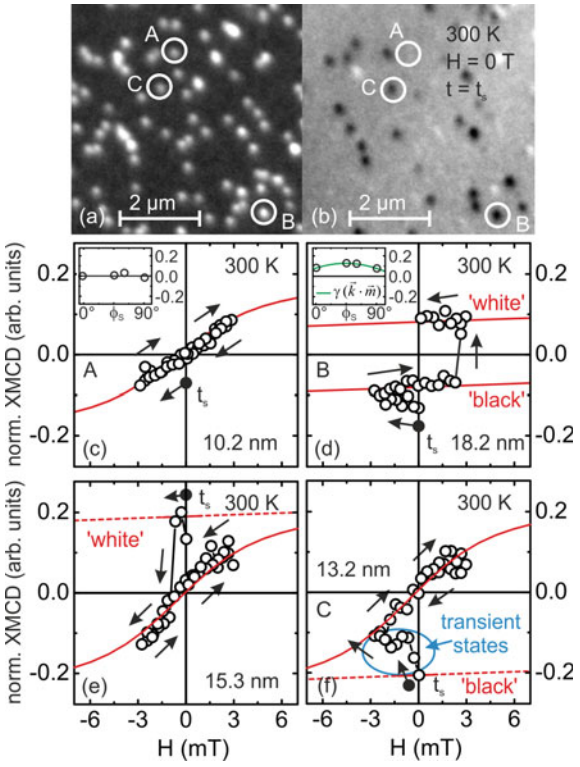

Fig. 9.3 **a**, **b** Elemental and magnetic contrast maps of iron nanoparticles on a silicon substrate. **c**–**f** Magnetization curves of individual nanoparticles (circles). The solid and the dashed lines are guides to the eye. The insets in **c**, **d** show the normalized XMCD recorded as a function of the azimuthal sample orientation φ_S as discussed in [38]. The dashed line in the inset of **d** is a fit to the data. The magnetization curves in **e**, **f** demonstrate spontaneous transitions from magnetically blocked states to superparamagnetic behavior. Reprinted with permission from [38]. Copyright (2014) by the American Physical Society

temperature in all nanoparticles. This observation demonstrates that the magnetic properties of iron nanoparticles critically depend on the thermal history of the sample, which could further explain some of the contradictory findings reported in the literature.

Some of the magnetically blocked nanoparticles could be switched between two states with opposite magnetization orientations, see Fig. 9.3d. This bistable behavior indicates a uniaxial magnetic anisotropy in the magnetically blocked nanoparticles. The associated magnetic energy barriers were found to be strongly enhanced when compared to those expected from the cubic magneto-crystalline anisotropy of bulk iron. Both characteristics, uniaxial magnetic anisotropy and enhanced magnetic energy barriers, were also found in several ensemble measurements of iron nanoparticles [23, 25] as well as in single particle measurements using microSQUID [27]. The authors of the latter work assigned those findings to surface and shape anisotropy contributions arising from deviations from the symmetric nanoparticle shape, which is for iron nanoparticles typically spherical, cubic, or truncated dodecahedra, as predicted by the Wulff theorem [5, 26, 27, 29, 46–49]. However, atomistic model calculations taking into account a Néel surface anisotropy with a negative Néel constant for iron and constraints on the nanoparticle shape (derived from TEM data),

revealed magnetic energy barriers that were still much lower when compared to the experimental values [27]. The authors assigned this discrepancy to an underestimated contribution of the Néel surface anisotropy in their calculations. Also in [38] it was shown by size and shape analysis that magnetic anisotropy contributions due to shape effects were too low to account for the observed magnetic energy barriers, which could similarly hint at an underestimated surface contribution to the magnetically blocked nanoparticles.

9.3.2 In Situ Oxidation of Iron Nanoparticles—The Role of the Surface

In a number of experiments it was observed that the effective magnetic anisotropy constants of iron nanoparticles increase with decreasing nanoparticle size [23, 24, 27]. In [24] this observation was explained by an effective surface anisotropy contribution which scales inversely with size and which adds to a bulk-like volume contribution. However, the large spread of the experimental data in the different reports does not permit the determination of an effective surface anisotropy constant which could be used to successfully predict the effective magnetic anisotropy of iron nanoparticles. This lack of understanding is partially related to the different surface states of the iron nanoparticles in the various experiments and the particular chemical reactivity of iron nanoparticles, which makes the control of their surface properties very difficult. For instance, the iron nanoparticles studied in [23] were covered with a native oxide layer, whereas the nanoparticles investigated in [27] were embedded in a niobium matrix, while pure iron nanoparticles were investigated in an inert gas atmosphere in [24]. Photoemission electron microscopy permits one to study samples under UHV conditions and under controlled exposure to reactive gases and has therefore been used to investigate chemical surface reactions [50–52]. By taking advantage of these capabilities, XPEEM was also used to investigate the evolution of magnetic properties and chemical states in iron nanoparticles directly during in situ oxidation experiments [53]. The latter work assumed that surface oxidation would drastically alter the electronic and magnetic properties of the free surface of the metal nanoparticles and would therefore be a direct probe of the role of the particle surface for the enhanced magnetic energy barriers of the magnetically blocked nanoparticles [38]. On the other side, the lattice mismatch between metallic iron and its oxides could give rise to significant strain in both the metallic core and the growing oxide shell and lead to sizeable modifications of the magnetic anisotropy energy due to magneto-elastic contributions, which in turn could lead to significantly altered properties in both superparamagnetic and magnetically blocked nanoparticles [54].

For the XPEEM in situ oxidation experiments, the iron nanoparticles were deposited on silicon wafers as in [38]. The pristine state of the samples revealed therefore a similar distribution of magnetically blocked and superparamagnetic nanoparticles. X-ray absorption (XA) spectra of individual nanoparticles recorded at the Fe

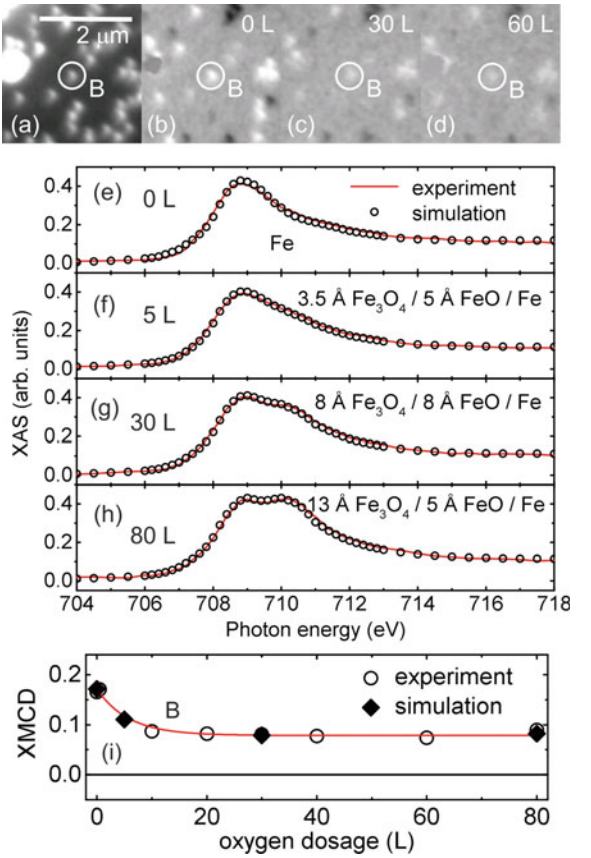

Fig. 9.4 **a** XPEEM elemental contrast map recorded with the photon energy set to the L_3 edge of metallic iron. **b–d** Magnetic contrast maps of the same area as in **a** recorded upon dosing the denoted amount of oxygen. The magnetically blocked particle "B" is highlighted with a solid circle in all images. **e–h** Simulated x-ray absorption spectra at the Fe L_3 edge as a function of oxygen dosage (circles) compared to the experimental data (red lines). The corresponding layer thicknesses used in the simulations are as denoted. **i** Magnetic contrast at the metallic Fe L_3 edge obtained from simulations (diamonds) and experimentally for particle "B" in **a–d** (circles). Line is a guide to the eye. Reproduced from [53] with permission from the PCCP Owner Societies

L_3 edge revealed that all nanoparticles consisted of pure metallic iron irrespective of their size or their magnetic state. This observation demonstrated that neither the superparamagnetic nor the magnetically blocked state originates from chemical surface modifications, which might occur during the nanoparticle growth or the sample preparation process. Stepwise exposure of the sample to molecular oxygen gave rise to a progressive stepwise oxidation of the nanoparticles. The oxidation state was probed after each exposure by recording XA spectra as shown in Fig. 9.4e–h. Similarly, the magnetic state of the nanoparticles was probed after each oxidation step, see Fig. 9.4b, c. The XA spectra revealed an evolution of the oxide layer from FeO at the lowest oxygen exposures towards Fe_3O_4 at higher dosages. The magnetic characterization showed that nearly all magnetically blocked nanoparticles preserved a stable orientation of their magnetic moments even after the longest exposure in the experiments, which led to the formation of a shell consisting mostly of Fe_3O_4 with an estimated thickness of about 2 nm. The latter value was deduced from fitting simulated XA spectra to the experimental data as discussed in detail in [38]. Likewise, no changes in the magnetic state of the superparamagnetic nanoparticles were observed.

These experiments directly demonstrate that the enhanced magnetic energy barriers in the magnetically blocked iron nanoparticles are not related with the free surface of the pure, metallic iron nanoparticles. The findings also confirm that a Néel-type surface anisotropy is not sufficient to explain the enhanced magnetic anisotropy observed in the magnetically blocked iron nanoparticles even when taking non-collinear surface spin configurations into account, as discussed in [5, 38, 55]. Moreover, the oxidation experiments confirm that enhanced magnetic energy barriers can be observed in partially oxidized iron nanoparticles and that interactions of the metallic core with the oxide layer are not necessary as proposed in [23], and, as seen in the in situ oxidation experiments, also not sufficient to establish magnetically blocked states in initially superparamagnetic nanoparticles. The in situ oxidation investigations show that the origin for the large magnetic anisotropy barriers is indeed very local and resides either deep in the particle volume or at the interface with the substrate, which is most likely not affected by the oxidation.

9.3.3 Iron Nanoparticles Deposited on Different Substrates—The Role of the Interface

In the previous sections it was shown that gas-phase grown iron nanoparticles with sizes ranging from 8 to 20 nm deposited on silicon substrates can exist in both a superparamagnetic state, as expected from bulk and surface contributions to the total magnetic anisotropy, and in a metastable state, with uniaxial anisotropy and significantly enhanced magnetic energy barriers when compared to the bulk properties [38]. It was further shown that the enhanced magnetic stability of the magnetically blocked nanoparticles is not related to their free surface [53]. In this section, we discuss the role of the interface to the substrate for the magnetic anisotropy of the iron nanopartices. The interface between different magnetic and non-magnetic materials is well known to modify magnetic phenomena in thin films and multilayers and can be used to control magnetism at the nanoscale [56]. Interface effects on the magnetic anisotropy of supported clusters and nanoparticles were also frequently reported, see for instance [57, 58]. Ensemble measurements performed under UHV conditions revealed, for instance, that iron nanoparticles deposited on single crystalline copper surfaces can have strongly enhanced magnetic anisotropy energies [28], which can even give rise to magnetically blocked states at room temperature [45], while deposition on W(110) leads only to a superparamagnetic state at room temperature with the magnetic fluctuations occuring mainly in the surface plane [59]. However, the sample preparation conditions varied in the different experiments and, therefore, it remained unclear whether the observed effects are indeed due to the interface or reflect intrinsic properties of the nanoparticles.

This issue was addressed in an XPEEM study, where iron nanoparticles with sizes in the range from 8 to 20 nm were deposited on three single crystalline substrates, namely Cu(001), NiO(110), and W(110) in addition to the Si substrates [60].

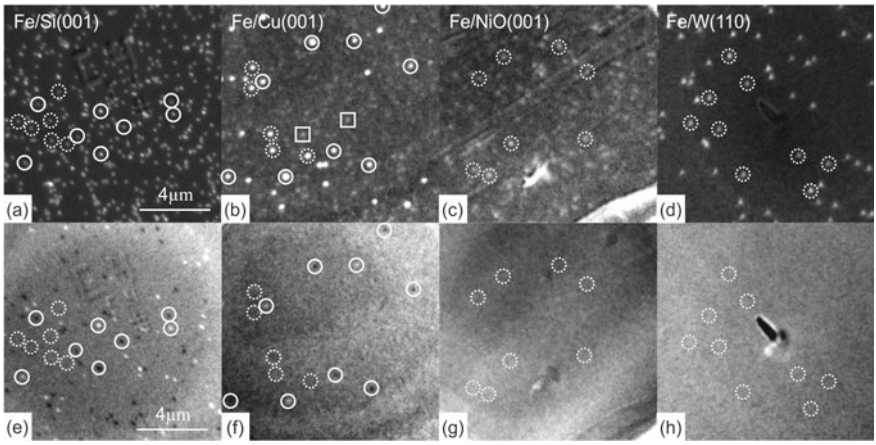

Fig. 9.5 **a–d** XPEEM elemental contrast maps of Fe nanoparticles (bright spots) deposited on **a** Si(001), **b** Cu(001), **c** NiO(001), and **d** W(110). The scale bar is the same for all images. **e–h** Corresponding magnetic contrast maps of the same areas on **e** Si(001), **f** Cu(001), **g** NiO(001), and **h** W(110). The position of a number of particles is denoted by circles as a guide to the eye. Solid circles denote magnetically blocked nanoparticles with magnetic contrast ranging from black to white. Dashed circles indicate a number of superparamagnetic particles, which show no magnetic contrast in **e–h**. All data are recorded at the Fe L_3 edge. Reprinted from [60], Copyright (2015), with permission from Elsevier

Similarly to the in situ oxidation, such investigation took advantage of the UHV compatibility of XPEEM to avoid modifications of the nanoparticle or substrate surface due to oxidation or interactions with matrix materials. The nanoparticles were prepared and deposited under identical conditions using the ACIS as in the previously discussed XPEEM works in [5, 38, 53]. Figure 9.5 shows the XPEEM elemental and magnetic contrast maps of the iron nanoparticles on the four different substrates. The data reveal that magnetically blocked nanoparticles are observed only on the silicon wafers and on the Cu(001) single crystal surface, but not on the antiferromagnetic NiO(110) and non-magnetic W(110) substrates, and therefore confirm the significant impact of the substrate on the magnetic properties of the nanoparticles. In particular, the data reveal that the magnetic energy barriers can be higher on silicon and copper surfaces when compared to NiO(110) and W(110). However, as discussed in [60], this behavior is ascribed to the nanoparticle deposition process and the different interfacial bonding energies of the four substrates rather than to different magnetic interface anisotropy contributions.

To rationalize this interpretation, we consider first the iron nanoparticles deposited on the W(110) surface. In thin films, the Fe/W(110) interface is known to possess a strong magnetic interface anisotropy with preferred in-plane magnetization axis, which could contribute to enhanced magnetic energy barriers in iron nanoparticles [61]. However, both ensemble and XPEEM measurements show that any interface-induced enhancement of the magnetic anisotropy of the nanoparticles by the interface

is not sufficient to induce magnetically blocked states at room temperature [59, 60]. Instead, the interface contribution leads to superparamagnetism with preferred in-plane magnetization as discussed in [59]. Also, in case of iron nanoparticles in contact with NiO(110), one could expect to find magnetically blocked states due to a strong exchange interaction with the antiferromagnetic substrate as observed in case of iron films grown on NiO [62, 63]. However, the absence of magnetically blocked states in iron nanoparticles on NiO(110) suggests a reduced interaction via the finite or imperfect contact interface when compared to the thin film systems. Imperfect interfaces are indeed likely for iron nanoparticles on all four investigated substrates, since RHEED experiments show that nanoparticles in the present size range are randomly oriented upon deposition on different substrates and under sample preparation conditions similar to the XPEEM works discussed here [5, 64]. For instance, in single crystalline fcc systems, the deposition of nanoparticles can lead to the formation of defects at the interface such as twin boundaries between epitaxial and non-epitaxial parts of the nanoparticles [65].

While for the iron nanoparticles on Cu(001) no particularly strong interface anisotropy is anticipated, enhanced magnetic energy barriers have been observed in ensemble measurements and in XPEEM investigations [28, 45, 60]. In [28, 45] the enhanced magnetic energy barriers of iron nanoparticles on copper substrates were attributed to indirect, surface state mediated interactions between the nanoparticles, which are expected to occur over short distance (few nm) and should only be present in dense samples. In the XPEEM experiments, the nanoparticles are separated by a few hundred nm and short range interactions can be excluded. Thus, the XPEEM data demonstrate that short range interactions are not necessary to establish enhanced magnetic energy barriers in iron nanoparticles on Cu(001), but suggest instead that they are intrinsic to the nanoparticles. Likewise, for the iron nanoparticles on the silicon substrates, no strong interface anisotropy or substrate induced magnetic interactions are expected, but magnetically blocked nanoparticles are observed at room temperature. Also this observation hints at an intrinsic rather then interface-induced origin of the enhanced magnetic energy barriers of the magnetically blocked nanoparticles. This conclusion is further supported by the fact that the magnetic moments of the magnetically blocked nanoparticles are randomly oriented on the silicon substrates [38], while a dominant interface-induced magnetic anisotropy would prefer either in-plane or out-of-plane oriented magnetic moments.

These considerations show that the magnetically blocked states of iron nanoparticles are not induced by interface effects, such as magnetic interface anisotropy, exchange interaction or surface-mediated magnetic interactions. Further, since the magnetically blocked states of iron nanoparticles can spontaneously relax towards a superparamagnetic state, as found in case of the silicon substrates, one is led to conclude that the enhanced magnetic energy barriers are an intrinsic, but metastable property of iron nanoparticles, possibly originating from the nanoparticle growth process [31]. This enhanced magnetic anisotropy is then preserved upon deposition on silicon wafers and on the Cu(001) single crystal surface, but lost upon deposition on NiO(110) and W(110). Such behavior could be assigned to the free surface energy E_s of the investigated substrates: SiO_x ($E_s \sim 0.2$ J/m^2) and Cu(001)

($E_s = 1.8$ J/m^2) have the lowest free surface energy, and interact therefore only weakly with the nanoparticles when the contact between the nanoparticle and the substrate is established. The higher free surface energy of NiO(110) ($E_s \sim 3.0$ J/m^2) and W(110) ($E_s = 3.5$ J/m^2) lead to a stronger interaction and to a relaxation of the high anisotropy state towards the superparamagnetic state upon impact of the nanoparticle on the substrate.

9.3.4 Comparison with Cobalt, Nickel and Iron–Cobalt-Alloy Nanoparticles

Finally, we address the question of whether strongly enhanced magnetic energy barriers and metastable states are only observed in iron nanoparticles or whether comparable behavior is found in other 3*d* transition metal nanoparticles as well. For this purpose fcc cobalt and fcc nickel nanoparticles were deposited on silicon substrates as in the case of the iron nanoparticles [5]. Surprisingly, for cobalt the same size-independent coexistence of superparamagnetic and magnetically blocked nanoparticles was found as observed for iron, see Fig. 9.6. Also in the case of fcc cobalt, the observation of magnetically blocked states at room temperature show the presence of significantly enhanced magnetic energy barriers when compared to the fcc bulk magneto-crystalline anisotropy and surface anisotropy contributions as discussed in detail in [5]. However, in contrast to iron nanoparticles, thermal annealing promotes transitions from superparamagnetic states into a magnetically blocked state in a large number of nanoparticles. In contrast to iron and cobalt, only superparamagnetic states were found in fcc nickel nanoparticles at room temperature [5]. Also $Fe_{50}Co_{50}$ alloy nanoparticles deposited on silicon substrates under similar conditions as the iron, cobalt, and nickel nanoparticles exhibit a coexistence of superparamagnetic and magnetically blocked nanoparticles at room temperature [66]. These findings demonstrate that the coexistence of states with distinct magnetic properties is not restricted to iron nanoparticles, but seems a more general phenomena among pure and alloyed 3*d* transition metal nanoparticles.

9.4 Conclusions and Perspectives

In this chapter we have demonstrated that XPEEM is a powerful tool for magnetic and chemical characterization of individual 3*d* transition metal nanoparticles under both UHV conditions and under reactive gas environments for in situ study of chemical reactions. Moreover, by combining XPEEM investigations with complementary structural characterization such as SEM and AFM, one is able to correlate directly magnetism, shape, and size of a large number of the very same nanoparticles and probe the actual distribution of magnetic properties in extended ensembles and

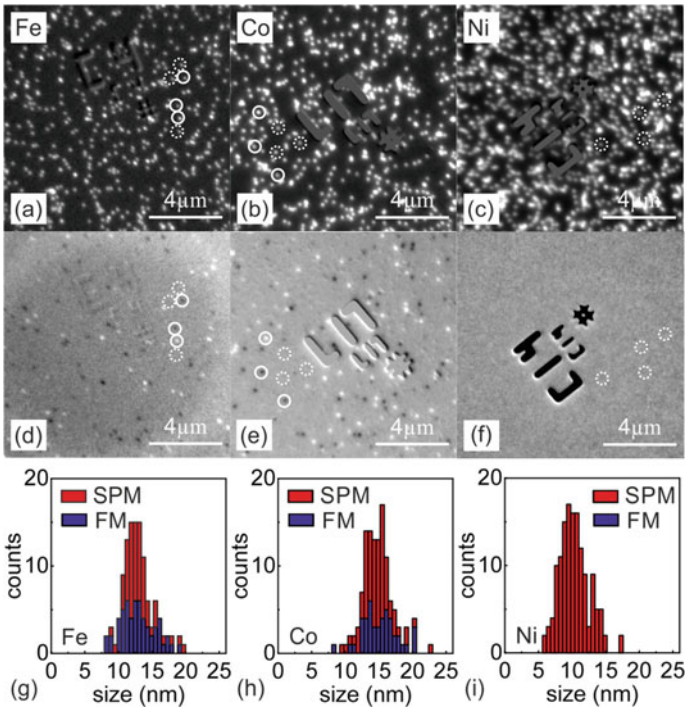

Fig. 9.6 **a**–**c** Elemental contrast maps of **a** iron, **b** cobalt, and **c** nickel nanoparticles in the as deposited state at room temperature. **d**–**f** Respective magnetic contrast maps. Examples of particles in superparamagnetic and magnetically blocked states are highlighted with dashed and solid circles, respectively. **g**–**i** Relative fraction of superparamagnetic (red) and magnetically blocked (blue) nanoparticles as a function of the particle size for **g** iron, **h** cobalt, and **i** nickel nanoparticles. Reprinted with permission from [5]. Copyright (2017) by the American Physical Society

under controlled conditions. The works presented here show that iron, cobalt, and iron–cobalt-alloy nanoparticles with sizes ranging from 8 to 20 nm can be found in a novel magnetically blocked state with significantly enhanced magnetic energy barriers when compared to the respective bulk and surface contributions to the magnetic anisotropy, while for nickel nanoparticles only the expected superparamagnetic states are observed [5, 38, 66]. For bcc iron and fcc cobalt nanoparticles it was further observed that magnetically blocked and superparamagnetic nanoparticles can coexist irrespective of size. In the case of iron nanoparticles, the magnetically blocked state is metastable and can relax towards the superparamagnetic state, while in the case of the cobalt nanoparticles, thermal excitation promotes a transition from the superparamagnetic state towards the magnetically blocked state [5, 38]. These findings demonstrate that the magnetic properties of iron and cobalt nanoparticles depend on the thermal history of the sample. In the case of iron nanoparticles it was further shown that the enhanced magnetic energy barriers are not due to surface or interface-related effects, but are rather intrinsic to the nanoparticles [53, 60].

While these findings contribute to a better understanding of the controversial reports on the magnetic anisotropy of 3*d* transition metal nanoparticles available in the literature, the actual microscopic origin of the enhanced magnetic anisotropy energy in iron, cobalt and iron–cobalt-alloy nanoparticles has yet to be clarified. The fact that the SEM and AFM characterization yield no discernible differences between magnetically blocked and superparamagnetic nanoparticles, strongly suggests that the origin of the enhanced magnetic energy barriers lies in the microstructure of the nanoparticles. Since the iron and cobalt nanoparticles in [5, 38] were only found in the well known bcc and fcc lattices, the enhanced magnetic energy barriers might be related to structural defects, such as dislocations or stacking faults, which could arise from the growth kinetics, for instance [31]. Dislocations give rise to local strain and therefore to magneto-elastic contributions to the total magnetic anisotropy. For iron and cobalt, the magnetic energy barriers due to dislocations can significantly exceed those arising from the respective magneto-crystalline anisotropy, and might therefore contribute to the enhanced magnetic energy barriers as discussed in more detail in [5]. Moreover, in the case of bcc iron, dislocations are highly mobile and might be ejected from the finite volume of iron nanoparticles upon thermal excitation. Such mechanism could explain the observed transitions from magnetically blocked to superparamagnetic states in individual iron nanoparticles. In the case of fcc cobalt nanoparticles, stacking faults are frequently observed, which can give rise to local hcp stacks within the nanoparticles [5, 67]. Based on the properties of bulk cobalt, hcp stacking could give rise to sizable uniaxial magnetic anisotropy contributions and lead to the observed magnetically blocked states at room temperature. Moreover, local hcp stacking may even increase the cohesion energy of nanoparticles and might therefore even be promoted by thermal annealing, which could explain the observed transition from superparamagnetic to magnetically blocked states in individual cobalt nanoparticles.

To achieve a direct correlation between microstructure and magnetic anisotropy energy requires one to combine magnetic characterization with structural characterization with atomic resolution of the very same nanoparticle. Such correlation can be achieved for instance by combining XPEEM with atomic resolution TEM. First successful experiments on cobalt nanoparticles show the feasibility of such approach, and hold the promise that the nature and orientation of the crystal lattice and defects together with the orientation of the magnetization of the nanoparticles can be obtained. Such results are expected to provide an unprecedented benchmark for the development of new theoretical models for nanoparticle magnetism that take both the impact of surface properties and structural defects on the magnetic properties into account. Experimentally, such approach will allow one to unambiguously address the impact of the many different structural motifs found in nanoparticles on their magnetic properties. Such motifs include multiply twinned structures, various truncated polyhedral forms, and the unique crystallographic phases, that can be found at the nanoscale, such as the ϵ–phase in cobalt or the hcp phase in nickel nanoparticles [40–43]. Such knowledge, will significantly improve our understanding of magnetism at the nanoscale and will enable one to achieve an increased control over the magnetic properties of nanoparticles. Finally, we note that magnetic charac-

terization using XPEEM is not restricted to ferromagnetic nanoparticles, but can also be used for the investigation of antiferromagnetic nanoparticles by means of the x-ray magnetic linear dichroism effect. Similar to the case of ferromagnetic nanoparticles, XPEEM can help to reveal finite size effects in nano-sized antiferromagnets, which are not only interesting for fundamental research on magnetism at the nanoscale, but also of great interest for spintronics applications [68].

Acknowledgements The author thanks J. Bansmann, A. Fraile Rodríguez, K.-H. Meiwes-Broer, and F. Nolting for their contributions and their support in establishing XPEEM as an in situ probe for studying individual nanoparticles. C. A. F. Vaz is acknowledged for his contribution to the experiments, fruitful discussions, and critical reading of this manuscript.

References

1. A.H. Lu, E.L. Salabas, F. Schüth, Angew. Chem. **46**, 1222 (2007)
2. D.L. Huber, Small **1**, 482 (2005)
3. J.L. Dormann, D. Fiorani, E. Tronc, *Magnetic Relaxation in Fine-Particle Systems* (Wiley, New York, 1997)
4. R.H. Kodama, J. Magn. Magn. Mater. **200**, 359 (1999)
5. A. Kleibert, A. Balan, R. Yanes, P.M. Derlet, C.A.F. Vaz, M. Timm, A. Fraile Rodríguez, A. Béché, J. Verbeeck, R.S. Dhaka, M. Radovic, U. Nowak, F. Nolting, Phys. Rev. B **95**, 195404 (2017)
6. D. Schmool, H. Kachkachi, Solid State Phys. **66**, 301 (2015)
7. M. Jamet, W. Wernsdorfer, C. Thirion, D. Mailly, V. Dupuis, P. Mélinon, A. Pérez, Phys. Rev. Lett. **86**, 4676 (2001)
8. C. Gatel, F.J. Bonilla, A. Meffre, E. Snoeck, B. Warot-Fonro, B. Chaudret, L.M. Lacroix, T. Blon, Nano Lett. **15**, 6952 (2015)
9. E. Bauer, *Surface Microscopy with Low Energy Electrons* (Springer, New York, 2014)
10. C.A.F. Vaz, A. Kleibert, M. El Kazzi, in *Nanoscale XPEEM Spectromicroscopy 21st Century Nanoscience–A Handbook: Advanced Analytical Methods and Intrumentation*, Vol. 3, ed. by D.S. Klaus (CRC Press, Taylor & Francis Group, Boca Raton, London, New York, 2020)
11. C.M. Schneider, J. Magn. Magn. Mater. **160**, 9517 (1997)
12. G. Schönhense, J. Phys.: Condens. Matter **11**, 9517 (1999)
13. A. Scholl, Curr. Opin. Solid State Mater. Sci. **7**, 59 (2003)
14. J. Stöhr, H.C. Siegmann, *Magnetism* (Springer, Berlin, 2006)
15. E. Beaurepaire, H. Bulou, F. Scheurer, J.P. Kappler (eds.), *Magnetism: A Synchrotron Radiation Approach*. Lect. Notes Phys. 697 (Springer, Berlin Heidelberg, 2006)
16. A. Locatelli, E. Bauer, J. Phys.: Condens. Matter **20**, 093002 (2008)
17. F. Nolting, in *Magnetism and Synchrotron Radiation*, ed. by E. Beaurepaire, H. Bulou, F. Scheurer, K. Jean-Paul (Springer, Berlin, 2010), pp. 345–366
18. W. Kuch, R. Schäfer, P. Fischer, F.U. Hillebrecht, *Magnetic Microscopy of Layered Structures*. Springer Series in Surface Sciences 57 (Springer, Berlin, Heidelberg, 2015)
19. J. Rockenberger, F. Nolting, J. Lüning, J. Hu, A.P. Alivisatos, J. Chem. Phys. **116**, 6322 (2002)
20. A. Fraile Rodríguez, F. Nolting, J. Bansmann, A. Kleibert, L.J. Heyderman, J. Magn. Magn. Mater. **316**, 426 (2007)
21. A. Fraile Rodríguez, A. Kleibert, J. Bansmann, A. Voitkans, L.J. Heyderman, F. Nolting, Phys. Rev. Lett. **104**, 127201 (2010)
22. A. Fraile Rodríguez, A. Kleibert, J. Bansmann, F. Nolting, J. Phys. D **43**, 474006 (2010)
23. S. Gangopadhyay, G.C. Hadjipanayis, B. Dale, C.M. Sorensen, K.J. Klabunde, V. Papaefthymiou, A. Kostikas, Phys. Rev. B **45**, 9778 (1992)

24. F. Bødker, S. Mørup, S. Linderoth, Phys. Rev. Lett. **72**, 282 (1994)
25. T. Ibusuki, S. Kojima, O. Kitakami, Y. Shimada, IEEE Trans. Magn. **37**, 2223 (2001)
26. D.L. Peng, T. Hihara, K. Sumiyama, H. Morikawa, J. Appl. Phys. **92**, 3075 (2002)
27. M. Jamet, W. Wernsdorfer, C. Thirion, V. Dupuis, P. Mélinon, A. Pérez, D. Mailly, Phys. Rev. B **69**, 024401 (2004)
28. J.P. Pierce, M.A. Torija, Z. Gai, J. Shi, T.C. Schulthess, G.A. Farnan, J.F. Wendelken, E.W. Plummer, J. Shen, Phys. Rev. Lett. **92**, 237201 (2004)
29. A.V. Trunova, R. Meckenstock, I. Barsukov, C. Hassel, O. Margeat, M. Spasova, J. Lindner, M. Farle, J. Appl. Phys. **104**, 093904 (2008)
30. J. Carvell, E. Ayieta, A. Garvin, R. Cheng, V.R. Shah, P. Sokol, J. Appl. Phys. **107**, 103913 (2010)
31. J. Liu, K. Schliep, S.H. He, B. Ma, Y. Jing, D.J. Flannigan, J.P. Wang, Phys. Rev. Mater. **2**, 054415 (2018)
32. F. Kronast, N. Friedenberger, K. Ollefs, S. Gliga, L. Tati-Bismaths, R. Thies, A. Ney, R. Weber, C. Hassel, F.M. Römer, A.V. Trunova, C. Wirtz, R. Hertel, H.A. Dürr, M. Farle, Nano Lett. **11**, 1710 (2011)
33. A.P. Hitchcock, J. Electron Spectrosc. Relat. Phenom. **200**, 49 (2015)
34. G. Tinti, H. Marchetto, C.A.F. Vaz, A. Kleibert, M. Andrä, R. Barten, A. Bergamaschi, M. Brückner, S. Cartier, R. Dinapoli, E. Fröjdh, D. Greiffenberg, C. Lopez-Cuenca, D. Mezza, A. Mozzanica, F. Nolting, M. Ramilli, S. Redford, M. Ruat, C. Ruder, L. Schädler, T. Schmidt, B. Schmitt, F. Schütz, X. Shi, D. Thattil, S. Vetter, J. Zhang, J. Synchrotron Radiat. **24**, 963 (2017)
35. L. Le Guyader, A. Kleibert, A. Fraile Rodríguez, S. El Moussaoui, A. Balan, M. Buzzi, J. Raabe, F. Nolting, J. Electron. Spectrosc. Relat. Phenom. **185**, 371 (2012)
36. J. Stöhr, *NEXAFS Spectroscopy* (Springer, Heidelberg, 1996)
37. A. Scholl, M.A. Marcus, A. Doran, J. Nasiatka, A.T. Young, A.A. MacDowell, R. Streubel, N. Kent, J. Feng, W. Wan, H.A. Padmore, Ultramicroscopy **188**, 77 (2018)
38. A. Balan, P.M. Derlet, A. Fraile Rodríguez, J. Bansmann, R. Yanes, U. Nowak, A. Kleibert, F. Nolting, Phys. Rev. Lett. **112**, 107201 (2014)
39. J. Stöhr, S. Anders, IBM, J. Res. Dev. **44**, 535 (2000)
40. V.F. Puntes, K.M. Krishnan, A.P. Alivisatos, Science **291**, 2115 (2001)
41. O. Kitakami, H. Sato, Y. Shimada, F. Sato, M. Tanaka, Phys. Rev. B **56**, 13849 (1997)
42. R. Morel, A. Brenac, C. Portemont, T. Deutsch, L. Notin, J. Magn. Magn. Mater. **308**, 296 (2007)
43. R. Masuda, Y. Kobayashi, S. Kitao, M. Kurokuzu, M. Saito, Y. Yoda, T. Mitsui, K. Hosoi, H. Kobayashi, H. Kitagawa, M. Seto, Sci. Rep. **6**, 20861 (2016)
44. H. Nagaoka, Ann. Phys. **295**, 66 (1896)
45. K. Fauth, G.A. Ballentine, C. Praetorius, A. Kleibert, N. Wilken, A. Voitkans, K.H. Meiwes-Broer, Phys. Status Solidi (b) **247**, 1170 (2010)
46. A. Kleibert, J. Passig, K.H. Meiwes-Broer, M. Getzlaff, J. Bansmann, J. Appl. Phys. **101**, 114318 (2007)
47. J. Bansmann, A. Kleibert, Appl. Phys. A **80**, 957 (2005)
48. T. Vystavel, G. Palasantzas, S.A. Koch, J.T.M. De Hosson, Appl. Phys. Lett. **82**, 197 (2003)
49. A. Kleibert, J. Bansmann, K.H. Meiwes-Broer, Phys. Rev. B **79**, 125423 (2009)
50. H.H. Rotermund, W. Engel, M. Kordesch, G. Ertl, Nature **343**, 355 (1990)
51. R. Imbihl, J. Electron Spectrosc. Relat. Phenom. **185**, 347 (2012)
52. W. Karim, C. Spreafico, A. Kleibert, J. Gobrecht, J. VandeVondele, Y. Ekinci, J.A. van Bokhoven, Nature **541**, 68 (2017)
53. C.A.F. Vaz, A. Balan, F. Nolting, A. Kleibert, Phys. Chem. Chem. Phys. **16**, 26624 (2014)
54. A. Pratt, L. Lari, O. Hovorka, A. Shah, C. Woffinden, S.P. Tear, C. Binns, R. Kroger, Nat. Mater. **13**, 26 (2014)
55. D.A. Garanin, H. Kachkachi, Phys. Rev. Lett. **90**, 065504 (2003)
56. C.A.F. Vaz, J.A.C. Bland, G. Lauhoff, Rep. Prog. Phys. **71**, 056501 (2008)

57. J. Bansmann, S. Baker, C. Binns, J. Blackman, J.P. Bucher, J. Dorantes-Dávila, V. Dupuis, L. Favre, D. Kechrakos, A. Kleibert, K.H. Meiwes-Broer, G. Pastor, A. Perez, O. Toulemonde, K. Trohidou, J. Tuaillon, Y. Xie, Surf. Sci. Rep. **56**, 189 (2005)
58. M. Martins, W. Wurth, J. Phys.: Condens. Matter **28**, 503002 (2016)
59. A. Kleibert, F. Bulut, R.K. Gebhardt, W. Rosellen, D. Sudfeld, J. Passig, J. Bansmann, K.H. Meiwes-Broer, M. Getzlaff, J. Phys.: Condens. Matter **20**, 445005 (2008)
60. A. Balan, A. Fraile Rodríguez, C.A.F. Vaz, A. Kleibert, F. Nolting, Ultramicroscopy **159**, 513 (2015)
61. H. Fritzsche, H.J. Elmers, U. Gradmann, J. Magn. Magn. Mater. **135**, 343 (1994)
62. E. Mlynczak, P. Luches, S. Valeri, J. Korecki, J. Appl. Phys. **113**, 234315 (2013)
63. P. Luches, S. Benedetti, A. di Bona, S. Valeri, Phys. Rev. B **81**, 054431 (2010)
64. A. Kleibert, A. Voitkans, K.H. Meiwes-Broer, Phys. Rev. B **81**, 073412 (2010)
65. T. Järvi, A. Kuronen, K. Meinander, K. Nordlund, K. Albe, Phys. Rev. B **75**, 115422 (2007)
66. A. Kleibert, A. Balan, A. Fraile Rodríguez, F. Nolting, J. Phys. Conf. Ser. **521**, 012003 (2014)
67. W. Wernsdorfer, C. Thirion, N. Demoncy, H. Pascard, D. Mailly, J. Magn. Magn. Mater. **242**, 132 (2002)
68. V. Baltz, A. Manchon, M. Tsoi, T. Moriyama, T. Ono, Y. Tserkovnyak, Rev. Mod. Phys. **90**, 015005 (2018)

Chapter 10
Measuring Atomic Magnetic Moments in Magnetic Nanostructures Using X-Ray Magnetic Circular Dichroism (XMCD)

Chris Binns, José Angel de Toro, and Peter Normile

Abstract The chapter describes the development of X-ray magnetic circular dichroism (XMCD) using circularly polarised soft X-ray photons from synchrotron sources. Following the derivation of X-ray absorption sum rules for magnetic materials, the technique became a powerful probe of magnetism able to separately measure the atomic and spin orbital magnetic moments independently for each magnetic element in the sample. The majority of the experiments have focused on the L-absorption edges of transition metals and the method has been particularly useful in identifying the source of enhanced magnetic moments in nanostructures. The chapter illustrates the power of the method with a specific example, that of Fe@Cr core–shell nanoparticles with different Cr shell thicknesses. Here, it was shown that at least two Cr atomic layers are required to see the onset of the exchange bias effect at the ferromagnetic–antiferromagnetic interface. The future perspectives of the technique are described including spatially resolved XMCD and time-resolved XMCD measurements.

10.1 Introduction

X-ray magnetic circular dichroism (XMCD) has emerged as a powerful tool that is capable of measuring element-specific atomic orbital and spin magnetic moments in materials. The technique has enabled some important breakthroughs in the understanding of the magnetic behaviour of nanostructures. Magnetic circular dichroism in the UV band has been known since the nineteenth century but X-ray magnetic circular dichroism began to be of interest as a magnetic measurement method in the 1970s. Erskine and Stern predicted in 1975 that circularly polarised X-rays could provide information on the valence band spin polarisation of Ni [1]. In 1987, a measurement of the transmission of synchrotron radiation through thin Fe films showed a difference

C. Binns (✉) · J. A. de Toro · P. Normile
Instituto Regional de Investigación Científica Aplicada (IRICA), Av. Camilo José Cela, 1, 13005 Ciudad Real, Spain
e-mail: christopher.binns@uclm.es

D. Peddis et al. (eds.), *New Trends in Nanoparticle Magnetism*,
Springer Series in Materials Science 308,
https://doi.org/10.1007/978-3-030-60473-8_10

in K-edge absorption for left and right circularly polarised photons [2]. As shown by Erskine and Stern, however, in the case of transition metals, $L_{2,3}$-edge absorption in the soft X-ray band is potentially a more powerful source of information though technically more difficult. An important breakthrough starting in the early 1980s was the emergence of dedicated synchrotron radiation sources that could produce high intensities of circularly polarised soft X-rays.

Figure 10.1 shows the two basic experimental set-ups for the measurement of dichroism in the *L*-edge absorption spectrum of a sample containing a transition metal. The photon beam is circularly polarised with the *L*-vector parallel or antiparallel to the beam and the sample magnetisation, ***M***, can be magnetised to saturation parallel or antiparallel to ***L***. Figure 10.1a shows a measurement where the sample can be deposited onto a substrate that is transparent to soft X-rays, for example, a carbon-coated transmission electron microscope (TEM) grid. In this case, the incident and transmitted beams are measured and the difference between them is the X-ray absorption. Figure 10.1b shows the other set-up when the sample is a bulk material or deposited on a substrate opaque to soft X-rays. In this case, the total secondary electron yield, which within certain assumptions is proportional to the X-ray absorption, is measured and normalised to the incident X-ray intensity. The

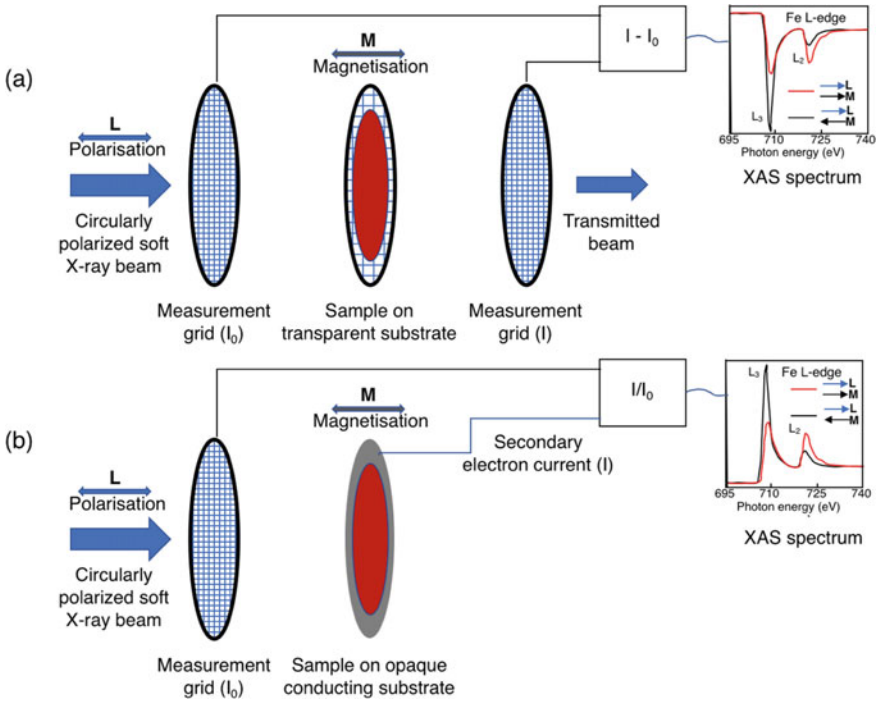

Fig. 10.1 The two basic configurations for measuring XMCD. **a** In transmission for transparent substrates. **b** By using secondary electron yield for opaque and conducting substrates or bulk samples. The example spectra shown are the *L*-edge absorption in samples containing Fe

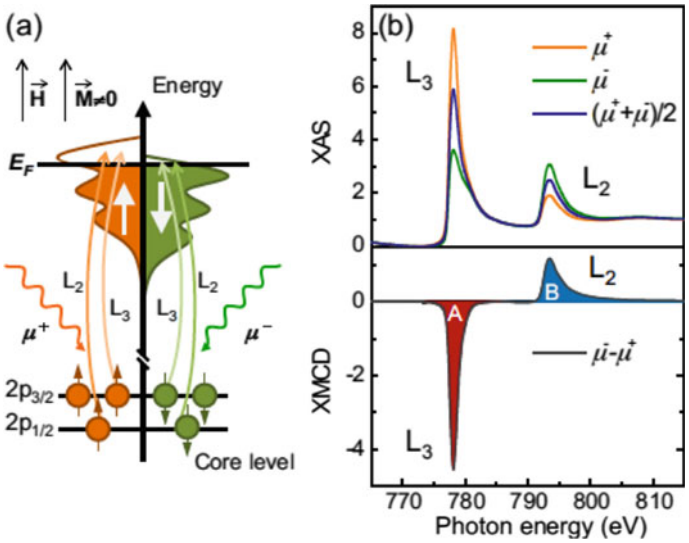

Fig. 10.2 The basic two-step process used to explain *L*-edge X-ray dichroism in a magnetic sample. Positive helicity μ^+ X-ray photons ($\boldsymbol{L} = +1$ excite mostly spin-up (majority band) electrons from the $2p_{3/2}$ level and since the empty states available at the fermi level are mostly spin-up, the absorption is enhanced relative to the unpolarised spectrum. The same photons excite mostly spin-down electrons from the $2p_{1/2}$ level so the absorption is reduced relative to the unpolarised spectrum. The opposite is true for the negative helicity μ^- photons ($\boldsymbol{L} = -1$). Reproduced from [4]

example spectra are from a sample containing Fe. The difference in the spectra between the parallel and antiparallel alignments of $\boldsymbol{L}$ and $\boldsymbol{M}$, that is, the dichroism, is clear and the dichroic spectrum can be analysed to determine the orbital and spin magnetic moments of the atoms.

The fundamental mechanism that produces the $L_{2,3}$-edge dichroism is normally described as a two-step process [3] illustrated in Fig. 10.2 [4]. In the first step, circularly polarised photons excite spin-polarised electrons from the spin–orbit split $2p$ level. In the case of positive helicity ($\boldsymbol{L} = +1$, electrons excited from the $2p_{3/2}$ level are 62.5% spin-up while those from the $2p_{1/2}$ level are 25% spin-up. The corresponding proportions for negative helicity ($\boldsymbol{L} = -1$) are 37.5% and 75%, respectively. These spin-polarised electrons are excited into the valence band and if this is spin-polarised then it acts as a spin filter for the polarised emission from the $2p$ level (step 2). Thus, in the case of a magnetised sample, the $L_{2,3}$ absorption spectrum shows a different spectral dependence for parallel and antiparallel alignments of $\boldsymbol{L}$ and $\boldsymbol{M}$.

As illustrated in Fig. 10.3 for Fe, Co, and Ni, the $L_{2,3}$ edges of the transition metals are at different X-ray energies [5]. The dichroism at each edge can be measured and thus the magnetic moments of the atoms of each element can be determined independently, which is especially important for samples containing more than one magnetic element.

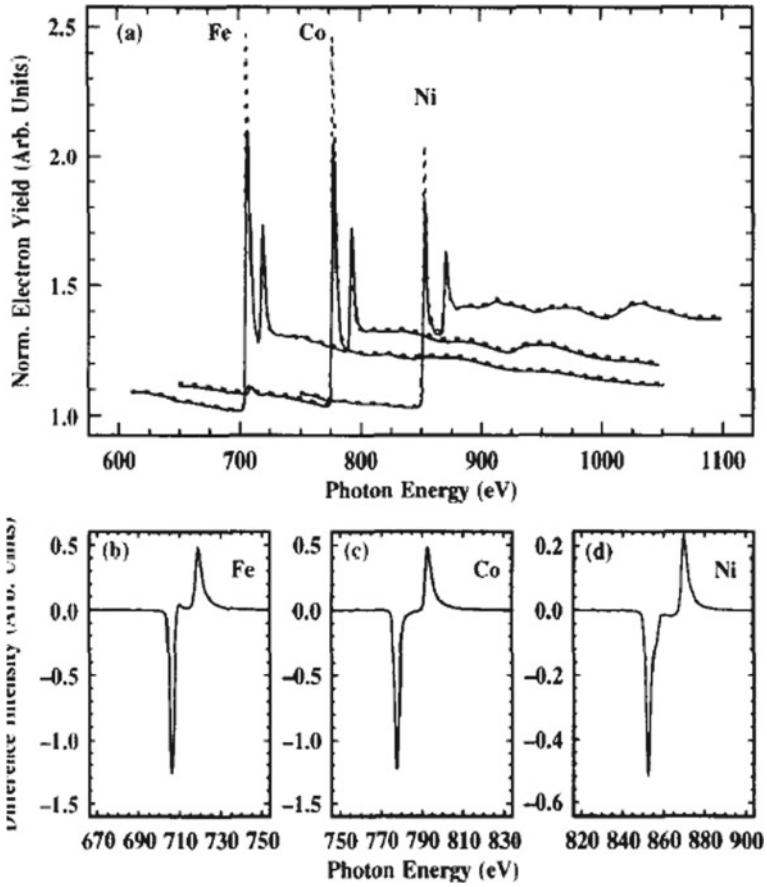

Fig. 10.3 XAS spectra and dichroism of the $L_{2,3}$ edges in thin films of Fe, Co, and Ni measured in transmission (Fig. 10.1a). Reproduced from [5]

The development of XMCD as a precise measuring tool of atomic magnetic moments began with the formulation of the sum rules for the absorption of circularly polarised X-rays by magnetic materials [6, 7]. The most important sum rules relate the projection of the spin $\langle S_Z \rangle$ and orbital $\langle L_Z \rangle$ magnetic moments along the photon polarisation direction to partial differential absorption cross sections at the L_2 and L_3 edges. Originally, these were derived using a graphical angular momentum technique [6, 7] but later, the same sum rules were obtained within a Fermi golden rule formalism [8, 9]. For transitions from core states with an angular momentum quantum number l_c to valence states with an angular momentum quantum number l_v, the orbital moment sum rule is given by [6]:

$$\langle L_z \rangle = 2\frac{l_v(l_v+1)}{l_c(l_c+1)-l_v(l_v+1)-2}\frac{\int_{\text{edge}}\left(\mu_{\uparrow\uparrow}(\omega)-\mu_{\uparrow\downarrow}(\omega)\right)\mathrm{d}\omega}{\int_{\text{edge}}\left(\mu_{\uparrow\uparrow}(\omega)+\mu_{\uparrow\downarrow}(\omega)+\mu_0\right)\mathrm{d}\omega}n_{\text{h}} \quad (10.1)$$

Here, $\mu_{\uparrow\uparrow}(\omega)$ and $\mu_{\uparrow\downarrow}(\omega)$ are the X-ray absorption spectra measured with the photon angular momentum parallel and antiparallel with the applied (saturating) magnetic field, respectively, and $\mu_0(\omega)$ is the average of the two, or, alternatively, the absorption spectrum measured with linearly polarised light. The term n_{h} is the number of holes per atom at the Fermi level, which for a solid state system, will be a non-integer number. For example, in the case of Fe, this is normally taken to be 3.39 holes per atom [10].

The integrals in this case are over the entire absorption edge. For absorption by a transition metal L edge, i.e. $2p$–$3d$ transitions, $l_c = 1$ and $l_v, = 2$ and using

$$\mu_0(\omega) = \frac{1}{2}\left(\mu_{\uparrow\uparrow}(\omega)+\mu_{\uparrow\downarrow}(\omega)\right) \quad (10.2)$$

(8.1) becomes:

$$L_z = \frac{4}{3}\frac{\int_{L_2+L_s}\left(\mu_{\uparrow\uparrow}(\omega)-\mu_{\uparrow\downarrow}(\omega)\right)\mathrm{d}\omega}{\int_{L_2+L_s}\left(\mu_{\uparrow\uparrow}(\omega)+\mu_{\uparrow\downarrow}(\omega)\right)\mathrm{d}\omega}n_{\text{h}} \quad (10.3)$$

Thus, the orbital moment is proportional to the total area in the dichroism spectrum.

The projection of the spin moment along the photon spin is given by [7]:

$$\begin{aligned}&\frac{l_v(l_v+1)-2-l_c(l_c+1)}{3l_c}S_z\\&+\frac{l_v(l_v+1)[l_v(l_v+1)+2l_c(l_c+1)+4]-3(l_c-1)^2(l_c+2)^2}{6l_vl_c(l_v+1)}T_z\\&=\frac{\int_{j^+}\left(\mu_{\uparrow\uparrow}(\omega)-\mu_{\uparrow\downarrow}(\omega)\right)\mathrm{d}\omega-\left(\frac{l_c+1}{l_c}\right)\int_{j^-}\left(\mu_{\uparrow\uparrow}(\omega)-\mu_{\uparrow\downarrow}(\omega)\right)\mathrm{d}\omega}{\int_{\text{edge}}\left(\mu_{\uparrow\uparrow}(\omega)+\mu_{\uparrow\downarrow}(\omega)+\mu_0\right)\mathrm{d}\omega}n_{\text{h}}\end{aligned} \quad (10.4)$$

where $< T_Z >$ is the expectation value of the magnetic dipole operator along the photon spin and is a measure of the anisotropy of the spin distribution, which XMCD is sensitive to since the photon polarisation samples a directional cut through the atomic electron density. This term, discussed in more detail below, is small relative to $<S_Z>$ and for bulk samples has often been assumed to be zero but its significance increases in nanoscale particles and it must be taken into consideration. Note that the integrals in the numerator of (4) are taken over individual j components of the L edge.

In the case of transition metal L edges (4) becomes.

$$\langle S_z \rangle + \frac{7}{2} T_z = \frac{\int_{L_s} \left(\mu_{\uparrow\uparrow}(\omega) - \mu_{\uparrow\downarrow}(\omega)\right) \mathrm{d}\omega - 2 \int_{L_2} \left(\mu_{\uparrow\uparrow}(\omega) - \mu_{\uparrow\downarrow}(\omega)\right) \mathrm{d}\omega}{\int_{L_2+L_s} \left(\mu_{\uparrow\uparrow}(\omega) + \mu_{\uparrow\downarrow}(\omega)\right) \mathrm{d}\omega} n_h \tag{10.5}$$

Figure 10.4 shows simulated dichroic XAS with a fitted integral background. Figure 4b, c shows the background-subtracted μ_0 signal and the dichroism. The relevant integrals appearing in the $<L_Z>$ and $<S_Z>$ sum rules are also indicated on

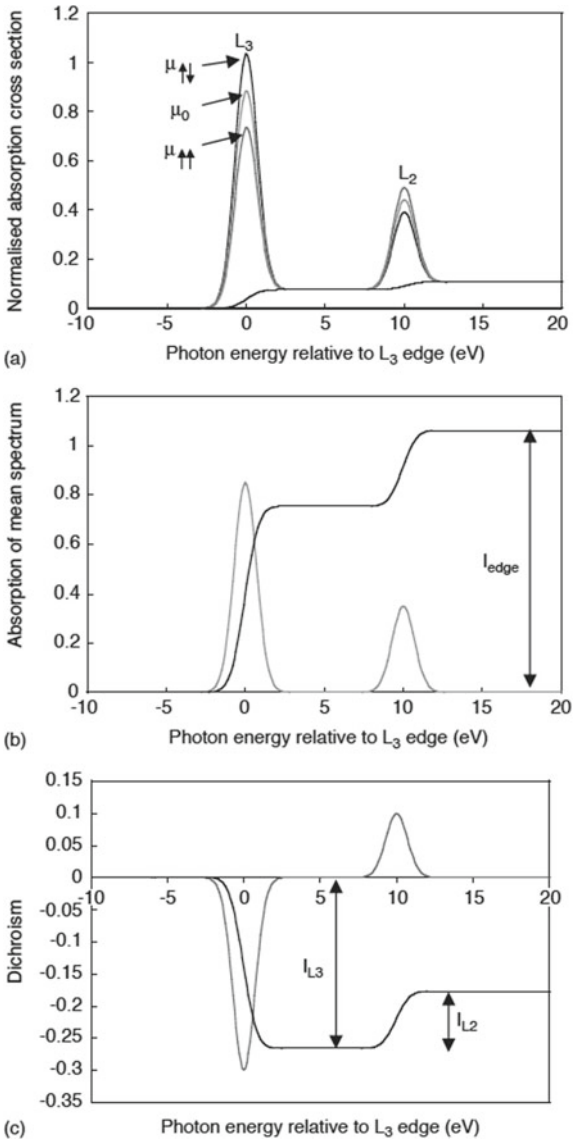

Fig. 10.4 XAS Simulated XAS and dichroism spectra for a transition metal *L* edge showing the relevant integrals used in the sum rules. Reproduced from [11]

the figure and labelled:

$$I_{\text{edge}} = \frac{1}{2} \int_{L_2+L_s} \left(\mu_{\uparrow\uparrow}(\omega) + \mu_{\uparrow\downarrow}(\omega)\right) \mathrm{d}\omega \tag{10.6}$$

$$I_{L3} = \int_{L_s} \left(\mu_{\uparrow\uparrow}(\omega) - \mu_{\uparrow\downarrow}(\omega)\right) \mathrm{d}\omega \tag{10.7}$$

$$I_{L2} = \int_{L_2} \left(\mu_{\uparrow\uparrow}(\omega) - \mu_{\uparrow\downarrow}(\omega)\right) \mathrm{d}\omega \tag{10.8}$$

In the simplest analysis for 3d transition metals, ignoring the $< T_Z >$ term, the spin and orbital sum rules reduce to:

$$\langle S_z \rangle = \frac{I_{L3} - 2I_{L2}}{I_{\text{edge}}} n_{\text{h}} \tag{10.9}$$

and

$$\langle L_z \rangle = \frac{4}{3} \frac{I_{L2} + I_{L3}}{I_{\text{edge}}} n_{\text{h}} \tag{10.10}$$

Since the quantities are normalised by the total edge absorption and given in terms of the number of valence band holes per atom, the values returned are the orbital and spin moments per atom.

The neglect of the $< T_Z >$ term is not valid in low-dimensional systems such as ultra-thin films since the high proportion of surface atoms introduces a significant anisotropy in the spin distribution and the spin term evaluated using (10.9) becomes measurably dependent on the angle of the sample normal with respect to the photon incidence direction. (Note that we assume throughout that the photon direction and sample magnetisation are parallel or antiparallel). It has been demonstrated that in the case of Fe nanoparticles, the dipole moment contribution increases as the particle size decreases [11].

Bruno has shown that the contribution of $< T_Z >$ to the measured spin moment with the sample normal at an angle θ with the photon beam varies as $\sin^2\theta$ [12]. If one can assume that the sample has rotational symmetry parallel to the substrate surface (the normal situation), then it can be shown [11] that the dipole moment goes to zero when $\tan^2 \theta = 2$, i.e. $\theta = 54.7°$, the so-called 'magic angle'. Thus, a measurement at the magic angle will yield the pure spin moment without the dipole contribution and is the value to be compared with other measurement techniques, for example, magnetometry (after including the orbital moment). Thus, the simple expedient of rotating the sample to an incidence angle of 55° relative to the photon

beam while maintaining the parallel and antiparallel alignment of the photon polarisation and sample magnetisation will eliminate the $<T_Z>$ term and (10.9) can be used to determine the spin moment.

10.2 Example System: Fe@Cr Core–Shell Nanoparticles

As pointed out earlier, XMCD is particularly powerful when investigating samples containing more than one element as it is able to chemically focus on the magnetic orbital and spin moments in individual elements. Whereas conventional magnetometry measures the average magnetic behaviour of all the elements in the sample. In recent years, the magnetic behaviour of ferromagnetic/antiferromagnetic interfaces has received particular attention due to the appearance of exchange bias after field-cooling, that is, a shift of the hysteresis loop of the magnetic material along the applied field axis [13, 14]. The effect is due to the 'pinning' of magnetic moments of the ferromagnetic material by exchange coupling with moments on the antiferromagnetic material at the interface and exchange bias is accompanied by an increase in coercivity. The effect is not only of interest from a fundamental perspective but is exploited in spin valves used for magnetic recording [15]. The majority of the work has focused on thin film interfaces but more recently an investigation using XMCD and magnetometry of the magnetic behaviour of Fe nanoparticles coated with one or two layers of Cr was reported [16].

The core–shell Fe@Cr nanoparticles were synthesised in ultra-high vacuum (UHV) in the gas-phase and matrix isolated in Ag films as illustrated in Fig. 10.5. The substrates used were C-coated Cu TEM grids and the finished samples had an X-ray transmission at the Fe L-edge in the range 10–90% and could be used for direct absorption measurements as illustrated in Fig. 10.1a. Three types of nanoparticles were prepared, that is, uncoated Fe nanoparticles, Fe cores with a single atomic layer of Cr, and Fe cores with two atomic layers of Cr (see Fig. 10.5c) thus the evolution of the magnetic behaviour as a function of the shell thickness could be studied.

The details of the analysis of the XMCD data is illustrated for the case of pure Fe nanoparticles in Fig. 10.6. The raw absorption data in transmission is shown in Fig. 10.6a and the same data after subtracting an integral background is plotted in Fig. 10.6b. The final dichroism spectrum after subtraction of a weak Ag N-edge absorption at 730 eV within the Fe $L_{2,3}$ absorption spectrum is shown in Fig. 10.6c. This is in a suitable form for sum rule analysis as illustrated in Fig. 10.4. In addition to obtaining the full XMCD spectrum, it is possible to obtain a magnetisation loop for a given element in the sample by simply measuring the intensity of the L_3 absorption edge as a function of the applied magnetic field intensity. The resulting curve is on a background signal that can easily be removed to produce loops such as that shown in Fig. 10.6d for pure Fe nanoparticles at a temperature of 204 K. The red line is a Langevin function at the same temperature that shows an optimum fit to the measured curve for a particle size of 2.68 nm (850 atoms). The inset in Fig. 10.6d compares the magnetisation measured by XMCD (black line) with that measured

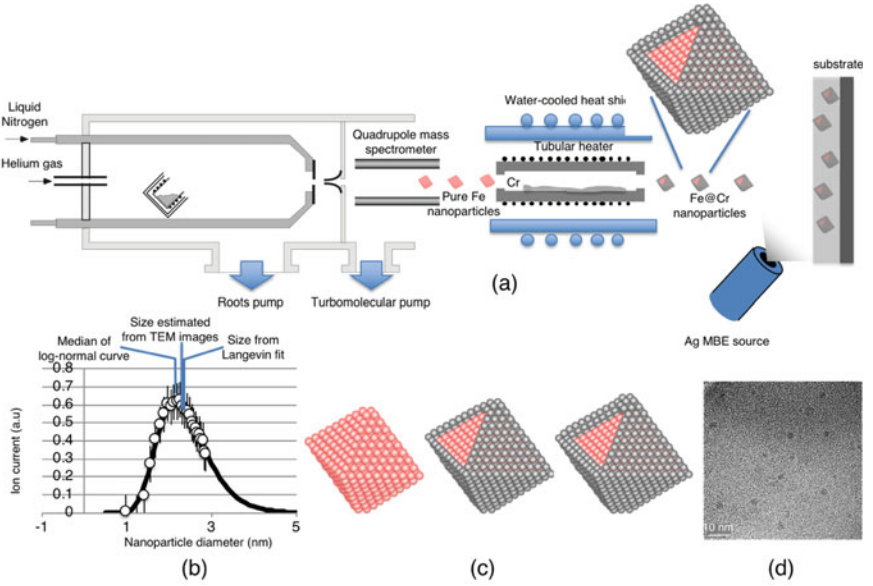

Fig. 10.5 **a** Synthesis of core−shell nanoparticles and production of matrix-isolated assemblies for XMCD and magnetometry studies. **b** Mass spectrum of pure Fe nanoparticles measured in the gas phase (open circles) fitted to a log−normal distribution (line). The spectrum is compared to the size determined by fitting Langevin functions to the magnetisation curves and estimated from TEM images. All three methods agree on the core particle diameter within the experimental uncertainty. **c** Illustration of the three types of nanoparticle studied, i.e. pure Fe, Fe@Cr with a monolayer shell, and Fe@Cr with a bilayer shell. **d** TEM image showing size distribution of Fe@Cr bilayer nanoparticles. Reproduced from [16]

from the same sample by a SQUID magnetometer (red line) demonstrating excellent agreement between the two methods.

The background subtracted XMCD spectra for pure Fe nanoparticles, Fe@Cr monolayer and Fe@Cr bilayer samples are compared in Fig. 10.7a. Even without detailed analysis, it is clear that the dichroism is weaker in the particles with the Cr shells showing that the magnetic moment of the Fe cores is reduced by the interaction with the Cr shell. The analysis using the sum rules presented in the previous section reveals the spin and orbital moments of the Fe cores plotted in the inset of Fig. 10.7a and listed in Table 10.1.

The general result is that coating the Fe cores with Cr does not significantly affect the orbital moment while the spin moment is reduced by around 40%. Note that the total Fe moment in the uncoated nanoparticles appears to be slightly less than the bulk value but this is an experimental artefact. The data above were taken at 204 K, whereas at 2 K, at which a higher level of saturation is reached, gives a measured total moment of 2.18 μ_B/atom. In addition, the data was taken at normal incidence at which, as discussed in the previous section, gives a contribution from the dipole

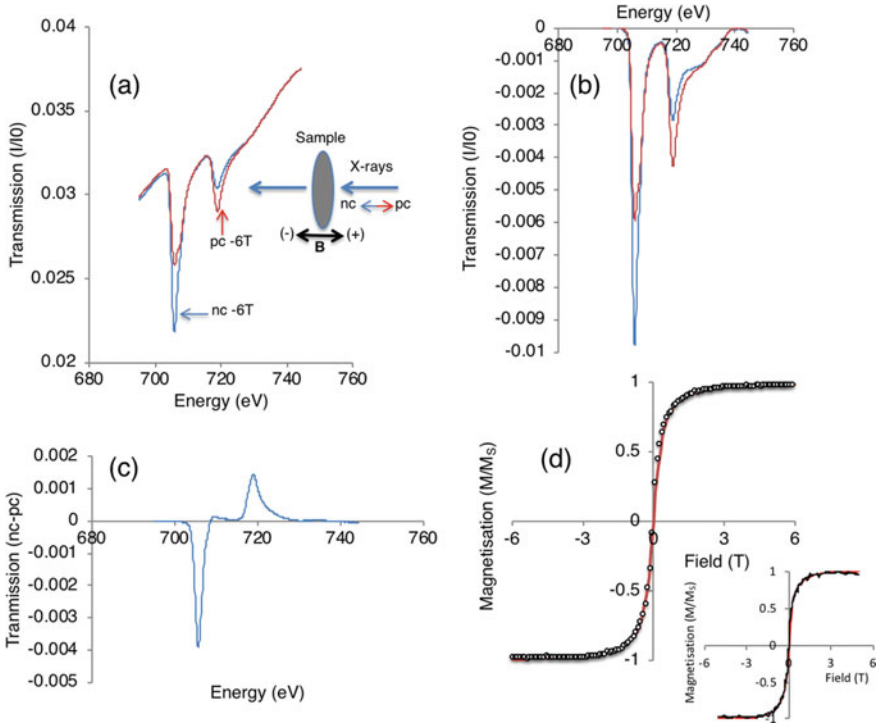

Fig. 10.6 **a** X-ray transmission in the Fe $L_{2,3}$ region of pure Fe nanoparticles in Ag with an applied field of − 6 T showing the difference in absorption between negative circular polarisation (nc) and positive circular polarisation (pc) of the X-rays. The inset shows the labeling of positive and negative directions of the applied field and photon angular momentum. **b** Absorption data after subtracting an integral background. **c** Fe $L_{2,3}$ dichroism used for sum rule analysis. **d** Sample magnetisation at 204 K (open circles) obtained by plotting the intensity of the Fe L_3 peak as a function of the applied field. The red line is a Langevin function plotted for a particle diameter of 2.68 nm. The inset compares the magnetisation measured by XMCD (black line) with that measured from the same sample by SQUID magnetometry (red line) showing excellent agreement. Reproduced from [16]

moment. Taking this into account gives a measured total Fe moment by XMCD of 2.28 μ_B/atom.

Whereas the low- temperature coercivity of the pure Fe nanoparticles and F@Cr monolayer particles is similar, there is a large increase observed in the Fe@Cr bilayer sample (Fig. 10.7b). In addition, field cooling the samples shows no indication of exchange bias on the pure Fe and F@Cr monolayer particles but a clear appearance of exchange bias in the Fe@Cr bilayer sample (Fig. 10.7c). The conclusion is that a shell thickness of at least two atomic layers of Cr around the Fe core is required to generate exchange bias and the accompanying increase in coercivity.

In an Fe nanoparticle containing 850 atoms, 40% of the atoms are at the surface so the XMCD data is suggestive that the layer of Fe atoms in contact with the Cr

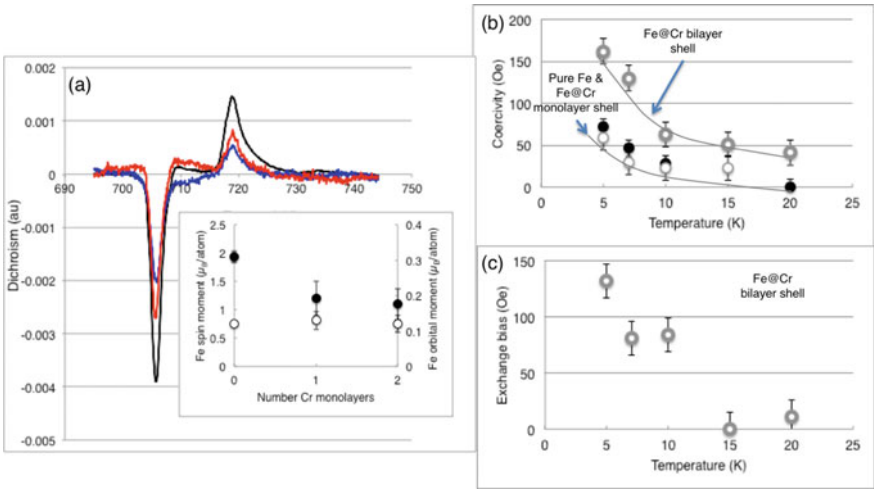

Fig. 10.7 **a** Normalised dichroism spectra (nc − pc, −6 T) for pure Fe (black line), Fe@Cr monolayer shell (red line), and Fe@Cr bilayer shell (blue line) nanoparticles in Ag matrices. The inset shows the variation of the Fe orbital (open circles) and spin (filled circles) magnetic moments with Cr shell thickness. **b** Coercivity after field cooling of pure Fe (filled circles), Fe@Cr monolayer shell (open circles with thin line), and Fe@Cr bilayer shell (open circles with thick line) nanoparticles in Ag matrices as a function of temperature. **c** Exchange bias of Fe@Cr bilayer shell nanoparticles in Ag matrices as a function of temperature after field cooling. Reproduced from [16]

Table 10.1 Fe orbital and spin moments bare Fe nanoparticles and for Fe nanoparticles coated with monolayer and bilayer Cr shells

Sample	Orbital moment/atom (μ_B)	Spin moment/atom (μ_B)	Total moment/atom (μ_B)
Fe nanoparticles	0.12 ± 0.02	1.83 ± 0.11	1.95 ± 0.11
Fe@Cr monolayer	0.13 ± 0.02	1.2 ± 0.3	1.3 ± 0.3
Fe@Cr bilayer	0.12 ± 0.02	1.1 ± 0.3	1.2 ± 0.3

shell is either magnetically disordered or antiferromagnetic. The conclusion of the work is that in the case of the monolayer shell, the interface is disordered while with the bilayer shell, some antiferromagnetic coupling is present. The level of exchange bias observed would require only a few Fe atoms to be pinned at the interface.

10.3 Future Perspectives

The emergence of the sum rules in the early 1990s was coincidental with an expansion in the number of third-generation synchrotron radiation sources, which use insertion devices to generate very high intensities of X-rays with variable polarisation. For a review of the development of the technique, see ref [17]. This led to a proliferation of XMCD experiments and initially the focus was on static thin films and nanostructures containing transition metals. The sum rules are equally applicable to rare-earth systems though a more complex analysis is required to extract the magnetic moments [18] and the field has matured and embraced complex rare-earth systems. These including magnetically doped topological insulators, important for spintronics applications [18] and DyFe/YFe exchange spring materials [4] that demonstrate giant magnetoresistance (GMR). The method has also evolved to include measurements with spatial and temporal resolutions and these developments are briefly illustrated with some examples in this section.

10.3.1 Spatially Resolved XMCD: Domain Imaging in Patterned Structures

XMCD can be combined with X-ray photoelectron microscopy (XPEEM) to provide spatially resolved images of magnetisation in samples. The principle of X-PEEM is illustrated in Fig. 10.8a and it consists of electron lenses that provide a magnified image of the sample at the image plane at which there is a two-dimensional detector. The secondary electrons are excited by a soft X-ray beam and as illustrated in Fig. 10.1b, if the photons are tuned to an element absorption edge, there will be a peak in the secondary electron yield at positions where that element is present, providing chemical mapping of a surface. If, in addition, the photon beam is circularly polarised, magnetic contrast at each position can be obtained by taking an image on and off the edge. This will reveal which regions have their magnetisation aligned with the photon spin (negative contrast) and which have their magnetisation aligned antiparallel to the photon spin (positive contrast). The direction of magnetisation sampled can be controlled by changing the angle of incidence of the photon beam. One of the major advantages of XMCD-XPEEM is that it combines magnetic imaging with chemical sensitivity.

Figure 10.8b–d shows domain patterns in micro-patterned Co rectangles with a thickness of 20 nm and aspect ratios of 1:1, 1:2, and 1:3. The Co squares show predominantly a vortex state domain structure, while the others show a variety of domain structures including symmetric and asymmetric vortex and antivortex states.

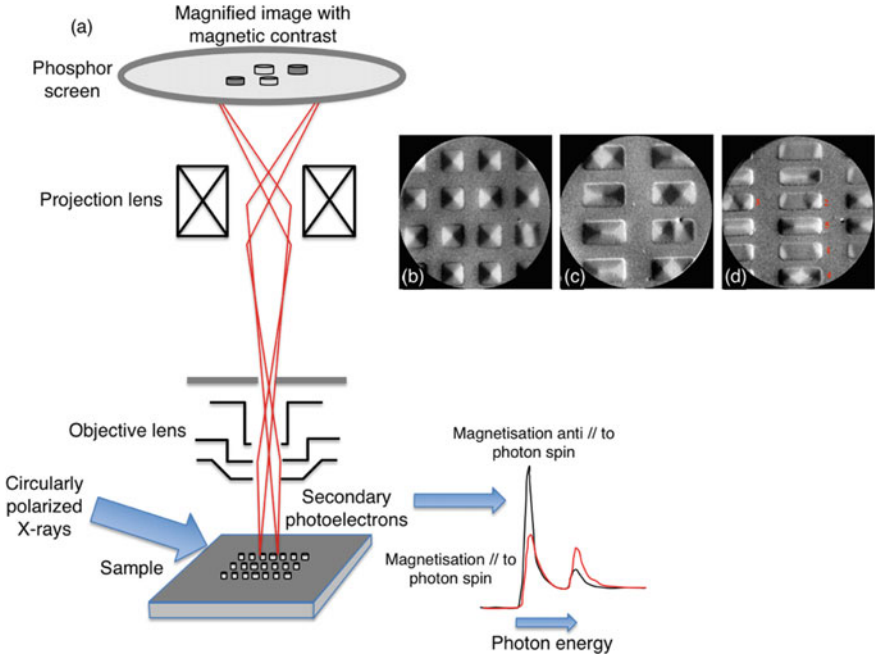

Fig. 10.8 **a** Schematic diagram of XPEEM combined with XMCD to produce surface magnetic imaging of a sample. **b–d** Magnetisation patterns in 20 nm thick Co rectangles with aspect ratios of 1:1, 1:2, and 1:3, respectively, with the photon beam from the left. Image size is 5 μm. Reproduced from [19]

10.3.2 Time-Resolved XMCD Measurements in Exchange-Coupled Layers

Synchrotrons that are mainly used for XMCD measurements are pulsed X-ray sources with a well-defined time structure. Thus, time-resolved magnetic measurements can be obtained by sampling the dichroism at a specific time from an X-ray pulse and this can be done simply by measuring the absorption intensity at an absorption edge for a fixed helicity of the X-rays. This will give the variation of magnetisation superimposed on a static background. A clock signal synchronous with the X-ray pulses can be used to drive a sample excitation, for example, a pulsed RF field that sets up ferromagnetic resonance (FMR) in a magnetic sample. Thus varying the time delay between the magnetisation pulse and the probing X-ray pulse enables a stroboscopic pump-probe measurement that measures the magnetisation state at a specific time following the excitation. The technique is referred to as X-ray-detected ferromagnetic resonance or XFMR [20]. A good demonstration of the technique has been published recently [21]investigating ferromagnetic resonance in exchange-coupled NiFe/CoNi bilayers (Fig. 10.9d). By measuring the dichroism at the Ni and

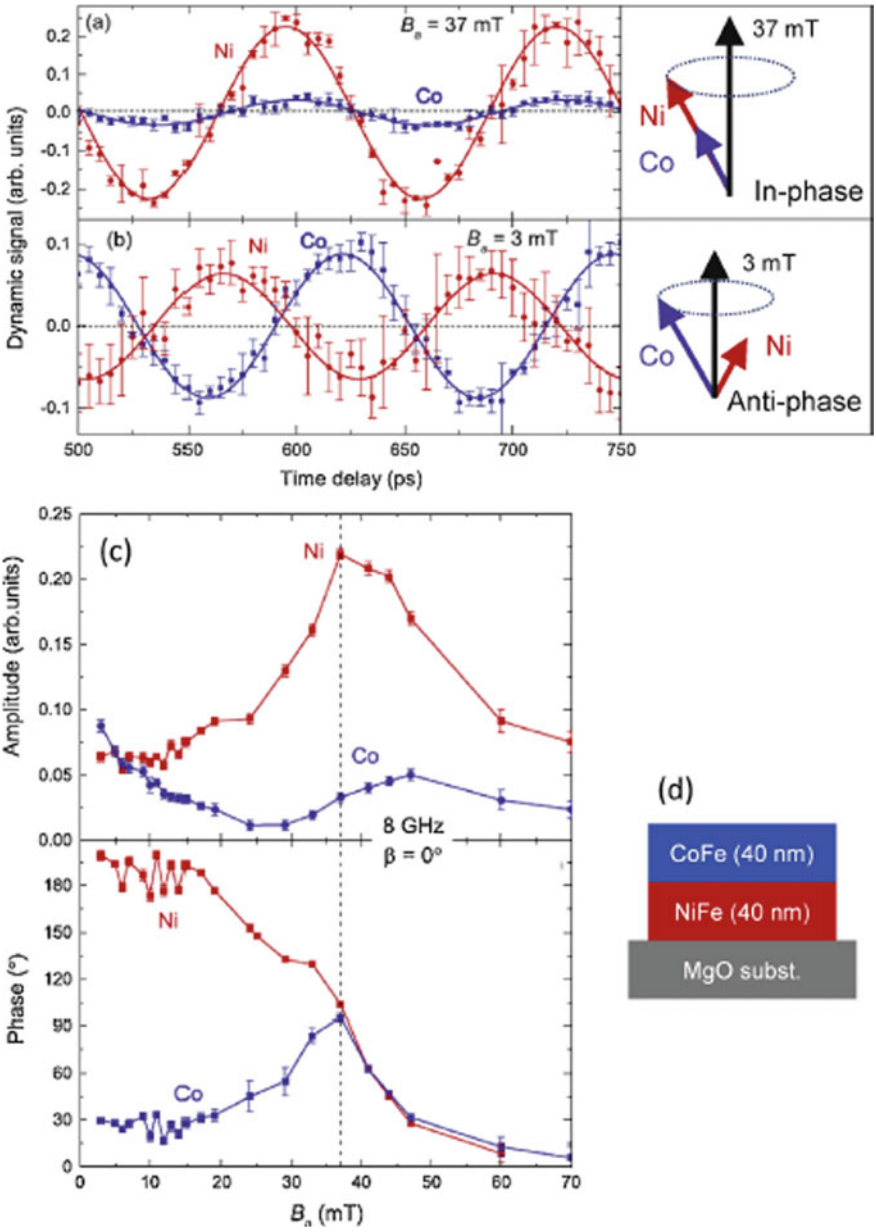

Fig. 10.9 XFMR results of exchange-coupled NiFe/CoFe bilayer. **a** and **b** XMCD signals measured at Co and Ni L_2 edges as a function of delay time between X-ray pulse and 8 GHz RF field. **a** and **b** show delay scans for the acoustic mode (at 37 mT) and optic mode (at 3 mT), respectively. The Co and Ni precession are anti-phase (167∘52) in the optic mode and in-phase (7∘52) in the acoustic mode. **c** XFMR precessional plots as a function of applied field showing the change in amplitude and phase of the Ni and Co precessions. **d** Schematics of the bilayer grown on MgO substrate. Reproduced from [20]

Co L-edge, it is possible to independently probe the dynamic behaviour in each section of the bilayer.

FMR measurements show two resonance states in the bilayer with applied static fields of 3 and 37 mT labelled the optic mode and the acoustic mode, respectively. In the acoustic mode, the magnetisation of both layers precesses in phase. The amplitude is strongest in the NiFe layer, and decays as it penetrates into the CoFe layer. In contrast, in the optic mode, magnetisations of the two layers precess in anti-phase and the amplitude is greatest in the CoFe layer. XFMR data was measured at the Ni and Co L_2 edges using circularly polarised X-rays with fixed helicity. The magnetic excitation pulse was at 8 GHz (125 ps period) and Fig. 10.9a, b shows the delay scans for the acoustic mode (at 37 mT) and optic mode (at 3 mT), respectively. In the acoustic mode, the Co and Ni spins precess in phase while in the optic mode, they are in anti-phase. The relative amplitudes confirm that the acoustic mode is mainly driven by the Ni layer and the optic mode is mainly driven by the Co layer.

The amplitude and phase of the Co and Ni signals are plotted in Fig. 10.3c and shows the behaviour expected of coupled driven oscillators.

References

1. J.L. Erskine, E.A. Stern, Phys. Rev. B **12**, 5016 (1975)
2. G. Schütz, W. Wagner, W. Wilhelm, P. Kienle, R. Zeller, R. Frahm, G. Materlik, Phys. Rev. Lett. **58**, 737 (1987)
3. J. Stöhr and Y. Wu, New directions in research with third generation synchrotron radiation sources, in *NATO ASI Series E: Applied Sciences*, eds. by A.S. Schlachter, F.J. Wuilleumier (Kluwer 1994), p. 221
4. G. Van der Laan, A.I. Figueroa, Co-ord. Chem Rev. **277–278**, 95 (2014)
5. J. Stöhr, J. Electr. Spectr. Re. Phenom. **75**, 253 (1995)
6. B.T. Thole, P. Carra, F. Sette, G Laan van der, Phys. Rev. B **68**, 1943 (1992)
7. P. Carra, B.T. Thole, M. Altarelli, X. Wang, Phys. Rev. Lett. **70**, 694 (1993)
8. M. Altarelli, Phys. Rev. B **47**, 597 (1993)
9. A. Ankudinov, J.J. Rehr, Phys. Rev. B **51**, 1282 (1995)
10. C.T. Chen, Y.U. Idzerda, H.-J. Lin, N.V. Smith, G. Meigs, E. Chaban, G.H. Ho, E. Pelligrin, F. Sette, Phys. Rev. Lett. **75**, 152–155 (1995)
11. C. Binns and J. Blackman, Chapter 9, section 9.2.6, in *Metallic Nanoparticles,* ed. by. J. Blackman (Elsevier, 2009). ISBN: 978-0-444-51240-6
12. P. Bruno, Phys. Rev. B **39**, 865 (1989)
13. J. Nogués, I.K.J. Schuller, J. Magn. Magn. Mater. **192**, 203–232 (1999)
14. A.E. Berkowitz, K.J. Takano, J. Magn. Magn. Mater. **200**, 552–570 (1999)
15. B. Dieny, V.S. Speriosu, S.S.P. Parkin, B.A. Gurney, D.R. Wilhoit, D. Mauri, Phys. Rev. B **43**, 1297–1300 (1991)
16. C. Binns, M.T. Qureshi, D. Peddis, S.H. Baker, P.B. Howes, A. Boatwright, S.A. Cavill, S.S. Dhesi, L. Lari, R. Kröger, S. Langridge, Nanoletters **13**, 3334–3339 (2013)
17. T. Funk, A. Deb, S.J. George, H. Wang, S.P. Cramer, Co-ord. Chem. Rev. **249**, 3–30 (2005)
18. A.I. Figueroa, A.A. Baker, S.E. Harrison, K. Kummer, G. van der Laan, T. Hesjedal, J. Magn. Magn. Mater. **422,** 93–99 (2017)
19. S. Cherifi, R. Hertel, J. Kirschner, H. Wang, R. Belkhou, A. Locatelli, S. Heun, A. Pavlocska, E. Bauer, J. Appl. Phys **98**, 043901 (2005)
20. G. van der Laan, J. Electr. Spectr. Rel. Phenom. **220**, 137–146 (2017)

21. G.B.G. Stenning, L.R. Shelford, S.A. Cavill, F. Hoffmann, M. Haertinger, T. Hesjedal, G. Woltersdorf, G.J. Bowden, S.A. Gregory, C.H. Back, P.A.J. de Groot, G. van der Laan, New J. Phys. **17**, 013019 (2015)

Chapter 11
Electron Tomography

P. Torruella, J. Blanco-Portals, Ll. Yedra, L. López-Conesa, J. M. Rebled, F. Peiró, and S. Estradé

Abstract The recent advances in TEM instrumentation with faster and more sensitive detectors, and the ever-increasing number of advanced algorithms capable of achieving quality 3D reconstructions with fewer acquired projections, are transforming electron tomography in one of the most versatile tools for a materials scientist, as the possible field of application for this technique is open to virtually any nanoscaled material. The complete three-dimensional characterization of magnetic nanoparticles is not an exception. Not only the 3D morphology is resolved, but also the elemental composition in 3D, by combining the available reconstruction algorithms and TEM spectral characterization techniques, seeking to retrieve the so-called spectrum volume. Among them, electron energy loss spectroscopy (EELS) stands out, given its unchallenged lateral resolution and its unique ability to resolve variations of the oxidation states, and even atomic coordination, through the analysis of the fine structure of the elemental edges in the acquired spectra. This chapter is a revision

P. Torruella (✉) · J. Blanco-Portals · Ll. Yedra · L. López-Conesa · J. M. Rebled · F. Peiró · S. Estradé
LENS-MIND, Electronics and Biomedical Engineering Department, Universitat de Barcelona, Barcelona, Spain
e-mail: ptorruella@el.ub.edu

J. Blanco-Portals
e-mail: jblanco@ub.edu

Ll. Yedra
e-mail: lluis.yedra@ub.edu

L. López-Conesa
e-mail: llopez@el.ub.edu

J. M. Rebled
e-mail: jmrebled@el.ub.es

F. Peiró
e-mail: francesca.peiro@ub.edu

S. Estradé
e-mail: sestrade@ub.edu

Institut de Nanociència i Nanotecnologia (IN2UB), Universitat de Barcelona, Barcelona, Spain

D. Peddis et al. (eds.), *New Trends in Nanoparticle Magnetism*,
Springer Series in Materials Science 308,
https://doi.org/10.1007/978-3-030-60473-8_11

of electron tomography strategies applied to magnetic nanomaterials, beginning in a chronologically ordered description of some of the commonly used algorithms and their underlying mathematical principles: from the historical Radon transform and the WBP, to the iterative ART and SIRT algorithms, the later DART and recently added compressed sensing-based algorithms with superior performance. Regarding the spectral reconstruction, dimensionality reduction techniques such as PCA and ICA are also presented here as a viable way to reduce the problem complexity, by applying the reconstruction algorithms to the weighted mappings of the physically meaningful resolved components. In this sense, the recent addition of clustering algorithms to the possible spectral unmixing tools is also described, as a proof of concept of its potentiality as part of an analytical electron tomography routine. Throughout the text, a series of published experiments are described, in which electron tomography and advanced EELS data treatment techniques are used in conjunction to retrieve the spectrum volume of several magnetic nanomaterials, revealing details of the NPs under study such as the 3D distribution of oxidation states.

11.1 Introduction: Fundamentals of Electron Tomography and Overview of Classic Reconstruction Methods

Electron tomography in the transmission electron microscope (TEM) refers to the reconstruction of 3D volumes from the 2D projection images obtained in the microscope. TEM tomography was first applied to the field of biology [1]. In the last couple of decades, the operational and instrumental advances, as well as the formulation of new reconstruction algorithms, have introduce tomography into the realm of materials and physical sciences. Nowadays, it plays a central role in the study and fabrication of nanostructured materials. Moreover, the combination of tomographic techniques with TEM spectroscopic techniques (electron energy loss spectroscopy EELS and energy-dispersive X-ray spectroscopy EDX/EDS) has recently opened new perspectives for the characterization of nanomaterials.

In order to successfully carry out tomography experiments in the TEM, the signal acquired (projected images) must fulfil the projection requirement: the contrast in the image must change monotonically with given property of the sample (e.g. thickness or Z number) [2]. This automatically discards high resolution TEM images, formed through phase contrast, and specifically bright and dark field diffraction contrast imaging modes. For crystalline samples, scanning-TEM high-angle annular dark field (STEM-HAADF) images are preferred, as HAADF incoherent signal is monotonically dependent on the thickness and the Z number.

Experimentally, tomography in the TEM is carried out through the acquisition of a set of images obtained at different tilt angles [3]. Hence, a certain degree of discretization is inherently introduced and, thus, the quality of the reconstruction will be affected by the number of projections (the angle step) and the considered angular range. The resolution in TEM tomography is anisotropic. For simplicity, let

us consider a single tilt axis experiment. In the tilt axis direction, the resolution is that of the projected images, but in the other two orthogonal axes, it is limited by the number of projections acquired and the diameter of the reconstruction volume, where lower step improves the resolution, especially at higher angles. However, this leads to an increment in the acquisition time, possibly jeopardizing sample stability and increasing sample damage. A compromise between angle step and acquisition time, avoiding a significant loss of resolution, is thus necessary.

Furthermore, since the space in the pole piece inside the TEM column is limited, it is practically impossible to cover the whole range of angles $\pm 90^{\circ}$ with conventional sample holders. This causes an undersampling in the illumination direction and is responsible of the most important artefact in TEM tomography: the missing wedge [2]. It degrades the resolution causing an elongation in the illumination direction, and it must be corrected by a factor of: $= \sqrt{(\alpha + \sin\alpha \cos\alpha)/(\alpha - \sin\alpha \cos\alpha)}$. There are several approaches to deal with the effect of the missing wedge. Experimentally, the preparation of samples in a needle shape [4, 5] is one possible solution (to cover the $\pm 90^{\circ}$ tilting range), but in principle excludes the study of nanoparticles. Double tilt experiments [6] are a viable option, reducing the missing wedge to a missing cone, at the cost of increasing the difficulty during image acquisition. DART [7, 8] algorithms appear as an alternative option when the composition of the sample is well known.

11.1.1 Mathematical Principles and Reconstruction Methods

11.1.1.1 Radon Transform and Fourier Methods

The first attempts to solve problems of reconstruction of 3D objects by tomography were based on the Radon transform [9] formulation and the Fourier space properties, through the application of the so-called *central section theorem*: the projection of an object at a given angle is a central section through the Fourier transform of that object (i.e. calculating the Fourier transform of the acquired projected images at different angles is equivalent to sampling the Fourier space of the projected object, that can be recovered performing an inverse Fourier transform).

The definition of the missing wedge is straightforward in terms of the Fourier space. Applying the central section theorem, we can relate the undersampling in the projection tilt series with non-sampled spatial frequencies in the Fourier space and, thus, to the resolution degradation and elongation of the reconstruction [2].

Although theoretically and historically relevant, the discretization imposed by the actual experiment inevitably forces a certain degree of interpolation in the reconstruction and, thus, an increment in the computational time. This triggered the development of the so-called direct methods. In them, the reconstruction is carried out in direct space instead of Fourier space.

11.1.1.2 Weighted Back-Projection (WBP)

This technique consists in the reconstruction of the original object from the projections in direct space [10]. To that end, the back-projection bodies are built, smearing the projected images back in the original projection angles. WBP has been extensively used for single tilt axis experiments (mainly in medical and biological applications [11, 12]). Not only it can be analytically resolved but it is also equivalent to Fourier methods. Besides, some of the artefacts intrinsically associated to WBP, due to the discrete nature of the experiments, are easily removed by applying a combination of ramp and low-pass filters. However, WBP performance is far from that of the iterative methods listed below.

11.1.1.3 Algebraic Reconstruction Techniques (ART)

To understand the mathematical procedure behind this first iterative method, let us consider a single axis tilt experiment [13]. The object to be reconstructed can be seen as a set of planes (slices) perpendicular to the tilting axis. Every and each one of these planes would then be a 1D line in the projected TEM image for each tilt angle in the experiment. By reconstructing the set of 2D planes, the 3D volume corresponding to the sample can be recovered, hence the problem dimensionality is reduced in the calculations (Fig. 11.1).

Each plane of the volume is regarded as a grid of $n \times n$ points (i, j) completely containing the sample slice into its boundaries (Fig. 11.1). In the reconstruction, each (i, j) position will have an optical density $\rho_{i,j}$, depending on the object and the angle of the projection. Each ray (k, θ) of the projection has the integrated density $R_{k,\theta} = \sum \rho_{i,j}$, where the summation is extended to all the grid points (i, j) contained within the ray. Experimentally, the acquired images are projections at a series of angles θ, and the measured intensities are $P_{k,\theta}$ for each (k, θ) ray. Therefore, obtaining the set of $\rho_{i,j}$ $(n \times n)$ from $P_{k,\theta}$ is the problem that needs to be solved

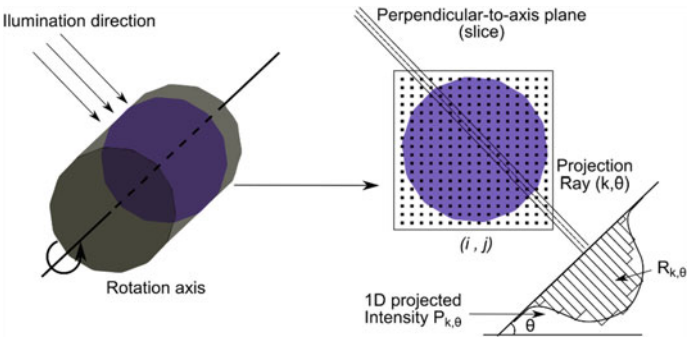

Fig. 11.1 Scheme of the mathematical impplementation of ART

The iterative nature of ART implies that the algorithm needs to converge. Two algorithms are available, multiplicative (mult.) and additive (add.):

$$\text{Mult.} : \rho_{i,j}^{q+1} = \frac{\left(P_{k,\theta}\right)}{\left(R_{k,\theta}^{q}\right)} \rho_{i,j}^{q}$$

$$\text{Add.} : \rho_{i,j}^{q+1};$$

$$= \max\left[\rho_{i,j}^{q} + \frac{\left(P_{k,\theta} - R_{k,\theta}^{q}\right)}{N_{k,\theta}}, 0\right]$$

where the initial guess for the optical density $\rho_{i,j}$ is to consider a homogeneous distribution of the total intensity (T) of a plane (slice) ${\rho_{i,j}}^{0} = T/n^2$. In the additive method, $N_{k,\theta}$ is the number of grid points (i, j) in the ray (k, θ). The algorithms positively define $\rho_{i,j} \geqslant 0$, as they take into account the fact that the signal is positively constrained ($\rho(x, y, z) \geqslant 0$).

11.1.1.4 Simultaneous Iterative Reconstruction Technique (SIRT)

This second iterative method for tomographic reconstruction arises from the same mathematical framework as ART [14]. The main difference lies in the use of information in the algorithms. ART gets $\rho_{i,j}$ in each iteration and for each projection (angle θ), only from information of the same projection. SIRT algorithms use all projections at the same time:

$$\text{Mult.} : \rho_{i,j}^{q+1} = \frac{\sum\left(P_{k,\theta}\right)}{\sum\left(L_{k,\theta}\right)} \frac{\sum\left(N_{k,\theta}\right)}{\sum\left(R_{k,\theta}^{q}\right)} \rho_{i,j}^{q}$$

$$\text{Add.} : \rho_{i,j}^{q+1}$$

$$= \max\left[\rho_{i,j}^{q} + \frac{\sum\left(P_{k,\theta}\right)}{\sum\left(L_{k,\theta}\right)} - \frac{\sum\left(R_{k,\theta}^{q}\right)}{\sum\left(N_{k,\theta}\right)}, 0\right]$$

The term $L_{k,\theta}$ is the length of the ray (k, θ).

Stability in noisy conditions is greatly enhanced in SIRT algorithms (specially compared to ART). SIRT converges more slowly than ART, but the quality of the results is overall better. Nonetheless, care is required when operating ART and SIRT algorithms. The results may converge after a few iterations and the algorithms may then begin to diverge again (i.e. the reproduced intensities for the projections may further differ from the measured projected values).

11.1.1.5 Discrete Algebraic Reconstruction Technique (DART)

DART algorithm belongs to the field of discrete tomography (DT), dealing with volume reconstruction from a low number of projections [7, 8]. It is driven by the idea of a priori object segmentation (i.e. component separation assigning a single grey level for each material present in the object). It operates iteratively in two steps: (1) reconstruction step, (2) segmentation step. For simplicity, let us consider a binary case (i.e. only one material species and the background) for a 2D reconstruction from 1D projections, that can be easily generalized to 3D volume reconstructions. The problem (reconstruction) can be represented by a linear system $\vec{p} = W\vec{x}$, where $\boldsymbol{p}$ are the projection values, $\boldsymbol{x}$ the image/object and $\boldsymbol{W}$ represents the projection process.

The reconstruction step is a continuous tomographic reconstruction method: ART [13], SIRT [14] or any other iterative algorithm can be used. From now on, we refer to this step as the algebraic reconstruction method (ARM). The segmentation is carried out separating the material and the background (thresholding the grey levels), and identifying the set boundary $B^{(t)}$ and 'fixed' $F^{(t)}$ pixels (where (t) accounts for the iteration step).

The set $B^{(t)}$ will be updated by the ARM algorithm in each iteration, while $F^{(t)}$ will remain fixed. This way, the number of variables in the linear system are reduced and the computational power required is greatly decreased. Since the segmentation is applied upon the ARM-reconstructed images (possibly suffering from missing wedge), the separation of grey levels can be defective at first. To allow the creation of boundary regions inside the material, a random set of pixels from $F^{(t)}$ is introduced in the ARM as well with a p probability (adjustable from 0 to 1, depending on each problem). Also, a smoothing filter is applied after each iteration, to counter the strong local oscillations in the grey levels of $B^{(t)}$ after the ARM step.

It has been proven that DART converges faster than any ARM available, when the number of grey levels does not exceed 5 [7]. The accuracy of the reconstruction (measured comparing phantom images and the results of the reconstruction for different algorithms) is usually higher, independently of the number of projections or the angular range. Tests on the effect of the missing wedge reveal a much-reduced impact in final solutions achieved by DART. Since electron dose is reduced when a lower number of projections are required, DART appears as a viable option in cases of severe sample damage due to beam sensitivity.

Despite the advantages described for DART, it remains a *heuristic* algorithm, meaning that convergence cannot always be assured. This circumstance makes the selection of a unique termination criteria difficult. It also relies on previous knowledge of the sample composition. Although it is robust with respect to the chosen segmentation criteria (threshold), if the number of components (different grey levels) is not correctly identified, the reconstruction may present serious image artefacts (Fig. 11.2).

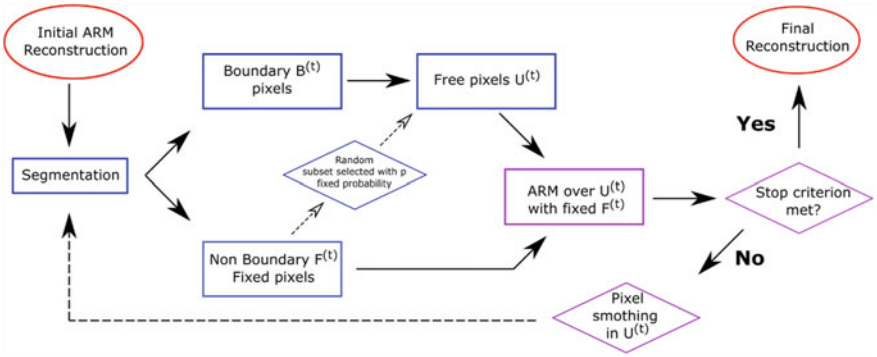

Fig. 11.2 Flow chart for DART algorithm. In blue, the steps corresponding to the segmentation process. In red, the ones belonging to the reconstruction process. In purple, reconstruction/segmentation steps

11.2 Analytical Tomography and the Spectrum Volume Approach

As tomographic reconstruction techniques become more accurate for volume reconstruction in materials science, and taking advantage of the new technical advances in transmission electron microscopes, the possibility of generalizing tomography to include spectroscopic signals arises. This is a particularly interesting approach in the case of magnetic nanostructures.

To this end, the combination of different analytical techniques in the TEM with tomographic reconstruction, such as energy filtered TEM tomography (EFTEM-Tomo), energy-dispersive X-ray tomography (EDX-Tomo) and electron energy loss spectroscopy tomography (EELS-Tomo) is considered.

EFTEM-Tomo [15, 16] is based on the idea of performing a classic tomography experiment from a data set of energy filtered TEM images. In this EFTEM imaging mode, a characteristic electron energy loss usually corresponding to an element specific signature (core level ionization, or bulk plasmon modes) is selected by the definition of three energy windows [3]. For each element present in the sample, an image is obtained at a characteristic electron energy loss, corresponding to a given transition of the element (or a characteristic plasmon energy of the compound). The lower acquisition times compared to other techniques and the sample stability during the acquisition (i.e. the minimization of spatial drift due to the low quantity of images needed) made it the technique of choice in the first experiments in analytical tomography. Nevertheless, EFTEM faces two shortcomings that are difficult to overcome. The first problem is the short energy resolution, implying that the elemental separation is compromised in cases where the energy window may span over various overlapping features on the spectrum. The second problem is the low energy range covered by each window. In order to be effective, each energy window must be as

small as possible to avoid misidentification (as already discussed). Hence, to cover large portions of the spectra, the quantity of required filtered images may be huge.

Nowadays, EDX-Tomo [17–19] is one of the most popular techniques to obtain a 3D elemental reconstruction in nanostructured materials. The new generation of detectors and the multi-detector geometries in the TEM column have largely decreased acquisition times and improved collection efficiency. This way, X-ray spectra can be collected fast enough to limit sample damage, as it is tilted to acquire the projections required for the tomographic reconstruction. Nonetheless, EDX is not as good as EELS in terms of spatial resolution and oxidation state information is not available from EDX.

Finally, EELS spectrum image (SI) [20, 21]—tomography reconstruction has become the option of choice to analytically reconstruct a 3D volume when high spatial and energy resolution are required. The advances in TEM instrumentation (e.g. Cs correctors [22], Cc correctors [23] and monochromators [24], Cold FEG [25] and better spectrometers) has allowed the acquisition time for EELS SI to decrease in recent years, as well as providing an access to higher resolution. Furthermore, EELS-SI contain more information than solely the elemental composition. Fine structure information about the local atomic environment in the sample is available through the analysis of the energy loss near-edge structure (ELNES), such as the atomic coordination, valence state, and type of bonding. Thus, the determination of the oxidation state is made possible by analysing EELS-SI data. ELNES arises from the quantum nature of the electronic excitation process for the electron in a certain atomic shell interacting with the electron beam, within the atom probed. Physically, the near-edge structure (spamming several tens of eV from the ionization edge) can be directly linked to the density of (empty) states above the Fermi level [3, 26]. Some of the more usually exploited ELNE-structures are the white lines (sharp peaks caused by the ionization to well-defined empty energy states of electros in transition metals and rare earths) [27].

In the following, a series of key experiments on the development of the EELS tomography technique carried out in recent years is described, as well as the mathematical and physical considerations that made them possible.

11.2.1 Compressed Sensing (CS)

Before the detailed description of the experiments, the introduction of one last reconstruction algorithm developed in recent times is advisable, due to the nature of the experiments themselves. Given the increment of the data volume required for analytical electron tomography experiments, faster and more accurate approaches must be pursued.

An alternative reconstruction method, based in the same theoretical background as the image compression algorithms (JPEG and JPEG-2000) [28], is proposed: compressed sensing *(CS)* [5, 29–32].

It has been proved that CS presents in general higher quality reconstructions than classic SIRT and WBP given the same number of iterations, and is capable to retrieve highly accurate reconstructed images in cases of severe undersampling (i.e. low number of projections available for the reconstruction). Examples of CS-ET reconstruction of magnetic nanoparticles are available in the literature [32–34], illustrating the power of this method to reconstruct accurately complex 3D structures for quantitative analysis and, thus, allowing the comparative study of magnetic properties and structural information.

11.2.1.1 Mathematical Principles

Understanding the principles behind the CS theoretical framework requires a fair knowledge of the concepts of sparse representation, compressible signal and sensing processes (measurement).

In a standard signal acquisition process (e.g. image acquisition in TEM), an initial signal $\vec{x}$ with n components will be measured against the so-called sensing waveform (i.e. a functional basis Φ) giving a recorded signal $\vec{p}$ with m components. This is:

$$\vec{p} = \Phi\vec{x}$$

In general, the process will suffer from undersampling (i.e. $m \ll n$) and the equation system is undetermined. CS theory shows that a unique solution can be calculated for this problem, with two major restrictions: (i) $\vec{x}$ is sparse in a certain basis Ψ. (ii) The basis for the sparse representation Ψ and for the sensing waveform Φ must be incoherent.

A signal $\vec{x}$ is considered sparse in a certain domain (i.e. basis Ψ), when all the information can be expressed through a small set s of $c_s \neq 0$ coefficients ($\vec{c}$). Mathematically, the sparse transform is expressed as:

$$\vec{c} = \Psi\vec{x}$$

The signal is said to be sparse only if $s \ll n$, being $\vec{c}$ the sparse representation of $\vec{x}$. In practical applications, CS allows the relaxation of the strict constraint of sparsity to compressibility. In a compressible $\vec{x}$, $\vec{c}$ would contain $k \neq 0$ elements such as $k > s$. Thus, the transform Ψ is allowed to retrieve a certain small number of coefficients $(k - s)$ with lower significance to the information recovery than the s remaining, but still $k \ll n$, whereas $\vec{x}$ is sufficiently represented by the $s < k \ll n$ coefficients with higher significance. Therefore, the small coefficients $(k - s)$ can be filtered away (or set to 0), providing that the inverse transform will be able to effectively recover the initial image with minimal information loss. Then, $\vec{x}$ is then said to be a compressible signal.

Ψ and Φ incoherence means that the sensing basis cannot be sparsely represented. Hence, it ensures that each p_i contains information about many of the coefficients

x_j and, thus, it guarantees that under sampling artefacts (Φ domain) are distributed in a noise-like fashion through the signal in the sparse domain (Ψ).

The practical application of CS requires of an optimization process to recover the sparse coefficients from measurements, since the signal acquired is compressed and the optimal transform Ψ is a priori unknown. To that end, a nonlinear algorithm is required, able to minimize the number of nonzero coefficients (promoting sparsity) without compromising the consistency of the measured data. It has been shown that the minimization can be carried out over the so-called l_1-norm [35] $\vec{c} = \sum_i |c_i|$.

11.2.1.2 Compressed Sensing in Electron Tomography (CS-ET)

CS-ET can be formulated from two different equivalent perspectives: (i) being $\vec{p}$ the projection image (sinogram) and Φ the real space projection operator in the frame of a discretized Radon transform or (ii) applying the central slice theorem in the frame of a discretized Fourier transform (FT). This second approach sets $\vec{p}$ as the FT of the projection data (i.e. discrete radial samples of the object in the Fourier space), and Φ as a discrete Fourier operator. Then, the under sampling artefacts (already discussed in the introduction) that arise from an uncomplete radial sampling of the Fourier space can be minimized through the effective application of a CS-based reconstruction algorithm.

The sparsity of the signals recorded (necessary condition for the application of CS) must be promoted through a certain transform Ψ. Several possibilities of transforms are described in the literature, depending on the sample nature and projection images information content (acquisition mode). The most common choice is a combination of sparse transform in the image domain itself ($\Psi = \mathbb{I}$ identity transform) and the spatial gradient domain ($\Psi =$ spatial finite-differences transform). The sparsity is then promoted by minimizing the l_1-norm in both spaces (being called the TV-norm in the spatial gradient space). This is a convex optimization problem that can be formulated as:

$$\vec{x}'_{\lambda_{\mathbb{I}},\,\lambda_{\mathrm{TV}}} = \arg\min_{\vec{x}'} \left\{ \Phi\vec{x}' - \vec{p}_{l2} + \lambda_{\mathbb{I}}\Psi\vec{x}'_{l1} + \lambda_{\mathrm{TV}}\mathrm{TV}\left(\vec{x}'\right) \right\}$$

where $\lambda_{\mathbb{I}}$, λ_{TV} coefficients are the weightings of the specific transforms l_1-norm minimization (image $\mathbb{I}$ and gradient TV), the l_2-norm term includes the tolerance to noise in the dataset ($\Phi\vec{x}' - \vec{p}_{l2} \leqslant \varepsilon$) and $\vec{x}'$ is the reconstruction of the $\vec{x}$ signal from the projection data $\vec{p}$. The minimization is an iterative process (see Fig. 11.3)

The quality of the reconstructed image will be affected by the values of the weighting factors $\lambda_{\mathbb{I}}, \lambda_{\mathrm{TV}}$. These values are not given a priori by any theory and must be approximated in each reconstruction problem independently. Under/overestimating them will lead to defective reconstructions, given that the minimization iterative process will incorrectly filter information in the sparse domain.

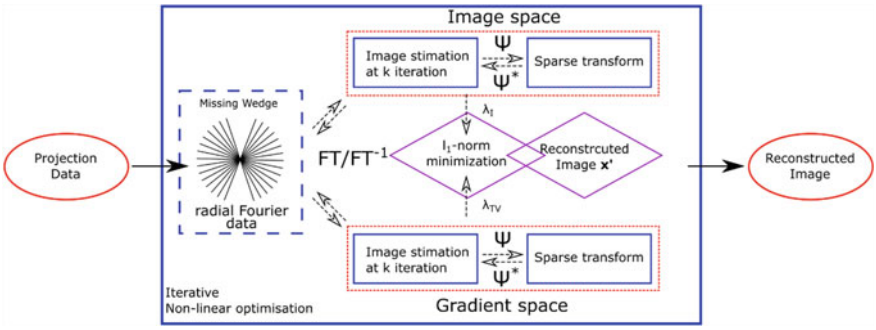

Fig. 11.3 Flow chart for the CS-ET process described in the text

11.2.2 EELS Tomography: From Spectrum Image Tilt Series to the Spectrum Volume

The end goal of analytical tomography is to retrieve the complete information about a 3D structure at the nanoscale. This is equivalent to reconstructing a four-dimensional object, where the first three dimensions correspond to the geometry of the sample, and the fourth dimension is related to the chemical composition. In the case of EELS tomography, the fourth dimension is the energy loss. This object is known as the spectrum volume (SV), where each voxel contains an EELS spectrum (see Fig. 11.4) [36, 37].

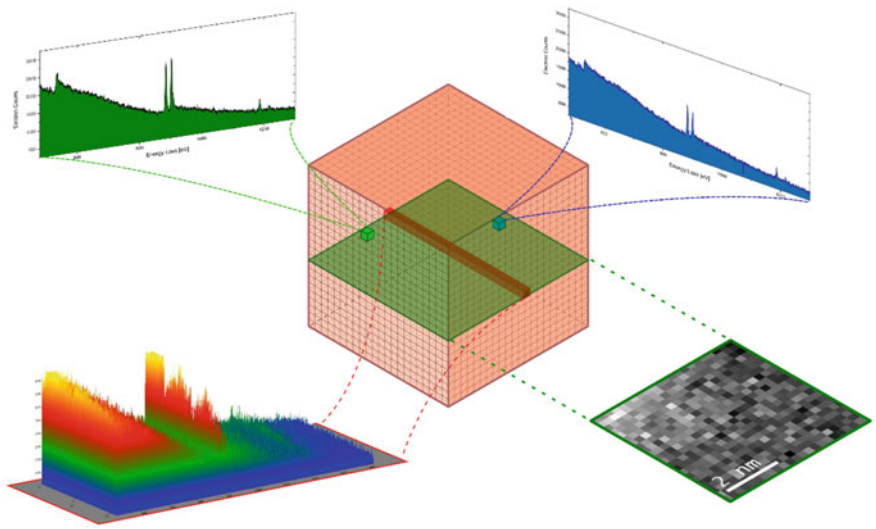

Fig. 11.4 Schematics of the spectrum volume approach for electron tomography. The individual spectra and spectrum line spectrum profile shown correspond to cerium oxide (CeO_2) doped with gad5olinium (Gd)

The first approximation to the spectrum volume reconstruction was carried out by acquiring sets of spectrum images (SI) at different tilt angles, simultaneous with the acquisition of HAADF images [37]. To avoid sample damage, the experiments are usually performed using short acquisition times for the EEL spectra. These conditions reduce the signal to noise ratio (SNR) of the spectra; thus, statistical treatment is routinely required to retrieve significant information. The large number of spectra acquired for the complete set of projections increases the statistics, allowing the successful retrieval of a denoised signal through multivariable analysis methods (MVA) [20, 38–40].

The information fed to the tomographic reconstruction algorithms is intended to be the intensity of the EELS edges on the spectrum images acquired $I(x, y, \theta)$ (i.e. the integrated area under the curve for each edge). This way, a map of separated elements according to EELS edge intensities is available for each projected image. The intensity of EELS edges in the core-loss region is given by:

$$I_k{}^A(\beta, \Delta) = N^A \, \sigma_k{}^A(\beta, \Delta) \, I_T(\beta) \, e^{(-t/\lambda)}$$

for the k edge of element A integrating over a collection angle β along an energy range Δ, $I_K{}^A$ is the integrated intensity, N^A is the areal density, $\sigma_k{}^A$ is the ionization cross-section and I_T is the total transmitted beam intensity; t is the sample thickness and λ the inelastic mean free path. (If $t/\lambda \geqslant 0.3$, plural scattering events are expected, and the equation may not hold). Avoiding plural scattering, the edge intensities will vary monotonically with thickness (material property), and the signals are suitable for tomographic reconstruction. This will be the usual scenario for magnetic nanoparticles due to their reduced size.

In cases where plural scattering is relevant (thicker or larger samples), some problems may arise. One clear example is the case of the 'cupping artefact', characterized by an inversion of the spectrum image contrast in thicker zones of the sample [41]. This leads to a miscalculation of the edge intensity and, thus, of the elemental quantification. Hence, in those cases, EELS edge intensities may no longer be suitable signals for tomography reconstruction.

The correct identification of cupping artefact effects in SI is not always straightforward, since they can be mistaken by a structural effect on the image (e.g. core-shell structure). Thereby, a thorough study of the material is required before undertaking the tomographic reconstruction. Although the spectrum volume cannot be retrieved if EELS edge intensities are unsuitable for tomographic reconstruction, 3D information for the elemental distribution in the samples can still be extracted [37].

11.2.2.1 Multivariable Analysis Methods (MVA)

SNR is usually low in EELS-SI experiments, due to image acquisition constraints to avoid sample damage. Hence, statistical treatment of the signals in the SI and

noise reduction are imperative. Besides, the problem requires the separation of the contribution of each element to the spectra per pixel and their identification, which can be regarded as a blind source separation *(BSS)* problem [20, 38–40].

First, the data $(x, y, \theta, \Delta E)$ needs to be treated to correct energy drift. Then, weighted principal component analysis (wPCA) [38] is applied. The weighting of the PCA is adapted to the dominant Poissonian noise. The PCA algorithm computes a new spectral base for the spectrum image, where the base components are ordered by the spectral variance in the original SI. Thus, the dimensionality is transformed from intensity of each energy loss channel at a given point to weight of each new base component in that given point. The method is based on three major assumptions: (i) the problem to be solved is linear, (ii) the signal has higher variance than noise and (iii) there is component orthogonality. The linearity and orthogonality mean that the separated components can be treated as a basis for the energy loss spectra space (i.e. each spectrum can be expressed as a weighted sum of the components). The higher variance components resolved by the algorithm are generally related with meaningful features of the sample (e.g. thickness and elemental composition), whereas the components of lower variance are usually associated with pure noise and do not offer further information pertaining to the spatial distribution of the elements.

The problem with PCA, and the reason it is not regarded as a valid BSS by itself, is that it relies in second order statistics (variance) to separate components. This is, the separation of components in PCA is not based on physical considerations, so they may have no physical meaning [42]. Thereby, they are also, in principle, unsuitable for tomographic reconstruction, since they may fail to fulfil the projection requirement. Nonetheless, as a noise reduction step, wPCA plays an important role since the BSS algorithms described ahead are not to be applied to noisy datasets. It also plays the important role of reducing the number of components in the calculation, thus reducing the computational time required.

Independent component analysis (ICA) is the first possible method for BSS. It deals with the data as a mixture of independent, and therefore uncorrelated, components. Those components are found according to their non-Gaussian distribution and they should unveil physically meaningful components of the dataset [39, 40].

A second possible method for BSS is the Bayesian linear unmixing (BLU) [42, 43] approximation, described by N. Dobigeon. One reason to choose BLU over ICA is that the latter has been shown to fail performing endmember extraction precisely when the spectral sources (components or endmembers) are not statistically independent, a strict condition for the implementation of ICA [42, 44]. Besides, this Bayesian formulation allows the introduction of several constraints for the calculations, such as (1) sparsity, (2) non-negativity and (3) full additivity. The case of the EELS-SV [36] calculation can clearly benefit from the introduction of the number of components, non-negativity nature of the signal, and the proportions limitation (i.e. full additivity for the proportions of the components expected in the sample) into the data treatment, as a way of increasing the endmember identification accuracy. Alongside, Dobigeon model [42] is characterized by estimating the parameters of the new basis in a lower dimension space identified by a standard dimension reduction

technique, such as PCA, within a Bayesian framework. This is ought to reduce the degrees of freedom in the parameters.

Although both methods described have proven to solve the BSS problem for tomography reconstruction, new advances are expected in the field, driven by the growing resources dedicated to the treatment of big data in a wide spectrum of scientific and technological fields [45].

11.2.2.2 EELS-SV. Tomographic Reconstruction from the Elemental Maps

After the PCA noise reduction and the EEL Spectra separation as a sum of weighted spectral components identified by ICA/BLU, these are set as the orthogonal axes of the new spectral basis. Every single EEL spectrum on every SI of the tilt series dataset acquired is represented as a weighted sum of the identified spectral components.

The final step is the tomographic reconstruction itself, using the spectral weighted component map separated from the SI as the projections fed to the algorithms. The quality of the reconstruction, the number of projections and the computational resources available, will determine the algorithm of choice, as already discussed.

At this point, EELS-SV is already available, since the full spectra in each reconstructed voxel have been calculated from the separated components and the corresponding weighting factors.

As a paradigmatic example, let us briefly revise the results achieved on the reconstruction of ferromagnetic (FM) $CoFe_2O_4$ (CFO) nanocolumns embedded in a ferroelectric (FE) $BiFeO_3$ (BFO) matrix grown on a $LaNiO_3$ buffered $LaAlO_3$ substrate (BFO–CFO//LNO/LAO) (see Fig. 11.5a). It is a prototypical multiferroic vertical nanostructure, where the magnetic properties are strongly dependent of the substrate material and orientation, ferroic phases, and phase ratio. Thus, a complete characterization, expected to bind functional properties and material structure, requires precise knowledge of the local composition (EELS) coupled with 3D structure reconstruction (electron tomography) [36].

A focus ion beam (FIB) [46] preparation of a nanopillar TEM specimen ensured almost constant thickness in the projections regardless the tilt angle. Electron mean free path exceeds sample thickness in all possible transmitted trajectories. Hence, multiple scattering events should remain as a residual contribution to EELS signal. This is confirmed by the absence of contrast inversion towards the centre of the nanocolumn in the SI and, thus, enables the use of EELS component as the input dataset for tomographic reconstruction.

BLU along with PCA where carried out for the endmember separation, and SIRT was the algorithm of choice for tomographic reconstruction, requiring 20 iterations before convergence. The parametric basis extracted after MVA consisted of four components, identified as: (1) iron oxide (Fe_xO_y), (2) lanthanum oxide(La_xO_y), (3) background contribution, and (4) noise in vacuum contribution (kept for calculations but not reconstructed), as shown in Fig. 11.5b. The results of the volume reconstructions for each component in the basis in Fig. 11.5b are shown in Fig. 11.5d.

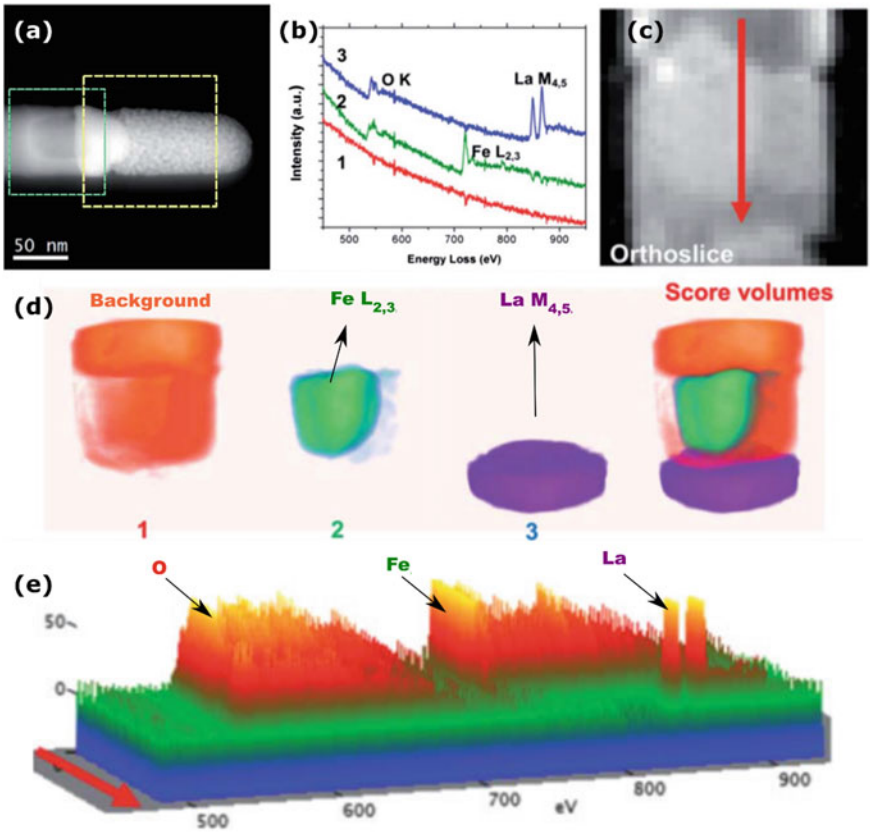

Fig. 11.5 **a** HAADF image of a projection of the multiferroic compound. Green: area chosen for the EELS-SV reconstruction. **b** EELS Spectrum components extracted from the BSS process as the new parametric basis: 1—Background, 2—Fe_xO_y 3—La_xO_y. **c** SI corresponding to a vertical orthoslice through the reconstructed SV. **d** Volume reconstructions for the parametric basis in **b**. **e** Spectrum profile for the spectrum line shown in red in **c**

One of the multiple advantages of the access to the EELS-SV can be easily understood through the images in Fig. 11.5c, e. The first one is a vertical orthoslice through the EELS-SV, and the second displays the spectra profile through the spectrum line traced in the orthoslice. The possibility to access spectral information in the inside of the structure, unaffected by the material above and below, as in the selected spectrum line, is unique of this technique.

11.2.2.3 Cupping Artefact and the Spectrum Volume

Unfortunately, EELS edge intensity does not always fulfil the projection requirement. In cases where plural scattering is not negligible, thickness effects causing contrast

inversion (i.e. cupping artefact) prevent a monotonical behavior of the intensity with the material composition and, thus, tomography algorithms fail to reconstruct the SV [37].

One possible solution to overcome this problem is to extract the concentration of the elements from the intensity edges. Let us consider the case of three elements identified after MVA. The concentration of element *A* (taking advantage of the exponential relation shown in subsection 11.2.2 for the intensity, $I_{kA(beta,\ delta)}$ of core loss EELS edges) is

$$A\% = \frac{N^A}{N^A + N^B + N^C} \approx \frac{{I_k}^A/{\sigma_k}^A}{{I_k}^A/{\sigma_k}^A + {I_k}^B/{\sigma_k}^B + {I_k}^C/{\sigma_k}^C}$$

assuming that the mean free path λ does not effectively change in these materials. This signal already fulfils the projection requirement and is suitable for the algorithms of ET.

Besides, it is common to extract from the MVA process a component of the spectra related to sample thickness and, thus, suitable for tomography reconstruction. If this thickness-related signal is merged with quantification data pixel by pixel, the intensity of this new signal will fulfil the projection requirement, as it can be regarded as the contribution of a given element to the thickness found for every pixel (density-thickness contrast images). The thickness inversion effect ('cupping artefact') is eliminated, and a signal fulfilling the projection requirement and containing elemental quantification is available for tomography reconstruction [37].

This method allows to recover a 3D reconstruction segmenting the identified elements through MVA, although the SV is not recovered (i.e. each voxel in the reconstructed volume will not contain the whole EEL Spectra). It proves to be an effective way of minimizing the negative effects of spectrum image artefacts and retains as much chemical quantitative information as possible in a reconstructed 3D volume.

11.2.3 A Case Study: 3D Visualization of Iron Oxidation State in FeO/Fe_3O_4 Core–Shell Nanocubes Through Compressed Sensing

The determination of the oxidation state of chemical species is of paramount importance to understand the physicochemical properties of nanomaterials for a wide range of applications, and particularly in the case of studying magnetic properties in nanostructured materials [34]. The high spatial and spectral resolution that characterizes EELS spectroscopy makes this technique suitable to recover detailed compositional and electronic information, relevant in such cases as core-shell magnetic nanoparticles. Furthermore, the energy loss near-edge structure (ELNES) can be used to determine the oxidation state of the probed chemical species. The combination of

this technique with a highly accurate ET reconstruction method (i.e. CS), able to retrieve fine structural details in a 3D distribution from fewer projection images and, thus, reducing sample damage, enables the recovery of the complete EELS-SV with access to oxidation state information.

To test this possibility, an experiment was proposed, aiming to recover the EELS-SV reconstruction of an iron oxide nanocube, with a FeO_x/FeO_y core-shell structure (*Torruella, Pau* et al. *2016. 3D Visualization of the Iron Oxidation State in FeO/Fe3O4 Core–Shell Nanocubes from Electron Energy Loss Tomography. Nano letters, 16(8), 5068–5073*) [34]. This particular problem poses a challenge due to the fact that the contrast difference between shell and core was not enough, neither in HREM nor in STEM-HAADF, to accurately segment the image.

In order to obtain a quantitative 3D oxidation state map of the particle, a EELS-SI tilt series was acquired in low voltage conditions (80 keV) from $-69°$ to $+67°$, every $4°$ each containing 64×64 pixels with spectra in the energy range 478−888 eV.

The high spectral resolution (given a dispersion of 0.2 eV/pixel and 0.015 s/pixel), much needed to analyze ELNES features, meant severe sample damage by beam focus during the second half of the tilt series acquisition, due to accumulated dose. Furthermore, some SI were also discarded because the evidences of the significant coherent diffraction occurring at specific angles. Fortunately, the high symmetry of the nanocube allowed the reconstruction assuming a mirror effect in the projections for positive tilting angles.

The procedure followed in MVA for noise reduction (namely PCA) and BSS was applied only to the area of interest in the EEL spectra, i.e. around the iron $L_{2,3}$ edges. This effectively reduced the computational time. The BSS algorithm chosen was Fast-ICA, implemented in Hyperspy [47]. Fast-ICA was performed over the first derivative of the six remaining spectral components after PCA (denoising). Among the six components, two were related to the Fe ionization edge, labelled as C_1 and C_2. They show clear ELNES features that can be identified as the Fe $L_{2,3}$ white lines (Fig. 11.6). The position of the maximum of the Fe L_3 of C_2 is shifted +1.9 eV with respect to Fe L_3 maximum in C_1. For comparison, Fig. 11.6 also shows reference EEL spectra corresponding to the Fe $L_{3,2}$ edges for wüstite ($Fe_{1-x}O$), Fe^{2+} and haematite (Fe_2O_3) Fe^{3+}. This allowed the extraction of the Fe oxidation state maps, depicted as the weight of the respective components in each pixel as shown in Fig. 11.6 (right) for the $0°$ projection. Similar maps are obtained for the whole SI angular range, giving rise to two set of images suitable for 3D reconstruction.

For the tomographic reconstruction of the SV, the obtained components fulfilled the projection requirement, given that the nanocube size ranged between 35 and 40 nm and no cupping artefact was observed. CS was chosen as the reconstruction algorithm, given the low number of projections available and the precision expected in the SV. The sparsity promoting transform was the one described in the previous section (both image and gradient spaces where sparsely transformed).

The results of the reconstruction are shown in Fig. 11.7. The orthoslice for the Fe^{2+} Fig. 11.7d reveals the presence of this oxidation state in the core and the shell of the nanoparticle, whereas the presence of Fe^{3+} Fig. 11.7e is confined to the shell. This is consistent with the shell Fig. 11.7b being Fe_3O_4 and the core Fig. 11.7a FeO.

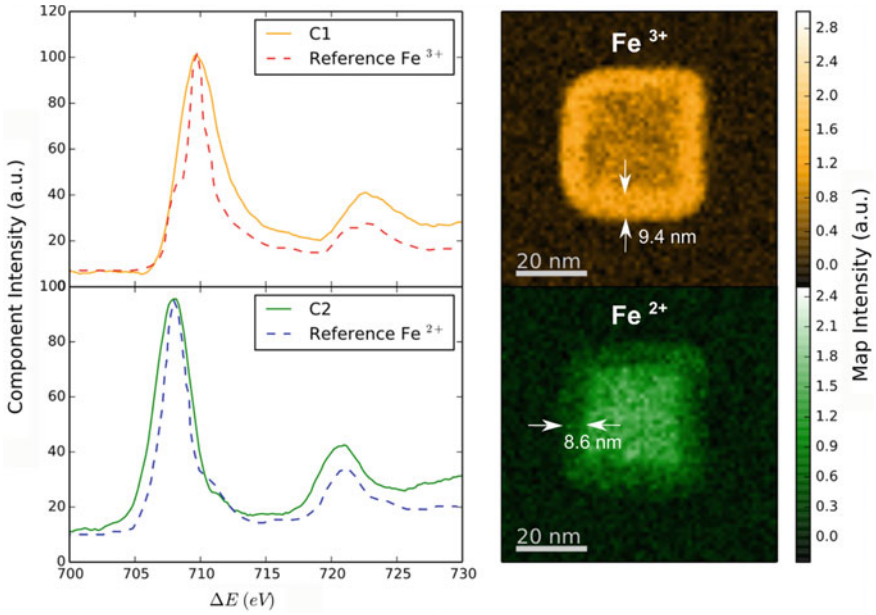

Fig. 11.6 C1 and C2 components extracted after the BSS process (ICA), and reference EEL spectra of the Fe white lines for the two oxidation states 3+ and 2+ . Right panels: Oxidation state maps calculated as weighted contribution of the C2 (Fe^{2+}) and C1 (Fe^{3+}) components shown in the EEL spectra on the left

The object reconstructed is a perfect example of an EELS-SV containing information about the oxidation state through ELNES analysis. Again, one of the clear advantages of the SV reconstruction is that information that usually would not be accessible experimentally is easily recovered by isolating specific voxels, for example, single spectra from the core region without shell contribution (Fig. 11.8a). In particular, spectrum lines, where the different oxidation states are clearly separated and spatially resolved, are accessible inside the reconstructed volume. This is shown in Fig. 11.8c, where a 2D vision of the EEL spectra along the line marked in 11.8b is depicted, being the ordinate axis the position in the line and the abscissa axis the energy loss. The intensity for each of the energy channels is represented by a colour scale (see Fig. 11.8c). The chemical shift of 1.4 eV for the different oxidation states in the iron edge is observable in the single spectrum and the spectrum line extracted from the SV reconstruction, proving the success in the reconstruction.

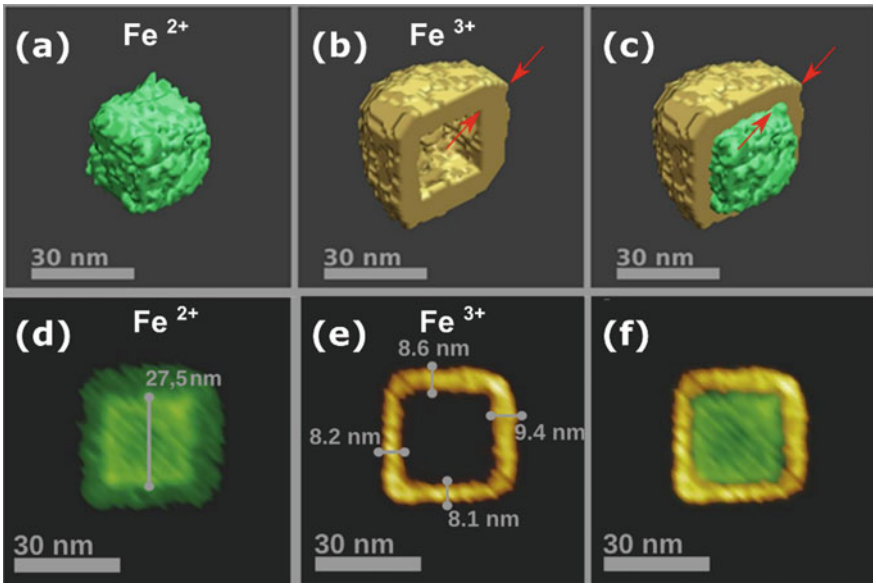

Fig. 11.7 3D visualization (AVIZO software) of the reconstructed volume for the **a** Fe^{2+}, **b** Fe^{3+} and **c** assembly of both. Orthoslices of the reconstructed volume for the **d** Fe^{2+}, **e** Fe^{3+} and **f** assembly of both. In **b** and **c**, the overlapping of core and shell is clearly observable (red arrows as visual guides)

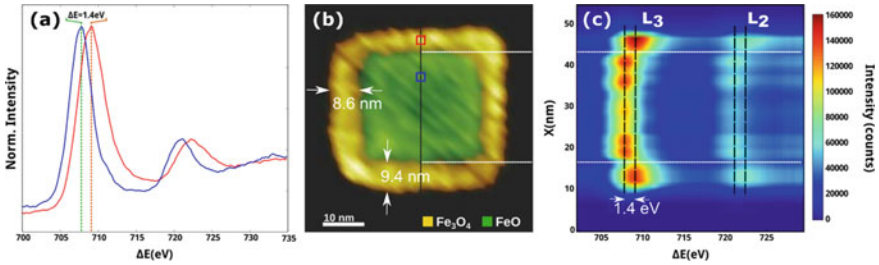

Fig. 11.8 **a** EELS spectra extracted from the SV reconstructed, corresponding to the voxels marked in red and blue in **b** and where the energy shift between both oxidation states is visible. **b** Orthoslice of the SV. **c** Stack of spectra corresponding to the spectrum line marked in **b**

11.3 Emerging Techniques and Future Perspectives for EELS-SV

The incorporation of EEL Spectra into electron tomography reconstruction resulted in the possibility of reconstructing the spectrum volume for a given sample (i.e.

the 4D dataset containing both structural and compositional information of a three-dimensional sample). Although the obtained results proved the successful implementation of this technique, allowing even the recovery of ELNES features from the reconstructed SV, there is clearly room for further improvements.

The separation of spectral components with physical meaningful information and suitable for tomographic reconstruction remains the main issue in the standard process described for EELS-SV recovery. Up to now, a combination of PCA (signal denoising) and ICA or BLU (BSS technique) has been used as the core of the MVA approximation for data treatment of the EELS-SI datasets. Although these methods have so far yielded good results, they rely on the ability of the scientist to make a physical interpretation of the output components, something that is not always straightforward. Hence, the implementation of clustering (or cluster analysis) to EELS SV recovery is considered.

11.3.1 Clustering Analysis: Mathematical Principles

An EELS-SI of $n = X \cdot Y$ pixels and $E = p$ channels per spectra can be represented by a $n \times p$ matrix, each spectrum a different row. Any given clustering algorithm will try to group spectra according to the similarity of their characteristic features (e.g. position of a certain intensity edge, or intensity ratios for edges in the same positions). Many options for the clustering implementation, such as K-means [48], density-based methods, [49] and agglomerative clustering algorithms [50] are available. In this case, the implementation of the hierarchical agglomerative clustering (HAC) for the segmentation of EELS-SI is briefly described, following the work done in [45].

Let us consider each spectrum (1 per pixel) a single object in a p-dimensional (pD) space. This is, all the different characteristics in the spectrum contained in a single pixel describe a single point in this new pD space. The distance between pD points in any given metric will characterize the similarity between spectra. For instance, let us consider the Euclidean metric:

$$d_{i,j} = \sqrt{\sum_{i=1}^{p} \left({x^i}_k - {x^j}_k \right)^2}$$

where ${x^{i,j}}_k$ $(k = 1, \ldots, p)$ are the coordinates for the spectra at the (i, j) points in the pD space. The HAC algorithm will measure this distance, grouping the closest elements in clusters iteratively. In each h iteration, the number of clusters will effectively decrease, and the distance $(d_{i,j})^h$ measured between the closest clusters will increase. At the end, if no stopping condition is set, all spectra would be grouped in a single cluster, losing the relevant information of the segmentation. In general, the value of $(d_{i,j})^h$ will suffer a sudden increment (orders of magnitude) after a certain number of iterations, which can be related to having achieved a certain degree of segmentation. This can be used as the stopping criteria. A very illustrative way to

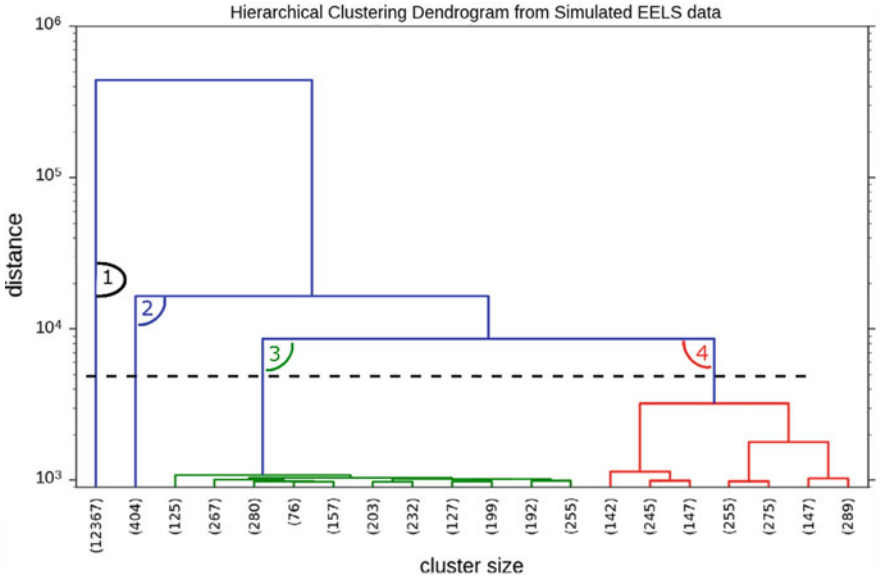

Fig. 11.9 Denogram plot for the HAC process in a simulated EELS-SP. The dashed line represents the reference distance for the HAC algorithm to classify the spectra in four clusters

understand the process is through the so-called *denogram plots* (Fig. 11.9), a 'tree' representation for the number of elements in a cluster against the minimum distance between them (at which a new cluster was formed from two previous different clusters, linked by a horizontal line).

11.3.2 Application of Clustering to EELS

EELS-SI and the data analysis techniques introduced so far, PCA and ICA/BLU, aimed to map the spatial distribution of compounds and properties of the sample through the study of the shape of individual EEL spectra. The nature of the problem, along with the characteristics of EEL spectra (good energy resolution and differentiated spectral features for each compound), makes it a suitable candidate for the implementation of clustering techniques.

Furthermore, clustering presents the advantage of resolving different regions without any prior assumption over the data. Also, due to the nature of cluster analysis techniques, the averaged signal in a single cluster will always contain physical meaningful information (absent of negative edges and other features commonly found in ICA or PCA, that require further manual analysis). This presents clustering as a new step towards the automatization on EEL spectroscopic techniques, especially in EELS-SI segmentation.

The first practical approximation to the implementation of clustering algorithms in EELS data treatment can be found in *Torruella, Pau,* et al. *2018. Clustering analysis strategies for electron energy loss spectroscopy (EELS). Ultramicroscopy*, *185*, 42–48 [45].

In it, EELS simulation and experimental datasets were successfully segmented after the implementation of the HAC algorithm following three different strategies: (i) HAC in raw data, (ii) HAC followed by PCA, and (iii) PCA followed by HAC separation. All three strategies successfully retrieved segmented results, but the accuracy and quantity of information provided was different in each case.

11.3.2.1 EELS Simulation Dataset

The simulated artificial EELS dataset consisted of a 128 × 128 pixels SI, with 1024 channels per spectrum. Four zones with different spectral features were created to test the proficiency of the algorithm to segregate spectral components when detailed analysis is required. The basic structure resembles a spherical core-shell NP, with two additional elliptical internal zones (see Fig. 11.10a). The core of the particle was filled with spectra corresponding a constant FeO composition. The shell was filled with $Fe_{x-1}O_{x+1}$, where the ratio Fe/O linearly varied increasing O towards the exterior. One of the elliptical zones inside the core was filled with FeCoO spectra to simulate a precipitate of Co, and the other one was a void. All spectra were filled with Gaussian and Poissonian noise to represent a real study case.

Raw data clustering segmentation was able to identify the regions of different composition without any prior assumption of the data (such as the composition and expected distribution of elements), identifying the four different zones of the phantom. Despite the acceptable separation (Fig. 11.10b), some problems with the cluster assignation for the FeO are present near the frontier core/shell, and the Fe/O gradient is not well represented for the shell. This accounts for the incapacity of clustering approach to retrieve negative non-physical edges in the spectral components separated and, thus, the incapacity of gradient composition detection. One hint of the presence of this gradient can be obtained by the relaxation of the pD distance threshold (i.e. relaxing the stopping criteria). Then, the shell will appear to contain three different clusters (Fig. 11.10).

To avoid the loss of this information, by grouping within the same cluster boundaries spectra with similar features arising from different physical properties in the sample, the first solution explored was the application of PCA to the HAC results. This proved capable of identifying the linear gradient of the Fe/O composition in the shell, retrieving a non-physical component with a negative edge in the decomposed cluster linked to a decreasing quantity of iron towards the exterior (Fig. 11.10c).

The second possible solution was the implementation of HAC algorithms over the score components extracted from the PCA calculations in the original EELS dataset. This method yielded similar results to the previous one (see Fig. 11.10d). The main difference resides now in the computational time. By first applying PCA, the number of spectral components is reduced to 3 and, thus, the HCA algorithm iterates over

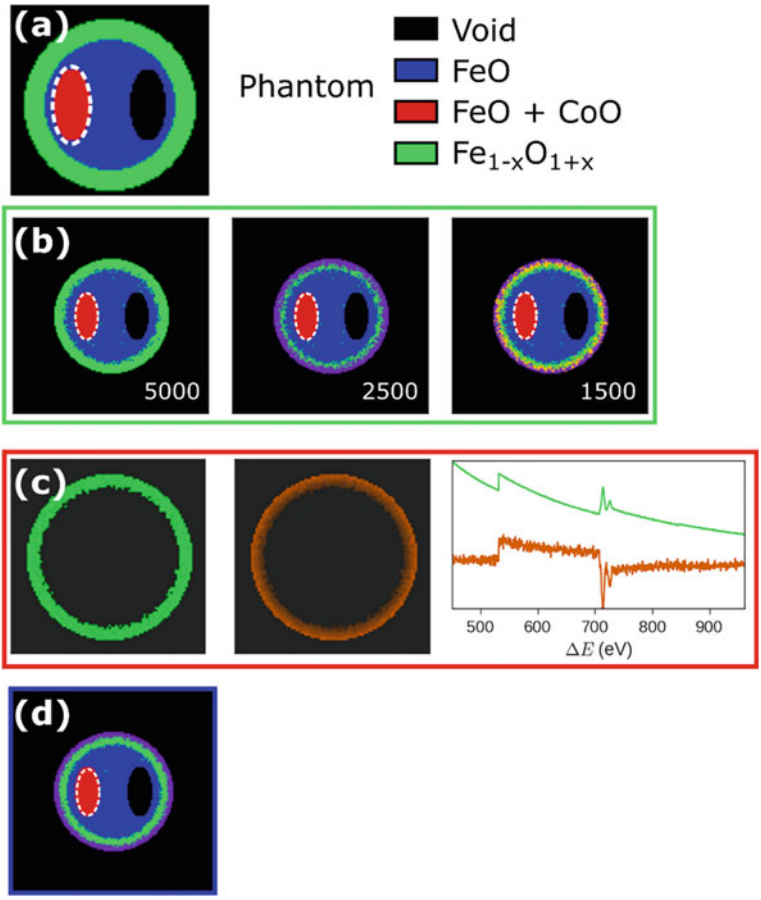

Fig. 11.10 **a** EEL spectral phantom used on the simulation of clustering techniques. **b** Results of the application of HAC on the raw data, showing the segmentation under three different threshold counts: 5000, 2500, and 1500. **c** Results of applying PCA to the shell region after HAC (green in **b**). **d** Result of applying HAC to the PCA scores of the phantom

$n = 128 \cdot 128 = 16384$ elements with only $p = 3$ possible spectral components (instead of the 1024 initial channels).

11.3.2.2 Example. Magnetic Fe_3O_4–Mn_3O_4/MnO Nanoparticle

The experimental dataset analyzed corresponds to a core-shell structure for a magnetic nanoparticle composed by a mixture of Fe_3O_4 and Mn_3O_4/MnO [51].

Once again, raw data clustering segmentation successfully separated regions of different composition. The core composition was identified as a majority of iron oxide with minor contributions of manganese oxide (presumably arising from the

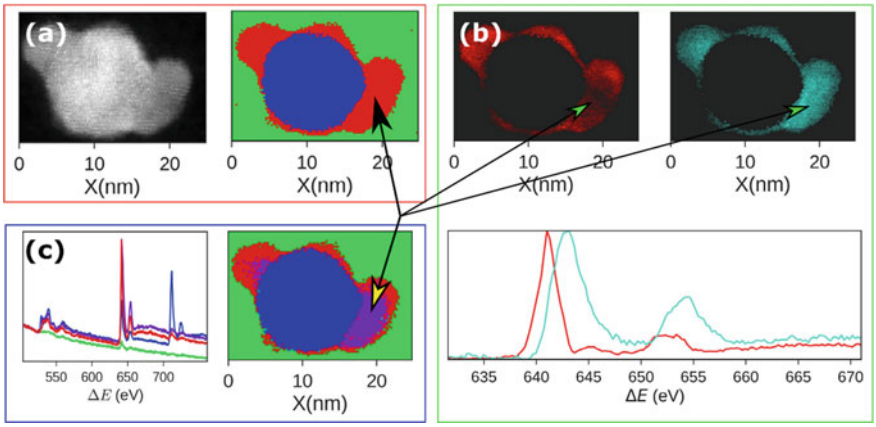

Fig. 11.11 Results for the HAC-EELS data treatment in the Fe_3O_4–Mn_3O_4/MnO magnetic nanoparticle. **a** HAC in raw data. Core and shell clearly separated. **b** Shell component separation by ELNES analysis, after applying PCA over the clusters retrieved by HAC. **c** HAC on the score spectra extracted by PCA over EELS dataset

shell beneath the core), and the shell composition was identified as manganese oxide. To accurately get the core–shell separation, a normalization step in the EELS dataset was imposed, to eliminate thickness effects in the signal. One main advantage over PCA + ICA approximation is that none of the segmented components contained non-physical features (such as negative edges) that required further interpretation.

Unfortunately, fine structure spectral information (ELNES) is lost if only HCA is performed. PCA was applied to the results of cluster analysis in the shell, as previously done in the phantom case. Two different components in the cluster were found, corresponding to different oxidation states of manganese oxide identified through ELNES analysis, separating Mn_3O_4 and MnO (see Fig. 11.11c). The results still lacked a good spatial resolution for the separation of each oxidation state, leading to a possible misinterpretation under the assumption of homogeneous mixing of states.

To that end, the implementation of HAC algorithms over the score signals extracted from the PCA calculations in the original EELS dataset was carried out, following the same procedure explained in the phantom case study. This method yielded an effective separation of the two zones with different oxidation states (Mn_3O_4 and MnO) in the shell of manganese oxide (Fig. 11.11b), improving the segmentation accuracy, the spatial resolution and reducing the computational time (since HCA is carried out over only four different spectral components).

11.3.3 Future Perspectives. Clustering Data in EELS-SV Tomographic Reconstructions

The potential benefits arising from the joint performance of new ET algorithms and better segmentation procedures are manifold: to overcome the problems arising from low acquisition times, few projections or reduced pixel time. This will lead to better EELS-SV reconstructions with a higher degree of complexity (ELNES analysis included), and in otherwise non-treatable cases (e.g. samples susceptible to beam damage). In this sense, systematic approaches have been recently reported, applying wavelet transform [28, 52] to reduce the incidence of Poissonian noise [53, 54] in HAADF images previous to the 3D reconstruction via TMV-algorithm [55, 56]. The same method is likely to be implemented in EELS-SV reconstruction, given the unavoidable Poissonian noise present in EELS due to the signal nature.

The recently introduced clustering approach for the EELS-SI segmentation is still to be tested on EELS-SV reconstructions. In principle, given the physical nature of the components extracted from cluster analysis, they should be a valid signal in most ET algorithms, whereas no thickness-related artefacts break the projection requirement. A systematic study on the accuracy of the EELS-SV reconstruction, using different algorithms, under different acquisition conditions and including clustering segmentation techniques, needs to be addressed shortly. Also, an in-depth study of the suitability of the wide variety of clustering algorithms available (e.g. the described HAC, *K*-means [48] and agglomerative clustering [57], among others) applied to EELS data treatment must be also undertaken.

References

1. V. Lučić, F. Förster, W. Baumeister, Structural studies by electron tomography: from cells to molecules. Annu. Rev. Biochem. **74**, 833–865 (2005)
2. P.A. Midgley, M. Weyland, 3D electron microscopy in the physical sciences: the development of Z-contrast and EFTEM tomography. Ultramicroscopy **96**, 413–431 (2003)
3. D.B. Williams, C.B. Carter, The transmission electron microscope. in *Transmission Electron Microscopy* (Springer US, 1996), pp. 3–17. https://doi.org/10.1007/978-1-4757-2519-3_1
4. P.A. Midgley, R.E. Dunin-Borkowski, Electron tomography and holography in materials science. Nat. Mater. **8**, 271–280 (2009)
5. Z. Saghi et al., Compressed sensing electron tomography of needle-shaped biological specimens—potential for improved reconstruction fidelity with reduced dose. Ultramicroscopy **160**, 230–238 (2016)
6. P. Penczek, M. Marko, K. Buttle, J. Frank, Double-tilt electron tomography. Ultramicroscopy **60**, 393–410 (1995)
7. K.J. Batenburg et al., 3D imaging of nanomaterials by discrete tomography. Ultramicroscopy **109**, 730–740 (2009)
8. T. Roelandts et al., Accurate segmentation of dense nanoparticles by partially discrete electron tomography. Ultramicroscopy **114**, 96–105 (2012)
9. J. Radon, Über die Bestimmung von Funktionen durch ihre Integralwerte längs gewisser Mannigfaltigkeiten. in *books.google.com*, pp. 71–86 (1983). https://doi.org/10.1090/psapm/027/692055

10. Radermacher, M. Weighted back-projection methods. in *Electron Tomography: Methods for Three-Dimensional Visualization of Structures in the Cell* (Springer New York, 2006), pp. 245–273. https://doi.org/10.1007/978-0-387-69008-7_9
11. R.A. Brooks, D.G. Chiro, Principles of computer assisted tomography (CAT) in radiographic and radioisotopic imaging. Phys. Med. Biol. **21**, 689–732 (1976)
12. G.A. Perkins et al., Electron tomography of large, multicomponent biological structures. J. Struct. Biol. **120**, 219–227 (1997)
13. R.B. Der, T. Gabor, Algebraic reconstruction techniques (ART) for three-dimensional electron microscopy and X-ray photography (1970) (Elsevier)
14. P. Gilbert, Iterative methods for three dimensional reconstruction of an object from projections. J. Theor. Biol. **36**, 105–117 (1972)
15. M. Weyland, P.A. Midgley, Extending energy-filtered transmission electron microscopy (EFTEM) into three dimensions using electron tomography. Microsc. Microanal. **9**, 542–555 (2003)
16. B. Goris, S. Bals, W. Van den Broek, J. Verbeeck, G. Van Tendeloo, Exploring different inelastic projection mechanisms for electron tomography. Ultramicroscopy **111**, 1262–1267 (2011)
17. G. Möbus, R.C. Doole, B.J. Inkson, Spectroscopic electron tomography. Ultramicroscopy **96**, 433–451 (2003)
18. G. Möbus, B.J. Inkson, Nanoscale tomography in materials science. Mater. Today **10**, 18–25 (2007)
19. J. Frank, S. Edition, J. Frank, S. Edition, in *Electron Tomography*. (Springer, 2006). doi:10.1007/978-0-387-69008-7
20. N. Dobigeon, N. Brun, Spectral mixture analysis of EELS spectrum-images. Ultramicroscopy **120**, 25–34 (2012)
21. C. Jeanguillaume, C. Colliex, Spectrum-image: the next step in EELS digital acquisition and processing. Ultramicroscopy **28**, 252–257 (1989)
22. B. Freitag, S. Kujawa, P.M. Mul, J. Ringnalda, P.C. Tiemeijer, Breaking the spherical and chromatic aberration barrier in transmission electron microscopy. Ultramicroscopy **102**, 209–214 (2005)
23. B. Kabius et al., First application of Cc-corrected imaging for high-resolution and energy-filtered TEM. J. Electron. Microsc. (Tokyo) **58**, 147–155 (2009)
24. K. Kimoto, G. Kothleitner, W. Grogger, Y. Matsui, F. Hofer, Advantages of a monochromator for bandgap measurements using electron energy-loss spectroscopy. Micron **36**, 185–189 (2005)
25. M.T. Otten, W.M.J. Coene, High-resolution imaging on a field emission TEM. Ultramicroscopy **48**, 77–91 (1993)
26. R.F. Egerton, in *Electron Energy-Loss Spectroscopy in the Electron Microscope*. (Springer, 2011)
27. L. Cavé, T. Al, D. Loomer, S. Cogswell, L. Weaver, A STEM/EELS method for mapping iron valence ratios in oxide minerals. Micron **37**, 301–309 (2006)
28. Q. Du, J.E. Fowler, Hyperspectral image compression using JPEG2000 and principal component analysis. IEEE Geosci. Remote Sens. Lett. **4**, 201–205 (2007)
29. E. Candès, J. Romberg, Sparsity and incoherence in compressive sampling. Inverse Probl. **23**, 969–985 (2007)
30. B. Bougher, Introduction to compressed sensing. Lead. Edge 1256–1258 (2015). doi:http://dx.doi.org/10.1190/tle34101256.1
31. R. Leary, Z. Saghi, P.A. Midgley, D.J. Holland, Compressed sensing electron tomography. Ultramicroscopy **131**, 70–91 (2013)
32. J.M. Thomas, R. Leary, P.A. Midgley, D.J. Holland, A new approach to the investigation of nanoparticles: electron tomography with compressed sensing. J. Colloid Interface Sci. **392**, 7–14 (2013)
33. Z. Saghi, et al., Three-dimensional morphology of iron oxide nanoparticles with reactive concave surfaces. a compressed sensing-electron tomography (CS-ET) approach. Nano Lett. **11**, 4666–4673 (2011)

34. P. Torruella et al., 3D visualization of the iron oxidation state in FeO/Fe_3 O_4 core-shell nanocubes from electron energy loss tomography. Nano Lett. **16**, 5068–5073 (2016)
35. L. Rudin, Nonlinear total variation based noise removal algorithms. Physica D **60**, 259–268 (1992)
36. L. Yedra et al., EELS tomography in multiferroic nanocomposites: from spectrum images to the spectrum volume. Nanoscale **6**, 6646–6650 (2014)
37. L. Yedra et al., EEL spectroscopic tomography: towards a new dimension in nanomaterials analysis. Ultramicroscopy **122**, 12–18 (2012)
38. H. Abdi, L.J. Williams, Principal component analysis. WIREs Comp. Stat. **2**, 433–459 (2010)
39. A. Hyvärinen, J. Karhunen, E. Oja, Independent component analysis (2004)
40. J.D. Bayliss, J.A. Gualtieri, R.F. Cromp, Analyzing hyperspectral data with independent component analysis, in (ed. J.M. Selander) vol. 3240, pp. 133–143 (International Society for Optics and Photonics, 1998)
41. W. Van den Broek et al., Correction of non-linear thickness effects in HAADF STEM electron tomography. Ultramicroscopy **116**, 8–12 (2012)
42. N. Dobigeon, S. Moussaoui, M. Coulon, J.-Y. Tourneret, A.O. Hero, Joint bayesian end member extraction and linear unmixing for hyperspectral imagery. IEEE Trans. Signal Process. **57**, 4355–4368 (2009)
43. N. Dobigeon, N. Brun, Ultramicroscopy spectral mixture analysis of EELS spectrum-images. Ultramicroscopy **120**, (2012)
44. J. Nascimento, J. Bioucas-Dias, Does independent component analysis play a role in unmixing hyperspectral data? IEEE Trans. Geosci. Remote Sens. **43**, 175–187 (2005)
45. P. Torruella et al., Clustering analysis strategies for electron energy loss spectroscopy (EELS). Ultramicroscopy **185**, 42–48 (2018)
46. L.A. Giannuzzi, F.A. Stevie, A review of focused ion beam milling techniques for TEM specimen preparation 10_1016-S0968-4328(99), 00005–0 Micron ScienceDirect_com. Micron **30**, 197–204 (1999)
47. F. de la Peña, et al., Hyperspy/Hyperspy: Hyperspy 1.3. *hyperspy/hyperspy: HyperSpy 1.3* (2017). https://doi.org/10.5281/zenodo.583693
48. A.K. Jain, Data clustering: 50 years beyond K-means. Pattern Recognit. Lett. **31**, 651–666 (2010)
49. J. Sander, M. Ester, H.P.P. Kriegel, X. Xu, Density-based clustering in spatial databases: the algorithm GDBSCAN and its applications. Data Min. Knowl. Discovery **194**, 169–194 (1998)
50. I. Davidson, S.S. Ravi, Agglomerative hierarchical clustering with constraints: theory and empirical resutls, in *9th European Conference on Principles of Data Mining and Knowledge Discovery Databases, PKDD 2005*, pp. 59–70 (2005)
51. L. Yedra et al., Oxide wizard: an EELS application to characterize the white lines of transition metal edges. Microsc. Microanal. **20**, 698–705 (2014)
52. T. Printemps et al., Self-adapting denoising, alignment and reconstruction in electron tomography in materials science. Ultramicroscopy **160**, 23–34 (2016)
53. M. Makitalo, A. Foi, Optimal inversion of the Anscombe transformation in low-count Poisson image denoising. IEEE Trans. Image Process. **20**, 99–109 (2011)
54. M. Makitalo, A. Foi, Optimal inversion of the generalized Anscombe transformation for Poisson-Gaussian noise. IEEE Trans. Image Process. **22**, 91–103 (2013)
55. M. López-Haro et al., A macroscopically relevant 3D-metrology approach for nanocatalysis research. Part. Part. Syst. Charact. **35**, 1700343 (2018)
56. B. Goris, W. Van den Broek, K.J. Batenburg, H.H. Mezerji, S. Bals, Electron tomography based on a total variation minimization reconstruction technique. Ultramicroscopy **113**, 120–130 (2012)
57. F. Murtagh, P. Legendre, Ward's hierarchical agglomerative clustering method: which algorithms implement ward's criterion? J. Classif. **31**, 274–295 (2014)

Chapter 12
Magnetic Force Microscopy and Magnetic Nanoparticles: Perspectives and Challenges

Daniele Passeri, Livia Angeloni, and Marco Rossi

Abstract Among the various techniques for the characterization of magnetic NPs, magnetic force microscopy (MFM) represent one of the most widespread and versatile methods due to its lateral resolution, sensitivity, imaging capability, the need for a relatively simple and widespread experimental setup, minimal/no specific requirements about sample preparations, capability to operate in air at room conditions as well as in vacuum or liquid environment. Indeed, MFM enables the quantitative characterization of magnetic properties of single magnetic NPs, can be used to detect single magnetic NPs in nonmagnetic (e.g., polymeric or biological) matrices, as well as to perform mechanical or magnetic nanomanipulation of single NPs. In this chapter, applications of MFM in the study of magnetic NPs are briefly reviewed and intriguing perspectives are depicted, focusing on current limitations to overcome and challenges to take up.

12.1 Introduction

The invention of atomic force microscopy (AFM) [1] put at disposal of the scientific community an experimental setup in which a nanometer sized tip can be maintained either in contact with a sample surface with controlled force or in close proximity of the surface with controlled distance, the tip location on the surface can be

D. Passeri (✉) · L. Angeloni · M. Rossi
Department of Basic and Applied Sciences for Engineering,
Sapienza University of Rome, Via A. Scarpa 16, 00161 Rome, Italy
e-mail: daniele.passeri@uniroma1.it

L. Angeloni
e-mail: livia.angeloni@uniroma1.it

M. Rossi
e-mail: marco.rossi@uniroma1.it

D. Passeri · M. Rossi
Research Center for Nanotechnology Applied to Engineering of SAPIENZA University of Rome (CNIS), Piazzale A. Moro 5, 00185 Rome, Italy

D. Peddis et al. (eds.), *New Trends in Nanoparticle Magnetism*,
Springer Series in Materials Science 308,
https://doi.org/10.1007/978-3-030-60473-8_12

controlled using accurate positioning systems, and the tip can be used to scan the sample surface in order to image it reconstructing its morphology with nanometer lateral resolution. The availability of such nanocharacterization platforms has stimulated the development of several AFM-based methods for the qualitative and quantitative investigation—both single-point measurements at selected location and mapping on a surface simultaneously to the topographical reconstruction—of different physical properties, e.g., magnetic, electric, mechanical, and thermal [2]. Indeed, while microscopy techniques based on the interaction between the matter and an electromagnetic radiation (e.g., optical, electron, or X-ray microscopy) can image the sample by 'seeing' its surface, the sample morphology is reconstructed with AFM by 'touching' the surface with the tip. Therefore, the tip can be used as a probe to measure a physical signal originating from a nanosized volume of material. Depending on the specific physical properties to be characterized, AFM-based techniques can use standard AFM tips can be used or require *ad hoc* realized probes, e.g., standard tips coated with conductive or magnetic layers. Among the latter techniques, magnetic force microscopy (MFM) is an AFM-based technique proposed in the the late 1980s [3–6] which enables one to image magnetic domains of a sample using a magnetic tip, i.e., a tip coated with a layer of magnetic material such as Co or Fe. MFM has been originally employed to study recording media [7, 8], allowing one to clearly and easily visualize their magnetic domains. Also, comprehensive analytical models have been developed to describe the interaction between the MFM tip and periodically patterned magnetic materials [9] and the pretty good qualitative and quantitative agreement with MFM data confirmed this technique as a powerful method to study magnetic recording media [10–12]. With the advent of nanotechnology, MFM has been quite naturally proposed for the characterization of magnetic nanoparticles (NPs) and other nanomaterials [13]. Indeed, MFM has been considered the par excellence technique for magnetic characterization of nanosized magnetic materials due to its lateral resolution, imaging capability and the need for a relatively simple and widespread experimental setup, i.e., a standard AFM apparatus with slight modifications to feature MFM facility, now routinely included in standard AFM setups. Nevertheless, more recently the awareness of some limitations in the use of MFM to study magnetic nanomaterials has been gaining a foothold in the MFM users community. Among these limitations, in particular the presence of nonmagnetic artifacts in MFM images may lead to misinterpretation of experimental data and severely hamper the use of MFM as an accurate quantitative tool for magnetic characterizations of materials at the nanoscale.

In this chapter, we review some applications of MFM in the study of magnetic NPs and magnetic nanomaterials, in particular focusing on current trends, perspectives, expected innovations, and highlighting the challenges to be taken up and present limitations to overcome.

12.2 Magnetic Force Microscopy

MFM experimental setups are based on a standard AFM apparatus equipped with a magnetic tip interacting with the sample through long-range magnetic forces. Some different MFM experimental approaches have been proposed to detect low-intensity magnetic fields originated from nanosized samples, e.g., using static or dynamic detection system, employing ferromagnetic or superparamagnetic tips, involving or not the application of an external magnetic field, which can be static and/or alternating.

The most common MFM configuration is based on a two-pass approach, i.e., the sample surface is scanned two times [12]. In the first pass, a line is scanned in tapping mode in order to record the line profile which is used to reconstruct the sample topography. The line profile is eventually used to scan again the same line maintaining the tip at fixed distance from the sample surface, namely the lift height Δz, which allows the tip to be not sensitive to short range interaction forces, but only to long range ones such as electrostatic or magnetic forces. During this second pass, the cantilever is set into oscillation at its first free resonance frequency f_0 (or at a frequency close to f_0) using a bimorph coupled with the cantilever chip. The presence of a static magnetic field uniform along the direction z perpendicular to the sample surface modifies equilibrium position of the cantilever without affecting its oscillation parameters, i.e., the resonance frequency f_0 and the phase shift at resonance with respect to the excitation $\theta_0 = -\pi/2$ [12, 14]. Conversely, if the external magnetic force F is not uniform, the oscillation parameters of the cantilever depend on the gradient F_1 along z of the component along the same direction of the force (F_z), i.e., $F_1 = \partial F_z/\partial z$, in correspondence of the equilibrium point of the cantilever. In particular, the shift in the resonance frequency Δf_0 and in the phase $\Delta\theta$ is given by

$$\Delta f_0 = -\frac{1}{2} f_0 \frac{F_1}{k_c} \tag{12.1}$$

and

$$\Delta\theta = -Q_c \frac{F_1}{k_c}, \tag{12.2}$$

where k_c and Q_c are the cantilever spring constant and the quality factor at the first resonance. Therefore, Δf_0 and $\Delta\theta$ contain information about the magnetic stray field near the sample. Thus, maps of the shift in the phase and/or in the resonance frequency of the cantilever can be acquired which qualitatively and quantitatively reflect the magnetic stray field generated by the sample. In particular, if the MFM tip can be considered as a permanent magnetic dipole and the imaged sample possesses permanent magnetic domains, the maps of $\Delta\theta$ (or Δf_0) provide the direct visualization of the vertical gradient of the component along z of the magnetic stray field H_z generated by the sample. If the sample to be imaged is a magnetic NP, its magnetic domains must be oriented so that an effective force can be experienced by the tip. While some authors reported that the magnetic stray field originated by the

tip can be sufficient to polarize small ferromagnetic or superparamagnetic NPs [15], the application of an external static magnetic field to polarize the NPs undoubtedly leads to improved detection capabilities of MFM [16]. The intensity of the magnetic field, and thus of the tip-sample interaction force, dramatically depends on the tip-sample distance. Thus, the use of lift mode allows the tip to interact with the sample at fixed distance Δz, which is constant on the scanned surface, and avoids the tip to experience variations in the magnetic field caused not by the variation of sample magnetic properties, but by the modulation of the tip-sample distance. Therefore, lift mode effectively reduces the presence of anomalous contrast in magnetic images due to changes in the tip-sample distance in case of uniform magnetic properties of the sample [17]. Nevertheless, when the length scale of the features of the investigated sample is comparable with that of the AFM tip, which typically occurs when NPs are analyzed, even in lift mode variation in the local value of the tip-sample capacitance C_{ts} are observed [18]. If a nonzero voltage V_{ts} is present between the tip and the sample, the existence of a tip-sample capacitance which depends on the tip-sample distance results in an electrostatic force acting on the tip which is given by [19]

$$F = \frac{1}{2}\frac{\partial C_{ts}}{\partial z} V_{ts}^2 \ . \tag{12.3}$$

This additional force, which varies on the surface, affects the contrast in second-pass phase or frequency shift maps, resulting in the presence of topography-induced electrostatic artifacts in magnetic images [20, 21]. In order to compensate such spurious signals to obtain accurate quantitative nanomagnetic characterizations using MFM, different approaches have been proposed. For instance, Jaafar et al. [21] demonstrated the effectiveness of the combination of MFM with Kelvin probe force microscopy (KPFM), in which KPFM is used to maintain $V_{ts} = 0$ at each point during the MFM imaging, thus nullify the tip-sample electrostatic force. Also, Angeloni et al. [15, 22] proposed the MFM with controlled magnetization of the tip (CM-MFM), in which the same surface is scanned twice, first in standard MFM and then with the tip demagnetized in order to acquire the electrostatic contribution which is eventually subtracted from the MFM image.

Other approach have been developed to enhance the nanocharacterization capabilities of MFM. In particular, while standard MFM is sensitive to static magnetic fields, in recent years frequency modulated MFM (FM-MFM), also referred to as ac field modulated MFM, has been developed to study the response of magnetic NPs to oscillating magnetic fields [23]. In FM-MFM, during the second pass the cantilever is set into oscillation at a frequency f_c close to its free resonance frequency f_0, which is generally has high as a few hundreds of kilohertz. In addition to the static magnetic field, applied by an external magnet and/or generated by the magnetic sample, an oscillating magnetic field at frequency f_m generally ranging from hundreds of hertz to a few kilohertz is applied to the system. As a result, two sideband peaks at frequencies $f_c \pm f_m$ appear in the spectrum of the cantilever oscillation. If a hard magnetic tip is used, the amplitude of the sideband peaks is proportional to the vertical gradient of the vertical component of the ac magnetic field, i.e., to $\partial H_z^{ac}/\partial z$ [24]. Conversely,

if a soft magnetic tip is used and the vertical component of the ac magnetic field ∂H_z^{ac} is spatially homogeneous, the amplitude of the cantilever oscillation at $f_c \pm f_m$ is proportional to the gradient along z of the vertical component of the dc magnetic field, i.e., to $\partial H_z^{dc}/\partial z$ [24]. Therefore, depending on the magnetic properties of the tip, FM-MFM can be used to detect static or dynamic magnetic fields. Notably, FM-MFM has been demonstrated to minimize the presence of artifacts in the magnetic images due to topographical crosstalk [25].

In the previously described methods, the cantilever is set into oscillation along the vertical z axis. This, combined with the orientation of the magnetization of the tip which is generally along the z axis, makes the techniques sensitive to the vertical component of the magnetic stray field generated by the sample. Really, MFM tips can be magnetized along one in-plane direction and in this case the vertical oscillation of the cantilever is affected by the in-plane direction of the sample magnetic field [12, 26]. A more effective method to probe horizontal magnetic fields is represented by torsional resonance MFM (TR-MFM). In TR-MFM the first torsional resonance is excited in order to set the cantilever into oscillation at the first torsional resonance $f_{0,TR}$ along the scan direction, i.e., the y axis [27]. In presence of a magnetic field with a component along the y axis, a shift of the torsional resonance frequency $\Delta f_{0,TR}$ is observed which is given by

$$\Delta f_{0,TR} = -\frac{1}{2k_{TR}} f_{0,TR} \frac{\partial F_y}{\partial y}, \tag{12.4}$$

where k_{TR} is the torsional spring constant of the cantilever, F_y is the component of the tip-sample interaction force along the y axis and $\partial F_y/\partial y$ is its gradient along the y axis. Notably, TR-MFM is free from topographical artifacts which originate from the tip-sample electrostatic force along z [27].

12.3 Magnetic Force Microscopy and Magnetic Nanoparticles

12.3.1 Quantitative Nanomagnetic Characterization

The constantly growing interest for the use of magnetic NPs in many different scientific and technological fields has increased the demand for NPs with optimized performances. This, in turns, requires the availability of methods capable to characterize magnetic properties of NPs at the nanometer scale and to relate them to 'tunable' physical parameters, e.g., size or shape, in order to tailor them for specific applications. Really, several methods for the characterization of magnetic properties of ensembles of NPs are available, e.g., vibrating sample magnetometry (VSM) [29], superconducting quantum interference devices (SQUID) [30], or alternating gradient field magnetometry (AGFM) [31]. These methods are well-established and

standardized and allow one to accurately quantify magnetic properties of materials, i.e., to acquire their characteristic magnetization curve and to evaluate magnetic parameters like saturation magnetization M_s and coercivity H_c. Due to their sensitivity, however, these techniques allow the analysis of samples containing a significant number of NPs and thus the measured magnetic characteristics are averaged on the whole ensemble of NPs. This approach is obviously effective in those cases in which 'macroscopic' amounts of NPs are needed for specific applications and their average magnetic properties have to be characterized. Conversely, the possibility of retrieving only average magnetic properties may represent a severe limitation when their dependence on physical parameters of the NPs are investigated, e.g., to obtain a more comprehensive knowledge of magnetisms at the nanometer scale and to design and optimize innovative magnetic nanomaterials. Indeed, the capability to relate the obtained results to specific physical parameters of the NPs dramatically depends on the homogeneity of the NPs in the analyzed sample. Therefore, the scientific and technological research in the field of characterization methods in nanomagnetisms has been recently focused on the development of techniques capable to analyze magnetic properties of nanomaterials combining satisfying accuracy and sensitivity with high spatial resolution. Ideally, these techniques should replicate the performances of standardized methods on individual nanomaterials, which should be visualized, selected and probed with nanometer scale spatial resolution. Different methods specifically developed to this purposed have been proposed by miniaturizing standard techniques, e.g., in the case micro and nano-SQUID [32–35]. In these methods, however, a certain limitation may be related to the actual sensitivity an to the capability to select the sample to be investigated. Methods have been also developed based on beam microscopy (e.g., electron or X-ray) approaches, such as off-axis electron holography [36, 37], differential phase contrast mode (DPC) [38], X-ray holography [39], transmission X-ray microscopy [40–42], X-ray photoemission electron microscopy (XPEEM) [43, 44]. Overall and with the due distinctions, the performances of these methods in terms of sensitivity and capability to image and select the single nanomaterial to probe undoubtedly represent significant advantages. However, some limitations may be related to the required characterization environment, e.g., vacuum or low temperature, to the sample preparation as well as to the relative complexity of the experimental setups. Combining high resolution imaging capabilities, possibility of probing a selected location on the sample with nanometer lateral resolution, flexibility of characterization conditions (e.g., air as well as in liquid, inert gas, vacuum and at room or low temperature), simplicity of sample preparation, scanning probe microscopy (SPM) has been used as a platform to develop advanced and very effective methods for magnetic characterization at the nanoscale, such as MFM, magneto-optical scanning near field optical microscopy [45] or scanning magnetometry with nitrogen-vacancy color centers in diamond [46–49]. Among them, standard MFM and advanced MFM-based methods are undoubtedly the most widespread techniques due to relative popularity of AFM setups, in which MFM is generally featured or can be easily included. While MFM has been widely used to qualitatively image magnetic NPs, one of the most intriguing possibilities offered by

MFM is the quantitative determination of magnetic parameters of isolated NPs by analyzing MFM images, which however has been only rarely reported.

In particular, the magnetic moment m_{NP} of a single NP can be evaluated from $\Delta\theta$ or Δf measured in correspondence of the center of the NP as a function of the lift height Δz. To this purpose, a suitable model to describe the tip-sample interaction must be assumed. The NP is generally described as a sphere uniformly magnetized, possibly with a core-shell structure a magnetic dipole with moment m_{NP}, different models have been assumed to describe the tip. For instance, Angeloni et al. [28] obtained m_{NP} of Fe_3O_4 NPs with diameter in the range 18–32 nm describing the tip as a single dipole with moment m_{tip} which was previously calibrated. Passeri et al. [50] analyzed the moment of the magnetic core 11 nm sized magnetoferritin explicitly considering the magnetic coating of the tip and describing the latter as a uniformly magnetized hemispherical shell. A more comprehensive model has been introduced by Schreiber et al. [16] who developed a model including the hemispherical apex and the side surface of the cone-shaped tip and used it to evaluated m_{NP} of iron oxide NPs in the range 5–35 nm. Other authors proposed different models, e.g., Haberle et al. [51] who described the probe as the magnetized surface of a cone using pseudo-pole model validating the model 18 nm sized Co NPs on a Si substrate covered by 23 nm thick silicon oxide layer. Also, Raşa et al. proposed a uniformly magnetized ideally conical surface or a truncated conical one [52]. In an interesting work, Sievers et al. [53] proposed an experimental procedure to phenomenologically calibrate the magnetic moment of the tip without any assumption about its actual shape by using a magnetic NPs traceable reference material, and used this approach to evaluate the magnetic moment of magnetic NPs with diameter of about 17 nm. In addition to the description of the tip, when the NP magnetization M_{NP} must be evaluated, the actual shape of the NPs must be described with a suitable model, the simplest one being a uniformly magnetized perfect sphere [28].

In addition to the need for sufficiently comprehensive models, the quantification/deletion of tip-sample electrostatic artifacts is fundamental for the accurate determination of magnetic parameters of the investigated NPs. Really, when magnetic NPs deposited on flat substrates are analyzed, which is the common experimental configuration in the analysis of NPs using MFM, nonmagnetic artifacts in standard MFM images may be comparable to pure magnetic signals and their presence may lead to results difficult to rationalize [18]. Therefore, methods capable to decouple nonmagnetic artifacts should be preferred to standard MFM. For instance, Angeloni et al. [28] used CM-MFM for the determination of the magnetic moment of Fe_3O_4 NPs with diameter in the range 18–32 nm. Moreover, Li et al. [25] recently demonstrated the high sensitivity and accuracy of FM-MFM by measuring the magnetic moment of individual Fe_3O_4 NPs with diameter of about 14 nm.

Magnetic moment is undoubtedly the magnetic parameter of NPs more often investigated using MFM and related techniques, also due to the fact that the experimental configuration is relatively simple as the measurement is generally performed applying either no external static magnetic field or a single value of external magnetic field to maintain the magnetization of the NPs. Nevertheless, by varying the intensity and the direction of the external applied static magnetic field, complete magnetization

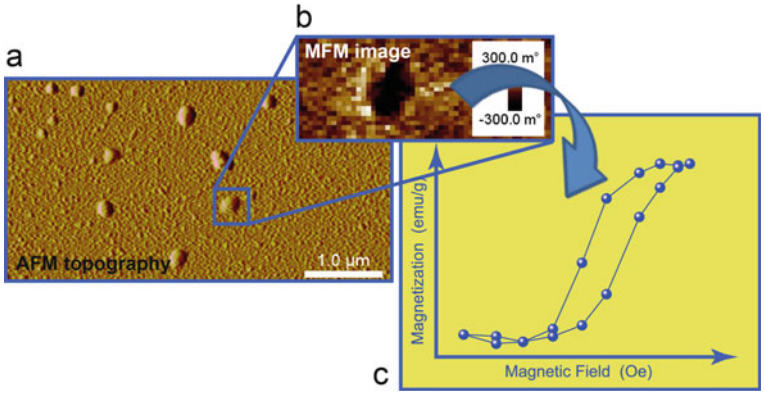

Fig. 12.1 Sketch of the working principle of reconstruction of magnetization curves of single NPs using MFM. **a** The NP to be investigated is selected in the AFM topographical image. **b** MFM phase images of the NP are acquired in correspondence of different values of the applied external magnetic field. **c** Values of phase contrast in MFM images are used to reconstruct the magnetization curve of the selected NP. Adapted from [28] by permission of The Royal Society of Chemistry

curves ca be obtained. Jaafar et al. [54] acquired the magnetization hysteresis curves of Co nanostripes using KPFM-MFM, also discriminating the domain configuration of the nanostructures, i.e., multi- or single-domain. Angeloni et al. [28] obtained magnetization curves of single magnetite NPs deposited on a flat Si substrate. The NPs to be analyzed are selected in the AFM topographical image (Fig. 12.1a), MFM phase images (an example of which is shown in 12.1b) are acquired at different values of the external static magnetic field. After subtraction of electrostatic artifacts and calibration of the MFM probe, the values of the contrast in magnetic phase images are converted into those of the magnetization, thus allowing one to reconstruct the magnetization curve of each single NP Fig. 12.1c). NPs with diameter ranging 18 nm 32 nm were analyzed, experimentally determining the coercivity H_c of individual NP, thus appreciating the transition from ferromagnetic to superparamagnetic behavior [28].

Although only a few studies have been reported, MFM-based techniques have shown an encouraging potential for the acquisition of quantitative magnetization curves of isolated NPs. However, some practical issues should be addressed when broadening their applications. The actual sensitivity of the techniques obviously affects the lower limit in the detectable magnetic moment (i.e., in the diameter for a given material) of the NPs. Conversely, the upper limit is affected, among other experimental parameters, by the tip coercivity. Indeed, the acquisition of NPs magnetization curves require the variation of the external magnetic field to change intensity and direction of the magnetization of the NP when the tip magnetization is constant. In case of tip with low coercivity, the magnetization of the tip itself is modified, thus affecting the accuracy of the reconstruction of the NPs magnetization curves.

The magnetic structure of NPs can be also investigated using MFM-based techniques. For instance, Moya et al. used KPFM-MFM to distinguish between ferromagnetic and superparamagnetic nature of NPs in aggregates [55] as well as study the polarity and reversal mechanism in single magnetic NPs [56].

Finally, other examples of applications of MFM-based techniques for the quantitative evaluation of physical parameters of NPs have been proposed. One of these applications is in the analysis of core-shell magnetic NPs, which are characterized by a magnetic (e.g., superparamagnetic) core and a nonmagnetic shell (e.g., gold) and have been proposed for different applications, e.g., in biomedicine to improve biocompatibility or to enhance cell internalization [57]. The determination of the diameter of the magnetic core and of the thickness of the nonmagnetic shell is fundamental in the design of these nanosystems and can be currently addressed for instance using transmission electron microscopy (TEM). Angeloni et al. [58] have recently reported preliminary results demonstrating the use of CM-MFM for the evaluation of core and shell dimensions on individual NPs. Also, using a phenomenological calibration Dong et al. [59] attempted to evaluate the diameter of magnetic NPs embedded into vesicular systems which are studied for applications in drug delivery. Recently, Krivcov at al. [60] demonstrated the capability to indirectly measure size of magnetite NPs with diameter ranging 10 nm 100 nm embedded in polymer films.

In conclusion, some issues require to be carefully addressed, such as the deletion of nonmagnetic artifacts, the development of comprehensive models and reliable experimental methodologies, as well as the need for a certain automatism to allow the characterization of a statistically significant number of NPs of the investigated sample with accurate but not too time-consuming procedures. Nonetheless, MFM-based techniques have demonstrated a great potential for the nondestructive quantitative characterization of magnetic properties at the nanoscale, which makes them a promising metrological tool for magnetic NPs not only in air and at room conditions, but also in liquid [61] or at low temperature [62].

12.3.2 Detection of Magnetic Nanoparticles in Nano-systems

Magnetic NPs have been proposed for a great number of scientific and technological applications. For instance, in the field of nano-bio-medicine they have been proposed in applications which can be summarized as theranostic applications, i.e., in which selected and functionalized nanomaterials are used as diagnostic materials, drug delivery vectors, in situ treatment tools, and instrument for the monitoring of the effectiveness of the treatment. For instance, magnetic NPs have been proposed in magnetic resonance imaging as nanomaterial-base contrast agents [64], in situ cancer treatments using hyperthermia [65], or for actively conveying drug delivery systems through the application of an external magnetic field [50, 66]. Also, magnetic nanocomposites based on the incorporation of magnetic NPs into polymeric matrices has been proposed for the realization of biocompatible microdevices, e.g., for drug release controlled by an external magnetic field. The common denomina-

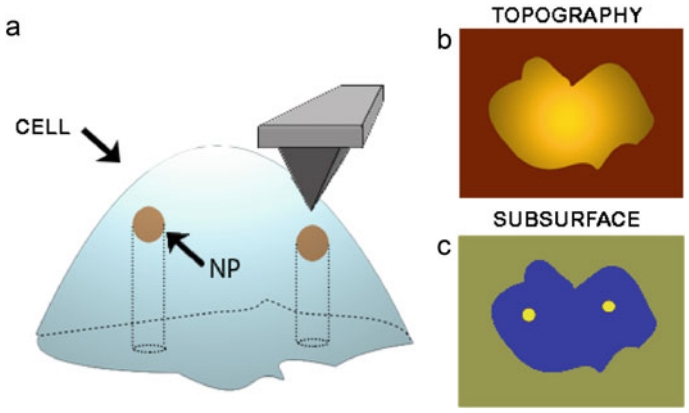

Fig. 12.2 Sketch of the working principle of MFM detection of buried magnetic NPs (e.g., in cells). **a** The magnetic MFM tip is sensitive to magnetic properties of the sample. Therefore, simultaneously to the topography (**b**), a map of the magnetic properties (**c**) is reconstructed in which subsurface magnetic NPs are visible. Reproduced from [63] by permission of John Wiley and Sons

tor of all these applications is that magnetic NPs are embedded into nonmagnetic matrices (e.g., niosomes, tissues, cells) either purposely or as the result of the interaction with a biological system. Thus, the development and the optimization of these nano-bio-systems requires the capability to detect the presence of magnetic NPs in different nonmagnetic matrices. Different techniques can be used, including fluorescence microscopy, scanning or transmission electron microscopy, or optical methods like two-photon microscopy. Besides their specific advantages in terms for instance of resolution or detection limits, these have some drawbacks among which the sample preparation requirements (e.g., NPs labeling and/or sample fixing and slicing). Being sensitive to long-range magnetic forces, MFM ca be used to detect magnetic NPs embedded in nonmagnetic matrices. Indeed, while AFM topography is not affected by buried magnetic NPs, their presence is observed in MFM images, where the nonmagnetic host matrix ideally does not give any signal, as sketched in Fig. 12.2. The requirement of no time consuming or destructive sample preparation, the possibility of analyzing the sample both in air and in liquid, and the high lateral resolution undoubtedly make MFM highly attractive for the detection of magnetic NPs in these systems. However, some drawbacks have to faced such as the limitation in the sensitivity, which may limit the minimum size and and maximum depth of detectable NPs, and the presence of electrostatic artifacts, which may conceal the signal from magnetic NPs.

12.3.2.1 Magnetic Nanocomposite

Magnetic nanocomposites, e.g., materials in which magnetic NPs are embedded in a nonmagnetic (e.g., polymeric) matrix, are a class of advanced materials recently

proposed, for instance, for the development of stimuli-responsive systems for application in biocompatible devices for the controlled release of drugs [67].

The detection of magnetite NPs with diameter ranging 10 nm 100 nm embedded in polymer films using MFM was demonstrated by Krivcov et al. [60]. In particular, while bigger NPs with diameter 80 nm could be detected under about 300 nm thick polymer layer, superparamagnetic NPs with diameter of 10 nm and 20 nm could be detected under polymer layers of 40 nm and 130 nm, respectively [60]. Slabu et al. [68] reported the use of MFM to detect superparamagnetic iron oxide NPs containing both magnetite and maghemite on the surface and into polyvinylidene fluoride (PVDF) based fibers. Alosmanov et al. [69] used MFM to study magnetic nanocomposites containing iron oxide nanoparticles formed in situ within a phosphorus-containing polymer matrix. Silva et al. [70] used iron-doped bismuth sulphide nanocrystals embedded in glass matrix. Marín et al. used MFM to detect magnetite NPs embedded in gelatin [71] or zein [67] based stimuli responsive films to control drug release triggered by the application of an external magnetic field. Arredondo et al. [72] recently proposed a method for the evaluation of enzyme activity, in which MFM images are used to real time monitor the degradation of enzyme responsive layer constituted by gelatin films loaded with magnetite NPs.

Among the different class of magnetic nanocomposites, vesicular systems loaded with magnetic NPs attract growing interest for their potential applications in theranostics. Passeri et al. [50] demonstrated the capability of MFM to distinguish between empty niosomes and niosomes encapsulating magnetic NPs. Dong et al. [59] attempted the determination of the diameter of magnetic NPs from MFM images using a phenomenological calibration procedure.

12.3.2.2 Nanoparticle Detection in Cells and Tissues

MFM has been also proposed as a diagnostic tool in biology and nanomedicine, i.e., as a nanoprobe for the detection of magnetic NPs in biological systems such as cells or tissues.

Taking advantage of its high spatial resolution and sensitivity, which allows one to detect a single magnetic NP, MFM has been demonstrated capable to probe the presence of ferritin by sensing its nanometer sized iron core [73]. In this field, they are worth mentioning the extensive and thorough studies by Agarwal and coworkers, who demonstrated the unique capability of MFM as a diagnostic tool to detect and evaluate the presence of ferritin in biological samples. First Nocera et al. [74] used MFM to distinguish ferritin from apoferritin, on the basis of the absence of the iron core in the latter, and to quantitatively evaluate the amount of ferritin in a sample. Then, Blissett et al. used MFM to evaluate the presence of ferritin in animal tissues, i.e., in spinal cord [75] or spleen [76].

Different works have been reported in which MFM is used to detect magnetic NPs on the surface as well as inside cells. In a first study, Shen et al. [77] detected silica-coated magnetic iron NPs coupled with antisense oligonucleotide in human leukemia (HL-60) cells. Wang and Cuschieri [78] successfully labeled human cancer

cells using magnetic NPs and determined the content and spatial distribution of intracellular iron. Passeri et al. [50] reported the labeling of leukemic cells using folic acid-coated core-shell superparamagnetic NPs in order to detect the presence of folate receptors on the surface of the cell membrane using MFM. MFM was also used by Reggente el at. [79] to confirm the presence of magnetite NPs internalized in microglial cells from mice cerebral cortices. Recently, Kim et al. [80] reported the used of MFM to analyze two breast cancer cell lines, MCF-7 and SK-BR-3, targeted with antibody conjugated magnetic NPs and demonstrated the capability of their MFM method to subtype cancer cells.

12.3.3 Manipulation

As previously discussed, since its invention, MFM has found larger and larger application in the world of magnetic micro- and nanomaterials as a powerful qualitative and, more recently, quantitative magnetic characterization technique. Nevertheless, the capability of applying and detecting magnetic forces at the nanoscale make MFM a powerful tool potentially applicable, not only for magnetic measurements, but also for magnetic and mechanical manipulation.

12.3.3.1 Magnetic Manipulation by MFM

While scanning the sample of interest, the magnetized MFM probe with its magnetic stray field can induce significant changes in the magnetization state of the sample, especially in case of soft magnetic materials (i.e., $H_c < H_{\text{tip}}$ where H_c is the coercivity of the sample and H_{tip} is the magnetic field generated by the tip). In case of multidomain ferromagnetic materials, slight changes in the configuration of the domains structure can be observed, while soft magnetic nanomaterials, e.g., single-domain ferro- and superpara-magnetic nanoparticles, could even exhibit a complete reversal of the magnetic moment [81–83]. When MFM technique needs to be used for the imaging of the magnetization state or for the quantitative measurement of the magnetic properties of the sample in certain conditions, this phenomenon is a negative effect which has to be quantified and carefully taken into account. Nevertheless, the same phenomenon can be positively used for active, controlled magnetic manipulation of nanofeatures and exploited, for example, for writing and reading nanostructured magnetic logic devices. The possibility of using the MFM tip to locally write a magnetic bit in patterned magnetic disks has been demonstrated for the first time in 90's, i.e., at the beginning of the application of MFM technique for recording industry [84, 85], but has never been fully exploited. The prerequisite for the writing process is that the effective tip stray field (H_{tip}) must be larger than the switching field of the particle (H_c) [84], while reading is possible only if the magnetization state of the bit is not varied during the scanning, i.e., if the tip stray field is significantly lower than the coercive field of the particle $H_{\text{tip}} \ll H_c$. In the

first works regarding the use of MFM for writing and reading processes, it has been demonstrated that writing and reading process can be performed using two MFM tips-a writing tip with a large magnetic moment and a reading tip with a very small magnetic moment [84]. Also, a method for recording and erasing using a MFM tip and the help of an external variable magnetic field has been proposed. In this method, writing is performed with the MFM tip into contact with the sample and by applying an external magnetic field parallel to the tip stray field; erasing is performed at a large tip-sample separation, while applying an external field antiparallel to the tip stray field [85]. The application of recent advances in the development of MFM technique could allow the complete exploiting of MFM as a magnetic manipulation method. As an example, a possible way to perform reading and writing processes has been more recently proposed. A suitable MFM can be used to read the magnetic-moment states of a particle at a large tip-particle separation, while it can be used for writing at a smaller tip-sample separation, exploiting its higher magnetic stray field. This method has been demonstrated to be effective for the control of the magnetic moment state of a single particle [86] and could be applied for writing input to magnetic logic devices. Furthermore, the recently developed capability of in situ controlling the magnetization state of the MFM probe by CM-MFM technique could be also applied [15] for magnetic manipulation purposes. Indeed, the writing process could be performed by using a strongly magnetized probe, e.g. in its saturation magnetization state. Then, the magnetic moment (and the corresponding stray field) of the probe could be opportunely decrease for reading by applying to the probe an appropriate 'demagnetizing' magnetic field. Recent developments in AFM instrumentation make the technique potentially scalable. Indeed, the operation of more than a thousand atomic force microscopes in parallel has recently been demonstrated [87].

12.3.3.2 Mechanical Manipulation by MFM

The growing interest in fabrication of nanostructures in several technology fields push researchers to look for new advanced fabrication methods with control and resolution at the nanometer scale. Beside imaging and physical characterization, SPM techniques, have started to be used also for nanofabrication and mechanical manipulation purposes, exploiting the high resolution and low forces control capabilities. As an example, local deposition of material has been obtained by using a scanning tunneling microscopy (STM) tip [88–90]. Mechanical manipulation of nanostructures is getting increasing interest in nanopattern fabrication and has been demonstrated to be doable by using a standard AFM probe, which can be used to push or slide with controllable force the nanostructures of interest [91, 92]. The magnetic stray field of the probe and the high resolution of MFM technique could be also used for mechanical entrapment and manipulation of magnetic nanostructures for nanofabrication purposes. Recently, Liu et al. [93] designed a helical capture path to precisely manipulate magnetic (paramagnetic and superparamagnetic) nanoparticles by a magnetized probe. The authors demonstrated the capability of MFM technique to pick up and remove from the surfaces nanoparticles with diameters in the range

of 10–200 nm [93]. The releasing and precise positioning of the grabbed nanoparticles has not been shown, yet. Nevertheless, the in situ demagnetization of the probe could allow the release of the NP in a determined position on the surface. CM-MFM [15] technique, thanks to its capability of in situ magnetizing and demagnetizing the probe could be applied to vary the magnetization state of the probe and allow the entrapment, the positioning and the release of the single nanoparticles and, in line of principle, used for magnetic nanopatterns fabrication.

12.4 Conclusions, Perspectives and Challenges

Due to its lateral resolution, sensitivity, imaging capability, the need for a relatively simple and widespread experimental setup, minimal/no specific requirements about sample preparations, capability to operate in air at room conditions as well as in vacuum or liquid environment, MFM can be considered one of the most effective and versatile techniques for the characterization of magnetic NPs. In particular, the potential of MFM for the quantitative characterization of magnetic properties of single magnetic NPs and, more in general, of nanomaterials, at the nanometer scale has been widely demonstrated. Also, being sensitive to long-range magnetic forces, MFM can be used to detect single magnetic NPs in nonmagnetic (e.g., biological) matrices allowing the characterization of magnetic nanocomposites. Also, MFM can be used as a tool to assess the presence of ferritin in biological tissues and to analyze cells labeled with functionalized magnetic NPs. Finally, not only can MFM be used as an imaging tool, but it can be used to modify the morphology and the magnetic state of magnetic NPs via mechanical or magnetic nanomanipulation. Despite its promising performances and encouraging results, however, several issues must be addressed such as: the enhancement of the sensitivity by developing improved MFM probes; the removal of nonmagnetic artifacts in MFM signal; the definition and improvement of lateral and vertical resolution; the comprehensive modeling of tip-sample interaction. Addressing these metrological aspects would result in a great improvement significance of MFM in the study of magnetic NPs, paving the way to the validation of truly accurate, sensitive and reliable MFM-based nanomagnetic characterization tools of magnetic NPs and, possibly, towards the development of MFM-based tomographic methods for the analysis of magnetic NPs in magnetic nanocomposites.

References

1. G. Binnig, C.F. Quate, C. Gerber, Phys. Rev. Lett. **56**, 930 (1986)
2. J. Zhong, J. Yan, RSC Adv. **6**, 1103 (2016)
3. Y. Martin, H.K. Wickramasinghe, Appl. Phys. Lett. **50**, 1455 (1987)
4. Y. Martin, C.C. Williams, H.K. Wickramasinghe, J. Appl. Phys. **61**, 4723 (1987)
5. J.J. Sáenz et al., J. Appl. Phys. **62**, 4293 (1987)

6. J.J. Sáenz, N. García, J.C. Sloczewski, Appl. Phys. Lett. **53**, 1449 (1988)
7. D.W. Abraham, C.C. Williams, H.K. Wickramasinghe, Appl. Phys. Lett. **53**, 1446 (1988)
8. A. Wadas, P. Grütter, H.J. Güntherodt, J. Appl. Phys. **67**, 3462 (1990)
9. I.G. Hughes, P.A. Barton, T.M. Roach, E.A. Hinds, J. Phys. B: At. Mol. Opt. Phys. **30**, 2119 (1997)
10. D. Rugar et al., J. Appl. Phys. **68**, 1169 (1990)
11. S. Porthun, L. Abelmann, C. Lodder, J. Magn. Magn. Mater. **182**, 238 (1998)
12. D. Passeri, L. Angeloni, M. Reggente, M. Rossi, Magnetic force microscopy, in *Magnetic Characterization Techniques for Nanomaterials*, ed. by C.S.S.R. Kumar, chapter 7, (Springer, Berlin Heidelberg, 2017), pp. 209–259
13. G. Agarwal, *Nanotechnologies for the Life Sciences* (2012)
14. D. Sarid, *Scanning Force Microscopy* (Oxford University Press, New York, 1994)
15. L. Angeloni, D. Passeri, M. Reggente, D. Mantovani, M. Rossi, Sci. Rep. **6**, 26293 (2016)
16. S. Schreiber et al., Small **4**, 270 (2008)
17. D. Passeri et al., Ultramicroscopy **136**, 96 (2014)
18. L. Angeloni et al., AIP Conf. Proc. **1667**, 020010 (2015)
19. P. Girard, Nanotechnology **12**, 485 (2001)
20. C.S. Neves et al., Nanotechnology **21**, 305706 (2010)
21. M. Jaafar et al., Beilstein J. Nanotechnol. **2**, 552 (2011)
22. L. Angeloni et al., AIP Conf. Proc. **1873**, 020008 (2017)
23. H. Saito, H. Ikeya, G. Egawa, S. Ishio, S. Yoshimura, J. Appl. Phys. **105**, 07D524 (2009)
24. H. Saito, R. Ito, G. Egawa, Z. Li, S. Yoshimura, J. Appl. Phys. **109**, 07E330 (2011)
25. Q. Li et al., Sci. Rep. **7**, 9894 (2017)
26. M. Jaafar, A. Asenjo, M. Vazquez, IEEE T. Nanotechnol. **7**, 245 (2008)
27. A. Kaidatzis, J.M. García-Martín, Nanotechnology **24**, 165704 (2013)
28. L. Angeloni et al., Nanoscale **9**, 18000 (2017)
29. J. Hu, I.M.C. Lo, G. Chen, Sep. Purif. Technol. **56**, 249 (2007)
30. M.M. Saari et al., J. Appl. Phys. **117**, 17B321 (2015)
31. A.L. Urbano-Bojorge et al., J. Nano Res. **31**, 129 (2015)
32. S.K.H. Lam, Supercond. Sci. Technol. **19**, 963 (2006)
33. S.K.H. Lam, W. Yang, H.T.R. Wiogo, C.P. Foley, Nanotechnology **19**, 285303 (2008)
34. C. Granata, E. Esposito, A. Vettoliere, L. Petti, M. Russo, Nanotechnology **19**, 275501 (2008)
35. L. Hao, D. Cox, P. See, J. Gallop, O. Kazakova, J. Phys. D Appl. Phys. **43**, 474004 (2010)
36. J.M. Thomas, E.T. Simpson, T. Kasama, R.E. Dunin-Borkowski, Acc. Chem. Res. **41**, 665 (2008)
37. E. Snoeck et al., Nano Lett. **8**, 4293 (2008)
38. T. Uhlig, J. Zweck, Ultramicroscopy **99**, 137 (2004)
39. S. Eisebitt et al., Nature **432**, 885 (2004)
40. E. Amaladass, B. Ludescher, G. Schütz, T. Tyliszczak, T. Eimüller, Appl. Phys. Lett. **91**, 172514 (2007)
41. P. Fischer et al., Rev. Sci. Instrum. **72**, 2322 (2001)
42. D.-H. Kim et al., J. Appl. Phys. **99**, 08H303 (2006)
43. F. Kronast et al., Nano Lett. **11**, 1710 (2011)
44. O. Sandig et al., J. Electron Spectrosc. Relat. Phenom. **185**, 365 (2012)
45. J. Schoenmaker et al., J. Appl. Phys. **98**, 086108 (2005)
46. C.L. Degen, Appl. Phys. Lett. **92**, 243111 (2008)
47. L.T. Hall, J.H. Cole, C.D. Hill, L.C.L. Hollenberg, Phys. Rev. Lett. **103**, 220802 (2009)
48. L. Rondin et al., Appl. Phys. Lett. **100**, 153118 (2012)
49. S. Hong et al., MRS Bull. **38**, 155 (2013)
50. D. Passeri et al., Biomatter **4**, e29507 (2014)
51. T. Häberle et al., New J. Phys. **14**, 043044 (2012)
52. M. Raşa, B.W.M. Kuipers, A.P. Philipse, J. Colloid Interface Sci. **250**, 303 (2002)
53. S. Sievers et al., Small **8**, 2675 (2012)
54. M. Jaafar et al., Nanoscale Res. Lett. **6**, 407 (2011)

55. C. Moya, O. Iglesias-Freire, X. Batlle, A. Labarta, A. Asenjo, Nanoscale **7**, 17764 (2015)
56. C. Moya et al., Nanoscale **7**, 8110 (2015)
57. F. De Angelis, G. Berardi, F.A. Scaramuzzo, M. Liberatore, M. Barteri, Int. J. Nanotechnol. **13**, 659 (2016)
58. L. Angeloni et al., AIP Conf. Proc. **1749**, 020006 (2016)
59. C. Dong et al., AIP Conf. Proc. **1667**, 020011 (2015)
60. A. Krivcov, J. Schneider, T. Junkers, H. Möbius, Phys. Stat. Sol. (a) **2018**, 1800753 (2018)
61. C. Dietz, E.T. Herruzo, J.R. Lozano, R. Garcia, Nanotechnology **22**, 125708 (2011)
62. E. Pinilla-Cienfuegos et al., Part. Part. Syst. Char. **32**, 693 (2015)
63. L. Angeloni, M. Reggente, D. Passeri, M. Natali, M. Rossi, Wiley Interdisciplinary Reviews: Nanomedicine and Nanobiotechnology **10**, e1521 (2018)
64. M. Corti et al., J. Mag. Magn. Mater. **320**, e320 (2008)
65. R.T. Gordon, J.R. Hines, D. Gordon, Med. Hypotheses **5**, 83 (1979)
66. M. Liberatore et al., Clin. Nucl. Med. **40**, e104 (2015)
67. T. Marín, P. Montoya, O. Arnache, R. Pinal, J. Calderón, J. Magn. Magn. Mater. **458**, 355 (2018)
68. I. Slabu et al., J. Phys. D: Appl. Phys. **50**, 315303 (2017)
69. R.M. Alosmanov et al., Nanotechnology **29**, 135708 (2018)
70. R.S. Silva et al., Molecules **22**, 1142 (2017)
71. T. Marín, P. Montoya, O. Arnache, R. Pinal, J. Calderón, Mater. Design **152**, 78 (2018)
72. M. Arredondo, M. Stoytcheva, I. Morales-Reyes, N. Batina, Biotechnol. Biotec. Eq. **32**, 1065 (2018)
73. C.W. Hsieh, B. Zheng, S. Hsieh, Chem. Commun. **46**, 1655 (2010)
74. T.M. Nocera, Y. Zeng, G. Agarwal, Nanotechnology **25**, 461001 (2014)
75. A.R. Blissett et al., Sci. Rep. **8**, 3567 (2018)
76. A.R. Blissett, B. Ollander, B. Penn, D.M. McTigue, G. Agarwal, Nanomedicine **13**, 977 (2017)
77. H.B. Shen et al., Biophys. Chem. **122**, 1 (2006)
78. Z. Wang, A. Cuschieri, Int. J. Mol. Sci. **14**, 9111 (2013)
79. M. Reggente et al., Nanoscale **9**, 5671 (2017)
80. K.-J. Kim, H.-Y. Cho, W.-J. Lee, J.-W. Choi, Biotechnol. J. **13**, 1700625 (2018)
81. X. Zhu et al., J. Appl. Phys. **93**, 8540 (2003)
82. W. Rave, L. Belliard, M. Labrune, A. Thiaville, J. Miltat, IEEE Trans. Magn. **30**, 4473 (1994)
83. T. Göddenhenrich, U. Hartmann, M. Anders, C. Heiden, J. Microsc. **152**, 527 (1988)
84. S.Y. Chou, Proc. IEEE **85**, 652 (1997)
85. O. Watanuki, Y. Sonobe, S. Tsuji, F. Sai, IEEE Trans. Magn. **27**, 5289 (1991)
86. X. Zhu, P. Grütter, MRS Bull. **29**, 457 (2004)
87. M.I. Lutwyche et al., Appl. Phys. Lett. **77**, 3299 (2000)
88. D.M. Kolb, R. Ullmann, T. Will, Science **275**, 1097 (1997)
89. R. Ullmann, T. Will, D.M. Kolb, Chem. Phys. Lett. **209**, 238 (1993)
90. F.P. Zamborini, R.M. Crooks, J. Am. Chem. Soc. **120**, 9700 (1998)
91. S. Hsieh et al., J. Phys. Chem. B **106**, 231 (2002)
92. A.A.G. Requicha, D.J. Arbuckle, B. Mokaberi, J. Yun, Int. J. Robot. Res. **28**, 512 (2009)
93. J. Liu et al., J. Magn. Magn. Mater. **443**, 184 (2017)

Part IV
Advanced Magnetic Nanoparticles Systems for Applications

Chapter 13
Magnetic Nanoparticles for Life Sciences Applications

C. Marquina

Abstract The ongoing research on the applications of magnetic nanoparticles in Bio-medicine and the results obtained up to now open a wide range of possibilities for their use in Life Science disciplines, for example in general plant research and agronomy. The work presented here focuses on the interaction of two types of magnetic core-shell nanoparticles with plants and microorganisms. The research carried out with carbon coated iron nanoparticles aims to investigate their penetration and translocation in whole living plants and into plant cells, as response of the nanoparticles to magnetic field gradients. This study is essential to evaluate the suitability of any nanoparticles as magnetic responsive carriers for the localized delivery of phytosanitary or pest control treatments. The study carried out with silica coated nanoparticles focuses on their interaction with fungal cells, taking a soil borne plant pathogen as in vitro model. Our research paves the way to use magnetic nanoparticles for detection, selective control and eventual elimination of pathogenic fungi.

13.1 Introduction

Life Sciences encompass the study of living organisms, which concerns not only animals (including human beings) but also plants and microorganisms, covering fields of knowledge such as Medicine, Biotechnology, Environmental Sciences, Botany and other branches of Biology, among many others. Research on these subjects has acquired a marked interdisciplinary character which has made it benefit, for example, from the knowledge, materials, devices and tools of Nanoscience and Nanotechnology. An example is the increasingly frequent use of nanoparticles, and in particular, of magnetic nanoparticles, in Biomedicine. Here we will focus on the use

C. Marquina (✉)
Instituto de Nanociencia y Materiales de Aragón (INMA), Consejo Superior de Investigaciones Científicas (CSIC)-Universidad de Zaragoza, Pedro Cerbuna 12, 50009 Zaragoza, Spain
e-mail: clara@unizar.es

Departamento de Física de la Materia Condensada, Facultad de Ciencias, Universidad de Zaragoza, Pedro Cerbuna 12, 50009 Zaragoza, Spain

D. Peddis et al. (eds.), *New Trends in Nanoparticle Magnetism*,
Springer Series in Materials Science 308,
https://doi.org/10.1007/978-3-030-60473-8_13

of magnetic nanoparticles in Life Sciences fields dealing with plants and microorganisms. Although Nanoscience and Nanotechnology are more and more present in areas such as plant research, agriculture and agronomy, and the incorporation to these areas of new strategies and methodologies based on the use of nanoparticles is growing, the particular case of magnetic nanoparticles is still little explored.

One of the first works dealing with nanoparticles in plant research is the one carried out by Torney et al. [1] in which mesoporous silica nanoparticles act as vehicles to transport DNA and chemicals into isolated plant cells and intact leaves. The delivery of DNA by means of mesoporous SiO_2 nanoparticles was studied also by Martín-Ortigosa et al. making use of different strategies for the penetration of the nanoparticles into the plant cell [2–4]. Polymeric nanoparticles [5], fluorescent chromophores [6], ZnO nanoparticles [7], among many others have also been used as carriers for plant cell genetic engineering, one of the most studied applications in plant research. Another topic that has aroused great interest is the study of how nanoparticles can influence the plant growth and germination and the functionality of plant cell organelles. Hong et al. studied effect of TiO_2 nanoparticles on the photochemical reaction of chloroplast of *Spinacia oleracea* [8], and on the growth of spinach plants [9]. Recently, Frazier et al. studied the influence of these nanoparticles on the growth and microRNA expression of tobacco (*Nicotiana tabacum*) [10]. The effect of ZnO nanoparticles on the inhibition of seed germination and root growth was also studied by Lin and coworkers [11, 12]. Efforts have also been focused on enhancing crop yields and controlling/suppressing plant diseases and parasites. With these objectives in mind, studies have been carried out with a variety of nanoparticles (made of polymers, liposomes, 3d-metals and 3d-metal oxides, carbon nanostructures etc.) as reported for example in the works of Perez de Luque et al. [13], Servin and coworkers [14] and Yasmeen et al. [15]. For the control of diseases and pests, the rapid and easy detection of the causative agent is crucial. In this respect, Nanotechnology has provided us with highly sensitive, versatile, inexpensive and user-friendly biosensors [16–19]. Among the different types, nano-devices based on the localized surface plasmon resonance (LSPR) have been developed, for example, for the detection of the maize chlorotic mottle virus in infected maize seeds [20, 21]; or for detecting biomarkers associated with nutritional deficiencies in crops [22]; or to elucidate the effect of a T-DNA insertion on mRNA transcripts in plants [23, 24], among other applications. With regard to microorganisms, the use of micro- and nano-particles as an antibacterial and antifungal agent is widespread. Silver is one of the most frequently used materials [25], working for example against phytopathogenic fungi [26] and bacteria such as *Pseudomonas aeruginosa* and *Staphylococcus aureus* [27]. Recent studies carried out on plant pathogenic fungi, oomycete and bacteria, have shown that copper nanoparticles can enhance the effect of commercial antimicrobial copper formulations and even represent an efficient alternative [28]. Zinc oxide and magnesium oxide nanoparticles have also demonstrated their effectiveness as antimicrobials [29–33].

The significant progress made in Biomedicine derived from the use of magnetic nanoparticles in diagnostic and therapy has opened the doors to their implementation

in the applications just mentioned. In addition, the capability of magnetic nanoparticles to interact with a magnetic field increases the possibilities for their exploitation. For instance, in the same way as nanoparticles can act as vehicles for magnetically targeted drug delivery in chemotherapy against cancer [34, 35] they could be implemented in phytosanitary treatments, for the selective and controlled delivery of agrochemicals or other biomolecules, or to induce genetic transformations etc. [13]. Also in the analogy with biomedical applications, magnetic nanoparticles could play a role as MRI contrast agents for plant research. In fact this technique is as well suitable for studying the health of a plant in a non-destructive way [36], and has made possible the study of the modifications of the biophysical parameters of a cucumber plant as response to environmental changes [37], the changes in the dynamics of the sap flow [38], or the damage induced by plant parasitic nematodes and soil borne pathogens on sugar beet plants [39]. Even the localized heating by magnetic hyperthermia [40] might be as well a useful treatment in agriculture and agronomy. As suggested by Pérez de Luque and Rubiales [13], it might be applied to eliminate parasitic weeds, assuming that nanoparticles are able to accumulate in a specific plant organ. This could be the case, for example, of tubercles in *Orobanche crenata*, where the nanoparticles (administered for example by the roots) would accumulate due to their sink effect.

As is well known, magnetic nanoparticles can be coated with biocompatible materials as silica [41, 42], dextran [43], polyvinyl alcohol (PVA) [44], poly(ethylene glycol) (PEG) [45] etc., which allows modifying the particle surface with a large number of molecules of biological interest, and therefore broadening the functionality of the nanoparticle. The coating can be functionalized with bio-molecules, as for instance antibodies [46, 47], able to recognize a specific pathogen in a culture or soil, making the nanoparticle act as a magnetic label for the pathogen to be detected by a biosensor [17, 18, 48]. The diversity of materials that can be used as coating and the wide variety of functionalization protocols make the magnetic nanoparticles very promising tools for plant biology and biotechnology.

In the following sections we will deal with two types of core-shell magnetic nanoparticles. In the first case, they consist of an iron core coated with graphite/graphene layers; from here on they will be called carbon-coated (Fe@C) nanoparticles. The second type is magnetite coated with silica (i.e., $Fe_3O_4@SiO_2$) nanoparticles; this coating, besides being biocompatible, stable and suitable for the encapsulation of biomolecules, [49] is very easy to be functionalized with biological moieties [46]. Likewise, the biocompatibility of the Fe@C nanoparticles has been successfully tested in in vitro and in vivo animal models [35, 50, 51]. In particular, the experiments carried out in New Zeeland rabbits have shown that these nanoparticles, once injected into the animal, can be located in the desired organ or tissue with the aid of a magnetic field gradient created by an implanted magnet. In addition, it has been shown that the nanoparticle coating can adsorb and desorb a chemotherapeutic agent, so they can be used for magnetically driven drug delivery [35]. These experiments suggest that nanoparticles could also be utilized *in planta*, as magnetic carriers of phytosanitary agents, nutrients, enzymes, nucleic

acids etc. to be concentrated in a specific part or organ of a plant (e.g., where a parasite or infection is located, or where the nutrients are going to be adsorbed in a more effective manner, etc. [52]). An advantage of using the Fe@C and the Fe_3O_4@SiO_2 nanoparticles in these applications is the high specific surface area of the coating, which offers a high load capacity [49, 53]. This could help in the optimization of the dose to be delivered, without the need of repeating the treatment, which would lead to more efficient and sustainable agricultural practices and methods.

In any case, taking these ideas to practice requires, among other issues, the study of the nanoparticle response when a magnetic field gradient is applied to the plant, and the analysis of their transport and distribution *in planta.* The experiments conducted for this purpose are presented in the following sections. They were carried out with Fe@C nanoparticles and different type of crops [52, 54, 55], constituting a pioneering work regarding the use of magnetic nanoparticles in whole alive plants. Next section also reports what, to our knowledge, is the first study on the interaction between magnetic nanoparticles and fungal cells. The final objective was to evaluate the feasibility of new nanotechnology-based strategies for the early detection and control of pathogenic fungi in plants, crops and soils [48]. The final goal was the design of a biosensor combining immunological recognition and magnetic detection [17, 18]. In this case, the study was performed with Fe_3O_4@SiO_2 nanoparticles, given the possibility to functionalize the coating with an antibody that recognized the pathogenic fungus. The target is *Fusarium oxysporum*, a soil borne plant pathogen that infects a vast variety of crops and is the cause of important economic losses [56]. It is also an opportunistic human pathogen and infection can also result in the death of immunocompromised patients [57]. To date there are neither effective methods for an early detection of the fungus, nor treatments for a complete elimination. In the case of *F. oxysporum* the problem is even more complex, because pathogenic strains cohabit in the rhizosphere with nonpathogenic strains, leading to biological control [58]. Therefore, in the present case an adequate functionalization strategy that ensures the high selectivity and sensitivity in the detection prior to the treatment is crucial. In addition, a comprehensive study of the behavior of the fungus in the presence of the nanoparticles, as the one reported here, and a deep knowledge of the toxicity profile of these nanomaterials are also decisive.

13.2 Penetration and Transport of Magnetic Nanoparticles in Living Plants

The aim of this work was to visualize the transport of nanoparticles inside living plants, and also to investigate whether the nanoparticles respond to the application of magnetic field gradients, with the objective of concentrating them in localized areas of the plants by the use of small magnets. As mentioned before, the work described from here on was carried out with whole living plants.

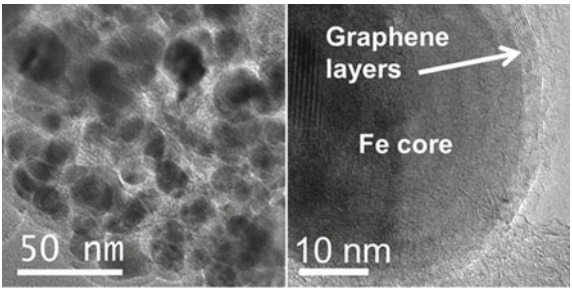

Fig. 13.1 High Resolution-TEM images of Fe@C nanoparticles (left) and magnification showing the graphene layers coating the Fe core (right)

The Fe@C nanoparticles were synthesized in an arc-discharge furnace [50, 59–61] by a method based on the previously followed by Krätschmer and coworkers [62]. The nanoparticles are produced by the sublimation and subsequent condensation of the starting materials (iron micrometric powder inside a graphite rod) when the electric arc ionizes the helium gas in the furnace chamber. The sublimation of graphite and iron produces a soot that, when condensed, deposits on the chamber walls. This soot was analyzed by X-ray diffraction (XRD). According to the XRD spectrum this powder contains mainly α-Fe, and some small traces of magnetite/maghemite. A more detailed characterization was carried out by Transmission Electron Microscopy (TEM) [50, 59, 61]. TEM images showed that the obtained black powder contained a variety of carbon nanostructures, including carbon onions, some nanotubes, amorphous carbon and a large proportion of iron/iron oxide nanoparticles encapsulated in graphene/graphite layers, as the ones displayed in Fig. 13.1.

The size of the nanoparticles ranged between 5 and 50 nm, with the size distribution center at 10 nm. The TEM images showed as well that the soot contained a small amount of non-coated or partially coated metallic particles. These are not biocompatible and therefore had to be eliminated from the sample by chemical etching [35, 61]. To increase the concentration of magnetic nanoparticles in the final sample, a magnetic purification of the powder was carried out to eliminate the amorphous carbon and all those carbon structures not containing any magnetic nanoparticle. For this purpose, particles were suspended in distilled water and the separation was carried out by placing the suspension in a magnetic field gradient produced by 3kOe permanent magnet [35]. After drying the fraction containing the magnetic nanoparticles these were suspended in two different biocompatible fluids, keeping the suspension in an ultrasonic bath for several minutes. A suspension was prepared with gelafundin, as this a biocompatible commercial succinated gel had been already tested in the above mentioned in vivo experiments with New Zeeland rabbits [35] and mice [51]. The other suspension was prepared with mannitol, a solution commonly used in experiments with plants [63]. These biocompatible magnetic fluids were subsequently administered to the plants, which represents an alternative to other methods used when working with plants [2, 3, 64]. To study the possible differences in the translocation and accumulation of the nanoparticles inside the plant, three different administration methods were tested: by injection, by spraying and by immersing the plant roots directly into the nanoparticle solution.

13.2.1 Nanoparticle Application by Injection

These experiments were carried out on living pumpkin plants and with the Fe@C nanoparticles suspended in gelafundine. The pumpkin plants were selected because of the large size of their vessels, to make the transport of the nanoparticles through the vascular system easier. Plants were grown as described in [52, 54, 63]. In a first series of experiments, the biocompatible magnetic fluid was injected inside the internal cavity of a leaf petiole (see Fig. 13.2 left), on the assumption that it would penetrate into the plant and translocate to other areas through the vascular tissues. To check if after injection it was possible to concentrate the nanoparticles in certain regions of the plant, permanent magnets (in the form of small discs about 5 mm diameter) were placed on the leaf petiole opposite to the injection point and on the roots, as shown in Fig. 13.2 left [52, 54]. On the right, the figure shows as well an optical micrograph of the transverse section of a pumpkin stem, with the main structural elements.

Plant tissue samples were collected 24, 48, 72 and 168 h after the injection of the magnetic fluid and processed for microscopy analysis. Tissue was cut from the stem and leaf petiole at the injection point. Roots and petiole samples were collected at the point of magnets localization but also before and after the magnet position (i.e., facing the expected movement of the nanoparticles from the injection point through the vascular tissue towards the magnet). The collected samples were observed using light microscopy, under a confocal laser scanning microscope and by TEM. Details on sample processing and observing protocols for the respective methods can be found in [52, 54].

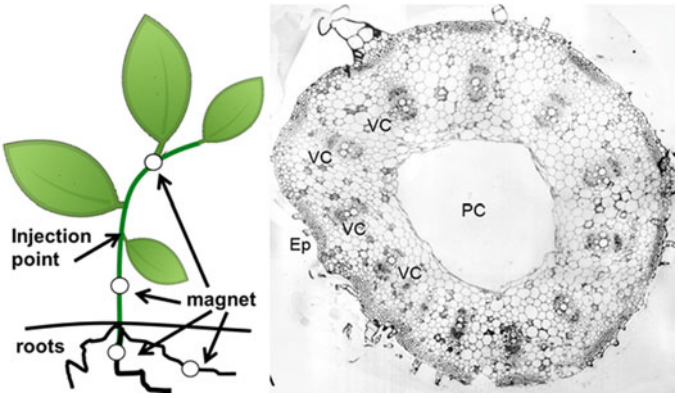

Fig. 13.2 Scheme showing the nanoparticle suspension injection point and the magnet positions (left). Optical micrograph of a pumpkin stem transversal section (right); VC stands for the vascular core, Ep for the epidermis and PC for the pit cavity. Reprinted by permission from Springer Nature Customer Service Centre GmbH: Springer Nature BMC Plant Biology Nanoparticle Penetration and transport in living pumpkin plants: in situ subcellular identification, Corredor et al. [54]. Copyright © 2009. https://doi.org/10.1186/1471-2229-9-45

To assess whether the nanoparticles would penetrate into the living plant and travel through the vascular system to the places where the magnets were located hand-cut sections of petioles and roots were observed on a light microscope. Figure 13.3 shows the images corresponding to sections of petioles (upper row) and of roots (lower row), taken at the injection point (a), before the position of the magnet (d), at the magnet point (b and e) and after the magnet position (c and f). The dark colored areas correspond to the accumulation of the nanoparticles suspension. Figure 13.3a shows a detail of the vascular tissue (vc in Fig. 13.2 right) at the application point where nanoparticles penetrated. They further moved to other parts of the plant and the magnets concentrated the fluid in the vascular tissues adjacent to their localization in the petiole (Fig. 13.3b) and roots (Fig. 13.3d, e). By comparison, images taken in vascular areas opposite to the magnet point of the same sections (Fig. 13.3c) or in samples located after the magnet position (Fig. 13.3f) display almost no black color, indicating that the nanoparticles in the fluid are trapped by the magnet and they do not travel further.

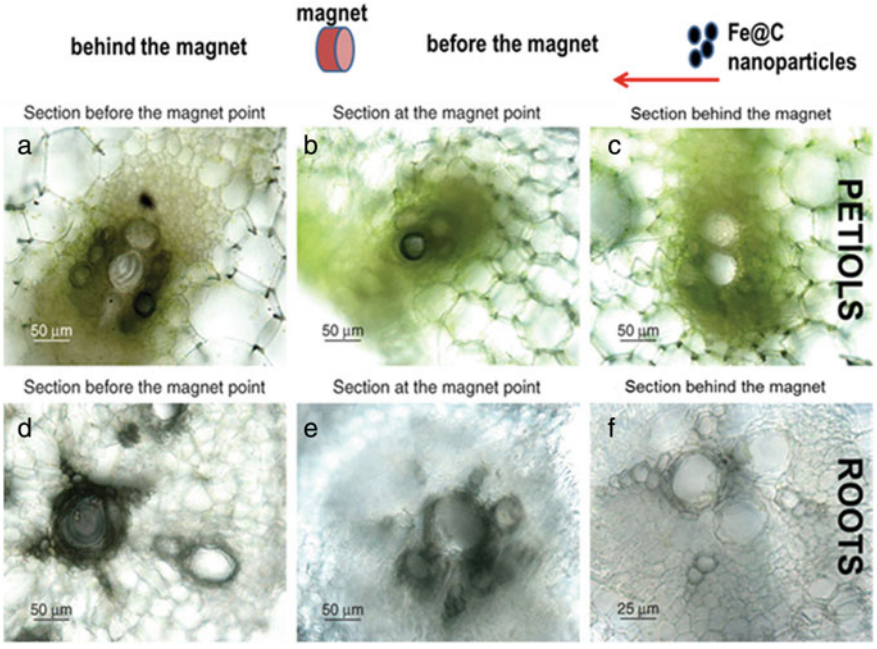

Fig. 13.3 Light microscopy images of vascular tissue of the petiole cut **a** at the application point; **b** adjacent to a magnet; **c** opposite to a magnet. Light microscopy images of vascular tissue of the root tissue cut **d** before the position of the magnet; **e** at the position of the magnet; **f** behind the magnet. Printed by permission from Oxford University Press Annals of Botany Nanoparticles as Smart Treatment-delivery Systems in Plants: assessment of different techniques of Microscopy for their Visualization in Plant Tissues, González-Melendi et al. [52]. Copyright © 2007 https://doi.org/10.1093/aob/mcm283

Tissue sections were also imaged by confocal and fluorescence microscopies. Despite the fact that the size of the nanoparticles is below the resolution limit of the light microscope, nanoparticle aggregates were clearly visualized by the differential interference contrast (DIC) or Nomarski technique on a projection of a 3D confocal stacks, and also in reflection mode. Figure 13.4a shows nanoparticles inside a cell of the cortex next to the internal hollow of the petiole just before the position of the magnet, 72 h after the injection. The image corresponds to the overlay of the respective images taken in Nomarski and reflection modes. On the contrary, no particles were observed in images from the untreated plant used as controls. Nanoparticles were also detected in the cell wall of the xylem vessel cells. This cell wall is naturally auto-fluorescent due to the lignin as its major component. Due to their black color (because their graphitic shell) the Fe@C nanoparticles are very suitable for working with plant tissues, as they can be easily identified in bright field images (as the one in Fig. 13.4b), and also be seen as non-auto-fluorescent dots in the cell wall, like in Fig. 13.4c.

Some samples were studied by light microscopy, and then the same regions were analyzed by TEM. Unlike in the control samples, aggregates of nanoparticles were detected at the injection site 24 h after administration, in the epidermis and in the extracellular space in between cells of the epidermal layer, on a light microscope under phase contrast (Fig. 13.5a). Electron microscopy correlative analysis displayed several nanoparticle aggregates (marked by asterisks in Fig. 13.5b) that would correspond to those previously detected by light microscopy. Increasing the magnification, individual nanoparticles could be clearly visualized (Fig. 13.5c), to measure their size. The diameter of the biggest particles is around 50 nm, although they represent the

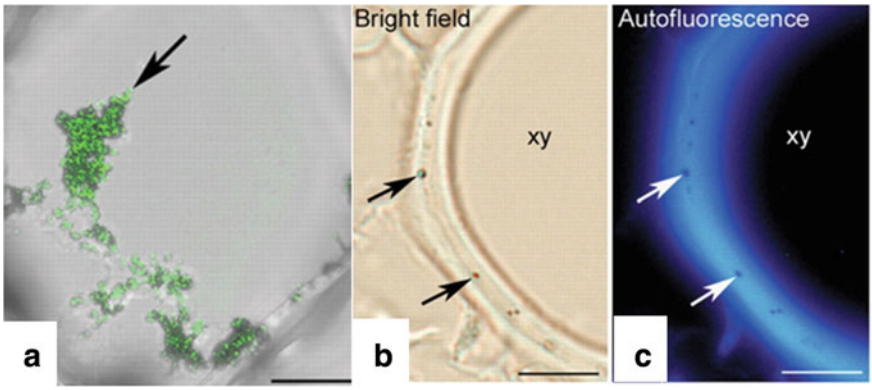

Fig. 13.4 Nanoparticles (pointed by arrows) in a projection of 3-D confocal stacks of a cell of a plant stem at the position of the magnet, 72 h after the suspension injection **a**. Nanoparticles (pointed by arrows) in a confocal bright-field image **b** and in a fluorescence microscope image **c** of a section of plant tissue. Printed by permission from Oxford University Press Annals of Botany Nanoparticles as Smart Treatment-delivery Systems in Plants: assessment of different techniques of Microscopy for their Visualization in Plant Tissues, González-Melendi et al. [52]. Copyright © 2007. https://doi.org/10.1093/aob/mcm283

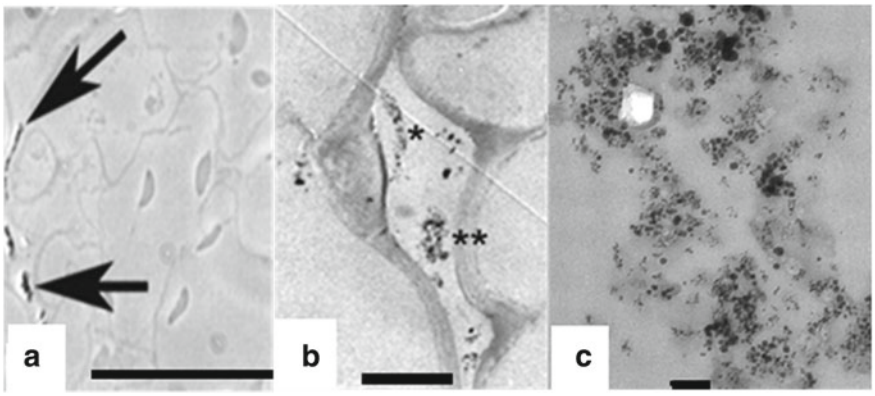

Fig. 13.5 **a** Phase contrast light microscope image of a string of nanoparticles (pointed by arrows) along the cells on the outer side of the cell wall at the epidermis. **b** TEM image of nanoparticle aggregates, marked with asterisks. **c** TEM magnification of the aggregate marked with two asterisks. in **b** The same Scale bars: 50 μm, 5 μm and 0.1 μm, respectively. Printed by permission from Oxford University Press Annals of Botany Nanoparticles as Smart Treatment-delivery Systems in Plants: assessment of different techniques of Microscopy for their Visualization in Plant Tissues, González-Melendi et al. Copyright © 2007. https://doi.org/10.1093/aob/mcm283

smallest population. The majority of the observed nanoparticles has a diameter equal or below 10 nm. In solution, these nanoparticles form aggregates with a diameter ranging from 5 to 200 nm [61]. The fact that no particles bigger than 50 nm were detected in the plant tissues suggest a size selection mechanism (maybe due to the cell walls and waxes), although more studies are necessary to clarify the nanoparticles penetration mechanisms in their movement to and through the plant vascular system.

The observation of all the samples taken from different points of the plant and at different time intervals, suggests that the nanoparticles move from the point of application progressively penetrating the different tissues of the plant. Analyzing samples taken near the application point, aggregates of nanoparticles were detected in the internal wall of the pit cavity (see Fig. 13.2 right) at the point of administration 24 h after injection, and 48 h after administration these nanoparticles had migrated into the stem parenchima. It is significant that these aggregates appeared in adjacent cells forming chains (with 2–5 cells) between the vascular cores and radially oriented to the stem surface, suggesting than the nanoparticles move from cell to cell. It seems unlikely that in this movement the aggregates of nanoparticles enter directly into cytoplasm; therefore, it is most likely that the nanoparticles enter individually, and aggregate spontaneously once inside the cell. Some aggregates were also visualized in the extracellular space between cells. Results also showed the presence of nanoparticles in the outer surface of the plant, both inside and outside of the trichomes, 24 h after application. This fact indicates that at least part of the nanoparticle suspension was expelled in a short time, as if the plant got rid of the excess of nanoparticles, maybe as a kind of detoxification mechanism. At 48 h nanoparticle aggregates were

also observed inside the xylem vessels. After 168 h there were almost no nanoparticles, neither in the pit cavity, nor in the tissues of the stem near the point of application. TEM analysis of samples collected 48 h after the administration, close to the magnets placed far from the point of injection, revealed the presence of individual nanoparticles in the cytoplasm of cells close to the vascular system. Nanoparticles were also observed inside the xylem vessels, suggesting that the nanoparticles use them for travelling long distances inside the plant. The microscopy study carried out in the different samples allowed also to analyze the structure of the cytoplasm. A dense cytoplasm with starch-containing organelles was observed in those cells collected 24 h after injection, with nanoparticle aggregates in the cytosol. However these starch structures were neither detected in adjacent cells without nanoparticles, nor in the cytoplasm of cells in tissues collected far from the application point 48 h later, containing individual nanoparticles. This fact suggests that these changes in their subcellular organization could be a plant response to the presence of a high density of nanoparticles. Cytotoxicity has been associated with the dose of nanoparticles [65], in particular with those in a magnetic ferrofluid [66–68]. However, only with our experiments it is not possible to assess if the observed reaction to the Fe@C nanoparticles is specific of the plant cells, or is a common cell reaction to high nanoparticle concentrations in the cytoplasm. Moreover, an effect of the calcium in the gelafundine in which nanoparticles are suspended cannot be completely excluded.

13.2.2 Nanoparticle Application by Spray

This methodology was chosen because is more similar to that used by agronomists in cultivated plants, for example for phytosanitary control. The experiments were as well carried out on living pumpkin plants and with the Fe@C nanoparticles suspended in gelafundine [52]. Drops of nanoparticle suspension were sprayed of the surface of leaves close to the insertion of the petiole. Tissue samples (close and far from the application point) were also collected 24, 48 and 168 h after spraying. In this case, nanoparticles were only observed in samples taken 168 h after application. It was not possible to distinguish any nanoparticle aggregates by light microscopy, and the nanoparticles were only visible in TEM images of cells from the epidermis of the petiole close to the application point. Moreover, there were no nanoparticles in cells beyond the first epidermal layer. In these cells the nanoparticles appeared isolated, not in aggregates. There was no difference between the intracellular structure density observed in those cells with nanoparticles and in the neighboring cells without nanoparticles in their cytoplasm. As the epidermic outer cell wall has a considerable thickness and is covered by protective waxes, it is quite likely that the nanoparticles penetrate through the stomata and the subestomatic chambers. In fact, this is a route used by pathogens of different species [69, 70]. The fact that nanoparticles passed through the epidermal cell wall opens up the possible application of these nanotechnology tools for agronomical purposes. However, these results should be taken as preliminary. For example, the fact that the amount of nanoparticles found in

the tissue samples was less than that found when applying the nanoparticles by injection, raises the need to optimize the suspension of nanoparticles, testing for example other biocompatible liquid carriers, functionalized nanoparticles for a higher affinity with the leave tissues etc.

13.2.3 Nanoparticle Application by the Roots

The study on the nanoparticle absorption and translocation was extended to the case in which the nanoparticles penetrate through the roots into the plant. In this case no magnets were used, to study the free movement of the nanoparticles inside the plant. A comparative analysis was carried out in four living crop plants belonging to different families, to unveil whether there were differences regarding the transport routes, the organs and tissues where nanoparticles tend to accumulate. This research was carried out on sunflower (*Helianthus annuus*) from the family *Compositae*; tomato (*Lycopersicum sculentum*) from the *Solanaceae*; pea (*Pisum sativum*), from the *Fabaceae*; and wheat (*Triticum aestivum*), from the *Triticeae* [55]. In this case, the plants were grown in vitro using a Petri dish system (rhizotron) allowing the visualization of the roots [71]. A biocompatible magnetic fluid was prepared suspending the Fe@C nanoparticles in manitol solution (1%). Once the plants developed the second pair of leaves some of the roots were immersed in the suspension (see Fig. 13.6a). Tissues

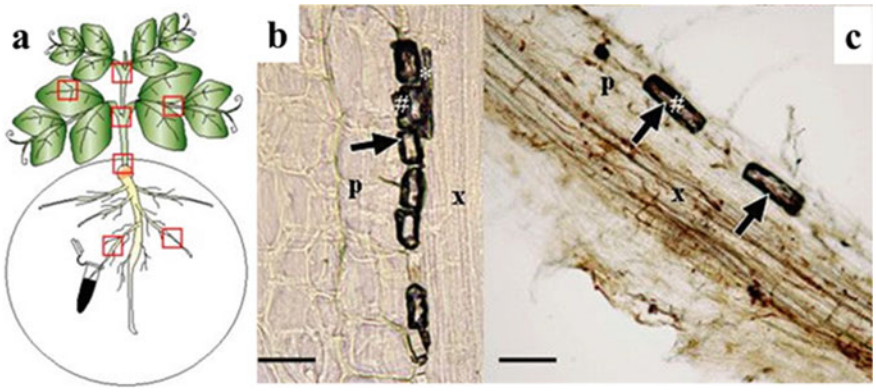

Fig. 13.6 Scheme of the plant showing the nanoparticle administration procedure and the tissue sections for microscopy analysis. **a** Root longitudinal sections of pea **b** and sunflower. **c** Samples were taken 24 h after nanoparticle administration. Arrows point to nanoparticle accumulations. Symbols # and * indicate cells from the parenchyma (p) and from the xylem (x), respectively. Scale bars are 25 μm in **b** and 50 μm in (**c**). Reprinted by permission from Springer Nature Customer Service Centre GmbH: Springer Nature Journal of Nanobiotechnology Absorption and traslocation to the aerial part of magnetic carbon-coated nanoparticles through the root of different crop plants Cifuentes et al. [55]. Copyright © 2010. https://doi.org/10.1186/1477-3155-8-26

from different parts of the plants were taken after 24 and 48 h, from the sections drawn in (Fig. 13.6a, and fixed for conventional light microscope analysis.

Big amounts of nanoparticles (in the form of a black staining corresponding to nanoparticle aggregates) were observed in samples of root tissue collected after 24 h (see Fig. 13.6b, c). These observations led to the conclusion that nanoparticle application by immersing the roots into the nanoparticle solution is faster, more reliable and efficient (in terms of the amount of nanoparticles) than application by pulverization or injection [52, 54]. This conclusion is common to the four crops analyzed in this study. Although in all cases nanoparticles were easily detected in the xylem vessels, some differences were observed depending on the species. Pea roots accumulated higher contents of nanoparticles than sunflower or wheat, for example. This difference still remained after 48 h of exposure to the nanoparticle fluid, suggesting that pea roots could be more permeable to nanoparticle penetration. Looking for the presence of nanoparticles in roots not exposed directly to the suspension, the characteristic black deposit was detected within the central cylinder of roots located diametrically opposite to the treated roots. Therefore, the nanoparticles had moved there probably through the phloem and using the source-sink pressure gradient [72]. This is also in good agreement with the observations in pumpkin plants with respect to the radial transport of nanoparticles from cell to cell [52, 54].

The translocation of the nanoparticles into the aerial parts of the plant was also studied, taking tissue samples from the plant crown 24 and 48 h after nanoparticle application. After 24 h the black deposit was observed in the xylem vessels of the four crops as shown in Fig. 13.7a–d, which means that the nanoparticles had quickly moved most likely by the transpiration stream.

As in the case of the roots, there were differences between species. Pea and wheat showed a high concentration of nanoparticles in the vascular tissues of the crown, whereas the black staining was less intense in tomato and sunflower. In the case of sunflower, it seems that the nanoparticle uptake through the roots is much slower than in the other species, and for that reason there is a lower accumulation after 24 h of nanoparticle treatment. In addition, in this case the nanoparticle suspension seems to be more restricted to the vascular tissues than in the other species. The observation of subsequent upper part sections confirmed that nanoparticles reached most of them also after 24 h of exposure to the suspension. The samples taken 48 h after nanoparticle application (see Fig. 13.7e–j) showed no significant differences from crop to crop, as an intense accumulation of nanoparticles was detected in all the cases. According to the microscopy analysis, the nanoparticles moved also towards the leaves and leaf petioles. Another striking result is that large accumulations of nanoparticles were detected in the leaf trichomes of the wheat plants, but not in the other three crop species. As mentioned in previous sections, the same was observed in pumpkin plants [52, 54], although not in such a high amount. This fact would confirm the secretory function of the trichomes [73], being this a putative detoxifying pathway. Different behavior regarding accumulation and excretion of heavy metals has been reported for different plant species [74], suggesting that such differences can also be found when working with metal nanoparticles. The reasons for the observed differences between crops are unclear, but they should be related to the physiology

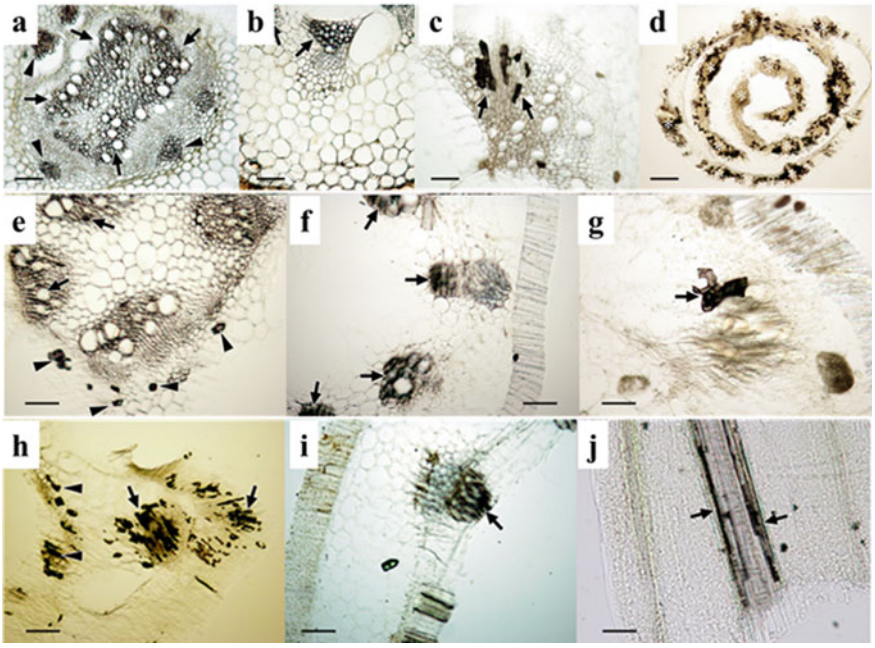

Fig. 13.7 Tissues from the crown of pea **a**, sunflower **b**, tomato **c** and wheat **d** cut 24 h after suspension administration. Detail of the first internode cross section of pea **e**, sunflower **f** and tomato **g** 48 h after suspension administration. Detail of the second internode cross section of pea **h**, sunflower **i** and wheat **j** 48 h after suspension administration. Scale bars in images (a)-**i** correspond to 100 μm; scale bar in images **j** corresponds to 50 μm. Reprinted by permission from Springer Nature Customer Service Centre GmbH: Springer Nature Journal of Nanobiotechnology Absorption and traslocation to the aerial part of magnetic carbon-coated nanoparticles through the root of different crop plants Cifuentes et al. [55]. Copyright © 2010. https://doi.org/10.1186/1477-3155-8-26

of the plants: wheat belongs to the monocot plant group, whereas the other three crops are dicots.

Therefore, these results and those obtained in pumpkin plants have shown that biocompatible nanoparticle suspensions can be administered to whole living plants, can circulate through their vascular system, either by themselves or by applying magnetic field gradients, and can also be located on specific places, from the root to the aerial parts. The study carried out by different microscopy techniques has allowed the accurate visualization of nanoparticles in tissues and cells. However, more detailed studies at cell level, including HR-TEM, are necessary to clarify the mechanisms by which nanoparticles can penetrate into the plant cells, as this is currently a controversial subject. In addition, special attention has to be paid to toxicity studies. In the work with pumpkin plants, some of the specimens treated with nanoparticles were transplanted to pots where they continued to grow, and no damage was observed. However, these results should be viewed with caution because it has been reported that in in vitro treatments [66–68], nanoparticles may cause some

local damage at cell level. Moreover, as cyto- and phyto-toxicity are dose-dependent, they cannot be discarded in case of treatments with more concentrated nanoparticle suspensions.

13.3 Interaction of Silica Coated Magnetic Nanoparticles with Pathogenic Fungi

In this section, the study of the interaction between silica coated iron oxide ($Fe_3O_4@SiO_2$) nanoparticles and fungal cells is presented, paying attention to the affinity and internalization of the particles by hyphal cells, and to their toxicity [48].

The core-shell nanoparticles were synthesized in two steps. First, the magnetite core was synthesized by coprecipitation, as described in De Matteis et al. [75]. According to the X-ray diffraction pattern and HR-TEM images of the synthesized powders, the nanoparticles were mainly composed by magnetite and only in some batches a small fraction of maghemite was detected. The particles were subsequently coated with an aminated silica shell and functionalized with protein G following the protocols reported in [47]. The diameter of the silica-coated nanoparticles was about 50–100 nm. The protein G on the surface was afterwards conjugated to AlexaFluor488, to visualize the nanoparticles by confocal microscopy when studying their interaction with the Fusarium. In addition, when the nanoparticles were going to be used for sensing purposes, the protein G would easily allow their further conjugation with the biomolecule that specifically recognizes the pathogenic fungus [47]. All the experiments described from here on were carried out on *F. oxysporum forma specialis lycopersici*. The fungal strain was stored as microconidial suspension in 30% glycerol at −80 °C. For microconidia production, cultures were grown in potato dextrose broth [48].

13.3.1 Internalization of $Fe_3O_4@SiO_2$ Nanoparticles by Fungal Cells

First of all, the affinity between the $Fe_3O_4@SiO_2$ nanoparticles and the fungus was studied. With this purpose, turbidity (or relative absorbance) measurements were performed on conidial suspensions incubated with magnetic nanoparticles, after different incubation times. In all the cases, 5×10^6 microconidia were grown for 16 h at 28 °C under agitation at 170 rpm in 1 mL of minimum medium (MM) [76]. The measurements were performed after long-term and short-term incubation experiments. In the first case the conidia were grown in MM supplemented with nanoparticles at 200 $\mu g\ ml^{-1}$. In short-term incubation experiments, conidia were grown in the absence of nanoparticles. They were added to the MM after 16 h of conidia growth and incubated there for 5 s, 15 min and 30 min. After incubation with

the nanoparticles, the suspensions were filtered to remove nanoparticles not internalized/not attached in/to the conidia, and the filtrate was resuspended in new fresh MM. This suspension was introduced in a magnetic separator, and kept under the action of the magnetic field for 1, 3 and 5 min. At these times, an aliquot of the medium was taken for turbidity measurements. All those fungi attached to the magnetic nanoparticles were going to be trapped by the magnet, decreasing the conidia concentration in the aliquot, and consequently, decreasing its turbidity. The optical density of this aliquot was measured at 600 nm (A600), and compared with the absorbance of a control sample (a sample not introduced in the magnetic separator). The reduction in absorbance was correlated with the nanoparticle attachment/internalization in/to the fungus. After long-term incubation with magnetic nanoparticles, the conidia were attracted by the magnet as early as 1 min after being introduced in the magnetic separator, and the turbidity of the medium was reduced dramatically, confirming the attachment of the nanoparticles to the hyphae. The long-term incubation experiments were also performed with the $Fe_3O_4@SiO_2$ nanoparticles after their functionalization with protein G, to verify whether the protein influenced the fungus-nanoparticle interaction. In fact, the functionalization of the nanoparticle surface delayed the particle movement towards the magnet, although a turbidity decrease similar to that observed when working with the non-functionalized nanoparticles was detected after 5 min. Short-term incubation experiments were also performed incubating the grown conidia with functionalized and non-functionalized $Fe_3O_4@SiO_2$ nanoparticles. The turbidity measurements were carried out following the protocol described above for long term experiments. A drastic reduction of the turbidity was observed after incubating fungal conidia with both functionalized and non-functionalized nanoparticles for as short as 5 s. These results evidence the high affinity of the functionalized and non-functionalized $Fe_3O_4@SiO_2$ nanoparticles for the fungal hyphae.

In order to investigate whether the nanoparticles were able to penetrate the fungal hypha or remained attached to its surface, visible, confocal and transmission electron (TEM) microscopies on conidia cultures after long-term and short-term incubation with $Fe_3O_4@SiO_2$ nanoparticles were carried out. For these studies, 5×10^6 conidia were grown for 16 h at 28 °C under agitation at 170 rpm in 1 ml of MM. For long-term studies, 200 $\mu g\ ml^{-1}$ of nanoparticle suspension was added at the time of fungus inoculation, while for short-term studies the nanoparticles were added to MM after 16 h growth and incubated for either 10 min or 3 h before visualization. First of all, confocal images of thin time-course confocal optical sections (~1 μm thick) were acquired. Details about the microscope and the instrumental conditions can be found in [48]. The results are displayed in Fig. 13.8. After 10 min of incubation, fluorescent $Fe_3O_4@SiO_2$ nanoparticle aggregates attached to the fungal hyphal surfaces were clearly seen (pointed by an arrow head at visible field and stack projection in Fig. 13.8a). However, theses aggregates did not penetrate the fungal hyphae since 3D optical sections showed a clear signal only for the largest aggregates attached to the hypha. Although the penetration of non-aggregated nanoparticles could not be inferred from the confocal images, it cannot be discarded. After 16 h of incubation, nanoparticle aggregates were still visible and attached on the hyphal surface, although they were smaller than those attached after 10 min incubation, and no signal

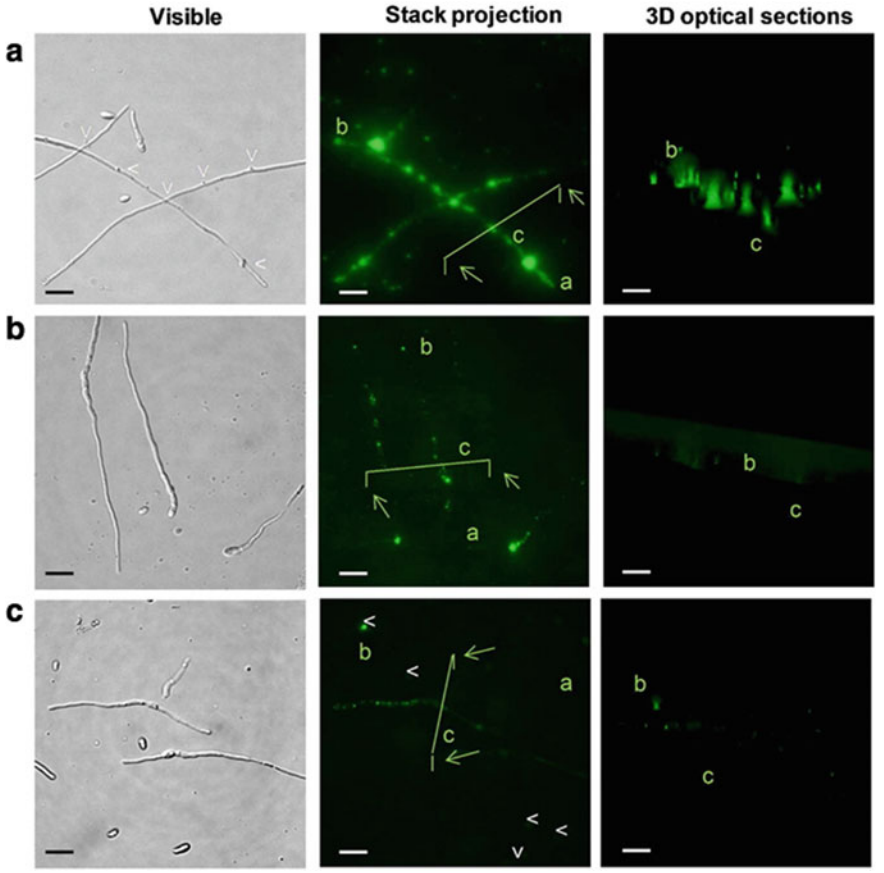

Fig. 13.8 Visible and confocal micrographs of overview images (stack projections) and the transverse optical section of *F. oxysporum* incubated with Fe_3O_4@SiO_2 nanoparticles for 10 min **a**, and 16 h **b**, and of the filtered sample re-suspended for 4 h in fresh MM **c**. The orientation of the images is indicated by lower case letters, for ease of understanding. *T* plane of the section shown in the 3D images is indicated by the green hurdle in the overview. Scale bars correspond to 10 μm. Reprinted with permission from Rispail et al. [48]. https://doi.org/10.1021/am501029gCopyright © 2014 American Chemical Society

was observed in the 3D optical sections (Fig. 13.8b). The eventual detachment of the nanoparticles from the fungal cells was also studied. With this purpose 16 h conidial suspensions already incubated with nanoparticles were filtered through a 0.45 μm filter to remove all the nanoparticles that could be in the medium, not attached to the hypha. The filtered sample was re-suspended in sterile MM for 4 h at 28 °C. Confocal images taken afterwards (Fig. 13.8c, arrow heads) showed that after 4 h some aggregates remained in the hypha, although some of them detached and were suspended in de medium.

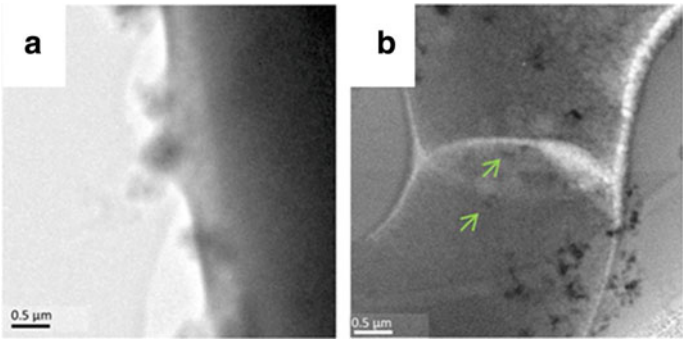

Fig. 13.9 BF-TEM image showing a detail of a *F. oxysporum* hypha **a** and a detail of the hyphal septum. **b** Arrows point to nanoparticles in the septum. Scale bars correspond to 0.5 µm. Adapted with permission from Rispail et al. [48]. https://doi.org/10.1021/am501029g. Copyright 2014 American Chemical Society

The confocal microscopy study was completed by TEM and Scanning Transmission Electron Microscopy-High Angle Annular Dark Field (STEM-HAADF) observation in a Tecnai F30 (FEI), operated at 300 kV. Samples were carefully prepared following cryo-TEM protocols [48]. Bright field (BF)-TEM images taken after 16 h incubation showed a range of small to medium aggregates corresponding to the $Fe_3O_4@SiO_2$ nanoparticles attached to the fungal surface and some individual nanoparticles moving through the fungal cell wall, as shown in Fig. 13.9a. Careful observations near to the fungal septum (see Fig. 13.9b) suggested that few individual nanoparticles (pointed by arrows in the figure) could enter the fungal cells. This assumption was also supported by focal series of STEM-HAADF images.

The chemical composition of the aggregates was analyzed by STEM-HAADF (see Fig. 13.10a, b) and Dispersive X-Ray Spectroscopy (EDS). The EDS spectra as the ones presented in Fig. 13.10c, d confirmed that the nanoparticles consist of an iron oxide core coated by a SiO_2 shell.

The fact that only a small fraction of individual nanoparticles penetrated the fungal cells whereas a large fraction of particles remain attached to the hypha coincides with the results obtained by confocal microscopy. This makes a difference with other nanomaterials, such as quantum dots. A similar study carried out in the same *forma specialis* of *F. oxysporum* indicated that quantum dots penetrate in a much larger amount into the cell [48]. As cellular uptake is closely related to the physicochemical properties of the nanosized objects, the different behavior of the quantum dots and the $Fe_3O_4@SiO_2$ nanoparticles in this study could be due to the different size of both nanomaterials (13–15 nm in the case of quantum dots versus 50–100 nm in the case of nanoparticles). In addition, although both nanomaterials were incubated together with the fungal conidia in MM at the same pH, their respective surface charge was different (approximately -35 mV in the case of quantum dots and about +25 mV the one of the nanoparticles). This different sign would determine the interaction with the proteins of the fungal cell wall characteristic of hyphal cells. The

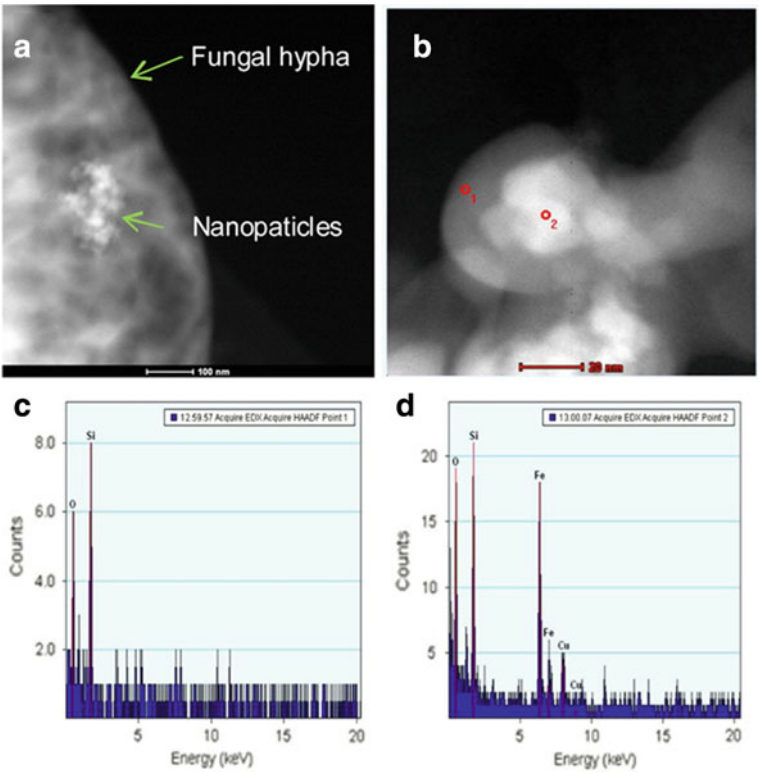

Fig. 13.10 STEM-HAADF images of a Fe_3O_4@SiO_2 nanoparticle aggregate adhered to a fungal hypha **a** and of a nanoparticle **b**. Here the o1 and o2 spots correspond to the EDS spectra shown in **c** and **d**. Scale bars in **a** and **b** represent 100 and 20 nm, respectively. Reprinted with permission from Rispail et al. [48]. https://doi.org/10.1021/am501029g. Copyright © 2014 American Chemical Society

outer layer of the cell wall of *F. oxysporum* is enriched in glycoproteins [77]. Since the glycoproteins are negatively charged, they will attract the positively charged nanoparticles by electrostatic interactions. This would favor the formation of the observed large nanoparticle aggregates, large enough to be observed in the confocal and even visible field. This large size might as well hamper their uptake. In addition, the images taken after the longest incubation periods showed that the number of aggregates decreased with time. This fact could be ascribed to the increase in the acidification of the incubation medium during *F. oxysporum* growth [78], that might increase the nanoparticle surface charge and in turn improve the stability of the isolated nanoparticles.

13.3.2 *Fe_3O_4@SiO_2 Nanoparticle Toxicity on* F. Oxysporum *Hyphal Cells*

The experiments performed to outline the toxicity profile of the synthesized Fe_3O_4@SiO_2 nanoparticles included colony growth assessment, the study of the reactive oxygen species (ROS) accumulation and oxidative stress, and the study of the fungal cell viability. In each case microconidia were grown in MM supplemented with nanoparticle concentrations equal to 25, 50, 100 and 500 $\mu g\ ml^{-1}$. The results demonstrated the low toxicity of the nanoparticles to these *forma specialis*, even at the highest nanoparticle concentration.

The experiments described above show that, although the fraction of Fe_3O_4@SiO_2 nanoparticles that penetrate the hypha is not very large, they remain as magnetic aggregates adhered to the fungus surface, which is already enough to be separated magnetically and to be detected by the magnetic reader of a biosensor. In addition, these nanoparticles in usual working doses are per se not toxic, so in principle they are not harmful to other non-pathogenic/beneficial fungi that may exist in the environment. This research constitutes the stage before the functionalization of the nanoparticles for the detection of the pathogen and also paves the way for the search of other biomolecules or active principles that could also be housed on the nanoparticle surface. This would result in multifunctional nanoparticles that could be used not only for detection, but also for the selective control and eventual elimination of the pathogenic fungus.

13.4 Summary and Persperctives

The work presented here evidences that magnetic nanoparticles are very attractive nanomaterials to be considered in research related to Life Sciences areas different from those more explored up to now, as the ones directly connected to Bio-medicine. The results presented here show how these nanosystems can be very useful, first of all, for basic research, to study the fundamental problems concerning their interaction with plants and microorganisms. In addition, these studies open the way to solve a large list of practical problems in agriculture, agronomy, environment, biotechnology, food industry, etc., which in the short and/or long term also influence health, quality of life and global welfare.

The work carried out with the Fe@C nanoparticles has shown that these nanoparticles are very appropriate for *in-planta* application and for plant cell research. First, because they are suitable for the synthesis of different biocompatible magnetic fluids easy to administer to living whole plants by different routes (injection, spray and immersion of the roots in the fluid). Second, they have an adequate response to magnetic field gradients. This characteristic, together with the high porosity and high specific surface area of their coating makes them very appropriate as magnetically responsive carriers for the localized delivery of different chemical substances,

such as those used in phytosanitary treatments, for pest control, etc. Although there are still many problems to be solved for their large-scale use, the work presented here can help in preliminary studies at laboratory scale (for instance, in those necessary for the optimization of the routes and doses to be administered in a specific treatment). Regarding their use in the laboratory, the Fe@C nanoparticles have been found as very convenient when working with plants and plant cells, as they are very easy to be visualized (without the need of any extra marker) by the microscopy techniques and protocols that have been developed during the execution of the different experiments. Therefore, the Fe@C magnetic nanoparticles can be of great help in elucidating the penetration mechanisms and the localization of the nanoparticles into the cell (for instance, by HR-TEM experiments) as well as the cell response to the nanocarriers. These topics are currently under discussion and are of great importance from the point of view of both basic and applied research (for example for the case of genetic engineering). Moreover, cell viability and cytotoxicity assays as well as the study of the relationship between cytotoxicity and phytotoxicity are of paramount importance prior their use in practice.

The use of magnetic nanoparticles coated with silica is much more exploited than that of the other magnetic nanoparticles. Their widespread implementation in biomedical applications has stimulated the rapid growth that their utilization in areas such as biotechnology, agriculture and agronomy is currently experiencing. The previous section summarizes what constitutes a systematic study of the interaction of $Fe_3O_4@SiO_2$ nanoparticles with a fungus that in one of its *forma specialis* is a plant pathogen and even an opportunistic human pathogen. One aspect that this work has highlighted is the importance of the physicochemical properties of the nanoparticles that have to be precisely tuned for each particular application. In this particular case, the size of the nanoparticles and their electrical charge has been determinant for their application in a biosensor that detects and allows the separation of the pathogenic fungus from infected soils, plants and crops. In particular, the different sign of the charge of the fungal cell wall of these hyphal cells and that of the silica coating causes the nanoparticles to be located in the form of relatively large magnetic aggregates on the fungal hypha. This has turned out to be decisive for the development of the future device, facilitating the detection and subsequent magnetic separation of the pathogen. Therefore, in the same way as for a given cell model it is necessary to know the toxicity profile of a particular nanomaterial, an exhaustive characterization of the physicochemical properties of this nanomaterial is also essential. At present, nanotechnology offers us advanced characterization techniques (which include magnetic characterization techniques, advanced microscopy, different spectroscopies etc.) that are more and more intended for the characterization of materials of biological interest, as well as biomaterials. In addition, the methodology and protocols developed for the case of the silica coated nanoparticles interacting with *Fusarium oxisporum* might then be implemented in the detection and control of other pathogens and pests, which would have a major impact on areas such as agronomy and agriculture, food industry etc. Moreover, this study could be extended to other fungi that are or can become pathogenic for humans, as for example those of *Candida* genus. Just as the resistance to antibiotics developed by bacteria

is a serious problem and is the cause of many deaths, certain pathogenic fungi have also become resistant to antifungals, and hence, there are fewer and fewer effective treatments. This opens a wide research field, and the fact that Nanoscience and Nanotechnology could contribute to finding solutions for their treatment and definitive elimination would represent a great benefit for the patient health In addition, the treatment of hospital acquired infections represents one of the highest costs of the health system and therefore, the solution to these problems would be enormously beneficial, also from the economic point of view.

When working with nanoparticles for applications as the ones discussed here, that involve plants and microorganisms present in our environment, it is essential to keep in mind that particles could in principle enter the food chain of animals and humans, with the consequent health impact. Therefore, before putting these ideas into practice, an exhaustive assessment of the nanoparticle fate is necessary, studying their degradability, their accumulation in fruits, seeds, roots, etc., and their possible excretion and effects on soils. Rigorous toxicity and ecotoxicity studies, leading to standardized nanorisk assessment protocols are mandatory. All this will contribute to improving the public perception of these new advances, and making people more confident about the use of new products based on nanotechnology.

Acknowledgements The author wish to thank the following colleagues: M. R. Ibarra, R. Fernández-Pacheco, D. Serrate, Z. Cifuentes, M. J. Coronado, E. Corredor, L. Custardoy, L. De Matteis, P. Fevereiro, J. M. de la Fuente, P. González-Melendi, C. Maycock, A. S. Miguel, A. Oliva, A. Pérez de Luque, E. Prats, N. Rispail, M. C. Risueño, D. Rubiales, R. Santos and P. S. Testillano. Financial support from the Spanish Ministerio de Economía y Competitividad (MINECO) through project MAT2016-78,201-P, and from the Department of Innovation, Research and University of the Government of Aragon through the Research Groups grants program co-financed by the FEDER Operational Program Aragón 2014–2020 "Building Europe from Aragon", is also acknowledged. The author also thanks the following publishers and journals: Springer Nature BMC Plant Biology (https://bmcplantbiol.biomedcentral.com/), as the original source of Fig. 13.2 published in Corredor et al. 2009, https://doi.org/10.1186/1471-2229-9-45; Oxford University Press Annals of Botany (www.aob.oxfordjournals.org), as original source of Figs. 13.3, 13.4 and 13.5, published in González-Melendi et al. 2008, https://doi.org/10.1093/aob/mcm283; BioMed Central Journal of Nanobiotechnology (https://jnanobiotechnology.biomedcentral.com/), as the original source of Figs. 13.6 and 13.7, published in Cifuentes et al. 2010. https://doi.org/10.1186/1477-3155-8-26; and American Chemical Society ASC Applied Materials and Interfaces, as the original source of Figs. 13.8, 13.9 and 13.10, published in Rispail et al. ACS Appl. Mater. Interfaces, 2014, 6 (12), pp 9100–9110 https://doi.org/10.1021/am501029g.

References

1. F. Torney, B.G. Trewyn, V.S.Y. Lin, K. Wang, Nat. Nanotechnol. **2**, 295 (2007)
2. S. Martin-Ortigosa, J.S. Valenstein, W. Sun, L. Moeller, N. Fang, B.G. Trewyn, V.S.Y. Lin, K. Wang, Small **8**, 413 (2012)
3. S. Martin-Ortigosa, J.S. Valenstein, V.S.Y. Lin, B.G. Trewyn, K. Wang, Adv. Func. Mater. **22**, 3576 (2012)
4. S. Martin-Ortigosa, D.J. Peterson, J.S. Valenstein, V.S.Y. Lin, B.G. Trewyn, L.A. Lyznik, K. Wang, Plant Physiol. **164**, 537 (2014)

5. A.T. Silva, N. Alien, C.M. Ye, J. Verchot, J.H. Moon, BMC Plant Biol. **10**, 291 (2010)
6. L. Jiang, L. Ding, B.C. He, J. Shen, Z.J. Xu, M.Z. Yin, X.L. Zhang, Nanoscale **6**, 9965 (2014)
7. H.W. Xun et al., Environ. Pollut. **229**, 479 (2017)
8. F.H. Hong, J. Zhou, C. Liu, F. Yang, C. Wu, L. Zheng, P. Yang, Biol. Trace Elem. Res. **105**, 269 (2005)
9. L. Zheng, F.S. Hong, S.P. Lu, C. Liu, Biol. Trace Elem. Res. **104**, 83 (2005)
10. T.P. Frazier, C.E. Burklew, B.H. Zhang, Funct. Integr. Genomics **14**, 75 (2014)
11. D.H. Lin, B.S. Xing, Environ. Pollut. **150**, 243 (2007)
12. D.H. Lin, B.S. Xing, Environ. Sci. Technol. **42**, 5580 (2008)
13. A. Perez de Luque, D. Rubiales, Pest Manag. Sci. **65**, 540 (2009)
14. A. Servin, W. Elmer, A. Mukherjee, R. De la Torre-Roche, H. Hamdi, J.C. White, P. Bindraban, C. Dimkpa, J. Nanopart. Res. **17**, 92 (2015)
15. F. Yasmeen, N.I. Raja, A. Razzaq, S. Komatsu, Biochimica Et Biophysica Acta-Proteins and Proteomics **1865**, 28 (2017)
16. D.L. Graham, H.A. Ferreira, P.P. Freitas, Trends Biotechnol. **22**, 455 (2004)
17. C. Marquina, J.M. de Teresa, D. Serrate, J. Marzo, F.A. Cardoso, D. Saurel, S. Cardoso, P.P. Freitas, M.R. Ibarra, J. Magn. Magn. Mater. **324**, 3495 (2012)
18. D. Serrate, J.M. De Teresa, C. Marquina, J. Marzo, D. Saurel, F.A. Cardoso, S. Cardoso, P.P. Freitas, M.R. Ibarra, Biosens. Bioelectron. **35**, 206 (2012)
19. B. Sepulveda, P.C. Angelome, L.M. Lechuga, L.M. Liz-Marzan, Nano Today **4**, 244 (2009)
20. Z.M. Liu, X.Y. Xia, C.Y. Yang, L. Wang, Rsc Advances **5**, 100891 (2015)
21. L. Wang, Z.M. Liu, X.Y. Xia, J.Y. Huang, Anal. Methods **8**, 6959 (2016)
22. D. Giust, M.I. Lucio, A.H. El-Sagheer, T. Brown, L.E. Williams, O.L. Muskens, A.G. Kanaras, ACS Nano **12**, 6273 (2018)
23. U. Kadam, C.A. Moeller, J. Irudayaraj, B. Schulz, Plant Biotechnol. J. **12**, 568 (2014)
24. U.S. Kadam, B. Schulz, J.M.K. Irudayaraj, Plant Journal **90**, 1187 (2017)
25. V.K. Sharma, R.A. Yngard, Y. Lin, Adv. Coll. Interface. Sci. **145**, 83 (2009)
26. Y.K. Jo, B.H. Kim, G. Jung, Plant Dis. **93**, 1037 (2009)
27. S. Gurunathan, J.W. Han, D.N. Kwon, J.H. Kim, Nanoscale Res. Lett. **9**, 373 (2014)
28. S. Banik, A. Perez-de-Luque, Spanish Journal of Agricultural Research **15**, e1005 (2017)
29. A. Sirelkhatim, S. Mahmud, A. Seeni, N.H.M. Kaus, L.C. Ann, S.K.M. Bakhori, H. Hasan, D. Mohamad, Nano-Micro Letters **7**, 219 (2015)
30. N. Padmavathy, R. Vijayaraghavan, Sci. Technol. Adv. Mater. **9**, 035004 (2008)
31. T. Jin, Y.P. He, J. Nanopart. Res. **13**, 6877 (2011)
32. Y.H. Leung et al., Small **10**, 1171 (2014)
33. I.F. Castillo, L. De Matteis, C. Marquina, E. García Guillén, J.M. de la Fuente, S. G. Mitchell, Int. Biodeterior. Biodegradation **141**, 79 (2018)
34. C. Alexiou, W. Arnold, R.J. Klein, F.G. Parak, P. Hulin, C. Bergemann, W. Erhardt, S. Wagenpfeil, A.S. Lubbe, Can. Res. **60**, 6641 (2000)
35. R. Fernandez-Pacheco et al., J. Magn. Magn. Mater. **311**, 318 (2007)
36. H. Van As, T. Scheenen, F.J. Vergeldt, Photosynth. Res. **102**, 213 (2009)
37. T. Scheenen, A. Heemskerk, A. de Jager, F. Vergeldt, H. Van As, Biophys. J. **82**, 481 (2002)
38. T.W.J. Scheenen, F.J. Vergeldt, A.M. Heemskerk, H. Van As, Plant Physiol. **144**, 1157 (2007)
39. C. Hillnhutter, R.A. Sikora, E.C. Oerke, D. van Dusschoten, J. Exp. Bot. **63**, 319 (2012)
40. V. Grazu, A.M. Silber, M. Moros, L. Asin, T.E. Torres, C. Marquina, M.R. Ibarra, G.F. Goya, Int. J. Nanomed. **7**, 5351 (2012)
41. F.G. Aliev, M.A. Correa-Duarte, A. Mamedov, J.W. Ostrander, M. Giersig, L.M. Liz-Marzan, N.A. Kotov, Adv. Mater. **11**, 1006 (1999)
42. R. Fernandez-Pacheco, M. Arruebo, C. Marquina, R. Ibarra, J. Arbiol, J. Santamaria, Nanotechnology **17**, 1188 (2006)
43. C. Gruttner, S. Rudershausen, J. Teller, J. Magn. Magn. Mater. **225**, 1 (2001)
44. H. Pardoe, W. Chua-anusorn, T.G. St Pierre, J. Dobson, J. Magn. Magn. Mater. **225**, 41 (2001)
45. A. Zahr, C. Davis, M. Pishko, Langmuir **22**, 8178 (2006)

46. M. Arruebo, R. Fernandez-Pacheco, B. Velasco, C. Marquina, J. Arbiol, S. Irusta, M.R. Ibarra, J. Santamaria, Adv. Func. Mater. **17**, 1473 (2007)
47. R. Arenal, L. De Matteis, L. Custardoy, A. Mayoral, M. Tence, V. Grazu, J.M. De La Fuente, C. Marquina, M.R. Ibarra, ACS Nano **7**, 4006 (2013)
48. N. Rispail et al., ACS Appl. Mater. Interfaces. **6**(12), 9100–9110 (2014)
49. C. Barbe, J. Bartlett, L.G. Kong, K. Finnie, H.Q. Lin, M. Larkin, S. Calleja, A. Bush, G. Calleja, Adv. Mater. **16**, 1959 (2004)
50. J.M. De Teresa, C. Marquina, D. Serrate, R. Fernandez-Pacheco, L. Morellon, P.A. Algarabel, M.R. Ibarra, Int. J. Nanotechnol. **2**, 3 (2005)
51. E. Escribano, R. Fernandez-Pacheco, J. Valdivia, M. Ibarra, C. Marquina, J. Queralt, Arch. Pharmacal Res. **35**, 93 (2012)
52. P. Gonzalez-Melendi et al., Ann. Bot. **101**, 187 (2008)
53. A.A. Kuznetsov, V.I. Filippov, O.A. Kuznetsov, V.G. Gerlivanov, E.K. Dobrinsky, S.I. Malashin, J. Magn. Magn. Mater. **194**, 22 (1999)
54. E. Corredor et al., BMC Plant Biol. **9**, 45 (2009)
55. Z. Cifuentes, L. Custardoy, J.M. de la Fuente, C. Marquina, M.R. Ibarra, D. Rubiales, A. Perez-De-Luque, J. Nanobiotechnol. **8**, 26 (2010)
56. A. Di Pietro, M.P. Madrid, Z. Caracuel, J. Delgado-Jarana, M.I.G. Roncero, Mol. Plant Pathol. **4**, 315 (2003)
57. E.I. Boutati, E.J. Anaissie, Blood **90**, 999 (1997)
58. S.Z. Validov, F.D. Kamilova, B.J.J. Lugtenberg, Microb. Biotechnol. **4**, 82 (2011)
59. H.R. Rechenberg, J.A.H. Coaquira, C. Marquina, B. Garcia-Landa, M.R. Ibarra, A.M. Benito, W. Maser, E. Munoz, M.T. Martinez, J. Magn. Magn. Mater. **226**, 1930 (2001)
60. J.A.H. Coaquira, H.R. Rechenberg, C. Marquina, M.R. Ibarra, A.M. Benito, W. Maser, E. Munoz, M.T. Martinez, Hyperfine Interact. **134**, 103 (2001)
61. R. Fernández-Pacheco, Ph.D. Thesis, Universidad de Zaragoza, 2008
62. W. Kratschmer, L.D. Lamb, K. Fostiropoulos, D.R. Huffman, Nature **347**, 354 (1990)
63. A. Perez de Luque, M.D. Lozano, J.I. Cubero, P. Gonzalez-Melendi, M.C. Risueno, D. Rubiales, J. Exp. Bot. **57**, 931 (2006)
64. S. Martin-Ortigosa, K. Wang, Transgenic Res. **23**, 743 (2014)
65. M. Bottini, S. Bruckner, K. Nika, N. Bottini, S. Bellucci, A. Magrini, A. Bergamaschi, T. Mustelin, Toxicol. Lett. **160**, 121 (2006)
66. A. Pavel, M. Trifan, Bara, II, D.E. Creanga, C. Cotae, J. Magn. Magn. Mater. **201**, 443 (1999)
67. V. Cotae, L. Creanga, J. Magn. Magn. Mater. **289**, 459 (2005)
68. A. Pavel, D.E. Creanga, J. Magn. Magn. Mater. **289**, 469 (2005)
69. A.K.M. Ekramoddoullah, R.S. Hunt, Can. J. Plant Pathol.-Rev. Canadienne De Phytopathologie **24**, 408 (2002)
70. T. Eichert, A. Kurtz, U. Steiner, H.E. Goldbach, Physiol. Plant. **134**, 151 (2008)
71. A. Perez de Luque, J. Jorrin, J.I. Cubero, D. Rubiales, Weed Res. **45**, 379 (2005)
72. K.J. Oparka, S.S. Cruz, Annu. Rev. Plant Physiol. Plant Mol. Biol. **51**, 323 (2000)
73. E. Onelli, C. Prescianotto-Baschong, M. Caccianiga, A. Moscatelli, J. Exp. Bot. **59**, 3051 (2008)
74. G. Sarret et al., Plant Physiol. **141**, 1021 (2006)
75. L. De Matteis, L. Custardoy, R. Fernandez-Pacheco, C. Magen, J.M. de la Fuente, C. Marquina, M. Ricardo Ibarra, Chem. Mater. **24**, 451 (2012)
76. J.E. Puhalla, Canadian J. Botany-Revue Canadienne De Botanique **63**, 179 (1985)
77. E.A.M. Schoffelmeer, F.M. Klis, J.H. Sietsma, B.J.C. Cornelissen, Fungal Genet. Biol. **27**, 275 (1999)
78. R.L. Brandao, I.M. Castro, J.B. Passos, J.R. Nicoli, J.M. Thevelein, J. Gen. Microbiol. **138**, 1579 (1992)

Chapter 14
Medical Applications of Magnetic Nanoparticles

Matteo Avolio, Claudia Innocenti, Alessandro Lascialfari, Manuel Mariani, and Claudio Sangregorio

Abstract The increased ability in manipulating matter at the nanoscale has paved the way towards the creation of a plethora of novel systems endowed with extremely appealing properties exploitable in a wide number of clinical applications, the two most prominent being, undoubtedly, Magnetic Resonance Imaging (MRI) and Magnetic Fluid Hyperthermia (MFH). In this Chapter, we review a few recent examples to convey to the reader a picture of the promising role magnetic nanoparticles (MNPs) may play in the medicine of the next future. After a general overview of the two techniques, we summarize the physical principles at their base to provide the reader the necessary tools to understand limits and advantages of employing MNPs as contrast agents in MRI and heat mediators in MFH. Among the countless examples of MNP-based materials proposed in the recent years for these applications, we select and report in detail some of the most representative and promising ones to underline the challenges that this branch of the material science must address to interplay with the complexity of the human body. Finally, we try to photograph the

M. Avolio · A. Lascialfari · M. Mariani
Dipartimento di Fisica, INFN and INSTM, Università degli Studi di Pavia, Via Bassi 6, 27100 Pavia, Italy
e-mail: matteo.avolio01@universitadipavia.it

A. Lascialfari
e-mail: alessandro.lascialfari@unipv.it

M. Mariani
e-mail: manuel.mariani@unipv.it

C. Innocenti (✉)
Dipartimento di Chimica "U.Shiff", Università degli Studi di Firenze and INSTM, Via della Lastruccia 3-13, Sesto Fiorentino (FI) 50019, Italy
e-mail: claudia.innocenti@unifi.it

C. Innocenti · C. Sangregorio
ICCOM, CNR, Via Madonna del Piano 10, Sesto Fiorentino (FI) 50019, Italy
e-mail: claudio.sangregorio@iccom.cnr.it

A. Lascialfari
Dipartimento Di Fisica, INFN and INSTM, Università degli Studi di Milano, Via Celoria 16, 20133 Milan, Italy

D. Peddis et al. (eds.), *New Trends in Nanoparticle Magnetism*,
Springer Series in Materials Science 308,
https://doi.org/10.1007/978-3-030-60473-8_14

state of the art of the clinical applications, which, mainly concerning MFH, is in continuous evolution.

14.1 Introduction

In the recent past, magnetic nanoparticles (MNPs) emerged as the most promising building blocks to realize multifunctional devices to be used in the biomedical field (Fig. 14.1). The greatest interest for MNPs resides in the possibility of exploiting their unique properties for both diagnostic and therapeutic purposes (i.e., theranostics). For example, the interactions between the particle's magnetization and the ^{1}H nuclear magnetization strongly affect the nuclear relaxation times, making MNPs powerful contrast agents for magnetic resonance imaging (MRI) applications [1]. Furthermore, the interaction of the MNP's magnetization with an alternating magnetic field of appropriate frequency and amplitude can cause a strong heating of the magnetic cores subsequently released to the surrounding tissues. This effect is known as magnetic fluid hyperthermia (MFH) [2–4], and it is already applied in clinics for the therapeutic treatment of glioblastoma, prostate cancer, and some other tumors [5]. Moreover, it has been extensively demonstrated in the literature that the MNP surface can be easily functionalized with ligands or biomolecules for the selective accumulation in target tissues (chemical targeting) [6]. Although simple in principle, the many barriers posed by biological processes make the application of this approach in clinics still

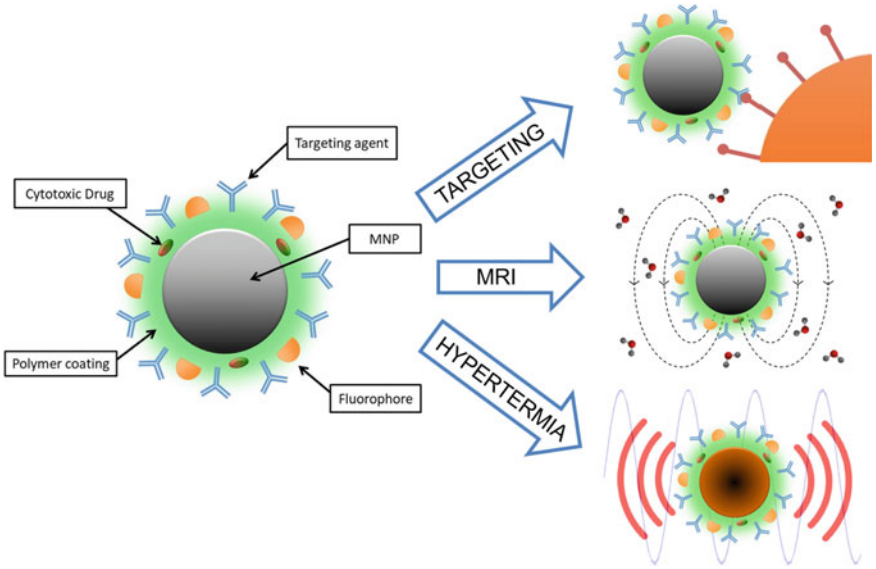

Fig. 14.1 Schematic representation of a multifunctional magnetic nanoparticle with its main components and some of its most interesting applications in the biomedical field

far from being realized. MNPs could offer a unique possibility to by-pass this hurdle, as they can be driven to a desired site by the application of an external magnetic field gradient (magnetic targeting) [7].

An overview of some of the many applications where MNPs have been proposed as main players is provided in Sect. 4.1 (Smart platforms for biomedical applications). Here, we will focus on the two most important ones, namely, magnetic resonance imaging (MRI) and magnetic fluid hyperthermia (MFH), whose impact has already been (MRI) or is expected to be in the next future (MFH) fundamental in clinics, both as diagnostic and therapeutic tools [1].

14.2 Magnetic Resonance Imaging and Magnetic Fluid Hyperthermia: An Overview

Nuclear magnetic resonance (NMR) is a powerful technique that has come into being in 1946, when pioneer scientists as Bloch [8] and Purcell [9] firstly discovered the possibility to manipulate the time evolution of the nuclear magnetization by applying radiofrequency (RF) pulse sequences. The RF field has the capability to slightly perturb a system generating a resonance signal that behaves as a fingerprint of its characteristics, therefore, providing multiple information about the system itself. The type of information acquired by the NMR analysis depends on the design of the RF pulse sequence [10, 11]. The advantages of NMR are its high versatility and a very low invasiveness, since differently from other diagnostic techniques such as computed tomography (CT), it makes no use of ionizing radiations. Moreover, the versatility of this technique, which allows obtaining multiple information depending on the RF pulses sequence designed for a specific diagnostic purpose, led to a rapid spread of magnetic resonance imaging (MRI) apparatus in the hospitals [12–15].

The dissemination of different kinds of contrast agents (CAs), which increased the readability of the MR images, has improved further the development of MRI in the latest decades. At first, paramagnetic molecules (for example, Gadolinium-based agents) were applied to affect the nuclear relaxation times on the site of interest [16]. Subsequently, and particularly in the latest years, an increasing interest in the field of nanomedicine led to the development of nanoparticles made of biocompatible magnetic materials, typically iron oxides, which act as efficient CA.

Contrary to MRI, which has been routinely employed in clinics for several years, magnetic fluid hyperthermia application as therapeutic tool is still limited to a few experimental cases. Despite MFH has been approved in Europe for glioblastoma multiforme, clinical trials involving this technique have been conducted solely by MagForce (Berlin, Germany) for treating glioblastoma, prostate, and other kinds of cancers [17, 18]. Although some important steps have been done in the last decades, further work is needed for translating MFH to the clinic, and thus, fully exploit the great potential of this promising cancer therapy. The attractiveness of MFH

treatment, indeed, relies in its potential for greater selectivity, as MFH allows extra-heating, induced by the controlled application of an external alternating magnetic field (AMF), only in the region where the heat mediators (MNPs) are localized. In principle, MNPs are delivered near or inside the tumor cells where, depending on the temperature reached, it is possible to cause an irreversible damage without tissue necrosis (41–46 °C) or the complete necrosis of the tumor by thermoablation (more than 46 °C, up to 56 °C) [19, 20]. It has been also demonstrated that, in the case of moderate temperature increase (41–43 °C), the hyperthermia treatment enhances the effect of conventional therapies, as chemotherapy or radiotherapy [21, 22]. The temperature rise of the tumor cells and the consequent destroying effect is directly related to the heating power of the MNP, i.e., its specific absorption rate (SAR) value. In the last decades, the number of publications proposing new nanodevices based on inorganic core with large SAR values has increased exponentially [23]. The macroscopic temperature rise of the target tissue, however, is not the only parameter to be considered. The capability of the nanoplatform to be internalized by the cells [24] or to provide a "Magnetically Mediated Energy Delivery" (MagMED [25]) able to amplify the effectiveness of the construct are additional items that must be taken into account. For efficiently realizing a nano-device with the best performance and multiple features, it is thus important to make it able to reach the target, by direct injection or by chemical targeting delivery, and directly interact with the tumor cells and sub-cellular elements. The mean to achieve this goal is the surface coating of the MNPs, which determines their interaction with the cells and all the elements of the physiological environment and provides multiple functionalities. The major aim of the surface coating is indeed to protect the magnetic core from degradation while preserving its properties over time, and at the same time, to allow overcoming the physiological barriers, increasing the circulation time by shielding the MNP inorganic core from the reticulo-endothelial system captures [26, 27]. The complexity of the MNPs bio-distribution inside the body and their interaction with it at all the scales, from organs, down to sub-cellular elements, makes very hard predicting the behavior, and thus, in vivo effectiveness of all the proposed nanosystems. The need of a better knowledge of MNP fate inside the body and the comprehension of the cellular uptake mechanisms are at the base of the development of this therapeutic approach, which represents a potential breakthrough for cancer treatment.

14.3 Physical Principles

14.3.1 Magnetic Resonance Imaging

In nuclear magnetic resonance (NMR), a radiofrequency (RF) signal is collected from the nuclei of a given species to investigate the properties of matter. Nuclear spins are in fact used as local probes, undergoing static homogeneous magnetic field

H_0, to study, thanks to the hyperfine interactions, the spin dynamics experienced by the nuclei depending on the environment surrounding them.

Although NMR is a low-sensitivity technique, since it is necessary to collect the signal of a huge number of nuclei (at least 10^{-4} to 10^{-6} mol) to detect a macroscopic nuclear signal (in a common field of 1.41 T used in MRI applications only 1 nucleus over 40,000 is aligned to H_0 and contributes to the generation of the NMR signal), clinical MRI is generally exploited by collecting the signal of hydrogen (^{1}H) nuclei, which are characterized by a strong gyromagnetic ratio ($\gamma = 42.5756$ MHz/T) and a high concentration water-rich soft tissues. This allows MRI images to have a very good space resolution, a property that merged with the MRI capability of investigating internal organs non-invasively, has made this technique one of the most powerful and intriguing modalities to perform in vivo imaging both in clinics and in the biological research field [28].

The parameters measured in a NMR experiment, once the nuclei are driven out of thermal equilibrium by radiofrequency pulses, are the absorption spectrum, obtained from the Fourier Transform of the NMR signal, and the relaxation times T_1 and T_2 (nuclear spin–lattice and spin–spin relaxation times, respectively). T_1 measures the interval for the recovery of the thermal equilibrium of the longitudinal component of the nuclear magnetization, governed by the interactions between the spins and the lattice (*i.e.*, the surrounding environment). T_2 describes the vanishing of transverse components of the nuclear magnetization, driven by the interactions among the nuclear spins. However, other factors besides the atomic and molecular mechanisms here cited, as the inhomogeneities of the field H_0, also contribute to the decay of the transverse magnetization in real NMR experiments, leading to the measurement of an "effective" T_2* always faster than the "real" T_2.

The possibility to produce a MR image of the body comes from the peculiar characteristics of each human tissue. Soft tissues as fat or muscle, hard tissues as bones, liquid tissues as blood or cerebrospinal fluid, are all characterized by different amount of ^{1}H nuclei (in most cases mainly belonging to water) and different T_1 and T_2 relaxation times, which allow to collect a pixel-by-pixel signal subsequently associated to a gray scale (i.e. to an image contrast). In particular, the NMR signal acquired in an MRI experiment can be expressed as:

$$S(t) \propto \rho(^1\mathrm{H})\, \mathrm{e}^{-\mathrm{TE}/T_2}\left(1 - \mathrm{e}^{-\mathrm{TR}/T_1}\right)\mathrm{e}^{-bD} \tag{14.1}$$

where $\rho(^1\mathrm{H})$ is the proton density within the analyzed object, TE (echo time) and TR (repetition time) are characteristic parameters of the sequence which can be adjusted by the operator, and the last term accounts for diffusive phenomena within the object, with D the diffusion coefficient of the medium. Choosing different values of TE and TR compared to the ones of the relaxation times, it is possible to obtain MR images that are proton density-weighted, T_1-weighted orT_2-weighted, thus changing the image contrast among tissues for obtaining different diagnostic information [29].

In a classic NMR experiment, the signal is collected from all the resonant nuclei of the system in the presence of the static homogeneous magnetic field H_0, thus

no information about their spatial distribution can be obtained. The main difference between NMR and MRI techniques is the ability of the latter to give information on the localization of the nuclei by superimposing to H_0 a combination of gradients along the three directions, causing a bijective correspondence between magnetic field value and the nucleus position. These conditions are the basis for the methods of image reconstruction first described by Lauterbur and Mansfield in 1973, who were awarded with the Nobel prize in medicine in 2003 [12, 14].

An easy formalism that allows describing the MR image reconstruction is the one based on the Fourier Transform (FT) operation [29]. First, the signal produced over the acquisition time by the ^{1}H spins can be written as

$$S(t) = \int d^3 r \rho(\vec{r}) \mathrm{e}^{i(\Omega t + \Phi(\vec{r},t)} \tag{14.2}$$

where Ω and Φ are the demodulation frequency and the spin phase in a given position of the space. In presence of field gradients, by introducing three new variables, $k_x = \gamma G_x t_x/2\pi$, $k_y = \gamma G_y t_y/2\pi$ and $k_z = \gamma G_z t_z/2\pi$, it is possible to define the k-space, which is related to the real space by the FT operation. An equivalent expression for the signal coming from the nuclei can therefore be written as

$$S(\vec{k}) = \int d^3 r \rho(\vec{r}) \mathrm{e}^{-i2\pi \vec{k}\cdot\vec{r}}. \tag{14.3}$$

The MR image can be obtained by the inverse FT of the information $S\left(\overrightarrow{k}\right)$ collected in the reciprocal space (Fig. 14.2), i.e.,

$$\rho(\vec{r}) = \int d^3 k S(\vec{k}) \mathrm{e}^{i2\pi \vec{k}\cdot\vec{r}}. \tag{14.4}$$

The MRI acquisition procedure can be consequently described as a mapping along tunable trajectories of the k-space, which can be further converted into an image in

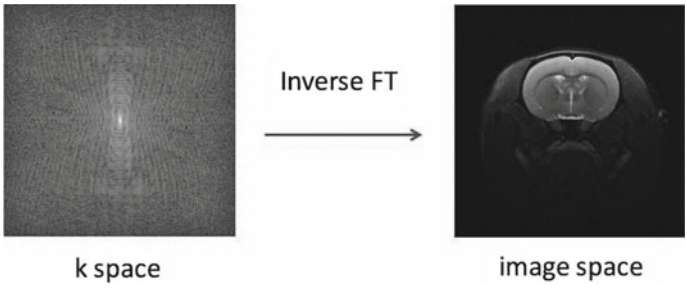

Fig. 14.2 Example of an MRI image acquired in the k-space (row data image) and the final MRI image in the real space obtained by mean of the Inverse Fourier Transform. Reprinted with permission of Società Italiana di Fisica from [28]

the real space through an inverse FT operation (Fig. 14.2). For the sake of clarity, it is necessary to note that this formalism can be applied only if the k-space is sampled continuously. This is not the common case, since the k-space is generally sampled discretely at Δk intervals. It is therefore necessary to modify the previous expressions to consider a Discrete Fast Fourier Transform (DFFT) operation, which produces a matrix of voxels in the 3D space.

14.3.2 Magnetic Fluid Hyperthermia

The capability of superparamagnetic materials to absorb energy from an external alternating magnetic field (AMF) is due to the hysteretic behavior induced by the lag of the magnetization to follow the external field. Unlike bulk ferro/ferromagnetic materials, for which the magnetic hysteresis depends on the instantaneous reorientation of the magnetic domains, single domain MNPs present magnetic irreversibility only if the field variation is faster than the characteristic time of the magnetization reversal. In both cases, however, the energy stored for each field cycle can be quantified by the hysteresis area. In a very general way, thus, the heating efficiency, or SAR, i.e., the energy adsorbed and converted in full into heat per unit of mass, can be defined as follows:

$$\mathrm{SAR} = \mu_0 \nu \oint M(H)\mathrm{d}H \tag{14.5}$$

where ν is the frequency of the AMF, that is the number of field cycle repetition in the unit of time. The evaluation of the area of the hysteresis is not an easy task, as it depends on the features of the material and can be hardly estimated a priori, particularly when minor loops are concerned, as in the case of MFH applications. On the other hand, the experimental measurement of this quantity, if feasible in principle for multidomain material, becomes impossible for superparamagnetic material, where the hysteresis area extent varies with the field scan speed and thus with the acquisition time. To overcome this problem, some models, that provide values whose approximation mainly depends on the mean size of the MNPs and on the strength of the applied field, H_0, can be adopted. Among the theoretical formulations, the most popular for mono-dispersed MNPs, is the linear response theory (LRT) [30], the main assumption of which is that the magnetization varies linearly with the oscillating magnetic field as

$$M(t) = \chi \cdot H(t) = H_0\left(\chi' \cos 2\pi \nu t + \chi'' \sin 2\pi \nu t\right) \tag{14.6}$$

where χ' and χ'' represent the in-phase and out-of-phase components of the magnetic susceptibility, respectively, that, intrinsically, depends on the field frequency. This hypothesis is valid when the magnetic anisotropy barrier, KV, and the field oscillation amplitude are small compared to thermal energy, $k_B T$, i.e., $KV/k_B T \ll 1$ and

$\mu_0 \mu H_0 / k_B T \ll 1$, where K is the anisotropy constant, V and μ are the mean volume and magnetic moment of the MNPs, respectively. When these conditions are met, the dissipated power is given by

$$\mathrm{SAR} = \frac{\pi \nu \mu_0 H_0^2}{\rho} \cdot \chi'' = \frac{\pi \nu \mu_0^2 H_0^2 M_S^2 V}{3 \rho k_B T} \cdot \frac{2\pi \nu \tau_{\mathrm{eff}}}{1 + (2\pi \nu \tau_{\mathrm{eff}})^2} \tag{14.7}$$

where ρ is the density of the material, and τ_{eff} is the effective relaxation time of the magnetization, which, for an MNP system suspended in a fluid matrix, is

$$\frac{1}{\tau_{\mathrm{eff}}} = \frac{1}{\tau_N} + \frac{1}{\tau_B} \tag{14.8}$$

where $\tau_N = \tau_0 e^{\frac{KV}{k_B T}}$, is Néel (or "internal") relaxation time, and $\tau_B = \frac{3\eta V_H}{k_B T}$, is the Brown relaxation, where V_H is the hydrodynamic volume and η the viscosity.

Equation (14.7) allows one to foresee the conditions for SAR maximization, occurring when $2\pi \nu \tau_{\mathrm{eff}} = \omega \tau_{\mathrm{eff}} = 1$, namely when the relaxation time is equal to the characteristic time of the measurement (in this case the inverse of the applied field angular frequency, $2\pi\ \nu$). With the aid of (14.7), the role of the parameters which mostly influence the heat power dissipation (saturation magnetization, magnetic anisotropy, and mean particle diameter) can be evaluated analytically, as in Fig. 14.3, where the typical example of magnetite MNPs are reported. Figure 14.3a shows that the SAR has a well pronounced, sharp maximum arising from the sum of the contribution of Néel and Brown relaxations. Evaluations of Fig. 14.3b, c demonstrate how

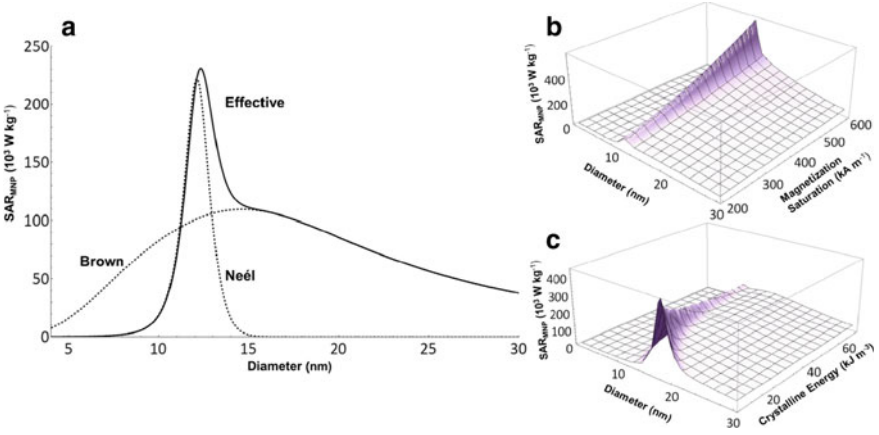

Fig. 14.3 Dependence of SAR for monodisperse magnetite MNPs evaluated from (14.7) on **a** size ($K = 15\mathrm{kJm}^{-3}$, $M_S = 450\mathrm{kAm}^{-1}$), **b** magnetization saturation ($K = 15\mathrm{kJm}^{-3}$), and C) magnetic anisotropy energy ($M_S = 450\mathrm{KAm}^{-1}$). Calculations were performed for $H_0 = 10\mathrm{kAm}^{-1}$ and $f = 500$kH z. Reprinted with permission from [31]

the maximum of SAR grows as the magnetization saturation increases and as the magneto-crystalline energy decreases, respectively.

The LRT model provides useful indications to foresee the behavior of a magnetic nanomaterial under the application of an AFM and thus to tune its main features to optimize the heating process. With this purpose, many other, more sophisticated, models have been developed in the past years to make the prevision more and more reliable and thus to address the research on material synthesis toward more effective devices. Efforts have been made to extend the LRT model by perturbative methods to include the treatment of larger MNPs, the magnetic behavior of which is at the borderline between the frequency independent description of the Stoner-Wohlfarth model and the pure superparamagnetic model referring to the Neél theory [32]. Beside analytical models to attempt the description of the MNP behavior in this transition region, computational models, mainly based on Montecarlo simulations, have been recently developed for accurately evaluating the SAR of a specific nanomaterial as well as to assess the temperature rise in the surrounding tissues [23, 33].

As established by (14.7), SAR is proportional to the square of the applied field amplitude, H_0, and the operating frequency ν. In principle, thus, it might be thought that the simplest way to increase SAR is to increase the parameters of the external applied AMF. However, only a narrow window of H_0 and ν are allowed for in vivo application. Figure 14.4 shows AMF exposure limit values beyond which eddy currents are generated in the tissues by the external electromagnetic excitation, which can lead to peripheral nerves and heart tissue uncontrolled, dangerous stimulations [34]. The gray area represents the safety area in terms of frequency and field strength, in which it is possible to operate without side effects. In the figure there are also reported the field values used in clinical trials carried out by Jordan et al. [17, 18]

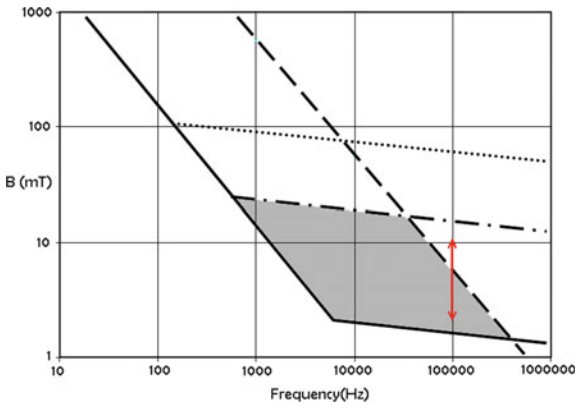

Fig. 14.4 Stimulus thresholds of peripheral nerves and heart tissue under the action of an AMF for an average adult. The dotted line represents the threshold for cardiac tissues, the dot-dashed line the peripheral nerves while the dashed line the threshold beyond which eddy current are generated. Red arrow represents experimental conditions in MFH clinical trials. Adapted with permission from [34]

(red arrow), which partially exceed the theoretical limit. Indeed, these estimates were obtained by theoretical modeling and have not been experimentally verified on human beings yet. In the absence of a thorough clinical study on safety limits and regulations about human body exposure to AMF, the human tolerance limit routinely accepted by the scientific and physician communities, concerns a constraint on the maximum value of the product $H_0\nu$ which is recommended not to exceed $4.84 \times 10^8 \mathrm{Am}^{-1}\mathrm{s}^{-1}$ [35] or $5 \times 10^9 \mathrm{Am}^{-1}\mathrm{s}^{-1}$ [36] for total or partial body exposure, respectively. To better understand the need of a reformulation of this issue, we would like to remind that the first of this threshold values, also known as Brezovich condition, which is the most popular and cited, dates by 1988, and was empirically established by recording the subjective discomfort of a few adults directly exposed to an increasing AMF.

14.4 Design of MNPs as Contrast Agents and Heat Mediators

In common clinical applications of MRI, the static field $\mu_0 H_0$ has a maximum value of 1.5 T. Lowest values of $\mu_0 H_0$, around 0.2–0.5 T, are sometimes applied for the imaging of the joints of the body. Higher values of $\mu_0 H_0$, and particularly systems working from 3 to 11 T, would allow to reach outstanding values of contrast, spatial resolution and signal-to-noise ratio in the final image. However, these systems are nowadays being tested only for research purposes, since the application of such strong fields on the human body is susceptible to (i) high values of SAR, (ii) low RF field penetration through the body at high resonant frequencies, and (iii) other potentially dangerous side effects, which need to be carefully evaluated before moving to the clinical practice [19–21]. The amplitude of the magnetic field gradients is instead much weaker, since for clinical applications it reaches a maximum value of about 45 mT/m.

To increase the contrast of the MR image and, especially, to better define the borders of a lesion are the main goals of MRI in clinics. For this purpose, magnetic CAs are administered to the patient and targeted to the organ or tissue of interest. Here, they generally shorten the characteristic relaxation times of the tissue, allowing its better detection in the MR image [37]. Molecules that mainly shorten T_1 are called positive CAs, since according to (14.1) they increase the brightness of the interested region. On the contrary, negative CAs have the property of shortening mainly T_2, and consequently to darken a portion of the image.

The efficiency of a CA is quantified through the longitudinal (r_1) or transversal (r_2) relaxivity, which is defined as

$$r_i = \frac{1}{C}\left(\frac{1}{T_{i,\mathrm{obs}}} - \frac{1}{T_{i,\mathrm{diam}}}\right), \quad i = 1, 2, \ldots \tag{14.9}$$

where C is the molar concentration of the magnetic center of the CA in mmol/L, and $T_{i,\text{obs}}$ and $T_{i,\text{diam}}$ are the relaxation times of the water protons with and without the magnetic contribution coming from the CAs, respectively [38]. The larger the difference in the relaxation rates induced by the CA, the higher its efficiency.

MRI CAs are divided in two main categories: paramagnetic and superparamagnetic compounds. Paramagnetic compounds are typically made of lanthanides or metal ions embedded in an organic shell, as for example Gd-based molecules [39–41]. Dipolar fluctuating magnetic fields characterize these ions, due to the presence of one or more free electrons. Commercial superparamagnetic compounds are instead made of a low crystallinity, non-stoichiometric iron oxide core of about 5 nm diameter coated by polymers or sugars with a total diameter of about 150–200 nm [42–44]. The particle magnetic moment (also called "superspin") fluctuates due to the thermal energy and interacts with the nuclear magnetization of the surrounding water protons. All these CAs generally present non-specificity and diffuse freely in the extracellular space.

In the latest years, a lot of attention has been focused on the development of MNPs, which can be used as multifunctional agents in the biomedical field, including the capability to work as CAs in MRI [34, 45–51]. These particles are typically made of an iron oxide magnetic core with mean size lower than 20 nm. Magnetite (Fe_3O_4) and maghemite (γ-Fe_2O_3) are generally the preferred materials due to their low toxicity for the body, which has its own metabolic pathways for the iron absorption and disposal. The very small size is often preferred, since small MNPs better interact with the cells and remain for a longer time in the bloodstream.

Iron oxide superparamagnetic nanoparticles (SPIO, i.e., superparamagnetic iron oxides, core size bigger than 50 nm or USPIO, i.e., ultra-small superparamagnetic iron oxides, core size smaller than 50 nm), could be applied as T_2* relaxation enhancing CAs. The susceptibility effects of the iron oxide cores are indeed able to determine a signal loss and consequently to darken the MR image in the region where they accumulate, increasing the contrast in the region of interest. T_2*-weighted pulse sequences are generally applied to acquire a MR image after SPIO or USPIO administration to the patient. From a technical point of view, differences between the T_2* measured before and after the administration of SPIOs could be correlated to the concentration of iron in the region of interest. However, the relation among the amount of SPIOs administered to the region and the T_2* enhancement obtained in the image is linear only when the iron concentration is low [52]. It will be possible to obtain good enhancement in the MR image giving small amounts of SPIOs only when strong magnetic fields, as the ones used by 7.0 T MRI apparatus, will be available in the clinical practice. Until then, the iron concentration evaluated by the measured ΔT_2* is susceptible to be highly inaccurate. Moreover, this inaccuracy is increased by the magnetic field inhomogeneities typically unavoidable in an MRI setup [53–55].

In this framework, the T_2 enhancement was proved by Tong et al. [56] with a new method for coating and functionalizing superparamagnetic iron oxide nanoparticles with biocompatible DSPE-PEG copolymers. They systematically studied the

variation of T_2 as a function of coating thickness on MNPs of two different diameter (5 and 14 nm) and found that SPIOs with 14 nm core and DSPE-mPEG1000 coating provides the highest T_2 relaxivity per-Fe atom among iron oxide nanoparticles reported to date. Also, by means of an in vitro assay mimicking an enzyme-linked immunosorbent assay (ELISA) they demonstrated that 14 nm SPIOs coated with DSPE-mPEG1000 and conjugated with specific antibodies can be used for molecular targeting with very high detection sensitivity. Moreover, they proved a great potential of these SPIOs as MRI CAs for detection of early stage tumors in animal studies of in vivo tumor imaging. In details, they implanted human U87 glioblastoma cells subcutaneously in nude mice to induce a tumor, that was subsequently investigated both before and after DSPE-PEG coated SPIOs administration using a 7 T MRI scanner. Results showed a significant enhancement of the contrast in the tumor region 1 h after the injection of 14 nm SPIOs through the tail vein, confirming both the high T_2 relaxivity and the targeting capability of these systems.

Although SPIOs in MRI are more suitable to obtain T_2* relaxation enhancement, also T_1-weighted pulse sequences can be executed [57]. However, the contrast effect is generally appreciable only in the case of the smaller USPIOs, since the required close interaction between protons and CA can be hampered by the thickness of the coating on the MNP [58, 59]. In particular, small Manganese ferrite nanoparticles have been proved to efficiently work as positive contrast agents for MRI by Li et al. [60], who first reported T_1-enhanced effects in in vivo MR Images. Despite the high toxicity of Manganese compounds limits their usage in clinical applications, 2.2 nm superparamagnetic $MnFe_2O_4$ nanoparticles resulted to be non-toxic in vitro and to have such a small r_2/r_1 ratio to allow their usage as positive MRI CAs. MR Images of mice livers and kidneys acquired under a 4.7 T magnetic field and using T_1-weighted sequences showed high positive contrast after administration of Manganese ferrite MNPs, in comparison with the pre-contrast images of the control. Indeed, the longitudinal relaxivity of these particles resulted to be much higher than the typical r_1 values of molecular Mn agents or Gd-based CAs, being $r_1 = 6.61\ mM^{-1}\ s^{-1}$ at 4.7 T. Moreover, thanks to the ultra-small size of the particles, which allow long blood circulation time, MR Images were observed to remain brighter than those of controls for more than 10 h [60].

The biocompatibility of MNPs for clinical application is controlled by using appropriate coatings of organic moieties, like sugars or other polymers, which are attached to the core surface and prevent MNPs elimination by the immune system of the body. Moreover, the coating can be exploited for multiple and even active functions: (i) it can be functionalized with antibodies or other molecules which allow selective targeting of an objective within the body [61]; (ii) drugs can be embedded within the coating to be specifically sent to malignant cells (i.e., cancer cells) and here to work as therapeutic agents [47, 48]; (iii) fluorescent molecules can be attached to the coating, allowing for the MNPs localization within the body thanks to their light emission.

In vitro and in vivo application of MNPs must face the problem of the particle toxicity, for which it is primarily necessary to better distinguish among SPIOs and USPIOs. Their different size is responsible for different fate of these particles inside

the body: SPIOs are sequestered by the Kupffer cells in the reticuloendothelial system, primarily in the liver, while USPIOs circulate longer into the blood before being captured by macrophages (monocytes) and to accumulate in liver and spleen [62, 63]. Particularly, the blood pool half-life of USPIOs in humans is more than 24 h [64], while for SPIOs it has been estimated to be shorter than 6 min [65]. More generally, the cellular uptake by monocytes increases with the particle size [59]; in this regard, Engberink et al. [59] reported a significant hypointense signal (increased r_2) coming from human monocytes labelled with 150 nm SPIOs compared to cells incubated with 30 nm USPIOs, proving a size-dependent uptake.

On the other hand, a high heating power, or SAR value, of the inorganic magnetic component of the nanodevice is the first requirement to assure its effectiveness for therapeutic application by MFH. In principle, this can be achieved by choosing a material with enhanced magnetic properties in its bulk phase and tuning them at the nanoscale as exemplified in Fig. 14.3. In fact, while the magnetization saturation and the magnetic anisotropy are intrinsic properties of the chosen material, its size and the size dispersion can be accurately tuned to fit the frequency of the external field [see (14.7)]. Based on this simple concept, many MNPs with different composition and morphological structure have been proposed as heat mediators for MFH. Unfortunately, most of those reporting huge SAR values are made of pure metal or metallic alloys, including potentially toxic elements, like cobalt [66, 67], which, due to their high concentration and weak chemical stability, have poor chance of being approved by the competent authorities in Europe and USA for use in medicine. Since the beginning, when MFH was proposed by Gilchrist in 1957 [68], iron oxide nanoparticles have been suggested as appropriate candidates for heat mediators because of their biological compatibility as the iron accidentally released can be recycled through the metabolic pathways. Also in this case the most commonly proposed materials are spinel ferrite magnetite (Fe_3O4) and maghemite (γ-Fe_2O_3) thanks to their superior magnetic properties, which, adopting simple, accurate synthetic procedures, can be maintained at the nanoscale size [69]. Nanoparticles of excellent crystallinity and chemical purity can be routinely obtained in the range of sizes established by the theory and confirmed by the experiments for optimizing the hyperthermic efficacy (12–20 nm for magnetite [70], and 15–25 nm for maghemite [71, 72]). In this class of materials, improvements have been done by using mixed ferrites ($M_xFe_{3-x}O_4$ where M is a divalent metallic cation), containing low percentage of other metals to not compromise the natural biocompatibility of the compound. Following this strategy, notable results have been recently reported for maghemite MNPs weakly-doped by magnesium ions [73]. Highly controlled synthetic procedure allowed preparation of monodispersed ($\delta < 10\%$) MNPs of $Mg_{0.13}$-γFe_2O_3 of 7 nm average size with giant (>10 kW/g) SAR value (Fig. 14.5). We stress that this result was obtained by applying an AFM within the tolerance limit (partial body exposure) and that the Mg-doping assures a good biocompatibility. It should be remarked, indeed, that, even though the tolerance limit condition needs a better definition, many of the highest SAR values reported in the literature [74] were obtained using field parameters well outside any theoretical or empirical constrains, making the translation to clinics trails unfeasible.

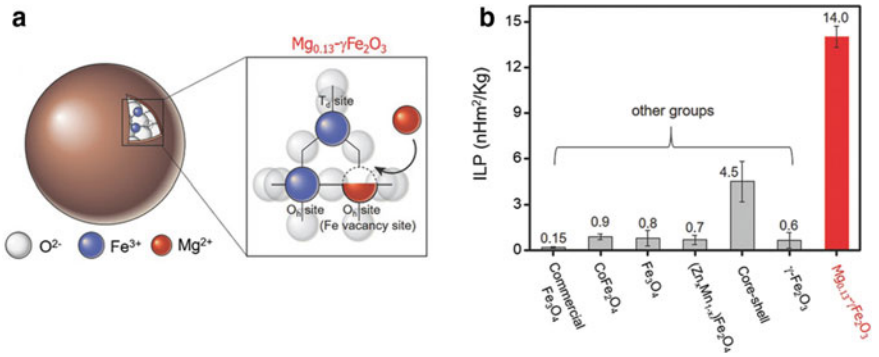

Fig. 14.5 **a** Diagram of spinel structure of $Mg_{0.13}$-γFe_2O_3 with the face-centered cubic lattices of oxygen enlarged on the right. **b** Comparison of ILP = SAR/$H\nu$ value of $Mg_{0.13}$-γFe_2O_3 MNPs to selected superparamagnetic nanoparticles reported in the literature and two commercial Fe_3O_4 MNPs (Feridex and Combidex), used for references. Adapted with permission from [73]

Another appreciable feature of the MNPs just mentioned is their ultra-small size, which, in principle, allows longer time circulation in the blood, a property becoming essential when chemical targeting through intravenous or "systemic" administration is envisaged. In the classical case of iron ferrites, the reduction of the average size of the constructs while keeping the high SAR values of magnetite or maghemite, has been obtained by partially substituting divalent iron ions of the spinel ferrite with much more anisotropic divalent cobalt ions, obtaining doped $Co_xFe_{3-x}O_4$ ferrites. A weak Co-doping (5% w/w) allows increasing SAR values of 3–5 times with respect to pure iron oxide MNPs of similar size grown within the biocompatible shell of human ferritin (Fig. 14.6) [24].

Other iron oxide-based samples with enhanced hyperthermic properties have been recently proposed in the literature, reflecting the renewed importance of this class of materials in the MFH context. Taking inspiration from the so called magnetosomes, naturally formed chains of cubic-shaped MNPs of 30–100 nm, the effect of the MNP

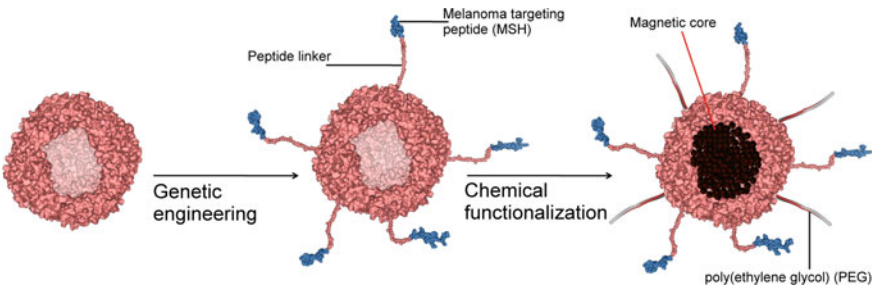

Fig. 14.6 Theranostic nanoplatform based on human ferritin (HFt) shell filled with a magnetic core of co-doped magnetite. The HFt protein is genetically functionalized with R-MSH peptide for melanoma cell targeting and conjugated with PEG. Reprinted with permission from [24]

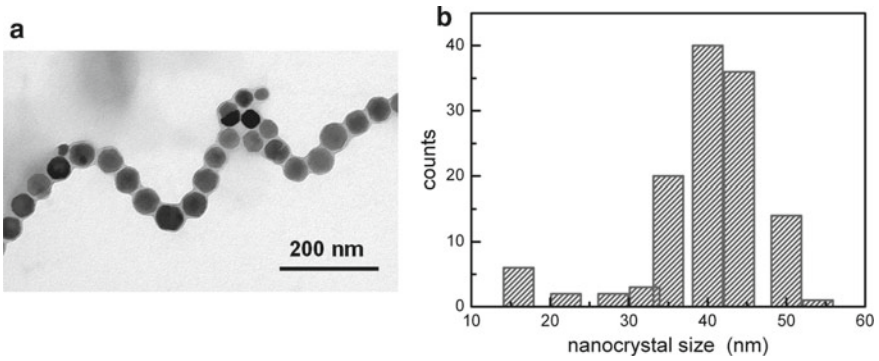

Fig. 14.7 Transmission electron microscopy image of MNPs extracted from *Magnetospirillum gryphiswaldense* and corresponding size distribution obtained from statistical analysis over around 200 MNPs. Reprinted with permission from [78]

shape and the interparticle interaction on the main magnetic properties that influence the heat capability has been deeply investigated [75, 76]. Good results were obtained for nanocubes of 20–40 nm, chemically or naturally synthesized [77, 78] and for strongly interacting cubic or spherical-shaped MNPs aligned in chain, as observed in bacterial magnetosomes (Fig. 14.7) [79]. Magnetic interparticle interaction and the consequent mutual disposition of the MNPs once they are introduced in the cellular environment, however, is not easily predictable. As recently discussed in [80], the uncontrolled interaction leading to a disordered aggregation in the cellular medium has a negative impact on the hyperthermal efficacy of MNPs, drastically reducing the heating power they show in water suspension. This result enlightens once again the complexity of the problem to realize an effective nanodevice for MFH and recalls how "robust" it must be so that its expected behavior is not altered by the biological interaction.

Despite this recommendation, more complex, multicomponent systems with dimer or core–shell architectures were also proposed [81]. Combination of ferrite with noble metals (Au, Ag) has been suggested for associating MFH with photothermal therapy, where heating is induced by plasmonic excitation in the metal component by a laser source of appropriate wavelength. In the field of combined therapy, however, it is worth to stress the good results obtained by using single component core in [82], where a large increase (2–5 times) of the heating power of 20 nm cubic MNPs of magnetite was obtained by simultaneous application of an AFM (12 mT, 110 kHz) and NIR laser irradiation (808 nm, 0.3 W/cm^2). DUAL-mode treatment was tested in vivo on subcutaneous tumors induced in mice and compared with MFH and laser irradiation modes applied separately. The advantage of the combined therapy is clearly demonstrated as it leaded to the complete eradication of the tumor, while the effect of the separate modalities showed significant, but partial regression.

The intense research activity of the last decades led to notable improvement of the hyperthermic properties of MNP mediators, reaching SAR (1–10 kW/g) that will

be hardly overcome in the future. These huge SAR values are useful to reduce the concentration needed to be targeted to the tumor, so limiting possible side effects after a direct injection of the MNPs suspension and, mainly, they open a new perspective for developing an effective systemic MNP administration by intravenous mode. Actually, delivery of MNPs to the target tumor by introduction in the blood stream and in situ accumulation is the main challenge and the most attractive potentiality of this cancer therapy. Up to now, however, the most effective MFH tests have been carried out by direct local injection into accessible, massive cancers, typically, subcutaneous tumors induced on mice. As demonstrated by estimates obtained through simple models [36, 83], indeed, the thermal dose (concentration of mediators multiplied by the SAR value and exposure time) needed to produce a sufficient heat to successfully eradicate cancer is very high because of the heat losses due to conduction towards surrounding tissue and to blood perfusion. Required thermal dose, and thus amount of MNPs deposited at the target, increases drastically for small cancer masses, including metastasis, where dissipative effects are more effective. As an example, a concentration of 1 mg/cm^3 of the best magnetic mediators mentioned above [73] is required to increase the temperature of a 3 mm tumor by 5 °C, and the concentration rapidly increases upon decreasing tumor size (~1/R^2). Up to now, the amount of MNPs delivered by systemic administration, i.e., cellular targeting or EPR (Enhanced Permeability and Retention) mechanism, seems far from satisfy these requirements [25].

A further effort of comprehension of the biological processes is also required to elucidate the killing mechanism induced by the MNP systems activated by an AFM in the cellular environment at the nanoscale. In many cases, indeed, significant results in destroying cancer cells have been observed without recording temperature increase of the culture medium up to hyperthermic range [84]. The hypothesis to account for this result is that local thermal or mechanical effects induced by the AFM application can lead to disruption of specific cellular structures. The absence of a macroscopic temperature increase suggested to rename these phenomena as 'magnetically mediated energy delivery' (MagMED) [25], instead of MFH. Investigations of the biological interaction at the nanoscale in order to promote MNP-cell internalization as well as achieving an effective capability of reaching the target cancer cell by systemic administration are fundamental to develop new engineered system to overcome the intrinsic limitations of MFH to treat cancer at the metastatic stage. The relevance of this task represents one of the most attractive challenge for the research activity in the field of nanotechnology application in medicine.

14.5 Clinical Applications: State of the Art and Perspectives

To date, several SPIOs and USPIOs compounds have been approved by Food and Drug Administration (FDA) for in vivo applications on humans. Feridex® (or

Endorem®, ferumoxides) and Resovist® (ferucarbotran) are two common examples, although they have been withdrawn from the market due to few number of users, and only Resovist® is still available in some countries [58, 63]. More recently, other SPIO CAs have been developed to be injected intravenously, as for example the Sienna plus® compound [85] that is exploited to localize sentinel lymph nodes.

SPIOs major quality in MRI is their higher capability to increase the image contrast compared to Gd-complexes. This quality comes from the high saturation magnetization of SPIOs and USPIOs and it is due to the presence of a higher number of magnetic ions, which are responsible for such magnetization [86, 87].

In addition to their capability as MRI CAs, SPIOs and USPIOs can be used also for other applications, for example to treat iron deficiencies in patient with specific diseases as the iron deficiency anemia caused by chronic kidney disease [88, 89]. The latter is for example the case of Ferumoxytol (Feraheme®, AMAG Pharmaceuticals, Cambridge, MA), a compound made of iron oxides nanoparticles with a carbohydrate coating. Ferumoxytol has also interesting properties as MRI CA but it is not yet approved for this purpose [62, 90].

In the latest years a great interest around SPIOs has born for application in stem cell labeling and tracking for cell therapy. This application consists in a long-term imaging of transplanted stem cells in vivo in order to monitor non-invasively their survival, differentiation, migration, etc.[57]. Stem cells are interesting due to their self-renewal and differentiation potency, i.e., their capability to perform several cell cycle divisions and to differentiate into various mature specialized cell types (i.e., muscle cells, bone cells, nerve cells, blood cells, etc.). Modern therapies aim to use human stem cells to repair defects in numerous diseases [91–96].

SPIOs were efficiently used to label hematopoietic and mesenchymal stem cells, or human prostate and melanoma cancer cells [97–102], or inflamed endothelial cells associated with atherosclerotic plaques [103]. With clinical 1.5 T or 3.0 T MRI scanners, the minimum detectable quantity of stem cells was reported to vary from 1000 to 100,000 cells, depending also on the cellular uptake. MRI performed on SPIO-labelled stem cells represents a safe, non-invasive and repeatable imaging technique to track mesenchymal stromal cells after transplantation, and it could facilitate clinical application of cell therapy.

To date, these particles have been tested for several clinical applications and particularly for interstitial MR lymphography [104–106], MRI for lymph node metastasis evaluation [107], MR angiography [108–114], inflammation process evaluation [115], molecular imaging for apoptosis detection [116], liver imaging [117], blood volume measurements [118] and MRI detection of amyloid plaques in Alzheimer's disease [119] and others [120].

Sentinel lymph node detection and dissection is the latest evolution of a common procedure in the field of metastases control and tumor staging, especially for patients affected by breast cancer. This technique consists in mapping the lymphatic path from the first lymph node, the sentinel one, to the regional nodes. The sentinel lymph node is the one with the highest probability of metastatic tumor occurrence, and whose pathologic examination allows a faithful staging of the regional nodes [104]. The sentinel lymph node identification usually consists in (i) injection of a short half-life

radiotracer, as the Technetium^{99m} ($T_{1/2} = 6$ h); (ii) injection of a carbon or blue dye directly around the tumor or close to the breast areola [104]. However, these two methods expose both the patient and the physician to dose risks and side effects related to the injection of dyes.

Interstitial MR lymphography exploiting USPIO CAs such as Resovist® or Sienna plus® are a promising alternative for this purpose as their small size enables them to reach the lymphatic system by crossing the capillary wall [63]. In this technique USPIOs are directly injected into the tumor region and the image acquisition is performed 18 or 24 h later.

Motomura et al. [106] reported excellent results from combining Computed Tomography (CT) lymphography and SPIO-enhanced MRI (Fig. 14.8). Particularly, in a study performed over 102 patient presenting breast cancer, macro-metastases were identified in the 100% of cases, while micro-metastases (smaller than 2 mm) were detected only in the 60% cases. Despite the very positive results reported, the current sensitivity and specificity of MRI, and the lack of statistically powered studies on this subject, make sentinel lymph node biopsy the best choice to date for detecting axillary nodes metastases in breast cancer patients.

MR angiography consists in exploiting MR techniques to visualize the blood vessels of the body, and even organs as heart and its chambers. It is a good alternative

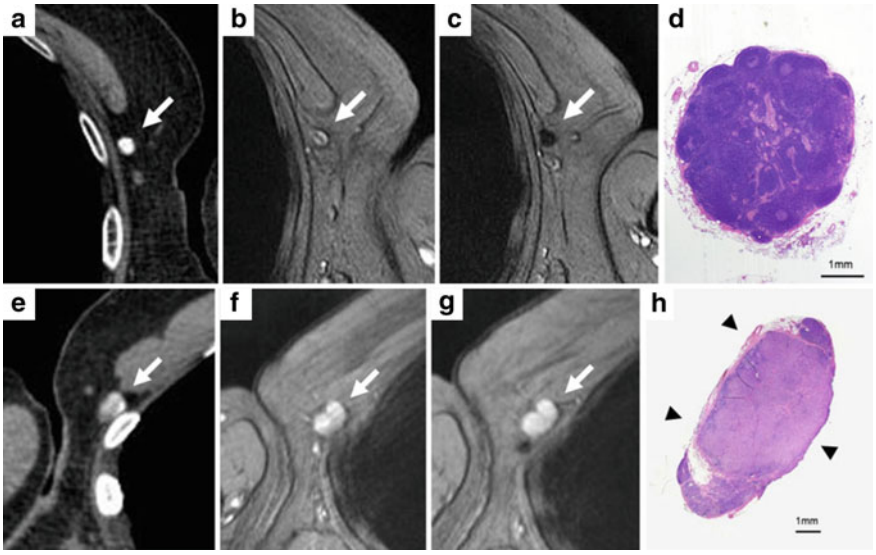

Fig. 14.8 Example of how MRI performed with Resovist® allows recognizing negative and positive metastatic lymph nodes. In **a** and **e** two sentinel nodes are identified (white arrows) with CT lymphography. The same node is in each case recognized also by pre-USPIO-contrast T_2*-weighted axial MRI in **b** and **f**. After USPIO injection, a strong contrast enhancement is recorded in (C), whose node is diagnosed as benign, but not in **g**, whose node is diagnosed as malignant. In **d** and **h** the histological analysis confirmed the diagnosis. Adapted with permission from [106]

to other medical imaging techniques, which allow the collection of similar information typically by using X-rays and appropriate opaque contrast agents injected into the blood vessels (i.e., fluoroscopy). The USPIO iron-based MRI CA Ferumoxytol is commonly used to produce enhanced T_1-weighted MR images of blood vessels, since it has a 14–15 h long intravascular half-life, allowing imaging to be repeated from the early arterial phase to the later ones with high signal-to-noise ratio and resolution [108–114].

SPIO-based CAs can be used to evaluate inflammatory responses in the human body, which can be caused by tumors or other serious diseases such as diabetes, atherosclerosis, multiple sclerosis and so on. All the inflammatory processes involve macrophages, whose tendency is to incorporate SPIOs. A first example of application of SPIOs for MR evaluation of inflammatory processes is the case of type-1 diabetes patients, which is strictly correlated to a pancreatic inflammation. A totally new approach based on SPIOs, and particularly on Ferumoxytol, described by Gaglia et al. [121], exploits SPIOs uptake by macrophages in the inflamed pancreatic region to obtain an enhancement in the MR image.

Another application of USPIOs and SPIOs is the diagnosis of atherosclerosis, and particularly the identification of high-risk atherosclerotic plaques. USPIOs (as Ferumoxtran-10) exploit the dysfunctional endothelium typical of atherosclerotic plaques to penetrate the macrophage-rich inflamed region, where they induce a MRI signal loss, allowing to differentiate among symptomatic and asymptomatic patients.

Unlikely MRI, where the use of MNPs is a routinely clinical practice, their application as heat mediators in tumor therapy by MFH is still at its infancy. Feasibility and efficacy of single or recursive MFH treatments of several kinds of cancers (glioblastoma, mammary and prostate carcinoma) by local MNPs injection have been demonstrated on animal models since the last decade of the 1900s.[122–125]. Concerning translation to humans, a first clinical application of interstitial MFH using MNPs for treating a patient with previously irradiated and locally recurrent prostate carcinoma was carried out by Johannsen et al. in the early 2000s [126]. After this pilot study, that demonstrated how MFH was feasible and well-tolerated, clinical trials on patients with glioblastoma multiforme, prostate, esophagus, and liver cancers were performed to investigate the potentiality of MFH [127–129]. MFH experimental applications and systematic clinical studies have been performed by Jordan et al. [127, 130–132] on patients suffering from glioblastoma multiforme, prostate and pancreas tumors. Since 2010, when MagForce company (https://www.magforce.de/en/home.html) presented the first prototype able to host a whole human body [133], a magnetic field applicator (NanoActivator®), operating with alternating magnetic field of 2–15 kA/m amplitude and 100 kHz frequency, is in current use at Charité Hospital in Berlin for treatment of glioblastoma.

Nowadays the NanoTherm® therapy has been clinically tested or is under clinical evaluation in other hospitals both in Europe and in the Unites States. At present the therapy has been applied on 90 patients suffering from brain cancer and 80 patients affected by inter alia, pancreatic, prostate, breast and oesophageal tumor were treated as part of a pilot study. The therapy procedure consists in the direct injection in the tumor mass of a high dose (ca. 30 mg per cm^3 of tissue) of NanoTherm®, a suspension

of coated spinel ferrite iron oxide MNPs of ca. 15 nm diameter, as heat mediators. Despite the apparatus and the magnetic fluid employed demonstrated the feasibility in clinical routine, significant benefits of MFH were obtained only in combination with radiotherapy (RT). Indeed, studies conducted by Wust et al. [134] using the first prototype of MagForce with different field applied on 22 patients with various types of recurrent tumors (sarcoma, rectal cancer, cancer cervix, ovarian cancer, and prostate cancer) previously heavily treated, led to unsatisfactory results. The SAR achieved in the target was 60–380 W/kg, depending on the pathology and on the maximum field applicable, but despite most of the tumor was heated to more than 40 C, the >42 °C overheating coverage was limited.

The feasibility and efficacy of the combination of MFH with standard RT on recurrent glioblastoma multiforme was established by the studies by Maier-Hauff et al. [132] conducted on 14 patients recruited in a phase I trial. After injection of a suspension of 12 nm iron oxide MNPs coated by aminosilane in the tumor, recursive sessions of MFH (median 6) and RT (median 30 Gy, by 2 Gy per session) were carried out. The combination treatment was well tolerated by all patients with minor or none side effects. The median maximum intratumoral temperature was 44.6 °C and the 90% of the tumor experienced a temperature over 40.5 °C, which, based on previous results, is too low to produce significant and durable damages to the tumor mass. In the phase II study [127] conducted on 59 patients, the MFH (twice weekly) and RT (five times/week) treatments were repeated with the same modality after direct injection of the MNPs suspension into recurrent glioblastomas. The main result concerning the patient survival is promising as the median overall survival (13.4 months) is more than the double of the typical 6 months median survival recorded in these cases [135, 136].

14.6 Conclusions

The increased ability in manipulating matter at the nanoscale has paved the way towards the creation of a plethora of novel systems endowed with extremely appealing properties exploitable in a wide number of clinical applications, the two most prominent being magnetic resonance imaging and magnetic fluid hyperthermia. In this chapter, we reviewed a few recent examples to convey to the reader a picture of the promising role MNPs may play in the medicine of the next future. Nevertheless, the exploitation of the full clinical potential of MNPs still requires addressing some major issues, mostly related to the complex interaction with the human body. Despite the countless examples of promising MNP-based materials, indeed, the translation to clinics is still limited to few, although effective, examples.

A major challenge is represented by site-specific delivery of a large enough amount of material via a systemic route, such as intravenous injection, which is opposed by the many biological barriers seizing foreign objects in the liver and spleen. On the other hand, a better understanding of the multifaceted MNP-cell interplay, is also mandatory to reach the goal. The solution of such a complex problem requires the

joint effort by researchers working in several different fields, from material scientists to physicians. Such an approach will allow to build-up an effective strategy to select the best candidates for clinical validation. The latter is indeed a long and expensive procedure, which often discourages pharmaceutical companies from investing resources unless a sure financial return is granted. To set in motion the process, a further step is a more effective dissemination of the many advantages provided by material nanotechnologies, aimed at increasing the awareness of hospital doctors.

References

1. A. Lascialfari, C. Sangregorio, Chimica Oggi-Chem. Today **29**(2), 20–23 (2011)
2. S. Dutz, R. Hergt, Nanotechnology **25**(45), 452001 (2014)
3. E.A. Périgo, G. Hemery, O. Sandre, D. Ortega, E. Garaio, F. Plazaola, F.J. Teran, Appl. Phys. Rev. **2**(4), 041302 (2015)
4. S. Laurent, S. Dutz, U.O. Häfeli, M. Mahmoudi, Adv. Colloid Interface Sci. **166**(1–2), 8–23 (2011)
5. A. Jordan, in *Hyperthermia*, in *Cancer Treatment: A Primer*. ed. by G.F. Baronzio, E.D. Hager (Springer, Boston, MA, 2006), pp. 60–63
6. K. Ulbrich, K. Hola, V. Subr, A. Bakandritos, J. Tucek, R. Zboril, Chem. Rev. **116**, 5338–5431 (2016)
7. C. Sun, J.S. Lee, M. Zhang, Adv. Drug Deliv. Rew. **60**(11), 1252–1265 (2008)
8. F. Bloch, Phys. Rev. **70**(7–8), 460 (1946)
9. E.M. Purcell, H.C. Torrey, R.V. Pound, Phys. Rev. **69**(1–2), 37 (1946)
10. C.P. Slichter, *Principles of Magnetic Resonance* (Springer-Verlag, Berlin, 1996)
11. A. Abragam, *The Principles of Nuclear Magnetism* (Oxford University Press, Oxford, 1961)
12. P.C. Lauterbur, Nature **242**, 190 (1973)
13. C. Guy, D. Ffytche, *An Introduction to the Principles of Medical Imaging* (Imperial College Press, London, 2000)
14. P. Mansfield, P.G. Morris, *NMR Imaging in Biomedicine* (Academic Press, New York, 1982)
15. M. Corti, A. Lascialfari, in *NMR-MRI, μSR and M̈ossbauer Spectroscopies*, in *Molecular Magnets*. ed. by P. Carretta, A. Lascialfari (Springer, Milan, 2007), pp. 89–110
16. R.N. Muller, S. Laurent, L. Vander Elst, A. Roch, in *NMR-MRI, μSR and M̈ossbauer Spectroscopies in Molecular Magnets*. ed. by P. Carretta, A. Lascialfari (Springer, Milan, 2007), pp. 71–87
17. M. Johannsen, U. Gneveckow, K. Taymoorian, B. Thiesen, N. Waldöfner, R. Scholz, K. Jung, A. Jordan, P. Wust, S.A. Loening, Int. J. Hyperth. **23**, 315–323 (2007)
18. B. Thiesen, A. Jordan, Int. J. Hyperth. **24**, 467–474 (2008)
19. S. Mornet, S. Vasseur, F. Grasset, E. Duguet, J. Mater. Chem. **14**, 2161–2175 (2004)
20. E. Garaio, O. Sandre, J.M. Collantes, J.A. Garcia, S. Mornet, F. Plazaola. Nanotechnology **26**, 15704 (2015)
21. F. Mohamed, P. Marchettini, O. Stuart, M. Urano, P. Sugarbaker, Ann. Surg. Oncol. **10**, 463–468 (2003)
22. S.V. Spirou, M. Basini, A. Lascialfari, C. Sangregorio, C. Innocenti, Nanomaterials **8**, 401–4022 (2018)
23. C. Blanco-Andujar, F.J. Teran, D. Ortega, in *Iron Oxide Nanoparticles for Biomedical Applications*, 1st edn., ed. by L. Sophie and L. Mahmoudi (Amsterdam, Elsevier, 2018), p. 197–245.
24. E. Fantechi, C. Innocenti, M. Zanardelli, M. Fittipaldi, E. Falvo, M. Carbo, V. Shullani, L. Di Cesare Mannelli, C. Ghelardini, A.M. Ferretti, A. Ponti, C. Sangregorio, P. Ceci, ACS Nano **8**, 4705–4719 (2014)

25. B. Kozissnik, A.C. Bohorquez, J. Dobson, C. Rinaldi, Int. J. Hyperthermia **29**(8), 706–714 (2013)
26. S. Mirsadeghi, S. Shanehsazzadeh, F. Atyabi, R. Dinarvand, Mater. Sci. Eng. C **59**, 390–397 (2016)
27. K. Riehemann, S.W. Schneider, T.A. Luger, B. Godin, M. Ferrari, H. Fuchs, Angew. Chemie Int. Ed. **48**, 872–897 (2009)
28. A. Lascialfari, F. Filibian, C. Sangregorio, P. Carretta, Riv. Nuovo Cimento **36**, 211–271 (2013)
29. E.M. Haacke, R.W. Brown, M.R. Thompson, R. Venkatesan, *Magnetic Resonance Imaging: Physical Principles and Sequence Design* (Wiley, New York, 1999)
30. R.E. Rosenweig, J. Magn. Magn. Mater. **252**, 370 (2002)
31. A. Cervadoro, C. Giverso, R. Pande, S. Sarangi, L. Preziosi, J. Wosik, A. Brazdeikis, P. Decuzzi, PLoS ONE **8**, e57332 (2013)
32. J. Carrey, B. Mehdaoui, M. Respaud, J. Appl. Phys. **109**, 083921 (2011)
33. H. Mamiya, J. Nanomater. **2013**, 752973 (2013)
34. Q.A. Pankhurst, N.T.K. Thanh, S.K. Jones, J. Dobson, J. Phys. D: Appl. Phys. **42**(22), 224001 (2009)
35. I.A. Brezovich, in *Biological, Physical and Clinical Aspects of Hyperthermia*, ed. By B.R. Paliwal, F.W. Hetzel, M.W. Dewhirst (Medical Physics Publishing, Madison, WI, USA, 1988), p. 82
36. R. Hergt, S. Dutz, S., J. Magn. Magn. Mater. **311**, 187–192 (2007)
37. P. Caravan, J.J. Ellison, T.J. McMurry, R.B. Lauffer, Chem. Rev. **99**(9), 2293–2352 (1999)
38. R.N. Muller, *Encyclopedia of Nuclear Magnetic Resonance* (Wiley, New York, 1996), p. 1438
39. S. Laurent, L. Vander Elst, S. Houzé, N. Guérit, R. N. Muller, Helv. Chim. Acta **83**(2), 394 (2000)
40. S. Laurent, D. Forge, M. Port, A. Roch, C. Robic, L. Vander Elst, R. N. Muller, Chem. Rev. **108**(6), 2064 (2008)
41. E. Taboada, R. Solanas, E. Rodríguez, R. Weissleder, A. Roig, Adv. Funct. Mater. **19**(14), 2319 (2009)
42. D. Pouliquen, H. Perroud, F. Calza, P. Jallet, J.J. Le Jeune, Magn. Reson. Med. **24**(1), 75 (1992)
43. W. Reith, M. Forsting, H. Vogler, S. Heiland, K. Sartor, Am. J. Neuroradiol. **16**(1), 53 (1995)
44. M.F. Casula, P. Floris, C. Innocenti, A. Lascialfari, M. Marinone, M. Corti, R.A. Sperling, W.J. Parak, C. Sangregorio, Chem. Mater. **22**, 1739–1748 (2010)
45. A.G. Roca, R. Costo, A.F. Rebolledo, S. Veintemillas-Verdaguer, P. Tartaj, T. González-Carreño, M.P. Morales, C.J. Serna, J. Phys. D: Appl. Phys. **42**(22), 224002 (2009)
46. P. Tartaj, M.P. Morales, S. Veintemillas-Verdaguer, T. González-Carreño, C.J. Serna, J. Phys. D: Appl. Phys. **36**(13), R182 (2003)
47. C.C. Berry, J. Phys. D: Appl. Phys. **42**(22), 224003 (2009)
48. C.C. Berry, A.S. Curtis, J. Phys. D: Appl. Phys. **36**(13), R198 (2003)
49. Q.A. Pankhurst, J. Connolly, S.K. Jones, J.J. Dobson, J. Phys. D: Appl. Phys. **36**(13), R167 (2003)
50. J.B. Haun, T.J. Yoon, H. Lee, R. Weissleder, Nanomed. Nanobiotechnol. **2**(3), 291 (2010)
51. C.T. Yavuz, J.T. Mayo, W.W. Yu, A. Prakash, J.C. Falkner, S. Yean, L. Cong, H.J. Shipley, A. Kan, M. Tomson, D. Natelson, V.L. Colvin, Science **314**(5801), 964 (2006)
52. L.A. Crowe, Y.X. Wang, P. Gatehouse, J. Tessier, J. Waterton, P. Robert, G. Bydder, D.N. Firmin, in *Proceedings of International Society for Magnetic Resonance in Medicine*, vol. 13 (2005), p. 115
53. T. Cukur, M. Yamada, W.R. Overall, P. Yang, D.G. Nishimura, Magn. Reson. Med. **63**(2), 427–437 (2010)
54. W. Chen, Quant. Imag. Med. Surg. **5**(4), 583–591 (2015)
55. W. Chen, J. Magn. Reson. **274**, 13–23 (2017)
56. S. Tong, S. Hou, Z. Zheng, J. Zhou, G. Bao, Nano Lett. **10**(11), 4607–4613 (2010)

57. C. Chambon, O. Clement, A. Le Blanche, E. Schouman-Claeys, G. Frija, Magn. Reason. Imaging **11**(4), 509–519 (1993)
58. M.A. Kirchin, V.M. Runge, Topics in magnetic resonance. Imaging **14**(5), 426–435 (2003)
59. R.D. Oude Engberink, S.M. van der Pol, E.A. Dopp, H.E. de Vries, E.L. Blezer, Radiology **243**(2), 467–474 (2007)
60. Z. Li, S.X. Wang, Q. Sun, H.L. Zhao, H. Lei, M.B. Lan, Z.X. Cheng, X.L. Wang, S.X. Dou, G.Q. Lu, Adv. Healthc. Mater. **2**(7), 958–964 (2013)
61. L. Shen, A. Stachowiak, A. Hatton, P.E. Laibinis, Langmuir **16**(25), 9907 (2000)
62. Y.X.J. Wáng, J.M. Idée, Quant. Imag. Med. Surg. **7**(1), 88 (2017)
63. M. Mahmoudi, H. Hosseinkhani, M. Hosseinkhani, S. Boutry, A. Simchi, W.S. Journeay, K. Subramani, S. Laurent, Chem. Rev. **111**(2), 253–280 (2010)
64. S.J. McLachlan, M.R. Morris, M.A. Lucas, R.A. FIsco, M.N. Eakins, D.R. Fowler, R.B. Scheetz, A.Y. Olukotun, J. Magn. Reson. Imaging **4**(3), 301–307 (1994)
65. R. Weissleder, D.D. Stark, B.L. Engelstad, B.R. Bacon, C.C. Compton, D.L. White, P. Jacobs, J. Lewis, A.J.R. Am, J. Roentgenol. **152**(1), 167–173 (1989)
66. M. Zeisberger, S. Dutz, R. Müller, R. Hergt, N. Matoussevitch, H. Bönnemann, J. Magn. Magn. Mater. **311**, 224–227 (2007)
67. B. Mehdaoui, A. Meffre, L.M. Lacroix, J. Carrey, S. Lachaize, M. Gougeon, M. Respaud, B. Chaudret, J. Magn. Magn. Mater. **322**, L49–L52 (2010)
68. R.K. Gilchrist, R. Medal, W.D. Shorey, R.C. Hanselman, J.C. Parrott, C.B. Taylor Ann. Surg. **146**, 596–606 (1957)
69. I. Hilger, W.A. Kaiser, Nanomedicine **7**, 1443–1459 (2012)
70. J.-P. Fortin, C. Wilhelm, J. Servais, C. Ménager, J.-C. Bacri, F. Gazeau, J. Am. Chem. Soc. **129**, 2628–2635 (2007)
71. L. Lartigue, C. Innocenti, T. Kalaivani, A. Awwad, M.D.M. Sanchez Duque, Y. Guari, J. Larionova, G. Guérin, J.-L.G. Montero, V. Barragan-Montero, P. Arosio, A. Lascialfari, D. Gatteschi, C. Sangregorio, J. Am. Chem. Soc. **133**, 10459–10472 (2011)
72. S. Purushotham, R.V. Ramanujan, J. Appl. Phys. **107**, 114701 (2010)
73. J. Jang, J. Lee, J. Seon, E. Ju, M. Kim, Y.I. Kim, M.G. Kim, Y. Takemura, A.S. Arbab, K.W. Kang, K.H. Park, S.H. Paek, S. Bae, Adv. Mater. **30**, 1704362 (2018)
74. J.-H. Lee, J.-T. Jang, J.-S. Choi, S.H. Moon, S.-H. Noh, J.-W. Kim, J.-G. Kim, I.-S. Kim, K.I. Park, J. Cheon, Nat. Nanotechnol. **6**, 418–422 (2011)
75. P. Guardia, R. Di Corato, L. Lartigue, C. Wilhelm, A. Espinosa, M. Garcia-Hernandez, F. Gazeau, L. Manna, T. Pellegrino, ACS Nano **10**, 7627–7638 (2016)
76. L. Gutiérrez, L. de la Cueva, M. Moros, E. Mazarío, S. de Bernardo, J. M. de la Fuente, M. Puerto Morales, G. Salas, Nanotechnology **30**, 112001 (14pp) (2019)
77. R. Hergt, R. Hiergeist, M. Zeisberger, D. Schüler, U. Heyen, I. Hilger, W.A. Kaiser, J. Magn. Magn. Mater. **293**, 80–86 (2005)
78. T. Orlando, S. Mannucci, E. Fantechi, G. Conti, S. Tambalo, A. Busato, C. Innocenti, L. Ghin, R. Bassi, P. Arosio, F. Orsini, C. Sangregorio, M. Corti, M.F. Casula, P. Marzola, A. Lascialfari, A. Sbarbati, Contrast Media Mol. **I**(11), 139–145 (2015)
79. E. Alphandery, S. Faure, O. Seksek, F. Guyot, I. Chebbi, ACS Nano **5**, 6279–6296 (2011)
80. R. Mejías, P. Hernández Flores, M. Talelli, J. L. Tajada-Herráiz, M. E.F. Brollo, Y. Portilla, M. P. Morales, D. F. Barber, ACS Appl. Mater. Interfaces **11**, 340−355 (2019)
81. N. Lee, D. Yoo, D. Ling, M.H. Cho, T. Hyeon, J. Cheon, Chem. Rev. **115**, 10637–10689 (2015)
82. A. Espinosa, R. Di Corato, J. Kolosnjaj-Tabi, P. Flaud, T. Pellegrino, C. Wilhelm, ACS Nano **10**(2), 2436–2446 (2016)
83. A. Chiu-Lam, C. Rinaldi, Adv. Funct. Mater. **22**, 3933–3941 (2016)
84. M. Creixell, A.C. Bohorquez, M. Torres-Lugo, C. Rinaldi, ACS Nano **5**, 7124–7129 (2011)
85. M. Teshome, C. Wei, K.K. Hunt, A. Thompson, K. Rodriguez, E.A. Mittendorf, Ann. Surg. Oncol. **23**(5), 1508–1514 (2016)
86. G. Kandasamy, D. Maity, Int. J. Pharm. **496**(2), 191–218 (2015)

87. Y. Gossuin, P. Gillis, A. Hocq, Q.L. Vuong, A. Roch, Wiley Interdiscip. Rev. Nanomed. Nanobiotechnol. **1**(3), 299–310 (2009)
88. M.R. Bashir, L. Bhatti, D. Marin, R.C. Nelson, J. Magn. Reson. Imaging **41**(4), 884–898 (2015)
89. J. Albaramki, E.M. Hodson, J.C. Craig, A.C. Webster, Cochrane Database Syst. Rev. **1**, CD007857 (2012)
90. M. Lu, M.H. Cohen, D. Rieves, R. Pazdur, Am. J. Hematol. **85**(5), 315–319 (2010)
91. J.A. Thomson, Science **282**(5391), 1145–1147 (1998)
92. M. Morigi, A. Benigni, G. Remuzzi, B. Imberti, Cell Transplant. **15**(1), 111 (2006)
93. E. Sykova, P. Jendelova, Cell Death Differ. **14**(7), 1336 (2007)
94. M.Z. Ratajczak, B. Machalinski, W. Wojakowski, J. Ratajczak, M. Kucia, Leukemia **21**(5), 860 (2007)
95. S. Bobis, D. Jarocha, M. Majka, Folia Histochem. Cytobiol. **44**(4), 215 (2006)
96. A. Bongso, E.H. Lee, *Stem Cells* (World Scientific Publishing Co., Singapore, 2005)
97. D. Spira, R. Bantleon, H. Wolburg, F. Schick, G. Groezinger, J. Wiskirchen, B. Wiesinger, Mol. Imaging **15**, 1536012115624915 (2016)
98. T.J. England, P.M. Bath, M. Abaei, D. Auer, D.R. Jones, Cytotherapy **15**(3), 384–390 (2013)
99. J.K. Hsiao, M.F. Tai, H.H. Chu, S.T. Chen, H. Li, D.M. Lai, S.T. Hsieh, J.L. Wang, H.M. Liu, Magn. Reson. Med. **58**(4), 717–724 (2007)
100. J. Jiang, Y. Chen, Y. Zhu, X. Yao, J. Qi, Cancer Biother. Radiopharm. **26**(4), 461–467 (2011)
101. H.E. Daldrup-Link, M. Rudelius, R.A. Oostendorp, M. Settles, G. Piontek, S. Metz, H. Rosenbrock, U. Keller, U. Heinzmann, E.J. Rummeny, J. Schlegel, T.M. Link, Radiology **228**(3), 760–767 (2003)
102. M. Oppitz, J. Pintaske, R. Kehlbach, F. Schick, G. Schriek, C. Busch, Magn. Reason. Mater. Phys. **20**(1), 1–9 (2007)
103. J.M. Chan, M.S. Cheung, R.G. Gibbs, K.K. Bhakoo, Clin. Trans. Med. **6**(1), 1 (2017)
104. A.J. Cochran, R. Essner, D.M. Rose, E.C. Glass, Langenbecks Arch. Surg. **385**(4), 252–260 (2000)
105. C. Bézu, C. Coutant, A. Salengro, E. Daraï, R. Rouzier, S. Uzan, Surg. Oncol. **20**(1), e55–e59 (2011)
106. K. Motomura, M. Ishitobi, Y. Komoike, H. Koyama, A. Noguchi, H. Sumino, Y. Kumatani, H. Inaji, T. Horinouchi, K. Nakanishi, Ann. Surg. Oncol. **18**, 3422–3429 (2011)
107. R.A. Heesakkers, A.M. Hövels, G.J. Jager, H.C. van den Bosch, J.A. Witjes, H.P. Raat, J.L. Severens, E.M. Adang, C.H. van der Kaa, J.J. Fütterer, J. Barentsz, Lancet. Oncol. **9**(9), 850–856 (2008)
108. A. Schwein, P. Chinnadurai, D.J. Shan, A.B. Lumsden, C.F. Bechara, J. Bismuth, J. Vasc. Surg. **65**(5), 1440–1452 (2017)
109. Z. Zhou, F. Han, S. Rapacchi, K.L. Nguyen, D.Z. Brunengraber, G.J. Kim, J.P. Finn, P. Hu, NMR Biomed. **30**(1), e3663 (2017)
110. P. Ning, E.J. Zucker, P. Wong, S. Vasanawala, Magn. Reson. Imaging **34**(2), 152–8 (2016)
111. L.M. Lai, J.Y. Cheng, M.T. Alley, T. Zhang, M. Lustig, S.S. Vasanawala, J. Magn. Reson. Imaging **45**(5), 1407–1418 (2017)
112. T. Schubert, U. Motosugi, S. Kinner, T.J. Colgan, S.D. Sharma, S. Hetzel, S. Wells, C.A. Campo, S.B. Reeder, J. Magn. Reson. Imaging **45**(6), 1617–1626 (2017)
113. M. Sigovan, W. Gasper, H.F. Alley, C.D. Owens, D. Saloner, Radiology **265**(2), 584–590 (2012)
114. A. Luhar, S. Khan, J.P. Finn, S. Ghahremani, R. Griggs, J. Zaritsky, I. Salusky, T.R. Hall, Pediatr. Radiol. **46**(9), 1332–1340 (2016)
115. T. Tourdias, S. Roggerone, M. Filippi, M. Kanagaki, M. Rovaris, D.H. Miller, K.G. Petry, B. Brochet, J.P. Pruvo, E.W. Radüe, V. Dousset, Radiology **264**(1), 225–233 (2012)
116. E.A. Schellenberger, D. Sosnovik, R. Weissleder, L. Josephson, Bioconjugate Chem. **15**(5), 1062–1067 (2004)
117. S. Maurea, P.P. Mainenti, A. Tambasco, M. Imbriaco, C. Mollica, E. Laccetti, L. Camera, R. Liuzzi, M. Salvatore, Quant. Imag. Med. Surg. **4**(3), 181–189 (2014)

118. C.G. Varallyay, E. Nesbit, R. Fu, S. Gahramanov, B. Moloney, E. Earl, L.L. Muldoon, X. Li, W.D. Rooney, E.A. Neuwelt, J. Cereb. Blood Flow Metab. **33**(5), 780–786 (2013)
119. K.K. Cheng, P.S. Chan, S. Fan, S.M. Kwan, K.L. Yeung, Y.X. J. Wang, A.H. Lum Chow, E.X. Wu, L. Baum, Biomaterials **44**, 155–172 (2015)
120. C. Sun, J.S. Lee, M. Zhang, Adv. Drug Deliv. Rev. **60**(11), 1252–1265 (2008)
121. E.A. Sadowski, L.K. Bennett, M.R. Chan, A.L. Wentland, A.L. Garrett, R.W. Garrett, A. Djamali, Radiology **243**(1), 148–157 (2007)
122. I. Hilger, R. Hergt, W.A. Kaiser, Investig. Radiol. **35**, 170–179 (2000)
123. M. Johannsen, A. Jordan, R. Scholz, M. Koch, M. Lein, S. Deger, J. Roigas, K. Jung, S. Loening, J. Endourol. **18**, 495–500 (2004)
124. A. Jordan, R. Scholz, K. Maier-Hauff, F.K.H. van Landeghem, N. Waldoefner, U. Teichgraeber, J. Pinkernelle, H. Bruhn, F. Neumann, B. Thiesen, A. von Deimling, F. Felix, J. Neuro-Oncol. **78**, 7–14 (2006)
125. A. Jordan, R. Scholz, P. Wust, H. Fähling, J. Krause, W. Wlodarczyk, B. Sander, T. Vogl, R. Felix, Int. J. Hyperth. **13**, 587–605 (1997)
126. M. Johannsen, U. Gneveckow, L. Eckelt, A. Feussner, N. WaldoFner, R. Scholz, S. Deger, P. Wust, S.A. Loening, A. Jordan, Int. J. Hyperth. **21**, 637–647 (2005)
127. K. Maier-Hauff, F. Ulrich, D. Nestler, H. Niehoff, P. Wust, B. Thiesen, H. Orawa, V. Budach, A. Jordan, J. Neuro-Oncol. **103**, 317–324 (2011)
128. A. Attaluri, S.K. Kandala, M. Wabler, H. Zhou, C. Cornejo, M. Armour, M. Hedayati, Y. Zhang, T.L. DeWeese, C. Herman, R. Ivkov, Int. J. Hyperth. **31**, 359–374 (2015)
129. S. Kunjachan, A. Detappe, R. Kumar, T. Ireland, L. Cameron, D.E. Biancur, V. Motto-Ros, L. Sancey, S. Sridhar, G.M. Makrigiorgos, R.I. Berbeco, Nano Lett. **15**, 7488–7496 (2015)
130. A. Jordan, R. Scholz, K. Maier-Hauff, M. Johannsen, P. Wust, J. Nadobny, H. Schirra, H. Schmidt, S. Deger, S. Loening, W. Lanksch, R. Felix, J. Magn. Magn. Mater. **225**, 118–126 (2001)
131. A. Jordan, R. Scholz, P. Wust, H. Fähling, F. Roland, J. Magn. Magn. Mater. **201**, 413–419 (1999)
132. K. Maier-Hauff, R. Rothe, R. Scholz, U. Gneveckow, P. Wust, B. Thiesen, A. Feussner, A. von Deimling, N. Waldoefner, R. Felix, A. Jordan, J. Neuro-Oncol. **81**, 53–60 (2007)
133. M. Johannsen, B. Thiesen, P. Wust, A. Jordan, Int. J. Hyperth. **26**, 790–795 (2010)
134. P. Wust, U. Gneveckow, M. Johannsen, D. Böhmer, T. Henkel, F. Kahmann, J. Sehouli, R. Felix, J. Ricke, A. Jordan, Int. J. Hyperth. **22**, 673–685 (2006)
135. R. Stupp, M.E. Hegi, W.P. Mason, M.J. van den Bent, M.J.B. Taphoorn, R.C. Janzer, S.K. Ludwin, A. Allgeier, B. Fisher, K. Belanger, P. Hau, A.A. Brandes, J. Gijtenbeek, C. Marosi, C.J. Vecht, K. Mokhtari, P. Wesseling, S. Villa, E. Eisenhauer, T. Gorlia, M. Weller, D. Lacombe, J.G. Cairncross, R.O. Mirimanoff, Lancet Oncol. **10**, 459–466 (2009)
136. R. Stupp, W.P. Mason, M.J. van den Bent, M. Weller, B. Fisher, M.J.B. Taphoorn, K. Belanger, A.A. Brandes, C. Marosi, U. Bogdahn, J. Curschmann, R.C. Janzer, S.K. Ludwin, T. Gorlia, A. Allgeier, D. Lacombe, J.G. Cairncross, E. Eisenhauer, R.O. Mirimanoff, N. Engl, J. Med. **352**, 987–996 (2005)

Chapter 15
Smart Platforms for Biomedical Applications

Tarun Vemulkar and Russell P. Cowburn

Abstract This chapter provides an overview of the various types of magnetic micro- and nanoparticle systems used in biomedical applications. We broadly divide particle types into colloidally synthesized and lithographically defined on silicon wafers. The applications relevant to each particle type are highlighted followed by research case studies. Each case study highlights a novel approach to the engineering of magnetic particles for a specific application. Finally, future perspectives for the field are described with an emphasis on the challenges remaining to be solved for all the main application areas of magnetic particles.

15.1 Colloidally Synthesized Nanoparticles

Superparamagnetic iron oxide nanoparticles (SPIONs) have largely been the foundational materials system for the biomedical applications of magnetic nanoparticles [1–8]. These γ-Fe_2O_3 (maghemite)- or Fe_3O_4 (magnetite)-based single domain nanoparticles possess a net zero remanent magnetic state due to the thermal fluctuation of their magnetic moments via Néel–Brown relaxation [9, 10]. SPIONs have been particularly useful in the biomedical space because of their biocompatibility, relative ease of colloidal chemistry-based fabrication, and resistance to magnetically driven aggregation in the absence of an applied field. Colloidally fabricated nanoparticles may also be synthesized at sizes larger than the superparamagnetic limit at which point they become single domain nanoparticles, and then multidomain. Other materials including Ni- and Co-based nanoparticles [11, 12], as well as mixed oxides [11–16] based on Fe and other transition metals are also of relevance to this space.

T. Vemulkar (✉) · R. P. Cowburn
Cavendish Laboratory, University of Cambridge, JJ Thomson Ave, Cambridge CB3 0HE, UK
e-mail: tv243@cam.ac.uk

D. Peddis et al. (eds.), *New Trends in Nanoparticle Magnetism*,
Springer Series in Materials Science 308,
https://doi.org/10.1007/978-3-030-60473-8_15

The most clinically advanced application involves the use of magnetic nanoparticles as contrast agents in the imaging of biological tissue [17–22]. This encompasses the more established technique of magnetic resonance imaging (MRI) and the comparatively more recent approach of magnetic particle imaging (MPI) [23].

For therapeutics, the heat generated when magnetic nanoparticles are exposed to alternating magnetic fields in the 100–1000 kHz range has been harnessed as a cell killing mechanism [24–29]. By increasing the temperature of the environment near a concentrated dose of SPIONS in biological tissue such as a tumour for example, a localized, triggered, tumour destroying therapeutic may be realized. This heat generation may also be used as the trigger for a thermally sensitive drug delivery mechanism [24–29].

Magnetic nanoparticles are also used extensively within the biomedical research space due to the ease of mechanical actuation of magnetic materials. This allows for their deployment in assays where biomolecules may need to be captured, concentrated, and re-suspended in solution [30, 31]. With the development of extremely sensitive magnetic field sensors based on magnetoresistance device architectures [32–34], magnetic nanoparticles may also be used as the detection moiety in biosensing systems instead of simply as a means of purifying samples for the elution of analytes. And finally, mechanical actuation has also been used to stimulate cells and tissue to trigger downstream phenotypic effects [35], as well as trigger cell death [36] in a different take on the therapeutic approach.

15.1.1 Applications

15.1.1.1 Magnetic Resonance Imaging

Magnetic resonance imaging (MRI) is a ubiquitous tool that has given clinicians the ability to achieve huge improvements in soft tissue contrast, opening a wide array of diagnostic procedures beyond that offered by X-ray radiation. Rooted firmly in the principles of nuclear magnetic resonance [37, 38], MRI imaging is based on the relaxation of the nuclear magnetic spins of hydrogen atoms, present in water and organic material that comprises human tissue (Fig. 15.1).

Since the inherent variation in signal between tissues is often insufficient for clinical requirements, contrast agents are used to significantly enhance MRI signals by modifying the values of the characteristic relaxation times, T_1, T_2, and T_2* [39–41], of the nuclear spins in the applied static and dynamic fields of an MRI scanner. T_1 contrast agents work by significantly shortening the T_1 of hydrogen nuclei in their vicinity, thereby significantly boosting the T_1 positive signal. High-spin paramagnetic ions are typical T_1 contrast agents [42–45], of which Gd^{3+} [42, 46, 47] is the clinical contrast agent of choice when chelated with various organic molecules for safety. However, significant effort is being expended in to the incorporation of Gd^{3+} into nanoparticles [48–51] to increase sensitivity, specificity, and reduce clearance time and toxicity (particularly nephrotic cystic fibrosis in patients with impaired

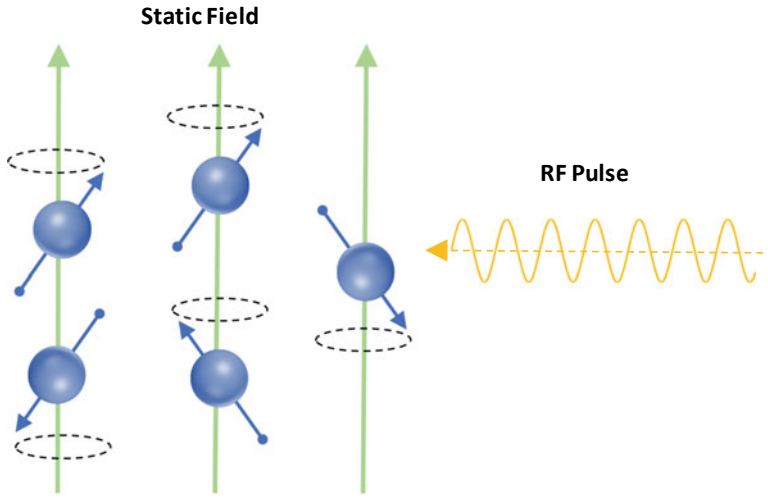

Fig. 15.1 In an MRI measurement, hydrogen nuclei in the water and hydrocarbons in tissue align in and precess to a static field of 1.5–3 T. An orthogonal RF pulse at the Larmor precession frequency of the nuclei misaligns them to the static field and causes them to precess in phase with each other. Over time, they relax back to alignment with the static field with a characteristic time T_1 and dephase with each other with a characteristic time T_2. T_2* is the observed T_2 and is usually much shorter due to field inhomogeneities

renal function [52]). Further optimization along this direction may prove extremely beneficial to the space of MRI contrast agents.

SPIONS, on the other hand, are used as T_2* contrast agents [48–51, 53] and operate by shortening T_2* relaxation times and thus locally reducing image intensity (termed negative contrast agents). The local magnetic field gradient and inhomogeneity from the presence of the magnetic nanoparticles results in rapid dephasing of the nuclear moments causing a significant reduction in signal. It should be noted that magnetic nanoparticles influence T_2* relaxation times in a much larger volume than T_1 contrast agents because of the relatively strong stray fields from their high magnetic moment [20, 54]. Particularly relevant here are SPIONs of sizes of a few hundred nanometres, as well as ultra-small SPIONs or USPIONs (diameter less than 50 nm) [55], where the size of the particle determines biodistribution and clearance from the body. Generally, SPIONs tend to interact with the phagocytic cells of the immune system and tend to rapidly make their way to the liver and spleen that are the nodes of the macrophage system [55]. USPIONs due to their small size make their way into the blood stream with a much lower clearance time increasing their chances of reaching tumours in the rest of the body. Further, systems that have higher saturation magnetization M_S than iron oxide (including Fe-, Mn-, Co-, Ni-based nanoparticles and Dy^{3+} chelates) [54–58] are of interest, since the particle stray field and hence the effect on T_2* scales with the magnetization [59]. However, contrast agents that shorten T_2* result in a reduced signal intensity can be confused for other pathogenic conditions, such as blood clots, and may reduce the signal intensity in

neighbouring tissue resulting in reduced resolution for diagnosis [55]. Reference [55] provides a thorough overview of nanoparticle design for MRI contrast and will be of relevance to the reader.

15.1.1.2 Magnetic Particle Imaging

While MRI had its origins in the 1970s [60], the concept of magnetic particle imaging (MPI) is relatively recent. It was demonstrated in 2005 by Gleich and Weizenecker [23]. Core to this imaging technique is the use of SPIONs as tracers (*not* contrast agents) due to their zero magnetization remanent state, and their nonlinear, saturating magnetization response in an applied field [61–63].

In the presence of a driving alternating applied field at a specific frequency termed the modulation field, the magnetization response of SPIONs is time-dependent and contains both the frequency of the driving field, but also contains higher harmonics. If a strong saturating static field is also applied to the SPIONs, then they remain saturated despite the presence of the alternating field and the generation of the higher harmonics in their magnetization response with time is suppressed. If the spatial configuration of the static field is such that it has a zero (or low) field at its centre and higher fields at the edges, then any SPIONs in the centre of this field retain their higher harmonics in conjunction with the driving field, whereas the SPIONs in the high static field region lose their higher harmonic responses. This is known as the application of a "selection field". MPI thus works by scanning the position of the field-free point (FFP) in the selection field throughout a sample volume containing SPIONs. By mapping the suppression of the higher harmonics of the SPIONs, a tomographic image of the sample volume is generated (Fig. 15.2).

This imaging modality is of extreme interest in the biomedical space. The magnetization response of the SPIONs is the sole contribution to the signal in this technique (hence "tracers"), and it is not confounded with artefacts related to proton relaxation. Further, the higher magnetization and much shorter relaxation times of SPIONs in MPI compared to protons in a 1.5 T applied field means MPI has comparatively extremely high temporal resolution [64] and higher signal to noise than MRI [65]. Further, MPI systems do not need to necessarily be as large as MRI systems and offer flexibility in their design for use [66]. MPI is thus a technique that is of extremely high interest, particularly for cardiovascular diagnostics, tissue perfusion and vascular anomalies, as well as situations where the use of standard MRI contrast agents is not possible from a toxicology perspective such as in patients with compromised renal function [52]. MPI has advanced rapidly since its conception because of its huge potential in the imaging space, and [67–69] will provide the reader with a more detailed overview on MPI in its current state.

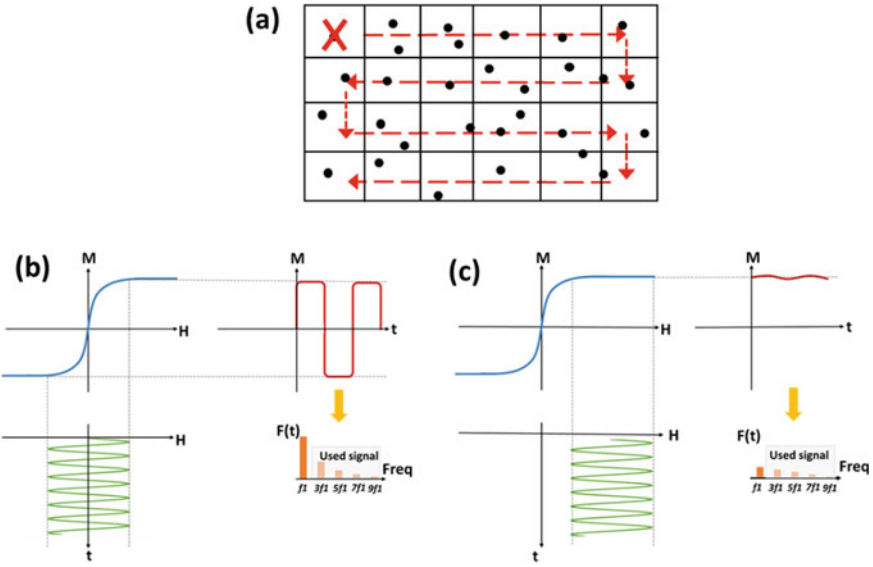

Fig. 15.2 **a** An FFP is scanned through a volume of material containing tracer particles. **b** The magnetization response of particles to the driving field (green) inside the FFP contains higher harmonics. **c** Outside the FFP the higher harmonics are suppressed allowing for tracer mapping as the FFP is scanned over the volume.

15.1.1.3 Magnetic Fluid Hyperthermia

In contrast to the imaging techniques discussed above where diagnostics is the main biomedical focus, magnetic particle hyperthermia is a therapy focussed discipline [29]. Hyperthermia utilizes the energy loss modes available to magnetic nanoparticles in an alternating magnetic field to generate heat in the environment containing the particles. The loss modes that are generally considered are hysteresis losses, Néel (particle magnetization relaxation) and Brown relaxation (particle orientation relaxation) losses, and viscous frictional losses arising from interactions with the fluid during Brown relaxation [70]. The heat generated from these losses is generally lumped into one single figure of merit termed the specific loss power or SLP (termed specific absorption rate or SAR historically). The SLP is defined as the thermal power dissipated per unit mass (typically per gram) of the magnetic material [25, 71].

Magnetic particle hyperthermia is typically conducted at a frequency of 0.05–1.2 MHz and a field amplitude of 0–15 kA/m [8]. The three loss mechanisms are size-dependent, and hence a consideration of magnetic core and hydrodynamic volume are important for evaluating the SLP of a given SPION formulation. Brown and Néel relaxation mechanisms (or a combination of the two) are more relevant for small particles (below the 10 nm range for SPIONs) [70]. Between 10–15 nm, the frequency of the applied field is too high to allow for susceptibility losses, and magnetic switching begins to occur in a coercive manner [70, 70]. This leads to hysteretic losses from

the nanoparticles that are moving away from the superparamagnetic regime. In the 20 nm and above range for iron oxide nanoparticles, the dominant heating process is frictional losses with the fluid due to stirring and the particles are no longer superparamagnetic. This is because the magnetic moment of the larger particles cannot be switched by the field magnitude typically used for hyperthermia [70]. The combination of multiple heating mechanisms, the finite size distribution in nanoparticle formulations [72] and effects such as anisotropy distributions [73–75] and interparticle dipolar interactions [75, 76] has made a comprehensive theoretical model of heat losses in magnetic particle systems quite elusive.

15.1.1.4 Mechanical Actuation

While initial work by F. Crick et al. used magnetic nanoparticles to investigate the microrheology of cell cytoplasm [77], the field has progressed to the point where functionalized blocked magnetic nanoparticles have been attached to individual integrin receptors on the cell membrane. Using a rotating magnetic field, the blocked particles applied torque to the cell membrane providing insight into the mechanical properties of the cytoskeleton [78]. Beyond providing a means to probe mechanical properties, the mechanical actuation of cells via membrane receptors can have significant downstream consequences [79], going as far as to influence gene transcription within the cell [80]. The reader will find [35] that provides a thorough overview of mechanical actuation techniques for cell behavioural modification.

There is also interest in mechanical actuation of cells from a clinical perspective. An area of interest is the directed mediation of mesenchymal stem cell (MSC) differentiation. MSCs differentiate into the various skeletal tissue structures and are a very relevant cell type for tissue engineering and regeneration to grow replacement tissue for a patient. The mechanical loading the cells experience is crucial to the differentiation process [81–83]. Using magnetic nanoparticles to condition cells allows for the mechanical stimulation of cells without a three-dimensional tissue scaffold which is important for the tissue engineering post the culture process [82].

Since mechanical forces can stimulate cells, the forces and torques they exert can also be used to destroy cells by damaging the cytoskeleton [84] or cellular components [85]. There has been work on using iron oxide nanoparticles to destroy cancer cells, where spherical- and rod-shaped iron oxide nanoparticles in an oscillating field have been shown to destroy human cervical cancer cells in vitro [84]. This field, however, has recently received significant attention when highly effective glioblastoma cell killing was demonstrated using a new class of magnetic particle [36]—lithographically defined micro- and nanoparticles which will be discussed further on in this chapter.

15.1.1.5 Biosensing

The sensing of biological analytes is at the core of clinical diagnostics. Magnetic nanoparticles typically used in the biosensing space are iron oxide based, either in core shell structures or functionalized for stability in solution [86]. There are a variety of sensing device architectures for magnetic particles [30, 33, 34, 87–91] but the primary architecture of interest has been magnetoresistance-based devices [92]. An example of such a system would be a giant magnetoresistance (GMR) or spin valve sensor-based assay [32, 93–96]. These are extremely sensitive magnetic field sensors, and here the detection of the analyte is determined by the presence of the stray field of a magnetic nanoparticle near the surface of the sensor. The localization of the nanoparticle on the sensor occurs by specific binding events between biomolecules such as antibody–antigen binding or complementary nucleic acid sequences [93, 97, 98], where the sensor and nanoparticle are both functionalized with the appropriate biomolecule. Magnetic approaches may be the most relevant for assays in biological samples that do not allow for standard optical detection techniques such as fluorescence. Line-of-sight considerations are generally eliminated with magnetic signals and as such magnetic nanoparticle-based assays may be relevant for sensing molecules directly in fluids such as blood [98]. References [82, 88, 89] and [91] provide a broader review of sensing device architectures and nanoparticle formulations in this space (Fig. 15.3).

15.2 Lithographically Defined Particles

Solution suspended lithographically defined magnetic micro- and nanodiscs are a relatively recent development [36, 99–102]. They have emerged because of the interest in transferring the knowledge gained in the fabrication of magnetic memory and logic devices to the biotechnology field. Lithographically defined particles are planar in shape and are generally in the range of 200 nm–2 μm in planar dimensions and 10–200 nm in thickness.

These microdiscs are fabricated with standard lithographic techniques, where most generally a magnetic thin film is grown via physical vapour deposition on patterned photoresist that is spun cast on a silicon wafer. The photoresist is then dissolved and the structures atop the resist are lifted off into solution. The control of magnetic thin-film growth allows for magnetic properties that can be engineered to extreme precision, with resolutions for individual layer thicknesses in the sub-nm range.

The primary challenge with lithographic microdiscs is ensuring a zero remanent magnetization state since they are far too large to be superparamagnetic in nature, and their stray fields are easily sufficient to drive strong magnetic agglomeration. There are two primary approaches used to create microdiscs that do not agglomerate.

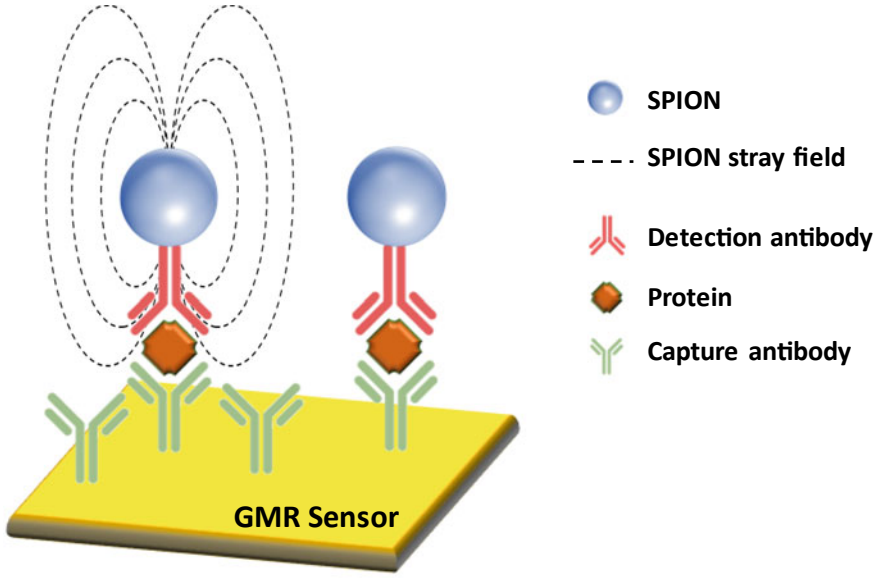

Fig. 15.3 A schematic immunoassay utilizing SPIONs and a GMR type sensor. The sensor top surface is biofunctionalized with a capture antibody. The sample solution containing the protein of interest is poured over the sensor, allowing the protein to be captured by the capture antibody. The sensor surface is then washed and a detection reagent consisting of a complementary detection antibody attached to a SPION is used to confirm the presence of the analyte. Binding of the detection antibody is confirmed by a resistance change in the sensor caused by the stray field of the SPION

The first approach uses magnetically soft materials magnetized in the plane of the particle with weak intrinsic in-plane anisotropy and a symmetric planar shape minimizing in-plane configurational anisotropy [103]. For circular disc configurations in the 200 nm–2 μm diameter range and thicknesses ranging from approximately 10–60 nm (aspect ratios of thickness/diameter typically ranging from 4–40) [104–106], a magnetic flux closure state may be exhibited at remanence known as a magnetic vortex. In such a configuration, the magnetization vector of the disc remains parallel to the nearest disc edge at all points.

The second approach makes use of Ruderman-Kittel-Kasuya-Yoshida (RKKY) [107–109] coupling between adjacent magnetic layers in a multilayer thin film. A phenomenon originally of interest in magnetic memory and logic elements [110–112], it has been of great interest in the space of lithographically fabricated microdiscs. In RKKY coupled systems, two adjacent magnetic layers may be coupled either ferromagnetically or antiferromagnetically (AF) [113, 114] depending on the thickness and composition of the interlayer separating the magnetic layers [115, 116]. A typical example of an RKKY coupling interlayer that can be sandwiched between two magnetic layers is 0.5–1 nm of Ru [116, 117]. When the thickness of the interlayer is tuned to lie in the AF regime, the two magnetic layers lie antiparallel (AP) to each other in the absence of a magnetic field. This AP configuration arising from the

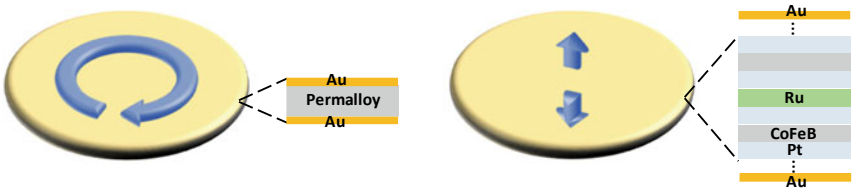

Fig. 15.4 Schematic of two types of microdiscs. The permalloy vortex microdisc (left) has a flux closure magnetization state to ensure a net zero remanent state. The out-of-plane magnetized microdisc (right) utilizes a heterostructure of CoFeB/Pt (for example) to achieve a magnetization perpendicular to the plane of the disc. The Ru interlayer creates an AP remanent state. Both microdiscs are capped with Au for biofunctionalization. The blue arrows denote the magnetization vectors of the magnetic layers in expanded views

AF coupling causes the thin film to have a net zero magnetization at remanence. AF RKKY coupling has been used to create microdiscs with the remanent AP configuration in in-plane magnetic layers (both with and without the vortex configuration) [118, 119], as well as in microdiscs based on perpendicularly magnetized [120–123] magnetic layers [101, 124, 125] (Fig. 15.4).

15.2.1 Applications

15.2.1.1 Mechanical Actuation

Solution suspended lithographically defined microdiscs have been used almost solely for the mechanical destruction of cancer cells, the original application for which they were conceived [36]. The high anisotropy of magnetic thin films translates to the generation of extremely high magnetic torques that are effectively transduced by the planar microdiscs themselves.

Initial work in this space used 2 μm vortex microdiscs in an oscillating magnetic field to destroy glioblastoma cells in vitro [36]. More recently, there has also been interest in using microdiscs fabricated from perpendicularly magnetized thin films for mechanical actuation [101, 124–127]. The mechanical actuation of micro- and nanodiscs structures has been shown to cause significant cell death both in vitro [36, 125] and in vivo [127] and has also been demonstrated in drug delivery-type systems where the actuation can trigger release of a therapeutic [126, 128, 129]. Recent work has been focussed on elucidating the most efficient systems for torque transduction from an applied field, and how that affects the therapeutic efficacy of the particles in a biological system [125].

15.3 Case Studies

15.3.1 Exploring the Potential of MPI In Vivo for the First Time

The first in vivo demonstration of MPI [130] as an imaging modality for cancer detection is of great interest to the field of nanoparticle magnetism. With potential as a high resolution, high sensitivity, safe, and cheap medical imaging technique, MPI is expected to be a field of both commercial and research interest in the biomedical space in the coming decade. The technique is presently capable of imaging ngs of Fe tracer in the form of SPIONs which can correspond to volume of a few hundred cells [131]. Since there is no signal attenuation, and no signal from surrounding tissue, the extremely high contrast technique allows for the visualization of tissue perfusion with resolution potentially down to hundreds of microns [130].

This in vivo study imaged a new SPION-based tracer injected into rats bearing breast cancer tumours. The biodistribution of the tracer was tracked over 6 days providing excellent insight into the behaviour of the tracer for MPI, as well as highlighting the strengths of the technique very effectively.

The LS-008 SPION formulation used for this study was developed by Lodespin Labs has been optimized in other work [132]. The nanoparticles consist of monodisperse oleic acid capped SPION cores around 25 nm that are then coated with poly(maleic anhydride-alt-1-octadecene) (PMAO)—polyethylene glycol (PEG) polymer chains for colloidal stability. This formulation was found to be stable in the high salt concentrations that are found physiologically and that often drive nanoparticle aggregation and impair colloidal stability.

The six-day evolution of the biodistribution of the tracer was tracked with MPI in tumour bearing rats. Seven athymic nude rats were prepared with subcutaneous implantation of breast cancer tumours. The tracer was intravenously injected in the tail 4 weeks after the tumour implantation. Three groups were prepared for the experiment. Group A was a high dose group at 15 mg/kg, group B was a low dose group at 5 mg/kg, and the control group C received no tumour and the high dose. No biofunctionalization was used to target the tumour, but instead the study relied on the fact that tumours preferentially accumulate nanoparticles because of their leakier vasculature than regular tissue, known as the enhanced permeability and retention (EPR) effect [133]. In fact, the study could directly observe the EPR effect and the dynamics of the tracer accumulation in the tumour. An initial enhancement in signal was observed at the edges of the tumour, followed by accumulation, and then the tracer was cleared over the course of 4–6 days (Fig. 15.5).

The quantitative nature of MPI (via a calibration sample) meant that the study could track the amount of tracer in the various organs over time. The pharmacokinetics of the tracer was modelled by a two-compartment method, the blood pool and the tumour. The model fits the experimental results for both the high dose and low-dose group which allowed tracer distribution to be quantified directly from the MPI signal intensity.

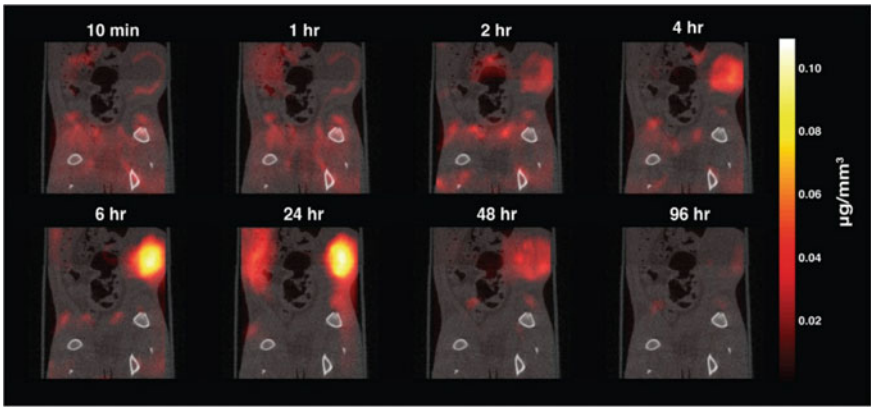

Fig. 15.5 Tracer dynamics observed via MPI for an individual in the high-dose group of rats. Slices through the MPI volume are overlaid with a computed tomography (CT) scan for visualization. The high contrast afforded by the tracer clearly shows three phases of the tracer interaction with the tumour—initial rim enhancement is observed in 10 min, after which the tracer accumulates in the tumour over the course of 24 h, and is subsequently cleared in the next 72 h. Reprinted with permission from Yu et al. [130]. Copyright 2017 American Chemical Society

This study demonstrated the extremely high signal to noise, a factor of 50 here, of which MPI is capable. Further, the high resolution of the technique allowed it to directly observe specific characteristics of the EPR effect, as well as accurately characterize the pharmacokinetics of the tracer. Next steps in this area will be to target tumours actively instead of passively through the EPR mechanism as this may not work with all tumour types. Other exciting prospects will include the combined use of the tracer as a hyperthermia therapy or drug delivery trigger, allowing the tracking of the tumour mass with the ongoing therapy. This two-pronged diagnostic-therapeutic approach could have strong implications in clinical oncology and the development of nanoparticle tracers with characteristics that optimize the efficacy of these two modalities is crucial going forward.

15.3.2 Fuller Treatments of Hyperthermia in Nanoparticle Systems

Moving towards an exploration of all the factors that contribute to the SLP for nanoparticles is necessary to both maximize, and get a better understanding of heat generation for hyperthermia applications. In the work in [134], the authors compare iron oxide nanospheres and nanocubes of 20 nm in diameter (or side length) for their heat generation efficacy. Focussed on magnetic nanoparticles in the single domain regime above the superparamagnetic limit, the work considers the effect

of differences in anisotropy, the presence of interparticle interactions and shape on hyperthermia efficiency.

Inspired by work into bacterial magnetosomes [135], this study demonstrates through experiment the effect of shape and nanoparticle concentration on the SLP and also looks to numerical calculations of the hysteresis loops of the different particle types to draw connections between the structural and magnetic properties of each particle type, and the measured hyperthermia results.

Focussing first on establishing well-characterized nanoparticle formulations as the core of this study, the team fabricated iron oxide nanocubes of 20 and 40 nm in size, as well as nanospheres of 20 nm in size. The different shaped nanoparticles have the same crystal structure (as characterized by transmission electron microscopy (TEM)) and the same size, and the two different sizes of nanocubes allow for a comparison of the effect of size while keeping the shape constant.

The interparticle interaction of the nanocubes is clear in the formation of chain-like aggregates verified by TEM imaging, even in the absence of an applied magnetic field. The effect of these aggregates may seem evident in the concentration dependence of the SLP for both the 20 and 40 nm nanocubes, as well as in the plateauing of the field-cooled curves for the SLP measurements which is not expected for a system of non-interacting particles [134]. Since the SLP decreases with concentration, it seems to suggest from this study that minimizing the interparticle interactions may be of benefit. It was also found via dynamic light scattering measurements that the nanocubes self-assembled into chain-like structures at remanence while the nanospheres did not, showing the importance of shape in interparticle interactions. A curious point of note, however, is that in the simulations conducted it was shown that the SLP appears to monotonically increase with increasing chain length up to ten particles, which would be expected to occur in the samples of higher concentration. Why then does the SAR not similarly increase in the samples where longer chains of particles are to be expected? It may perhaps be the case that minimal ordering on the scale of simple short chains is desirable, but at high concentrations interactions between chains may lead to large clusters that reduce SLP efficiency. A better understanding of the effect of such interparticle interactions is clinically relevant because of the localization of a high dose of nanoparticles in a tumour mass for therapy.

The 20 nm nanocubes were then compared to 20 nm nanospheres, and it was found that there was a 20% increase in the SAR compared to the spheres both experimentally, and this quite closely matched Monte-Carlo simulations of the SAR of the two systems that considered dipolar interactions. The nanocubes were estimated to have an anisotropy approximately 25% higher than the nanospheres at room temperature accounting for dipolar interactions. The higher anisotropy was attributed primarily to the higher surface area of the cubic particles that leads to a higher surface anisotropy contribution since exchange bias effects were shown to be non-existent and a homogenous oxide composition was assumed.

Tuning the shape of nanoparticles thus can have a significant effect on their effectiveness in hyperthermia applications. However, this work highlights some interesting questions about interparticle interactions and their effect on the SAR. Aggregates of particles in chains, for example, have an anisotropy that can be assigned to the entire

chain in addition to the magnetic anisotropy of the individual particle. A thorough understanding of the effect of these dipolar interactions on the SLP and in which regimes they are desirable is needed [136–139].

15.3.3 The Top-Down Engineering of Application Specific Nanoparticles

Lithographically defined microdiscs made from permalloy were shown to be effective at triggering apoptotic cell death in glioblastoma cells in vitro [36] which sparked investigation into the mechanical destruction of cancer cells as a viable cancer therapy. The study featured here [125] began with the hypothesis that the permalloy vortex magnetic configuration was not the most efficient method of torque generation from an applied field, and that magnetic microdiscs with a strong uniaxial anisotropy are more desirable for this application.

Mechanical actuation of magnetic particles in an applied field is dictated largely by the magnetic anisotropy of the particle. The magnetic anisotropy can be thought of as a measure of how strongly the magnetization vector of the particle is linked to its mechanical structure. Optimizing the actuation of magnetic particles for such an application involves engineering its magnetic anisotropy to best fit the type of applied field being used.

Lithographically defined microdiscs are based on thin-film magnetic systems and may have the easy magnetic axis in the plane of the film, or out of the plane of the film. The permalloy vortex is a special case of the in-plane system, where the shape constraints from patterning and the inherently soft material lead to a magnetic system with an easy plane of magnetization (the plane of the microdisc). When a field is applied in the plane of the microdisc the vortex core is displaced resulting in a net magnetization in the direction of the applied field, and this is achieved equally "easily" in any direction in the plane of the disc. Perpendicular magnetic thin films are constructed by alternating layers of a magnetic material (CoFeB) with a heavy metal (Pt) in a multilayer heterostructure. The out-of-plane magnetization is driven by spin–orbit coupling at the CoFeB/Pt interface [120–123]. The perpendicular microdiscs achieve a net zero remanent state by utilizing RKKY AF coupling between adjacent magnetic layers in the multilayer stack. Both sets of discs in this study were 2 μm in diameter. The permalloy vortex discs were 60 nm in permalloy thickness with 5 nm gold caps, and the perpendicular microdisc contained a total of 21.6 nm of CoFeB dispersed in a multilayer heterostructure approximately 110 nm in thickness with 5 nm gold caps. The vortex microdisc thus has a higher magnetic moment than the perpendicular microdiscs, with an easy plane of magnetization as opposed to an easy axis. It should be noted that the hard axis saturation field for the vortex microdiscs was approximately 1 T, and the effective hard axis anisotropy field for the perpendicular particles (once the RKKY coupling is accounted for) was approximately 0.5 T.

Both discs were used to mechanically disrupt glioblastoma cells in vitro, under an applied rotating field of 1 T at 20 Hz for 60 s. This was carried out by incubating the cells with the microdiscs for 24 h which led to the internalization of the microdiscs by the cells. They were then exposed to the magnetic field treatment, and it was found that the perpendicular microdiscs demonstrated approximately 60% cell killing, whereas the vortex microdiscs displayed just 12% cell killing. To understand the large difference in cell killing efficiency, the difference in the magnitude of the magnetic torque and the symmetry of the anisotropy between the two particles was considered.

The study simulated the torque as a function of field angle using a Stoner-Wohlfarth-like model, and compared this to experimental measurements of the magnetization angle as a function of field angle. Both the simulation and experimental results estimated the peak torque of approximately 75 pNm for the vortex microdiscs, and approximately 20 pNm for the perpendicular microdiscs. The difference in peak torque is due to the difference in magnetic moment and anisotropy fields between the two microdiscs. Thus, the magnitude of the torque did not provide an explanation for the difference in performance between the two types of particles since the vortex microdiscs exerted higher peak torques (Fig. 15.6).

It was noted that the symmetry of the anisotropy is the cruci6al difference between the two particles. With a rotating magnetic field, a particle with an easy plane of magnetization will first align its easy plane to the plane of the applied field. The magnetization will then rotate in the plane of the particle without transducing any mechanical torque from the field. The microdisc with the easy magnetization axis,

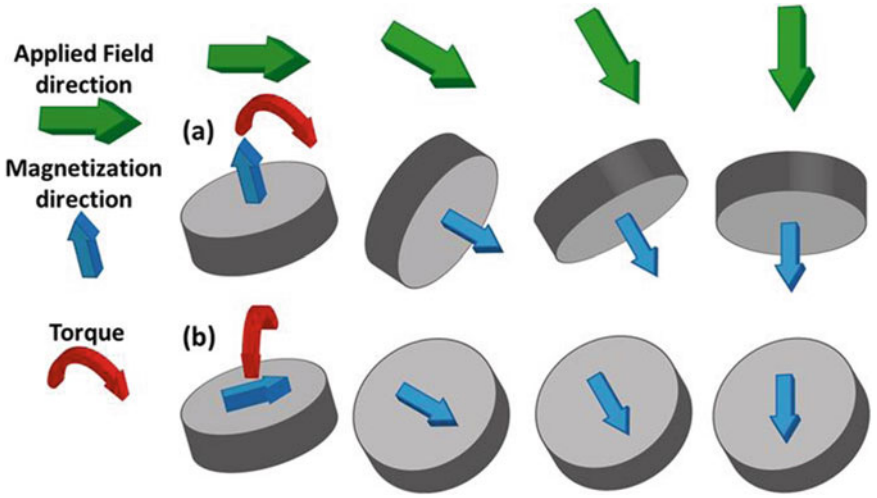

Fig. 15.6 A schematic showing the importance of considering the symmetry of anisotropy in relation to the applied field configuration for mechanical actuation. The magnetization direction and torques on **a** perpendicular particles (top row) and **b** permalloy vortex particles (bottom row) under an applied rotating field. Figure reproduced from [125] with permission

however, will continuously mechanically rotate to align its magnetization with the applied field transducing torque over the entire field duration. Over even the 60 s field duration this proved to be enough to result in a 50% difference in cell killing capability between the two sets of particles. This study clearly highlighted the need to engineer magnetic particles to their application to ensure maximum efficiency. Lithographic techniques offer great precision in this regard and are expected to be of significant interest for the fabrication of magnetic micro- and nanoparticles for biotechnology applications.

15.3.4 Magnetically Driven Labs-On-Chips

The transport of magnetic beads using either domain walls [140] or periodic magnetic elements [141] is an interesting prospect technologically and may offer a new take on lab-on-chip processes where the analyte of interest is not transported by fluid flow as in microfluidics, but via the motion of magnetic beads. The study here [142] demonstrates an architecture of patterned permalloy nanotracks on a Si chip that creates a magnetic domain wall routing network capable of transporting magnetic beads along paths selected by the application of external fields. This has exciting implications for more complex operations such as dynamic sorting of magnetic particles allowing for intricate downstream processing and sensing.

Magnetic domain walls are localized sources of stray field capable of trapping superparamagnetic beads with forces in the range of hundreds of pN [143–146]. Domain walls, and hence the particles they trap, may be moved in micro- and nanowire structures with an applied field at speeds approaching 1 mm/s [140]. A permalloy curvilinear nanotrack was fabricated consisting of semi-circular links, with track width of 800 nm, thickness of 40 nm and an outer diameter of 20 μm for the semi-circular links. A junction was created that spits the track into two paths. This study focussed on vortex-type domain walls [147], a magnetic texture analogous to the vortex flux closure state in a patterned microdisc. A vortex domain wall exists in thin magnetic strips where two in-plane domains of the opposite magnetization direction meet. At this intersection between the two domains, the domain wall forms with a magnetic vortex core in the centre of the wall, and a chirality given by the direction that the magnetization rotates about the core of the wall [148]. The domain wall can be formed in a head-to-head or tail-to-tail configuration according to the direction of the domains in the magnetic strip, and these two configurations may be thought of as having opposite signs, and their stray fields (pointing out of the plane of the track) are of opposite sign as well.

The vortex domain walls in this study are moved in the permalloy nanotrack by a rotating magnetic field of the appropriate rotational direction in the plane of the track. As the domain wall is moved through the junction, it splits and creates two domain walls in each of the new paths, one of the same sign and one of the opposite sign. The crucial point of this work shows that since the domain wall splits into two domain walls of the opposite sign, a field pulse applied out of the plane of the system

is additive for the stray field of one of the domain wall configurations and subtractive for the other. This creates a selection mechanism for the bead as it approaches the junction that is reminiscent of a train switching tracks. The bead is driven to the path with the domain wall that has had its field enhanced at the junction as determined by the sign of the out of plane field pulse.

This selection process is simulated in a model track junction of permalloy 100 nm wide, 60 nm thick, and with a 2 μm outer diameter. An in-plane rotating field of 625 Oe was simulated to drive the domain wall motion, and a ±250 Oe out of plane field was used to create the asymmetric magnetostatic potential energy surface that the bead observes as it exits the junction. Experimentally this process was demonstrated on a series of 2.8 μm beads going through a junction in the fabricated track described above, where the bead switching to path 2 was looked at under various conditions. The out-of-plane fields ranged from −150 to +150 Oe. It was found that the bead does not switch to path 2 if its domain wall stray field is diminished by the applied field which agrees with the simulated result. When the applied field is additive to the domain wall stray field in path 2, the bead only switches to path 2 where the applied filed pulse is above approximately 57 Oe. This minimum magnitude of applied field necessary for switching paths is interesting. It shows that the magnetostatic potential energy surface the bead experiences needs to be modified by a significant external field to drive path switching. It was explained that this is perhaps due to differences in domain wall depinning in the two paths as the domain wall goes through the junction requiring some minimum field magnitude to remove the inherent bias to the bead motion.

This study takes the demonstration one step further by experimentally demonstrating that beads of different sizes can be sorted based on this technique since the potential energy well of interaction of each bead is modified by its magnetic moment. Each bead size thus has different threshold out-of-plane field pulses necessary to switch it to path 2 in the system. Populations of 2.8 and 5.8 μm beads were robustly sorted through a junction using the appropriate out-of-plane fields. If the beads were functionalized to capture different bioanalytes, for example, this sorting mechanism would allow for separation of these analytes, an important step towards multiplexed detection. This study showed a simple but powerful method to transport and sort magnetic beads on a silicon chip. This is an exciting route forward for lab-on-chip-type applications driven largely by magnetic forces and torques and potentially getting around the challenges associated with microfluidic systems [149] (Fig. 15.7).

15.4 Future Perspectives

The fundamental challenge for materials developed for clinical techniques is in achieving the desired materials performance within the required bounds of toxicity that are defined by any in vivo application. Iron oxide-based nanoparticles still form the mainstay of magnetic nanoparticles relevant for this field particularly

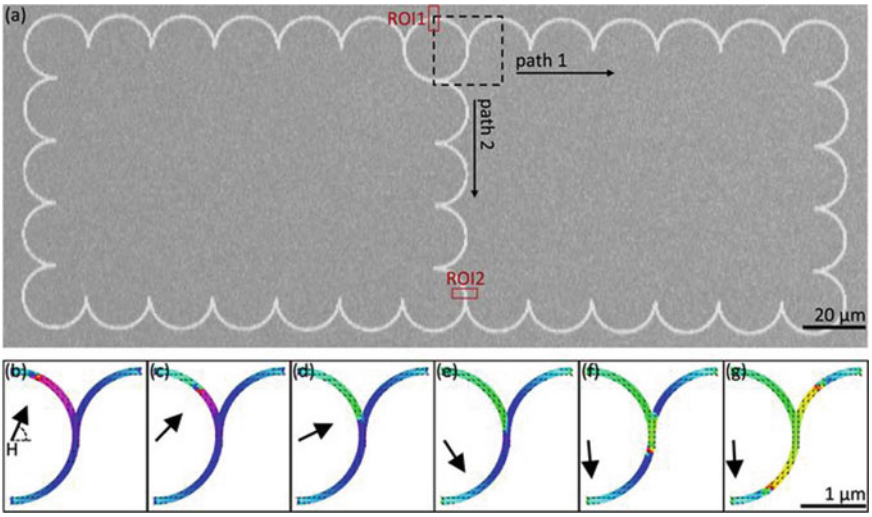

Fig. 15.7 Magnetic nanotrack configuration used to transport magnetic beads with domain walls and simulations of domain wall motion. **a** An optical image of the curvilinear permalloy track composed of 20 µm outer diameter, 800 nm wide, 40 nm thick linked semi-circular segments. The dashed square shows the micromagnetically simulated junction region consisting of a full circle that links two independent paths to an incoming track. **b–g** Evolution of the simulated magnetization configuration in junction region with the rotation of an applied magnetic field (black arrow) in the plane of the track. As the applied in-plane field is rotated in time, a head-to-head domain wall enters the junction, and two domain walls, one head-to-head and one tail-to-tail, exit the junction, one on each path. Figure reproduced from [142] with permission

because they are minimally toxic. Working within these limits, significant progress has been made in the development of iron oxide nanoparticle synthesis that are effective for hyperthermia or imaging applications [150, 151]. The pharmacokinetics and biodistribution of the nanoparticles are also important once they meet the toxicology requirements [152]. Here, size and functional coatings and encapsulations are crucial in ensuring that the nanoparticles remain in the body for long enough to be relevant as therapeutics or image enhancing agents [153]. The optimization of nanoparticle formulations for biostability and minimal toxicity will continue to be a challenge as new nanoparticle systems are developed with better magnetic properties.

For MRI imaging, an area of extreme interest is a dual-mode contrast agent, where both T_1 and T_2* imaging modes may be enhanced and used simultaneously with the same probe [55, 154]. Work in this direction has thus far focussed on core–shell-type nanoparticle structures with a transition metal-based core and a Gd-based shell [154–158]. The Gd shell is in direct contact with the liquid to ensure that the T_1 contrast agent can operate on the short length scale (in "direct contact" with the hydrogen atoms), and the superparamagnetic core is still able to influence the T_2* relaxation process via the stray magnetic field generated [55]. The development of a successful, high-performance, dual-mode probe would be a paradigm shift in the MRI field and work in this area is worthy of attention.

In the imaging space, optimizing SPIONs for the MPI field is an extremely relevant challenge with significant expected impact in the next decade. The performance of SPIONs as MPI tracers is generally evaluated by a combination of the Langevin theory of paramagnetism and understanding the relaxation processes for a magnetized nanoparticle [159, 160]. Magnetic nanoparticles typically consist of a magnetic centre and a coating of a capping polymer or organic molecules. Particles with a larger core have a higher magnetic moment and generally produce higher signal increasing imaging sensitivity. As particles get larger, however, their relaxation time (typically dominated by Brownian processes in MPI) increases [161]. This affects spatial resolution since the particle response to the FFP should be as near to instantaneous as possible to allow for the detection of the higher-order harmonics in the magnetization response to the modulation field. Typically, for a given applied field configuration, the goal is to maximize the size of the SPIONs until particle relaxation begins to impede spatial resolution. The polydispersity of SPION formulations can also have a large impact on MPI performance [160] since both the Langevin function for the magnetization and the Brownian function for relaxation are strongly dependent on particle size [161]. Particles that are smaller than ideal do not have high enough signals, and particles that are larger have long relaxation times, and so the monodispersity of SPION tracers is crucial to maximize MPI signal per unit gram of tracer used. Further, since SPIONs are typically fabricated with an encapsulation for stability and Brownian relaxation processes are dependent on the effective hydrodynamic radius, the optimum coating thickness to magnetic core ratio is also a factor of consideration. With MPI performance so closely tied to the quality of the SPION tracers, there is significant potential for concerted SPION development that may be specific to a given diagnostic application. The commercial interest in development of MPI nanoparticle formulations is evident in that Lodespin Labs has been founded around this goal and has already created the first commercial SPION-based tracer dedicated for MPI [132].

From the thermal ablation perspective, there are two overarching goals moving forward. The first is to develop nanoparticle formulations to maximize the SLP, with a minimum figure of merit of 1000 W/g at 100 kHz and 20 mT [162]. This is already significantly higher than the 200–600 W/g obtained from commercially available SPION formulations [133]. The work in this area has moved towards modifying the nanoparticle structure and material composition with a variety of core–shell structures utilizing exchange coupling [28, 131, 163, 164] to massively increase the SLP. Three materials properties that are of importance here are nanoparticles diameter D, anisotropy K, the nanoparticle shape and saturation magnetization M_S. The particularly relevant parameter to tune is the anisotropy of the nanoparticles used [75, 165–167], and it is here that the interfacial coupling between core–shell nanoparticles becomes relevant. By using a hard magnetic core and soft magnetic shell that are magnetically coupled, the anisotropy can be tuned to be close to the theoretically ideal point for maximizing the SLP with values of 1000–4000 W/g [28] demonstrated. With nanoparticle shape and size, optimized values in excess of 10,000 W/g have been observed [167]. Most of this work has focussed on Mn, Zn and Co ferrites which may prove to be challenging with regard to regulatory approval

for clinical deployment. These approaches may feed into novel iron oxide-based nanoparticle development with interesting shape and magnetic structures that could unlock high SAR values while allowing for safe clinical deployment [168, 169]. The second goal for magnetic hyperthermia has been in establishing a general theoretical framework. Strong steps forward have been made by creating theoretical models for the various aspects comprising the whole. This includes modelling hysteresis processes [170, 171], understanding the role of interparticle dipolar interactions on the SLP [136–139, 172, 173], and the role of the anisotropy of magnetic particle aggregates [75, 174]. Developing a theoretical framework that encapsulates the full complexity of hyperthermia processes, along with a strong push towards optimizing nanoparticle fabrication within the toxicity restrictions of an in vivo application is crucial for the commercial future of clinical magnetically driven thermal ablation techniques. It is expected to be unlikely [175] that magnetic particle hyperthermia will in the short term be the silver bullet that entirely replaces the more damaging cancer therapies of chemo and radiotherapy, but it may find applicability in specific instances of cancer treatment [176, 177].

Diagnostics applications that do not require in vivo deployment of magnetic nanoparticles allow more flexibility in particle composition as they are not as restricted by toxicity considerations. This may be of relevance for MR-based sensing techniques where the sensor detects the stray field from a nanoparticle as a positive signal. Here, nanoparticle development may be towards developing techniques that maximize the stray field of the particles while minimizing agglomeration, and developing nanoparticles optimized for detection by MR type sensors may prove worthwhile [96]. With recent interest in the manipulation of magnetic beads on chips using the motion of domain walls or patterned magnetic structures [140–145, 178, 179], there is potentially an alternative to microfluidic-based approaches to biomolecule capture, transport and detection. Combined with optical, electrical or magnetic sensing-based approaches, this is an interesting way forward for nanoparticle techniques in the biosensing space.

In addition to colloidally synthesized magnetic nanoparticles, lithographically defined structures for biotechnology applications have also been discussed here. The attraction of lithographically defined microdiscs is the ability to engineer magnetic particles with a precision that is simply not offered by colloidal chemistry fabrication techniques [99]. By being able to finely tune the size and shape of the discs, as well as the amount of magnetic material, and the strength and orientation of the magnetic anisotropy, local forces and torques may be applied with a high degree of control. This is particularly relevant in cell manipulation for downstream responses as cellular processes may be triggered by mechanical stimulation. For cancer cell death, for example, torques in the range of aNm may trigger apoptotic cell death [36] via ion channel mediation, a mechanism that does not trigger an inflammatory response in the body and is important for treatments in the brain.

While work thus far has focussed on their use in therapy type applications, it will be worthwhile to explore the potential of lithographically defined particles in lab-on-chip-type systems. A need for the controlled manipulation of magnetic particles on chip may better suit the lower fabrication yields and precisely tunable magnetic

characteristics of magnetic thin-film-based fabrication techniques. While defining the application space where these particles will be the most effective has proved challenging, general insights may be gained by their use since their properties may be conveniently engineered. A thorough exploration of the available existing and potential future applications with regard to these types of particles will be a worthwhile undertaking to best understand where they may be most effectively deployed.

Lithographically defined particles represent systems where the magnetic properties can be extremely accurately tuned but are limited in the volume that they can be fabricated. Colloidal synthesis is on the other end of the spectrum and offers an approach for high volume fabrication of magnetic nanoparticles but is somewhat limited in the precision engineering of the magnetic properties of the particles. As both these techniques evolve further the gap between them is likely to be bridged allowing a broader range of magnetic micro- and nanoparticles that will be exciting for the biomedical field.

Magnetic nanoparticles cover a wide range of applications in the biomedical space, ranging from in vivo imaging and therapy to ex vivo diagnostics. Nanoparticle synthesis and fabrication has continually evolved and opened new areas where these systems offer benefit and insight. It is expected that this community will continue to make strong contributions towards solving the varied and exciting challenges offered by the biomedical space.

References

1. U. Jeong, X. Teng, Y. Wang, H. Yang, Y. Xia, Adv. Mater. **19**, 33 (2007). https://doi.org/10.1002/adma.200600674
2. R. Hao, R. Xing, Z. Xu, Y. Hou, S. Gao, S. Sun, Adv. Mater. **22**, 2729 (2010). https://doi.org/10.1002/adma.201000260
3. T. Neuberger, B. Schöpf, H. Hofmann, M. Hofmann, B. von Rechenberg, J. Magn. Magn. Mater. **293**, 483 (2005). https://doi.org/10.1016/j.jmmm.2005.01.064
4. S. Sun, H. Zeng, J. Am. Chem. Soc. **124**, 8204 (2002). https://doi.org/10.1021/ja026501x
5. S. Laurent, D. Forge, M. Port, A. Roch, C. Robic, L. Vander Elst, R.N. Muller, Chem. Rev. **108**, 2064 (2008). https://doi.org/10.1021/cr068445e
6. A.K. Gupta, M. Gupta, Biomaterials **26**, 3995 (2005). https://doi.org/10.1016/j.biomaterials.2004.10.012
7. L.H. Reddy, J.L. Arias, J. Nicolas, P. Couvreur, Chem. Rev. **112**, 5818 (2012). https://doi.org/10.1021/cr300068p
8. Q.A Pankhurst, J. Connolly, S.K. Jones, J. Dobson, J. Phys. D. Appl. Phys. **36**, R167 (2003). https://doi.org/10.1088/0022-3727/36/13/201
9. M.L. Néel, Ann. Geophys. **5**, 99 (1949). https://doi.org/10.1017/CBO9781107415324.004
10. W.F. Brown, Phys. Rev. **130**, 1677 (1963). https://doi.org/10.1103/PhysRev.130.1677
11. A.-H. Lu, E.L. Salabas, F. Schüth, Angew. Chemie Int. Ed. **46**, 1222 (2007). https://doi.org/10.1002/anie.200602866
12. R.H. Kodama, J. Magn. Magn. Mater. **200**, 359 (1999). https://doi.org/10.1016/S0304-8853(99)00347-9
13. I. Sharifi, H. Shokrollahi, S. Amiri, J. Magn. Magn. Mater. **324**, 903 (2012). https://doi.org/10.1016/j.jmmm.2011.10.017

14. H. Deng, X. Li, Q. Peng, X. Wang, J. Chen, Y. Li, Angew. Chemie Int. Ed. **44**, 2782 (2005). https://doi.org/10.1002/anie.200462551
15. M. Bellusci, C. Aliotta, D. Fiorani, A. La Barbera, F. Padella, D. Peddis, M. Pilloni, D. Secci, J. Nanoparticle Res. **14**, 904 (2012). https://doi.org/10.1007/s11051-012-0904-7
16. D. Peddis, N. Yaacoub, M. Ferretti, A. Martinelli, G. Piccaluga, A. Musinu, C. Cannas, G. Navarra, J.M. Greneche, D. Fiorani, J. Phys. Condens. Matter **23**, 426004 (2011). https://doi.org/10.1088/0953-8984/23/42/426004
17. J. McCarthy, R. Weissleder, Adv. Drug Deliv. Rev. **60**, 1241 (2008). https://doi.org/10.1016/j.addr.2008.03.014
18. Y. Jun, J. Lee, J. Cheon, Angew. Chemie Int. Ed. **47**, 5122 (2008). https://doi.org/10.1002/anie.200701674
19. A. Louie, Chem. Rev. **110**, 3146 (2010). https://doi.org/10.1021/cr9003538
20. Y.-X.J. Wang, S.M. Hussain, G.P. Krestin, Eur. Radiol. **11**, 2319 (2001). https://doi.org/10.1007/s003300100908
21. H. Bin Na, I.C. Song, T. Hyeon, Adv. Mater. **21**, 2133 (2009). https://doi.org/10.1002/adma.200802366.
22. J.W.M. Bulte, D.L. Kraitchman, NMR Biomed. **17**, 484 (2004). https://doi.org/10.1002/nbm.924
23. B. Gleich, J. Weizenecker, Nature **435**, 1214 (2005). https://doi.org/10.1038/nature03808
24. A. Jordan, R. Scholz, K. Maier-Hauff, M. Johannsen, P. Wust, J. Nadobny, H. Schirra, H. Schmidt, S. Deger, S. Loening, W. Lanksch, R. Felix, J. Magn. Magn. Mater. **225**, 118 (2001). https://doi.org/10.1016/S0304-8853(00)01239-7
25. R. Hergt, S. Dutz, R. Müller, M. Zeisberger, J. Phys. Condens. Matter **18**, S2919 (2006). https://doi.org/10.1088/0953-8984/18/38/S26
26. S. Laurent, S. Dutz, U.O. Häfeli, M. Mahmoudi, Adv. Colloid Interface Sci. **166**, 8 (2011). https://doi.org/10.1016/j.cis.2011.04.003
27. C.S.S.R. Kumar, F. Mohammad, Adv. Drug Deliv. Rev. **63**, 789 (2011). https://doi.org/10.1016/j.addr.2011.03.008
28. J.H. Lee, J.T. Jang, J.S. Choi, S.H. Moon, S.H. Noh, J.W. Kim, J.G. Kim, I.S. Kim, K.I. Park, J. Cheon, Nat. Nanotechnol. **6**, 418 (2011). https://doi.org/10.1038/nnano.2011.95
29. A. Jordan, R. Scholz, P. Wust, H. Fähling, R. Felix, J. Magn. Magn. Mater. **201**, 413 (1999). https://doi.org/10.1016/S0304-8853(99)00088-8
30. Y.R. Chemla, H.L. Grossman, Y. Poon, R. McDermott, R. Stevens, M.D. Alper, J. Clarke, Proc. Natl. Acad. Sci. U. S. A. **97**, 14268 (2000). https://doi.org/10.1073/pnas.97.26.14268
31. J.M. Nam, C.S. Thaxton, C.A. Mirkin, Science (80-.) **301**, 1884 (2003). https://doi.org/10.1126/science.1088755
32. D.A. Hall, R.S. Gaster, T. Lin, S.J. Osterfeld, S. Han, B. Murmann, S.X. Wang, Biosens. Bioelectron. **25**, 2051 (2010). https://doi.org/10.1016/j.bios.2010.01.038
33. G. Li, S. Sun, R.J. Wilson, R.L. White, N. Pourmand, S.X. Wang, Sensors Actuators. a Sens. Actuators Phys. **126**, 98 (2006). https://doi.org/10.1016/j.sna.2005.10.001
34. S.X. Wang, G. Li, in IEEE Trans. Magn. 1687–1702 (2008). https://doi.org/10.1109/TMAG.2008.920962.
35. J. Dobson, Nat. Nanotechnol. **3**, 139 (2008). https://doi.org/10.1038/nnano.2008.39
36. D.-H. Kim, E.A Rozhkova, I.V Ulasov, S.D. Bader, T. Rajh, M.S. Lesniak, V. Novosad, Nat. Mater. **9**, 165 (2010). https://doi.org/10.1038/nmat2591
37. F. Bloch, Phys. Rev. **70**, 460 (1946). https://doi.org/10.1103/PhysRev.70.460
38. E.M. Purcell, H.C. Torrey, R.V. Pound, Phys. Rev. **69**, 37 (1946). https://doi.org/10.1103/PhysRev.69.37
39. C.F.G.C. Geraldes, S. Laurent, Contrast Media Mol. Imaging **4**, 1 (2009). https://doi.org/10.1002/cmmi.265
40. R.A. Pooley, Radiographics **25**, 1087 (2005). https://doi.org/10.1148/rg.254055027
41. P.A. Bottomley, C.J. Hardy, R.E. Argersinger, G. Allen Moore, Med. Phys. **14**, 1 (1987). https://doi.org/10.1118/1.596111

42. C.T. Yang, P. Padmanabhan, B.Z. Gulyás, RSC Adv. **6**, 60945 (2016). https://doi.org/10.1039/c6ra07782j
43. G. Marchal, Y. Ni, P. Herijgers, W. Flameng, C. Petré, H. Bosmans, J. Yu, W. Ebert, C.S. Hilger, D. Pfefferer, W. Semmler, A.L. Baert, Eur. Radiol. **6**, 2 (1996). https://doi.org/10.1007/BF00619942
44. H. Bin Na, T. Hyeon, J. Mater. Chem. **19**, 6267 (2009). https://doi.org/10.1039/b902685a
45. S. Flacke, S. Fischer, M.J. Scott, R.J. Fuhrhop, J.S. Allen, M. McLean, P. Winter, G.A. Sicard, P.J. Gaffney, S.A. Wickline, G.M. Lanza, Circulation **104**, 1280 (2001). https://doi.org/10.1161/hc3601.094303
46. R.J. Kim, E.L. Chen, J.A.C. Lima, R.M. Judd, Circulation **94**, 3318 (1996). https://doi.org/10.1161/01.CIR.94.12.3318
47. E. Wiener, M.W. Brechbiel, H. Brothers, R.L. Magin, O.A. Gansow, D.A. Tomalia, P.C. Lauterbur, Magn. Reson. Med. **31**, 1 (1994). https://doi.org/10.1002/mrm.1910310102
48. V. Trubetskoy, Adv. Drug Deliv. Rev. **37**, 81 (1999). https://doi.org/10.1016/S0169-409X(98)00100-8
49. C.H. Reynolds, N. Annan, K. Beshah, J.H. Huber, S.H. Shaber, R.E. Lenkinski, J.A. Wortman, J. Am. Chem. Soc. **122**, 8940 (2000). https://doi.org/10.1021/ja001426g
50. P. Chandran, A. Sasidharan, A. Ashokan, D. Menon, S. Nair, M. Koyakutty, Nanoscale **3**, 4150 (2011). https://doi.org/10.1039/c1nr10591d
51. J. Kukowska-Latallo, Int. J. Nanomedicine **3**, 201 (2008). https://doi.org/10.2147/ijn.s2696
52. Y. Wang, T.K. Alkasab, O. Narin, R.M. Nazarian, R. Kaewlai, J. Kay, H.H. Abujudeh, Int. Braz J Urol **37**, 541 (2011). https://doi.org/10.1590/S1677-55382011000400018
53. T.G. St. Pierre, P.R. Clark, W. Chua-Anusorn, A.J. Fleming, G.P. Jeffrey, J.K. Olynyk, P. Pootrakul, E. Robins, R. Lindeman, Blood **105**, 855 (2005). https://doi.org/10.1182/blood-2004-01-0177
54. Z.R. Stephen, F.M. Kievit, M. Zhang, Mater. Today **14**, 330 (2011). https://doi.org/10.1016/S1369-7021(11)70163-8
55. M.A. Busquets, J. Estelrich, M.J. Sánchez-Martín, Int. J. Nanomedicine **10**, 1727 (2015). https://doi.org/10.2147/IJN.S76501
56. G.K. Das, N.J.J. Johnson, J. Cramen, B. Blasiak, P. Latta, B. Tomanek, F.C.J.M. Van Veggel, J. Phys. Chem. Lett. **3**, 524 (2012). https://doi.org/10.1021/jz201664h
57. H. Yang, C. Zhang, X. Shi, H. Hu, X. Du, Y. Fang, Y. Ma, H. Wu, S. Yang, Biomaterials **31**, 3667 (2010). https://doi.org/10.1016/j.biomaterials.2010.01.055
58. C.G. Hadjipanayis, M.J. Bonder, S. Balakrishnan, X. Wang, H. Mao, G.C. Hadjipanayis, Small **4**, 1925 (2008). https://doi.org/10.1002/smll.200800261
59. Q.L. Vuong, J.F. Berret, J. Fresnais, Y. Gossuin, O. Sandre, Adv. Healthc. Mater. **1**, 502 (2012). https://doi.org/10.1002/adhm.201200078
60. P.C. Lauterbur, Nature **242**, 190 (1973). https://doi.org/10.1038/242190a0
61. A.P. Khandhar, R.M. Ferguson, H. Arami, K.M. Krishnan, Biomaterials **34**, 3837 (2013). https://doi.org/10.1016/j.biomaterials.2013.01.087
62. D. Eberbeck, F. Wiekhorst, S. Wagner, L. Trahms, Appl. Phys. Lett. **98**, 182502 (2011). https://doi.org/10.1063/1.3586776
63. S. Biederer, T. Knopp, T.F. Sattel, K. Lüdtke-Buzug, B. Gleich, J. Weizenecker, J. Borgert, T.M. Buzug, J. Phys. D. Appl. Phys. **42**, 205007 (2009). https://doi.org/10.1088/0022-3727/42/20/205007
64. P.C. Fannin, S.W. Charles, J. Phys. D. Appl. Phys. **22**, 187 (1989). https://doi.org/10.1088/0022-3727/22/1/027
65. P.W. Goodwill, A. Tamrazian, L.R. Croft, C.D. Lu, E.M. Johnson, R. Pidaparthi, R.M. Ferguson, A.P. Khandhar, K.M. Krishnan, S.M. Conolly, Appl. Phys. Lett. **98**, 262502 (2011). https://doi.org/10.1063/1.3604009
66. N. Panagiotopoulos, F. Vogt, J. Barkhausen, T.M. Buzug, R.L. Duschka, K. Lüdtke-Buzug, M. Ahlborg, G. Bringout, C. Debbeler, M. Gräser, C. Kaethner, J. Stelzner, H. Medimagh, J. Haegele, Int. J. Nanomedicine **10**, 3097 (2015). https://doi.org/10.2147/IJN.S70488

67. J. Weizenecker, B. Gleich, J. Rahmer, H. Dahnke, J. Borgert, Phys. Med. Biol. **54**, L1 (2009). https://doi.org/10.1088/0031-9155/54/5/L01
68. R.M. Ferguson, A.P. Khandhar, K.M. Krishnan, J. Appl. Phys. **111**, 07B318 (2012). https://doi.org/10.1063/1.3676053
69. M.H. Pablico-Lansigan, S.F. Situ, A.C.S. Samia, Nanoscale **5**, 4040 (2013). https://doi.org/10.1039/c3nr00544e
70. G. Vallejo-Fernandez, O. Whear, A.G. Roca, S. Hussain, J. Timmis, V. Patel, K. O'Grady, J. Phys. D. Appl. Phys. **46**, 312001 (2013). https://doi.org/10.1088/0022-3727/46/31/312001
71. R. Hergt, R. Hiergeist, M. Zeisberger, G. Glöckl, W. Weitschies, L.P. Ramirez, I. Hilger, W.A. Kaiser, J. Magn. Magn. Mater. **280**, 358 (2004). https://doi.org/10.1016/j.jmmm.2004.03.034
72. R. Hergt, S. Dutz, M. Röder, J. Phys. Condens. Matter **20**, 385214 (2008). https://doi.org/10.1088/0953-8984/20/38/385214
73. A.A. McGhie, C. Marquina, K. O'Grady, G. Vallejo-Fernandez, J. Phys. D. Appl. Phys. **50**, 455003 (2017). https://doi.org/10.1088/1361-6463/aa88ed
74. G. Vallejo-Fernandez, K. O'Grady, Appl. Phys. Lett. **103**, 142417 (2013). https://doi.org/10.1063/1.4824649
75. C.L. Dennis, R. Ivkov, Int. J. Hyperth. **29**, 715 (2013). https://doi.org/10.3109/02656736.2013.836758
76. I.M. Obaidat, B. Issa, Y. Haik, Nanomaterials **5**, 63 (2014). https://doi.org/10.3390/nano5010063
77. F.H.C. Crick, A.F.W. Hughes, Exp. Cell Res. **1**, 37 (1950). https://doi.org/10.1016/0014-4827(50)90048-6
78. N. Wang, J.P. Butler, D.E. Ingber, Science (80-.). **260**, 1124 (1993). https://doi.org/10.1126/science.7684161
79. A. Du Toit, Nat. Rev. Mol. Cell Biol. **14**, 196 (2013). https://doi.org/10.1038/nrm3534
80. C.J. Meyer, F.J. Alenghat, P. Rim, J.H.J. Fong, B. Fabry, D.E. Ingber, Nat. Cell Biol. **2**, 666 (2000). https://doi.org/10.1038/35023621
81. H.A. Benhardt, E.M. Cosgriff-Hernandez, Tissue Eng. Part B Rev. **15**, 467 (2009). https://doi.org/10.1089/ten.teb.2008.0687
82. S.H. Cartmell, J. Dobson, S.B. Verschueren, A.J. El Haj, IEEE Trans. Nanobioscience **1**, 92 (2002). https://doi.org/10.1109/TNB.2002.806945
83. G.R. Kirkham, K.J. Elliot, A. Keramane, D.M. Salter, J.P. Dobson, A.J. El Haj, S.H. Cartmell, IEEE Trans. Nanobioscience **9**, 71 (2010). https://doi.org/10.1109/TNB.2010.2042065
84. D. Cheng, X. Li, G. Zhang, H. Shi, Nanoscale Res. Lett. **9**, 195 (2014). https://doi.org/10.1186/1556-276X-9-195
85. M. Domenech, I. Marrero-Berrios, M. Torres-Lugo, C. Rinaldi, ACS Nano **7**, 5091 (2013). https://doi.org/10.1021/nn4007048
86. T.A.P. Rocha-Santos, TtrAc Trends Anal. Chem. **62**, 28 (2014). https://doi.org/10.1016/j.trac.2014.06.016
87. S.X. Wang, S.Y. Bae, G. Li, S. Sun, R.L. White, J.T. Kemp, C.D. Webb, J. Magn. Magn. Mater. 731–736 (2005). https://doi.org/10.1016/j.jmmm.2005.02.054
88. P.I. Nikitin, P.M. Vetoshko, T.I. Ksenevich, J. Magn. Magn. Mater. **311**, 445 (2007). https://doi.org/10.1016/j.jmmm.2006.10.1180
89. I. Koh, L. Josephson, Sensors **9**, 8130 (2009). https://doi.org/10.3390/s91008130
90. J.B. Haun, T.J. Yoon, H. Lee, R. Weissleder, Wiley Interdiscip. Rev. Nanomedicine. NanoBiotechnology **2**, 291 (2010). https://doi.org/10.1002/wnan.84
91. J. Connolly, T.G. St Pierre, J. Magn. Magn. Mater. **225**, 156 (2001). https://doi.org/10.1016/S0304-8853(00)01245-2
92. G. Lin, D. Makarov, O.G. Schmidt, Lab Chip **17**, 1884 (2017). https://doi.org/10.1039/c7lc00026j
93. S.J. Osterfeld, H. Yu, R.S. Gaster, S. Caramuta, L. Xu, S.J. Han, D.A. Hall, R.J. Wilson, S. Sun, R.L. White, R.W. Davis, N. Pourmand, S.X. Wang, Proc. Natl. Acad. Sci. U. S. A. **105**, 20637 (2008). https://doi.org/10.1073/pnas.0810822105

94. D.L. Graham, H.A. Ferreira, P.P. Freitas, Trends Biotechnol. **22**, 455 (2004). https://doi.org/10.1016/j.tibtech.2004.06.006
95. J. Schotter, P.B. Kamp, A. Becker, A. Pühler, G. Reiss, H. Brückl, Biosens. Bioelectron. **19**, 1149 (2004). https://doi.org/10.1016/j.bios.2003.11.007
96. W. Wang, Y. Wang, L. Tu, Y. Feng, T. Klein, J.-P. Wang, Sci. Rep. **4**, 5716 (2015). https://doi.org/10.1038/srep05716
97. J.R. Lee, C.T. Chan, D. Ruderman, H.Y. Chuang, R.S. Gaster, M. Atallah, P. Mallick, S.W. Lowe, S.S. Gambhir, S.X. Wang, Nano Lett. **17**, 6644 (2017). https://doi.org/10.1021/acs.nanolett.7b02591
98. R.S. Gaster, D.A. Hall, C.H. Nielsen, S.J. Osterfeld, H. Yu, K.E. MacH, R.J. Wilson, B. Murmann, J.C. Liao, S.S. Gambhir, S.X. Wang, Nat. Med. **15**, 1327 (2009). https://doi.org/10.1038/nm.2032
99. E.A. Vitol, V. Novosad, E.A. Rozhkova, Nanomedicine **7**, 1611 (2012). https://doi.org/10.2217/nnm.12.133
100. E.A. Vitol, V. Novosad, E.A. Rozhkova, IEEE Trans. Magn. **48**, 3269 (2012). https://doi.org/10.1109/TMAG.2012.2198209
101. T. Vemulkar, E.N. Welbourne, R. Mansell, D.C.M.C. Petit, R.P. Cowburn, Appl. Phys. Lett. **110**, 042402 (2017). https://doi.org/10.1063/1.4974211
102. W. Hu, R.J. Wilson, A. Koh, A. Fu, A.Z. Faranesh, C.M. Earhart, S.J. Osterfeld, S.J. Han, L. Xu, S. Guccione, R. Sinclair, S.X. Wang, Adv. Mater. **20**, 1479 (2008). https://doi.org/10.1002/adma.200703077
103. R.P. Cowburn, D.K. Koltsov, A.O. Adeyeye, M.E. Welland, 2 (1999)
104. W. Scholz, K.Y. Guslienko, V. Novosad, D. Suess, T. Schrefl, R. Chantrell, J. Fidler, J. Magn. Magn. Mater. **266**, 155 (2003). https://doi.org/10.1016/S0304-8853(03)00466-9
105. K.Y. Guslienko, V. Novosad, Y. Otani, H. Shima, K. Fukamichi, Appl. Phys. Lett. **78**, 3848 (2001). https://doi.org/10.1063/1.1377850
106. K.Y. Guslienko, V. Novosad, Y. Otani, H. Shima, K. Fukamichi, Phys. Rev. B Condens. Matter Mater. Phys. **65**, 244141 (2002). https://doi.org/10.1103/PhysRevB.65.024414
107. T. Kasuya, Prog. Theor. Phys. **16**, 45 (1956)
108. C. Kittel, M.A. Ruderman, Phsyical Rev. **96**, 72 (1954)
109. K. Yosida, Phys. Rev. **106** (1957)
110. J.L. Leal, M.H. Kryder, J. Appl. Phys. **83**, 3720 (1998). https://doi.org/10.1063/1.366597
111. S. Bandiera, R.C. Sousa, Y. Dahmane, C. Ducruet, C. Portemont, V. Baltz, S. Auffret, I.L. Prejbeanu, B. Dieny, I.E.E.E. Magn, Lett. **1**, 3000204 (2010). https://doi.org/10.1109/LMAG.2010.2052238
112. R. Lavrijsen, J.H. Lee, A. Fernández-Pacheco, D.C.M.C. Petit, R. Mansell, R.P. Cowburn, Nature **493**, 647 (2013). https://doi.org/10.1038/nature11733
113. P. Bruno, J. Phys. Condens. Matter **11**, 9403 (1999). https://doi.org/10.1088/0953-8984/11/48/305
114. P. Bruno, C. Chappert, Phys. Rev. Lett. **67**, 1602 (1991)
115. D. Mauri, S.S. Parkin, **44**, 7131 (1991)
116. S.S. Parkin, Phys. Rev. Lett. **67**, 3598 (1991)
117. M. D. Stiles, **2**, 1 (2002).
118. S. Leulmi, H. Joisten, T. Dietsch, C. Iss, M. Morcrette, S. Auffret, P. Sabon, B. Dieny, Appl. Phys. Lett. **103**, 132412 (2013). https://doi.org/10.1063/1.4821854
119. T. Courcier, H. Joisten, P. Sabon, S. Leulmi, T. Dietsch, J. Faure-Vincent, S. Auffret, B. Dieny, Appl. Phys. Lett. **99**, 093107 (2011). https://doi.org/10.1063/1.3633121
120. M.T. Johnson, P.J.H. Bloemen, F.J.A. Den Broeder, J.J. De Vries, Reports. Prog. Phys. **59**, 1409 (1996). https://doi.org/10.1088/0034-4885/59/11/002
121. P. Bruno, Phys. Rev. B **39**, 865 (1989). https://doi.org/10.1103/PhysRevB.39.865
122. G.C. Fletcher, Proc. Phys. Soc. Sect. A **67**, 505 (1954). https://doi.org/10.1088/0370-1298/67/6/303
123. J.H. Van Vleck, Phys. Rev. **52**, 1178 (1937). https://doi.org/10.1103/PhysRev.52.1178

124. T. Vemulkar, R. Mansell, D.C.M.C. Petit, R.P. Cowburn, M.S. Lesniak, Appl. Phys. Lett. **107**, 012403 (2015). https://doi.org/10.1063/1.4926336
125. R. Mansell, T. Vemulkar, D.C.M.C. Petit, Y. Cheng, J. Murphy, M.S. Lesniak, R.P. Cowburn, Sci. Rep. **7**, 4257 (2017). https://doi.org/10.1038/s41598-017-04154-1
126. M.E. Muroski, R.A. Morshed, Y. Cheng, T. Vemulkar, R. Mansell, Y. Han, L. Zhang, K.S. Aboody, R.P. Cowburn, M.S. Lesniak, PLoS ONE **11**, e0145129 (2016). https://doi.org/10.1371/journal.pone.0145129
127. Y. Cheng, M.E. Muroski, D.C.M.C. Petit, R. Mansell, T. Vemulkar, R.A. Morshed, Y. Han, I.V. Balyasnikova, C.M. Horbinski, X. Huang, L. Zhang, R.P. Cowburn, M.S. Lesniak, J. Control. Release **223**, 75 (2016). https://doi.org/10.1016/j.jconrel.2015.12.028
128. Y. Zhang, J. Yu, H.N. Bomba, Y. Zhu, Z. Gu, Chem. Rev. **116**, 12536 (2016). https://doi.org/10.1021/acs.chemrev.6b00369
129. Y. Qiu, S. Tong, L. Zhang, Y. Sakurai, D.R. Myers, L. Hong, W.A. Lam, G. Bao, Nat. Commun. **8**, 15594 (2017). https://doi.org/10.1038/ncomms15594
130. E.Y. Yu, M. Bishop, B. Zheng, R.M. Ferguson, A.P. Khandhar, S.J. Kemp, K.M. Krishnan, P.W. Goodwill, S.M. Conolly, Nano Lett. (2017). https://doi.org/10.1021/acs.nanolett.6b04865
131. G. Song, C. Liang, H. Gong, M. Li, X. Zheng, L. Cheng, K. Yang, X. Jiang, Z. Liu, Adv. Mater. **27**, 6110 (2015). https://doi.org/10.1002/adma.201503006
132. A.P. Khandhar, P. Keselman, S.J. Kemp, R.M. Ferguson, P.W. Goodwill, S.M. Conolly, K.M. Krishnan, Nanoscale **9**, 1299 (2017). https://doi.org/10.1039/c6nr08468k
133. H. Kobayashi, R. Watanabe, P.L. Choyke, Theranostics **4**, 81 (2014). https://doi.org/10.7150/thno.7193
134. C. Martinez-Boubeta, K. Simeonidis, A. Makridis, M. Angelakeris, O. Iglesias, P. Guardia, A. Cabot, L. Yedra, S. Estradé, F. Peiró, Z. Saghi, P.A. Midgley, I. Conde-Leborán, D. Serantes, D. Baldomir, Sci. Rep. **3**, 1652 (2013). https://doi.org/10.1038/srep01652
135. R. Hergt, R. Hiergeist, M. Zeisberger, D. Schüler, U. Heyen, I. Hilger, W.A. Kaiser, J. Magn. Magn. Mater. **293**, 80 (2005). https://doi.org/10.1016/j.jmmm.2005.01.047
136. J.G. Ovejero, D. Cabrera, J. Carrey, T. Valdivielso, G. Salas, F.J. Teran, Phys. Chem. Chem. Phys. **18**, 10954 (2016). https://doi.org/10.1039/c6cp00468g
137. M.E. Sadat, R. Patel, J. Sookoor, S.L. Bud'Ko, R.C. Ewing, J. Zhang, H. Xu, Y. Wang, G.M. Pauletti, D.B. Mast, D. Shi, Mater. Sci. Eng. C **42**, 52 (2014). https://doi.org/10.1016/j.msec.2014.04.064
138. D.F. Coral, P. Mendoza Zélis, M. Marciello, M.D.P. Morales, A. Craievich, F.H. Sánchez, M.B. Fernández Van Raap, Langmuir **32**, 1201 (2016). https://doi.org/10.1021/acs.langmuir.5b03559
139. L.C. Branquinho, M.S. Carrião, A.S. Costa, N. Zufelato, M.H. Sousa, R. Miotto, R. Ivkov, A.F. Bakuzis, Sci. Rep. **3**, 2887 (2013). https://doi.org/10.1038/srep02887
140. E. Rapoport, D. Montana, G.S.D. Beach, Lab Chip **12**, 4433 (2012). https://doi.org/10.1039/c2lc40715a
141. G. Vieira, T. Henighan, A. Chen, A.J. Hauser, F.Y. Yang, J.J. Chalmers, R. Sooryakumar, Phys. Rev. Lett. **103**, 128101 (2009). https://doi.org/10.1103/PhysRevLett.103.128101
142. E. Rapoport, G.S.D. Beach, Sci. Rep. **7**, 10139 (2017). https://doi.org/10.1038/s41598-017-10149-9
143. E. Rapoport, G.S.D. Beach, Phys. Rev. B Condens. Matter Mater. Phys. **87**, 174426 (2013). https://doi.org/10.1103/PhysRevB.87.174426.
144. E. Rapoport, G.S.D. Beach, Appl. Phys. Lett. **100**, 082401 (2012). https://doi.org/10.1063/1.3684972
145. M. Donolato, B.T. Dalslet, M.F. Hansen, Biomicrofluidics **6**, 024110 (2012). https://doi.org/10.1063/1.4704520
146. G. Vieira, A. Chen, T. Henighan, J. Lucy, F.Y. Yang, R. Sooryakumar, Phys. Rev. B **85**, 174440 (2012). https://doi.org/10.1103/PhysRevB.85.174440
147. R.D. McMichael, M.J. Donahue, IEEE Trans. Magn. **33**, 4167 (1997). https://doi.org/10.1109/20.619698

148. W.C. Uhlig, M.J. Donahue, D.T. Pierce, J. Unguris, J. Appl. Phys. **105**, 103902 (2009). https://doi.org/10.1063/1.3125526
149. D.T. Chiu, A.J. DeMello, D. Di Carlo, P.S. Doyle, C. Hansen, R.M. Maceiczyk, R.C.R. Wootton, Chem **2**, 201 (2017). https://doi.org/10.1016/j.chempr.2017.01.009
150. Y.M. Wang, X. Cao, G.H. Liu, R.Y. Hong, Y.M. Chen, X.F. Chen, H.Z. Li, B. Xu, D.G. Wei, J. Magn. Magn. Mater. **323**, 2953 (2011). https://doi.org/10.1016/j.jmmm.2011.05.060
151. R. Qiao, C. Yang, M. Gao, J. Mater. Chem. **19**, 6274 (2009). https://doi.org/10.1039/b902394a
152. R.A. Petros, J.M. Desimone, Nat. Rev. Drug Discov. **9**, 615 (2010). https://doi.org/10.1038/nrd2591
153. K.M. Krishnan, IEEE Trans. Magn. **46**, 2523 (2010). https://doi.org/10.1109/TMAG.2010.2046907
154. T.H. Shin, Y. Choi, S. Kim, J. Cheon, Chem. Soc. Rev. **44**, 4501 (2015). https://doi.org/10.1039/c4cs00345d
155. M.W. Ahmad, W. Xu, S.J. Kim, J.S. Baeck, Y. Chang, J.E. Bae, K.S. Chae, J.A. Park, T.J. Kim, G.H. Lee, Sci. Rep. **5**, 8549 (2015). https://doi.org/10.1038/srep08549
156. R. Anbazhagan, Y.A. Su, H.C. Tsai, R.J. Jeng, A.C.S. Appl, Mater. Interfaces **8**, 1827 (2016). https://doi.org/10.1021/acsami.5b09722
157. Y.K. Peng, C.N.P. Lui, Y.W. Chen, S.W. Chou, P.T. Chou, K.K.L. Yung, S.C. Edman Tsang, Nanotechnology **29**, 015102 (2018). https://doi.org/10.1088/1361-6528/aa96eb
158. M. Yang, L. Gao, K. Liu, C. Luo, Y. Wang, L. Yu, H. Peng, W. Zhang, Talanta **131**, 661 (2015). https://doi.org/10.1016/j.talanta.2014.08.042
159. R.M. Ferguson, K.R. Minard, K.M. Krishnan, J. Magn. Magn. Mater. **321**, 1548 (2009). https://doi.org/10.1016/j.jmmm.2009.02.083
160. Y. Du, P.T. Lai, C.H. Leung, P.W.T. Pong, Int. J. Mol. Sci. **14**, 18682 (2013). https://doi.org/10.3390/ijms140918682
161. R. Dhavalikar, C. Rinaldi, J. Appl. Phys. **115**, 074308 (2014). https://doi.org/10.1063/1.4866680
162. L. Kafrouni, O. Savadogo, Prog. Biomater. **5**, 147 (2016). https://doi.org/10.1007/s40204-016-0054-6
163. M.R. Phadatare, J.V. Meshram, K.V. Gurav, J.H. Kim, S.H. Pawar, J. Phys. D. Appl. Phys. **49**, 095004 (2016). https://doi.org/10.1088/0022-3727/49/9/095004
164. S.H. Moon, S.H. Noh, J.H. Lee, T.H. Shin, Y. Lim, J. Cheon, Nano Lett. **17**, 800 (2017). https://doi.org/10.1021/acs.nanolett.6b04016
165. H. Khurshid, J. Alonso, Z. Nemati, M.H. Phan, P. Mukherjee, M.L. Fdez-Gubieda, J.M. Barandiarán, H. Srikanth, J. Appl. Phys. **117**, 17A337 (2015). https://doi.org/10.1063/1.4919250
166. N.A. Usov, B.Y. Liubimov, J. Appl. Phys. **112**, 023901 (2012). https://doi.org/10.1063/1.4737126
167. S.H. Noh, W. Na, J.T. Jang, J.H. Lee, E.J. Lee, S.H. Moon, Y. Lim, J.S. Shin, J. Cheon, Nano Lett. **12**, 3716 (2012). https://doi.org/10.1021/nl301499u
168. N.A. Usov, M.S. Nesmeyanov, V.P. Tarasov, Sci. Rep. **8**, 1224 (2018). https://doi.org/10.1038/s41598-017-18162-8
169. X.L. Liu, Y. Yang, C.T. Ng, L.Y. Zhao, Y. Zhang, B.H. Bay, H.M. Fan, J. Ding, Adv. Mater. **27**, 1939 (2015). https://doi.org/10.1002/adma.201405036
170. S. Ruta, R. Chantrell, O. Hovorka, Sci. Rep. **5**, 9090 (2015). https://doi.org/10.1038/srep09090
171. D.B. Reeves, J.B. Weaver, Appl. Phys. Lett. **104**, 102403 (2014). https://doi.org/10.1063/1.4867987
172. C. Haase, U. Nowak, Phys. Rev. B **85**, 045435 (2012). https://doi.org/10.1103/PhysRevB.85.045435
173. G.T. Landi, Phys. Rev. B **89**, 014403 (2014). https://doi.org/10.1103/PhysRevB.89.014403
174. R. Fu, Y. Yan, C. Roberts, Z. Liu, Y. Chen, Sci. Rep. **8**, 4704 (2018). https://doi.org/10.1038/s41598-018-23225-5
175. S. Dutz, R. Hergt, Nanotechnology **25**, 452001 (2014). https://doi.org/10.1088/0957-4484/25/45/452001

176. M. Johannsen, U. Gneveckow, L. Eckelt, A. Feussner, N. WaldÖFner, R. Scholz, S. Deger, P. Wust, S.A. Loening, A. Jordan, Int. J. Hyperth. **21**, 637 (2005). https://doi.org/10.1080/02656730500158360
177. M. Johannsen, B. Thiesen, P. Wust, A. Jordan, Int. J. Hyperth. **26**, 790 (2010). https://doi.org/10.3109/02656731003745740
178. M.T. Bryan, K.H. Smith, M.E. Real, M.A. Bashir, P.W. Fry, P. Fischer, M.-Y. Im, T. Schrefl, D.A. Allwood, J.W. Haycock, IEEE Magn. Lett. **1**, 1500104 (2010). https://doi.org/10.1109/LMAG.2010.2046143
179. B. Lim, V. Reddy, X. Hu, K. Kim, M. Jadhav, R. Abedini-Nassab, Y.-W. Noh, Y.T. Lim, B.B. Yellen, C. Kim, Nat. Commun. **5**, 3846 (2014). https://doi.org/10.1038/ncomms4846

Chapter 16
Magnetic Fluids for Thermoelectricity

Sawako Nakamae

Abstract The unique properties of magnetic nanoparticles (MNP) and their interactions with their environment have given rise to innovative R&D possibilities outside the field of conventional magnetism. One such example is in the field of energy science, and in particular, the thermal engineering. In this respect, research on refrigeration technology based on the magnetoconvection property of ferrofluids (FF) has attracted great attention in the past decades. On the other hand, the thermoelectric energy conversion (or more commonly known as "thermopower") in ferrofluids has so far remained underexplored. This subchapter describes this very new research path in the field of magnetic nanoparticle science, from its theoretical background and motivation, a few existing example of experimental investigations and the future perspectives. The unique properties of magnetic nanoparticles (MNP) and their interactions with their environment have given rise to innovative R&D possibilities outside the field of conventional magnetism. One such example is in the field of energy science, and in particular, the thermal engineering. In this respect, research on refrigeration technology based on the magnetoconvection property of ferrofluids (FF) has attracted great attention in the past decades. On the other hand, the thermoelectric energy conversion (or more commonly known as "thermopower") in ferrofluids has so far remained underexplored. This subchapter describes this very new research path in the field of magnetic nanoparticle science, from its theoretical background and motivation, a few existing example of experimental investigations and the future perspectives.

16.1 Introduction

Thermoelectric (TE) materials are capable of directly converting thermal energy to electricity. As such, they can offer a possible solution for low-grade waste heat

S. Nakamae (✉)
Service de Physique de L'état Condensé, SPEC, CEA, CNRS, Université Paris-Saclay, CEA Saclay, 91191 Gif sur Yvette CEDEX, France
e-mail: sawako.nakamae@cea.fr

D. Peddis et al. (eds.), *New Trends in Nanoparticle Magnetism*,
Springer Series in Materials Science 308,
https://doi.org/10.1007/978-3-030-60473-8_16

recovery at all levels of human activities, from industrial waste stream, internal combustion car engines, electronic appliances to body heat. Solid semiconductor-based TE modules entered the commercial application many decades ago and they still are dominant in the TE market today. Despite their technical advantages including simple usage with no moving parts and high reliability, however, the TE technology is still limited to low-power applications due to their poor efficiency. The latter is generally expressed by a dimensionless parameter called "figure of merit" *ZT*. *ZT* combines materials' three transport properties, namely the electrical conductivity σ, the thermal conductivity κ, and the Seebeck (thermoelectric) coefficient S_e:

$$ZT = (\sigma S_e^2/k)T \tag{16.1}$$

where T is the operation temperature, and the Seebeck coefficient is defined by:

$$Se = -\frac{\Delta V}{\Delta T} \tag{16.2}$$

ΔV is the potential difference generated in a material in response to a temperature gradient ΔT.[1] It is said that *ZT* values greater than 4 are needed for TE devices to be competitive against other renewable energy technology (*e.g.* solar and geothermal) [1]. To achieve this goal, a tremendous amount of research effort has been dedicated to nanostructuring the semiconductor-based TE materials in the last 20 years, primarily aiming to lower the lattice thermal conductivity while enhancing the Seebeck coefficient[2–4]. This has led to some notable improvements in thermal-to-electric energy conversion capacity. However, even the most "promising" materials are yet to overcome the minimum *ZT* requirement. Furthermore, these nanostructured TE materials suffer from operational, environmental and economic obstacles such as their limited sizes, considerable production costs and the presence of rare and toxic materials. For the thermoelectric technology to become environmentally friendly and economically viable, alternative solutions are being sought in new types of TE materials such as polymers [5], ionic conductors (see, for example, [6, 7] etc.)

One such possibility can be found in liquid electrolytes. Reported values of Seebeck coefficients[2] are generally larger that the semiconductor counterparts (including the nanostructured) by an order of magnitude or more. Furthermore, they are made with Earth-abundant and non-toxic elements. Unfortunately, the electrical conductivity of such liquids is a few orders of magnitude smaller and thus, liquid electrolytes were considered ineffective for waste heat recovery technology until very recently. Ionic liquids and ionic liquids/solvent binary mixtures, however, are giving renewed hope in the development of liquid thermoelectrics. Ionic liquids (IL)

[1] The Seebeck coefficient is defined here in the same manner as in solids, i.e. $\vec{E} = Se\vec{\nabla}T$ [12]. Note that in the thermogalvanic cell community, it is not uncommon to see the following definition: Se $= \Delta V/\Delta T$.

[2] Here, we apply the term "Seebeck" loosely to describe all types of thermoelectric coefficient (also known as temperature coefficient) found in the liquid systems. The distinction between different thermoelectric phenomena are given further down in the chapter.

are molten salts that are liquid at room temperature and stay liquid up to temperatures much higher than 100 °C (some can exceed 300 °C). ILs possess large ionic conductivity values and wider electrochemical windows compared to other liquid electrolytes [8, [9] making them a promising candidate for a variety of low-grade waste heat recovery applications.

Today, the most widely studied TE property in liquid electrolytes is that of thermogalvanic effects, *i.e.* the temperature dependent electrochemical reactions between the redox couple molecules and the electrodes. The highest Seebeck coefficient reported is found with Cobalt-based redox couple mixed in ionic liquids larger than 2 mV/K over a wide temperature range extending well above 100 °C. For interested readers, Dupont et al. [10] has compiled a review of thermoelectrochemical cells containing a variety of ionic liquids, redox couples, electrode materials and their combinations.

The Seebeck coefficient in liquid electrolytes was also found to increase by inclusion of colloidal magnetic nanoparticles (ferrofluids) [11]. These nanoparticles are "charge"-stabilized and their thermodiffusion under a thermal gradient and the adsorption by the electrodes are believed to influence the fluid's thermoelectric potential. In the following sections, brief and salient descriptions of three most dominant physical origins of thermoelectric potential production in complex liquids are given.[3] Then recent experimental evidences on the combined thermoelectrochemical and thermodiffusion effects in ferrofluids are recounted. As it will be clear, our current understanding of thermoelectrochemical nature of complex fluids is far from complete, encouraging further experimental and theoretical research and development efforts in this exciting field of liquid thermoelectrics.

16.1.1 Basic Mechanisms of Thermoelectric Conversion in Fluids (3 Pages)

In solid materials, the production of thermoelectric potential is well understood from the out-of-equilibrium thermodynamics of heat and charge flows (of electrons or holes), expressed in terms of Onsager relations [12]. The situation is quite different for liquid thermoelectric materials. First, there are multiple types of charge carriers, i.e. electrolyte ions and other solutes such as colloidal particles or macromolecules. These carriers are all susceptible to thermodiffusion as well as interactions among themselves, and certain ions react electrochemically with the electrodes, hugely complicating the experimental data interpretation of such systems [13, 14]. Furthermore, a liquid sample must be placed inside a container (called thermocell) to be examined, thus additional precautions must be taken in order to minimize experimental errors due to thermal and electrical losses to its surroundings.

[3] Note that in-depth introduction on the physics and electrochemistry of these phenomena are beyond the scope of the current article, but references to useful articles and books are given for interested readers.

A thermoelectric module containing such a liquid is often referred to as a "thermoelectrochemical cell", a "thermally charged supercapacitor", or simply a "thermocell", depending on which TE effects dominates its thermoelectric energy conversion process. Here, we focus our attention on a thermocell containing ionic colloidal fluids (e.g. ferrofluids) where two sources of thermoelectric phenomena coexist, namely the thermogalvanic Seebeck effect and the internal Seebeck effect. As described in Fig. 6.1, the liquid (not an ionic liquid) is considered as a continuous medium inside which the charged (magnetic) particles, counterions (for electric neutrality of the solution) and the redox couple molecules are dissolved. The two ends of the cell are sealed hermetically with identical and metallic electrodes. When a temperature gradient (ΔT) is applied, an electrical potential (ΔV) appears across these electrodes. Note that to avoid convection, we assume that the cell is heated from the top.

In the simplest case, the electrochemical reaction between the redox couple species and the metallic electrodes results in the transfer of one electron either from the solution to the electrode (reduction), or vice-versa (oxidation), i.e.

$$Ox^{n-} + e \leftrightarrow \mathrm{Red}^{(n+1)-} \tag{16.3}$$

The most common example of such a reaction is that of ferro/ferricyanide redox couple $Fe(CN)_6^{3-}/Fe(CN)_6^{4-}$ (see for example, [15, 16]). By considering the local thermodynamic equilibrium of these redox reactions and one can show that the electrochemical potential difference at the hot and the cold electrodes to be [17]:

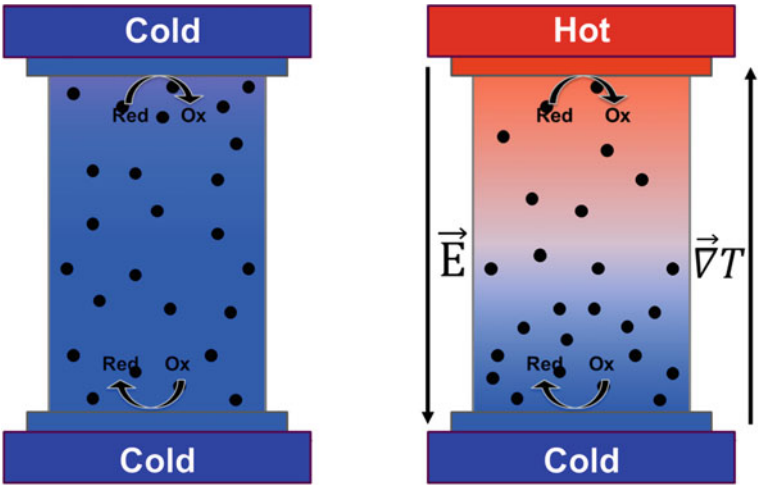

Fig. 6.1 Schematic view of an up-right thermocells in an isothermal condition (left panel) and under a thermal gradient ∇T (right panel). Upon the application of ∇T, the thermodiffusion of ionic species and the thermogalvanic reactions of redox species take place, both contributing to the overall Seebeck potential across the cell

$$\Delta V = \frac{\sum_{rc} v_{rc} \Delta \mu_{rc}}{e} \Delta T - Se_{\text{int}}.\Delta T \tag{16.4}$$

where the first term corresponds to the difference in the Gibbs free energy of the redox reaction with v_{rc} the stoichiometric number and μ_{rc} the chemical potential of the reducing and oxidizing molecules. Note that here we consider that the Seebeck coefficient of the metal electrodes ($\sim \mu V/K$) is negligibly small compared to those of the thermogalvanic and the internal ones (of the order of mV/K). The second term, Se_{int}, is the internal Seebeck coefficient. It is created by the internal electric field, $\vec{E}_{\text{int}}$, stemming from the distribution of all ions/particles in the solution, i.e.

$$\vec{E}_{\text{int}} = Se_{\text{int}} \vec{\nabla} T \tag{16.5}$$

$\vec{E}_{\text{int}}$ is known to influence a large number of diffusion phenomena of charged species in electrolytes [18–23] and can be determined from the current $\vec{J}_i$ of all charged ions/particle in the solution,

$$\vec{J}_i = -D_i \left[\vec{\nabla} n_i + n_i \frac{\hat{S}_i}{k_B T} \vec{\nabla} T - n_i \frac{\xi_i e}{k_B T} \vec{E}_{int} \right] \tag{16.6}$$

D_i, the diffusion coefficient, $\hat{S}_i$, the Eastman entropy of transfer (see below for more explanation), ξ_i the effective *electrophoretic* charge number and n_i the number density of the i_{th} charged ion/particle. These quantities depend on experimental variables such as the particle concentration, n_i, temperature and magnetic field strength, whose analytical expressions have recently been reported in [24] by Salez et al. While in most liquid electrolytes containing small ions, the thermogalvanic terms is predominant and thus the internal Seebeck term is often ignored (see, for example, [10, 17]). However, in ionic nanofluids containing large ions and particles such as ferrofluids, the Se_{int} is known to make non-negligible contributions to the liquid's overall thermoelectric potential.

Another distinct feature of the thermoelectric phenomena in nanofluids is the slow time constant involved inthe thermodiffusion process. That is, while the thermogalvanic term is established immediately upon the application of a temperature gradient,[4] the ions and particles will continue to diffuse until the equilibrium is reached between the thermal and the electrical forces. The corollary of such time dependency is that the thermoelectric potential also evolves with time, and one can distinguish between the initial Seebeck coefficient (Se_{ini}) and the stationary one (Se_{st}).

At the initial state, the ion/particle concentration of all species is still uniform within the fluid ($\forall i, \vec{\nabla} n_i = \vec{0}$), which simplifies the (16.6) to:

[4]The temperature gradient is supposed to be established instantaneously here, *i.e.* the thermal diffusivity of the liquid is much faster than the ions/particles diffusion time.

$$\vec{J}_i = -D_i \left[n_i \frac{\hat{S}_i}{k_B T} \vec{\nabla} T - n_i \frac{\xi_i e}{k_B T} \vec{E}_{\text{int}}^{\text{ini}} \right] \tag{16.7}$$

In an open-circuit configuration, the total electric current is null, $\sum_i z_i e \vec{\nabla} n_i = \vec{0}$, where z_i is the effective static charge. (For small ions, z_i and ξ_i are equal, but they can take different values for charged nanoparticles and large molecules.) This leads to the expression for the *initial* internal electric field:

$$\vec{E}_{\text{int}}^{\text{ini}} = -\left[\sum_i t_i \frac{\hat{S}_i}{\xi_i e} \right] \vec{\nabla} T \quad \text{with} \quad t_i = -\frac{z_i \xi_i e^2 n_i D_i}{\sum_i z_i \xi_i e^2 n_i D_i} = \frac{\sigma_i}{\sigma_{\text{total}}} \tag{16.8}$$

t_i is known as the Hittorf number, which is the ratio between the electrical conductivity of the i_{th} species to the total conductivity of the liquid. The initial internal electrical field, $\vec{E}_{\text{int}}^{\text{ini}}$, describes the thermal force experienced by the ions/particles causing them to *thermodiffuse*.

The initial internal Seebeck coefficient can then be written as:

$$Se_{\text{int}}^{\text{ini}} = \sum_i t_i \frac{\hat{S}_i}{\xi_i e} \tag{16.9}$$

Combined with (16.4), one obtains the total initial Seebeck coefficient to be

$$Se^{\text{ini}} = \frac{1}{e} \left(-\Delta_{rc} S + \sum_i \frac{t_i \hat{S}_i}{\xi_i} \right) \tag{16.10}$$

$\Delta_{\text{rc}} S$, the redox reaction entropy can be determined by the Nernst equation [25] which depends on the type of redox species and on the ionic strength of the surrounding electrolytes.

After a sufficiently long time and still under a temperature gradient, the ion/particle current due to the thermal force is cancelled by the concentration gradient, $\vec{\nabla} n_i$ and the resulting internal electric field of charged particles/ions. At that point, the system is said to be in an equilibrium state (*Soret* equilibrium state, see next section for more detail), i.e. $\forall i, \vec{J}_i = \vec{0}$. The corresponding particle current equation for all particles/ions is:

$$\vec{0} = \left[\vec{\nabla} n_i + n_i \frac{\hat{S}_i}{k_B T} \vec{\nabla} T - n_i \frac{\xi_i e}{k_B T} \vec{E}_{\text{int}} \right] \tag{16.11}$$

From the electrical neutrality, one can arrive to the expression for the *Soret equilibrium* internal Seebeck coefficient as:

$$Se_{\text{int}}^{\text{Eq}} = \frac{\sum_i z_i n_i \hat{S}_i}{e \sum_i z_i \xi_i n_i} \tag{16.12}$$

The equilibrium internal Seebeck coefficient is thus independent of the diffusion coefficients. Furthermore, it can be shown that at the equilibrium state, the redox couple molecules arranges themselves to screen entirely the internal electric field of the solution resulting in the total equilibrium state Seebeck coefficient:

$$Se^{\text{eq}} = \frac{1}{e}\left(-\Delta_{rc} S + \sum_{rc} v_{rc} \hat{S}_{rc}\right) \tag{16.13}$$

Therefore, all thermoelectrodiffusion-related effects in charged nanofluids (including magnetic field and concentration effects) are present only during the initial state of the thermocell operation.

16.1.2 Motivation for Using Ferrofluids (2 Pages)

In order to maximize the internal electric field contribution in ionic nanofluids (see 16.15), then it is desirable to increase the Eastman entropy of transfer of the charged particles and to tailor their sign and the size of the effective electrophoretic charge. The Eastman entropy of transfer is a thermodynamic quantity associated with the enthalphy, *i.e.* the difference between the partial molar entropy and the transported entropy of the particles (cite Groot and Agar). As the enthalpy is born out of the interactions between a given particle and its environment (solvent molecules, other particles and ions, etc.), $\hat{S}_{np}$ generally scales with the particle's surface area and it can take both positive and negative values. If $\hat{S}_{np}$ is positive, the particles have the tendency to "structure" the surrounding molecules and thus they move towards the cold region (thermophobic), while the opposite is true for a negative $\hat{S}_{np}$ (thermophilic).

Naturally, the Eastman entropy of transfer is also a key parameter in the thermodiffusion phenomena, known as the Ludwig–Soret effect. The thermodiffusion coefficient, or more widely known as Soret coefficient, S_T describes the ratio between the concentration gradient of particles/ions and the applied temperature gradient in the *equilibrium state.*

$$\frac{\vec{\nabla} n}{n} = -S_T \vec{\nabla} T \quad \text{and} \quad S_T = \frac{\hat{S}_i}{k_B T} - \frac{\xi_i e}{k_B T} Se_{\text{int}}^{\text{Eq}} \tag{16.14}$$

The influence of internal electric field on the thermodiffusion of charged colloidal particles became an active area of research in the last decade and the theoretical models were used to explain experimental observations in various colloidal fluids (See for example [19, 22, 26, 27]). The parameters $\hat{S}$ and ξ have been shown to depend on the particle concentration, and the interparticle interactions can generally

be described by Carnahan–Starling hard sphere (cite 25) model as:

$$\hat{S} = \hat{S}_0 \chi(\phi) \quad \text{and} \quad \xi = \xi_0 \chi(\phi) \tag{16.15}$$

where ϕ is the volume fraction of nanoparticles, i.e. $\phi = V_{np}.n$ (V_{np} is the nanoparticle volume) and χ is the isothermal osmotic compressibility (cite 5—Vigolo).

$$\chi(\phi) = \frac{(1-\phi)^4}{1 + 4\phi + 4\phi^2 - 4\phi^3 + 4\phi^4} \tag{16.16}$$

χ tends to unity as $\phi \to 0$, thus $\hat{S}_0$ and ϕ_0 correspond to the nanoparticles' Eastman entropy and the effective charge values at the infinite dilution limit.

Among a variety of charged colloidal solution, ferrofluids containing nanometre-sized magnetic nanoparticles show very high Soret coefficient values. Furthermore, the "magnetic" nature gives an additional degree of experimental control (magnetic field) on the thermodiffusion property of these nanoparticles [28, 29]. Interestingly, Filomeno et al., have recently demonstrated that the substitution of counterion (lithium) by another type (tetrabutylammonium) not only changes the magnitude but also can reverse the sign of the Soret coefficient (and thus the thermophoretic direction) of the identical magnetic nanoparticles [30]. As both Soret and Seebeck (initial) coefficients depend directly on the Eastman entropy of transfer, it is of great interest to explore the thermoelectric nature of ferrofluids.

The first experimental study combining thermoelectric and thermos(electro)diffusion in ferrofluid was reported by Huang et al., where a *quantitative* agreement was found on the Eastman entropy of transfer values determined independently from Soret coefficient and (initial) Seebeck coefficient measurements [31]. This work laid down the experimental foothold supporting the existing theoretical models describing the thermoelectric and thermodiffusive properties in charged colloidal solutions through a common parameter, $\hat{S}$. Several more experimental and theoretical investigations have followed since (and still continue to follow) elucidating the effects from other control parameters such as the ionic strength and the particle sizes, etc., examples of which are described in the following sections.

16.2 Experimental Investigation of Seebeck Coefficients in Ferrofluids

16.2.1 Experimental Approach

The technical difficulties for measuring and analysing thermoelectric properties of liquids were discussed in the previous section. It also needs to be mentioned that

preparation of ionic nanofluids made of interacting nanoparticles is faced with a formidable challenge on its own. Ferrofluids, in particular, contain freely moving magnetic nanoparticles that tend to form chains and aggregates through attractive magnetic forces, unless screened properly by other repulsive forces (electrostatic, steric, etc.) which require a fine tuning of the coating ions of individual nanoparticles as well as the surrounding ionic condition (e.g. electrolyte ions, counter- and co-ions). The ferrofluids used in the following example studies are composed of maghemite (γ-Fe_2O_3) nanoparticles with average particle diameters in the range of 6–8 nm. They are either ionically stabilized ([30, 32, 33]) or with polymers ([34]) and dispersed in polar liquids (water and organic solvent). The thermoelectric measurements were performed in the thermogalvanic cell condition, i.e. a small amount of redox couple molecules were always present.

A schematic image of the thermoelectric measurement cell is shown below. In order to properly measure the "basic" liquid TE property, following precautions should be taken.

- Cell body: The thermal conductance of the material should be smaller or comparable to that of the liquid sample. The material or the design must be able to accommodate the liquid dilation at high temperature. The material must be inert (no chemical reactions with the fluid can occur) and impermeable.
- Electrodes: The material must be electrochemically stable, possess high thermal conductivity (to ensure good heat transfer from the heater/cooler to the liquid).
- Faraday cage, electrometer: For highly resistive samples, it is desirable to shield the cell from the environmental EM waves, and use a high input-impedance voltmeters (10^{11} Ω or higher).
- Measurements: In order to avoid introducing convective motions of the fluid and/or nanoparticles, the cell should be heated from the top (Fig. 16.2).

Due to the thermodiffusion effect, especially that of magnetic nanoparticles, the thermoelectric voltage (thus the Seebeck coefficient) of nanofluids evolves over a long period of time, from several minutes to several days, depending on the viscosity of the liquid, the cell geometry, the hydrodynamic size of the nanoparticles and their concentration. Such a slow process can become experimentally cumbersome; however, it is precisely this time dependency of *Se* that provides us the means to distinguish between different thermoelectric phenomena taking place inside the complex, magnetic nanofluids.

16.2.2 Experimental Determination of Eastman Entropy of Transfer in Ferrofluids

In 2015, Huang et al. have published the first experimental study on the Seebeck coefficient (S_e^{ini}) in ferrofluids, combined with the corresponding Soret coefficient S_T [31]. The ferrofluids used here consist of charge-stabilized nanoparticles dispersed

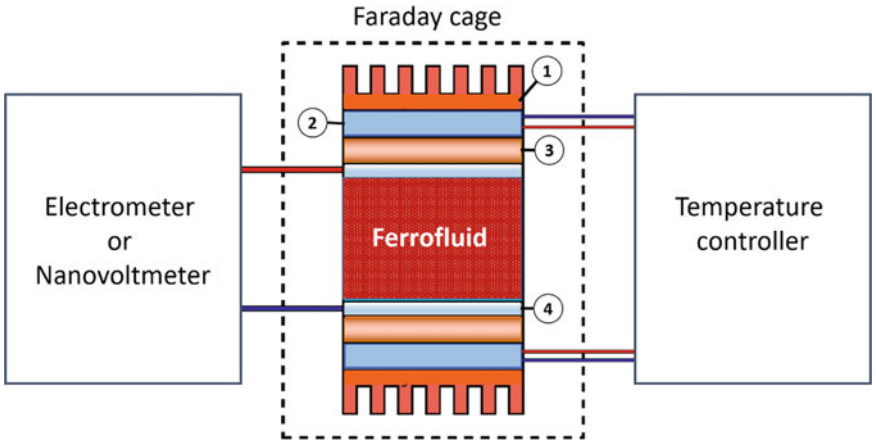

Fig. 16.2 Schematic image of thermoelectric measurement principle used in the experimental studies presented in this chapter. Cell parts: ⊖ heat exchanger, ⊖ heating/cooling module, ⊖ heat sink and ⊖ electrodes in contact with the liquid

in dimethyl sulfoxide (DMSO) and ferrocene/ferrocenium ($Fe(C_5H_5)_2$/[$Fe(C_5H_{52}$]+) were used as a redox couple. The Soret coefficient was obtained via forced Rayleigh scattering technique, which also gives an access to the NPs diffusion coefficients (cite Demouchy).

Both coefficients were measured as a function of magnetic nanoparticles volume fraction, ϕ and presented in Fig. 16.3. The Seebeck coefficient at zero nanoparticle concentration, $Se^{ini}(\phi)$, corresponds to the thermogalvanic potential of the redox couple. The change in Se^{ini} is due to the presence of nanoparticles, i.e. $Se^{ini}(\phi)$ - $Se^{ini}(0)$ and $S_T(\phi)$ were fitted using the theoretical model (as discussed above) from which, the nanoparticle's effective electrophoretic charge number $\hat{S}_0$ and the Eastman entropy of transfer $\hat{S}_o$ were extracted.

As can be seen from Fig. 16.3, the values of the Eastman entropy of transfer determined *independently* from the Soret and Seebeck coefficient measurements are in quantitative agreement confirming the common physical origin of the two phenomena. Furthermore, the determined $\hat{S}_0$ value is quite large, ~75 meV.K^{-1}, a few orders of magnitude larger than those of small electrolyte ions. This observation further endorses the supposition that the thermodiffusion of charged nanoparticles with large Eastman entropy of transfer (and large effective charge number) can influence both the thermodiffusive and thermoelectric properties of colloidal solutions. Although the Seebeck coefficient was found to decrease, unfortunately, in this particular ferrofluid, this study served to open a new route in the thermoelectric materials research and development.

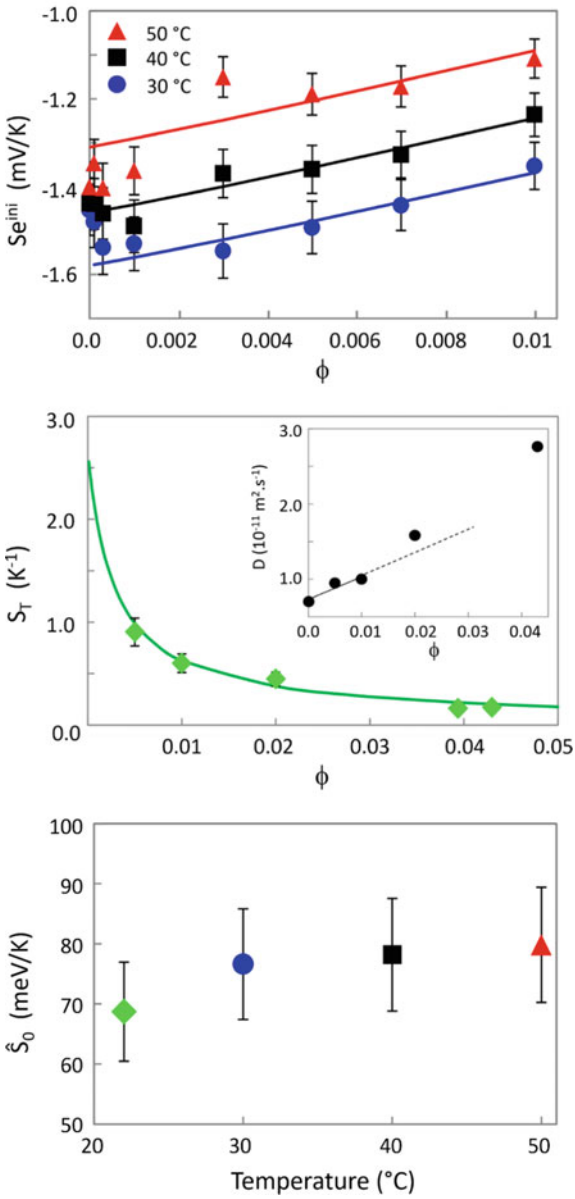

Fig. 16.3 (Top) Se^{ini} measured at 30, 40 and 50 °C as a function of NP concentration (volume fraction). (Middle) S_T as a function of NP concentration (volume fraction) measured at $T = 23$ °C. The inset: Diffusion coefficient of magnetic nanoparticles in DMSO also obtained from the forced Rayleigh scattering measurements. In both graphs, the solid lines are the fitting results using the model equations presented in the previous section. (Bottom) The values of Eastman entropy of transfer extracted from Se^{ini} and S_T using a common ξ_0 value of 30

16.2.3 The Effect of Ionic Environment on the Initial Seebeck Coefficient of Aqueous Ferrofluids

In this example, the effect of ionic environment on $\hat{S}_0$, and ξ_0 (and ultimately, the Seebeck coefficient) was explored in aqueous ferrofluids by changing the counterions

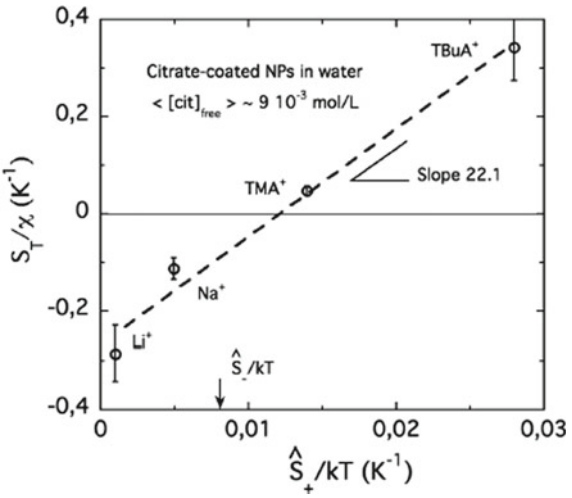

Fig. 16.4 Measured Soret coefficient ratio, S_T/χ, of citrate-coated nanoparticles dispersed in water at room temperature as a function of $\hat{S}/k_BT$ of the counterions in the ferrofluid. ϕ~0.043 was used for all ferrofluids. (Image reproduced from[30], © Elservier 2016)

used to stabilize the colloidal magnetic nanoparticles. The nanoparticle material (maghemite) and size, as well as the pH level of the solution were identical for both ferrofluids, and only the counterion types are modified. This study was motivated by the work by Filomeno et al., where the effect of counterions on the magnitude and the sign of the nanoparticles Soret coefficients was demonstrated in a series of aqueous ferrofluids [30].

In their study, four monovalent counterions were explored; Li^+, Na^+, TMA^+ (tetramethyl ammonium) and TBA^+ (tetrabutyl ammonium) in the order of increasing ion size. In sum, it was concluded that by changing the size of the counterion, the $\hat{S}_0$ can be *tuned* from a "larger, positive" (thermophobic) value for TBA-coated NPs to a "smaller, negative" (thermophilic) value for Li-coated ones. The effective charge number of the particles was also affected, showing a larger value for TBA-ions than for Li-ions (Figs. 16.4).

Here, we have taken these two counterions, $TBuA^+$ and Li^+, which resulted in the extreme S_T values to verify the impact on the Seebeck coefficient counterpart. As expected, the concentration dependence of the initial Seebeck coefficient in these ferrofluids behave dissimilarly between the two counterion types (Fig. 16.5). Note that a small amount of ferro/ferricyanide redox couple was added to the solutions.

In the case of ferrofluids with TBA^+ as counterions, Se^{ini}*increase* as much as 15% by the inclusion of nanoparticles at a volume fraction of 1%. On the other hand, with Li^+ as counterions, no appreciable change was observed. The difference between the two ferrofluids can be explained in terms of 1) large Eastman entropy of transfer values of nanoparticles (14 meV/K) *and* TBA^+; and 2) a large effective electrophoretic charge (estimated to be of the order of -300 of nanoparticle in the presence of TBA-ions. This study highlights the importance of the ionic environment on $\hat{S}$ and ξ of magnetic nanoparticles. With a proper control of such parameters, one can indeed increase the thermoelectric power of liquid thermocells.

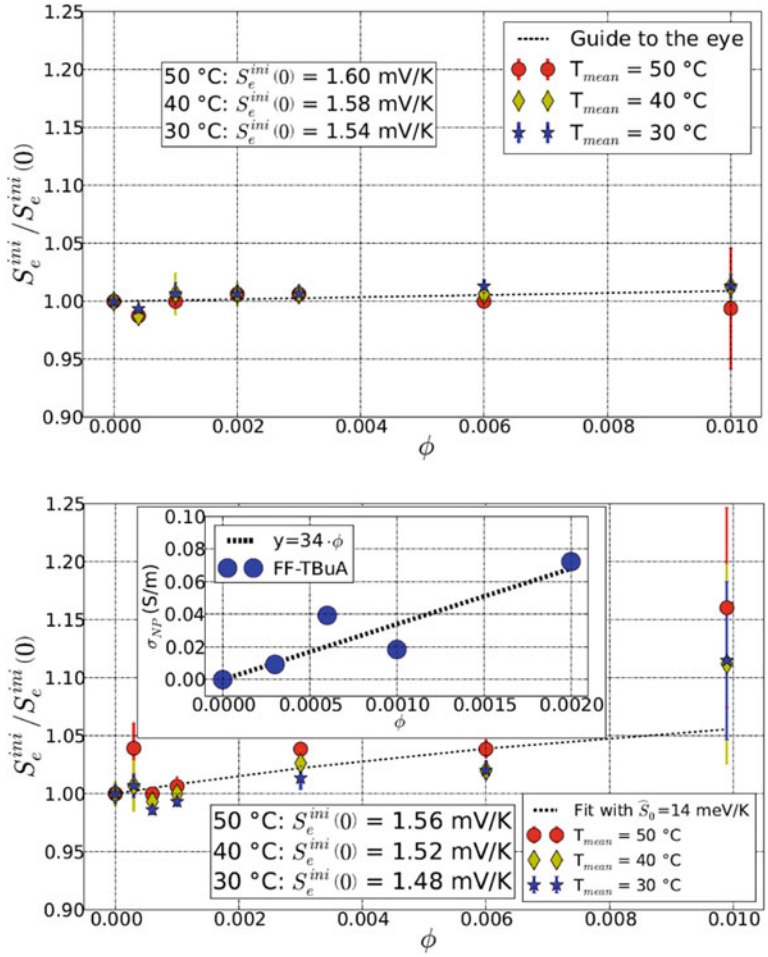

Fig. 16.5 Normalized initial state Seebeck coefficient as a function of ϕ with Li^+ (top) and TBA^+ (bottom) counterions measured at three different temperature values. $Se^{ini}(0)$ values indicated in the inset correspond to the thermogalvanic potential of ferro/ferricyanide redox couple in water. The inset shows the experimentally determined electrical conductivity of the ferrofluid (with TBA^+ counterion) as a function of nanoparticle concentration

16.2.4 Magnetic Nanoparticle Adsorption Phenomena at the Liquid/metal Interface

While the initial Seebeck coefficient analysis leads to a conclusion coherent with the existing theoretical model, the time evolution of Se and the steady-state values exhibited surprising behaviour. First, the *apparent* steady state is reached only 6–8 h after the application of temperature gradient. Considering the diffusion coefficient

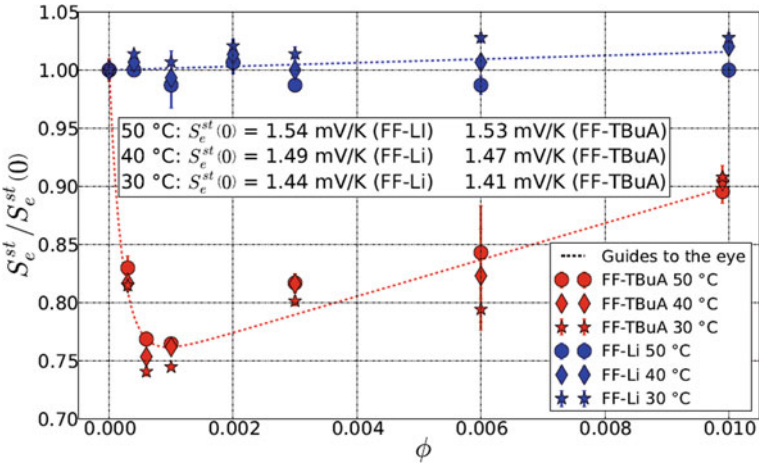

Fig. 16.6 Normalized "apparent" steady state Seebeck coefficient as a function of nanoparticle concentration for ferrofluid samples containing Li^+ (blue) and TBA^+ (red) counterions. (Image taken from [11] © Elsevier 2017)

of nanoparticles in water ($D_{NP} = 10^{-11}$ m^2 s^{-1}) and the characteristic length of the thermocell ($l = 6$ mm), it should take $\tau = l^2/(\pi^2 D_{NP}) = 100$ h for the magnetic nanoparticles reach the true Soret equilibrium state. Moreover, in thermodiffusion measurements on ferrofluids with a comparable experimental parameter (in terms of cell size, fluid and particle characteristics), nanoparticles are found to continue to thermodiffuse over several days and longer [28]. Secondly, according to 16.5, the Se^{st} should only depend on the redox couples and thus one would expect $Se^{st}(\phi)$ to be constant (and close to $Se^{ini}((0))$, regardless of the nanoparticle concentration. While the sample containing Li^+ counterions $Se^{st}(\phi)$ is nearly concentration independent at all temperatures studies, the sample with TBA^+ counterion shows a minimum around $\phi = 0.001\%$ (Fig. 16.6). Additionally, the $Se^{st}(\phi)$ behaviour above $\phi = 0.001$ resembles that of $Se^{ini}(\phi)$ very closely.

The numerical simulations on the nanoparticle concentration performed on two concentration values ($\phi = 0.004$ and 0.01) confirm that the NP distribution in the bulk is indeed much closer to that of the initial state after the time lapse of 6–8 h (*i.e.* t ~ 0.1 τ) as seen in Fig. 16.6. In other words, the experimentally determined "apparent" stationary state corresponds to a physical phenomenon different from the Soret equilibrium, and this effect saturates beyond a critical concentration value of about 0.001 (Fig. 16.7).

At present, it is supposed that the apparent steady state is due to the magnetic nanoparticles adsorption (at the electrodes) modifying the ionic environment at the hot and the cold electrodes asymmetrically. As the redox reaction entropy (16.18) depends on the ionic strength surrounding the redox couple, this results in the modification of the Nernst term, $\Delta_{rc}S$. Once a critical concentration value is reached, however, the electrostatic repulsion created by the already adsorbed nanoparticles

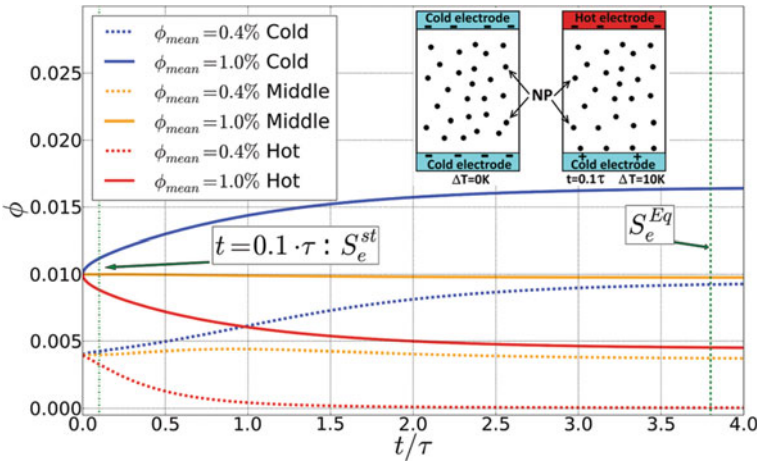

Fig. 16.7 Time evolution of the concentration under a temperature gradient of 10 K (applied at $t = 0$) calculated at three different locations within a thermocell. Two starting nanoparticle concentrations (0.01 and 0.004) are considered. (Image taken from [11] Elsevier 2017.) ©
/Credit>

prevents additional particles from approaching, resulting in a saturation observed for $\phi = 0.001$.

16.2.5 Magnetic Field Effect (3 Pages)

Theoretical investigation on the magnetic field effect on the Seebeck coefficient has been carried out starting from Onsager's theorem applied to liquid electrolyte systems. A full derivation of the model is out of scope of the present chapter, and here we will only indicate the final expression on the diffusion coefficient, D_i, the Eastman entropy of transfer, $\hat{S}_i$ and the effective electrophoretic number ξ_i under the influence of magnetic field, H.

$$D_i(\varphi_i, H) = D_i^0(\varphi_i)\left(\frac{1}{\chi_{CS}(\varphi_i)} - \alpha_\lambda(\varphi_i, H) + \delta.\beta_\lambda(\varphi_i, H)\right) \tag{16.17}$$

$$\hat{S}_i(\varphi_i, H) = \frac{\hat{S}_i^0(\varphi_i) + k_B(S_1(\varphi_i, H) - \delta.S_2(\varphi_i, H))}{\frac{1}{\chi_{CS}(\varphi_i)} - \alpha_\lambda(\varphi_i, H) + \delta.\beta_\lambda(\varphi_i, H)} \tag{16.18}$$

$$\xi_i(\varphi_i, H) = \frac{\xi_i^0(\varphi_i)}{\frac{1}{\chi_{CS}(\varphi_i)} - \alpha_\lambda(\varphi_i, H) + \delta.\beta_\lambda(\varphi_i, H)} \tag{16.19}$$

where $D_i^0(\varphi_i)$, $\hat{S}_i^0(\varphi_i)$ and $\xi_i^0(\varphi_i)$ refer to the corresponding quantities in the absence of applied magnetic field. The field-dependent modifications, externally applied field and dipolar interactions, are contained in the parameters $\alpha\lambda$, S_1, $\beta\lambda$ and S_2. These terms appear as the magnetic component of the chemical potential gradient in response to $\vec{\nabla}\varphi$ (α_λ), to $\vec{\nabla}T$ (S_1) and β_λ and S_2 both arise from the local field perturbations. δ is a Kronecker-like parameter which is equal to 0 if the temperature and field gradients are perpendicular to one another and to -1 if the two gradients are in parallel. While more detailed derivations and the exact forms of these parameters are be found in [24], here we simply show the qualitative behaviour as a function of magnetic field, expressed in terms of the Langevin parameter, x (Fig. 16.8).

The field-dependent values of D_i, $\hat{S}_i$ and ξ_i are expected to modify the initial (internal) Seebeck coefficient of ferrofluids as described in 16.8 and 16.10. The next step will compare these theoretical models to the experimental measurements. Preliminary results (cite thesis Salez) indicate, however, that the application of magnetic field not only influence the internal electric field (as predicted here) but also induce field-dependent nanoparticle layering, in addition to the temperature gradient-induced adsorption effect already described in the previous section.

16.3 Future Research Direction and Perspectives

16.3.1 Fundamental Challenge—Understanding the Phenomena Through Theoretical and Experimental Explorations

The thermoelectric potential production in ferrofluids and other charged nanofluids arise from multiple components (electrolytes, nanoparticles, redox couples, etc.), thermoelectric phenomena (thermogalvanic effect, thermodiffusion, electrostatic adsoption, magneto-diffusion, etc.) and the interplay between them. The underlying mechanisms of these newly discovered phenomena are only beginning to be understood. Thus, theoretical/mathematical modelling and simulations of constituents at multiscale levels, from molecular orbital interactions to collective thermodiffusion of particles, as well as the formation of adsorption layers at the liquid/electrode interface will become crucial for building foundational knowledge for the proposed magnetothermoelectric materials research in liquids. A few other experiments were performed on the Seebeck effect and TE electricity production using ferrofluids [39] and other nanofluids [40, 41], which have brought into light rather unexpected and new phenomena such as a field-dependent layering (may be similar to what is described (numerical simulation) by Richardi and Weiss [42]) and a percolation of nano-objects. Withall, it is truly an uncharted and exciting field of research to explore.

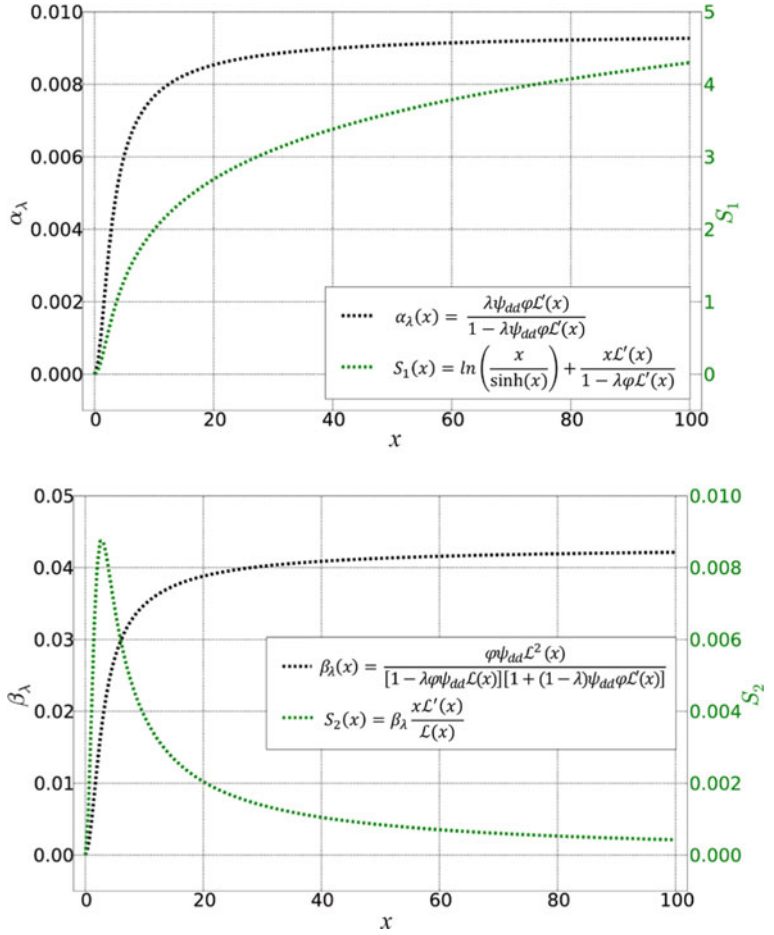

Fig. 16.8 Functions Al and S1 (top panel) and bl and S2 (bottom panel) as a function of Langevin parameter x. Here the particle concentration φ is fixed to 0.01. The parameters l and zdd represent the non-dimensional proportionality coefficient and the dipolar interaction parameter whose values are close to 0.22 and 4.3 for aqueous ferrofluids as determined experimentally by [35–38]. More explanation can be found in [24]

16.3.2 Possible Research Directions in Light of Increasing Thermoelectric Energy Conversion Efficiency

From the application point of view, we have seen that by selecting the right combination of electrolytes, one can tune the Eastman entropy of transfer and the effective charge number of magnetic nanoparticles to enhance the initial Seebeck coefficient by 15%. Since, for the first approximation, the efficiency of a thermocell is proportional to the figure of merit (see 16.1) and therefore to the Seebeck coefficient squared, one

can expect a 30% efficiency increase. Within the existing theoretical framework, the increase in Se^{ini} is ascribed to the large Eastman entropy of transfer and possibly a large effective surface charge of magnetic nanoparticles. As the thermodiffusion term is lost from the thermoelectric potential once the steady state is reached, it is desirable to operate the thermocell in its (close to) initial state; a condition that can easily be achieved in a flow-cell.

A promising technological path for the future exploration of ferrofluids as a thermoelectric material can be found in combining magnetic nanoparticles with ionic liquids introduced at the beginning of this chapter. The use of ionic liquids will expand both the operation temperature and the voltage (and thus power) range of liquid thermoelectric devices due to their higher boiling temperature and the electrochemical stability. There are only a few examples of IL-based ferrofluids in existence today, either charge-stabilized or with surfactants (see for example [43–46]) but the Seebeck coefficient (thermogalvanic or thermodiffusion) has not been examined for any of them. The preliminary results obtained in an ionic liquid ferrofluid (based on EAN (ethylammonium acetate) containing maghemite nanoparticles with a redox couple of I_2/I^- shows a maximum initial Seebeck coefficient at the particle (volume) concentration as small as 0.005 (of about 60% increase) whose origin is yet to be confirmed [39].

Another interesting thermoelectric application route for ferrofluids is that of thermally chargeable (super)capacitors [47–49]. In the absence of a redox couple, the electrons cannot be extracted from the liquids. In that case, a thermocell will function as a capacitor, where electric charges are stored at the electrode/liquid interface through an electronic double layer (EDL) effect. The asymmetry in the EDL at two electrodes is induced due to the temperature difference applied across the thermocell. The temperature (gradient)-dependent adsorption of magnetic nanoparticles as discussed in this chapter is a very promising candidate for amplifying the EDL in thermocells.

In addition to these, there are alternative and unique ways to improve the efficiency of liquid thermoelectric materials. In fact, in a liquid and non-Ohmic conductor, the electrical conductivity to be included in the ZT calculation is that of the redox couple (at a low frequency), rather than the ionic conductivity of the liquid itself. The more realistic figure of merit ZT for a thermocell is proposed [10]:

$$ZT^* = \frac{Se^2.z^2.e^2D.n}{k_B.\kappa}T \tag{16.20}$$

D, z and n are the diffusion coefficient, the effective charge number and the number concentration of the slowest species of the redox couple and κ is the thermal conductivity of the liquid. This expression is suitable for a thermocell in the absence of convection. A more general the above expression should be modified to include the convection term to:

$$ZT^* = \frac{Se^2.l}{R_{\mathrm{exp}}.A.\kappa.\mathrm{Nu}}T \tag{16.21}$$

With R_{exp} the experimentally determined resistance of the cell (from an *I-V* curve, for example), *l* and *A* are the thermocell constant (length and the effective electrode area, respectively) and Nu is the Nusselt number, which equals to unity in the absence of convection. Note that while the convection ($Nu > 1$) will increase the effective thermal conductivity, it also helps to increase the mass transport of the redox couples (thus reduces the R_{exp}). In certain cases, it is found that the reduction in R_{exp} is larger than the increase in k, resulting in the enhancement of ZT^* of the thermocell [39, 50]. Therefore, in addition to improving the materials' intrinsic thermoelectric property, many opportunities exist in the device engineering (cell dimensions, heating directions, etc.) for improving the performance of liquid thermocells.

Last, but not least, the application of magnetic field is known to increase the Soret coefficients of ferrofluids and influence the layering behaviour of nanoparticles near the electrodes. These experimental observations further encourage the use of magnetic nanoparticles' unique and tunable properties [51] in the development of magnetothermoelectric energy conversion applications.

References

1. C.B. Vinning, An inconvenient truth about thermoelectrics. Nat. Mater. **8**, 83 (2009)
2. J.P. Heremans et al., When thermoelectrics reached the nanoscale. Nat. Nanotechnol. **8**, 471 (2013)
3. A.I. Hochbaum et al., Enhanced thermoelectric performance of rough silicon nanowires. Nature **451**, 163 (2007)
4. L.D. Hicks et M.S. Dresselhaus, Effect of quantum-well structures on the thermoelectric figure of merit. Phys. Rev. B. **47**, 12727–12731 (1993)
5. A. Fina, S. Colonna, L. Maddalena et M. Tortello, A facile and low environmental impact approach to prepare thermally conductive nanocomposites based on polylactide and graphite nanoplatelets. ACS Sustain Chem Eng (2018). https://doi.org/10.1021/acssuschemeng.8b03013
6. D. Zhao, H. Wanga, Z. U. Khana, J. C. Chen, R. Gabrielssona, M.P. Jonssona, M. Berggrena et X. Crispin, Ionic thermoelectric supercapacitor. Energy Environ. Sci. **9**, 1450 (2016).
7. V. Zinovyeva, S. Nakamae, M. Bonetti, et M. Roger, Enhanced thermoelectric power in ionic liquids. Chem. Electr. Chem. (2013). https://doi.org/10.1002/celc.201300074
8. M. Hayyan et al., J. Ind Eng. Chem. **19**, 106 (2013)
9. S. Uhl et al., J. Electron. Mater. **43**, 3758 (2014)
10. M.F. Dupont, D.R. MacFarlane et J.M. Pringle, Thermo-electrochemical cells for waste heat harvesting—progress and perspectives. Chem. Comm. (2017)
11. T.J. Salez, B.T. Huang, M. Rietjens, M. Bonetti, C. Wiertel-Gasquet, R.M. Gasquet, C.L. Filomeno, E. Dubois, R. Perzynski et S. Nakamae, Can charged colloidal particles increase the thermoelectric energy conversion efficiency? Phys. Chem. Chem. Phys. (2017). https://doi.org/10.1039/C7CP01023K.
12. C. Goupil, W. Seifert, K. Zabrocki, E. Müller et G.J. Snyder, Thermodynamics of thermoelectric phenomena and applications. Entropy. **13**, 1481–1517 (2011)
13. J. Agar et J. Turner, Thermal diffusion in solutions of electrolytes. Proc. R. Soc. Lond. A Math. Phys; Eng. Sci. **255**, 307–330 (1960)
14. S. Di Lecce et F. Bresme, Thermal polarization of water influences the thermoelectric response of aqueous solutions. J. Phys. Chem. B. **122**, 1662–1668 (2018)

15. Y. Kuzminskii, V. Zasukha et G. Kuzminskaya, Thermoelectric effects in electrochemical systems. Nonconventional thermogalvanic cells. J. Power Sources. **52**, 231–242 (1994)
16. T. Ikeshoji, F. de Nahui, S. Kimura et M. Yoneya, Computer analysis on natural convection in thin-layer thermocells with a soluble redox couple. J. Electroanal. Chem. Interfacial Electrochem. **312**, 43–56 (1991)
17. J.N. Agar, *Thermogalvanic Cell, chez Advances in Electrochemistry and Electrochemical Engineering Interscience* (New York, 1963)
18. J. Burelbach, D. Frenkel, I. Pagonabarraga et E. Elser, A unified description of colloidal thermophoresis. Eur. Phys. J. E. **41**, 7 (2018)
19. K.A. Eslahian, A. Majee, M. Maskos et A. Würger, Specific salt effects on thermophoresis of charged colloids. Soft Matter. **10**, 1931 (2014)
20. A. Majee, Effet ThermoéLectrique Dans Les Dispersions Colloïdale, Ph.D. Thesis, Université Bordeaux I (2012)
21. A. Majee et A. Würger, Charging of heated colloidal particles using the electrolyte seebeck effect. Phys. Rev. Lett. **83**, 061403 (2012)
22. A. Würger, Transport in charged colloids driven by thermoelectricity. Phys. Rev. Lett. **101**, 108302 (2008)
23. A. Würger, Hydrodynamic boundary effects on thermophoresis of confined colloids. Phys. Rev. Lett. **116**, 138302 (2016)
24. T.J. Salez , S. Nakamae, R. Perzynski, G. Mériguet, A. Cebers et M. Roger, Thermoelectricity and thermodiffusion in magnetic nanofluids: entropic analysis. Entropy **1**, 220–405 (2018). https://doi.org/10.3390/e20060405
25. W. Nernst, Die elektromotorische wirksamkeit der jonen *Z*. Phys. Chem. **4**, 129–181 (1889)
26. S. Duhr et D. Braun, PNAS **103**, 19678–19682 (2006)
27. A. Parola et R. Piazza, Thermophoresis in colloidal suspensions J. Phys. Cond. Matt. **20**, 153102 (2008)
28. L. Sprenger, A. Lange et S. Odenbach, Thermodiffusion in ferrofluids regarding thermomagnetic convection. Phys. Fluids. **341**, 429–437 (2013)
29. T. Völker, E. Blums et S. Odenbach, Determination of the Soret coefficient of magnetic particles in a ferrofluid from the steady and unsteady part of the separation curve. Int. J. Heat Mass Tran. **47**, 4315–4325 (2004)
30. C.L. Filomeno, M. Kouyaté, F. Cousin, G. Demouchy, E. Dubois, L. Michot, G. Mérigue, R. Perzynski, V. Peyre, J. Sirieix-Plénet et F. A. Tourinho, J. Magn. Magn. Mater (2017)
31. B.T. Huang, M. Roge, M. Bonetti, T.J. Salez, C. Wiertel-Gasquet, E. Dubois, R. Cabreira Gomes, G. Demouchy, G. Mériguet, V. Peyre, M. Kouyaté, C.L. Filomeno, J. Depeyrot, F.A. Tourinho, R. Perzynski et S. Nakamae, Thermoelectricity and thermodiffusion in charged colloids. J. Chem. Phys. **143**, 054902 (2015)
32. I. Lucas, E. Dubois, J. Chevalet et S. Durand-Vidal, *Physical,* vol. 10, p. 3263–3273, 2008.
33. E. Massart, IEEE Tran. Magn. **17**, 1247–1250 (1981)
34. C. Guibert, *Etude des propriétés d'hyperthermie de nanoparticules dispersées dans.* PhD Thesis (2016)
35. J.C. Bacri, A. Cebers, A. Bourdon, G. Demouchy, B.M. Heegaard, B. Kashevsky et R. Perzynski, Transient grating in a ferrofluid under magnetic field: Effect of magnetic interactions on the diffusion coefficient of translation Phys. Rev. E. **52**, 3936–3942 (1995)
36. F. Gazeau, E. Dubois, J.C. Bacri, , F. Boué, A. Cebers et R. Perzynski, Anisotropy of the structure factor of magnetic fluids under a field probed by small-angle neutron scattering. Phys. Rev. E. **65**, 031403 (2002)
37. G. Mériguet, F. Cousin, E. Dubois, F. Boué, A. Cebers et R. Perzynski, What tunes the structural anisotropy of magnetic fluids under a magnetic field? J. Phys. Chem. B. **110**, 4378–4386 (2006)
38. E. Wandersman, E. Dubois, F. Cousin, V. Dupuis, G. Mériguet, R. Perzynski et A. Cebers, Relaxation of the field-induced structural anisotropy in a rotating magnetic fluid. Europhys. Lett. **86**, 10005 (2009)
39. T. J. Salez, Effets *thermoelectriques dans les fluides complexes: liquides ioniques et ferrofluides.* PhD Thesis (2017)

40. P.F. Salazar, S.T. Stephens, A.H. Kazim, J.M. Pringle et B.A. Colas, Enhanced thermo-electrochemical power using carbon nanotube additives in ionic liquid redox electrolytes. J. Mater. Chem. A. **2**, 20676 (2014)
41. R. Hu et al., Harvesting waste thermal energy using a carbon-nanotube-based thermo-electrochemical cell. Nanoletters **10**, 838 (2010)
42. J. Richardi et J.-J. Weiss, Influence of short range potential on field induced chain aggregation in low density dipolar particles. J. Chem. Phys. **138**, 244704 (2013)
43. M. Mamusa, J. Siriex-Plenet, F. Cousin, E. Dubois et V. Peyre, Tuning the colloidal stability in ionic liquids by controlling the nanoparticles/liquid interface. Soft Matter. **10**, 1097 (2014)
44. C. Guibert , V. Dupuis , J. Fresnais et V. Peyre, Controlling nanoparticles dispersion in ionic liquids by tuning the pH. J. Colloid Interf. Sci. **454**, 105 (2015)
45. P. Priyananda, H. Sabouri, N. Jain et B.S. Hawkett, Steric Stabilization of γ-Fe_2O_3 Superparamagnetic Nanoparticles in a Hydrophobic Ionic Liquid and the Magnetorheological Behavior of the ferrofluid. Langmuir,. **34**, 3068−3075 (2006)
46. X. He, W. Qiang, J. Wu, Q. Shao, P. Cao, L. Cheng, X. Zhang et Y. Deng, Manipulation of magnetic ionic liquid droplets and their application in energy harvesting. J. Phys. D Appl. Phys. **50**, 465002 (2017)
47. M. Bonetti et al., «Thermoelectric energy recovery at ionic-liquid/electrode interface,» *The Journal of Physical Chemistry,* vol. 142, p. 244708, 2015.
48. M. Bonetti, S. Nakamae, M. Roge et P. Guenoun, Huge Seebeck coefficients in nonaqueous electrolytes. J. Chem. Phys. **134**, 114513 (2011)
49. M. Chen, Z.A. Goodwi, G. Fenga et A.A. Kornyshev, On the temperature dependence of the double layer capacitance of ionic liquids. J. Electroanal. Chem (2017)
50. A. Gunawan, H. Li, C.-H. Lin, D.A. Buttry, V. Mujica, R.A. Taylor, R.S. Prasher et P.E. Phelan, The amplifying effect of natural convection on power generation of. Int. J. Heat Mass Trans. **78**, 423 (2014)
51. K. Trohidou, *Magnetic Nanoparticle Assmblies* (Taylor and Francis, Boca Raton, 2014)

Chapter 17
Nanocomposites for Permanent Magnets

Isabelle de Moraes and Nora M. Dempsey

Abstract Permanent magnets are exploited in a variety of devices (e.g. motors, generators, sensors, actuators) used in various fields of applications including transportation (e.g. (hybrid)electric vehicles), energy management (wind turbines…) and information technology (e.g. hard disc drives). Permanent magnet research today is concerned with improving the performance of magnets based on various hard magnetic phases while reducing dependence on any critical materials used. Nanocomposite magnets which combine a high coercivity hard magnetic phase with a high magnetisation soft magnetic phase hold great potential to rise to this challenge. In this chapter, we briefly outline the history of permanent magnets and explain the basic physical concepts behind nanocomposite permanent magnets. We recall the metallurgical and physical vapour deposition synthesis routes used to fabricate bulk and thin film nanocomposites, respectively. We then focus on chemical synthesis methods which offer the possibility to produce hard and soft magnetic nanoparticles or core-shell nanoparticles that can be used as building blocks to fabricate bulk hard-soft nanocomposites. We present three case studies concerning the fabrication and structural and magnetic characterisation of FePt-Fe_3Pt, FePd-Fe and $SmCo_5$-Fe nanocomposites. We wrap up the chapter with an outline of the challenges faced in producing hard-soft nanocomposite magnets using chemically synthesised nanoparticles, and an overview of the advanced magnetic characterisation tools being used to study the complex magnetisation reversal processes at play in hard-soft nanocomposites.

I. de Moraes · N. M. Dempsey (✉)
Institut Néel, CNRS and Université Grenoble Alpes, Grenoble, France
e-mail: nora.dempsey@neel.cnrs.fr

D. Peddis et al. (eds.), *New Trends in Nanoparticle Magnetism*,
Springer Series in Materials Science 308,
https://doi.org/10.1007/978-3-030-60473-8_17

17.1 Permanent Magnets

17.1.1 A Brief History of Permanent Magnets

Permanent magnets are exploited in a wide variety of applications, ranging from motors, generators, sensors, actuators, to simple latches. The defining characteristic of a permanent magnet is its resistance to demagnetisation, which is quantified by its coercivity, H_c (Fig. 17.1). The strength of interaction between a magnet and another object is proportional to its remanent magnetisation, $\mu_0 M_r$ (Fig. 17.1). Both coercivity and remanent magnetisation are extrinsic properties, their upper limits being set by the material's intrinsic properties (anisotropy field and saturation magnetisation), their actual values being determined by the magnet's microstructure. Magnetic anisotropy in magnets is due to either shape anisotropy or magnetocrystalline anisotropy, with much higher values achievable with the latter. The remanent magnetisation of a magnet is reduced with respect to its saturation magnetisation when the easy axes of individual grains are misaligned, and it is reduced with respect to the saturation magnetisation of the principle hard magnetic phase when the volume content of this phase is diluted by the presence of non-magnetic material or voids. A magnet's maximum energy product corresponds to twice the energy stored in the stray field of the magnet, and it quantifies the work that can be done by the magnet. Its value is given by the rectangle of maximum area in the second quadrant of the *B–H* loop, where *B* is the magnetic flux density (Fig. 17.1). The maximum energy product is a key figure of merit for comparing magnets. The evolution in the room temperature value of energy product achieved in bulk magnets over the last century (Fig. 17.2) is due to the discovery of new hard magnetic phases with improved intrinsic properties and the development of appropriate microstructures through complex processing techniques.

Steel and Alnico magnets exploit shape anisotropy, at the macroscopic scale in the case of steel magnets (thus the familiar horse-shoe shape of these magnets), at the nanoscale in the case of Alnico magnets (nanorods of CoFe in an AlNi-based matrix). Both ferrites and rare earth-transition metal (RE-TM) magnets exploit

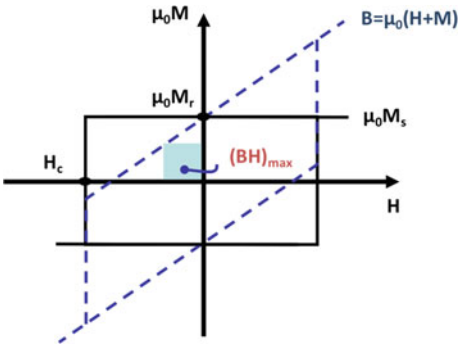

Fig. 17.1 Ideal hysteresis loops for a permanent magnet, M(H) and B(H), where M is magnetisation and B is magnetic flux density. The maximum possible energy product, $(BH)_{max}$, is represented by the area of the largest square that can be drawn in the second quadrant

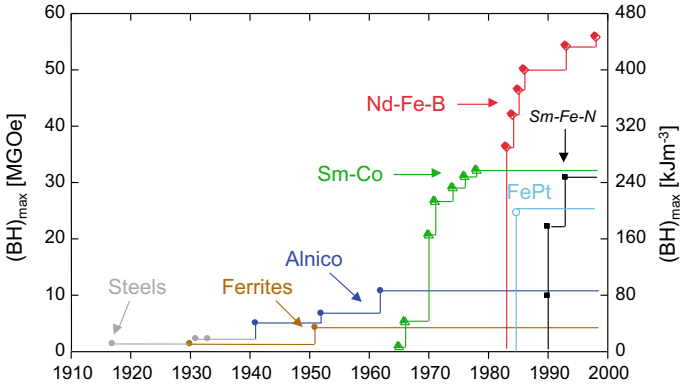

Fig. 17.2 Evolution in the room temperature energy product, $(BH)_{max}$, of hard magnetic materials in the twentieth century [1]

magnetocrystalline anisotropy. The anisotropic 4f charge distributions in rare earth ions together with strong spin-orbit coupling with the crystal electric field leads to very high magnetocrystalline anisotropy in RE-TM phases [2]. While horse-shoe-shaped steel magnets are now obsolete, the other classes of magnets represented in Fig. 17.2 are used in a wide range of applications. Ferrite magnets are used in devices such as motors, generators, actuators and latches, where their relatively low energy densities are sufficient (e.g. hand-held tools). Ferrites dominate world magnet production in tonnage. Alnicos are characterised by excellent temperature stability of remanence and are used in applications where this is critical (e.g. metrology). The emergence of RE-TM magnets has revolutionised the design of motors and generators and they are used in devices where their elevated energy products and other particular characteristics (e.g. high coercivity) off-set their relatively high cost. They account for the largest fraction of the magnet market in terms of revenue. The first mass market application of SmCo magnets was in the Sony walk-man, while now they are used in applications with extreme requirements such for very high-temperature use (>200 °C), very high resistance to demagnetisation (>2T), or very small magnets (mm to sub-mm range) produced by machining of bulk magnets. For applications in which energy density is a premium, NdFeB magnets are the magnets of choice. The first large-scale use of NdFeB magnets was in the voice-coil motors of computers, and they played a real role in reducing the size of mobile devices including computers and phones. The typical weight for NdFeB magnets used in these applications is in the gram range. Note that what are referred to as "NdFeB" magnets typically also contain Pr (another RE with properties similar to Nd), as well as minor additions of elements such as Al, Cu and Ga, that serve to produce an appropriate microstructure. The next big use to emerge for NdFeB-based magnets was in the generators and motors of hybrid electric vehicles (1 kg-range) and then in gearless wind turbines (1 tonne-range). The growth in room temperature energy product, which effectively doubled in value every 12 years in the last century (Fig. 17.2), has been practically stagnant

over the last 20 years. This is because, despite extensive searches for ternary and quaternary phases containing RE and TM elements, no new magnetic phases having intrinsic properties better than those of $Nd_2Fe_{14}B$ have been discovered.

The maximum operating temperature of NdFeB-based magnets in hybrid electric vehicles and wind turbines reaches as high as 180°C. The coercivity of RE-TM magnets decreases with increasing temperature, and to maintain sufficient coercivity at elevated temperature, magnet manufacturers increased the anisotropy of the main hard magnetic phase ($R_2Fe_{14}B$) through a partial substitution of Nd, which is a light rare earth (LRE) element, by a heavy rare earth (HRE) such as Dy or Tb. One drawback of substituting HRE for LRE is that the remanent magnetisation of the magnet is reduced, because while the moments on LRE atoms align parallel to the moments on the Fe atoms in the $R_2Fe_{14}B$ phase, those of HRE align anti-parallel. Another major concern with HRE substitution is that HREs are much less abundant, and thus much more expensive, than LREs. The growing demand for certain LREs and HREs for use in magnets and in other applications (e.g. lighting and visual displays, catalysers…) coupled with limited mining and separation of REs, essentially concentrated in China, led to the so-called RE-crisis. The cost and supply risks associated with REs have been a driving factor in defining the main directions in permanent magnet research today (Fig. 17.3). The rest of this chapter deals with one specific research direction, namely the development of hard—soft magnetic nanocomposites.

17.1.2 Hard—Soft Magnetic Nanocomposites

Following an experimental report by Coehoorn on the attainment of M_r/M_s values of over 0.5 and coercivity of 0.3T in isotropic Fe_3B–Fe–$Nd_2Fe_{14}B$ magnets containing just 15 vol.% hard magnetic phase [3], Kneller and Hawig proposed an approach to significantly increase the energy product of permanent magnets. Their idea was to produce a nanostructured composite material that combines a hard magnetic phase exchange coupled to a high magnetisation soft phase [4], as illustrated in Fig. 17.4. They showed that the length scale of the soft phase should be roughly of the order of the domain wall width of the hard phase, i.e. a few nanometres. The application of an external field to an exchange coupled hard-soft nanocomposite will produce a twisted spin state in the soft material, and upon removal of the external field, the twist will spring back to the original state of full remanence, giving rise to the term "spring magnet" (Fig. 17.4—right). The concept was further developed by Skomski and Coey, who predicted that it may be possible to achieve an energy product in excess of a megajoule per cubic metre in an optimised textured $Sm_2Fe_{17}N_3/Fe_{65}Co_{35}$ hard/soft nanocomposite [5]. Skomski recently revisited the idea of predicting the ideal nanostructure of aligned hard/soft nanocomposites and found that soft-in-hard structures should have higher coercivity than hard-in-soft structures and that ideal nanostructures should be made of soft cubes or long soft rods [6]. The intrinsic magnetic properties of candidate hard and soft magnetic materials are listed in Table 17.1.

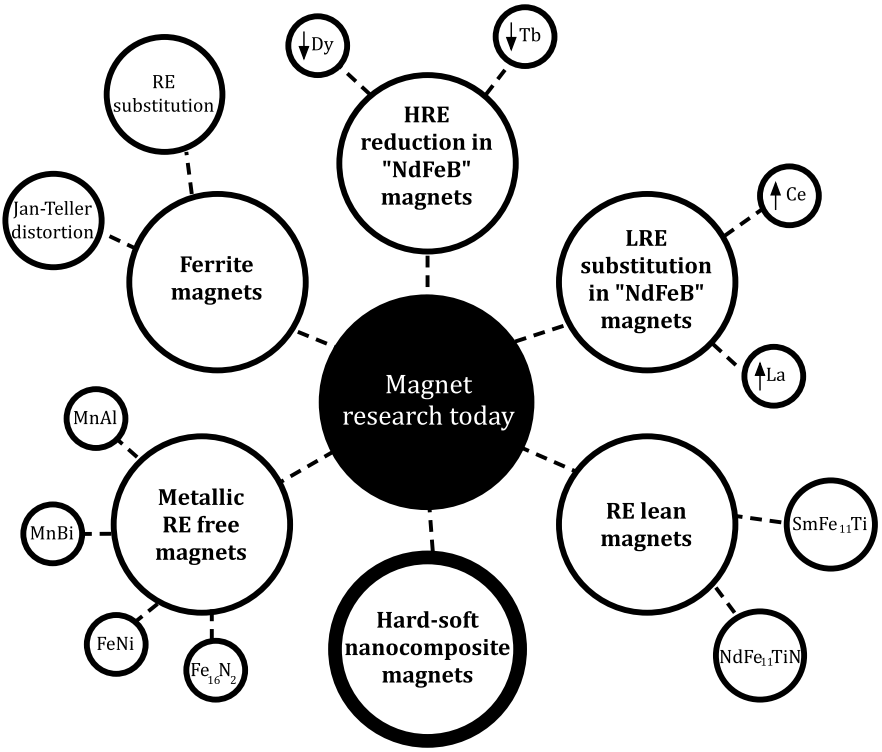

Fig. 17.3 Current directions in magnet research

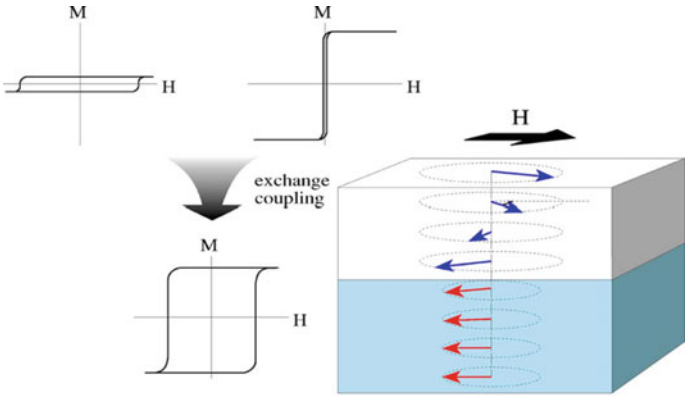

Fig. 17.4 Schematic of an exchange coupled nanocomposite "spring" magnet [7]

Table 17.1 Intrinsic properties of various soft magnetic and hard magnetic phases

Material	$\mu_0 M_s$(T)	$\mu_0 M_s$(emu/g)	K_1(MJ/m^3)	δ_w(nm)
Soft magnetic phases				
Co	1.81	161	0.410	24
Fe	2.15	218	0.048	64
$Fe_{65}Co_{35}$	2.45	240	0.018	90
$Fe_{20}Ni_{80}$	1.00	93	– 0.002	2000
Fe_3Pt	1.83	125	– 0.4	15
Fe_3O_4	0.63	92	– 0.013	73
Hard magnetic phases				
$Nd_2Fe_{14}B$	1.61	171	4.9	3.9
$SmCo_5$	1.07	110	17.2	3.6
Sm_2Co_{17}	1.25	120	3.3	10
$CoFe_2O_4$	0.56	80	0.18	13
$SrFe_{12}O_{19}$	0.48	71	0.35	14
$BaFe_{12}O_{19}$	0.48	71	0.33	14
FePt	1.43	74	6.6	3.7
CoPt	1.00	50	4.9	5.0
$Sm_2Fe_{17}N_3$	1.54	157	8.6	3.7
FePd	1.41	114	1.7	10
FeNi ($L1_0$)	1.6	154	1.0	–

Much effort has gone into fabricating hard-soft nanocomposite permanent magnets using a range of processing techniques based on (a) bulk metallurgical synthesis, (b) physical vapour deposition and (c) chemical synthesis. The bulk metallurgical synthesis route includes techniques already used in magnet fabrication (e.g. melt spinning) and the mass production of amorphous materials (e.g. ball milling) and could thus be considered a natural extension of today's magnet manufacturing industry. However, the maximum energy product of the attained hard-soft nanocomposites achieved to date is not better than that of single-phase magnets. This can be attributed to the technical challenges faced in preparing textured materials, to reach high remanence, with grain size below 10 nm, needed to reach coercivity in excess of 1T. The physical vapour deposition route is only suitable for the fabrication of thin and thick films. On the one hand, films can serve as model systems to study the link between micro/nanostructure and extrinsic magnetic properties in nanocomposite materials [8]. On the other hand, there is huge potential for their use in micro/nanosystems requiring high energy density but compact magnetic flux sources [9]. In this chapter, we chose to focus our attention on the chemical synthesis of hard-soft nanocomposite permanent magnets, but before presenting cases studies from literature, we will very briefly recall studies related to bulk metallurgical synthesis and physical vapour deposition of hard/soft nanocomposites.

(a) ***Bulk metallurgical synthesis***

Examples of bulk metallurgical processing include work on melt spinning to produce NdFeB–Fe [10–12], mechanical alloying to produce SmFeN–Fe [13], splat cooling to produce $RE_2TM_{14}B/Fe_3B$ [14] and ball milling to produce SmCo–Fe [15, 16] and NdFeB–Fe [17]. In all these studies, the influence of sample composition, preparation and annealing conditions on phase formation, phase content and microstructure (grain size) was probed. While cold welding limits the lower particle size achievable in classical ball milling to some hundreds of nm and more, surfactant assisted ball milling was developed to produce nanometre sized coercive SmCo and NdFeB hard magnetic particles [18, 19]. The motivation for this pioneering work was to fabricate nanocomposite magnets in a bottom-up approach by blending hard and soft magnetic nanopowders. The very small grain size reached constituted a significant advance of this type of approach, but the isotropic nature of the samples greatly limited the energy product value achieved. An increase in remanent magnetisation by nanoparticle alignment under magnetic field was reported [20]. More details on advances in bulk metallurgical synthesis of nanocomposites, including the use of novel powder consolidation techniques, can be found in a recent review by Yue et al. [21].

(b) ***Thin film physical vapour deposition synthesis***

Thin film fabrication techniques (sputtering, pulsed laser deposition, molecular beam epitaxy) have been used to study the fabrication of hard-soft nanocomposites. Thin film deposition has the advantage that full density samples can be produced and the crystallographic texture of the hard magnetic layer can be controlled through deposition conditions. Deposition onto heated substrates produces out-of-plane texture in NdFeB films [22, 23], and most generally in-plane texture in SmCo films [24]. On polycrystalline substrates, FePt films normally grow with [111] texture, but [001] texture with the easy magnetisation axis perpendicular to the film plane may be obtained by appropriate selection of the substrate [25]. The deposition of multilayer structures allows us to combine materials of our choice, thus by-passing the phase diagram, and the relative thickness of the different layers can be controlled by varying the deposition conditions. Exchange coupling has been demonstrated in a number of hard-soft multilayer stacks of different type, based on RFeB/Fe or RFeB/FeCo [26–28], SmCo/Fe or SmCo/Co [29, 30], and FePt/Fe_3Pt [31].

The deposition of in-flight-formed clusters has also been applied to the preparation of model hard magnetic materials. Cluster deposition may permit the crystallisation of the hard magnetic phase without grain growth. It was initially applied to the deposition of FePt nanoparticles [32]. More recently, YCo_5 and $SmCo_5$ nanomagnets were prepared by this approach [33, 34]. The nanoparticles are essentially monodisperse and they may be oriented under a magnetic field before landing on the substrate surface. Hard nanocomposites have been obtained by embedding hard $HfCo_7$ nanoparticles in a soft FeCo matrix [35]. To date, the materials prepared with this approach suffer from the fact that the matrix is soft, whereas soft magnetic inclusions in a hard magnetic matrix are predicted to permit much higher values of coercivity [6].

17.2 Chemical Synthesis of Hard-Soft Nanocomposites

Chemical synthesis, using a range of solution chemistry techniques (precipitation, hydride reduction, hydrothermal, reverse micelles, polyol, sol–gel, thermolysis, photolysis, sonolysis, electrochemical/electrodeposition…) is applied to the fabrication of a wide range of magnetic nanoparticles, including core-shell nanoparticles [36–39]. These bottom-up fabrication approaches allow to tune the size, shape and composition of the magnetic nanoparticles. Chemically synthesised magnetic nanoparticles are now used to make ferrofluids for applications in seals, bearings, dampers, stepper motors, loudspeakers and sensors [40]. In the field of bio-medicine, they are used as contrast agents in magnetic resonance imaging and for magnetic separation in diagnostic kits, while their potential use in drug delivery and magnetic hyperthermia in cancer treatment are being extensively explored [37–39]. Self-assembled periodic arrays of magnetic nanoparticles are being studied for use as magnetic recording media [39, 41], while they are also being considered for use in the ferrite cores of high frequency electronic components [40] and in microwave devices [38]. Our interest in chemical synthesis lies in the fact that it offers the possibility to produce hard and soft magnetic nanoparticles or core-shell nanoparticles that can be used as building blocks to fabricate bulk hard-soft nanocomposites. The potential to upscale chemical synthesis routes opens the possibility to fabricate bulk nanocomposite magnets on an industrial scale. A number of excellent review articles have dealt with the chemical synthesis of hard-soft magnetic nanocomposites [21, 38, 39, 42]. Here, we have selected three case studies to highlight advances made and the great potential which this approach holds for the fabrication of high-performance permanent magnets.

17.2.1 Case Study #1—FePt/Fe_3Pt Nanocomposites

This case study concerns the fabrication of FePt/Fe_3Pt nanocomposites [43] and is a follow on from the pioneering work by Sun and co-workers on the preparation of monodisperse nanoparticles of FePt [41] and magnetite (Fe_3O_4) [44]. We will begin by recalling the main results from these studies and will then describe the self-assembly of these precursors and further processing steps developed to fabricate hard-soft nanocomposites.

FePt nanoparticles were prepared from a mixture containing platinum acetylacetonate and iron pentacarbonyl. Reduction of the $Pt(acac)_2$ (acac = acetylacetonate, $CH_3COCHCOCH_3$) by a diol and thermal decomposition of iron pentacarbonyl followed by addition of a flocculent (ethanol) led to the preceipitation of FePt nanoparticles [41]. The addition of oleic acid and oleyl amine in the mixture served to stabilise monodisperse nanoparticles of diameter 3 nm. The size of the nanoparticles could be increased by adding additional reagents to 3 nm seed particles while the composition of the nanoparticles could be tuned by adjusting the molar ratio of

the Pt salt and the iron pentacarbonyl. Monodisperse nanoparticles of diameter up to 10 nm were isolated and purified by centrifugation and then redispersed at variable concentrations in nonpolar solvents. If a drop of such a dispersion is spread on a substrate and the carrier solvent is allowed to slowly evaporate, 3D superlattices of FePt nanoparticles are produced. The as-produced FePt nanoparticles are chemically disordered and thus magnetically soft. Annealing was used to transform the crystal structure from face centred cubic to face centred tetragonal, and the evolution in the XRD patterns of 1 μm-thick assemblies of 4 nm $Fe_{52}Pt_{48}$ nanoparticles, as a function of annealing temperature (for a fixed annealing time of 30 min.), is compared in Fig. 17.5. The observed shift in the position of the (111) peaks together with the evolution of the (001) and (110) peaks attests to the chemical ordering induced by annealing, though only partial ordering is achieved below 500 °C. Increasing the annealing temperature or the annealing time (data not shown) leads to increased chemical ordering. Representative in-plane coercivity values of a series of 140-nm-thick assemblies of 4 nm $Fe_{52}Pt_{48}$ nanoparticles, annealed in the same temperature range and for the same time, are compared in Fig. 17.6. The gradual increase in coercivity with annealing temperature is consistent with the concomitant increase in chemical ordering evidenced by x-ray diffraction, which leads to an increase in the magnetocrystalline anisotropy of the FePt phase. In-plane coercivity values of another series of 140-nm-thick assemblies of 4 nm Fe_xPt_{1-x} nanoparticles of variable composition are also shown in Fig. 17.6. The highest values of coercivity were found

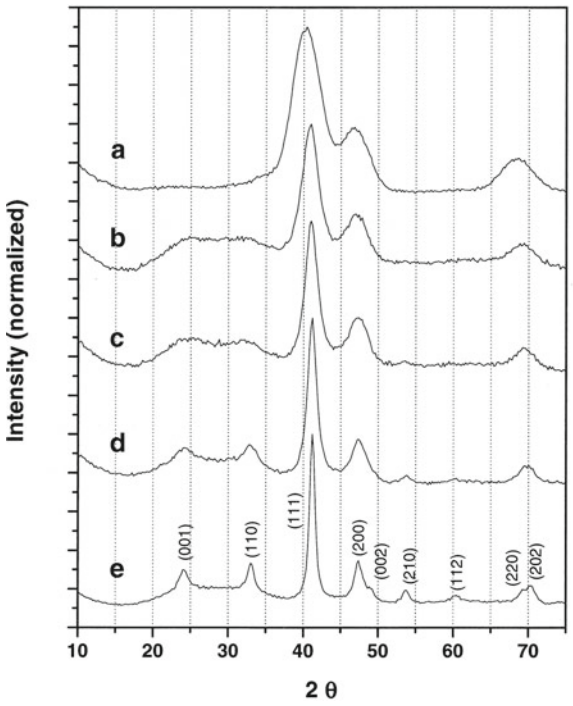

Fig. 17.5 XRD patterns of as-synthesised 4-nm $Fe_{52}Pt_{48}$ particle assemblies (**a**) and a series of similar assemblies annealed under N_2 for 30 min at temperatures of 450 °C (**b**), 500 °C (**c**), 550 °C (**d**), and 600 °C (**e**). The indexing is based on tabulated fct FePt reflections [41]

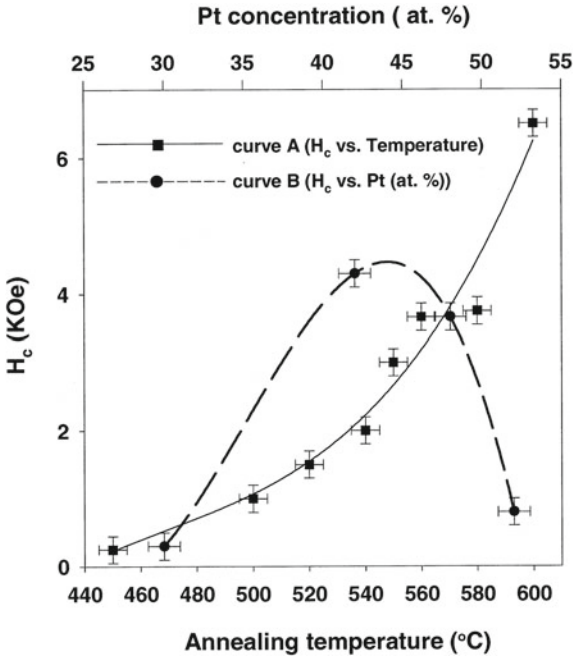

Fig. 17.6 In-plane coercivity values of 140-nm-thick assemblies of 4 nm FePt nanoparticles: Curve A—as a function of annealing temperature for a fixed annealing time (30 min.) and fixed composition ($Fe_{52}Pt_{48}$); Curve B—as a function of composition for fixed annealing conditions (560 °C, 30 min.) [41]

for Fe-rich samples ($x = 0.52$–0.6), a trend also reported for Fe_xPt_{1-x} films prepared by sputtering [45]. The maximum coercivity value was subsequently increased by further tuning of the composition and annealing conditions [46].

The precursors for the soft magnetic phase, Fe_3O_4 nanoparticles, were prepared by a high-temperature (265 °C) reaction of $Fe(acac)_3$ (acac = acetylacetonate) in phenyl ether in the presence of alcohol, oleic acid and oleylamine [44]. As with FePt nanoparticles, the particle size can be increased by seed mediated growth. In this way, monodisperse solutions of Fe_30_4 nanoparticles with diameters in the range 4–20 nm were prepared. The width of the XRD peaks of the nanoparticles decreased with nanoparticle size (Fig. 17.7, curves *a–d*) and estimates of the particle size from the Scherrer formula were in good agreement with TEM observations (Fig. 17.8). The thus synthesised Fe_3O_4 nanoparticles could be transformed to γ-Fe_2O_3 by annealing under oxygen or to α-Fe by annealing under Ar + 5% H_2 (Fig. 17.7, curves *e* , *f*). The saturation magnetisation of the transformed particles was estimated to be 70 and 186 emu/g, respectively, to be compared with 82 emu/g of the starting Fe_3O_4 nanoparticles. The apparent reduction in the saturation magnetisation of the α-Fe nanoparticles compared to the value of 210 emu/g of bulk α-Fe may be attributed to finite size effects [47] or surface oxidation [48].

Sun and co-workers then went on to exploit the progress they made in the synthesis of monodisperse hard and soft magnetic nanoparticles to fabricate FePt/Fe_3Pt nanocomposites [43]. To start, chemically disordered FePt and Fe_3O_4 nanoparticles were mixed in hexane, and evaporation of the hexane or addition of ethanol was

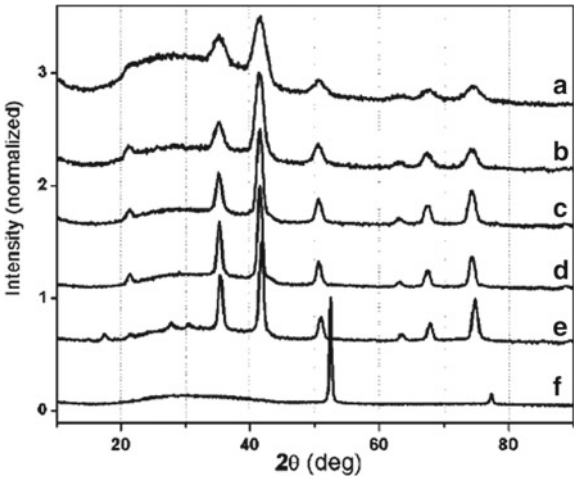

Fig. 17.7 X-ray diffraction patterns of 4 nm (**a**), 8 nm (**b**), 12 nm (**c**), 16 nm (**d**) Fe_3O_4 nanoparticle assemblies, and α-Fe_2O_3 nanoparticle assembly (**e**) obtained from the oxidation of a 16 nm Fe_3O_4 nanoparticle assembly under oxygen at 250°C for 2 h, α-Fe nanoparticle assembly (**f**) obtained from the reduction of a 16-nm Fe_3O_4 nanoparticle assembly under Ar + H_2 (5%) at 400 °C for 2 h [44]

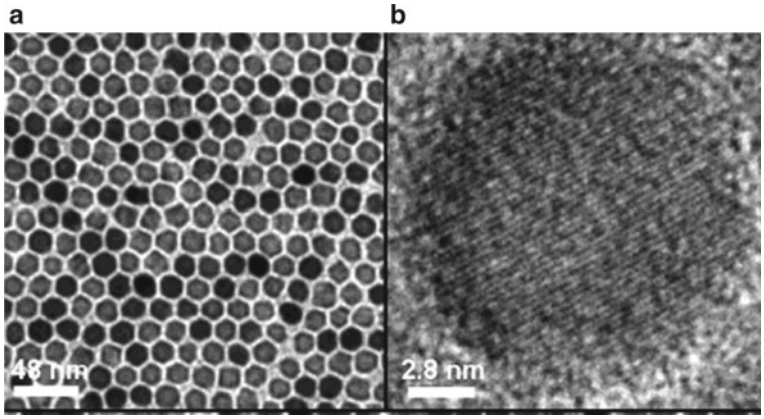

Fig. 17.8 **a** TEM bright field image of a monolayer assembly of 16-nm Fe_3O_4 nanoparticles, and **b** HRTEM image of a single Fe_3O_4 nanoparticle [44]

used to form 3D assemblies of the nanoparticles. The size and composition of the FePt nanoparticles were fixed (4 nm, $Fe_{58}Pt_{42}$) while the size of the Fe_3O_4 nanoparticles was varied from 4 to 12 nm and the mass ratio of Fe_3O_4 to FePt nanoparticles was varied from 1:5 to 1:20. The overall structure of the binary 3D assemblies was found to depend on the relative size of the nanoparticles. When both particle types had the same size (4 nm), a hexagonal lattice was formed in which the Fe_3O_4 and FePt nanoparticles occupied the sites of the lattice in a random fashion (Fig. 17.9a). When the diameter of the Fe_3O_4 nanoparticles was twice that of the FePt nanoparticles (8 nm: 4 nm), the bigger particles were typically surrounded by 6-8 smaller particles, giving rise to local ordering (Fig. 17.9b). An even greater different in the

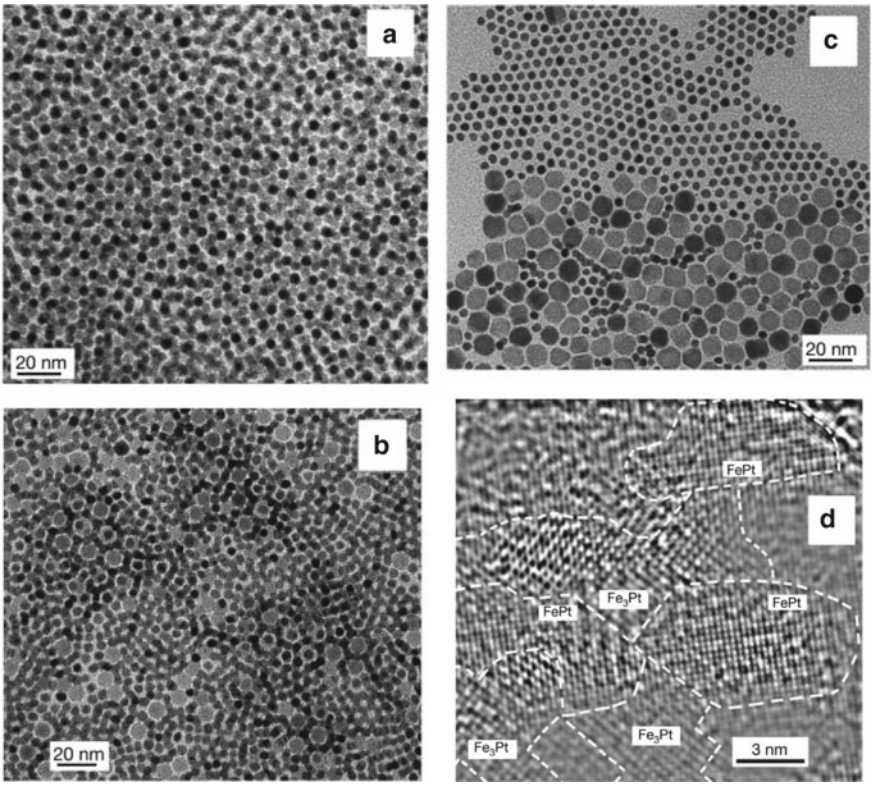

Fig. 17.9 **a–c** TEM images of Fe_3O_4: $Fe_{58}Pt_{42}$ nanoparticle assemblies of mass ratio 1:10, the size of the FePt is constant (4 nm) while that of the Fe_3O_4 nanoparticles was 4 nm, 8 nm and 12 nm, respectively; **d** HRTEM image of a sintered FePt–Fe_3Pt particle formed by annealing an assembly made of 4 nm Fe_3O_4 and $Fe_{58}Pt_{42}$ nanoparticles [43]

particle size (12 nm: 4 nm) led to phase segregation (Fig. 17.9c). The assembly structure was reported to be insensitive to the mass ratio, within the range studied.

Annealing of the assemblies under $Ar + H_2$ (5%) at 650 °C for 1 h led to chemical ordering of the FePt nanoparticles and to the reduction of Fe_3O_4 to form α-Fe. Desorption of the organic layers around the individual nanoparticles during the annealing step resulted in sintering of the particles, which in turn led to partial inter-particle diffusion. In the case of samples made with 4 nm and 8 nm Fe_3O_4 nanoparticles, this diffusion transformed the α-Fe into soft magnetic Fe_3Pt inclusions less than 10 nm in size, dispersed in a hard magnetic FePt matrix, as evidenced by high resolution TEM (Fig. 17.9d) and energy dispersive spectroscopy analysis. Selected area diffraction analysis showed that the thus formed FePt/Fe_3Pt nanocomposites are crystallographically isotropic. α-Fe particles larger than 20 nm in diameter were identified in the samples made using 12 nm Fe_3O_4 nanoparticles, which can be attributed to phase segregation during assembly of the constituent nanoparticles.

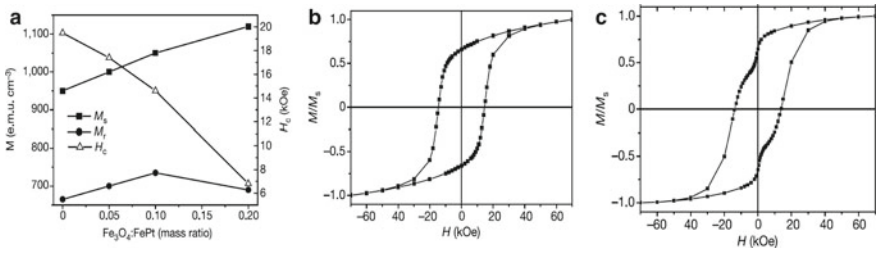

Fig. 17.10 **a** M_s, M_r and H_c values of FePt–Fe_3Pt nanocomposites made by annealing assemblies of 4 nm Fe_3O_4 and $Fe_{58}Pt_{42}$ nanoparticles, plotted as a function of the mass ratio of the precursors. **b**, **c** Hysteresis loops of FePt–Fe_3Pt nanocomposites made by annealing assemblies of Fe_3O_4 and $Fe_{58}Pt_{42}$ nanoparticles with a precursor mass ratio of 1:10 and an Fe_3O_4 nanoparticle size of 4 nm and 12 nm, respectively [43]

The saturation magnetisation, remanent magnetisation and coercivity of FePt–Fe_3Pt nanocomposites formed by annealing an assembly of 4 nm nanoparticles are plotted as a function of the mass ratio of Fe_3O_4 to $Fe_{58}Pt_{42}$ nanoparticles in Fig. 17.10a. The values measured for pure $Fe_{58}Pt_{42}$ annealed assemblies are also included, for comparison. The saturation magnetisation of the pure FePt sample is 15% lower than the value typically reported for bulk $L1_0$ FePt [45]. This is tentatively attributed to size, composition or surface effects. It is worth noting that the coercivity of the pure FePt sample reported in the nanocomposite study is more than twice that reported in the earlier studies by Sun and co-workers. Though not discussed, they may be due to a change in the annealing atmosphere from static nitrogen in the earlier studies to flowing Ar + H_2 in the present study. With increasing amount of the soft magnetic precursor phase, the saturation magnetisation of the nanocomposites monotonically increases while the coercivity monotonically decreases. The remanent magnetisation peaks for an intermediate precursor mass ratio of 1:10, at a value which is 17% higher than that of the pure FePt sample. The M_r/M_s ratio of all samples exceed 0.6, which is indicative of exchange coupling in these isotropic samples.

The shape of the measured hysteresis loops was found to depend of the size of the starting Fe_3O_4 nanoparticles. Those made from 4 nm (Fig. 17.10b) and 8 nm (data not shown) particles showed single-phase magnetic behaviour, indicative of exchange coupling between the hard magnetic matrix and the soft phase inclusions. On the other hand, those made from 12 nm Fe_3O_4 nanoparticles showed distinct two-phase behaviour (Fig. 17.10c) due to uncoupled switching of the hard and soft phases of the composite structure, owing to phase segregation. These results are in good agreement with the prediction that the soft phase inclusions of an exchange coupled nanocomposite should have an upper size limit close to twice the domain wall width of the hard phase, which is reported to be 3.7 nm for $L1_0$ FePt (Table 17.1). The energy product of the $Fe_{58}Pt_{42}$/Fe_3Pt nanocomposite with optimised properties shown in Fig. 17.10b was estimated to be 20.1 MGOe, which is 37% higher than that estimated for the single-phase $Fe_{58}Pt_{42}$ sample and over 50% higher than the

theoretical value of non-exchange coupled isotropic $L1_0$ FePt. However, it is far from the theoretical upper limit predicted for textured single-phase FePt ($1/4\mu_0 M_s^2 = 390\,kJ/m^3 = 49\,MGOe$). Nevertheless, this case study demonstrated the possibility to use chemical synthesis to fabricate exchange coupled hard-soft nanocomposites. Further improvements in the energy product can be expected with advances made in powder compaction and the inducement of crystallographic texture in the hard magnetic phase.

17.2.2 Case Study #2—FePd/α-Fe Nanocomposites

The second case study we selected to highlight concerns FePd/α-Fe nanocomposites [49]. The chemical approach used to fabricate these nanocomposites is somewhat different to the previous case and the authors used first-order reversal curve (FORC) analysis to study the magnetic switching behaviour. While FePd has a slightly lower magnetisation and significantly lower magnetocrystalline anisotropy than FePt, it has the advantage that according to its phase diagram it can co-exist with α-Fe, while the annealing of α-Fe in proximity to FePt tends to transform high magnetisation α-Fe into lower magnetisation Fe_3Pt. The authors argued that the coexistence of FePd and α-Fe in a thermodynamically stable state should favour the formation of coherent interfaces. This is expected to improve exchange coupling compared to NdFeB or FePt-based nanocomposites with amorphous or diffuse interfaces [50].

The sample preparation process began with fabrication of monodisperse trioctylphosphine (TOP) coated Pd nanoparticles by thermal decomposition of a Pd-surfactant complex [51]. Heterostructured Pd/γ-Fe_2O_3 nanoparticles, in which one, two or three γ-Fe_2O_3 nanoparticles are attached to a Pd nanoparticle, were then formed by dissolving the Pd nanoparticles in a solution of 1-octanol, $Fe(acac)_3$, oleylamine and oleic acid and heating the solution (180 °C/1 h) while bubbling N_2 through it [52]. TEM images of Pd nanoparticles and heterostructured Pd/γ-Fe_2O_3 nanoparticles are shown in Fig. 17.11. The Pd/γ-Fe_2O_3 nanoparticles were then mixed with Pd nanoparticles in n-hexane, annealed under O_3 (200 °C/2 h) to remove surface organic ligands and then annealed (10 h) at various temperatures under $Ar + H_2$. The volume fraction of the soft and hard phases was varied by changing the relative amount of Pd and Pd/γ-Fe_2O_3 nanoparticles in the mixture (Fig. 17.12). The second annealing step caused reduction of the γ-Fe_2O_3 and interfacial atom diffusion to form FePd/α-Fe and led to chemical ordering in the FePd phase, though too high a temperature (823 K) led to disordering of the phase, as evidenced by x-ray diffraction (Fig. 17.13a). Increasing the annealing temperature also led to an increase in grain size of both phases to above 30 nm, as estimated from Scherrer formula analysis of the XRD patterns (Fig. 17.13b), and confirmed by TEM analysis (data not shown). High resolution TEM analysis of some select samples annealed at 723 K (data not show) revealed an interfacial orientation relationship: α-Fe(110)//$L1_0$-FePd (111) and α-Fe (111)//$L1_0$-FePd(110), which indicates that the close packed planes of both phases are in coherent contact, though slightly distorted at the interface (lattice mismatch

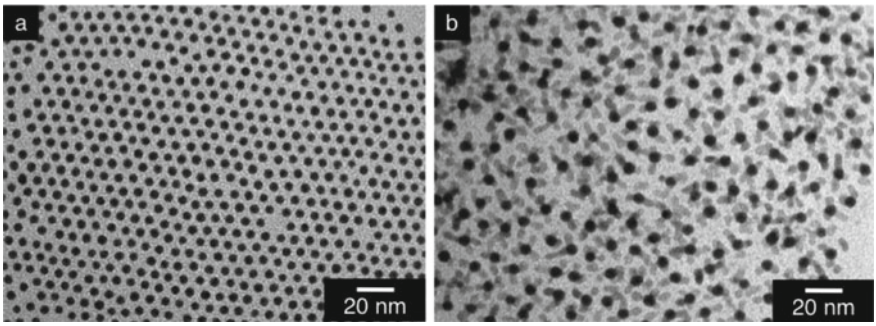

Fig. 17.11 TEM images of **a** Pd nanoparticles (4.9–0.3 nm) and **b** heterostructured Pd/γ-Fe_2O_3 nanoparticles (Fe/Pd molar ratio of 80/20) [49]

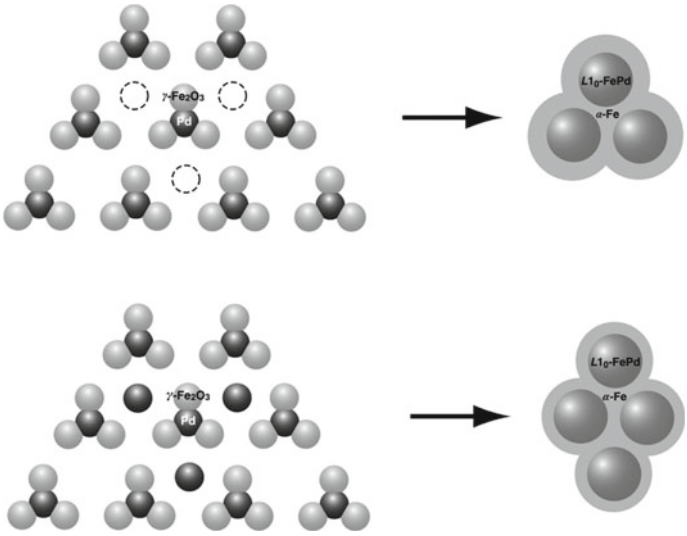

Fig. 17.12 Schematic illustration of the formation of FePd/Fe nanocomposites with different FePd/Fe volume ratios from mixtures of Pd/γ-Fe_2O_3 heterostructured nanoparticles and pure Pd nanoparticles [49]

4.7%). High resolution TEM analysis also revealed that annealing at 823 K led to a loss of lattice coherency at the interfaces (data not show).

The influence of annealing temperature on the magnetic properties of composites with 56 vol.% α-Fe is shown in Fig. 17.14. The samples annealed at the two lower temperatures (723 K, 798 K) showed single-phase loops, indicative of exchange coupling between the hard and soft constituent phases, while two-phase behaviour, indicative of non-coherent switching of magnetisation, was found for the sample annealed at the higher temperature (823 K). The reduction or loss in exchange coupling compared to the samples annealed at lower temperatures was attributed

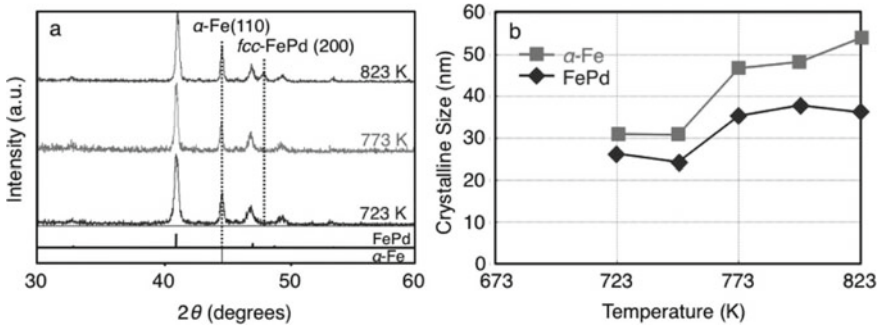

Fig. 17.13 **a** XRD patterns of FePd/Fe (44/56) nanocomposites formed by annealing at 723, 773, and 823 K. **b** Crystalline size of FePd (diamond) and α-Fe (square) of FePd/Fe (44/56) nanocomposites formed by annealing at various temperatures [49]

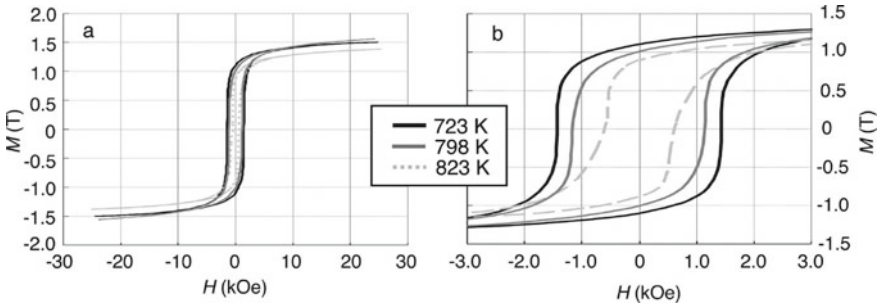

Fig. 17.14 Influence of annealing temperature on the MH loops of FePd/Fe nanocomposites with 56 vol.% soft phase. (**a** full loops, **b** zoom on low field regions) [49]

to the enlarged size of the soft grains, and possibly to chemical disordering of the hard grains.

The influence of soft phase content on the magnetic properties of composites annealed at 723 and 773 K is compared to those of a pure FePd sample in Fig. 17.15. As may be expected, the saturation and remanent magnetisation values increase with the soft phase content, while the coercivity decreases. Magetisation, coercivity and maximum energy product values are plotted as a function of soft phase content and annealing temperature in Fig. 17.16. The relative changes in these values are attributed to variations in the grain size of the soft phase, which depends on both the annealing temperature and volume content of the soft phase, and the degree of order of the hard phase, which depends on the annealing temperature. The maximum energy product value achieved was 10.3 MGOe, at an optimum annealing temperature of 773 K. Coalescence of α-Fe and disordering of the hard phase at the highest temperatures leads to a decrease in the average magnetic anisotropy of the nanocomposites and negatively affects exchange coupling.

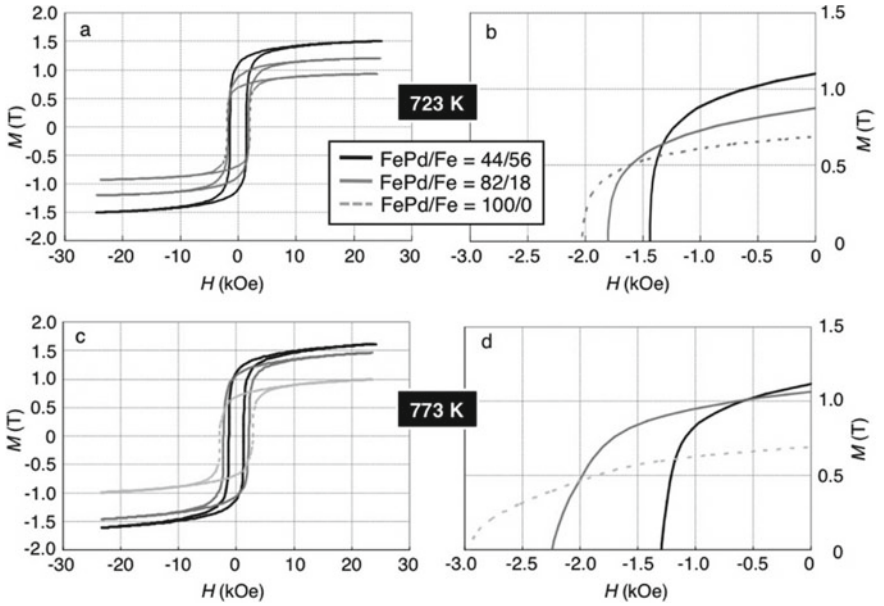

Fig. 17.15 Influence of relative volume content on the MH loops of FePd/Fe nanocomposites annealed at 723 K and 773 K. (**a**, **c** full loops, **b**, **d** zoom on 2nd quadrant) [49]

First-order reversal curve (FORC) analysis is a method based on hysteresis measurements that can be used to characterise magnetic interactions and switching field distributions [53]. It has been used to study magnetisation reversal in permanent magnets [54] as well as hard-soft nanocomposites made by thin film deposition of metallic multilayers [55] and chemical synthesis of oxides [56]. In this study, it was used to probe exchange interactions in select FePd/α-Fe nanocomposite samples. FORC diagrams of nanocomposites with 56 vol.% α-Fe annealed at two different temperatures (773 K, 823 K) are shown in Fig. 17.17. Only one peak was observed in the optimally annealed sample, indicating that the soft and hard phases are switching together. The observed distribution in switching fields is attributed to a distribution in the size of the constituent grains. The FORC diagram of the sample annealed at the higher temperature is characterised by two distinct coercivity distribution peaks. The peak centred around zero field is attributed to switching of the soft phase while the peak at higher field is attributed to switching of the hard phase. The decoupled switching can be explained by the fact that this sample has coarser α-Fe grains, which are not well exchange coupled with their neighbouring hard grains. The fact that the high field switching events are displaced below the H_c axis is attributed to magnetostatic interactions between the hard and soft grains [49]. This case study demonstrated the possibility to use chemical synthesis to fabricate hard-soft nanocomposites with coherent interfaces and has showcased the use of FORC analysis to study exchange coupling between the hard and soft phases in such samples.

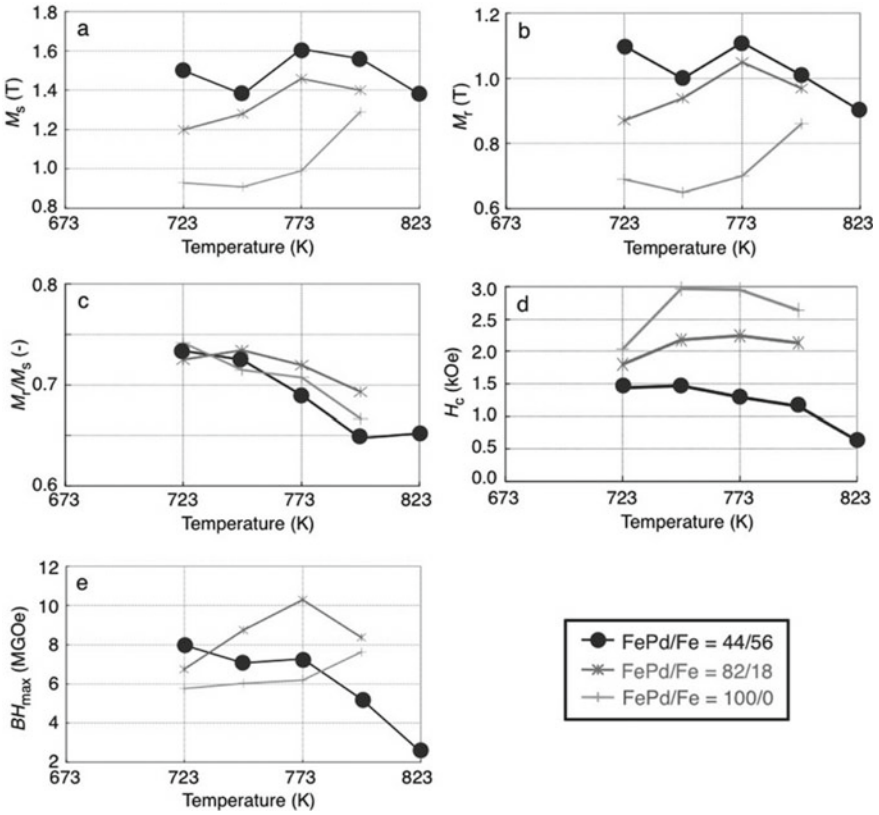

Fig. 17.16 Annealing temperature dependency of the magnetic properties of FePd/Fe nanocomposites with various hard/soft phase volume fractions: **a** saturation magnetisation, M_s, **b** remanent magnetisation, M_r, **c** M_r/M_s ratio, **d** coercivity, Hc, and **e** maximum energy product, BH_{max} [49]

17.2.3 Case Study #3—$SmCo_5$/α-Fe Nanocomposites

While the first two case studies concerned composites with Pt or Pd-based hard magnetic phases, our last case study involves a rare earth high anisotropy phase, namely $SmCo_5$ [57]. The preparation of rare earth-based phases by chemical routes rather than classical metallurgical routes is challenging because of the high affinity of rare earths for oxygen. Nevertheless, $SmCo_5$ nanocrystals displaying hard magnetic properties were produced by a combination of solution phase chemistry, to form core/shell Co/Sm_2O_3 nanoparticles, followed by solid-solution high-temperature reduction in the presence of metallic calcium [58]. A direct one-step chemical synthesis method involving the reduction of metallic salts in a liquid polyol medium was then developed to fabricate air-stable coercive Sm–Co nanoparticles of controlled size, shape and chemical composition [59]. The main challenge in producing hard-soft nanocomposites by chemical methods is to prevent growth in the size of the soft

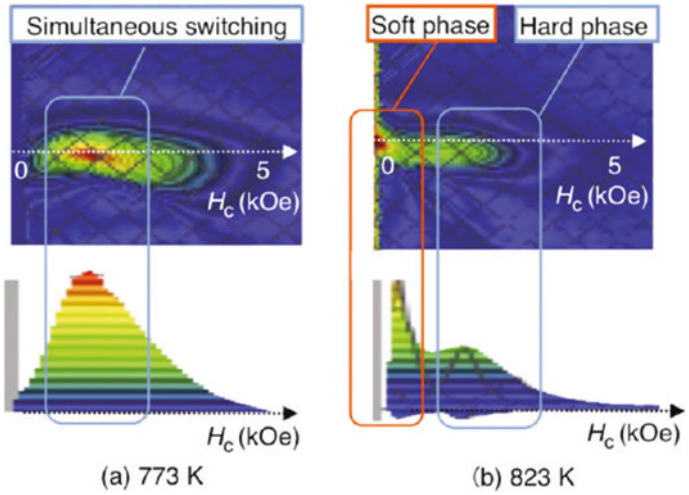

Fig. 17.17 FORC diagrams of FePd/Fe (44/56 vol.%) nanocomposites formed by annealing at **a** 773 and **b** 823 K [49]

phase grains during the harsh reductive annealing step needed to form $SmCo_5$. A combined solution phase chemistry and calciothermic reduction approach, in which Fe nanoparticles are temporarily coated to stabilize their size, has been successfully used to fabricate nanocomposites consisting of a high coercivity $SmCo_5$ matrix phase containing nanosized Fe inclusions [57]. Details of this case study will now be presented.

The complete synthesis route used to fabricate $SmCo_5$ – Fe nanocomposites is illustrated in Fig. 17.18. Fe nanoparticles of 12 nm in diameter were synthesised by decomposition of $Fe(CO)_5$ in the presence of oleyamine and hexadecylammonium chloride at 180 °C. The Fe nanoparticles were then coated in a 7-nm-thick layer of SiO_2 by controlled hydrolysis and condensation of tetraethyl orthosilicate (TEOS) in the presence of ammonia. TEM images of the as-prepared Fe nanoparticles and

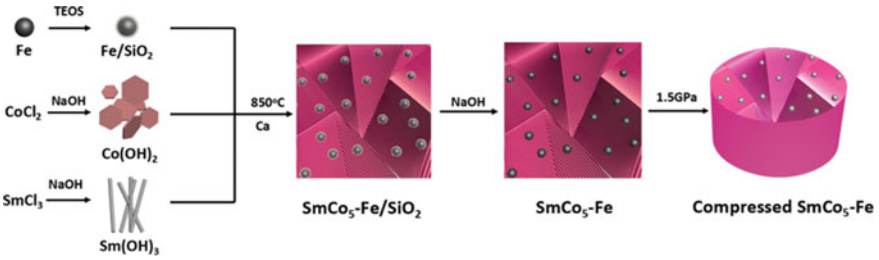

Fig. 17.18 Schematic illustration of the synthesis of $SmCo_5$ – Fe nanocomposites by assembling $Sm(OH)_3$ nanorods, $Co(OH)_2$ nanoplates, and Fe/SiO_2 nanoparticles, followed by reductive annealing, NaOH solution washing and compaction [57]

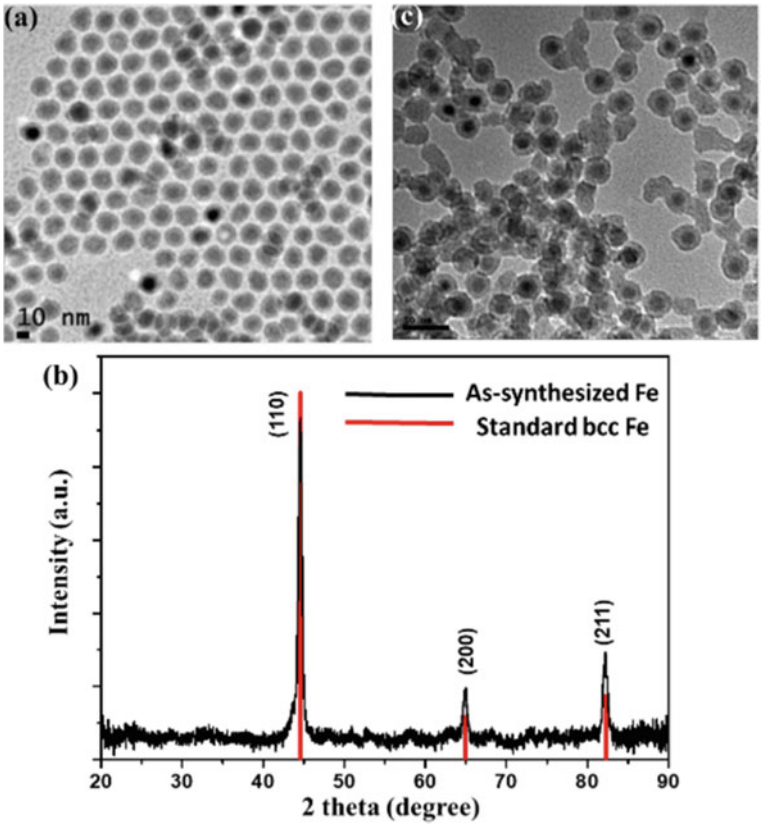

Fig. 17.19 TEM images of 12 nm Fe nanoparticles as-prepared (**a**) and coated with 7 nm of SiO_2 (**c**), XRD pattern of the as-prepared Fe nanoparticles (**b**) [57]

SiO_2 coated Fe nanoparticles are shown in Fig. 17.19a, c while an XRD pattern of the former is shown in Fig. 17.19b.

Rod-shaped $Sm(OH)_3$ and platelet-shaped $Co(OH)_2$ nanoparticles (Fig. 17.20a, b) were fabricated by adding drops of NaOH to aqueous solutions of $SmCl_3$ or $CoCl_2$ at 100 °C and refluxing the reaction mixture. Reduction of a mixture of $Sm(OH)_3$ and $Co(OH)_2$ nanoparticles with a specific molar ratio, by heating at 850°C under Ar and in the presence of calcium, leads to the formation of $SmCo_5$. An XRD diffraction pattern and hysteresis loop of thus formed nanocrystalline $SmCo_5$ are shown in Fig. 17.20c, d. To form $SmCo_5 - Fe$ nanocomposites, firstly $Sm(OH)_3$ and $Co(OH)_2$ nanoparticles were mixed together with the SiO_2 coated Fe nanoparticles by sonication in ethanol. The ethanol was removed and the dry powder that remained was ground together with calcium under argon, and then annealed at 850 °C. This high-temperature annealing step led to calciothermic reduction of the hydroxides and formation of $SmCo_5$. The powder was cooled to room temperature, washed in distilled water under Ar to remove CaO and subsequently sonicated in NaOH at

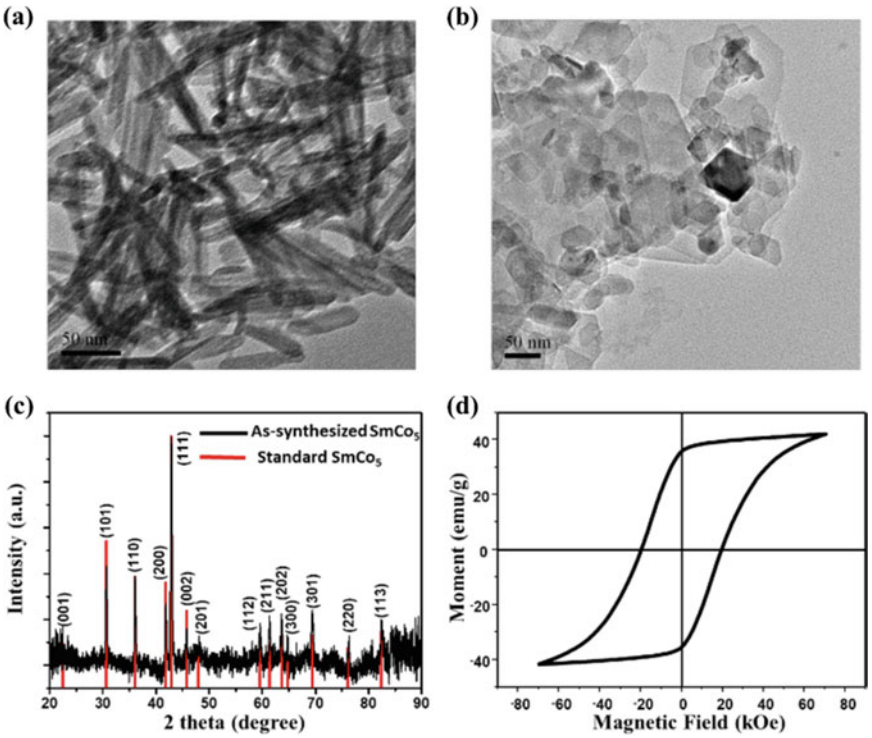

Fig. 17.20 TEM image of $Sm(OH)_3$ nanorods (**a**) and $Co(OH)_2$ nanoplates (**b**). XRD pattern of $SmCo_5$ powder produced by calciothermic co-reduction of these hydroxide nanoparticles, compared to the peak positions (red lines) expected for hexagonal $SmCo_5$ (JPCDS No. 65-8981) (**c**); Room temperature hysteresis loop of the $SmCo_5$ powder (**d**) [57]

60 °C to remove the SiO_2 coating from the Fe nanoparticles, and finally washed under water and ethanol and then vacuum dried. The ratio of $SmCo_5$ to Fe in the resultant $SmCo_5$ - Fe nanocomposites was controlled by varying the relative amount of SiO_2-coated Fe nanoparticles added to the mixture of $Sm(OH)_3$ and $Co(OH)_2$ nanoparticles. XRD patterns of samples with Fe content in the range 5–20 wt% are compared with that of a pure $SmCo_5$ sample in Fig. 17.21a, confirming that all the nanocomposites prepared consisted of hexagonal $SmCo_5$ and bcc α-Fe. High angle annular dark field scanning TEM (HAADF-STEM) imaging together with elemental mapping (Fig. 17.21b, c) showed that the composites consist of Fe inclusions of size 12–13 nm in a $SmCo_5$ matrix, validating the temporary use of a SiO_2 coating to prevent coalescence of Fe nanoparticles or inter-diffusion with SmCo nanoparticles during the high-temperature annealing process.

Hysteresis loops of $SmCo_5$ - Fe nanocomposites with Fe content in the range 5–20 wt% are compared with that of a pure $SmCo_5$ sample in Fig. 17.22a. The remanent and saturation magnetisation values increase with Fe content, while the coercivity

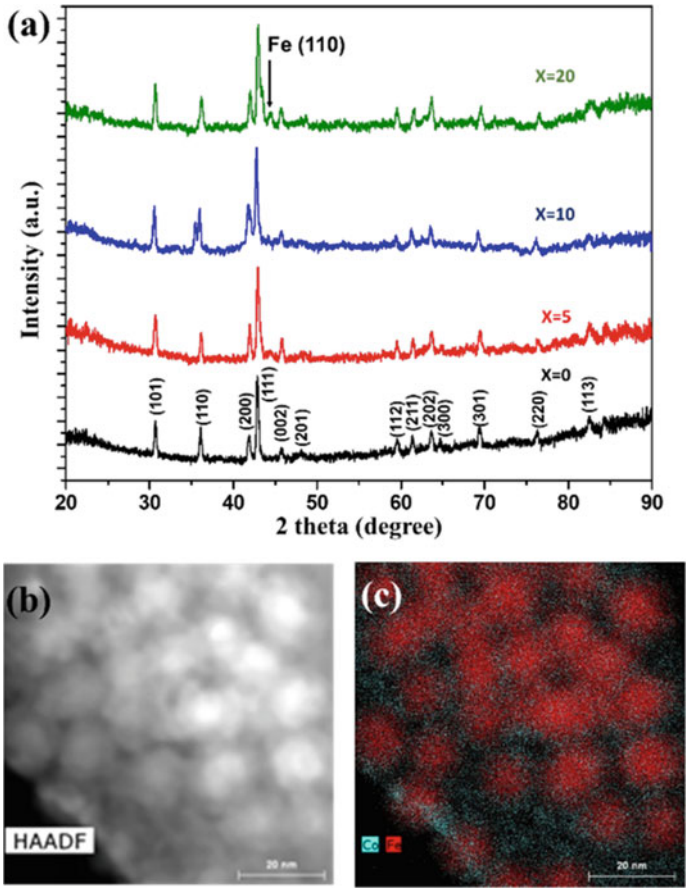

Fig. 17.21 **a** XRD patterns of $SmCo_5 - Fe$ (x wt%) composite with $x = 0, 5, 10$, and 20. **b** HAADF-STEM image and **c** elemental mapping of the $SmCo_5 - Fe$ (10 wt%) nanocomposite (the overall Fe content is 10 wt%, but the image shows an area enriched with Fe inclusions) [57]

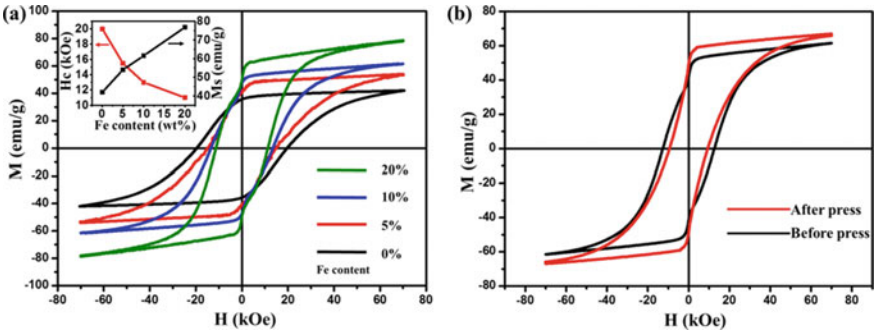

Fig. 17.22 **a** Magnetisation curves of $SmCo_5 - Fe$ (x wt%) composite with $x = 0, 5, 10$, and 20. **b**. Magnetisation curve of $SmCo_5 - Fe$ (10 wt%) before and after compaction at 300 K [57]

decreases, all in a monotonic fashion. All the nanocomposites showed apparent two-phase magnetic behaviour, despite the fact that the Fe inclusions should be small enough to be fully exchange coupled to the hard magnetic matrix. The authors suspected that the low field kink may be due to rotation of loosely packed Fe inclusions, and thus, they pressed the nanocomposites at room temperature under 1.5 GPa. This compaction step did indeed lead to an increase in the saturation magnetisation and suppression of the low field kink (Fig. 17.22b), which is indicative of exchange coupling between the soft inclusions and the hard matrix.

This case study has demonstrated the possibility to use chemical synthesis to fabricate hard-soft nanocomposites in which a high magnetisation phase (α-Fe) is stabilised within a hard matrix based on a RE-TM high anisotropy phase ($SmCo_5$). The soft-in-hard structure favours maximisation of coercivity while the temporary use of a SiO_2 shell to limit growth of Fe nanoparticles may facilitate the future use of novel consolidation methods being studied to densify and texture magnetic nanocomposites.

17.3 Challenges and Future Prospects for Hard-Soft Nanocomposites

17.3.1 Outline of the Challenges Faced in Producing Hard-Soft Nanocomposites

Key challenges facing the development of hard-soft nanocomposite magnets using chemically synthesised nanoparticles are identified in Fig. 17.23. The two most urgent challenges concern compaction to full density and alignment of the easy axes of the hard magnetic grains, both of which impact directly on the remanence and thus maximum energy product achievable. Both of these objectives are particularly challenging with nanoparticles. The coercivity values presently achieved in chemically synthesised hard magnetic nanoparticles are far below the theoretical upper limit given by the magnetocrystalline anisotropy of the hard magnetic phase. The coercivities reported for nanocomposites made using these hard magnetic nanoparticles are further reduced. Increasing the coercivities of the hard magnetic precursors and the final nanocomposites will increase the maximum energy product attainable and will increase the upper temperature limit for application of the nanocomposite magnets. Understanding magnetisation reversal in hard nanoparticles and hard/soft nanocomposites, with the aim to increase coercivity, will require advanced structural (e.g. high resolution TEM, atom probe) and magnetic characterisation (see below) and should be complemented with theoretical studies (e.g. micromagnetics).

The density, degree of alignment and coercivity values achieved in nanocomposite magnets are all influenced by the compaction process used, through its impact on the final nanostructure. A critical point here is to avoid grain growth which would lead to decoupling of the hard and soft phases. Thus, high-temperature sintering, now used to

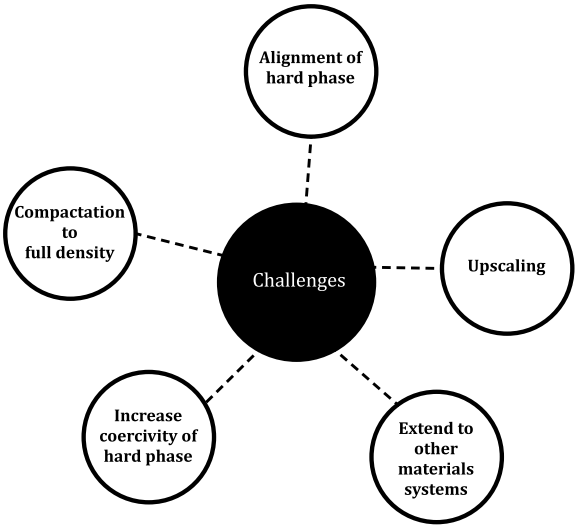

Fig. 17.23 Key challenges facing the development of hard-soft nanocomposite magnets using chemically synthesised nanoparticles

fabricate fully dense magnets by metallurgical routes, cannot be applied. Alternative novel techniques for the compaction of nanocomposites will be discussed in more detail below.

Upscaling the chemical synthesis of the nanoparticle precursors used as building blocks to fabricate hard-soft nanocomposites is expected to impact on the structural and magnetic properties of the nanoparticles. No doubt the processing conditions will need to be re-optimised with respect to small-scale fabrication. Recycling of precursors, solvents, reducing agents and other ingredients should be pursued to limit the cost and potential environmental impact of large-scale chemical synthesis of nanocomposite magnets.

Nd–Fe–B-based magnets have the highest room temperature maximum energy product among all known magnets, thanks to a combination of high saturation magnetisation and high magnetocrystalline anisotropy of the principle $Nd_2Fe_{14}B$ phase. What is more, the temperature range of application of such magnets can be increased up to 200 °C through partial substitution of Nd with heavy rare earths (Dy, Tb), which leads to an increase in the magnetocrystalline anisotropy of the main phase [2]. Thus, the successful application of the chemical synthesis route to the fabrication of nanocomposite magnets combining textured $Nd_2Fe_{14}B$-based nanograins with a high volume content of high magnetisation α-Fe or FeCo nanograins could lead to magnets with significantly enhanced energy products compared to today's best magnets. Surface modification of $Nd_2Fe_{14}B$ nanoparticles with heavy rare earths could lead to coercivity enhancement with a minimum use of strategic heavy rare earths, reminiscent of today's grain boundary diffusion processed magnets [60]. However, the chemical synthesis of RE-TM compounds is challenging because of the large difference in the reduction potential of transition metal and rare earth elements, and ternary $Nd_2Fe_{14}B$ is more challenging to prepare than binary Sm–Co phases.

Sol-gel synthesis followed by high-temperature reduction-diffusion was reported to lead to the formation of a mixture of $Nd_2Fe_{14}B$, Nd_2Fe_{17} and α-Fe [61]. However, further development is needed to produce pure $Nd_2Fe_{14}B$ nanoparticles of controllable size with high remanent magnetisation and coercivity values. The chemical synthesis of nanocomposites based on RE-lean (e.g. $SmFe_{11-1}Ti$) or RE-free (MnBi, FeNi, $Fe_{16}N_2$) phases having even mid-range magnetic properties is also very attractive. Their successful fabrication would free up Nd now used in bonded NdFeB-based magnets, allowing it to be reserved for where it is really needed, in very high energy product magnets [62].

17.3.2 Compaction of Hard-Soft Nanocomposites

A number of novel compaction routes exploiting either low temperatures (down to room temperature), short duration (down to microseconds) or high pressure (up to tens of GPa) have been used for the consolidation of bulk nanostructured permanent magnets, in most cases working with powders produced by melt spinning or high energy ball milling [21]. Careful control of the processing parameters resulted in a restraint of grain growth and in some cases actual grain refinement. Two such techniques, namely spark plasma sintering (SPS) and high-pressure warm compaction (HPWC), have been used for the consolidation of chemically synthesised nanocomposites. Spark plasma sintering was carried out on a mixture of fcc FePt and Fe_3O_4 nanoparticles under a pressure of 100 MPa, for a duration of 600 s and in the temperature range 400–600 °C [63]. Chemical ordering of the FePt nanoparticles to form $L1_0$ started at 500°C and was almost complete at 600°C. The average grain size of FePt, as estimated from XRD analysis, increased from about 7 nm in samples consolidated at 400°C to 17 nm in those consolidated at 600 °C. Fe_2O_3 remained in the samples consolidated at 400 and 500 °C but it was suppressed in the sample consolidated at 600 °C (Fig. 17.24). The latter sample contained 13 vol.% Fe_3Pt, formed by diffusion between thermally reduced Fe_2O_3 and neighbouring FePt grains. The maximum density measured in these FePt/Fe_3Pt hard/soft nanocomposite was 70% of theoretical full density. It remains to be seen if SPS can be used to consolidate to full density and with a higher soft phase volume content. High-pressure warm compaction was also used to produce FePt/Fe_3Pt by consolidation of a mixture of fcc FePt and Fe_3O_4 nanoparticles [64]. In this case, consolidation at 600 °C under a pressure of 3.8 GPa led to about 95% of the theoretical full density of an FePt/Fe_3Pt composite with 15% volume content of soft phase. The achievement of higher density with HPWC compared to SPS is attributed to significant plastic deformation of the nanoparticles under the much higher pressure used in HPWC. Lessons learned from the compaction of nanocrystalline powders produced by melt spinning or high energy ball milling using a range of consolidation techniques (SPS, HPWC, shock wave compaction, microwave compaction) [21] can guide the application of such techniques to the fabrication of fully dense chemically synthesised nanocomposites.

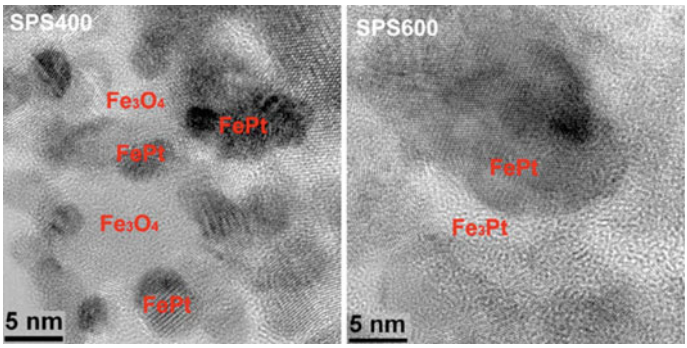

Fig. 17.24 TEM images of mixtures of chemically synthesised fcc FePt and Fe_3O_4 nanoparticles spark plasma sintered under a pressure of 100 MPa, for a duration of 600 s at 400°C (SPS400) and 600 °C (SPS600) [63]

17.3.3 Alignment of Hard-Soft Nanocomposites

Shortly after the discovery of the excellent hard magnetic properties of $Nd_2Fe_{14}B$, it was shown that die-upset hot deformation of fully dense compacts of nanocrystalline NdFeB leads to anisotropic grain shape and c-axis alignment along the deformation direction, with the c-axis of each grain being the short axis [65]. The degree of alignment was subsequently shown to depend on the deformation temperature, degree of deformation and deformation rate. Hot deformation was also applied to Sm–Co magnets and it was shown that the degree of texture achieved depended on the composition and crystal structure, with practically no alignment for ordered Sm_2Co_{17}, and successively greater alignment for disordered $SmCo_7$, $SmCo_5$ and Sm_2Co_7 [66]. The presence of a Nd-rich intergranular phase was reported to be important for the inducement of texture in NdFeB samples while strong texture was reported in $SmCo_5$ samples having no Sm-rich phase. It was also shown that under fixed hot deformation conditions, it is easier to induce texture in $PrCo_5$ than in $SmCo_5$. The actual mechanism responsible for inducing texture during hot deformation in these nanocrystalline materials has not been clearly identified, though it has been suggested that grain boundary mediated plasticity may play a role [21].

Some degree of texture inducement has been reported for consolidated hard-soft nanocomposites made from melt spun or ball milled precursors. Heating of a Nd-lean amorphous NdFeB precursor under high pressure (6 GPa) led to the crystallisation of aligned $Nd_2Fe_{14}B$ grains together with α-Fe grains [67]. Partial c-axis alignment of $Nd_2Fe_{14}B$ was achieved in $Nd_2Fe_{14}B$/α-Fe nanocomposites compacted by SPS. Hot deformation of $Nd_2Fe_{14}B$/α-Fe nanocomposites led to strong c-axis alignment of the $Nd_2Fe_{14}B$ grains for a low (2%) volume content of α-Fe, but increasing the volume content of the soft phase to just 5% led to a significant reduction in alignment of the hard phase [68]. However, hot deformation of an amorphous precursor led to *c*-axis alignment of $Nd_2Fe_{14}B$ grains in a $Nd_2Fe_{14}B$/α-Fe nanocomposite with 25 vol.% soft phase. Texture inducement is attributed to preferential nucleation and growth of

$Nd_2Fe_{14}B$ crystals in the highly stressed amorphous matrix. As with single-phase materials, more detailed studies are required to elucidate the texture inducing mechanism in nanocomposites during high-pressure compaction and hot deformation, and the applicability of such routes to inducing texture in chemically synthesised precursors needs to be assessed. Magnetic field alignment was used to induce texture in $SmCo_5$/α-Fe nanocomposites compacted by SPS [69]. In this case, alignment can be explained by the strong out-of-plane (001) texture of the starting $SmCo_5$ nanoflakes.

17.3.4 Advanced Magnetic Characterisation of Hard-Soft Nanocomposites

Measurement of the major hysteresis loop of a magnet gives information about its extrinsic magnetic properties (remanence, coercivity). In the case of hard-soft nanocomposite magnets, exchange coupled systems are characterised by single-phase hysteresis loops, while exchange decoupled systems are characterised by two-phase hysteresis loops [4]. It is worth noting that dipolar interactions have been shown to mask the presence of anisotropic soft phase inclusions in a hard magnetic matrix [70]. Information about switching field distributions and magnetic interactions between soft and hard phase components can be accessed by tracing minor loops, such as in first-order reversal curve (FORC) analysis mentioned above, and in recoil loop analysis. In the latter case, a sample previously saturated in positive field is exposed to a negative field of a certain value; the field is reduced to zero, and then brought back to the negative field value. The thus traced recoil loop is characterised by its slope and it may be "open" or hysteretic, meaning the ascendant and descendant curves do not coincide. Successive recoil loops can be measured by applying progressively stronger reversed fields. Irreversible magnetisation reversal in single-phase hard magnets leads to closed recoil loops characterised by low susceptibility while reversible magnetisation reversal in the soft phase of hard-soft nanocomposite magnets gives rise to high susceptibility recoil loops [4]. Hysteresis in the recoils loops of hard-soft nanocomposite magnets has been attributed to a breakdown in exchange coupling between the soft and hard phase, but mean field modelling indicates that distributions in coercivity values and the relative volume fraction of the two phases can also contribute to recoil loop hysteresis [71]. Recoil loop analysis has been applied to hard-soft nanocomposites made by bulk metallurgical synthesis [72, 73], and physical vapour deposition [8, 27, 74], and its application to hard-soft nanocomposites made by chemical synthesis should help shed light on magnetisation reversal processes in these materials, and thus serve to guide the enhancement of their magnetic performance through improved processing. What is more, micromagnetic modelling could be used as a support tool in FORC [54] and recoil curve analysis [8, 74] of chemically synthesised hard-soft nanocomposites.

Element selective magnetic measurement techniques allow studying magnetisation reversal in hard and soft phases independently. X-ray magnetic circular dichroism

(XMCD) spectroscopy is one such technique [75]. XMCD was used to measure reversal of the hard phase in hard/soft NdFeB and PrFeB-based ribbons, and comparison with global magnetisation reversal curves measured by classical magnetometry was used to extract soft phase reversal [76]. A spectacular illustration of full element selective reversal was reported for hard/soft $DyFe_2/YFe_2$ heterostructures [77, 78]. XMCD was also used to study interphase exchange coupling in hard/soft Sm–Co/Fe bilayers with a gradient in the thickness of the Fe layer [79]. XMCD can be performed with soft (low energy) or hard (high energy) x-rays, the low probing depth of soft x-rays limits it to surface studies while XMCD with hard x-rays can be used to probe bulk properties. Hard X-ray MCD under high magnetic fields and at variable temperature [80] holds great potential for the advanced magnetic characterisation of hard-soft magnetic nanocomposites.

17.4 Conclusions

Despite much effort and some progress, the promise of the hard-soft nanocomposite concept to produce ultra-strong magnets has not been realised to date. Initial efforts were based on bulk metallurgical synthesis and physical vapour deposition. More recently, much effort has gone into exploiting the unique advantages offered by chemical synthesis, to prepare hard-soft nanocomposites with controlled size and composition of the constituent phases. So far, the approach has been successfully applied to the fabrication of hard-soft composites with FePt (Pd) and SmCo-based hard phases. Further enhancement of the energy product achieved requires compaction to full density, alignment of the hard phase and increased coercivity, if such magnets are to match or go beyond today's high-performance NdFeB magnets. Extension of the approach to form nanocomposite magnets with mid-range energy products, based on a range of rare earth free hard magnetic materials, could free up rare earths presently used in bonded magnets, for use in high energy product magnets. Chemically synthesised hard-soft nanocomposite powders could also be used to make micro/nanosized magnets, using emerging fabrication techniques such as micromagnetic imprinting [81] and 3D-printing [82], for applications in bio-medicine, microrobotics and micro/nanosystems.

Acknowledgements The authors acknowledge funding from the French National Research Agency (project N° ANR-16-CE09-0019-01).

References

1. O. Gutfleisch, M.A. Willard, E. Brück, C.H. Chen, S.G. Sankar, J.P. Liu, Adv. Mater. **23**, 821–842 (2011)
2. J.M.D. Coey, *Magnetism and Magnetic Materials* (2010)

3. R. Coehoorn, D.B. De Mooij, C. de Waard, J. Magn. Magn. Mater. **80**, 101–104 (1989)
4. E.F. Kneller, R. Hawig, IEEE Trans. Magn. **27**, 3560–3588 (1991)
5. R. Skomski, J. Coey, Phys. Rev. B **48**, 15812–15816 (1993)
6. R. Skomski, P. Manchanda, I. Takeuchi, J. Cui, JOM **66**, 1144–1150 (2014)
7. S.D. Bader, Rev. Mod. Phys. **78**, 1–15 (2006)
8. W.B. Cui, H. Sepehri-Amin, Y.K. Takahashi, K. Hono, Acta Mater. **84**, 405–412 (2015)
9. N.M. Dempsey, in:, J.P. Liu, E. Fullerton, O. Gutfleisch, D.J. Sellmyer (Eds.), *Nanoscale Magnetic Materials and Applications*, 1st ed. (Springer, n.d.), pp. 661–684
10. A. Manaf, M. Al-Khafaji, P.Z. Zhang, H.A. Davies, R.A. Buckley, W.M. Rainforth, J. Magn. Magn. Mater. **128**, 307–312 (1993)
11. L. Withanawasam, G.C. Hadjipanayis, R.F. Krause, J. Appl. Phys. **75**, 6646–6648 (1994)
12. I. Panagiotopoulos, L. Withanawasam, A.S. Murthy, G.C. Hadjipanayis, E.W. Singleton, D.J. Sellmyer, J. Appl. Phys. **79**, 4827–4829 (1996)
13. J. Ding, Y. Liu, R. Street, P.G. McCormick, J. Appl. Phys. **75**, 1032–1035 (1994)
14. J. Bernardi, G.F. Soto, J. Fidler, S. David, D. Givord, J. Appl. Phys. **85**, 5905–5907 (1999)
15. J.M. Le Breton, R. Lardé, H. Chiron, V. Pop, D. Givord, O. Isnard, I. Chicinas, J. Phys. D Appl. Phys. **43**, 085001 (2010)
16. X.Y. Xiong, C.B. Rong, S. Rubanov, Y. Zhang, J.P. Liu, J. Magn. Magn. Mater. **323**, 2855–2858 (2011)
17. S. Mican, R. Hirian, O. Isnard, I. Chicinaş, V. Pop, Phys. Procedia **75**, 1314–1323 (2015)
18. Y. Wang, Y. Li, C. Rong, J.P. Liu, Nanotechnology **18**, 465701 (2007)
19. N.G. Akdogan, G.C. Hadjipanayis, D.J. Sellmyer, Nanotechnology **21**, 295705 (2010)
20. N. Poudyal, V. Vuong Nguyen, C.-B. Rong, J.P. Liu, J. Phys. D: Appl. Phys. **44**, 335002 (2011)
21. M. Yue, X. Zhang, J.P. Liu, Nanoscale **9**, 3674–3697 (2017)
22. F.J. Cadieu, T.D. Cheung, L. Wickramasekara, J. Magn. Magn. Mater. **54–57**, 535–536 (1986)
23. B.A. Kapitanov, N.V. Kornilov, Y.L. Linetsky, V.Y. Tsvetkov, J. Magn. Magn. Mater. **127**, 289–297 (1993)
24. F.J. Cadieu, S.H. Aly, T.D. Cheung, R.G. Pirich, J. Appl. Phys. **53**, 2401–2403 (1982)
25. T. Shima, K. Takanashi, Y.K. Takahashi, K. Hono, Appl. Phys. Lett. **81**, 1050–1052 (2002)
26. S.M. Parhofer, J. Wecker, C. Kuhrt, G. Gieres, L. Schultz, IEEE Trans. Magn. **32**, 4437–4439 (1996)
27. M. Shindo, M. Ishizone, H. Kato, T. Miyazaki, A. Sakuma, J. Magn. Magn. Mater. **161**, L1–L5 (1996)
28. W.-B. Cui, Y.K. Takahashi, K. Hono, Adv. Mater. **24**, 6530–6535 (2012)
29. E.E. Fullerton, J.S. Jiang, C.H. Sowers, J.E. Pearson, S.D. Bader, Appl. Phys. Lett. **72**, 380 (1998)
30. S. Sawatzki, R. Heller, C. Mickel, M. Seifert, L. Schultz, V. Neu, J. Appl. Phys. **109**, 123922–123927 (2011)
31. J.P. Liu, C.P. Luo, Y. Liu, D.J. Sellmyer, Appl. Phys. Lett. **72**, 483 (1998)
32. B. Rellinghaus, S. Stappert, M. Acet, E.F. Wassermann, J. Magn. Magn. Mater. **266**, 142–154 (2003)
33. B. Balasubramanian, R. Skomski, X. Li, S.R. Valloppilly, J.E. Shield, G.C. Hadjipanayis, D.J. Sellmyer, Nano Lett. **11**, 1747–1752 (2011)
34. O. Akdogan, W. Li, B. Balasubramanian, D.J. Sellmyer, G.C. Hadjipanayis, Adv. Funct. Mater. **23**, 3262–3267 (2013)
35. B. Balamurugan, B. Das, V.R. Shah, R. Skomski, X.Z. Li, D.J. Sellmyer, Appl. Phys. Lett. **101**, 122407 (2012)
36. M.A. Willard, L.K. Kurihara, E.E. Carpenter, S. Calvin, V.G. Harris, Int. Mater. Rev. **49**, 125–170 (2004)
37. S.A. Majetich, *Nanostructured Materials*, 2nd ed. William Andrew (2007)
38. A. López-Ortega, M. Estrader, G. Salazar-Alvarez, A.G. Roca, J. Nogués, Phys. Rep. **553**, 1–32 (2015)
39. L. Wu, A. Mendoza-Garcia, Q. Li, S. Sun, Chem. Rev. 10473–10512 (2016)

40. M.A. Willard, L.K. Kurihara, E.E. Carpenter, S. Calvin, V.G. Harris, Int. Mater. Rev. **49**, 125–170 (2013)
41. S. Sun, C.B. Murray, D. Weller, L. Folks, A. Moser, Science **287**, 1989–1992 (2000)
42. F. Liu, Y. Hou, S. Gao, Chem. Soc. Rev. **43**, 8098–8113 (2014)
43. H. Zeng, J. Li, J.P. Liu, Z.L. Wang, S. Sun, Nature **420**, 395–398 (2002)
44. S. Sun, H. Zeng, J. Am. Chem. Soc. **124**, 8204–8205 (2002)
45. D. Weller, A. Moser, IEEE Trans. Magn. **35**, 4423–4439 (1999)
46. S. Sun, E.E. Fullerton, D. Weller, C.B. Murray, IEEE Trans. Magn. **37**, 1239–1243 (2001)
47. D. Babonneau, J. Briatico, F. Petroff, T. Cabioc'h, A. Naudon, J. Appl. Phys. **87**, 3432–3443 (2000)
48. N.M. Dempsey, L. Ranno, D. Givord, J. Gonzalo, R. Serna, G.T. Fei, A.K. Petford-Long, R.C. Doole, D.E. Hole, J. Appl. Phys. **90**, 6268–6274 (2001)
49. N. Sakuma, T. Ohshima, T. Shoji, Y. Suzuki, R. Sato, A. Wachi, A. Kato, Y. Kawai, A. Manabe, T. Teranishi, ACS Nano **5**, 2806–2814 (2011)
50. Y.Q. Wu, D.H. Ping, K. Hono, M. Hamano, A. Inoue, J. Appl. Phys. **87**, 8658–8665 (2000)
51. S.-W. Kim, J. Park, Y. Jang, Y. Chung, S. Hwang, T. Hyeon, Y.W. Kim, Nano Lett. **3**, 1289–1291 (2003)
52. T. Teranishi, A. Wachi, M. Kanehara, T. Shoji, N. Sakuma, M. Nakaya, J. Am. Chem. Soc. **130**, 4210–4211 (2008)
53. C.R. Pike, A.P. Roberts, K.L. Verosub, J. Appl. Phys. **85**, 6660–6667 (1999)
54. T. Schrefl, T. Shoji, M. Winklhofer, H. Oezelt, M. Yano, G. Zimanyi, J. Appl. Phys. **111**, 07A728–07A728–3 (2012)
55. J.E. Davies, O. Hellwig, E.E. Fullerton, J.S. Jiang, S.D. Bader, G.T. Zimányi, K. Liu, Appl. Phys. Lett. **86**, 262503–262504 (2005)
56. D. Roy, K.V. Sreenivasulu, P.S. Anil Kumar, Appl. Phys. Lett. **103**, 222406–6 (2013)
57. B. Shen, A. Mendoza-Garcia, S.E. Baker, S.K. McCall, C. Yu, L. Wu, S. Sun, Nano Lett. **17**, 5695–5698 (2017)
58. Y. Hou, Z. Xu, S. Peng, C. Rong, J.P. Liu, S. Sun, Adv. Mater. **19**, 3349–3352 (2007)
59. C.N. Chinnasamy, J.Y. Huang, L.H. Lewis, B. Latha, C. Vittoria, V.G. Harris, Appl. Phys. Lett. **93**, 032504–032505 (2008)
60. K. Hirota, H. Nakamura, T. Minowa, M. Honshima, IEEE Trans. Magn. **42**, 2909–2911 (2006)
61. P.K. Deheri, S. Shukla, R.V. Ramanujan, J. Solid State Chem. **186**, 224–230 (2012)
62. J.M.D. Coey, Scripta Mater. **67**, 524–529 (2012)
63. C.-B. Rong, V. Nandwana, N. Poudyal, J.P. Liu, T. Saito, Y. Wu, M.J. Kramer, J. Appl. Phys. **101**, 09K51–09K515 (2007)
64. C.-B. Rong, V. Nandwana, N. Poudyal, J.P. Liu, M.E. Kozlov, R.H. Baughman, Y. Ding, Z.L. Wang, J. Appl. Phys. **102**, 023908 (2007)
65. R.W. Lee, Appl. Phys. Lett. **46**, 790–791 (1985)
66. A.M. Gabay, M. Marinescu, J.F. Liu, G.C. Hadjipanayis, J. Magn. Magn. Mater. **321**, 3318–3323 (2009)
67. W. Wu, W. Li, H. Sun, H. Li, X. Li, B. Liu, X. Zhang, Nanotechnology **19**, 285603–285605 (2008)
68. M. Yue, P.L. Niu, Y.L. Li, D.T. Zhang, W.Q. Liu, J.X. Zhang, C.H. Chen, S. Liu, D. Lee, A. Higgins, J. Appl. Phys. **103**, 07E101–07E104 (2008)
69. D.W. Hu, M. Yue, J.H. Zuo, R. Pan, D.T. Zhang, W.Q. Liu, J.X. Zhang, Z.H. Guo, W. Li, J. Alloy. Compd. **538**, 173–176 (2012)
70. N.H. Hai, N.M. Dempsey, D. Givord, J. Magn. Magn. Mater. **262**, 353–360 (2003)
71. R. William McCallum, Journal of Magnetism and Magnetic Materials **299**, 472–479 (2006)
72. M. Emura, D.R. Cornejo, F.P. Missell, J. Appl. Phys. **87**, 1387–1394 (2000)
73. A. Bollero, O. Gutfleisch, K.H. Müller, L. Schultz, G. Drazic, J. Appl. Phys. **91**, 8154–8159 (2002)
74. Y. Choi, J.S. Jiang, J.E. Pearson, S.D. Bader, J.P. Liu, Appl. Phys. Lett. **91**, 022502–022504 (2007)

75. G. Schütz, W. Wagner, W. Wilhelm, P. Kienle, R. Zeller, R. Frahm, G. Materlik, Phys. Rev. Lett. **58**, 737–740 (1987)
76. S. David, K. Mackay, M. Bonfim, S. Pizzii, A. Fontaine, D. Givord, MRS Online Proc. Lib. Arch. **577**, 175 (1999)
77. K. Dumesnil, C. Dufour, P. Mangin, A. Rogalev, Phys.l Rev. B **65**, 1135–1136 (2002)
78. K. Dumesnil, C. Dufour, P. Mangin, A. Rogalev, F. Wilhelm, J. Phys. Condens. Matter **17**, L215–L222 (2005)
79. M.-H. Yu, J. Hattrick-Simpers, I. Takeuchi, J. Li, Z.L. Wang, J.P. Liu, S.E. Lofland, S. Tyagi, J.W. Freeland, D. Giubertoni, M. Bersani, M. Anderle, J. Appl. Phys. **98**, 063905–063908 (2005)
80. A. Rogalev, F. Wilhelm, Phys. Metals Metallogr. **116**, 1285–1336 (2015)
81. N.M. Dempsey, D. Le Roy, H. Marelli-Mathevon, G. Shaw, A. Dias, R.B.G. Kramer, L. Viet Cuong, M. Kustov, L.F. Zanini, C. Villard, K. Hasselbach, C. Tomba, F. Dumas-Bouchiat, Appl. Phys. Lett. **104**, 262401 (2014)
82. Y. Kim, H. Yuk, R. Zhao, S.A. Chester, X. Zhao, Nature **558**, 274–279 (2018)

Index

D. Peddis et al. (eds.), *New Trends in Nanoparticle Magnetism*,
Springer Series in Materials Science 308,
https://doi.org/10.1007/978-3-030-60473-8